



UNIVERSITEIT VAN PRETORIA  
UNIVERSITY OF PRETORIA  
YUNIBESITHI YA PRETORIA

Denkleiers • Leading Minds • Dikgopolo tša Dihlalefi

# The Simultaneous Optimization of the Nose and Tail Geometry of a High-Speed Train for Drag and Crosswind Stability

---

By: A. Beneke

Submitted in partial fulfilment of the requirements for the degree:  
Master of Engineering

Department of Mechanical and Aeronautical Engineering  
University of Pretoria

Year: 2018

Supervisor: Prof K. J. Craig

## Abstract

The South African Government requires that a high-speed rail network is available to commuters by the year 2050. One of the key role players in achieving the aforementioned is Transnet Engineering (TE), which at present has neither experience in the field of high speed rail, nor a prototype train that would perform well aerodynamically travelling at speeds of approximately 350km/h. As such the final deliverable of this study was a nose and tail geometry for a train travelling at 350km/h, which had been optimized for total drag under windless conditions and drag as well as crosswind stability when subjected to crosswinds. In this study attention was thus given to the flow surrounding high-speed trains so as to address the knowledge deficit within TE, as well as the challenges typically faced in high speed rail applications with the purpose of ensuring the validity of the optimization goals set out by TE. This study furthermore identified appropriate geometric variables from literature which are important for an efficient aerodynamic nose and tail shape, i.e., the nose length (L), nose-tip height ( $Z_0$ ) and the inflection point height (H). Another objective was to identify an appropriate turbulence model that was able to accurately analyze the flow surrounding the train body, with attention also being given to the choice of a suitable optimization algorithm. The validation case completed on the Ahmed's body not only revealed an appropriate grid resolution to use for the optimization study on the train geometry, but further showed the aptness of the linear pressure-strain Reynold's stress turbulence model and the SHERPA optimization algorithm. For the optimization of the nose and tail geometry under windless conditions, the design space was sampled by making use of a 5-level full factorial, while the radial basis function with thin spline method was used to connect the data points obtained from simulation. The surrogate model was found to be highly predictive with the largest discrepancy between its results and simulation values being -1.6%. The SHERPA algorithm was used for the optimization study itself and identified an optimal geometry with  $L=7.7\text{m}$ ,  $H=2.73\text{m}$  and  $Z_0=1.364\text{m}$ . The associated minimized total drag force is 13.6kN which is 30.4% less than the maximum drag force that can be actualized by the geometric parameters within their respective ranges. In the case of a train subjected to crosswinds, the Latin Hypercube sampling method along with 27 designs points was made use of in order to sample the design space. The surrogate model was obtained by making use of the same fitting method as above and was once again found to be predictive with the greatest discrepancy reported being 1.6%. The same search algorithm as above was also used in order to identify the Pareto front, with the recommended geometry displaying the following features;  $L=7.7\text{m}$ ,  $H=2.71\text{m}$  and  $Z_0=1.364\text{m}$ . This yielded a minimum drag force of 14.6kN and rolling moment of 93.5kN, which corresponds to a reduction of 23.5% and 12.6%, respectively, from the maximum values that can be actualized by the geometric parameters within their respective ranges. Finally, it was found that either of the aforementioned optimized geometries is able to perform well when exposed to the other's load case.

# Table of Contents

Abstract .....	i
List of Figures .....	vi
List of Tables .....	xiii
Nomenclature .....	xvii
Abbreviations .....	xix
Rail Definitions .....	xx
1. Introduction .....	1
1.1. Background .....	1
1.2. Previous Work Completed on Nose Optimization .....	2
1.3. Problem Statement .....	2
1.4. Objectives of the Study .....	3
1.5. Scope of Work .....	4
1.6. Overview of Dissertation .....	5
2. Literature Review .....	6
2.1. External Flow around High-Speed Trains .....	6
2.1.1. Windless Conditions .....	6
2.1.2. Cross-wind Conditions .....	18
2.2. Aerodynamic Challenges in Rail Applications .....	23
2.2.1. Aerodynamic Drag Force .....	23
2.2.2. Crosswind Stability .....	24
2.2.3. Other Challenges .....	30
2.3. Previous Work Completed on Nose Optimization .....	34
2.4. Influential Geometric Parameters .....	35
2.4.1. Nose .....	35
2.4.2. Rear .....	38
2.5. Numerical Approaches used to solve Aerodynamics .....	47
2.5.1. Turbulence Models .....	47
2.5.2. Numerical Optimization Algorithms .....	50
2.6. Summary of Literature Study .....	53
3. Validation of Computational Fluid Dynamics .....	55
3.1. Introduction .....	55

3.2.	Simulated Configuration and Flow Parameters .....	55
3.3.	Mesh Independence .....	56
3.3.1.	The Grid Convergence Index .....	56
3.3.2.	The Mesh Construction .....	57
3.3.3.	Results from the Numerical Analysis .....	60
3.4.	Turbulence Model Validation .....	61
3.4.1.	Results from Numerical Analysis .....	61
3.5.	Minimization of drag on Ahmed’s body .....	70
4.	Optimization of the High-Speed Train Nose and Tail for Windless Conditions .....	73
4.1.	Simulated Geometry .....	73
4.2.	Configuration of the Computational Model .....	76
4.3.	Grid Convergence Study .....	77
4.3.1.	Transposed Computational Domain .....	78
4.3.2.	Mesh Construction .....	79
4.3.3.	Results from the Numerical Analysis .....	83
4.4.	Validate Computational Domain .....	84
4.4.1.	Sensitivity Results and Discussion .....	84
4.4.2.	The Unpredictability of the Lift Force and Hypothesis as to the Cause .....	86
4.5.	Optimization of the Nose and Tail Geometry .....	91
4.5.1.	Discretization of the Design Space .....	91
4.5.2.	Simulation of the Design Points .....	91
4.5.3.	Response Surface Model .....	94
4.5.4.	Optimization Algorithm Results .....	111
5.	Optimization of the High-Speed Train Nose and Tail for Crosswind Conditions .....	130
5.1.	Configuration of the Computational Model .....	130
5.2.	Validation of Computational Domain .....	135
5.3.	Optimization .....	140
5.3.1.	Response Surface Model .....	141
5.3.2.	Optimization Results .....	155
6.	Summary, Conclusions and Recommendations .....	167
6.1.	Summary .....	167
6.2.	Conclusions .....	168

6.3. Recommendations .....	170
Bibliography .....	172
Appendix .....	180
Appendix A.....	180
Prism Layer Mesh Construction .....	180
Appendix B.....	182
Appendix C.....	184
Appendix D.....	192
i. Determine Adequate Blockage Ratio.....	192
ii. Determine Adequate Inlet Distance .....	195
iii. Determine Adequate Outlet Distance .....	198
iv. Blockage Ratio Validation .....	199
Appendix E .....	203
i. Variable Nose Length: Kriging Surrogate Model.....	203
ii. Variable Nose-Tip Height: RBF vs. Kriging.....	206
iii. Variable Inflection Point Height: RBF vs. Kriging .....	212
Appendix F .....	216
i. Determine Adequate Front Inlet Distance.....	216
ii. Determine Adequate Side Inlet Distance.....	218
iii. Determine Adequate Back Outlet Distance .....	221
iv. Determine Adequate Side Outlet Distance.....	223
Appendix G.....	226
i. x-Force acting on the Tail.....	226
ii. y-Force acting on the Tail.....	228
iii. z-Force acting on the Tail.....	230
Appendix H.....	232
Appendix I .....	236
i. Drag Forces .....	236
ii. Side Forces .....	238
iii. Lift Forces.....	240
Appendix J.....	242
i. Inlet Distance .....	242

ii. Outlet Distance ..... 245

## List of Figures

Figure 1: A comparison between the nose pressure pulses obtained from both full scale (FS) as well as model scale (MS) experiments for an ICE-2 train (Baker, et al., 2013).	7
Figure 2: Velocity measurements about the nose of a train (Velaro S-103) (Baker, et al., 2013).	7
Figure 3: Ensemble average velocities measured for the S-100 TGV (Baker, et al., 2013).	8
Figure 4: Ensemble average velocities measured for the S-252 locomotive and trailing coaches (Baker, et al., 2013).	8
Figure 5: Ensemble average velocities for the ICE-2 train (Sterling, et al., 2008).	9
Figure 6: The boundary-layer velocity profiles measured at 0.5m above the track for the ICE-1 (Sterling, et al., 2008).	10
Figure 7: On-board measurements of a train boundary layer by making use of a laser anemometer (RAPIDE, 2001).	10
Figure 8: The displacement thickness for the ICE-1 train measured at 0.5m above the track and 0.5m above a platform (Sterling, et al., 2008).	11
Figure 9: The Boundary layer form parameter for the ICE-1 train measured at 0.5m above the track and 0.5m above a platform (Sterling, et al., 2008).	12
Figure 10: The boundary layer turbulence intensity for the ICE-1 train measured at 0.5m above the track and 0.5m above a platform (Sterling, et al., 2008).	12
Figure 11: The boundary layer displacement thickness over the roof of a 1/76 <sup>th</sup> model scale HST (Brockie & Baker, 1990).	13
Figure 12: Ensemble average velocities for the Class 43 HST (Baker, 2014).	13
Figure 13: Boundary layer parameters shown along the roof of a 1/25 <sup>th</sup> scale ICE model, measured during moving model tests (Baker, et al., 2001).	14
Figure 14: The variation of the pressure coefficient beneath a Eurostar train (Quinn & Hayward, 2008).	15
Figure 15: Velocity traces at various distances from the tie upper surface measured beneath Korean high-speed train (Kwon & Park, 2006).	15
Figure 16: Vertical (left) and horizontal (right) velocity profiles beneath Korean high-speed train (Kwon & Park, 2006).	15
Figure 17: The pressure and slipstream velocity measurements made around a four car ICE-2 train model (Baker, 2014).	17
Figure 18: The velocity decay in the wake of the Velaro S103 (Baker, et al., 2013).	17
Figure 19: The velocity vector diagram for a train exposed to a crosswind (Baker, 2014).	18
Figure 20: Wind parameters relative to a moving train (Baker, 2010).	19
Figure 21: The effect of crosswinds on the ensemble averaged velocities of the Velaro S-103 (Baker, et al., 2013).	20
Figure 22: The complex vortex structures that form around an idealized train body ( (Mair & Stewart, 1985) and (Copley, 1987)).	20
Figure 23: Pressure distribution around a two car ICE model (Hemida, 2006) and (Wu, 2004).	22
Figure 24: The variation of the drag coefficient with yaw angle, for various container configurations in the case of container trains (Beagles & Fletcher, 2012).	24
Figure 25: A lateral cross-section of a single track, ballasted rail configuration that is used for simulation in wind tunnel tests (CEN, 2010), is shown here on the yz-plane as per the document configuration.	26
Figure 26: The side and lift coefficients for the ICE3, TGV duplex and ETR500 at varying yaw angle (CEN, 2010).	26
Figure 27: The parameterization of lee rail rolling moment coefficients for various types of trains (Baker, 2014).	28
Figure 28: The Chinese hat wind gust profile (CEN, 2010).	29

Figure 29: The crosswind characteristics obtained for a Class 1 vehicle by making use of the Chinese hat gust (CEN, 2010).....	29
Figure 30: The effect of smoothing the data obtained from multiple runs for the pressure coefficient distribution of the Class 390 train passing an overbridge (Baker, et al., 2012)..	30
Figure 31: The pressure coefficient distribution measured on trackside hoardings during the passage of different train types (Baker, et al., 2012) and (Baker, et al., 2012).	31
Figure 32: Peak-to-peak pressure coefficients measured on an ETR 500 caused by the passing of another ETR 500, with variable nose shape (Johnson & Dalley, 2002).	31
Figure 33: The Gust positions and magnitudes for representative train types from the AeroTRAIN experiments (Baker, et al., 2013).	32
Figure 34: The cumulative distribution of the probability of human instability when exposed to sharp edged gusts (Jordan, et al., 2008).	32
Figure 35: The change in the drag coefficient of a vehicle plotted against the height of the stagnation point of that vehicle (Buchheim, et al., 1981).	36
Figure 36: The variation of the drag force coefficient with the bonnet slope ( $\alpha$ ) and the rake angle of the windshield ( $\delta$ ) (Carr, 1968/9).	36
Figure 37: Influence of the rake angle ( $\gamma$ ) on the location of flow separation on the bonnet and the reattachment point on the windshield (Scibor-Rylski, 1984)	37
Figure 38: The influence of the rake angle ( $\varphi$ ) on the drag coefficient of the VW 200 research vehicle (Buchheim, et al., 1979).	37
Figure 39: The change in the drag coefficient as a function of the front end shape (Buchheim, 1983)	38
Figure 40: The influence of the step height on the drag coefficient of the notchback car (Hucho, et al., 1976).	39
Figure 41: Drag reduction plotted as a function of increasing the trunk height ( $z$ ) [ (Buchheim & Leie, 1982) & (Buchheim, et al., 1983)].	39
Figure 42: Drag reduction plotted as a function of increasing the trunk length ( $x$ ) (Buchheim & Leie, 1982) and (Buchheim, et al., 1983).	39
Figure 43: The influence of the underbody diffuser length ( $l_u$ ) and angle ( $\alpha$ ) on the drag coefficient of a vehicle (Buchheim, et al., 1981).	40
Figure 44: The influence of the underbody diffuser geometry on the drag and rear-axle lift (Potthoff, 1982).	40
Figure 45: The influence of boat-tailing on the drag coefficient (Mair, 1969).	41
Figure 46: The effect of boat-tailing when applied to a notchback vehicle (Hucho, et al., 1976).	41
Figure 47: Various rear end configurations a) Squareback; b) & c) Fastback; d) Notchback (Hucho, 1986).	42
Figure 48: The influence of the rear end slope angle ( $\varphi$ ) on the separation line, wake and drag coefficient (measured on the VW Golf I) (Janssen & Hucho, 1975).	42
Figure 49: The effect of the rear end slope angle ( $\varphi$ ) on the drag and lift coefficients of an axisymmetric body off the ground (Bearmann, 1979).	44
Figure 50: The pressure distribution plotted over the rear end slope surface, measured along section YY (Bearmann, 1979).	45
Figure 51: The influence of the slope angle ( $\gamma$ , where $\gamma = 90^\circ - \varphi$ ) on the drag and lift coefficient and flow pattern for a body in close ground proximity (Morel, 1978).	45
Figure 52: Pressure distribution plotted on the slope's surface with quasi-two-dimensional wake flow (I) and vortex formations at the C-pillars (II) (Morel, 1978).	45
Figure 53: Notchback configuration: a) Rear defined by multiple geometric parameters b) Two-dimensional step model (Hucho, 1986).	46
Figure 54: Drag reduction plotted as a function of the rear window slope ( $\gamma$ ) (Buchheim & Leie, 1982) and (Buchheim, et al., 1983).	47

Figure 55: Comparison of velocity profiles obtained by using various turbulence models for the NACA 4412 airfoil ( $\alpha=13.87^\circ$ , $Re=1.5 \times 10^6$ ) (Coles & Wadcock, 1979). .....	49
Figure 56: The side profile of the train nose, whose geometry is to be optimized. ....	54
Figure 57: A schematic of the geometry of the Ahmed's body (Hinterberger, et al., n.d.). ....	55
Figure 58: The base mesh constructed for the Ahmed's body shown at the symmetry plane of the model .....	59
Figure 59: The near-wake and far-wake mesh refinements specified for the base mesh, shown at the symmetry plane of the model.....	59
Figure 60: The total and partial drag components of the Ahmed's body plotted against various slant angles of the rear-end slope ( $\varphi$ ) (Ahmed, et al., 1984). ....	60
Figure 61: The total drag of the Ahmed's body as obtained from various turbulence models.....	64
Figure 62: The Partial Drag Component of the Nose of the Ahmed's body as obtained by various turbulence models plotted together with the experimental values of the same as obtained by (Ahmed, et al., 1984). ....	65
Figure 63: The Nose Partial Drag component of the Ahmed's body as obtained from various turbulence models. ...	66
Figure 64: The Partial Drag Component of the sides and feet of the Ahmed's body as obtained by various turbulence models plotted together with the experimental values of the same as obtained by (Ahmed, et al., 1984). ....	66
Figure 65: The "Sides and Feet" Partial Drag component of the Ahmed's body as obtained from various turbulence models. ....	67
Figure 66: The Partial Drag Component of the Slope of the Ahmed's body as obtained by various turbulence models plotted together with the experimental values of the same as obtained by (Ahmed, et al., 1984). ....	67
Figure 67: The Slope Partial Drag component of the Ahmed's body as obtained from various turbulence models. ....	68
Figure 68: The Partial Drag Component of the Back of the Ahmed's body as obtained by various turbulence models plotted together with the experimental values of the same as obtained by (Ahmed, et al., 1984). ....	68
Figure 69: The Back Partial Drag component of the Ahmed's body as obtained from various turbulence models. ....	69
Figure 70: The total drag of the Ahmed's body as obtained from numerical analyses plotted against the experimental results. ....	72
Figure 71: The geometry of the train nose and tail that was to be optimized.....	75
Figure 72: The computational domain, not drawn to scale, of the symmetry model of the train and the chosen nomenclature of the boundary faces.....	77
Figure 73: The initial computational domain, not drawn to scale, that was used for the grid convergence study and was obtained by transposing the computational domain of the Ahmed's body. ....	79
Figure 74: The high $y^+$ -mesh constructed for the train body shown here at refinement level two on the symmetry plane of the model.....	81
Figure 75: The near-wake and far-wake mesh refinements specified for the high $y^+$ -mesh constructed for the train body, shown here at refinement level two on the symmetry plane of the model. ....	82
Figure 76: The subdivision of the train showing the nose (green), coaches (blue) and tail (yellow), with the wind moving in the positive $x$ -direction.....	84
Figure 77: The subdivision of the train showing the top (blue) and bottom (green) halves of it. ....	84
Figure 78: The normalised $x$ -force [N] acting on the train for various domain inlet distances. ....	85
Figure 79: The normalised $z$ -force [N] acting on the train for various domain inlet distances .....	85
Figure 80: The final computational domain, not drawn to scale, that was used for the grid convergence study and was obtained by transposing the computational domain of the Ahmed's body. ....	86
Figure 81: Velocity magnitude profiles as a function of the vertical height off the ground ( $z$ -axis) beneath the train .....	89
Figure 82: Velocity magnitude profiles as a function of the vertical height off the ground ( $z$ -axis) above the train... ..	90
Figure 83: The external velocity field surrounding the train for the optimized nose geometry in windless conditions as seen from the side. ....	93

Figure 84: The variation of the total x-force (vertical axis) acting on the train as a function of nose-tip height ( $Z_0$ ) and inflection point height ( $H$ ) for a constant nose length of $L=2m$ , top and $L=3.425m$ , bottom. ....	96
Figure 85: The variation of the total x-force (vertical axis) acting on the train as a function of nose-tip height ( $Z_0$ ) and inflection point height ( $H$ ) for a constant nose length of $L=4.85m$ , top and $L=6.275m$ , bottom. ....	97
Figure 86: The variation of the total x-force (vertical axis) acting on the train as a function of nose-tip height ( $Z_0$ ) and inflection point height ( $H$ ) for a constant nose length of $L=7.7m$ .....	98
Figure 87: The notch-back (left), optimal (middle) and fast-back (right) configurations for the train nose geometry at a nose length ( $L$ ) of $7.7m$ , a nose-tip height ( $Z_0$ ) of $1.364m$ and inflection point heights ( $H$ ) of $2m$ (lower-bound), $2.73m$ and $3m$ (upper-bound) for the left, middle and right noses, respectively. ....	100
Figure 88: The tail (and thus nose) configurations at the maximum length of $7.7m$ that yield the minimum (left) and maximum (right) drag force on the tail .....	103
Figure 89: The various nose geometries shown at different nose lengths, i.e., $2m$ , $4.85m$ and $7.7m$ respectively. ...	104
Figure 90: The behaviour of the drag force [N] components for the portion of the train above the stagnation point (left) and below the stagnation point (right) as a function of the nose-tip ( $Z_0$ ) and the inflection point height ( $H$ ), for a constant nose length of $2m$ .....	105
Figure 91: The behaviour of the drag force [N] components for the portion of the train above the stagnation point (left) and below the stagnation point (right) as a function of the nose-tip ( $Z_0$ ) and the inflection point height ( $H$ ), for a constant nose length of $4.85m$ .....	106
Figure 92: The behaviour of the drag force [N] components for the portion of the train above the stagnation point (left) and below the stagnation point (right) as a function of the nose-tip ( $Z_0$ ) and the inflection point height ( $H$ ), for a constant nose length of $7.7m$ .....	107
Figure 93: The behaviour of the drag force [N] components for the train nose (top, left), coaches (top, right) and train tail (bottom, left) as a function of the nose-tip ( $Z_0$ ) and the inflection point height ( $H$ ), for a constant nose length of $2m$ .....	108
Figure 94: The behaviour of the drag force [N] components for the train nose (top, left), coaches (top, right) and train tail (bottom, left) as a function of the nose-tip ( $Z_0$ ) and the inflection point height ( $H$ ), for a constant nose length of $4.85m$ . ....	109
Figure 95: The behaviour of the drag force [N] components for the train nose (top, left), coaches (top, right) and train tail (bottom, left) as a function of the nose-tip ( $Z_0$ ) and the inflection point height ( $H$ ), for a constant nose length of two meters $7.7m$ .....	110
Figure 96: The correlation plot that was obtained by making use of the Radial Basis Function Metamodel which was explored by the SHERPA optimization algorithm.....	114
Figure 97: The raw data obtained from the optimization study that shows the relationship between the total x-force acting on the train and the inflection point height (top), nose length (middle) and nose-tip height (bottom). ....	115
Figure 98: The final geometry of the train nose that was optimized for drag .....	116
Figure 99: The distribution of the velocity field around the train is shown on the symmetry plane, and the pressure field acting on the train nose (left) and tail (right), is shown on the three dimensional body, for the optimized nose design. ....	121
Figure 100: The external velocity field surrounding the train for the optimized nose geometry in windless conditions as seen on the symmetry plane, from the side .....	122
Figure 101: The external velocity field surrounding the train for the optimized nose geometry in windless conditions as seen on the xy-plane, from the top. ....	123
Figure 102: The distribution of the Q-criterion around the train body which was fitted with an optimized nose and tail geometry. ....	124
Figure 103: The Q-Criterion of the flow surrounding the train is shown, along with the locations of the various planes on which the convolution integral of the velocity is indicated in Table 21.....	125

Figure 104: The velocity streamlines of the flow as indicated over the tail of the train on the symmetry plane. ....	127
Figure 105: The distribution of the wall shear stress as shown over the tail portion of the train body.....	128
Figure 106: The density distribution surrounding the optimized tail shape. ....	128
Figure 107: The external pressure field surrounding the train for the optimized nose geometry in windless conditions is shown. ....	129
Figure 108: The computational domain of the full model of the train under crosswind conditions showing the chosen nomenclature of the boundary faces.....	132
Figure 109: A magnified view of the three distinct ground regions and associated boundary conditions used for the simulation of the train under crosswind conditions.....	132
Figure 110: The velocity vector diagram for a train exposed to a crosswind (Baker, 2014). ....	133
Figure 111: Parameters of the wind relative to the ground (top, left) as well as the moving train (top, right and bottom, left).....	134
Figure 112: The geometry of the nose that was used throughout the process of validating the computational domain for crosswind conditions. ....	135
Figure 113: The Normalised y-force [N] acting on the Train as a whole as well as its sub-components given for the various locations of the front inlet face. ....	136
Figure 114: The Normalised z-force [N] acting on the Train as a whole as well as its sub-components given for the various locations of the front inlet face. ....	137
Figure 115: The computational domain of the full model of the train under crosswind conditions showing the chosen nomenclature of the domain dimensions. ....	139
Figure 116: The spread of design points generated by the Latin Hyper-Cube sampling method, shown here for the stagnation point height ( $Z_0$ ) plotted against the nose length (L).....	142
Figure 117: The spread of design points generated by the Latin Hyper-Cube sampling method, shown here for the inflection point height (H) plotted against the stagnation point height ( $Z_0$ ). ....	142
Figure 118: The spread of design points generated by the Latin Hyper-Cube sampling method, shown here for the inflection point height (H) plotted against the nose length (L). ....	143
Figure 119: The variation of the total x-force (vertical axis) acting on the train as a function of nose-tip height ( $Z_0$ ) and inflection point height (H), shown here for nose lengths of 2.171m, 4.930m and 7.688m. ....	145
Figure 120: The variation of the leaside rolling moment (vertical axis) acting on the leading locomotive as a function of nose-tip height ( $Z_0$ ) and inflection point height (H), shown here for nose lengths of 2.171m, 4.930m and 7.688m. ....	148
Figure 121: The static pressure (Pa) distribution over the surface area of the leading locomotive under crosswind conditions, shown here for two geometries. ....	149
Figure 122: The variation of the side-force (vertical axis) acting on the leading locomotive as a function of nose-tip height ( $Z_0$ ) and inflection point height (H), shown here for nose lengths of 2.171m, 4.930m and 7.688m.....	153
Figure 123: The variation of the lift-force (vertical axis) acting on the leading locomotive as a function of nose-tip height ( $Z_0$ ) and inflection point height (H), shown here for nose lengths of 2.171m, 4.930m and 7.688m.....	154
Figure 124: The relationship between the nose length (L) and the total drag force acting on the train. ....	159
Figure 125: The relationship between the nose-tip height ( $Z_0$ ) and the rolling moment acting on the leading vehicle about the leaside rail. ....	159
Figure 126: The Pareto front that was obtained from the multi-objective optimization process of minimizing both the total drag as well as the rolling moment acting on the leading vehicle about the leaside rail. ....	160
Figure 127: The coefficient of pressure plotted against degrees at $x/L = 0.125$ of the leading locomotive ....	161
Figure 128: The coefficient of pressure plotted against degrees at $x/L = 0.25$ of the leading locomotive ....	161
Figure 129: The coefficient of pressure plotted against degrees at $x/L = 0.375$ of the leading locomotive ....	162
Figure 130: The coefficient of pressure plotted against degrees at $x/L = 0.5$ of the leading locomotive ....	162

Figure 131: The coefficient of pressure plotted against degrees at $x/L = 0.75$ of the leading locomotive .....	163
Figure 132: The coefficient of pressure plotted against degrees at $x/L = 1$ of the leading locomotive .....	163
Figure 133: The velocity field surrounding the train geometry associated with point 'a' (see Table 35) on the Pareto front is shown. The velocity field is displayed about the train's symmetry plane, i.e., on the $xz$ -plane. ....	164
Figure 134: The velocity field surrounding the train geometry associated with point 'a' (see Table 35) on the Pareto front is shown. The velocity field is displayed from the top on a $xy$ -plane located at a vertical height of $z = 1\text{m}$ .....	165
Figure 135: The vortex structures surrounding the train with the nose geometry associated with point 'a' on the Pareto front are shown.....	166
Figure 136: The normalised x-force [N] acting on the train for various domain cross-sectional areas .....	194
Figure 137: The normalised y-force [N] acting on the train for various domain cross-sectional areas .....	194
Figure 138: The normalised z-force [N] acting on the train for various domain cross-sectional areas .....	195
Figure 139: The normalised x-force [N] acting on the train for various domain inlet distances.....	196
Figure 140: The normalised y-force [N] acting on the train for various domain inlet distances.....	197
Figure 141: The normalised z-force [N] acting on the train for various domain inlet distances.....	197
Figure 142: The normalised x-force [N] acting on the train for various domain outlet distances .....	200
Figure 143: The normalised y-force [N] acting on the train for various domain outlet distances .....	200
Figure 144: The normalised z-force [N] acting on the train for various domain outlet distances .....	201
Figure 145: The variation of the total x-force (vertical axis) acting on the train as a function of nose-tip height ( $Z_0$ ) and inflection point height ( $H$ ) for a constant nose length of $L=2\text{m}$ , left and $L=3.425\text{m}$ , right.....	203
Figure 146: The variation of the total x-force (vertical axis) acting on the train as a function of nose-tip height ( $Z_0$ ) and inflection point height ( $H$ ) for a constant nose length of $L=4.85\text{m}$ , left and $L=6.275\text{m}$ , right.....	204
Figure 147: The variation of the total x-force (vertical axis) acting on the train as a function of nose-tip height ( $Z_0$ ) and inflection point height ( $H$ ) for a constant nose length of $L=7.7\text{m}$ .....	205
Figure 148: The variation of the total x-force (vertical axis) acting on the train as a function of nose length ( $L$ ) and inflection point height ( $H$ ) for a constant nose-tip height ( $Z_0=0.7\text{m}$ ).....	207
Figure 149: The variation of the total x-force (vertical axis) acting on the train as a function of nose length ( $L$ ) and inflection point height ( $H$ ) for a constant nose-tip height ( $Z_0=0.9\text{m}$ ).....	208
Figure 150: The variation of the total x-force (vertical axis) acting on the train as a function of nose length ( $L$ ) and inflection point height ( $H$ ) for a constant nose-tip height ( $Z_0=1.1\text{m}$ ).....	209
Figure 151: The variation of the total x-force (vertical axis) acting on the train as a function of nose length ( $L$ ) and inflection point height ( $H$ ) for a constant nose-tip height ( $Z_0=1.3\text{m}$ ).....	210
Figure 152: The variation of the total x-force (vertical axis) acting on the train as a function of nose length ( $L$ ) and inflection point height ( $H$ ) for a constant nose-tip height ( $Z_0=1.5\text{m}$ ).....	211
Figure 153: The variation of the total x-force (vertical axis) acting on the train as a function of nose length ( $L$ ) and nose-tip height ( $Z_0$ ) for a constant inflection point height ( $H=2\text{m}$ ).....	213
Figure 154: The variation of the total x-force (vertical axis) acting on the train as a function of nose length ( $L$ ) and nose-tip height ( $Z_0$ ) for a constant inflection point height ( $H=2.5\text{m}$ ).....	214
Figure 155: The variation of the total x-force (vertical axis) acting on the train as a function of nose length ( $L$ ) and nose-tip height ( $Z_0$ ) for a constant inflection point height ( $H=3\text{m}$ ).....	215
Figure 156: The Normalised x-force [N] acting on the Train as a whole as well as its sub-components given for the various locations of the front inlet face. ....	217
Figure 157: The Normalised y-force [N] acting on the Train as a whole as well as its sub-components given for the various locations of the front inlet face. ....	218
Figure 158: The Normalised z-force [N] acting on the Train as a whole as well as its sub-components given for the various locations of the front inlet face. ....	218

Figure 159: The Normalised x-force [N] acting on the Train as a whole as well as its sub-components given for the various locations of the side inlet face.....	219
Figure 160: The Normalised y-force [N] acting on the Train as a whole as well as its sub-components given for the various locations of the side inlet face.....	220
Figure 161: The Normalised z-force [N] acting on the Train as a whole as well as its sub-components given for the various locations of the side inlet face.....	220
Figure 162: The Normalised x-force [N] acting on the Train as a whole as well as its sub-components given for the various locations of the back outlet face. ....	221
Figure 163: The Normalised y-force [N] acting on the Train as a whole as well as its sub-components given for the various locations of the back outlet face. ....	222
Figure 164: The Normalised z-force [N] acting on the Train as a whole as well as its sub-components given for the various locations of the back outlet face. ....	222
Figure 165: The Normalised x-force [N] acting on the Train as a whole as well as its sub-components given for the various locations of the side outlet face. ....	224
Figure 166: The Normalised y-force [N] acting on the Train as a whole as well as its sub-components given for the various locations of the side outlet face. ....	224
Figure 167: The Normalised z-force [N] acting on the Train as a whole as well as its sub-components given for the various locations of the side outlet face. ....	225
Figure 168: The variation of the x-force (vertical axis) acting on the tail as a function of nose-tip height ( $Z_0$ ) and inflection point height (H), shown here for nose lengths of 2.1713m, left and 4.92979m, right.....	226
Figure 169: The variation of the x-force (vertical axis) acting on the tail as a function of nose-tip height ( $Z_0$ ) and inflection point height (H), shown here for a nose length of 7.68828m. ....	227
Figure 170: The variation of the y-force (vertical axis) acting on the tail as a function of nose-tip height ( $Z_0$ ) and inflection point height (H), shown here for nose lengths of 2.1713m, left and 4.92979m, right.....	228
Figure 171: The variation of the y-force (vertical axis) acting on the tail as a function of nose-tip height ( $Z_0$ ) and inflection point height (H), shown here for a nose length of 7.68828m. ....	229
Figure 172: The variation of the z-force (vertical axis) acting on the tail as a function of nose-tip height ( $Z_0$ ) and inflection point height (H), shown here for nose lengths of 2.1713m, left and 4.92979m, right.....	230
Figure 173: The variation of the z-force (vertical axis) acting on the tail as a function of nose-tip height ( $Z_0$ ) and inflection point height (H), shown here for a nose length of 7.68828m. ....	231
Figure 174: The drag forces [N] acting on the train for the various mesh refinement levels of the Low $y^+$ -Mesh (see Table 44) and the High $y^+$ -Mesh (see Table 45).. ....	237
Figure 175: The side forces [N] acting on the train for the various mesh refinement levels of the Low $y^+$ -Mesh (see Table 44) and the High $y^+$ -Mesh (see Table 45).....	239
Figure 176: The lift forces [N] acting on the train for the various mesh refinement levels of the Low $y^+$ -Mesh (see Table 44) and the High $y^+$ -Mesh (see Table 45). ....	241
Figure 177: The normalised x-force [N] acting on the train for various domain inlet distances.....	243
Figure 178: The normalised y-force [N] acting on the train for various domain inlet distances.....	244
Figure 179: The normalised z-force [N] acting on the train for various domain inlet distances. ....	244
Figure 180: The normalised x-force [N] acting on the train for various domain outlet distances. ....	247
Figure 181: The normalised y-force [N] acting on the train for various domain outlet distances. ....	247
Figure 182: The normalised z-force [N] acting on the train for various domain outlet distances. ....	248

## List of Tables

Table 1: Ballast definition and illustration (Terram, n.d.) _____	xx
Table 2: Bogie definition and illustration (The Railway Technical Website, 2018) _____	xx
Table 3: Cowcatcher definition and illustration (Your Dictionary, n.d.) _____	xx
Table 4: Pantograph definition and illustration (Auckland Transport, 2014) _____	xx
Table 5: The grid generation specifications for the three mesh independent models of the Ahmed’s body. _____	58
Table 6: Results of the GCI method applied to three successive grid refinements, for various values of the inclination angle of the slope, i.e., 5°, 15°, 25° and 35°. _____	60
Table 7: The deviation percentage from the experimental values for total drag associated with each respective turbulence model. _____	65
Table 8: The parameters that describe the single-objective optimization of the slope of the Ahmed’s body for the total drag coefficient _____	70
Table 9: The results of the optimization studies as obtained by making use of the Linear Pressure-Strain as well as the $k-\omega$ SST turbulence models respectively and the deviation of said results from the experimental values. _____	71
Table 10: Significant geometric parameters that define the shape of the train nose and which could alter the flow that surrounds the train. _____	74
Table 11: Examples of nose geometries that can be generated by varying the parameters as shown in Figure 71. _____	75
Table 12: The boundary conditions used for the simulation of the airflow around the symmetry model of the train under windless conditions. _____	76
Table 13: The material properties of air at standard atmospheric pressure. _____	77
Table 14: Dimensions of the Initial Computational Domain. _____	78
Table 15: The cell count [millions] and corresponding base cell sizes of the high $y^+$ - and the low $y^+$ -meshes, for both the case of the transposed mesh as well as the coarsened mesh respectively. _____	80
Table 16: The final dimensions that were verified for the computational domain for the symmetry model of the train. _____	86
Table 17: The three variables that parameterize the nose geometry and their respective values for the five design levels considered for the design sweep. _____	91
Table 18: The Pearson correlation coefficients obtained for the various nose parameters and the total x-force working on the half-model of the train for an increasing number of evaluations. All results shown here were obtained from the surrogate model created by making use of the radial basis function. _____	111
Table 19: The Pearson correlation coefficients obtained for the various nose parameters and the total x-force working on the half-model of the train for an increasing number of evaluations. All results shown here were obtained from the surrogate model created by making use of the Kriging interpolation function. _____	112
Table 20: The drag force components that were predicted for the various geometric portions of the half-model of the train, i.e., the nose, coaches and tail as well as the top and bottom portions thereof. _____	117
Table 21: The convolution integrals of the velocity of the flow surrounding the train body, is shown at various locations of the yz-Plane. _____	127
Table 22: The various constants and variables used both for the description of the logarithmic wind profile, as well as the wind’s behaviour relative to the moving train. _____	133
Table 23: The dimensions of the “base case” computational domain for a train exposed to crosswind conditions. _____	135
Table 24: The values of the parameters that govern the nose geometry. _____	135
Table 25: The x-force [N] components acting on the Train as a whole as well as its sub-components, given for the various locations of the back outlet face. _____	138
Table 26: The y-force [N] components acting on the Train as a whole as well as its sub-components, given for the various locations of the back outlet face. _____	138

Table 27: The z-force [N] components acting on the Train as a whole as well as its sub-components, given for the various locations of the back outlet face.	139
Table 28: The dimensions of the final computational domain for a train exposed to crosswind conditions	139
Table 29: The twenty-seven design points that were generated by making use of the Latin Hypercube statistical method and their near-random associated parameter values.	141
Table 30: The effect of a variable inflection point (H) on the nose geometry of the train for a constant nose length of $L = 2.171\text{m}$ and nose-tip height of $Z_0 = 0.709\text{m}$ .	149
Table 31: The nose geometries associated with the global (left) and local (right) minimum leeside rolling moment acting on the leading locomotive, shown here for a constant nose length (L) of 4.930m.	150
Table 32: A comparative table showing first the nose geometries that ensure a minimum leeside rolling moment for nose lengths of $L = 2.171\text{m}$ , $4.930\text{m}$ and $7.688\text{m}$ given at the location of both the minimum (left column) as well as the maximum (right column) nose-tip heights.	152
Table 33: The geometric description as well as the force and moment responses, as per surrogate model, of the extreme points of the Pareto front (see Figure 126, point 'a' and 'c') as well as its "trade-off" point (see Figure 126, point 'b').	155
Table 34: A comparison between the results predicted by the surrogate model and the simulation for the total drag force (N) and the leeside rolling moment (N-m) for various geometries.	156
Table 35: The nose geometries corresponding to point a, b and c on the Pareto front is shown here along with their associated force and moment responses (see Figure 126), from left to right respectively.	160
Table 36: The mesh settings used for the construction of a low $y^+$ -mesh for the Ahmed's body, the transposed mesh for the train body and the coarsened mesh for the train body.	183
Table 37: The mesh settings used for the construction of a high $y^+$ -mesh for the Ahmed's body, the transposed mesh for the train body and the coarsened mesh for the train body	183
Table 38: The results of the Grid Convergence Index study completed for the Low $y^+$ -Mesh.	186
Table 39: The results of the Grid Convergence Index study completed for the High $y^+$ -Mesh.	187
Table 40: The values obtained for the various force components at grid refinements levels 1,2 and 3, for the transposed and coarsened low $y^+$ -meshes (in conjunction with the SST $k-\omega$ model).	188
Table 41: The values obtained for the various force components at grid refinements levels 1,2 and 3, for the transposed and coarsened high $y^+$ -meshes (in conjunction with the LPS Two-Layer model).	188
Table 42: The percentage deviation between the subsequent x-, y- and z-force components associated with their respective grid refinement levels for the coarsened Low $y^+$ -Mesh.	188
Table 43: The percentage deviation between the subsequent x-, y- and z-force components associated with their respective grid refinement levels for the coarsened High $y^+$ -Mesh.	188
Table 44: The results of the Grid Convergence Index study completed for the Low $y^+$ -Mesh.	189
Table 45: The results of the Grid Convergence Index study completed for the High $y^+$ -Mesh.	190
Table 46: The values obtained for the various force components at grid refinements levels 1,2 and 3, for the transposed and coarsened low $y^+$ -meshes (in conjunction with the SST $k-\omega$ model).	191
Table 47: The values obtained for the various force components at grid refinements levels 1,2 and 3, for the transposed and coarsened high $y^+$ -meshes (in conjunction with the LPS Two-Layer model).	191
Table 48: The percentage deviation between the subsequent x-, y- and z-force components associated with their respective grid refinement levels for the coarsened Low $y^+$ -Mesh.	191
Table 49: The percentage deviation between the subsequent x-, y- and z-force components associated with their respective grid refinement levels for the coarsened High $y^+$ -Mesh.	191
Table 50: The values of the nose length (L), nose-tip height ( $Z_0$ ) and inflection point height (H) of the nose geometry used for the study of an adequate blockage ratio.	192

Table 51: The various simulation cases that were considered in order to determine an adequate blockage ratio and their associated domain heights. _____	192
Table 52: The values of the dimensions of the computational domain that was validated for a streamlined train nose. _____	193
Table 53: The various simulation cases that were considered in order to determine an adequate inlet distance and their associated values. _____	195
Table 54: The values of the nose length (L), nose-tip height ( $Z_0$ ) and inflection point height (H) of the nose geometry used for the study of an adequate inlet distance. _____	195
Table 55: The various simulation cases that were considered in order to determine an adequate outlet distance and their associated values. _____	198
Table 56: The values of the nose length (L), nose-tip height ( $Z_0$ ) and inflection point height (H) of the nose geometry used for the study of an adequate outlet distance. _____	198
Table 57: The drag force and its various components acting on the train as a whole as well as its various sub-divisions, i.e., nose, coaches, tail, top and bottom. _____	202
Table 58: The side force and its various components acting on the train as a whole as well as its various sub-divisions, i.e., nose, coaches, tail, top and bottom. _____	202
Table 59: The lift force and its various components acting on the train as a whole as well as its various sub-divisions, i.e., nose, coaches, tail, top and bottom. _____	202
Table 60: The various simulation cases that were considered in order to determine an adequate front inlet distance and their associated values. _____	217
Table 61: The various simulation cases that were considered in order to determine an adequate side inlet distance and their associated values. _____	219
Table 62: The various simulation cases that were considered in order to determine an adequate back outlet distance along with their associated values. _____	221
Table 63: The various simulation cases that were considered in order to determine an adequate side outlet distance along with their associated values. _____	223
Table 64: The complete table of the 125 design points ran for the various combinations of the parameters that define the train nose geometry and their respective total drag force response. _____	235
Table 65: The values of the nose length (L), nose-tip height ( $Z_0$ ) and inflection point height (H) of the nose geometry used for the study of an adequate inlet distance. _____	242
Table 66: The various simulation cases that were considered in order to determine an adequate inlet distance and their associated values. _____	242
Table 67: The total x-, y- and z-forces obtained from the simulation at various inlet boundary locations. The percentage deviation between subsequent values is also indicated. _____	242
Table 68: The drag force acting on the various sub-components of the train, i.e., the nose, coaches and tail, at various inlet boundary locations. The percentage deviation between subsequent values is also indicated. _____	242
Table 69: The side force acting on the various sub-components of the train, i.e., the nose, coaches and tail, at various inlet boundary locations. The percentage deviation between subsequent values is also indicated. _____	243
Table 70: The lift force acting on the various sub-components of the train, i.e., the nose, coaches and tail, at various inlet boundary locations. The percentage deviation between subsequent values is also indicated. _____	243
Table 71: The values of the nose length (L), nose-tip height ( $Z_0$ ) and inflection point height (H) of the nose geometry used for the study of an adequate outlet distance. _____	245
Table 72: The various simulation cases that were considered in order to determine an adequate outlet distance and their associated values. _____	245
Table 73: The total x-, y- and z-forces obtained from the simulation at various outlet boundary locations. _____	245

*Table 74: The drag force acting on the various sub-components of the train, i.e., the nose, coaches and tail, at various outlet boundary locations.* \_\_\_\_\_ 246

*Table 75: The side force acting on the various sub-components of the train, i.e., the nose, coaches and tail, at various outlet boundary locations.* \_\_\_\_\_ 246

*Table 76: The lift force acting on the various sub-components of the train, i.e., the nose, coaches and tail, at various outlet boundary locations.* \_\_\_\_\_ 246

## Nomenclature

$\delta$	Boundary layer thickness	m
$\delta^* / d^*$	Displacement thickness	m
$\theta$	Momentum thickness	m
$H$	Form or shape parameter ( $\frac{\delta^*}{\theta}$ )	-
$St$	Strouhal number	-
$z$	Height above ground	m
$\kappa$	Von Karman constant	-
$z_0$	Surface roughness height	m
$u(z)$	Mean velocity profile of wind	m/s
$u_*$	Surface friction velocity	m/s
$\sigma(z)$	Standard deviation of the velocity fluctuations of the wind at height 'z' above the ground	m/s
$I$	Turbulence intensity of the wind	-
$V$	Velocity of the wind relative to the train	m/s
$u(h)$	Mean velocity of wind at reference height 'h'	m/s
$h$	Reference height, usually taken to be 3m	m
$v$	Velocity of the train	m/s
$\beta$	Wind direction	Degrees
$\psi$	Yaw angle	Degrees
$C_D$	Drag Coefficient	-
$C_{D,\psi=0}$	Drag coefficient at zero yaw	-
$\alpha$	Variable that ranges between 0.5 - 1	-
$Z_s$	Position of the stagnation point	m
$\alpha$	Inclination angle of the hood	Degrees
$\gamma$	Rake angle of the windshield	Degrees
$\delta$	Lateral taper of nose	Degrees
$\varphi$	Slant angle of rear	Degrees
$C_p$	Pressure coefficient	-
$p$	Static Pressure	Pa
$p_\infty$	Far field pressure	Pa
$V_\infty$	Far field velocity	m/s
$\rho$	Density	kg/m <sup>3</sup>
$w_{vc}$	Velocity at vortex center	m/s
$w_{vp}$	Velocity at vortex periphery	m/s
$C_L$	Lift Coefficient	-
$L$	Nose length	m
$H$	Inflection point height	m
$Z_0$	Stagnation point height	m
$\mu$	Dynamic viscosity	kg/ms
$\nu$	Kinematic viscosity	m <sup>2</sup> /s
$Re$	Reynolds number	-
$p$	Order of convergence	-
$r$	Mesh refinement ratio	-
$f_i$	Performance parameter	-
$F_s$	Factor of safety	-
$\varepsilon$	Relative error	%

$C_B$	Partial drag coefficient acting on the back	-
$C_K$	Partial drag coefficient acting on the nose	-
$C_R$	Partial drag coefficient acting on the rest of the body	-
$C_S$	Partial drag coefficient acting on the slope	-
$D_I$	Domain inlet distance	m
$D_O$	Domain outlet distance	m
$W$	Domain width	m
$H$	Domain Height	m
$R^2$	Coefficient of multiple determination	-
$\dot{m}$	Mass flow rate	kg/s
$A$	Cross-sectional area	m <sup>2</sup>
$D_{FI}$	Front Inlet Distance	m
$D_{SI}$	Side Inlet Distance	m
$D_{BO}$	Back Outlet Distance	m
$D_{SO}$	Side Outlet Distance	m
$M_{R,LS}$	The leeside rolling moment coefficient acting on the leading locomotive	N-m
$F_{S,LL}$	The side force acting on the leading locomotive	N
$COG_{TE}$	Transnet's height limit on the center of gravity, i.e., 2.49m	m
$F_{L,LL}$	The lift force acting on the leading locomotive	N
$w_{rail}$	The width of the standard gauge rail, i.e., 1.435m	m
$M_{x,LL}$	The moment working about the longitudinal (x-) axis of the leading locomotive	N-m
$M_{max}$	Maximum moment	N-m
$M_{min}$	Minimum moment	N-m
$R$	Percentage deviation of a given maximum value from a corresponding minimum value	%
$F_{y,LL}$	Side force acting on the leading locomotive	N
$F_{z,LL}$	Lift force acting on the leading locomotive	N
$F_{x,Train}$	Drag force acting on the train	N
$M_{LL,COG}$	Moment about the COG of the leading locomotive	N-m
$M_{LL,LS}$	Moment about the leeside rail of the leading locomotive	N-m
$C_f$	Skin friction coefficient	-
$\tau_w$	Wall shear stress	kg/ms <sup>2</sup>
$U_\tau$	Near wall velocity	m/s
$y$	Height of first body adjacent cell	m

## Abbreviations

AIAA	American Institute of Aeronautics and Astronautics
BES	Base element size
CAD	Computed aided design
CEN	Comité Européen de Normalisation (European Committee for Standardization)
CFD	Computational fluid dynamics
CPU	Central processing unit
DNS	Direct Numerical Simulation
DTBR	Double track ballasted rail
RANS	Reynolds-Averaged Navier-Stokes
RSM	Reynolds stress model
RSM	Response surface model
EVM	Eddy viscosity model
GCI	Grid convergence index
HST	High-speed train
LES	Large eddy simulation
LPS	Linear Pressure-Strain
MO-SHERPA	Multi-Objective SHERPA
NCGA	Neighbourhood Cultivation Genetic Algorithm
NSGA	Non-dominated Sorting Genetic Algorithm
RBF	Radial basis function
RMSE	Root mean squared error
SST	Shear stress transport
STBR	Single track ballasted rail
TSI	Trading Standards Institute
VSM	Viscous sublayer model

## Rail Definitions

Ballast

Ballast forms the track bed on which the rails and railroad ties (sleepers) are laid. Usually made from crushed stone.

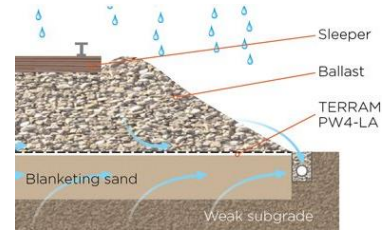


Table 1: Ballast definition and illustration (Terram, n.d.)

Bogie

An undercarriage that carries wheelsets, which pivots beneath a rail vehicle.

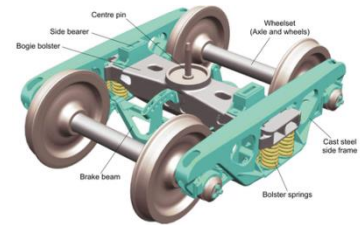


Table 2: Bogie definition and illustration (The Railway Technical Website, 2018)

Cowcatcher

A structure mounted to the front of a locomotive to deflect obstacles on the track.



Alamy/Lee Foster

Table 3: Cowcatcher definition and illustration (Your Dictionary, n.d.)

Pantograph

A device that conducts electricity from the overhead line to the train.



Table 4: Pantograph definition and illustration (Auckland Transport, 2014)

# 1. Introduction

## 1.1. Background

The rail industry in South Africa is a product of the colonization of the country with the first train introduced in Durban in 1860. While the home railways of European countries had already been standardized at standard gauge, save Portugal and Spain which standardized for broad gauge, the railways built in South Africa were narrow or Cape gauge, which are inherently uncompetitive. Due to many factors, at least one of which is a lack of funding, rails in South Africa have unfortunately not been replaced with a competitive gauge type as yet, which has left the country's rail industry financially impotent. That is, due to the low axle load offered by narrow gauge, road has been able to hit above its weight, the low implied speed has made rail solutions like the Gautrain more attractive than those offered by the South African government and finally given the general outdated nature of narrow gauge, new technologies are rendered unattainable which in turn has implications on efficiency and carbon emissions to name a few. In short, South Africa has missed the railway Renaissance and all the benefits it holds.

It is the intention of The National Rail Policy (Department: Transport , June 2017) to consciously address this void and to ensure that rail acts as the backbone of national land transport by 2050. A secondary motivator for the aforementioned is the potential economic benefits posed by developing the rail industry; not only does the initiative create jobs in and of itself, but it further serves to open the metropolitan job markets to residents of rural areas. Environmental concerns are however the primary motivator for the initiative, i.e., many governments have agreed to substantial international commitments regarding the reduction of greenhouse gas emissions associated with the transport sector. Given that rail is the most energy efficient transport mode and considering the substantial backlog in rail technology development in South Africa, the rail sector is well poised to make a considerable contribution towards reaching the agreed upon emissions targets. One of the ways in which The National Rail Policy hopes to bridge the technological gap in the rail sector is by implementing standard gauge technologies on the national rail network and developing a high-speed commuter to deliver long-distance services to passengers. The potential success of this initiative has already been proven by the Gautrain which has come close to matching its initial investment in its seventh year of active service, while simultaneously sustaining jobs and increasing tax revenues.

Unfortunately the loss of the rail industry's ability to develop and retain skills is one way in which the impact of the industry's decline over the last several decades can be felt. Given that this industry constitutes a specialized work environment which requires specific and sometimes scarce skills to support research, development and design, there is a clear obstacle which must be overcome in order to facilitate the revitalization of the South African rail network. With regard to high speed rail in particular, at present there doesn't exist any in-house expertise on the matter in Transnet, which has been identified by The National Rail Policy as one of the key role players in this endeavor. It is the purpose of this thesis to address this gap in knowledge and technology. Thus, while the optimized solution provided at the completion of the work at hand is purely a technology demonstrator model, the knowledge

acquired through the execution process constitutes an invaluable contribution to Transnet's resources when addressing the targets set for it by The National Rail Policy.

However, since the information garnered is meant to build towards a very real database of knowledge which is meant to contribute to very real targets and deadlines, it is imperative that the work done towards the completion of the technology demonstrator is well thought out. Consider for example that there are already coaches being developed, with the first prototypes in production, by Transnet Engineering's mechanical design office that will be suited for standard gauge track. The design of these coaches is subject to certain constraints, e.g., the dimensions of the vehicle gauge, ergonomics, passenger and luggage compartment capacity and ducting to name but a few. Modifying the geometry of the coaches is thus not feasible at present and as such they are not only precluded from the optimization problem but also act to further constrain it, i.e., the transverse cross-sectional area of the coaches and locomotives must align. In contrast, the development of locomotives within Transnet is still ongoing with the first prototype, namely the Trans-Africa locomotive, only having been launched in 2017. It is Transnet's hope to incrementally improve upon this initial locomotive design to address a multitude of rail challenges of which high speed rail is but one; modifying the shape of this locomotive is thus not only possible but encouraged. It is against this backdrop that it was decided to optimize for the geometry of the leading locomotive, or nose, of a high-speed train however, given that the tail is identical to the nose, a more accurate description may be the simultaneous optimization of the leading and trailing locomotives.

## **1.2. Previous Work Completed on Nose Optimization**

Previous studies completed on the optimization of the train nose or even the simultaneous optimization of the train nose and tail, includes, but is not limited to, some of the examples given in section 2.3 in the literature review. Some of the examples consider crosswind while others only look at windless conditions. Furthermore, the optimization objectives also vary from case to case with the most common objective being the reduction of aerodynamic drag although some cases also consider lift or crosswind stability etc.

## **1.3. Problem Statement**

The problem at hand is the geometric optimization of the nose, or leading locomotive, of a high-speed train travelling at 350km/h. Given however, that the nose and tail are identical, altering the nose geometry must necessarily alter the shape of the tail, or trailing locomotive, also. As such one might say that the optimization, rather than being limited to the nose, is a simultaneous one of both the nose and tail. Furthermore, the nose must be optimized for two travelling conditions; first, windless, i.e., normal operating conditions must be considered. For this design case the total drag of the train must be minimized so as to ensure maximum fuel efficiency, hereby aligning the locomotive design with the outcomes for 2050 as specified by The National Rail Policy. The second load case is that of the train travelling under storm, i.e., crosswind conditions. Under these circumstances there are two objectives that must be optimized for. Once again the total drag of the train is to be minimized but in addition, this design case necessitates the maximization of crosswind stability of the train so as to ensure the safety of the passengers. The study must further investigate the trade-off between the two optimized

geometries, when a given optimal geometry is exposed to the other wind load case so as to facilitate decision-making within Transnet.

Furthermore, there are certain constraints the optimal design must adhere to so as to comply with Transnet Engineering's criteria;

- The dimensions of the transverse cross-section of the locomotive at the location of its maximum cross-sectional area must be identical to that of the coaches already being developed by Transnet Engineering. This is such so as to facilitate a smooth coupling between the locomotive and the trailing coaches as well as to ensure that the risk of gauge infringement is minimized.
- As per Transnet standard the minimum gap between the cowcatcher (see Table 3) and the rail may not be less than 75mm. Since the ballast (see Table 1) height can vary arbitrarily along the track, the worst case of a ballast height equal to the rail height must be considered.
- The high-speed train configuration that must be considered is that of a power car and a non-powered driving trailer along with four passenger coaches. Given that each vehicle is 20m long, the entire train is thus 120m in length.

#### **1.4. Objectives of the Study**

The objective of this study is to find the nose geometry for a high-speed train that is most suitable for Transnet's specific operating conditions. This is to be accomplished by optimizing the nose for each of the most crucial load conditions as specified by Transnet, i.e., windless as well as storm condition crosswinds. Finally, the trade-off between the two optimized designs will be investigated when the given geometry is subjected to the remaining wind loading condition. In order to achieve this, the researcher will complete the following;

- A study on the external flow field surrounding a high-speed train for both windless as well as crosswind conditions, so as to facilitate understanding of the flow features that may be encountered in future work.
- A study on the aerodynamic challenges faced by the Rail industry, so as to verify that the optimization objectives stipulated by Transnet are indeed of concern.
- A study on geometric parameters that influence the external flow over vehicles, so as to facilitate sound decision making when constructing and parameterizing the geometry of the leading locomotive.
- A study on the numerical approaches available to solve for and optimize the aerodynamic characteristics of a given structure. This will include an investigation into some of the turbulence models offered by the computational fluid dynamics software that will be used to solve the flow surrounding the train body. Attention will also be given to numerical algorithms and approaches that are available to optimize for the train body.
- A computational fluid dynamics validation case in order to facilitate the choice of an appropriate grid construction and resolution as well as a suitable turbulence model that will be able to capture the flow phenomena associated with a vehicle in close ground proximity. This validation case will further allow for the accuracy of the chosen optimization algorithm to be verified.

- An optimization study on the nose geometry of a high-speed train travelling at 350km/h under windless, i.e., normal operating conditions. The geometric parameters that define the nose, as well as the computational model and optimization algorithm used will be informed by the results of the aforementioned studies.
- An optimization study on the nose geometry of a high-speed train travelling at 350km/h under storm, i.e., crosswind conditions. Once again the geometric parameters that define the nose, as well as the computational model and optimization algorithm used will be informed by the results of the above studies.
- Consideration will be given to the trade-offs between the two optimized geometries, i.e., the effect(s) on the optimization goal(s) when a given optimized geometry is exposed to the other's wind load case.

## 1.5. Scope of Work

This study is concerned with the optimized nose geometry of a high-speed train, and not with the actual values of the drag or rolling moment coefficients. The accurate prediction of the crosswind characteristic for the train, i.e., the wind speed vs. train speed at which derailment will occur, will thus not be considered here and therefore it is unnecessary to model or consider the multi-body dynamics of the train. Rather, the study will only attempt to provide an accurate prediction of the aforementioned coefficients' behaviour as a function of the identified geometric parameters, hereby allowing the optimization question to be answered. As such, those geometric features whose effect on either the flow field or the final optimized shape is considered to be insignificant, will be omitted from the train model, e.g., door handles, window handles, etc.

Another simplification was the omission of explicitly modelled bogies (see Table 2) in favour of the assumption that they were perfectly faired. Given that bogie fairings are a standard feature for high-speed trains, the assumption is not entirely unreasonable. It must however be noted that they hardly produce a perfectly smooth surface since the wheelsets must protrude for cooling purposes and as such they actually constitute a repeat friction load. Furthermore, the inter-carriage gaps of the high-speed train constitute the same but they too are faired in an attempt to mitigate their effect on the flow field. Thus, they are also not included in the train model.

With regard to the two load cases in question, i.e., windless and crosswind conditions, it is clear that the former is simpler to simulate than the latter. The study will thus not only attempt to determine an accurate approach to follow in order to account for the various relative velocity components experienced by the train when exposed to crosswinds, but will further attempt to find a suitable wind definition also. This definition must be such that it accurately describes the boundary layer of the wind in close ground proximity, accounts for the topography of the rural environment that the train will most commonly traverse and finally the worst case storm conditions that the train will be exposed to before being required to stop operation.

There are many additional aspects to high speed rail that will not be considered in this document; heat transfer, train-tunnel interaction and pantograph (see Table 4) dewirement to name a few and while

these and many other considerations are important, it simply isn't feasible to attempt to address them all.

## 1.6. Overview of Dissertation

**Chapter 2** contains an in depth literature review on the external flow field surrounding the train body under windless and crosswind conditions. The aerodynamic challenges faced by the rail industry are also considered along with the geometric parameters that define the nose shape, that influence the flow field around a vehicle in close ground proximity. Finally, attention is given to the numerical approaches available to optimize a body for aerodynamic considerations.

**Chapter 3** contains the description of, methodology followed and results obtained for the CFD validation case. The particular case study that was selected is the Ahmed's body on the basis that the train shares geometric and flow similarities with it. The grid refinement, appropriate turbulence model choices and suitable optimization algorithm are all justified in this chapter for future use, i.e., when the geometry of the train nose is to be optimized.

**Chapter 4** and **Chapter 5** relay the entire procedure followed to optimize the nose geometry for windless and crosswind conditions, respectively. Parameters such as domain size, boundary conditions, grid refinement and the optimization process itself are considered. The results obtained for each optimization case are discussed, the flow field associated with the optimal nose geometry analyzed and hypotheses as to the possible mechanisms driving the observed flow phenomena made.

**Chapter 6** serves to summarize and conclude the results. Recommendations for future work are made.

## 2. Literature Review

### 2.1. External Flow around High-Speed Trains

The external flow field surrounding a high-speed train is highly turbulent, three-dimensional and aerodynamically 'dirty'. Far from being predictable as one may expect the flow field surrounding a train to be, the complexity exhibited by the flow necessitates that the field be divided into separate regions in order to ease both the clarification and interpretation thereof. The regions that will be employed in order to discuss the flow field are those developed by Baker in (Baker, et al., 2001), these are;

- The nose region; extends upstream in order to include the oncoming flow, as well as approximately 5 to 10m downstream of the nose, usually terminating in a large velocity peak.
- The boundary layer region; starts at the end of the nose region and extends to the end of the train body. This region will address the train sides, roof and the region beneath its body.
- The near wake region; extends to approximately 100m behind the train and usually terminates with a large velocity peak.
- The far wake region; starts at the end of the near wake region and it is within this region that the velocities decay to zero.

It is worth noting that while the discussions that follow will describe the flow behaviour around a train, it will do so in general terms. The specific flow field associated with a given train will vary based on its unique geometric features and as such the aerodynamic behaviours given below should be seen as purely generic. In what follows, the coordinate system as discussed below will be adhered to as far as possible. Since this document does, however, contain material from various sources, it isn't always possible to do so. Throughout the document, the following coordinate system is used:

- X-coordinate: along train direction of travel (longitudinal of train body). It will generally be measured from the train nose.
- Y-coordinate: perpendicular to the train body (lateral direction). It will be measured from the centerline of the tracks.
- Z-coordinate: in the vertical direction and is measured from ground level.

#### 2.1.1. Windless Conditions

##### 2.1.1.1. *The Nose Region*

In the event that the train is travelling in windless conditions, the air several hydraulic diameters upstream of the train body may be regarded as relatively undisturbed, i.e., it has not yet come under the influence of the train body and may be regarded as stationary. Once the air comes in contact with, or in close proximity of the train, it is accelerated. This may be attributed, amongst others, to the viscosity of the air; adhesive forces dominate the fluid-solid interface which gives rise to some velocity profile of the air travelling over the moving vehicle. Since the flow remains largely attached over the nose the viscous effects of the air remains within close proximity of the train body, i.e., the boundary layer. The flow behaviour of the air beyond this boundary layer is dominated by inertial forces and as such it may be regarded as essentially inviscid with relatively low turbulence (Baker, 2014).

The pressure distribution along the centerline of a train's nose is illustrated in Figure 1. This pressure variation is well defined for train noses in general, all of which tend to follow the same trend. It can also be anticipated to some degree based on the expression for the non-dimensional pressure coefficient, i.e., a positive pressure peak is visible at the stagnation point at the tip of the train nose, followed by a negative peak as the air is accelerated over the nose.

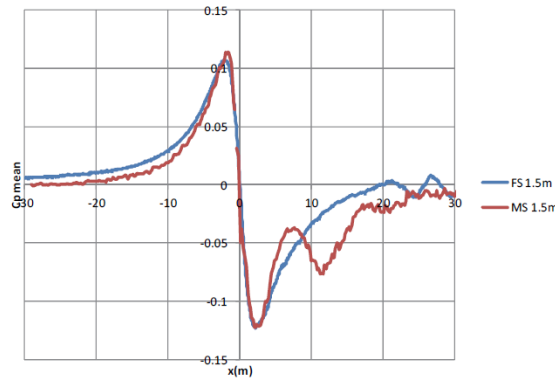


Figure 1: A comparison between the nose pressure pulses obtained from both full scale (FS) as well as model scale (MS) experiments for an ICE-2 train (Baker, et al., 2013).

In addition to these large pressure peaks, there are also large horizontal velocity peaks present in the flow about the nose (see Figure 2). The longitudinal velocity (in the x-direction) follows the same trend as that of the pressure variation displaying a positive and then a negative peak, the latter of which is indicative of flow separation and associated recirculation region. The lateral velocity also shows a large positive peak (in the positive y-direction) as the air is deflected away by the train passing through it. From Figure 2 it is clear that the behaviour of the overall horizontal velocity is dominated by the lateral velocity component. In fact, had the overall velocity, rather than its components been measured the negative velocity peak in the longitudinal velocity would have been overlooked.

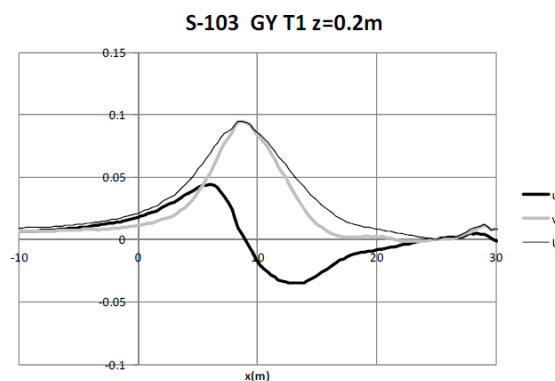


Figure 2: Velocity measurements about the nose of a train (Velaro S-103) (Baker, et al., 2013). In this figure  $u$  is the normalized longitudinal velocity,  $v$  is the normalized lateral velocity and  $U$  is the normalized overall horizontal velocity.

While this overall horizontal velocity peak may be present for all trains, it is more pronounced for trains with a blunt nose. Consider as an example the S-100 TGV (see Figure 3), which is 200m long with a pointed, streamlined nose, and the S-252, a rather blunt nosed locomotive with trailing coaches. In the

case of the streamlined nose, the non-dimensional horizontal velocity peaks at just over 0.05, whereas the blunt nose generates a velocity peak of approximately 0.15. In this instance then, the magnitude of the velocity peak associated with a blunt nosed train is nearly three times larger than that of a streamlined nose. According to (Baker, 2014) similar behaviour is however generally observable as well; the overall normalized velocity nose peaks for streamlined passenger trains are between 0.05 and 0.1, while that of blunt freight trains are much higher. It follows then, that at a fixed distance from the side of the train, the magnitude of the overall normalized horizontal nose peak velocity increases with the bluntness of the train nose. Finally, from Figure 4 it is clear that there are two velocity peaks present; at the nose of the locomotive, as well as at the discontinuity between the locomotive and its trailing coach which is indicative of disturbed flow in this area.

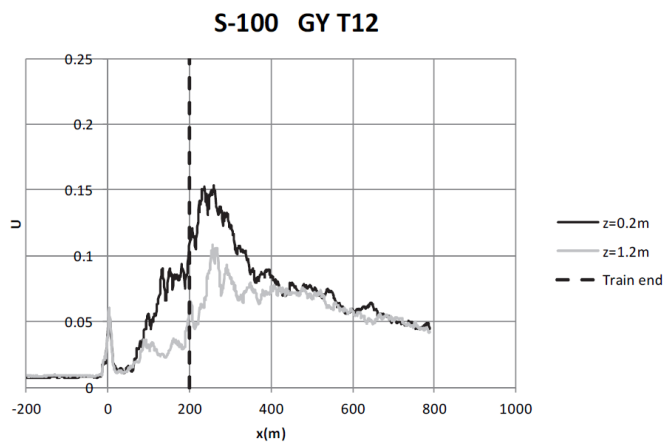


Figure 3: Ensemble average velocities measured for the S-100 TGV (Baker, et al., 2013), where the x-axis shows the distance from the train nose, the y-axis the overall, horizontal, normalized velocity. Measurements were made at heights of  $z$  as indicated, at a distance of  $y=3m$  from the centerline of the track.

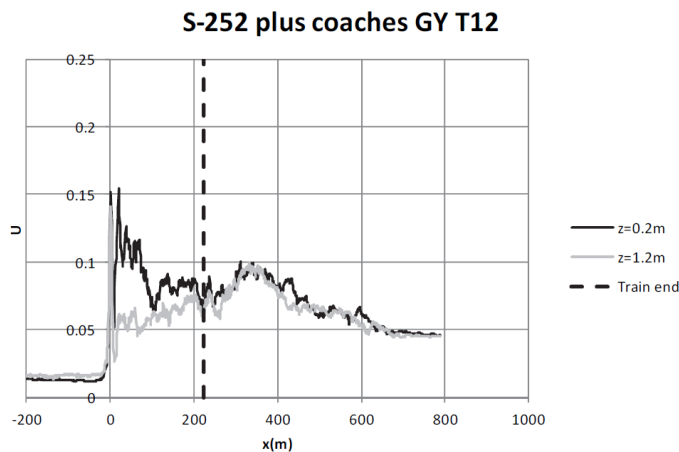


Figure 4: Ensemble average velocities measured for the S-252 locomotive and trailing coaches (Baker, et al., 2013), where the x-axis shows the distance from the train nose, the y-axis the overall, horizontal, normalized velocity. Measurements were made at heights of  $z$  as indicated, at a distance of  $y=3m$  from the centerline of the track.

### 2.1.1.2. The Boundary Layer Region

The boundary layer that develops along the length of the train body is highly turbulent and three-dimensional in nature. Additionally, the scale of the boundary layer is considerable and by the time it reaches the end of the train, can have lateral dimensions of the same order of magnitude as the width to height ratio of the train itself (Baker, 2014). Thus, in order to best describe the complex boundary layer region, the train sides, train roof and underbody flows will be discussed separately.

#### 2.1.1.2.1. Train Sides

During the RAPIDE experiments (Sterling, et al., 2008), measurements were taken of the flow field that surrounds the ICE-2 train. The normalized (with train velocity) ensemble averaged overall horizontal velocities that were measured along the side of the train can be seen in Figure 5. The sharp initial velocity peaks observable at the tip of the train nose ( $x=0\text{m}$ ) has already been discussed in the previous section, but their magnitude is small when compared to those observable in the boundary layer. What is however clear from the experimental results is the gradual development of the boundary layer along the train body, following these sharp nose peak velocities. It is also clear from the results that the values of the overall, non-dimensional horizontal velocity are at their highest nearest the train body while decreasing the further away from the track centerline they are measured. Considering that there exists a no-slip condition at the interface between the air and the train body, thus implying an air velocity equal to the train velocity and that under windless conditions, the air furthest away would have a zero velocity, the experimental measurements substantiate what is anticipated from theory. It is also interesting to note from Figure 5, the increase in the boundary layer thickness; at a distance of 2.42 meters away from the center of the nearest rail, the air velocity is initially rather low, thus indicating that the boundary layer has not yet grown sufficiently for the measuring point to lie within it. Larger velocity values are however observable at this point ( $y=2.42\text{m}$ ) once the boundary layer has developed sufficiently, implying a boundary layer thickness of approximately 2.42 meters in the lateral direction.

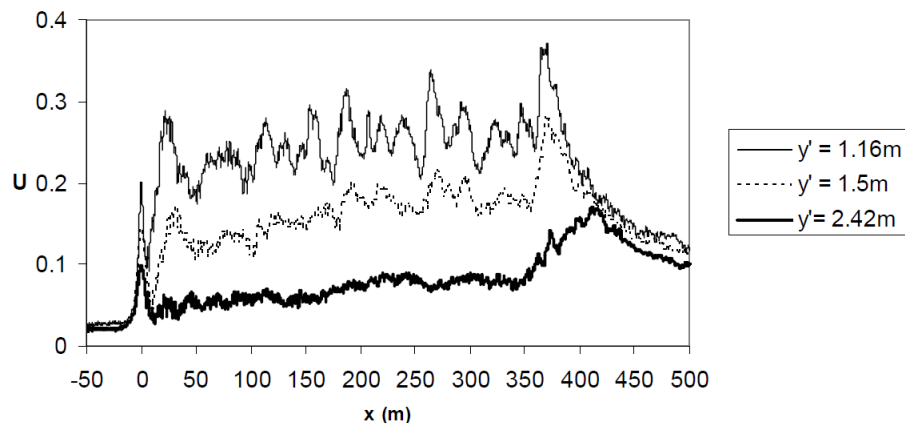


Figure 5: Ensemble average velocities for the ICE-2 train (Sterling, et al., 2008). The x-axis shows the distance from the train nose, the y-axis indicates the normalized horizontal slipstream velocity.  $y'$  is the distance from the center of the nearest rail. All measurements were made at a height of 0.5m from the top of the rail.

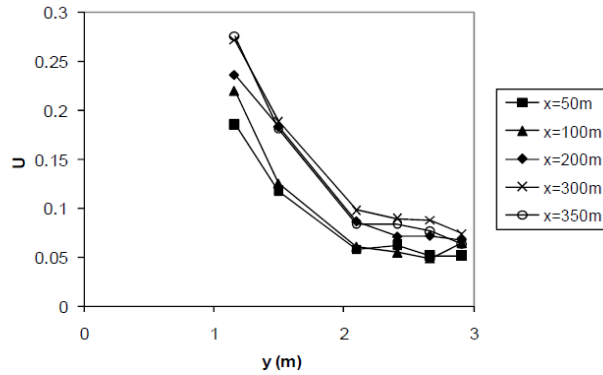


Figure 6: The boundary-layer velocity profiles measured at 0.5m above the track for the ICE-1 (Sterling, et al., 2008). The x-axis shows the distance from the nearest rail and the y-axis shows the normalized overall horizontal velocity at various distances from the side of the train. The various x-values (in the legend) are representative of the position along the train body where the velocities are measured. The train is 364m long.

A more conventional representation of the boundary layer profiles that can be found along the length of the train is shown in Figure 6. Once again, there is a visible increase in the thickness of the boundary layer as it develops, made clear by the larger velocities measured at the same distance from the side of the train, for increasing values of x (where x=0m is the tip of the train nose). During the RAPIDE experiments boundary layer measurements were also made for the ICE-2 by means of an on-board laser anemometer (see Figure 7) (RAPIDE, 2001). The figure shows a boundary layer with an approximate thickness of over 1m and while this is still considerable, it is noticeably less than predicted from the ground measurements shown in Figure 6; a fact indicated by the lower non-dimensional velocities at the same approximate x-location along the train. This phenomenon may be explained by considering the location on the train at which the measurements are made, i.e., in the case of the ground-based measurements the measuring point is closer to the ground than for the onboard measurements. Since there are multiple factors contributing to roughness closer to the ground such as the topography, bogies etc. there is a greater loss of energy in this region. Consider that the greater the energy of the flow is, the better the mixing that occurs and consequently, the thinner the boundary layer. Thus, when the flow loses energy, the boundary layer thickens. The experimental results are consistent with this flow behaviour; where the train is smoother, a thinner boundary layer is observed (Figure 7) than where the train (and surrounds) is rougher (Figure 6).

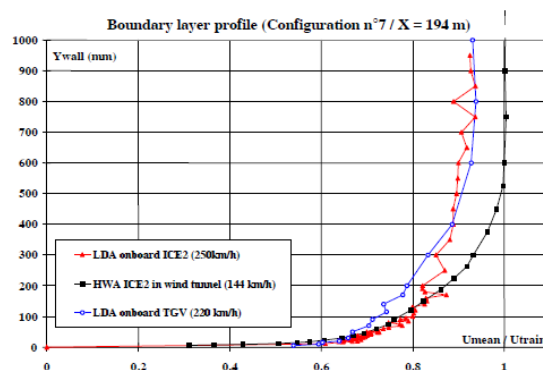


Figure 7: On-board measurements of a train boundary layer by making use of a laser anemometer (RAPIDE, 2001).

In addition to the boundary layer thickness, the displacement thickness, form parameter and turbulence intensity can also give valuable information regarding the boundary layer. Consider, for example, the displacement thickness of the boundary layer plotted along the length of the train (see Figure 8). For measurements made at full scale there is a definite peak at the nose, corresponding to the flow disturbances discussed previously. The displacement thickness also grows along the train length, hereby affirming the results obtained for the boundary layer thickness. Once again, the displacement thickness is larger for measurements near the ground (trackside) than for those higher up the train body. This phenomenon can once more be attributed to the roughness in the vicinity of the measuring point, which contributes to energy consuming processes. The form parameter in the case of both the trackside measurements as well as those taken from the platform show values of less than 1.3 to 1.4 (see Figure 9). Considering that turbulent flows are typically associated with  $H = 1.3$  to  $1.4$  for an equilibrium boundary layer, these lower values of the form parameter are indicative of the essential three-dimensionality of the flow (Baker, 2014). Figure 10 shows that the turbulence intensity, a measure of the magnitude of the turbulence, remains approximately constant along the length of the train. Both the trackside as well as the platform measurements fluctuates greatly, hereby affirming the unsteady characteristics of the flow. It is clear, as would be expected, that the values of turbulence intensity is much greater for trackside measurements (approximately 0.1) than for the platform measurements (approximately 0.05), with both the aforementioned values characteristic of flat plate boundary layers (Baker, 2014). Another boundary layer parameter that is of importance is the skin friction coefficient, especially so since it is the surface skin friction that determines the overall drag of the train to a large extent. According to (Baker, 2014), since most values for the local skin friction coefficient for a train fall on or below that of the accepted smooth wall correlations of skin friction and local Reynolds number for flow over a two-dimensional flat plate, the non-equilibrium, three-dimensional nature of the side wall boundary layers of a train is herewith reaffirmed. Additionally, in keeping with aforementioned behaviour, the value of the skin friction coefficient is larger nearer the ground, in the vicinity of the rough bogies, than higher up the train wall.

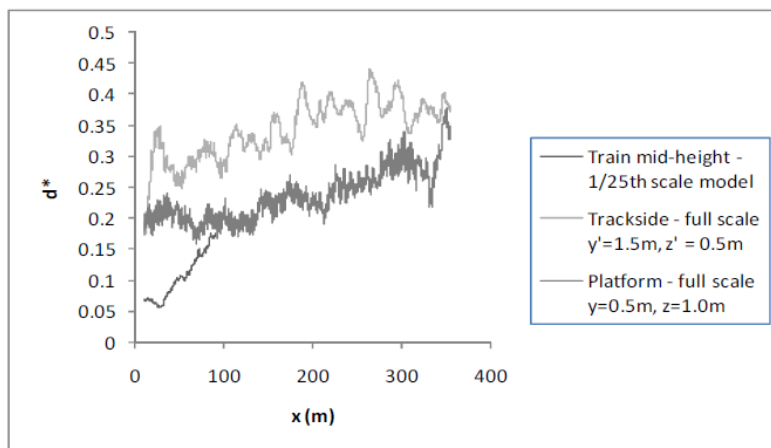


Figure 8: The displacement thickness for the ICE-1 train measured at 0.5m above the track and 0.5m above a platform (Sterling, et al., 2008).

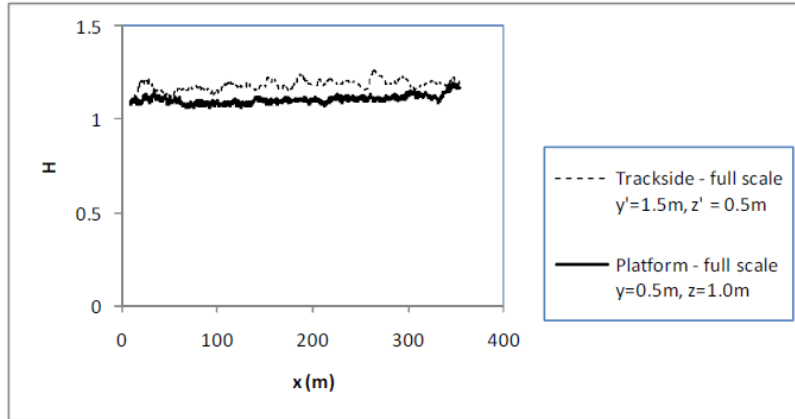


Figure 9: The Boundary layer form parameter for the ICE-1 train measured at 0.5m above the track and 0.5m above a platform (Sterling, et al., 2008).

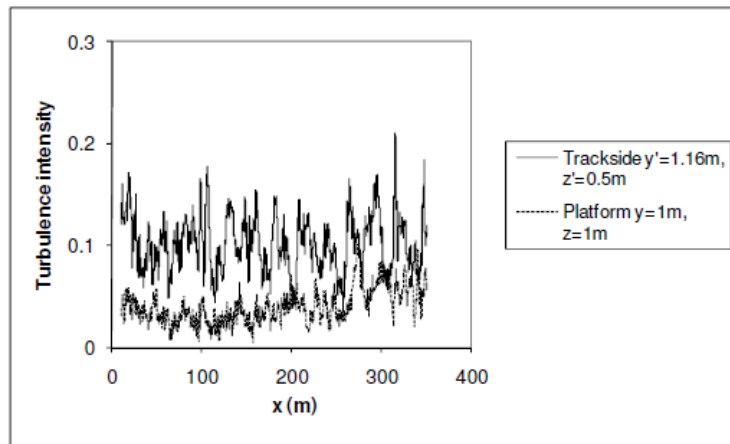


Figure 10: The boundary layer turbulence intensity for the ICE-1 train measured at 0.5m above the track and 0.5m above a platform (Sterling, et al., 2008).

#### 2.1.1.2.2. Train Roof

The flow over the train roof is of particular importance when considering the aerodynamics pertaining to pantographs. Unfortunately there aren't much experimental data available regarding the boundary layer development along the roof of the train as yet (Baker, 2014), with certain data sets even contradicting one another. An attempt will thus be made herein to discuss the available data, while accepting the potential of future contradiction.

Measurements of the boundary layer development along a train body were made by (Brockie & Baker, 1990) at model scale, with both the side and the roof boundary layers considered, as well as at full-scale, with only the side boundary layers considered. At model scale the measured momentum thickness growth of the side boundary layer was less than predicted for a purely two-dimensional boundary layer, hereby implying cross-flow velocity terms. Upon subsequent inclusion of three-dimensional effects in their mathematical model, (Brockie & Baker, 1990) found good correlation with the experimental data, leading to the conclusion that the boundary layer along the side of the train is diverging. Similarly, the two-dimensional boundary layer model failed to accurately predict the flow over the roof. From an

ensuing momentum balance calculation a convergent roof boundary layer was deduced. The aforementioned flow behaviours are compatible with one another, consider: the boundary layer flow along the side of the train has a vertical velocity component, hereby allowing the flow to wash up its sides and over the roof, effectively thickening the roof boundary layer. Furthermore, this flow behaviour was affirmed by two sets of model scale experimental data, as well as the full scale test data. Measurements of the boundary layer displacement thicknesses along the sides and roof of a model scale HST that were made by (Brockie & Baker, 1990) are shown in Figure 11. These results indicate a considerably thicker roof boundary layer than that of the sides, thus confirming the aforementioned flow behaviour, i.e., a diverging flow up the side of the train and a converging flow over its roof. Full-scale measurements of the flow around a 200m long HST at roof height further confirms this postulated behaviour (see Figure 12); once the initial flow disturbances in the vicinity of the nose have passed, there is a noticeable decrease in the normalized overall, horizontal velocity herewith affirming the proposed converging roof boundary layer.

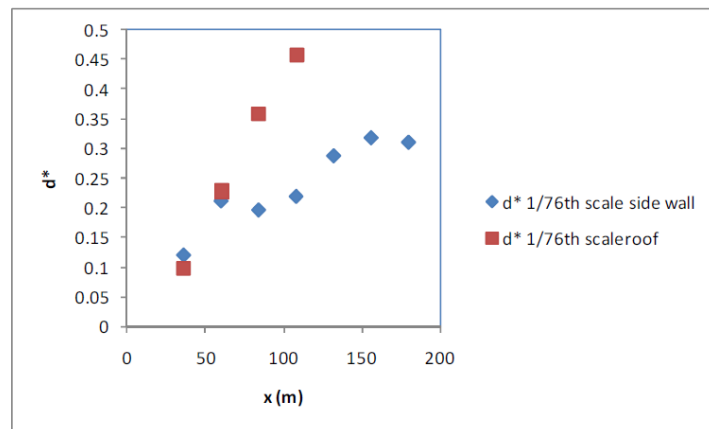


Figure 11: The boundary layer displacement thickness over the roof of a 1/76<sup>th</sup> model scale HST (Brockie & Baker, 1990).

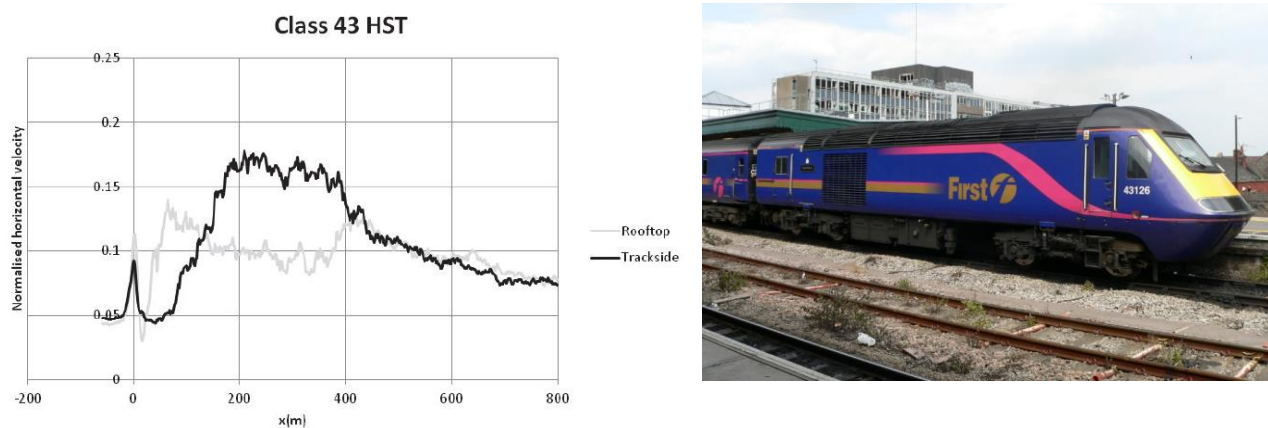


Figure 12: Ensemble average velocities for the Class 43 HST. The x-axis shows the distance from the train nose, the y-axis indicates the normalized horizontal velocity. Measurements were made at two locations. Firstly: 3.05m from the track centerline, at a height of 0.7m above the top of the rail. Secondly: 4.05m from the track centerline and 4.2m above the top of the rail (close to the roof top) (Baker, 2014).

Experiments conducted by (Baker, et al., 2001) contradict the aforementioned findings and show displacement thicknesses of similar magnitude along the side and the roof of the train (see Figure 13). Their findings do however show form parameters for both the roof and side of the train that are below 1.4 and as such, at least reaffirm the significant three-dimensionality of the developing boundary layer flow.

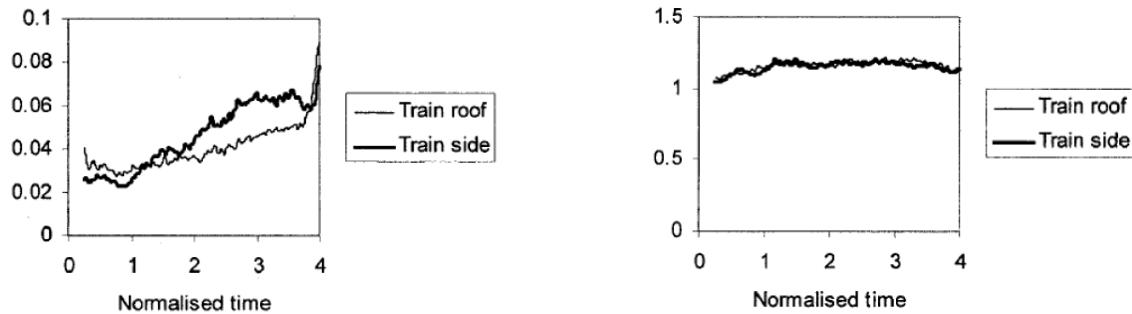


Figure 13: Boundary layer parameters shown along the roof of a 1/25<sup>th</sup> scale ICE model, measured during moving model tests (Baker, et al., 2001). The displacement thickness is shown on the left and the form parameter is the graph on the right. The x-axis shows normalized time, where T=0 is the point when the train nose passes and T=4 is when the train tail passes.

#### 2.1.1.2.3. Train Underbody

In contrast with the flow over the train roof, there exist ample experimental data for the flow underneath the train. Most of the available data were obtained in recent years, once the issue of 'ballast flight' came to light. These investigations have yielded typical pressure and velocity fields beneath the train, such as those shown in Figure 14 and Figure 15. As is the case with the flow over the top of the train, there is a clear positive pressure peak at the nose in the case of the air flowing underneath the train as well (see Figure 14). The positive peak is followed by a slightly less pronounced negative pressure peak, where after the pressure distribution beneath the train remains fairly constant before it reaches the tail. There are, however, smaller pressure peaks visible along the length of the train, indicating the locations of the bogies and inter-carriage gaps. There is also a slightly more pronounced peak at the point where the two units of the Eurostar are coupled together (at approximately ten units of non-dimensional time). Finally, a clear tail pressure peak is visible as the air exits the underside of the train body. Figure 15 shows the velocity profiles of the air flowing beneath the high speed Korean train (Kwon & Park, 2006). Measurements were made at various distances from the upper rail surface and as might be expected, the velocities are at a minimum at close proximity to the ground ( $z=-20\text{mm}$ ) and increase as they approach the underbody of the train ( $z=180\text{mm}$ ), reaching an astonishing 40 per cent of the train speed at heights of around 0.18m (Baker, 2008). The data reveal a small velocity peak as the train nose passes, where after the magnitude of the velocity increases and thereafter remains approximately constant along the length of the underbody, albeit with visibly large measures of turbulence. These considerable fluctuations in the velocity are, however, to be expected when considering the measure of roughness associated with the underside of the train. Figure 16 shows the vertical and horizontal velocity profiles measured beneath the same Korean train (Kwon & Park, 2006). The vertical velocity measurements reveal a profile that is not typical of a boundary layer; rather it resembles an annular flow profile with an inflection point located between the underbody and the ground. The aforementioned flow profile has also been confirmed by (Ido, et al., 2008), whose test results clearly show the point of inflection. From the horizontal profile it is clear that the velocity is a

maximum at the center line of the track, or train for that matter, and reduces in magnitude towards the outside of the track.

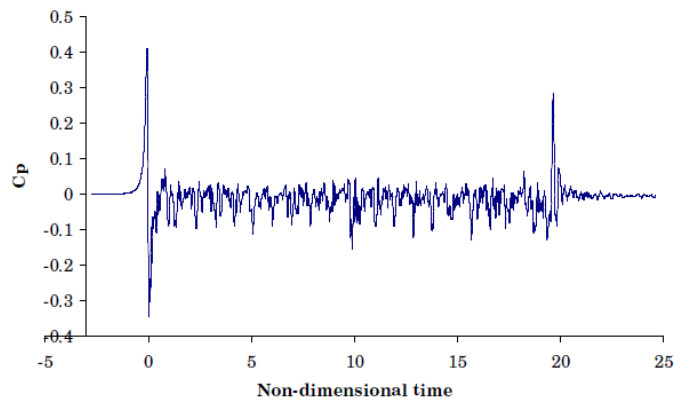


Figure 14: The variation of the pressure coefficient beneath a Eurostar train (Quinn & Hayward, 2008).

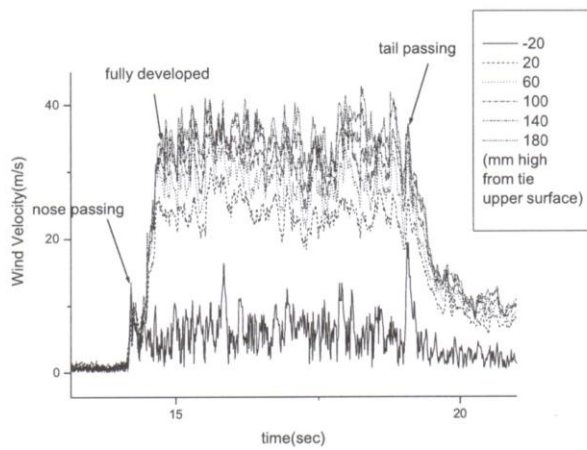


Figure 15: Velocity traces at various distances from the tie upper surface measured beneath Korean high-speed train (Kwon & Park, 2006).

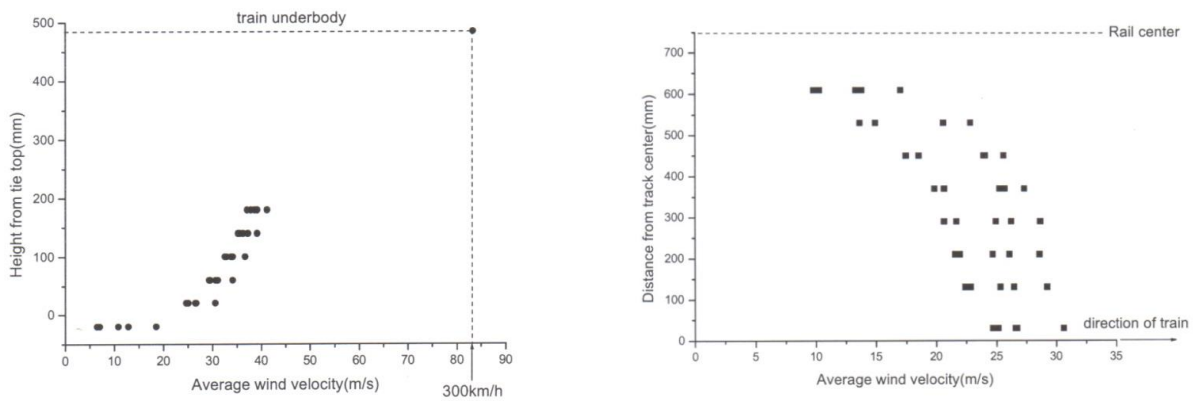


Figure 16: Vertical (left) and horizontal (right) velocity profiles beneath Korean high-speed train (Kwon & Park, 2006).

### **2.1.1.3. The Near Wake Region**

The wake region at the rear of the train is a consequence of flow separation; the boundary layer disperses and the flow is wholly governed by viscous effects. The ensuing flow patterns that govern the near wake region are a function of the specific tail geometry in question. While these patterns may vary, they are typically comprised out of a combination of the following flow mechanisms; shear layer separations, longitudinal helical flows, vortex streets and a separation cavity ( (Vino, et al., 2005), (Sims-Williams, et al., 2001) and (Nouzawa, et al., 1992)). It is interesting to note that the aforementioned behaviours were revealed by experimental studies done on road vehicles. While the shape of the train tail is somewhat different to that of road vehicles, the information obtained through their study can still be applied to trains, albeit slightly nuanced (Baker, 2008). Consider, for example, that since the boundary layer surrounding a train is significantly thicker in comparison with that of an automobile, any separated shear layers will also be much thicker (Baker, 2008). Yet similarities between the wake trailing a train and a car can also be observed; for streamlined trains and fastback cars a pair of longitudinal trailing vortices exists. These vortices generate very high velocities in the train wake (see the wake peaks in Figure 3) and are thus also responsible for low pressures. For blunt ended trains, or squareback cars, the flow separates at the trailing edge of the roof hereby reducing the flow velocity and increasing the base pressure (note the absence of velocity peaks in the wake of Figure 4). Figure 17 shows pressure and velocity measurements made around a model of the streamlined ICE 2 high-speed train (Baker, 2014). There is a clear peak observable in the normalised velocity trace that corresponds to a second minimum in the pressure plot, presumably indicating the existence of a longitudinal trailing vortex. These vortices are also believed to be unsteady as shown computationally by (Schulte-Werning, et al., 2003, 2, pp 332 - 333) and experimentally by (Sterling, et al., 2008) and as such, the approach of ensemble averaging might not be entirely suitable for the analysis of these structures (Baker, 2014). However, despite this inaccuracy inherent in the experimental results, there was good agreement between the Strouhal numbers obtained computationally ( $St = 0.14$ , (Schulte-Werning, et al., 2003, 2, pp 332 -333)) and those obtained experimentally ( $St = 0.11$ , (Sterling, et al., 2008)). Therefore, although a certain measure of accuracy is lost by making use of mean values when considering the flow surrounding a train, especially in the wake region, the loss is not significant.

### **2.1.1.4. The Far Wake Region**

The flow in the far wake of the train, i.e., several vehicle heights removed from the tail, exhibits little pressure variation as well as a gradual decay in velocity. Figure 5 shows the velocities measured at full-scale during the RAPIDE experiments where this behaviour in the far wake is clearly visible (the train is 365m long) (Sterling, et al., 2008). In the case of the velocity trace furthest away from the train, the velocity first increases and then decreases; this is indicative of the lateral spread of the wake before it starts to decay. While in the case of the velocity traces nearest the train, there is simply a steady decay in velocity observable. The aforementioned flow behaviour is also illustrated in Figure 18 for the Velaro S103, for which the nature of the decay was analysed. It was found by (Baker, et al., 2013) that the air velocity in the far wake is proportional to (the distance from the train tail) <sup>$n$</sup> , where the exponent  $n$  was found to be approximately equal to 0.5 for a wide range of trains.

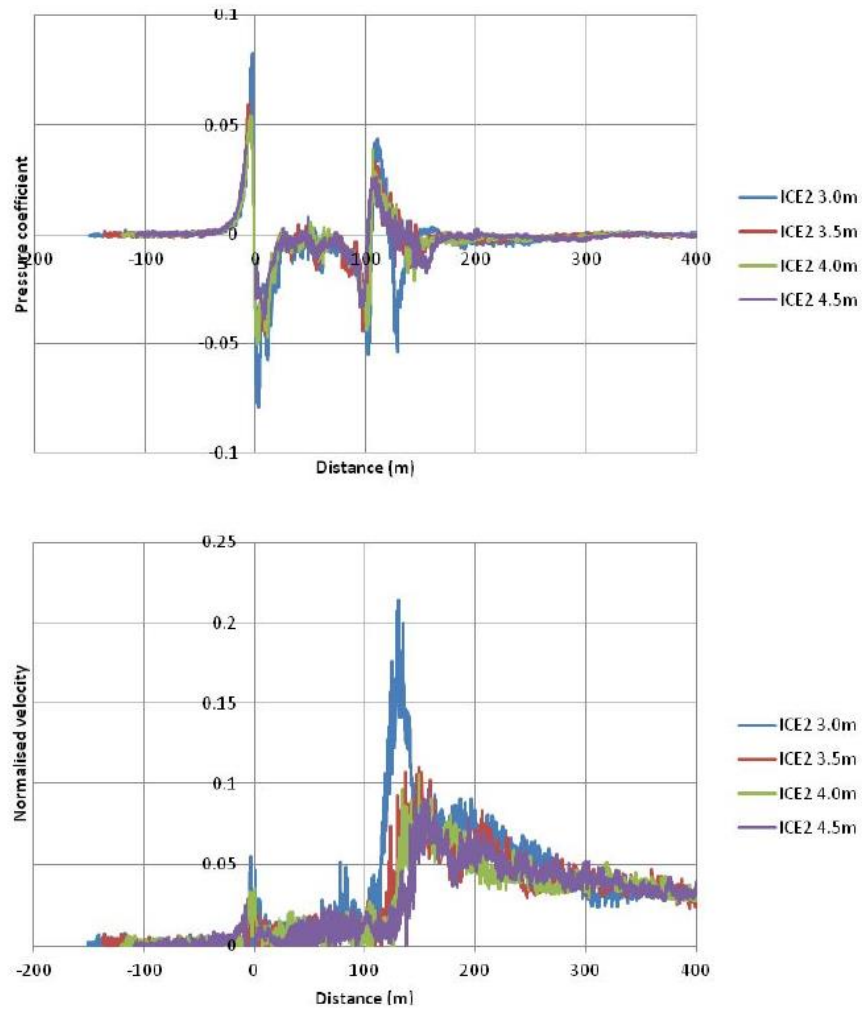


Figure 17: The pressure and slipstream velocity measurements made around a four car ICE-2 train model. The horizontal-axis shows the distance along the train. The vertical-axis shows either the pressure coefficient or the normalised, overall horizontal velocity. Measurements were made at a height of 0.2m above the top of the rail. The legend indicates the respective distances from the track center line (Baker, 2014).

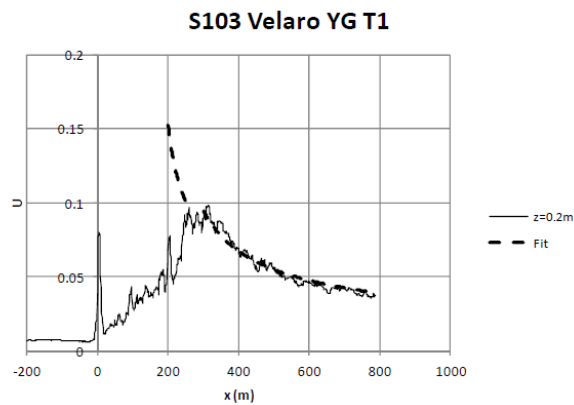


Figure 18: The velocity decay in the wake of the Velaro S103 (Baker, et al., 2013).

## 2.1.2. Cross-wind Conditions

### 2.1.2.1. Natural wind relative to a train

Natural wind that travels over earth has a distinctive boundary layer profile which is extremely thick in comparison to train height. It is a highly turbulent flow and is influenced significantly by the surroundings (city, open field, etc.) and ground condition (roughness). For the simple case of wind travelling over flat ground, its mean velocity profile  $u(z)$  is logarithmic and can be expressed as a function of surface roughness height ( $z_0$ ) and surface friction velocity ( $u_*$ ) (Cook, 1986):

$$u(z) = u_* \ln\left(\frac{z}{z_0}\right) \quad (1)$$

The turbulence intensity of the wind can be expressed as the ratio of the standard deviation  $\sigma(z)$  of the velocity fluctuations at a height  $z$  above the ground and the mean velocity of the wind at that height (Cook, 1986):

$$I = \frac{\sigma(z)}{u(z)} \approx 1/\ln\left(\frac{z}{z_0}\right) \quad (2)$$

According to (Baker, 2014), the scale of turbulence in close ground proximity is not well defined, although it does seem to show a linear variation with height. Likewise, the wind spectrum in close ground proximity is not well defined below heights of approximately five meters and is strongly influenced by local effects. An example of one such an effect is an embankment; as the wind travels over an embankment, the velocity component normal to it speeds up, while the velocity component along the embankment remains unchanged - a phenomenon known as the 'Baker hypothesis'. It is clear then, that under such circumstances the flat ground approximation is unsuitable. When considering crosswinds however, it is prudent to not only consider the wind, but also the wind relative to the train (see the vector diagram in Figure 19). The velocity of the wind relative to the train ( $V$ ) is given by;

$$V^2 = ((u(h) \cos \beta + v)^2 + (u(h) \sin \beta)^2) \quad (3)$$

where  $u(h)$  represents the mean velocity of the wind at some reference height ( $h$ ), usually taken to be three meters. The velocity of the train is represented by  $v$ , while the wind direction is given by  $\beta$ . The yaw angle ( $\psi$ ), that is the angle of the wind relative to the train, is given by;

$$\tan(\psi) = \frac{u(h) \sin \beta}{u(h) \cos \beta + v} \quad (4)$$

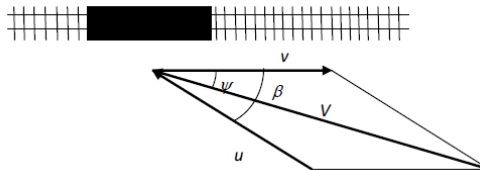


Figure 19: The velocity vector diagram for a train exposed to a crosswind (Baker, 2014).

Figure 20 shows the wind parameters as seen by a train travelling at various speeds ( $v$ ). The graphs were constructed by making use of the expressions discussed above, for a crosswind normal to the track. The

velocity magnitude of the wind at the reference height ( $h = 3m$ ) is  $20m/s$  and the surface roughness height is that of a typical rural upstream fetch ( $z_0 = 0.03m$ ). It is clear that at low train speeds the relative velocity profile assumes a typical boundary layer form, the yaw angle is approximately  $90$  degrees and the turbulence intensity is considerable. In addition, it is evident from Figure 20 that at these low train speeds, the velocity varies significantly across the train height, whereas the velocity across the train height remains approximately uniform for high train speeds. The yaw angle at higher train speeds is smaller and varies over the train height while the effective turbulence intensity is low and has values of the order of a few percent.

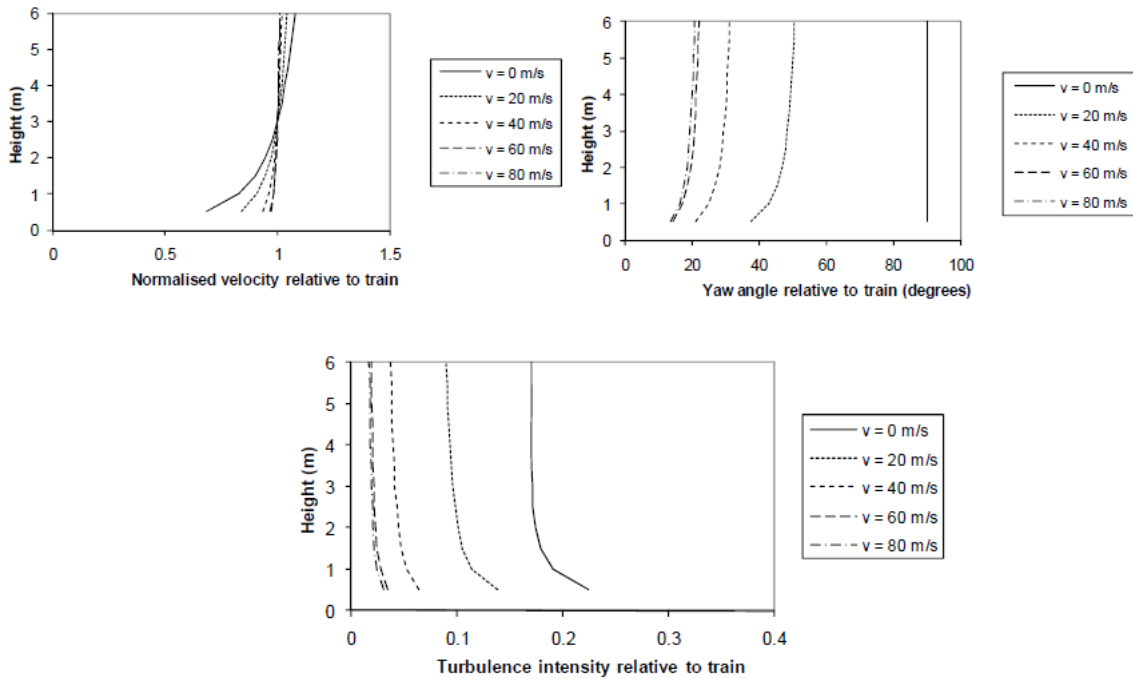


Figure 20: Wind parameters relative to a moving train (Baker, 2010).

### 2.1.2.2. Wake flow structure in cross winds

According to (Baker, 2014) the flow field surrounding a train can be altered in small, yet potentially significant ways, for even small yaw angles ( $0^\circ$  to  $5^\circ$ ). One example of this is that the boundary layer that develops along the train can be skewed, i.e., along the windward side the boundary layer is thinner while the leeward side displays a comparatively thick boundary layer. Measurements made during the AEROTRAIN project also showed the particular sensitivity of the near wake behaviour to the yaw angle (Baker, et al., 2013). Figure 21 shows the large effects even small yaw angle ranges can have on the velocity; this is presumably due to the lateral deflection of the longitudinal vortices to, or away from, the measuring equipment. It is interesting to note that the velocity measured for the yaw angle range  $-1.5^\circ$  to  $-0.5^\circ$ , is much larger when measured at  $1.2m$  above the ground than for  $0.2m$  above it. This may be a consequence of the location of the longitudinal vortices in space; the velocity of the longitudinal vortex increases as the radial distance from the core decreases. As such it is reasonable to hypothesize that the height of the vortex core off the ground is in closer proximity to  $1.2m$  than  $0.2m$ . Early work completed at Cambridge ( (Mair & Stewart, 1985) and (Copley, 1987)) show that for larger yaw angles ( $5^\circ$  to  $40^\circ$ )

longitudinal vortices form along the leeside of streamlined trains. The aforementioned experimental studies revealed the existence of a complex vortex structure along the train (Figure 22), a finding that has been confirmed by CFD studies in recent years (Diedrichs, 2003). It is, however, debatable to what extent these complex vortex structures manifest themselves in natural conditions, which are typically subject to turbulent winds and complex train geometries (rather than the idealized train body used by (Mair & Stewart, 1985) and (Copley, 1987)). For yaw angles larger than  $60^\circ$ , applicable only for slow or stationary trains, the flow field surrounding the train is similar to that of a prism normal to the flow (Baker, 2014). As such, there is large-scale separation at the leeside of the train with some measure of vortex shedding present, although the latter is somewhat inhibited by the influence of the ground (Baker, 2010). These changes in the flow field surrounding a train under crosswind conditions necessarily have an effect on the pressure field around trains as well.

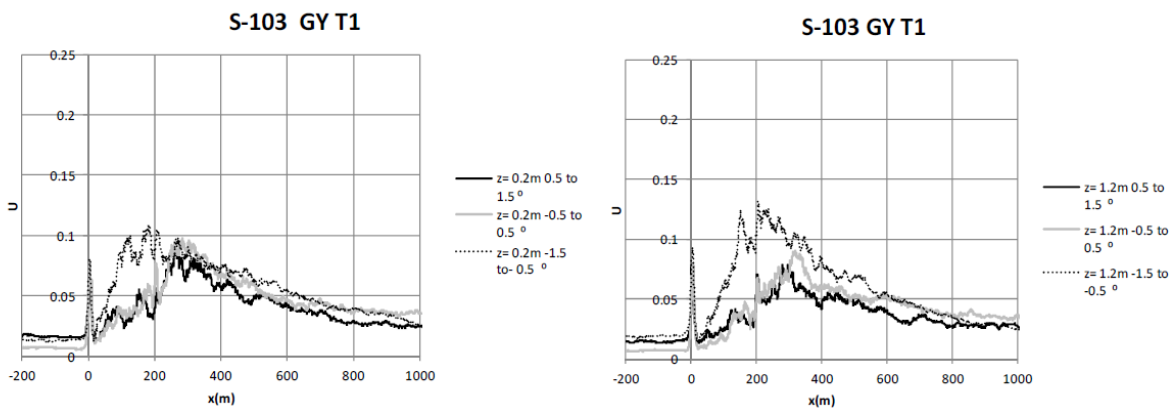


Figure 21: The effect of crosswinds on the ensemble averaged velocities of the Velaro S-103 (Baker, et al., 2013). Left: Velocities measured at 0.2m above the top of the rail. Right: Velocities measured at 1.2m above the top of the rail. The x-axis is distance along the train and the y-axis is the normalised horizontal velocity at different yaw angle ranges.

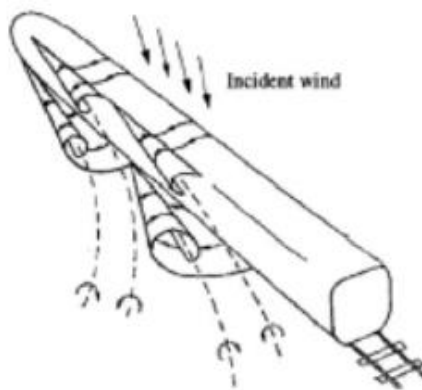


Figure 22: The complex vortex structures that form around an idealized train body ( (Mair & Stewart, 1985) and (Copley, 1987)).

### **2.1.2.3. Pressure distribution in cross winds**

In windless conditions the pressure distribution over a train body is somewhat predictable and can be reasonably described by considering the pressure distribution over the longitudinal symmetry plane of the train. When exposed to a crosswind however, the flow field varies considerably along the length of the train, necessitating the use of multiple sections in order to fully understand the pressure distribution over the body. Pressure measurements made by (Wu, 2004) for a two car ICE 2 model is shown in Figure 23 alongside LES results obtained by (Diedrichs, 2005). In order to effectively describe the flow behaviour, the results are shown for the train's cross-sectional perimeter at six locations, at various distances ( $x$ ) from the nose of the train. This distance ( $x$ ) has been normalised with the train length and the negative pressure coefficient is plotted in the positive  $y$ -direction. For those locations that are in close nose proximity, there is a strong suction peak present on the leeward side, possibly due to the air accelerating as a function of the nose-taper, or longitudinal vortex formation, or both. This suction peak contributes greatly to the side force exerted on the train (Baker, 2008). At those locations further away from the nose, there is a definite suction peak visible at the windward roof corner ( $\theta \approx 315^\circ$ ). Once again, the suction peak is indicative of the air velocity increasing. There are two possible modes that could be responsible for this; firstly Bernoulli's principle says that since the cross-sectional area available to the lateral flow decreases, the lateral velocity over the train roof must increase. Secondly, the static pressure along the train side under crosswind conditions is considerably higher than for windless conditions; a scenario that could very well cause the formation of longitudinal vortices along the windward side of the train roof. For all locations along the train, there is a definite stagnation region visible on the stream-wise face, indicated by the positive pressure coefficient on the windward wall for all instances. It is worth noting that in general the numerical and experimental results show a good level of correlation.

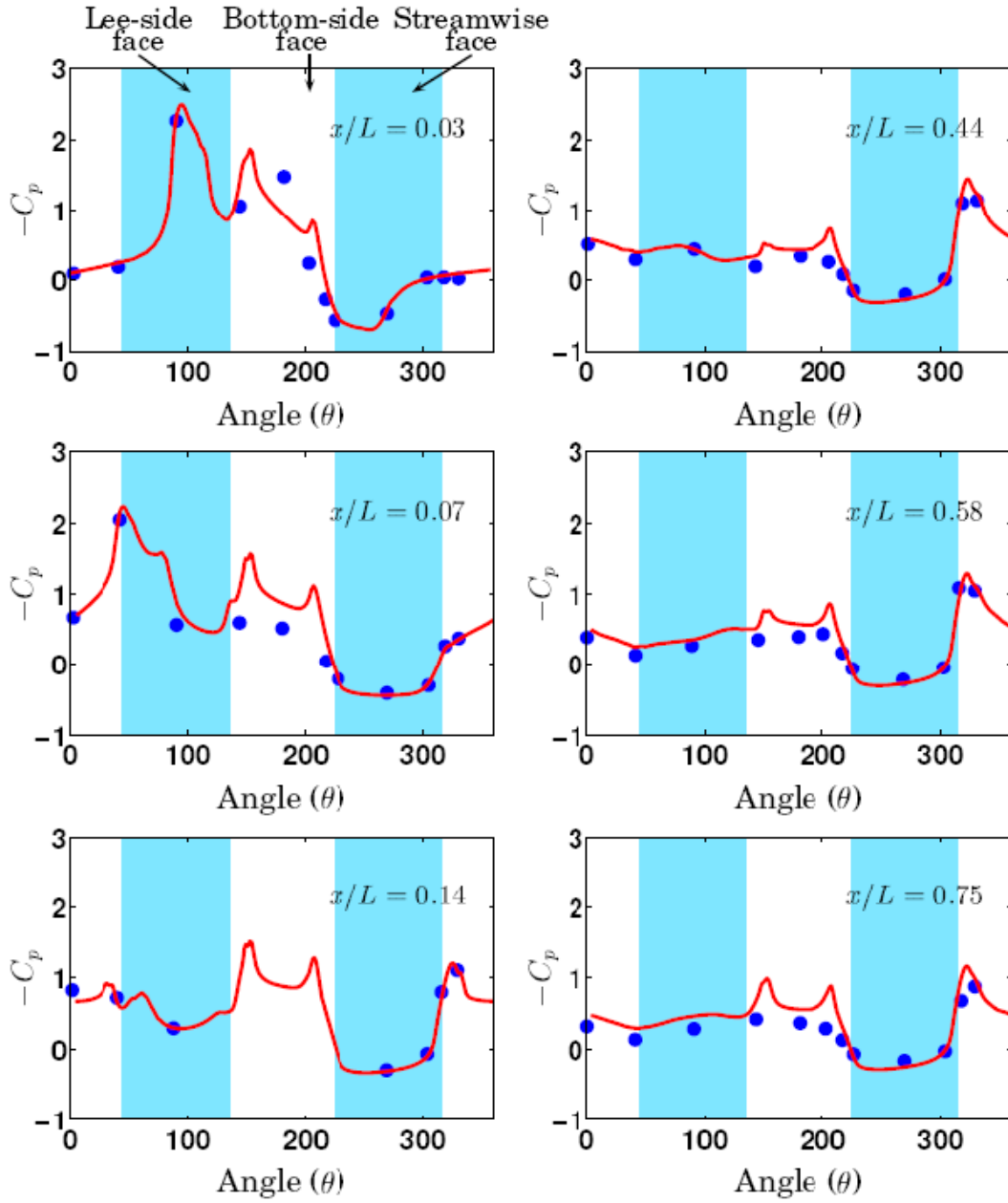


Figure 23: Pressure distribution around a two car ICE model. The lines indicate LES results (Hemida, 2006), the points are experimental values of (Wu, 2004). The front of the windward face is at 270 degrees.

## 2.2. Aerodynamic Challenges in Rail Applications

### 2.2.1. Aerodynamic Drag Force

The total resistance a train offers to motion is important to designers, not only in order to specify the necessary power requirements for the train, but also for the purposes of minimizing energy consumption. The total train resistance is a summation of mechanical resistance terms, air momentum drag and aerodynamic drag and is conventionally expressed by the Davis equation (Rochard & Schmid, 2000). It is well-known that the aerodynamic drag increases with the square of the wind speed, therefore as the train's travelling speed increases, the aerodynamic drag becomes of increasing significance. This tendency becomes clear for conventional passenger trains travelling at speeds greater than 200km/h where the aerodynamic resistance dominates over the mechanical resistance. Furthermore, for trains travelling at 250 km/h the aerodynamic drag contribution is approximately 75 to 80% of the total resistance (Gawthorpe, 1978). Aerodynamic drag can be divided into pressure drag and shear drag, both of which contribute to the total aerodynamic drag of the train in roughly the following ways; the first pressure drag component is caused by the pressure difference across the nose and tail of the train. This drag component is a function of the nose and tail shape, which are in turn defined by parameters such as the length to height ratio of the nose, the measure of streamlining thereof, etc. The second pressure drag component is a consequence of the pressure difference across the bogies and underfloor equipment. As such, it is a function of the train length, since this parameter determines the number of bogies and equipment carried by the train. The final component is shear drag which is a consequence of the friction caused along the train side, roof and underbody as the air flows over it. Shear drag is also the dominant contributor to total drag for passenger trains (Brockie & Baker, 1990) and is a function of the Reynolds number based on the length and overall 'roughness' of the train. It is therefore clear from the aforementioned, that the total drag coefficient is most strongly influenced by the train length. For a fixed train length it is, however, possible to reduce the drag coefficient. The possible ways in which this may be accomplished for trains in the open air, in windless conditions, are;

1. Streamlining the nose and tail. However, the drag component contributed by the nose and tail of most trains is comparatively small, with the largest contributor being the shear drag along the length of the train body. It was also found that the law of diminishing returns applies for the streamlining of the nose, where further streamlining beyond a certain point no longer yields significant drag reductions (Baker, 2014). Japanese investigators found that increasing the length to height ratio of the nose (or tail) beyond two has a negligible impact on drag (Raghunathan, et al., 2002). The extreme streamlining seen on high-speed trains in recent years is for the purpose of diminishing the pressure transients in the open air and in tunnels (Baker, 2014). Furthermore, by ensuring the flow over the nose remains as attached as possible, the flow along the remainder of the train body will be smoother and consequently the friction reduced.
2. Ensuring the surface of the train is as smooth and uniform as possible. This includes the detail design of door handles, inter-car gaps etc. as well as a general attempt to minimize the number of protuberances along the train (Baker, 2014).

- Fairing the train underbody. By fairing the underbody of the train as far as is practically possible, not only is the surface roughness (and consequently the friction drag) reduced, but the separation of flow around the bogies is also reduced.

The aforementioned recommendations are applicable for trains travelling through open air, in windless conditions. In reality however, still air conditions rarely occur and there is usually a crosswind present, which affects the drag coefficient. Figure 24 shows the variation of the drag coefficient with yaw angle for a container train (Beagles & Fletcher, 2012). For small yaw angles the drag coefficient may be expressed as;

$$C_D = C_{D,\psi=0}(1 + \alpha\psi) \quad (5)$$

where  $C_{D,\psi=0}$  is the drag coefficient at zero yaw and  $\psi$ , is the yaw angle in radians. The values of  $\alpha$  may vary from 0.5 to 1. From Figure 24, it is clear that the drag coefficient initially increases with yaw angle, reaching a maximum between 30° to 40° (depending on the container configuration), where after it decreases and finally stabilizes. The largest yaw angle therefore doesn't necessarily imply the largest drag experienced by the train. It is also clear, that the smaller the inter-container (or inter-body) gaps, the less the drag experienced by the train. This effect is broadly speaking exacerbated by an increase in yaw angle. Clearly then, ensuring the inter-carriage gaps are as small as possible, is advisable for crosswind conditions. In fact, (Gawthorpe, 1978) estimated that crosswinds can add around 10% to the total aerodynamic drag of a train travelling in typical UK weather conditions. Clearly then, crosswinds are of considerable importance when considering aerodynamic drag.

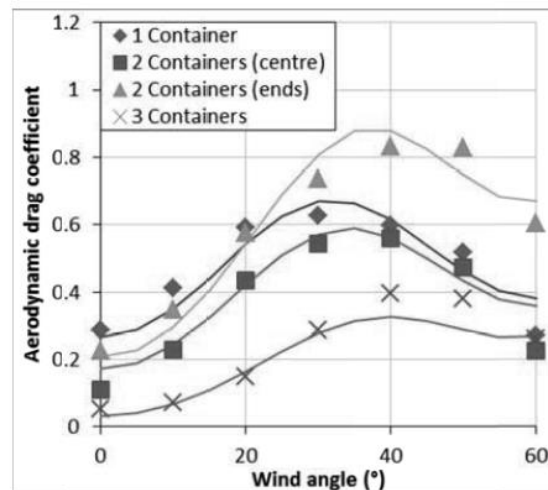


Figure 24: The variation of the drag coefficient with yaw angle, for various container configurations in the case of container trains (Beagles & Fletcher, 2012). Various numbers, as well as configurations of containers are illustrated. One container is in the center of the wagon (with gaps at either end) and the maximum number of containers the wagon can hold is three.

### 2.2.2. Crosswind Stability

Crosswinds are responsible for many concerns in the rail industry; excessive lateral forces on tracks (Andersson, et al., 2004), gauge infringements due to excessive displacement (O'Neil, 2008), dewirement of pantographs (Bouferrouk, et al., n.d.) and the overturning of trains. In this section

attention will be paid to the latter concern, which is certainly most serious due to the devastating consequences of train derailment (see (East Japan Railway Company, 2006) & (China Daily, 2007), as examples). While train derailment is not a new occurrence, one of the first reported incidences dates back to 1903, it has become of increasing importance since the advent of high speed rail (Baker, 2014). In Europe, the TSI requires the stability of trains travelling in excess of 160 km/h to be assessed under crosswind conditions (TSI, 2008/232/EC). The methodology that ought to be followed when doing so is given by the CEN code (CEN, 2010). This process yields the crosswind characteristic of the train in question as the deliverable, which is essentially a graph of the wind gust speed at which an accident will occur plotted against train speed and wind direction (Baker, 2014). Since this process does however, take the vehicle dynamics of the train into consideration as well, it lies outside the scope of this document and has only been mentioned for the sake of completeness. Rather, this document concerns itself with the aerodynamic characteristics of the train which in turn serves as an input to the aforementioned methodology.

A train exposed to crosswind conditions is subjected to three aerodynamic forces, i.e., drag, side and lift forces, which work along the x-, y- and z-axes respectively. These forces in turn also cause the following moments to act upon the train; the rolling moment about the x-axis, the pitching moment about the y-axis and the yawing moment about the z-axis. In order to obtain values for the aforementioned, either experimental procedures (e.g., wind tunnel tests) or numerical analyses (e.g., CFD) may be utilized (Baker, 2014). Both of these methods rely on the use of models, which can range from simple to complex, depending on what scenario is being analyzed or which phenomena are of importance. Consider for example, a simple approach commonly used for the analysis of high-speed trains which makes use of a stationary train model mounted on a representation of the track (Baker, 2014). The response of the train to various wind directions is studied by simply turning the model with respect to the incoming air, hereby varying the yaw angle. Clearly then, this approach does not take into consideration either the effects of the motion of the train relative to the ground, or the effects of atmospheric turbulence and shear. However, as discussed above (see Figure 20), the nature of the flow experienced by the train tends to an essentially steady flow wind at a small yaw angle, as the train's travelling speed increases (Baker, 2014). Thus, while the aforementioned modelling approach may be simple it remains quite valid for high-speed trains. Not so for low speed or stationary trains, rather for studies pertaining to these travelling conditions, the atmospheric turbulence and shear ought to be modelled (Baker, 2014). Finally, modelling decisions with respect to the ground representation must be made. Some standard configurations that are used include; flat ground, single track ballasted rail (STBR) (see Figure 25) and double track ballasted rail (DTBR) representations etc., although CEN (CEN, 2010) has adopted STBR. The ground can either be stationary or can be assigned movement, hereby taking into account the relative motion between the train and it. While it is very complex to accomplish this for experimental procedures (Dorigati, 2013), it is simpler to do for CFD simulations; the floor of the computational domain is assigned a 'moving wall' boundary condition.

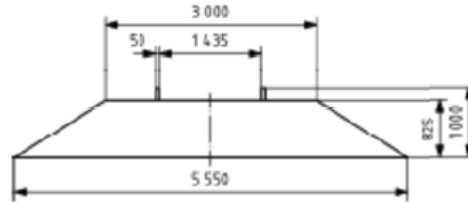


Figure 25: A lateral cross-section of a single track, ballasted rail configuration that is used for simulation in wind tunnel tests (CEN, 2010), is shown here on the yz-plane as per the document configuration.

A comparison of the side and lift coefficients at various yaw angles are shown in Figure 26 for the ICE3, TGV Duplex and ETR500 (CEN, 2010). The results were obtained from low turbulence wind tunnel tests and by making use of the standard ground configuration, i.e., STBR. All forces were normalized by  $0.5\rho AV^2$ , where  $A$  is the reference area, conventionally taken to be  $10m^2$  and where  $V$  is the wind velocity relative to the train. For yaw angles ranging from  $0^\circ$  to approximately  $40^\circ$ , both the side and lift coefficients increase, until ultimately reaching a maximum in the vicinity of  $40^\circ$ . Hereafter, both coefficients decrease with increasing yaw angle until approximately  $70^\circ$ . A further increase in yaw angle beyond this point does not seem to influence the coefficients significantly. It would thus appear, that the side and lift coefficients obtained experimentally, confirm the type of external flow field that exists at a given yaw angle range (discussed above); for yaw angles below approximately  $40^\circ$ , longitudinal vortices form on the leeside of the train body. As the yaw angle increases, the vortices develop and as such the side and lift coefficients increase. For yaw angles greater than roughly  $70^\circ$ , the flow field resembles that of a prism perpendicular to oncoming flow, i.e., large measures of leeside separation; consequently there are no significant changes to the coefficients. Finally, for the range of angles between roughly  $40^\circ$  and  $70^\circ$ , the flow is transitioning between regions. The general behaviour of the coefficients against yaw angle, as shown in Figure 26, typically remains unchanged for various types of trains (Baker, 2014). The only exception is that not all train types show the decrease at high yaw angles.

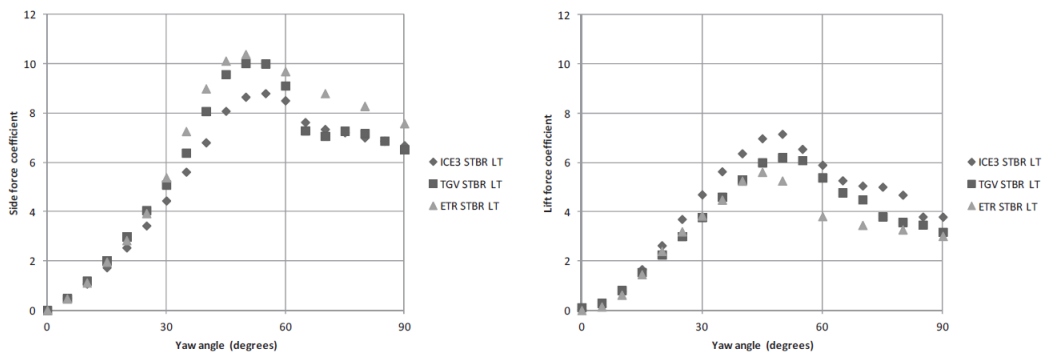


Figure 26: The side and lift coefficients for the ICE3, TGV duplex and ETR500 at varying yaw angle (CEN, 2010). The horizontal-axis indicates the yaw angle. The vertical-axis indicated the side and lift coefficient values.

The lift and side force coefficients discussed above are important parameters to consider during train design, e.g., negative lift is undesirable since it exacerbates rail wear, while a too large lift coefficient is dangerous, since it may cause derailment (especially in the case of the trailing vehicle). According to (Baker, 2014) however, the rolling moment coefficient about the leeside rail (tipping point) is most

important when addressing the overturning of a train. The largest contributors to this coefficient are the side and lift forces which cause a moment about the leese side rail and while the rolling moment about the x-axis also contributes, its influence is comparatively small. Studies pertaining to the side force, lift force and leese side rolling moment coefficients over a range of yaw angles, for different train types were completed by (Baker, 2014) and (Baker, 2011). It was found that when the aforementioned coefficients for each train were normalized by their values at 40°, the data collapsed onto a single curve in the low yaw angle range (the range of importance for high-speed trains) irrespective of train type (see Figure 27). This behaviour allows for an easy parametrization of these curves (Baker, 2014);

$$\frac{C_{RL}(\psi)}{C_{RL}(40^\circ)} = \left( \frac{\sin(\psi)}{\sin(40^\circ)} \right)^n \quad (6)$$

where 'n' is equal to 1.2 for non-streamlined leading vehicles, 1.5 for streamlined passenger trains and 1.7 for trailing vehicles.

The final topic that will be addressed in this section is the matter of the wind field that can be applied to a train, with the available methodologies varying in complexity. The simplest approach available has already been discussed above (reference discussion pertaining to Figure 20). It essentially specifies a wind profile and turbulence intensity based on parameters such as surface roughness. A more complex approach which is recommended by CEN (CEN, 2010) is known as the Chinese hat gust (see Figure 28). While it was originally developed as a time dependent gust for wind loading studies on wind turbines, it has been transformed for rail purposes into a spatially varying gust through which the train passes. This approach has been criticized by (Baker, 2014) as being theoretically unsound as well as unjustified. Rather, (Baker, 2014) recommends a gust that varies with both time and space. Lastly, the stochastic wind field is the most complex available formulation. It may also be used in conjunction with an aerodynamic admittance which allows for the non-correlation of turbulence along the train side (Baker, 2014). Irrespective of the wind field chosen, by following the approach recommended by CEN (CEN, 2010), the crosswind characteristics of any given train may be obtained (see Figure 29). As might be expected, an increase in the travel speed of the train shows a decrease in the wind speed required for an accident to occur.

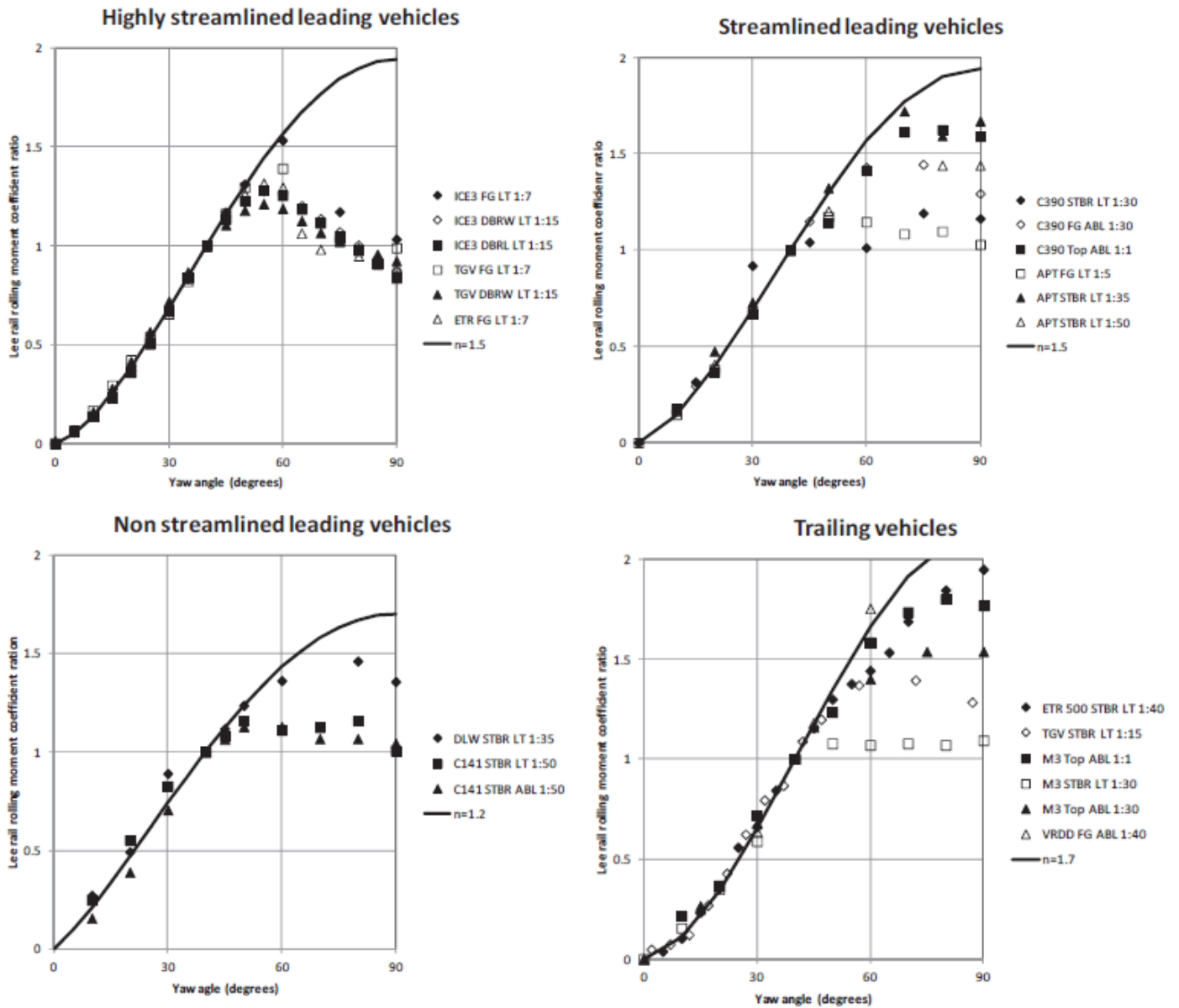


Figure 27: The parameterization of lee rail rolling moment coefficients for various types of trains (Baker, 2014). Ground simulation types indicated by; STBR – single track ballasted rail. DBRW – double ballasted rail windward. DBRL – double ballasted rail leeward. FG – flat ground. Wind simulation type; LT – low turbulence. ABL – atmospheric boundary layer. Source data given by (Baker, 2011).

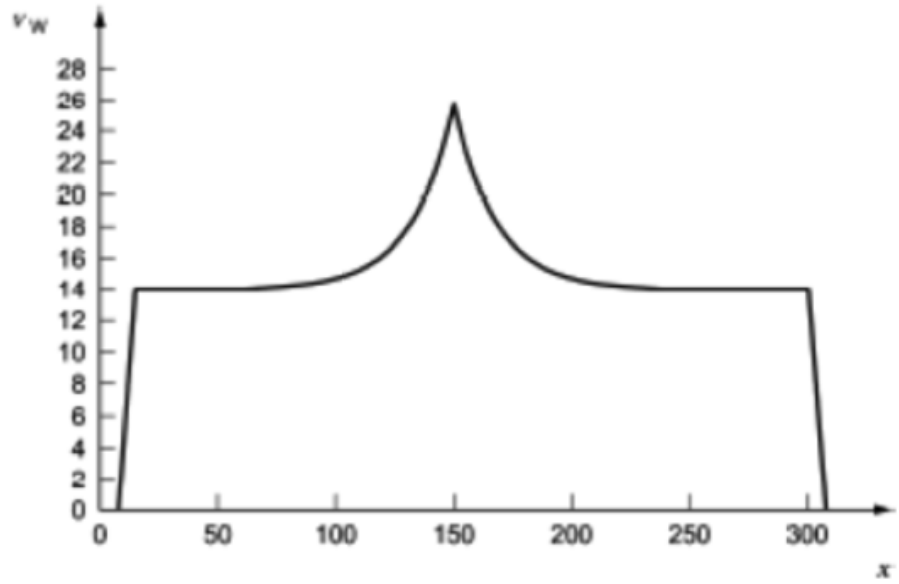


Figure 28: The Chinese hat wind gust profile (CEN, 2010).

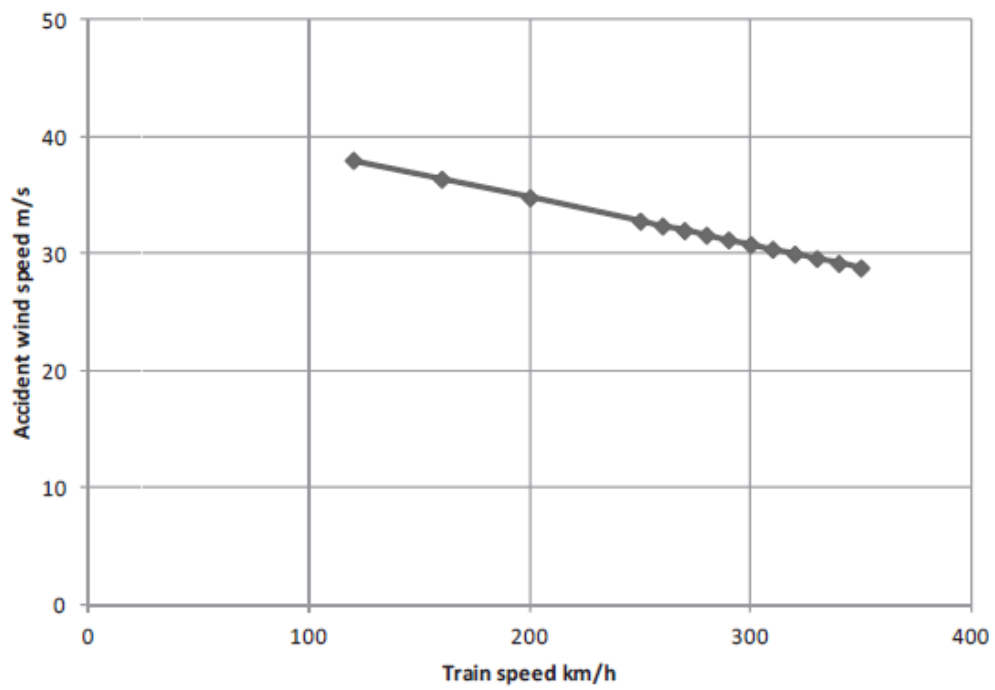


Figure 29: The crosswind characteristics obtained for a Class 1 vehicle by making use of the Chinese hat gust (CEN, 2010).

### 2.2.3. Other Challenges

In this section, a brief overview will be given of the most pressing aerodynamic problems facing the rail industry at present in addition to the aerodynamic drag and crosswind effects as discussed above. Some other important issues that will not be discussed here include airborne particles in the vicinity of the railway line (see (Ferreira & Vaz, 2004) and (Gustafsson, et al., n.d.)), pantograph 'dewirement' (see (Johnson , 2013)), gauge infringement due to high crosswinds (see (Baker, et al., 2009) & (Andersson, et al., 2004)) and the effect of the train flow field on birds and small animals in close proximity (see (Baker, 2014)).

#### 2.2.3.1. Pressure Loads Exerted on Nearby Bodies

The pressure field that is generated by the relative motion between a train and the surrounding air can be considerable, especially in the vicinity of the nose and tail which are accompanied by large (positive) pressure and suction peaks respectively. Consequently, a body that is subjected to a passing train, experiences a pressure loading which is defined from peak-to-peak, i.e., nose peak to tail peak of the moving train (see Figure 30, (Baker, et al., 2012)). Repeated loading on structures can cause fatigue failure, while trains passing one another can cause significant displacement on the suspension system which leads to passenger discomfort (Baker, 2014).

Studies done by (Baker, et al., 2012) and (Baker, et al., 2012) considered the effect of different types of trains passing various trackside structures. The trains in question varied from blunt to streamline and the results of the study can be seen in Figure 31. As is expected from the pressure and velocity fields discussed above, the freight locomotive exerts the largest pressure load on the hoardings and the streamlined train, the smallest. The characteristic form of the pressure load exerted by all three trains is, however, broadly speaking similar and has been parameterized by (Sanz-Andres, et al., 2004). The influence of nose length on the loading experienced by trains passing one another was investigated by (Johnson & Dalley, 2002). The results of this study are shown in Figure 32 and as is expected, the blunter the nose of the train is, the larger the pressure load exerted on the train it is passing. The study further showed, that as the track spacing between the passing trains increase, the pressure load decreases. Data such as this therefore not only allows acceptable track-spacing to be determined when building new lines, but also justifies the streamlining of train noses.

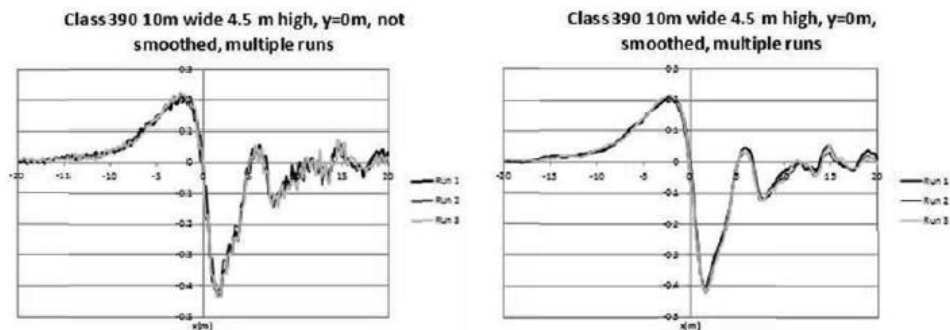


Figure 30: The effect of smoothing the data obtained from multiple runs for the pressure coefficient distribution of the Class 390 train passing an overbridge (Baker, et al., 2012). The horizontal-axis indicates the train's position relative to the bridge and the vertical-axis indicates the pressure coefficient.

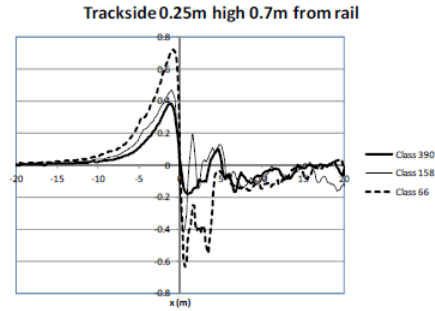


Figure 31: The pressure coefficient distribution measured on trackside hoardings during the passage of different train types (Baker, et al., 2012) and (Baker, et al., 2012). The horizontal-axis indicates the position of the train nose relative to the measurement position and the vertical-axis indicates the pressure coefficient.

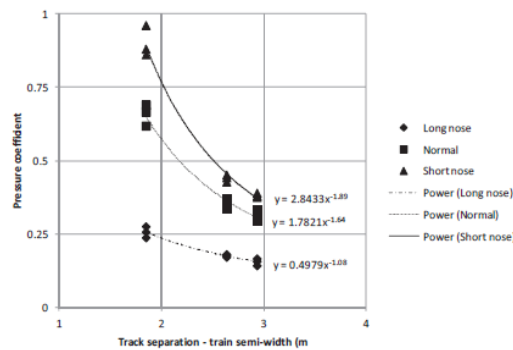


Figure 32: Peak-to-peak pressure coefficients measured on an ETR 500 caused by the passing of another ETR 500, with variable nose shape (Johnson & Dalley, 2002). The horizontal-axis indicates track separation (minus train half width). The vertical-axis indicates the peak-to-peak pressure coefficients.

### 2.2.3.2. Slipstream Effects

The boundary layer and wake regions of trains are associated with considerable air velocities, the magnitude of which is such that the question of the safety of people in close proximity to the train arises. Incidents have been reported of slipstreams displacing pushchairs towards the train, minor injuries caused to members of the public and some people nearly being swept of their feet (Temple & Johnson, 2003). Since the air velocity of slipstreams is proportional to the train velocity, an increase in train speed will necessarily exacerbate the effects of slipstreams. It is therefore prudent to assess the slipstream risk.

The underlying concept of the method proposed by the CEN (CEN, n.d.) and TSI (TSI, 2008/232/EC) codes to do this, is determining the characteristic velocity of a given train, which is defined as the mean plus two standard deviations of the gust values. Once this characteristic value has been obtained, it is compared to limit velocities which vary from code to code, e.g., TSI (TSI, 2008/232/EC) limits are given as 22m/s for trackside positions and 15.5m/s for platform positions. The typical characteristic velocity normalized by train speed for a non-streamlined train is 0.25 to 0.3, which is considerably higher than the 0.15 to 0.2 which is associated with a streamlined train (Baker, 2014). The location at which the gust maxima for streamlined and non-streamlined trains occur also varies; the maximum gust occurs in the near wake region for the former, whereas it occurs in the nose region for the latter (see Figure 33).

However, simply quantifying the gust and specifying its general location does not address the matter of the gust's effect on people in close proximity thereof. Studies on the response of real individuals exposed to various wind gusts were conducted by (Jordan, et al., 2008) by making use of large scale wind-tunnel tests. The data obtained allowed for the cumulative distribution of the probability of human instability to be determined for various gusts (see Figure 34). The results show that females are more susceptible to gusts than males and that the orientation of the individual with respect to the gust has an influence on their stability. Furthermore, the results show that the characteristic velocity limits deemed as acceptable by the TSI is too great, considering the rather large percentage of people displaced at these velocities.

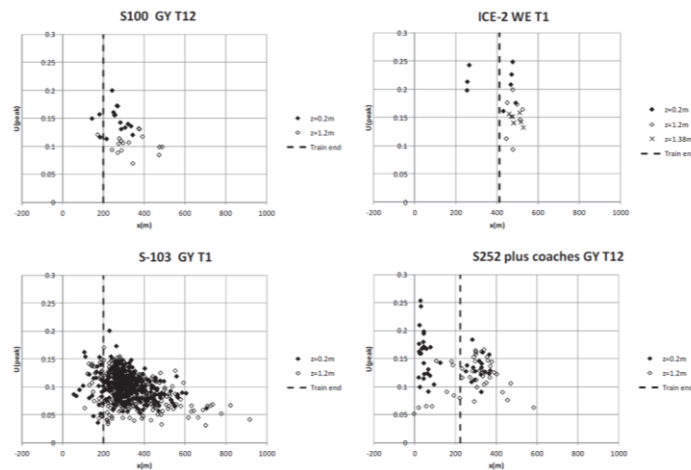


Figure 33: The Gust positions and magnitudes for representative train types from the AeroTRAIN experiments (Baker, et al., 2013). The x-axis indicates the position of the measurement point of the peak velocity relative to the train nose. The y-axis indicates the normalized TSI (TSI, 2008/232/EC) velocity.

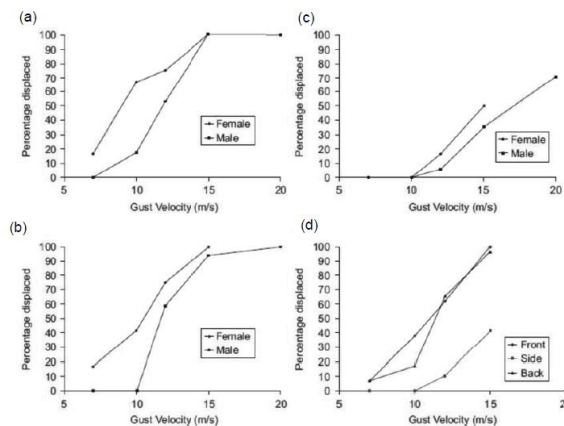


Figure 34: The cumulative distribution of the probability of human instability when exposed to sharp edged gusts (Jordan, et al., 2008). The horizontal-axis indicates the velocity of a gust produced in the wind tunnel. The vertical-axis indicates the percentage of displaced individuals. The results for males and females are shown separately. The following orientations of the subjects with respect to the wind was considered; a) Facing the oncoming wind, b) back to oncoming wind, c) side to oncoming wind, d) both genders.

### **2.2.3.3. Ballast Flight**

The phenomenon of ballast flight may be described as the ballast particles on the track becoming airborne, where after they could collide with the underbody of the train, hereby causing serious damage. Furthermore, the particles could also be lifted onto the track, where a passing wheel could crush them, leading to damage to both the wheel as well as the track. This will, in turn, increase the required wheel maintenance. According to (Baker, 2014) ballast flight has been a problem for many years, but as the travelling speed of trains have increased (and continues to do so) in recent years, the effects of flying ballast have been exacerbated also. Therefore the cause of ballast flight is clearly related to aerodynamic effects, although it is not the only contributing factor (Baker, 2014). There are usually three physical effects at play, these are; the suction peaks at the nose and rear of the train, the shear stresses due to the velocity of the air travelling beneath the train and the vibration between the wheelsets and the rails, which loosens the ballast.

Once the ballast has started moving, the particles can either continue creeping down the track, or should they gain sufficient energy, they will start “flying”. In order to determine the path of the flying ballast particles (Quinn , et al., 2010) made use of a formulation that is used to investigate the flight of wind borne debris during storms; the velocity profile of the air beneath the train serves as input to the three dimensional equations of motion for the flight of particles. The results of the work completed by (Quinn , et al., 2010) showed that it is entirely plausible for the flying ballast to impact the underbody of the train or the rail under the right circumstances. Furthermore, numerical measurements completed on ballast flight revealed that while shear stress acting on the particles causes a low and flat flight path, should the particles impact one another, considerable ballast motion could ensue, leading to higher, more destructive flight paths (Baker, 2014).

### **2.2.3.4. Train-Tunnel Interaction**

The entry of a train into a tunnel is associated with large pressure transients, which have implications on passenger comfort, the micro pressure waves at the tunnel exit and the structural integrity of the train nose. In order to ensure passenger comfort, limits are imposed on the pressure transients. These limits vary based on whether the train in question is sealed or unsealed, with the majority of modern high-speed trains being sealed (see for example, CEN (CEN, 2010)). The degree to which trains are considered as being sealed is determined by a leakage time constant, which is less than 0.5s for unsealed trains (Baker, 2014).

Micro-pressure waves, otherwise known as sonic booms, which occur when high-speed trains exit tunnels can frighten passengers, disturb nearby residents and possibly cause damage to trains and tunnel structures. The curious reader may turn to (Vardy, 2008) for further information on this matter. There are a few methods available to reduce the magnitude of the pressure wave at the tunnel exit. The modification of the tunnel entrance is one such way, which entails a decreasing cross-sectional area of the inlet. In so doing the gradient of the initial pressure wave is decreased as well, consequently reducing the gradient of the emitted wave. Another available method is to lengthen the train nose (Baker, 2014). Active devices may also be employed (Vardy, 2008); anti-noise generation can counteract the sonic boom, while releasing large quantities of air disrupts the pressure rise in a passing wave.

### 2.3. Previous Work Completed on Nose Optimization

S. Krajnović optimized the front shape of a generic train for drag and crosswind stability which were expressed in his work by the drag, lift and side force coefficients. The model geometry was modified by making use of control points specified on the body surface (CAD based modification), rather than using morphing tools which make changes to the body grid. A description of the geometry and the associated design constraints are given in (Krajnović, 2008). Krajnović considered a yaw angle of  $30^\circ$  used in conjunction with a full model and a constant velocity of 64.7m/s. This study found that while a short front and small measure of roundedness of the train nose was advantageous for reducing the lift force coefficient, this combination produces maximum drag and side force coefficients. Conversely a maximum nose length and roundedness produced minimal drag and side force coefficients but a maximal lift force coefficient. Krajnović's study thus indicates that a long, well-rounded nose is best for high-speed trains since it not only allows for savings in energy consumption but also ensures greater cross-wind stability.

Work completed by (Ming, et al., 2016) considered the multi-objective optimization of the head shape of a high-speed train for aerodynamic drag and noise. The parameters that were identified to be varied were the nose tip height, '*n<sub>scale</sub>*', expansion amount of the control points on the cowcatcher, '*deltax*', and the inclination angle of the bogie region baffle, '*theta*' (see (Ming, et al., 2016)). These parameters were varied within the CAD software in order to generate various head geometries for the symmetry model of the train utilized by the study. The study found that a positive correlation existed between *n<sub>scale</sub>* and both the aerodynamic resistance as well as the surface sound power level. It was further found that the correlation between *deltax* and the drag force was negative, while that of *deltax* and the surface sound power level was positive. Finally, an increase in *theta* increased the drag, while a decrease in *theta*, reduced the sound power level.

Work completed by (Monnoyer, et al., 2006) investigated not only the optimal nose shape for the purposes of drag reduction, but also the feasibility of conducting the optimization process by making use of a two-dimensional model, hereby saving on computational expense. The train model that was considered for both the two- as well as the three-dimensional case was exposed to a uniform incoming air velocity of 30m/s. The geometry was modified by varying four control points which essentially affected the nose sharpness, curvature and global shape of the profile (see (Monnoyer, et al., 2006) for a more detailed description). The two-dimensional model yielded a blunt-nose with a steep windshield as the optimal solution, while a slender nose had an adverse effect on drag reduction. However when the three-dimensional model was considered a slender nose shape was shown to be best, since the nose with the steep windshield allows more air to flow in from the sides of the train hereby feeding the vortices which produce a larger wake and consequently increase the drag. It is thus clear from this study that it is imperative to consider a full three-dimensional model when optimizing for train geometry due to the three-dimensional flow effects that necessarily accompany it.

A study conducted by (Li, et al., 2016) considered the multi-objective optimization of the CRH2 high-speed train head using the free-form deformation method, which modifies the train geometry by modifying the grid. According to (Tain, 2007) 75% of the total resistance of a high-speed train travelling at 300 km/h under windless conditions is comprised of aerodynamic drag. It is this consideration that (Li,

et al., 2016) cites as their motivation for the minimization of drag as their one objective, while the other is to keep the lift force relatively small; a negative lift exacerbates rail wear while a positive lift force increases vehicle instability. Five design variables were chosen to parametrize the nose shape, these are; window height, window edge height, nose length and height as well as the cowcatcher length. Their study revealed that there exists an approximately linear, positive correlation between the drag force and the window height, window-edge height and nose height. The primary influencing factor on the drag force was however determined to be the nose length which displayed a large reduction in drag for a slight increase in nose length. With regard to the lift force it was found that it remains relatively insensitive to changes in the window height, window-edge height and cowcatcher length. It was further shown that an increase in nose length reduces the lift force, while an increase in nose height reduces the lift force acting on the tail. Ultimately the optimal model showed a decrease in the cab window height, a forward motion of the nose, an increase in window edge height as well as the height of the train nose and an elongation of the cowcatcher. Generally speaking it was found that a reduction in the drag force leads to an increase in the lift force.

A similar yet parametric approach to the study conducted by (Li, et al., 2016) was followed by (Shuanbao, et al., 2014) who simultaneously optimized for the shape of the nose and tail of the CRH380A high-speed train, taking the lift force of the trailing car and the volume of the head as the objective functions. Their study yielded a streamlined head of similar volume to the original, while simultaneously ensuring a reduction of 27.86% in the lift force of the tail and a 3.34% reduction in the total drag under windless conditions. Under crosswind conditions the reduction of the lift force acting on the tail is 5.43%, the side force acting on the train reduces by 72.09% while the drag decreases by 2.1%.

## 2.4. Influential Geometric Parameters

It is important to note that while the discussion conducted in section 2.4.1 and section 2.4.2 below, mostly concerns road vehicles it is applicable to trains as well.

### 2.4.1. Nose

Broadly speaking it is desirable to prevent flow separation from occurring in order to reduce the aerodynamic drag. Although factors such as the fraction of air that passes over the vehicle relative to the fraction of flow that passes underneath it play a part as well. There are a number of parameters, which will be discussed in greater detail below, which can influence the flow of air over the nose of a vehicle; the position of the stagnation point ( $Z_s$ ), the inclination angle of the hood ( $\alpha$ ), the rake angle of the windshield ( $\gamma$ ) as well as the lateral taper of the nose ( $\delta$ ).

Research done by (Buchheim, et al., 1981) showed that for any given vehicle there is an optimum location for the stagnation point, at which a minimum drag coefficient is obtained (see Figure 35). This optimal location varies based on the specific vehicle in question since it is influenced by factors such as the vehicle shape and the design of its underside. However, the general rule that a lower stagnation point yields a lower drag, usually applies. Another parameter of importance is the inclination angle of the engine hood; (Carr, 1968/9) showed that by sloping the bonnet, the drag coefficient is reduced. It is

however clear from Figure 36 that once the inclination angle is such that the flow remains attached, sloping the hood further does not result in additional drag reduction.

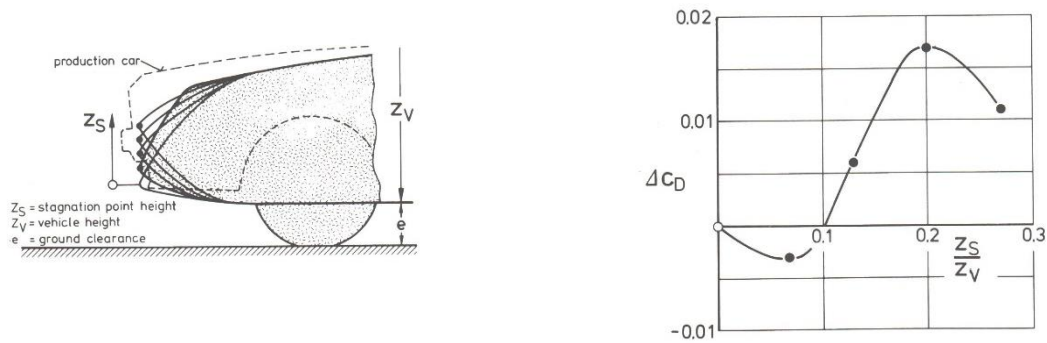


Figure 35: The change in the drag coefficient of a vehicle plotted against the height of the stagnation point of that vehicle (Buchheim, et al., 1981).

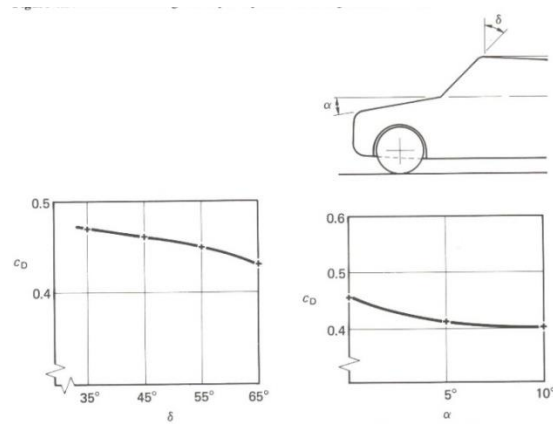


Figure 36: The variation of the drag force coefficient with the bonnet slope ( $\alpha$ ) and the rake angle of the windshield ( $\delta$ ) (Carr, 1968/9).

The air flowing over the nose of a road vehicle typically separates at some point on the hood where after it reattaches itself further downstream somewhere on the windshield. Studies completed by (Scibor-Rylski, 1984) investigated the locations of the aforementioned separation and reattachment points as a function of the windshield rake angle (see Figure 37) in the case of non-convex (flat) windshields; these windshields yield larger separation bubbles than their laterally curved counterparts which exist in practice (Hucho, 1986). It is clear from the figure that an increase in the rake angle ( $\delta$ ) moves the location of the separation point (point S) further upstream, while the location of the reattachment point (point R) moves further downstream. Figure 37 shows the results for the longitudinal midsection, for sections that lie outboard of the midsection however, points S and R move closer to one another. Furthermore (Scibor-Rylski, 1984) found that as the rake angle decreases (as defined in Figure 37), so does the aerodynamic drag; a phenomenon which has been confirmed by numerous authors including (Lay, 1933) and (Carr, 1968/9) (see Figure 36). The aforementioned findings are further illustrated in Figure 38, which shows the experimental results obtained by (Buchheim, et al., 1979) for the VW 200 research vehicle. It is clear then from the data published in Figure 36 and Figure 38, that the direct effect of the rake angle of the windshield on drag reduction is moderate. If, however,

the rake angle is such that the flow is routed over the vehicle its effect becomes more significant (Hucho, 1986).

Lastly, the effect of the rake angle ( $\alpha$ ) of a van's windshield as well as its front-end taper ( $\delta$ ) on its drag coefficient was investigated by (Buchheim, 1983) (see Figure 39). The results of this study are illustrated in Figure 39 and allow the following conclusions to be drawn:

1. When there is no front-end taper, the rake angle of the windshield has a substantial influence on the drag coefficient of the vehicle.
2. As the front-end taper increases, the influence of the rake angle on the drag coefficient reduces. However, for any taper angle, there is a reduction in drag with an increase in rake angle.
3. For all taper and rake angles, an enlargement of the front end radii has a favourable influence on the drag coefficient. However, the effect of increasing the front end radii becomes less pronounced with an increase in the rake angle.

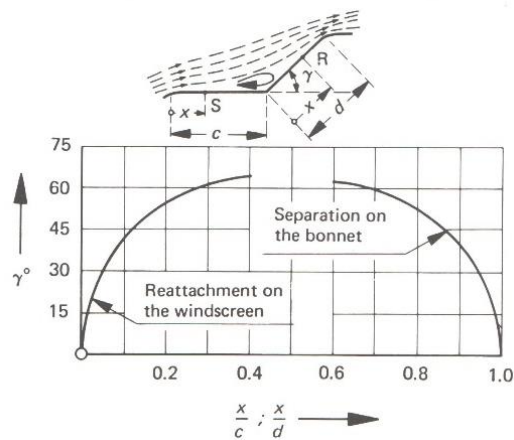


Figure 37: Influence of the rake angle ( $\gamma$ ) on the location of flow separation on the bonnet and the reattachment point on the windshield (Scibor-Rylski, 1984)

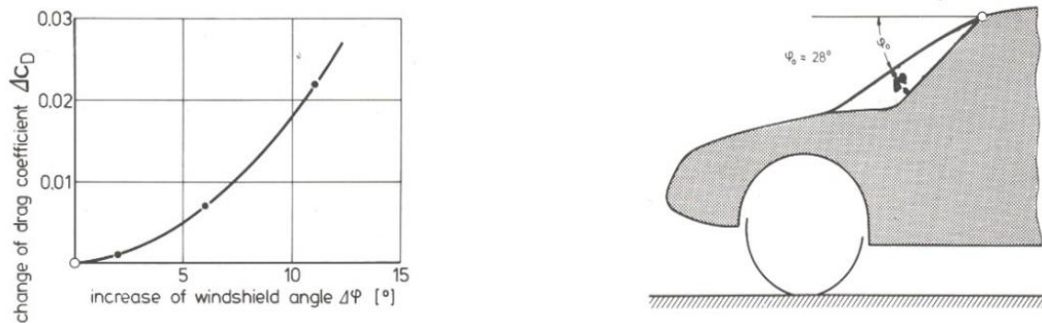


Figure 38: The influence of the rake angle ( $\phi$ ) on the drag coefficient of the VW 200 research vehicle (Buchheim, et al., 1979).

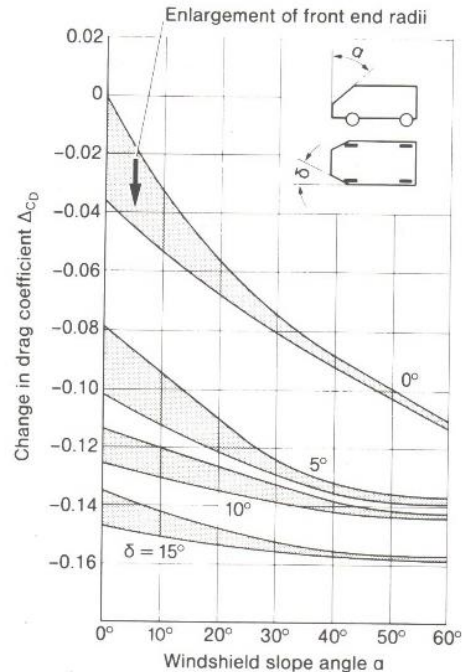


Figure 39: The change in the drag coefficient as a function of the front end shape (Buchheim, 1983)

#### 2.4.2. Rear

The geometry of the rear of the high-speed train is identical to that of its nose, consequently the parameters that are chosen to define the nose geometry, necessarily define the rear as well. As such, the effects of these nose parameters on the flow field surrounding the rear will be discussed here.

Varying the height of the stagnation point on the nose of the vehicle ( $Z_s$ ) will necessarily influence the 'diffuser' angle and 'trunk' height as well. The results of research completed by (Hucho, et al., 1976) on the effect of trunk height on the drag coefficient of a notchback are shown in Figure 40. It is clear that in order to reduce the drag, the trunk height must be sufficient for the flow to reattach on the lid of the trunk. If the lid is too low the flow is deflected over it entirely and there is no effect on the drag. The results further show that once the height is sufficient for the flow to reattach on the lid, increasing the height further has a minimal effect on the drag. The effect of increasing the trunk height on drag reduction was further confirmed by (Buchheim & Leie, 1982) and (Buchheim, et al., 1983) while developing the Audi 100 III (see Figure 41). However, in contrast with the findings of (Hucho, et al., 1976), (Buchheim & Leie, 1982) and (Buchheim, et al., 1983) found that for notchbacks with long trunks, there is a continued reduction in the drag coefficient as the trunk height increases. Furthermore (Buchheim & Leie, 1982) and (Buchheim, et al., 1983) showed that by lengthening the trunk of the vehicle the drag coefficient may also be reduced (see Figure 42).

In addition to the trunk height, the diffuser angle is also affected by varying the height of the stagnation point on the nose of the vehicle ( $Z_s$ ). Research done by (Buchheim, et al., 1981) showed that as the diffuser length increases, the necessary taper angle ( $\alpha$ ) to achieve notable drag reduction decreases (see Figure 43). These results are further verified by those obtained by (Potthoff, 1982) (see Figure 44). It is

worth noting that the diffuser has the added effect of reducing the lift at the rear axle. Furthermore, extremely high diffuser angles of the underbody produce vortices in a similar fashion to the fastback configuration, as determined by (George, 1979).

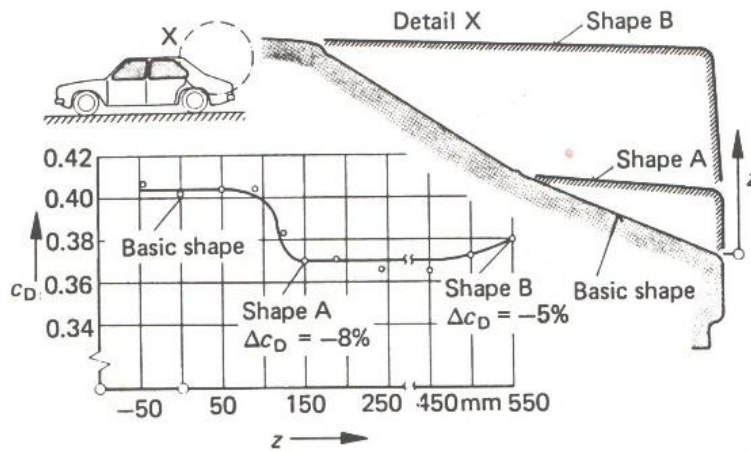


Figure 40: The influence of the step height on the drag coefficient of the notchback car (Hucho, et al., 1976).

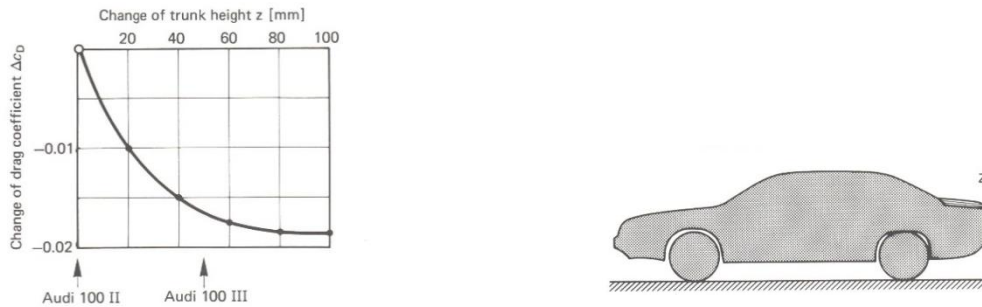


Figure 41: Drag reduction plotted as a function of increasing the trunk height ( $z$ ) [ (Buchheim & Leie, 1982) & (Buchheim, et al., 1983)].

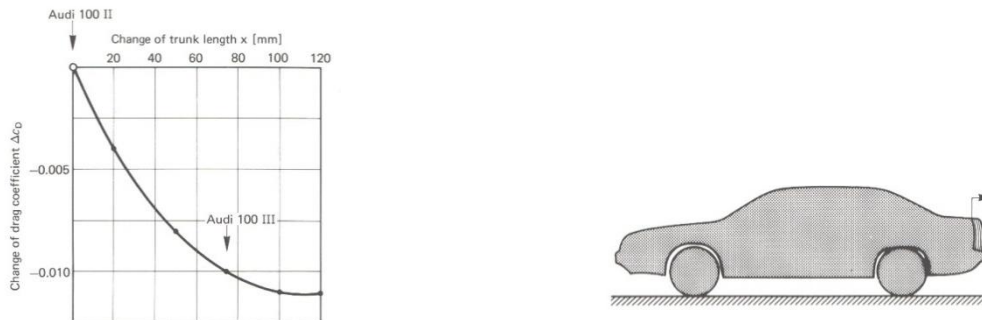


Figure 42: Drag reduction plotted as a function of increasing the trunk length ( $x$ ) (Buchheim & Leie, 1982) and (Buchheim, et al., 1983).

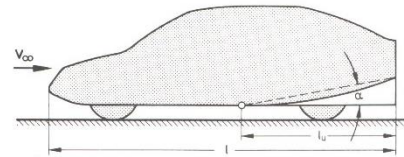
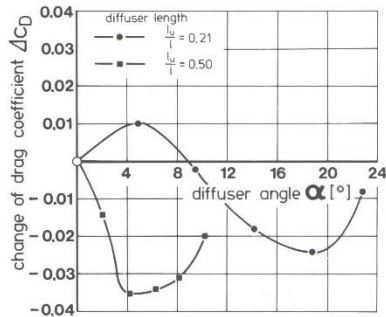


Figure 43: The influence of the underbody diffuser length ( $l_u$ ) and angle ( $\alpha$ ) on the drag coefficient of a vehicle (Buchheim, et al., 1981).

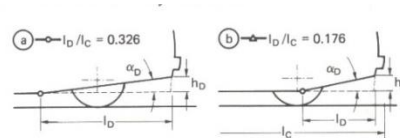
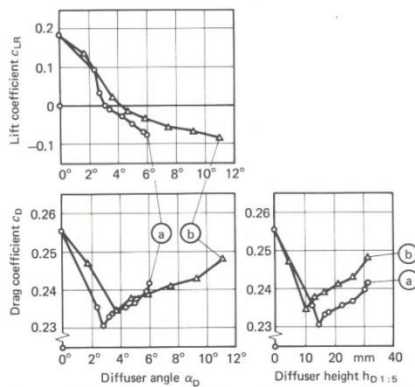


Figure 44: The influence of the underbody diffuser geometry on the drag and rear-axle lift (Potthoff, 1982).

By varying the taper of the front-end the rear is necessarily tapered accordingly. This lateral taper of the rear is commonly known as boat-tailing and is done in an attempt to keep the flow attached to the vehicle body, hereby reducing the drag. Studies done by (Mair, 1969) revealed that for a given body there exists an optimum angle for the boat tail and when the angle is increased further, the flow separates at the shoulder. The result of the investigation for the body and angle in question is illustrated in Figure 45. It is clear from the results that by extending the tail further (increasing the x-value), not much is won in terms of drag reduction. Work done by (Hucho, et al., 1976) confirms the merits of boat-tailing; at a constant trunk height the lateral taper of the vehicle was increased incrementally (see Figure 46). Initially there is a visible drag reduction as the sides move from perfectly parallel ( $y=0$ ), to an increasingly tapered configuration. This predictable behavior continues until shape B is assumed, where after an increase in taper no longer seems to reduce the drag; the flow remains attached up until a taper is reached which corresponds to shape B where after it separates.

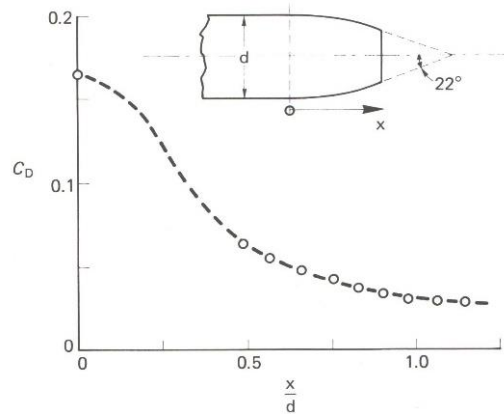


Figure 45: The influence of boat-tailing on the drag coefficient (Mair, 1969).

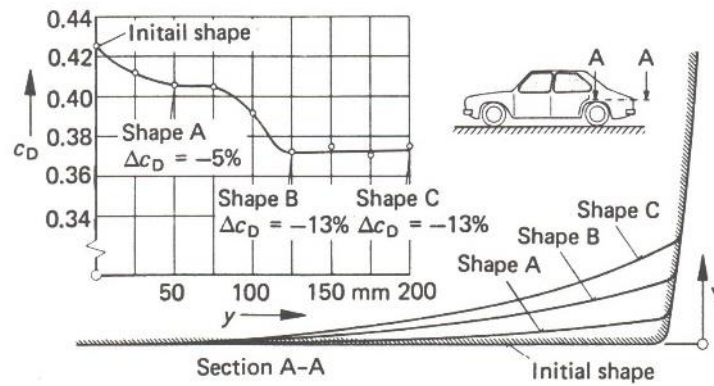


Figure 46: The effect of boat-tailing when applied to a notchback vehicle (Hucho, et al., 1976)

When the rake angle of the windshield is varied, the inclination angle of the rear window is varied accordingly. In so doing four basic rear-end shapes may be assumed, these are; squareback, notchback and two-variations of the fastback (see Figure 47). The flow associated with the squareback (see (a) in Figure 47) is purely quasi-two-dimensional; there is a separation bubble present at the rear of the vehicle and no longitudinal vortices form on the C-pillars. For a specific range of  $\phi$ , that will be discussed below, the fastback geometry is assumed (see (b) and (c) in Figure 47). Fastback configurations exhibit three-dimensional separation with longitudinal vortex trains present in the wake. In addition to the vortex trains, shape (c) also exhibits a quasi-two-dimensional wake at the perpendicular base.

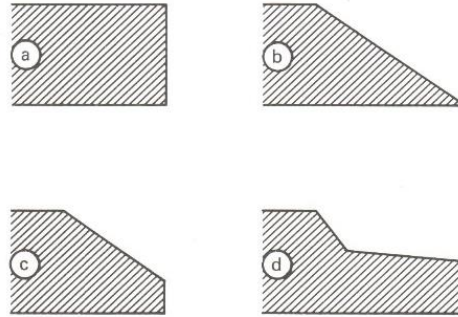


Figure 47: Various rear end configurations a) Squareback; b) & c) Fastback; d) Notchback (Hucho, 1986).

It was first noted by (Janssen & Hucho, 1975) that the inclination of the rear end of a vehicle can be responsible for entirely different flow types, consequently giving rise to different drag-values. It was while developing the VW Golf I that (Janssen & Hucho, 1975) incrementally reduced the value of the slant angle of the rear, starting from  $\varphi = 45^\circ$  (see Figure 48). Consider;

- 1)  $\varphi = 45^\circ$ ; The flow over the vehicle separated at the end of the roof and the corresponding drag coefficient was 0.40.
- 2)  $\varphi = 30^\circ$ ; With a decrease in the value of the inclination angle, there was a sudden 10% increase of the drag coefficient at an angle of thirty degrees. The separation line jumped to the lower edge of the inclined rear of the vehicle. A pair of strong, inward-rotating longitudinal vortices, which were responsible for the creation of a low pressure area on the inclined rear of the vehicle, was observed.
- 3)  $\varphi = 10^\circ$ ; As the inclination angle was reduced further, the drag coefficient once again started decreasing. A minimum value for the drag coefficient was reached at an angle of ten degrees. At even smaller angles, the flow regime returns to that associated with a squareback and the drag coefficient is once again 0.40.
- 4)  $28^\circ < \varphi < 32^\circ$ ; For inclination angles that fall within this range, the flow assumed a bi-stable condition. Whether the flow separated at the top or the bottom of the inclined rear end depended on the curvature of the roof's rear edge.

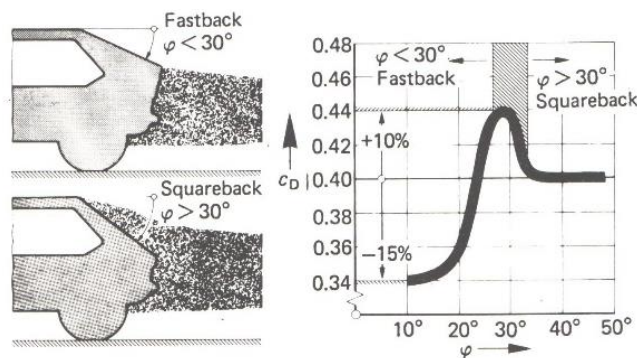


Figure 48: The influence of the rear end slope angle ( $\phi$ ) on the separation line, wake and drag coefficient (measured on the VW Golf I) (Janssen & Hucho, 1975).

Following the publication of the above results, studies were conducted by (Bearmann, 1979) into this effect by considering bodies of revolution which were exposed to free flow. The results obtained from

these studies are illustrated in Figure 49 and confirm the findings of (Janssen & Hucho, 1975); the drag coefficient of a body is clearly dependent on the slant angle of the rear. Furthermore, (Bearmann, 1979) found that the lift coefficient is also dependent on the slant angle. From the results shown in Figure 49 it is clear that there is an initial increase in the drag and lift coefficients with an increase in the angle of inclination, this is a consequence of the formation of longitudinal vortex trains in the wake region. For this body however, there occurs a limit angle ( $\phi$ ) between  $54^\circ$  and  $55^\circ$ , where the separation type changes; a large separation bubble is present in the wake rather than the aforementioned vortices and the drag and lift coefficients decrease. The results obtained by (Janssen & Hucho, 1975) and (Bearmann, 1979) therefore correspond well with one another, with the only discrepancy being the numerical value of the critical angle of inclination.

Pressure measurements were made on the same body as the one considered above, and the results may be seen in Figure 50. It is clear then, that these data confirm the information pertaining to the vortex formation and a characteristic pressure distribution develops over the base of the body under the influence of the longitudinal vortices.

Consider that the dimensionless pressure coefficient may be expressed as;

$$C_p = \frac{p-p_\infty}{\frac{1}{2}\rho V_\infty^2} = 1 - \left(\frac{w}{V_\infty}\right)^2 \quad (7)$$

Therefore;

$$-C_p = \left(\frac{w}{V_\infty}\right)^2 - 1 \quad (8)$$

However, as discussed previously, the velocity at the center of the vortex is comparatively high and from Bernoulli's equation it is known that the static pressure in the region is therefore comparatively low. Thus;

$$w_{vc} > w_{vp} \quad (9)$$

where;

$w_{vc}$ : Velocity at vortex center

$w_{vp}$ : Velocity at vortex periphery

Therefore;

$$\left(\frac{w_{vc}}{V_\infty}\right)^2 > \left(\frac{w_{vp}}{V_\infty}\right)^2 \quad (10)$$

and as such;

$$-C_{p,vc} > -C_{p,vp} \quad (11)$$

Figure 50 therefore not only confirms the increase in circumferential speed of the spinning vortex with a decrease in the radius (measured from the vortex center), but also confirms the increase in vortex strength with an increase in the inclination angle (for a given range of  $\phi$ ). It is also clear from the figure, that there is a critical point where the slant angle is too great for the flow to remain attached, consequently the longitudinal vortices burst, a quasi-two-dimensional separation bubble develops and the squareback flow regime is resumed. Since the velocity for this regime remains more or less constant over the rear of the body, the pressure coefficient follows suit (see the data points corresponding to  $\phi=70^\circ$  in Figure 50).

Finally, studies performed by (Morel, 1978) on prismatic bodies in ground proximity, confirm the vortex behaviour results obtained for bodies of revolution in free flow (see Figure 51). Additionally the critical angle determined by (Morel, 1978) corresponds with that obtained by (Janssen & Hucho, 1975) , i.e.,  $\phi = 30^\circ$  (or  $\gamma = 60^\circ$  for (Morel, 1978)). At this critical angle the flow transitions from type I (squareback flow with associated quasi-two-dimensional separation bubble) to type II (fastback flow with tip vortices present). The pressure distributions associated with these rear-end configurations can be seen in Figure 52, which also serves to confirm prior results obtained for bodies of revolution.

It is worth noting that the transition from squareback- to fastback-flow and vice versa occurs for a defined inclination angle only if the edge where the end of the roof and the inclined rear end meet is sharp. However, if this edge is rounded and the inclination angle lies within the range  $28^\circ < \phi < 32^\circ$ , the transition between flows is unstable. The separation line located at the inclined rear end of the vehicle may move from the top to the bottom and back again. This behaviour was first noted by (Janssen & Hucho, 1975) and later confirmed independently by (Morel, 1978) and (Ahmed, 1981).

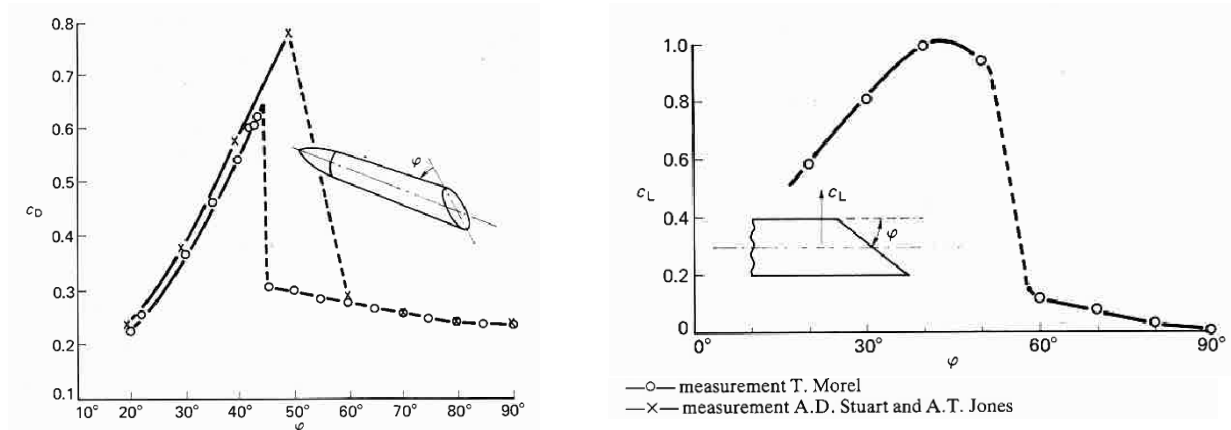


Figure 49: The effect of the rear end slope angle ( $\phi$ ) on the drag and lift coefficients of an axisymmetric body off the ground (Bearmann, 1979).

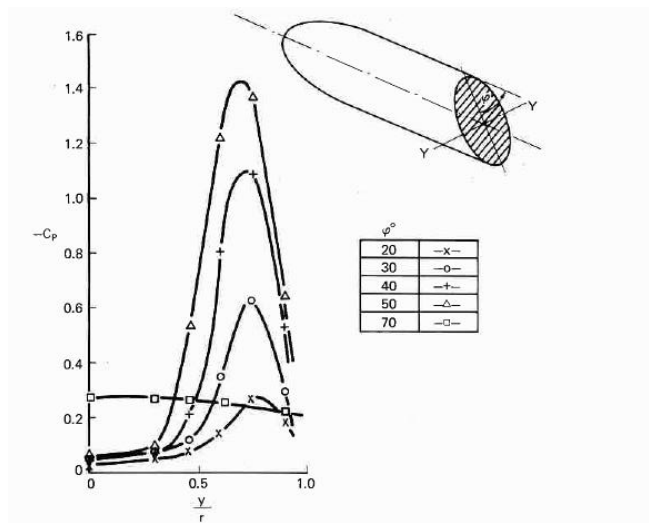


Figure 50: The pressure distribution plotted over the rear end slope surface, measured along section YY (Bearmann, 1979).

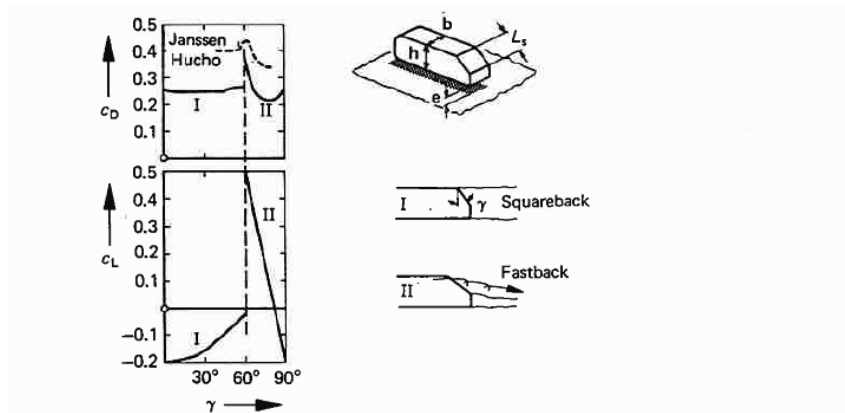


Figure 51: The influence of the slope angle ( $\gamma$ , where  $\gamma = 90^\circ - \phi$ ) on the drag and lift coefficient and flow pattern for a body in close ground proximity (Morel, 1978).

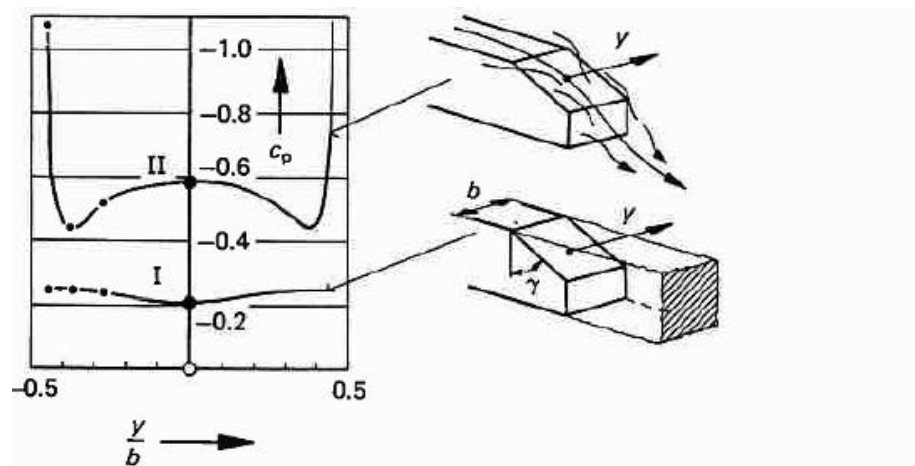


Figure 52: Pressure distribution plotted on the slope's surface with quasi-two-dimensional wake flow (I) and vortex formations at the C-pillars (II) (Morel, 1978).

The final parameter that defines the nose geometry, that necessarily influences the rear as well, is the slope of the 'bonnet' (which is synonymous to the slope of the 'trunk' at the rear). This parameter is, however, only relevant in the case of a notchback configuration (see Figure 47), which has a larger number of parameters that influences its flow pattern (see Figure 53) than does the square or fastback configurations. While it may be tempting to apply the theories derived for the fastback, directly onto the inclined rear window of the notchback, according to (Hucho, 1986) there are two differences between these configurations which render the approximation inaccurate;

The aspect ratio of the inclination ( $\lambda = \frac{w}{L_S}$ ) of the respective configurations is the first difference (see Figure 53). The length of the rear window ( $L_S$ ) of the fastback is larger than that of the notchback; consequently the associated aspect ratio of the fastback ( $\lambda \approx 1.5$ ) is smaller than that of the notchback ( $\lambda \approx 3$  to 4). Thus, for the same inclination angle ( $\varphi$ ), a notchback will experience smaller negative pressures and a weaker downwash on its slanted rear end, than its fastback counterpart.

The second difference is a consequence of the step that follows the slanted part of the notchback. According to (Hummel, 1978) the step, which causes a positive pressure gradient, may cause the side vortices to burst. In so doing, the already comparatively small negative pressure on the slanted rear as well as the induced downwash velocities, which are responsible for the deflection of the flow in the vicinity of the rear-end, are reduced even further. The flow over the rear of the notchback reattaches itself at a point 'A' after the step (see Figure 53). Studies of the flow over two-dimensional, vertical ( $\gamma_1 = 0$ ) steps were conducted by (Arnold, 1965); the reattachment point of the flow in relation to the height of the step was determined while also considering the boundary layer parameters in front of the step. It was found that the thicker the boundary layer of the oncoming flow was, the later the flow would reattach itself after the step. For three-dimensional flow, such as the case of a vehicle travelling through space, it is expected that the reattachment point A would move forward (see Figure 53). This phenomenon may be attributed to the downwash caused by the longitudinal vortex trains located at the rear window.

Lastly, the inclination angle of the rear window (corresponding to the rake angle of the windshield of the nose) of the notchback may be varied in order to reduce the drag coefficient (see Figure 54, (Buchheim & Leie, 1982) and (Buchheim, et al., 1983)).

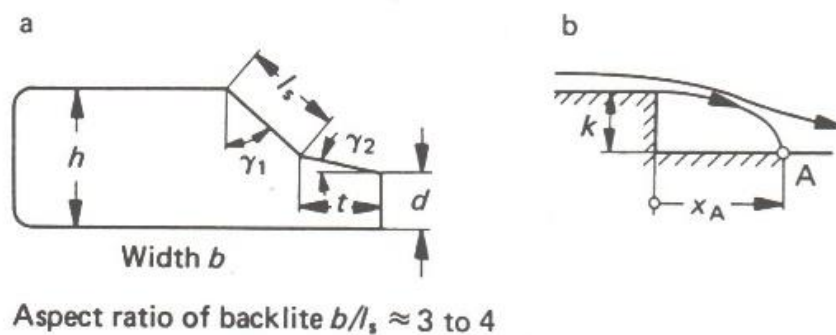


Figure 53: Notchback configuration: a) Rear defined by multiple geometric parameters b) Two-dimensional step model (Hucho, 1986).

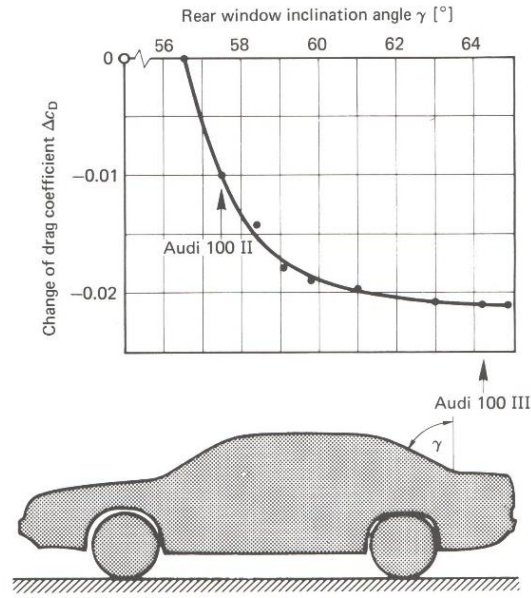


Figure 54: Drag reduction plotted as a function of the rear window slope ( $\gamma$ ) (Buchheim & Leie, 1982) and (Buchheim, et al., 1983).

## 2.5. Numerical Approaches used to solve Aerodynamics

### 2.5.1. Turbulence Models

According to (Menter, 2011) turbulence is arguably the most challenging subject matter in fluid dynamics and the factor that limits the accurate computer simulation of engineering flow to the greatest extent. Furthermore, turbulence is a classical multi-scale problem and the understanding of such complex nonlinear problems does not come intuitively to the human mind. (Menter, 2011) however argues that a complete understanding of turbulence is unnecessary and that a sufficiently accurate solution of the underlying equations is adequate.

When conducting a simulation using computational fluid dynamics (CFD), turbulence may either be solved directly using direct numerical simulation (DNS) or it may be modelled. While solving the Navier-Stokes equations in space and time for all turbulence scales is certainly more accurate than modelling turbulence, it requires immense computational power and the associated solving time is considerable. From a pragmatic point of view then, DNS is not a feasible approach for solving engineering flow problems. Modelling turbulence is an attempt to allow for approximate solutions to be obtained by engineers for their flow-related problems. It is however, important to note that turbulence models are inexact representations of the physical phenomenon they are meant to be modelling and there is single turbulence model that is able to model every type of flow problem best. Rather, careful consideration should be given to the various turbulence models available and the most appropriate one for the problem at hand selected.

#### 2.5.1.1. In General

Osborne Reynolds first introduced the concept of averaging the Navier-Stokes equations, during which instantaneous quantities are decomposed into their time-averaged and fluctuating quantities, hereby

eliminating turbulence fluctuations and resulting in equations which are less computationally expensive. This simplification process results in the presence of an additional term in the momentum transport equation which is known as the Reynolds stress tensor.

Since there are more unknowns than equations now, in order to provide closure of the governing equations, the Reynolds stress tensor is modelled in terms of the mean flow quantities. There are two basic approaches to accomplish this; the first is by means of eddy viscosity models, the second by means of Reynolds stress transport models. No matter the approach chosen, the turbulence in either case is modelled rather than resolved. Consequently the turbulence modelling approach will not necessarily be able to yield results within a narrow margin of error.

Finally, it is worth noting that while the Reynolds-averaged Navier-Stokes (RANS) equations are usually used in a steady-state approach, there are certain transient situations which validate the use of the unsteady RANS equations in order to obtain more accurate results. Some examples of such scenarios are the unsteadiness imposed by a time-varying boundary condition or highly anisotropic flows, such as vortex shedding that occurs in flows with large separation regions.

#### **2.5.1.2. *Near-wall Treatment***

In most engineering problems walls act as sources of vorticity for the flow and as such the ability to accurately predict the flow and turbulence parameters across the boundary layer is critical. Almost all RANS turbulence models are able to accomplish this under a zero-pressure gradient, however under an adverse pressure gradient not all models perform equally well. The success of a turbulence model to predict separation under such a pressure gradient lies in its ability to integrate to the wall. These models are known as viscous sublayer models (VSM) and solve flow across the boundary layer rather than modelling it. The alternative is to make use of a wall-function which derives the flow parameters from the equilibrium turbulent boundary layer theory. Models making use of wall-functions have, however, proven to be somewhat unsuccessful at predicting flow separation (Menter, 2011). There are also models available that allow for  $y^+$ -insensitive wall formulations to be used, this allows the model to switch between integration to the wall or utilizing a wall function based on the near-wall resolution. Making use of a  $y^+$ -insensitive wall formulation offers the advantage that the user is able to distinguish between numerical and modeling errors during the mesh refinement process. Furthermore, the use of  $y^+$ -insensitive wall formulations is prudent, since it reduces the influence the user has on the predictive accuracy of the simulation as a function of grid generation (Menter, 2011).

#### **2.5.1.3. *The Scale Equation***

The scale equation selected can have an important influence on the results obtained from a simulation, especially for wall boundary layers. While the  $\epsilon$ -equation with wall functions has proved successful under a zero-pressure gradient, it is well known that it performs poorly under adverse pressure gradients and consequently tends to miss or under-predict separation (Menter, 2011). This is a serious flaw in the  $\epsilon$ -equation, since it leads to overly optimistic loss/stall predictions; the results from the simulation may indicate that the flow is still attached, when in fact, it has already separated and the body consequently subjected to large separation-related losses. An additional challenge posed by the  $\epsilon$ -equation is the difficulty for it to be extended for integration through the viscous sublayer. There are

many viscous sublayer model extensions available that have been developed for the  $\epsilon$ -equation. In general they do however, have difficulty converging and in some cases can even lead to multiple results for simple flow problems (e.g., laminarization).

(Menter, 2011) therefore suggest the use of the  $\omega$ -equation in order to ensure a more accurate and robust modeling framework for boundary layers. The  $\omega$ -equation not only offers a more accurate near-wall formulation, but also performs well under adverse pressure gradients. The  $\omega$ -equation has however been proven by (Menter, 1992) and (Menter, 2009) to be disturbingly sensitive to the freestream  $\omega$ -values imposed at the boundary layer edge through the inlet values. Consequently a model known as the baseline (BSL) model was developed which combines the advantages offered by both the  $\epsilon$ - and the  $\omega$ -equation (Menter, 1994). The baseline model serves as a basis for many turbulence models available today, such as the SST model or the DES models to name a few (Strelets, 2001).

Since the introduction of the SST model, it has gained popularity not only in the field of aerodynamics but also for general CFD applications (Menter, 1994) and (Menter, 2009)). Consider as an example the results obtained from various eddy viscosity models, including the SST model, for flow over a NACA 4412 airfoil shown in Figure 55 (Coles & Wadcock, 1979). The simulation results are shown alongside the experimental results for the same, allowing clear comparisons to be drawn. From Figure 55, it is clear that the SST model shows the best correlation with the experimental results and is even able to closely capture the flow separation present over the airfoil. The absence of  $k$ - $\epsilon$  solutions is a consequence of their inability to capture the aforementioned flow separation observed in the experiment. The SST model was also used in the more severe test cases of the 2003 AIAA Drag Prediction Workshop and performed very well (Langtry, et al., 2004). The accuracy that can be obtained under adverse pressure gradients for wall-bounded flows by making use of  $\omega$ -equation-based RANS models is thus considerable. Furthermore, the ability of the SST model in particular to predict separation lines accurately makes it a prudent modeling choice (Menter, 2011).

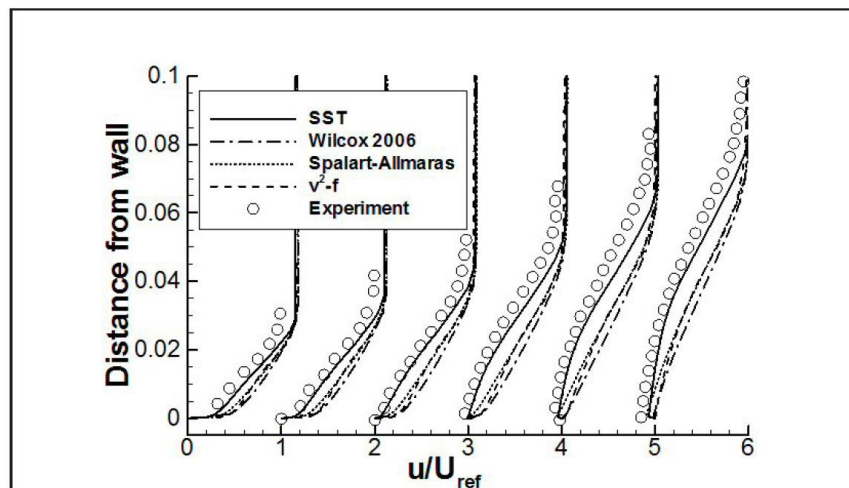


Figure 55: Comparison of velocity profiles obtained by using various turbulence models for the NACA 4412 airfoil ( $\alpha=13.87^\circ$ ,  $Re=1.5 \times 10^6$ ) (Coles & Wadcock, 1979).

#### **2.5.1.4. Transition Modelling**

The ability to accurately model the transition from laminar to turbulent flow can have a considerable influence on the accuracy of the results obtained from the simulation; the skin friction in the laminar boundary layer portion is significantly lower than that of the turbulent part. Additionally, heat transfer is much higher in the turbulent boundary layer region as a consequence of turbulent mixing. Finally, the flow separation that occurs under adverse pressure gradients, where a laminar separation bubble with turbulent reattachment appears, has already been discussed above. While the accurate modeling of transition in boundary layers has proved challenging in the past, a new transition model which is compatible with the SST turbulence model has been developed recently (Menter, et al., 2006) and (Langtry & Menter, 2009). The model, known as the Gamma-Re Theta ( $\gamma-Re_{\theta}$ ) or Transition SST, solves two additional transport equations and also incorporates experimental correlations that act as a trigger for the onset of transition. It has also been validated against multiple sets of experimental results such as the flat plate test cases (T3C), the McDonald Douglas 30P-30N flap and the Pratt and Whitney PAK-B low pressure turbine blade, to name but a few (Menter, 2011). It was found that the Gamma-Re Theta model was able to describe separation-induced transition well. This is of significance, since separation-induced transition is one of the most important and frequently encountered transition mechanisms in industrial flow applications. Transition models should however, only be used in combination with turbulence models whose viscous sublayer model formulation does not already enable them to mimic transitional behaviour; the use of both formulations would necessarily interfere with one another, consequently resulting in unpredictable behaviour (Menter, 2011). The most suitable choice would be the use of the  $\omega$ -equation-based transition models.

#### **2.5.1.5. Reynolds Stress Models**

Eddy viscosity turbulence models are able to yield accurate results at relatively low computational cost, making them attractive modeling approaches but they do have their limitations. For flows that exhibit strong swirl behaviour or where turbulence anisotropies drive secondary motion, eddy viscosity models may fail. In these cases, the next step has historically been to resort to Reynolds stress models (see (Wilcox, 2006)).

These models require a scale equation as well as one transport equation for each of the components of the Reynolds stress tensor (due to the symmetry of the tensor there are six equations) to be solved. Using Reynolds stress models (RSM) do, however, pose their own set of challenges; RSMs tend to not be as numerically robust as eddy viscosity models, especially when integration of the equations through the viscous sublayer is required. Rather, they have proven more successful when applied to flows for which the boundary layer behaviour is not central or where a wall-function resolution is adequate (Menter, 2011).

### **2.5.2. Numerical Optimization Algorithms**

#### **2.5.2.1. Introduction**

Automated design optimization technology allows engineers to deliver better designs in less time and as such it is a very attractive tool from a technical and business perspective. Optimization does however, offer some obstacles that can prevent engineers from fully realizing its potential, these are primarily the

choice of an appropriate algorithm and the efficiency of the algorithm in question. In order to choose an appropriate search algorithm, the characteristics of the design space must be known. Unfortunately, these characteristics aren't typically known beforehand and it is in fact the role of the search algorithm to identify them. Clearly then, this offers a typical causality dilemma and the trial-and-error process of selecting the appropriate algorithm and tuning its parameters can be time-consuming. An algorithm that doesn't require manual tuning and which can find the optimal solution within a single run can therefore effectively reduce the required manual effort as well as the design cycle time. Furthermore, it is advantageous that a given algorithm performs well irrespective of the type of problem being solved or the starting conditions thereof. Such an algorithm is said to be robust and it allows for the results of the optimization to be trusted, i.e., it would find approximately the same optimal solution irrespective of design problem or initial conditions. It is also desirable that the algorithm is efficient enough to solve large-scale optimization problems. Since a single evaluation may require several hours of CPU time to solve and considering that the optimization process may require several evaluations, it is clearly beneficial if the search algorithm in question requires a minimal number of evaluations to find the optimal solution. The two primary characteristics of a successful algorithm are thus its effectiveness and efficiency over a wide range of problems (Chase, et al., Retrieved on: 24 November 2016).

#### **2.5.2.2. Classification of Search Algorithms**

In this dissertation algorithms will be classified as either monolithic or hybrid and as either static or adaptive. The term "monolithic algorithm" will be used to refer to algorithms that use a single strategy for all cycles in an optimization study, e.g., simplex methods, genetic algorithms and response surface methods to name but a few. All monolithic algorithms are however, subject to limitations irrespective of the specific type that is chosen and there is no single algorithm that performs best for all, or even a wide range of, problems. Challenges posed by monolithic algorithms include, but aren't limited to; finding the local optimum but failing to broaden the search in order to find the global optimum, requiring a large number of design evaluations in order to find the optimum and being able to work with either continuous or discrete variables, but not both. "Hybrid algorithms" will denote algorithms which are able to utilize multiple strategies within a cycle and for all cycles during a study. Thus, a clear advantage of a hybrid algorithm is that it is able to utilize the strengths of various strategies during a single optimization study and as such, is not encumbered by the same limitations a monolithic algorithm faces.

The term "static" will denote an algorithm which requires its tuning parameters to be defined prior to the commencement of the optimization study and where after those parameters remain fixed throughout. The genetic algorithm is a well-known example of a static algorithm where parameters such as population size, cross-over type and rate, selection method, etc., must be defined by the user a priori. Unfortunately, the solution that is found by the algorithm may be sensitive to the values of the aforementioned parameters. As such, it is beneficial for the accuracy of the result that the user be well-trained in the use of the algorithm in question. Furthermore, the algorithm's parameters are usually tuned by a trial-and-error approach until its performance is adequate, which may be a time-consuming process. "Adaptive" algorithms on the other hand, neither require their parameters to be defined prior to the commencement of the study, nor do they remain constant throughout it. These parameters are, in fact, variable and are continuously changing to the most suitable values based on statistical,

heuristic and other feedback from the solution process. These characteristics allow the algorithm to automatically adapt in such a way as to best describe the behaviour of the design space it is busy exploring, hereby continuously improving its performance. Since these algorithms do not require predefined parameters they are accessible to users who aren't experts in the field of optimization, while their ability to learn and adapt allows them to exceed the performance of manually tuned, static algorithms if the adaptation process works well.

### **2.5.2.3. Multi-Objective Optimization**

Multi-objective tradeoff studies, otherwise known as Pareto optimization, refer to problems that require more than one competing objective function to be optimized simultaneously. For these types of optimization studies there is no one optimal design, rather there exists a collection of optimal designs known as the Pareto front. The designs comprising this front are all optimal in one objective for given values of the other objectives, this is otherwise known as the non-dominated design condition. Since a large number of design evaluations are necessary to find the Pareto front when optimizing for more than two objective functions, it is recommended to combine those objectives which are analogous. An alternative approach is to attempt to define the problem in terms of two objective functions and constraints. Irrespective of the approach taken to determine the Pareto front, ultimately any decision made based on the results would be a trade-off between the objectives. As such, the onus of responsibility lies with the engineer to make an appropriate decision based on a more comprehensive understanding of the true implications of the tradeoffs at hand.

A benchmark study on the efficiency and robustness of three multi-objective optimization algorithms was conducted by (Chase, et al., 2014), by making use of the so-called ZDT functions. The algorithms that were considered in this study are the NSGA-II, NCGA and MO-SHERPA;

1. NSGA-II; this genetic algorithm makes use of non-dominated sorting in order to rank individual designs and a secondary crowding measure enables the algorithm to distribute design points evenly along the Pareto front. The NSGA-II assigns ranks in ascending order based on the performance of a design, i.e., a rank of 1 is assigned to the design point that performs best. The lower-numbered ranks therefore have a higher probability of producing offspring in the following generation or cycle (Chase, et al., 2014). The inquisitive reader may refer to (Pratap, et al., 2000), (Deb, 2001) and (Deb, et al., 2002) for a more detailed mathematical formulation.
2. NCGA; while this genetic algorithm is similar to the NSGA-II in many ways, it also makes use of a neighbourhood crossover operator which allows the algorithm to converge more rapidly by enhancing the degree of exploitation versus exploration. This algorithm does not arbitrarily select individuals to crossover, rather the pairs used to produce children are chosen based on their close proximity to one another in the objective space. Consequently, the children that are produced by the aforementioned crossover are also more likely to be in close proximity of the parents in the objective space. The inquisitive reader may refer to (Watanabe, et al., 2002) for a more detailed mathematical formulation.
3. MO-SHERPA; The multi-objective SHERPA algorithm also makes use of non-dominated sorting in order to rank designs, but varies from NSGA-II and NCGA in other aspects. It is based on the SHERPA algorithm and fundamentally works the same, but has been adapted in order to allow

for multiple objective functions to be optimized. The SHERPA algorithm is both hybrid and adaptive and as such it makes use of elements of many different local and/or global search algorithms simultaneously (not sequentially) in order to explore the design space and find the optimal result. As SHERPA learns about the design space it is able to not only make more informed decisions regarding the appropriate algorithm (or elements thereof) to use and to what extent to use it, but since it is adaptive it also automatically tunes the internal parameters of the chosen algorithms to the most suitable values for the given design space. Lastly, SHERPA is a direct algorithm and thus makes use of the actual model to perform its evaluations, rather than some derivative such as the response surface model (Chase, et al., 2014).

The study completed by (Chase, et al., 2014) found that for all the ZDT functions the MO-SHERPA algorithm significantly outperformed the NSGA-II and the NCGA in terms of efficiency and robustness, irrespective of population size. The superior performance of the MO-SHERPA algorithm may be ascribed to its adaptive and hybrid nature, which allows it to be effective over a wide range of problems.

## 2.6. Summary of Literature Study

To summarize, the research conducted in Chapter 2 revealed the following; the flow field that surrounds a train body is three-dimensional in nature and its boundary layer, in addition to being highly turbulent, can grow to a considerable thickness. Longitudinal vortices may also present themselves, either trailing the tail under windless conditions or on the leeward side when the train is subjected to crosswinds. An investigation into commercially available turbulence models revealed that should the flow surrounding the train prove sufficiently complex, an occurrence that seems extremely likely given the aforementioned, a Reynolds' stress turbulence model would be necessary to accurately predict the flow behaviour.

Furthermore, it was found that the rail industry is faced with a number of challenges which include, but is not limited to, the aerodynamic drag force acting on the train as well as the train's stability under crosswind conditions. In addition to the literature affirming the choice of the optimization objectives described in this thesis as valid, it further served to confirm the grounds for their selection, i.e., a reduction in the total drag force, reduces the train's fuel consumption and consequently the greenhouse gases emitted by it as well. With regard to maximizing the train's crosswind stability, it was found that while crosswinds are responsible for many concerns in the rail industry, it is their ability to overturn trains that is most serious due to the devastating consequences this can have on infrastructure as well as human life. Thus two separate geometric optimization cases will be considered; for a train travelling in windless conditions the reduction of the total drag will serve as the optimization objective. For a train travelling under crosswind conditions however, the reduction of both the total drag acting on the entire train as well as the rolling moment acting on the leading locomotive (CEN, 2010) about the leeward rail, since the literature revealed that this moment is the principal cause for the derailment of high-speed trains, will serve as optimization objectives.

In order to complete a geometric optimization however, the geometry in question must first be parameterized. To this end, significant geometric parameters that could influence the flow around the train nose and tail and in so doing influence the optimization goals also, were identified from the

literature as the; nose length ('L'), nose-tip height ( $Z_0$ ) and inflection point height ('H') (see Figure 56). Finally, an investigation into optimization algorithms was necessary, so that an efficient and robust algorithm could be identified for future use. From this study it was decided to make use of the self-taught, hybrid search algorithm known as SHERPA.

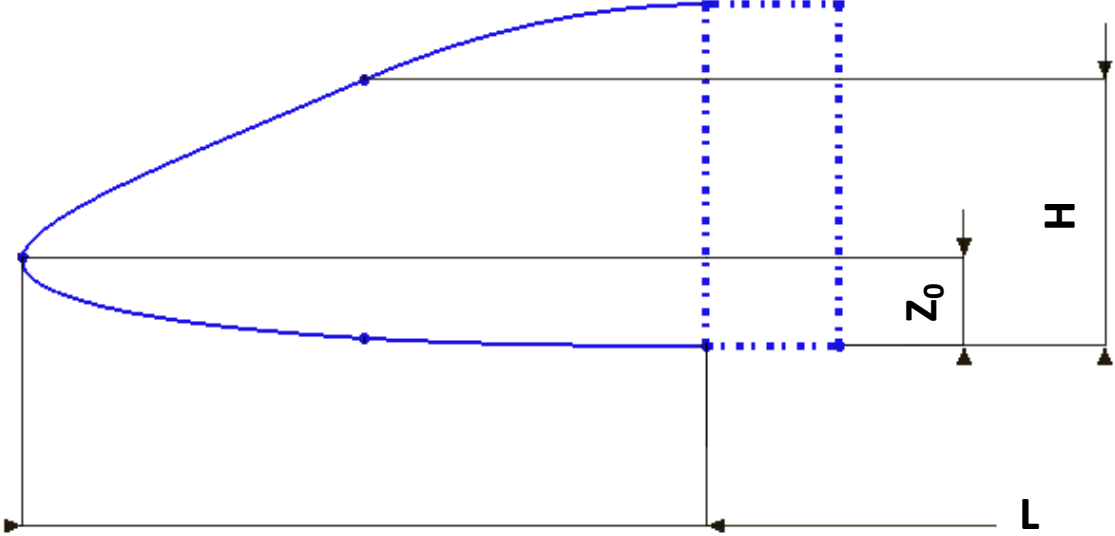


Figure 56: The side profile of the train nose, whose geometry is to be optimized. The significant parameters identified from the literature are also shown, i.e., the nose length ('L'), the nose-tip height ('Z<sub>0</sub>') and the inflection point height ('H').

### 3. Validation of Computational Fluid Dynamics

In order to affirm trust in the results obtained from a CFD analysis, the computational model that is made use of must first be validated. One way to accomplish this is to make use of a validation case which is accompanied by published experimental data available for comparative purposes. In general past CFD simulations have also been completed for these cases by various authors and their results published. The validation case that was selected for the high-speed train is the well-known Ahmed's Body. This body shares important commonalities with the high-speed train such as the stagnation point on the nose as well as the wake flow at the rear, making it a rather suitable choice for model validation. Once the computational model used for solving the Ahmed's body has been validated, it will be transposed onto the high-speed train, i.e., the size of the computational domain, the mesh discretization and choice of turbulence model used for solving the high-speed train will all be informed by the Ahmed's body benchmark case.

#### 3.1. Introduction

The Ahmed's body was first defined by S. R. Ahmed in 1984. While its geometry may be relatively simple, i.e., a bluff body with slanted back, it still allows the main features of the wake flow that may present itself as a function of the inclination angle, to be generated. Since the ability to reliably simulate such complex turbulent flows surrounding vehicles is of great industry value, the Ahmed's body can prove very useful as a benchmark test case for simulation purposes. This can be attributed in part to the wide range of experimental results available for the Ahmed's body as captured by (Lienhart, et al., 2000) which allows for the extensive validation of the simulation results. Successful validation therefore allows the mesh refinement level, boundary conditions, computational domain size and turbulence model used, etc., to be justified and confirmed.

#### 3.2. Simulated Configuration and Flow Parameters

The dimensions of the Ahmed's body that were modelled are shown in Figure 57 and are synonymous with those of the body used by (Lienhart, et al., 2000).

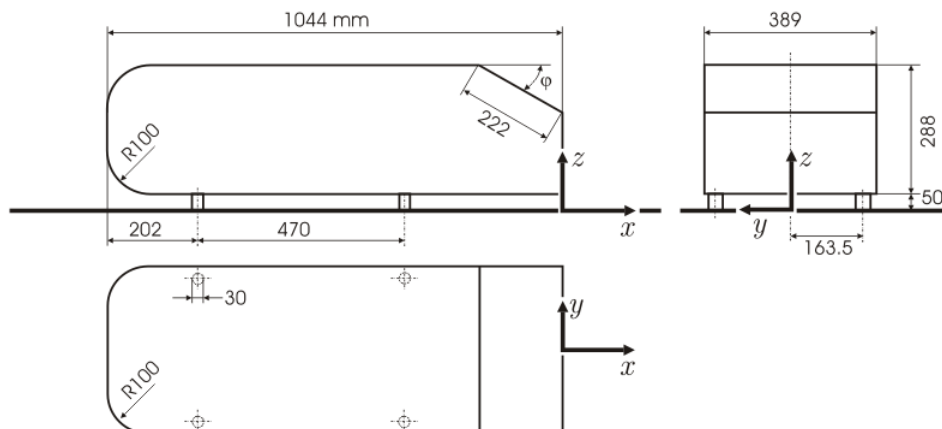


Figure 57: A schematic of the geometry of the Ahmed's body (Hinterberger, et al., n.d.).

The CFD model was set-up in a way that attempts to mimic the experimental set-up used by (Lienhart, et al., 2000) when taking measurements for the body in the LSTM low-speed wind-tunnel. The tunnel configuration used by (Lienhart, et al., 2000) was a ¾ open test section; there is a floor, but no walls or ceiling. Although the cross-sectional area of the tunnel is  $1.87 \times 1.4\text{m}^2$ , a symmetry CFD model was made use of in order to lower computational time and cost and as such the cross-section of the simulated domain is  $0.935 \times 1.4\text{m}^2$ . Furthermore, the computational domain was extended ten body-widths in front of the body (3.89m), as measured from the tip of the nose. The domain was also extended twenty body-widths behind the body as measured from its rear face (7.78m). This yields a total domain length of 12.714m and was determined to be such by ensuring the solution is independent of the locations of inlet and outlet boundary locations. The bulk velocity of the air at the inflow plane is 40m/s in keeping with the experiment (Lienhart, et al., 2000). The side and top boundaries were designated as free-slip walls. Since the simulation was conducted using a half-model, a symmetry boundary condition was allocated to the symmetry plane of the model. At the outflow of the domain, an atmospheric pressure boundary condition was applied. The ground was modelled as a no-slip, stationary wall.

The flow parameters and initial conditions that were used in this model are;

$$V_{\infty,air} = 40 \text{ m/s (Lienhart, et al., n.d.)}$$

$$\rho = 1.18415 \text{ kg/m}^3 \text{ [Star-CCM+ standard atmospheric air definition]}$$

$$\mu = 1.85508 \times 10^{-5} \text{ kg/ms [Star-CCM+ standard atmospheric air definition]}$$

$$\therefore \nu = 15.67 \times 10^{-6} \approx 15 \times 10^{-6} \text{m}^2/\text{s (Lienhart, et al., n.d.)}$$

$$I_2 = 0.2\% = 0.002 \text{ (Liu \& Moser, 2003)}$$

$$Re_{Height} = 768 \text{ 000 (Lienhart, et al., n.d.)}$$

### 3.3. Mesh Independence

An adequate mesh resolution is critical for eliminating possible discretization errors. These numerical errors arise as a consequence of the governing flow equations and other physical models being applied as algebraic expressions to the discrete volumes that comprise the mesh, rather than being applied to a continuum. For a given numerical method, the solution will approach that of the continuum as the mesh resolution increases. Once the solutions obtained from successive grid refinements show less sensitivity to a further reduction in grid spacing, the mesh is said to be converged, i.e., the discretization error tends to zero.

#### 3.3.1. The Grid Convergence Index

The methodology used here to verify mesh convergence was suggested by (Roache, 1998) and is known as the Grid Convergence Index (GCI), which is able to provide an approximation for the discretization error for both integer and non-integer grid refinement ratios. The GCI provides an error band which indicates a measure of the percentage that the solution value deviates from the asymptotic numerical value (it is important to note that this value is not synonymous with the true value). Therefore, a small value of the GCI is indicative that the numerical solution obtained from a given grid, lies within the

asymptotic range. Furthermore, it is able to provide an estimation of the solution given a grid-spacing of zero (Roache, 1998).

The GCI method requires successive grids to be refined (or coarsened) by a constant ratio,  $r$ . As mentioned previously, this ratio needn't be an integer. It is, however, important that the same mesh generation parameters are used throughout irrespective of the chosen mesh refinement ratio ( $r$ ). For all successive grids in this study the total drag coefficient of the Ahmed' body will act as the performance parameter ( $f$ ). The order of convergence ( $p$ ) can be calculated from the performance parameters obtained for three successive grid refinements as follows:

$$p = \frac{\ln\left(\frac{f_{i+2}-f_{i+1}}{f_{i+1}-f_i}\right)}{\ln(r)} \quad (12)$$

where  $f_i$  is associated with the finest mesh. The relative error (shown here for the two finer meshes) of the performance parameters obtained from two successive grid refinements may be calculated as:

$$\varepsilon_{i,i+1} = \frac{f_{i+1}-f_i}{f_i} \quad (13)$$

In the instance where three successive grids are used to determine the GCI, as is the case in this study, it is recommended to make use of a factor of safety ( $F_s$ ) of 1.25 (Roache, 1998). The GCI for the fine grid may thus be determined in the following manner:

$$GCI_{i,i+1} = \frac{F_s |\varepsilon_{i,i+1}|}{r^p - 1} \quad (14)$$

Similarly, the GCI for the coarse grid may thus be calculated as:

$$GCI_{i+1,i+2} = \frac{F_s |\varepsilon_{i+1,i+2}|}{r^p - 1} \quad (15)$$

The asymptotic range of convergence, i.e., mesh independence, is said to have been reached once three successive grids obey the following rule:

$$\frac{GCI_{i+1,i+2}}{r^p GCI_{i,i+1}} \approx 1 \quad (16)$$

### 3.3.2. The Mesh Construction

Three grids were used for the mesh independence study of which the base grid had the finest mesh resolution. The remaining grids were generated by successively coarsening the preceding mesh by a factor of 1.7 ( $r = 1.7$ ). The construction of the base grid will be discussed here in some detail and a summary of the remaining grids and their corresponding specifications will follow (see Table 5).

A low  $y^+$ -mesh was constructed on the Ahmed's body itself as well as on the ground beneath and in close proximity to it (Figure 58). The near wall mesh on the Ahmed's body had a total height of seven millimeters, consisted of twenty prism layers and was assigned a stretching factor of 1.3. In close proximity of the body (the near-wake and far-wake regions as indicated in Figure 59), the total height of the prism layer was seven millimeters and comprised of fifteen layers that were stretched by a factor of

1.4. In the remainder of the domain a high  $y^+$ -mesh was constructed on the ground surface; it consisted of three prism layers that were stretched by a factor of 1.1 to occupy a total height of 7.5 millimeters. These near-wall mesh settings resulted in  $y^+$ -values well below one on the Ahmed's body, thus allowing for the viscous sublayer to be solved accurately. In close proximity of the body the maximum  $y^+$ -value on the ground surface was 1.728, which is well below the maximum limit of five, hereby avoiding the blended region. In the far-field the  $y^+$ -values comfortably lie within the acceptable range for a high  $y^+$ -mesh. Lastly, it is worth noting that there were a small number of cells that lay within the blended region ( $5 < y^+ < 30$ ), where the near-wall mesh transitioned from a low to a high  $y^+$ -mesh (see Figure 59).

On the surface of the Ahmed body itself the minimum element size was 2.13mm (2.13% of the base element size [BES]) and the target size of the element 4.27mm (4.27% of the BES). These elements were allowed to grow to a maximum size of 5.12mm (5.12% of the BES) in the near wake region, where after the elements could further grow to 7.68mm (7.68% of BES) in the far-wake region. The minimum surface element size in the far-field was 10mm (10% of BES) and the target size 30mm (30% of BES). Once again these surface elements were permitted to grow to the base element size of 100mm and in all instances the allowable surface growth rate was 1.2. The volume mesh that resulted from these grid generation specifications comprised of 15.71 million cells and more detail regarding the base mesh can be seen in Table 5.

Grid Specifications		Grid 1	Grid 2	Grid 3
Base Element Size		100mm	120mm	146mm
Number of cells normal to ground in far-field		3	3	3
Number of cells normal to ground in proximity of the Ahmed's body, the near-wake and far-wake		15	15	15
Number of cells normal to Ahmed body's surface		20	20	20
Number of surface elements on Ahmed's body		46 180	31 487	21 834
y <sup>+</sup> -values	Ahmed's Body	0.010 < y <sup>+</sup> < 0.487	0.007 < y <sup>+</sup> < 0.472	0.011 < y <sup>+</sup> < 0.482
	Ground in close proximity of body	0.040 < y <sup>+</sup> < 1.591	0.068 < y <sup>+</sup> < 1.548	0.103 < y <sup>+</sup> < 1.496
	Ground in far-field	30 < y <sup>+</sup> < 146.13	30 < y <sup>+</sup> < 145.79	30 < y <sup>+</sup> < 145.67
Number of cells in the proximity of the Ahmed's body and the near-wake		9 681 659	5 739 876	3 328 409
Number of cells in far-wake		983 698	593 551	381 140
Number of cells in domain		15 714 321	9 337 327	5 438 413

Table 5: The grid generation specifications for the three mesh independent models of the Ahmed's body. All results are given for an inclination angle of the rear-end slope of twenty-five degrees ( $\varphi = 25^\circ$ ).

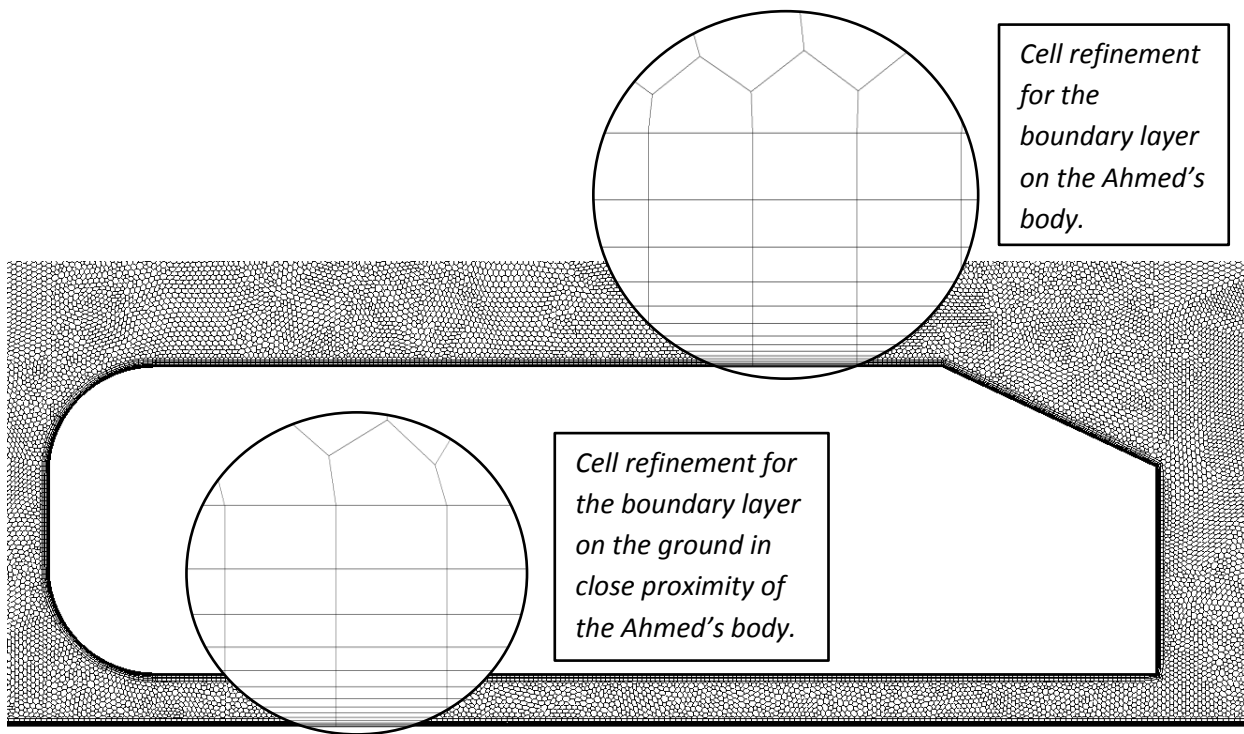


Figure 58: The base mesh constructed for the Ahmed's body shown at the symmetry plane of the model. The magnified views show the boundary layer cell refinements for the Ahmed's body, as well as the ground in close proximity of the Ahmed's body. All results are given for an inclination angle of the rear-end slope of twenty-five degrees ( $\varphi = 25^\circ$ )

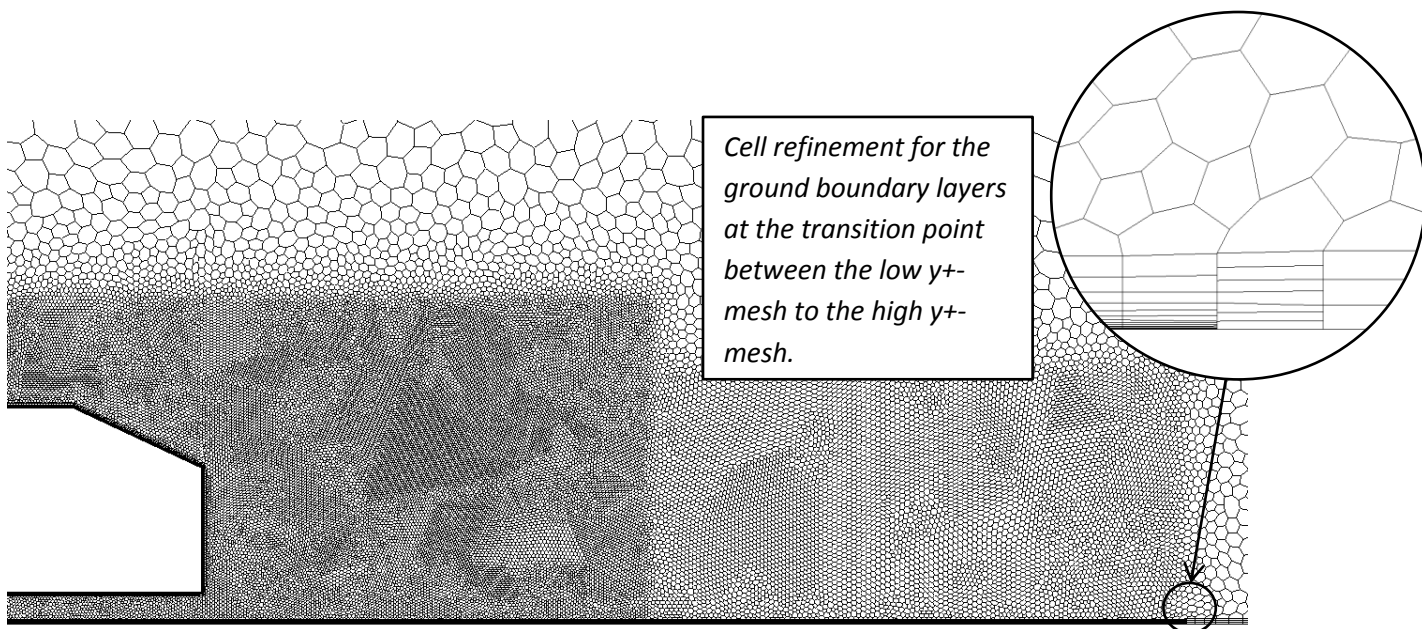


Figure 59: The near-wake and far-wake mesh refinements specified for the base mesh, shown at the symmetry plane of the model. The magnified view shows the boundary layer cell refinements for the low  $y^+$ -mesh in the far-wake region (left), the high  $y^+$ -mesh in the far-field (right) and the transition between the two (middle). All results are given for an inclination angle of the rear-end slope of twenty-five degrees ( $\varphi = 25^\circ$ )

### 3.3.3. Results from the Numerical Analysis

A mesh independence study using the GCI approach was performed on the Ahmed's body for various inclination angles of the slope, namely; 5°, 15°, 25° and 35° for the grid specifications as discussed above. The chosen performance parameter for the study was the total drag of the Ahmed's body and all results (see Table 6) were compared with those published in the literature (see Figure 60). The results showed that mesh independence had been reached for all the grids in question and for all inclination angles considered; the total drag obtained from all the models in question converged to values well within the asymptotic range of convergence.

Grid Convergence Index Outputs and Variables	Inclination Angle of Slope			
	5 Degrees	15 Degrees	25 Degrees	35 Degrees
<b>Total Drag Coefficient [<math>C_D</math>]:</b>				
Grid 1	0.272	0.281	0.308	0.291
Grid 2	0.276	0.283	0.310	0.297
Grid 3	0.284	0.293	0.315	0.306
<b>Order of Convergence:</b>	1.119	2.544	2.553	0.788
<b>Relative Error:</b>				
$\epsilon_{12}$	0.016	0.009	0.004	0.020
$\epsilon_{23}$	0.029	0.033	0.017	0.030
<b>Grid Convergence Index:</b>				
$GCI_{12}$	0.025	0.004	0.002	0.048
$GCI_{23}$	0.044	0.014	0.007	0.072
$\frac{GCI_{i+1,i+2}}{r^p GCI_{i,i+1}}$	0.984	0.992	0.996	0.980

Table 6: Results of the GCI method applied to three successive grid refinements, for various values of the inclination angle of the slope, i.e., 5°, 15°, 25° and 35°. NB. These values have been rounded to three decimal places in order to ease reading thereof. The original and complete results are available upon request.

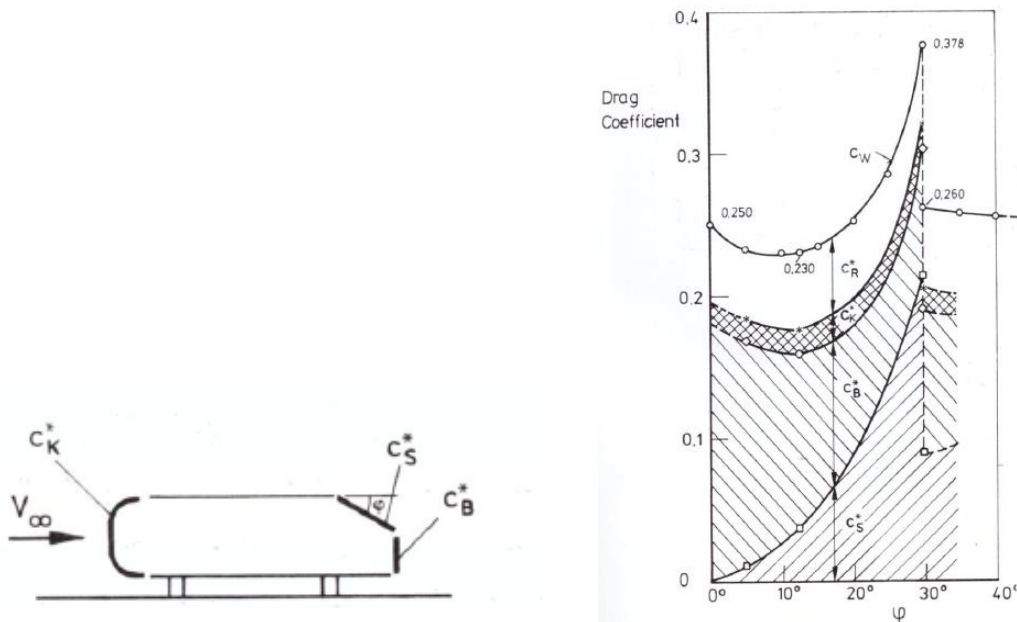


Figure 60: The total and partial drag components of the Ahmed's body plotted against various slant angles of the rear-end slope ( $\phi$ ) (Ahmed, et al., 1984).

### 3.4. Turbulence Model Validation

In the foregoing section mesh independence was proven. This allows for the further study of the influence that other factors may have on the solution obtained from a given model, without the concern of multiple factors simultaneously influencing said solution. One such an additional factor that ought to be studied is the choice of turbulence model used to solve the flow problem. In this section both eddy viscosity as well as Reynolds stress models will be investigated. However, since a theoretical discussion on turbulence modelling is already included in this document it will not be repeated here. Rather, the turbulence models that were considered in the analysis will only be mentioned for the sake of clarity. These are;

1. The K-Epsilon Model:
  - a. Realizable Two-Layer model.
  - b. Used in conjunction with a high  $y^+$ -mesh.
2. The K-Omega Model:
  - a. Shear-Stress-Transport (Menter) model.
  - b. Used in conjunction with a low  $y^+$ -mesh.
  - c. This model was run with and without the  $\gamma$ -Re- $\theta$  transition model enabled.
3. The Reynolds Stress Model:
  - a. Linear Pressure-Strain Two-Layer Model.
  - b. This model was run on both a high  $y^+$ -mesh as well as a low  $y^+$ -mesh.

Grid 1 as described in Table 5 was used for all the simulations that were conducted in this section, with the exception of those turbulence models that were run on a high  $y^+$ -mesh. In these instances the mesh in the far-field is identical to that of Grid 1 but the boundary layer, i.e., the near-wall mesh varies. The construction of this high  $y^+$ - boundary layer mesh can be found in Appendix A.

#### 3.4.1. Results from Numerical Analysis

The results obtained from the analyses were compared to results published in the literature. First, the total and partial drag components were compared to the experimental results that were published by (Ahmed, et al., 1984). Thereafter the velocity profiles obtained from the simulations were compared to the experimental results obtained by (Lienhart, et al., n.d.). It was by investigating the ability of a given turbulence model to accurately capture both the drag as well as the velocity profiles of the Ahmed's body, that an informed decision could be made regarding an appropriate turbulence model to use.

##### 3.4.1.1. Drag Coefficient Results

Experimental work completed by (Ahmed, et al., 1984) measured not only the total drag experienced by the Ahmed's body, but also the various partial drag components the respective portions of the body, i.e., the nose, sides and feet, slope and the back, contribute. The results of this study were used to construct the graph displayed in Figure 60. This graph shows the systematic, cumulative effect of the respective partial drag components, but for the evaluation of the turbulence models it was deconstructed into its various components. This was done in order to identify the flow phenomenon that a given turbulence model captures best, since no single turbulence model is able to capture all phenomena precisely. Thus, by considering the various drag contributions in isolation, a more informed

decision may be made with regard to the appropriate turbulence model to use in the future train-nose optimization problem. That is, which flow phenomena must be captured as precisely as possible and which may be reasonably compromised. In order to have allowed for a holistic decision making process, simulations were conducted for slope angles of five, fifteen, twenty-five and thirty-five degrees respectively. The results that were obtained from these simulations will be discussed below, both in terms of the total drag as well as the component wise partial drag contributions.

The results obtained for the total drag of the Ahmed's body (see Figure 61 and Table 7) show that the RSM (High  $y^+$ -mesh) performs best with the smallest average deviation from the experimental results (8.71%), followed by the  $k-\omega$  SST (13.87%),  $k-\epsilon$  Realizable Two-Layer (14%),  $k-\omega$  SST with transition (14.03%) and finally the RSM (Low  $y^+$ -mesh) (17.56%) respectively. It is, however, worth noting that the RSM (high  $y^+$ -mesh) also has the greatest deviation range (16.10%) and as such the greatest measure of uncertainty in the results that it yields, i.e., it is unknown to what extent the drag result it yields is truly a function of the change in geometry rather than a consequence of numerical error. Clearly then, the choice of appropriate turbulence model is not quite as simple as selecting the model which yields the smallest average deviation from the experimental results. It is therefore pragmatic to also consider the variation in a given turbulence model's performance for the individual regions of the Ahmed's body, hereby allowing for the quantification of the error made as well as identifying the region and associated flow-type contributing most to the total error.

Since this study concerns itself with the optimization of the train nose, it is important that the chosen turbulence model is able to capture the flow behaviour over the nose with reasonable accuracy. Figure 62 shows the partial drag results for the nose as obtained by various turbulence models. While it is evident that the RSM (High  $y^+$ -mesh) may have the largest offset from the experimental values, this offset remains approximately constant. The RSM (High  $y^+$ -mesh) is also the only turbulence model able to capture the trend of the partial drag component as a function of the inclination angle, i.e., the partial drag component increases steadily until approximately thirty degrees, where after the value decreases. The  $k-\omega$  SST model also performs well and while it does not capture the trend as accurately as the RSM (High  $y^+$ -mesh) its average offset from the experimental values is considerably smaller. Thus either one of these two turbulence models is a viable option for the future optimization of the train nose. It is also worth noting that the Ahmed's body has a very blunt nose and as such its design is not advantageous to drag reduction, rather the sizable stagnation region will contribute to pressure drag. From aerodynamic principals it is expected that the optimized nose be longer, with a smoother transition between it and the remainder of the train body. Furthermore, it is known from the theory that the  $k-\omega$  SST model does well for flows over a flat plate, as well as for flows under an adverse pressure gradient (Menter, 2011). As the optimization process generates increasingly more streamlined nose shapes, the flow over the nose will tend to the aforementioned flat-plate flow. The  $k-\omega$  SST model is therefore a reasonable choice, not only based on the results in Figure 62 and Figure 63, but also because its performance is expected to improve for those nose shapes that are in fact favourable for drag considerations.

The experimental results obtained by Ahmed combined the partial drag coefficients of the sides of the body with that of the feet. This is unfortunate to some degree since the flow phenomena along the sides of the body resembles that of flow over a flat plate, while the feet are bluff bodies with some measure

of stagnation expected on their upstream faces followed by vortex shedding further downstream. These are two decidedly different flow phenomena and as such the turbulence model that predicts one of the phenomena well, might not be as successful with the other. It is therefore not very telling to consider the results of Figure 64 and Figure 65 in isolation. Be that as it may, it is of some value to note that all the turbulence models that were considered predicted an approximately constant partial drag coefficient irrespective of the inclination angle of the slope. In fact, the only real difference between them lies in the magnitude of the offset from the experimental values. Consequently, based purely on Figure 64 and Figure 65, it is somewhat irrelevant which turbulence model is chosen since the error that is made remains approximately constant. Another consideration to be borne in mind is that the bogies of the high-speed train will be fitted with fairings and as such the performance of a given turbulence model pertaining to the feet region is not critical. Rather, it is the accurate prediction of the flow along the sides of the body that is of greater importance.

The simulation results for the partial drag component of the slope are given in Figure 66 and Figure 67. While all the turbulence models perform reasonably well for most inclination angles, there are a few exceptions. The  $k-\omega$  SST model performed well for all angles save for twenty-five degrees where it under-predicted the partial drag by approximately twenty-seven percent (see Figure 67). Since the slope is an area where flow separation occurs, it is expected that the eddy viscosity models find it challenging to predict the flow behaviour accurately in this region. What is, however, somewhat peculiar is the superior performance of the  $k-\epsilon$  Realizable Two-Layer model (henceforth referred to simply as the  $k-\epsilon$  model). Since both the  $k-\omega$  SST as well as the  $k-\epsilon$  model uses the  $\epsilon$ -scale equation in the far-field and both models make use of realizability, hereby mitigating the effects of separation on accuracy to some extent, a similar performance is expected from these models in the separation region. A plausible hypothesis is the strong measure of turbulence anisotropy associated with the irrotational longitudinal vortices present on the slope at this angle (see section 2.4.2); the  $k-\omega$  SST model makes use of a linear relation between the Reynolds stresses and the mean strain rate which tends to strongly under predict the anisotropy of the turbulence. The performance of the RSM (High  $y^+$ -mesh) and the  $k-\epsilon$  model at thirty-five degrees are also outliers in the otherwise well-performing simulation results. It is known from the theory that at thirty-five degrees the flow separates at the trailing edge of the roof (see section 2.4.2). It is therefore plausible that the poor performance of these models at this angle may be attributed to the  $\epsilon$ -scale equation's notorious under-prediction of separation and implied over-prediction of the fluid's viscosity. Consequently, it is expected that the wall shear stress as determined by these models is over-predicted, as is observable in the over-estimation of the partial drag component of the slope in Figure 66.

Figure 68 and Figure 69 show the simulation results obtained for the partial drag of the back region. From these figures it is clear that all the turbulence models perform well save for a few outliers at twenty-five degrees, these are the  $k-\omega$  SST, the  $k-\omega$  SST (with transition) and the  $k-\epsilon$  model. It was mentioned previously that at twenty-five degrees there exists irrotational longitudinal vortices in the wake region (see section 2.4.2). These vortices have their origin at the top corners of the slope but extend into the back region and trail some distance behind the body. It is therefore plausible that the inaccurate results yielded by the eddy viscosity models at this angle are a consequence of these vortices.

The shortcomings of these models when faced with highly anisotropic turbulent flows have already been discussed above.

In conclusion, all the turbulence models that were considered performed well in some way. There are however two models that consistently performed well, namely the RSM (High  $y^+$ -mesh) and the  $k-\omega$  SST. If the only consideration when selecting a turbulence model were accuracy, the RSM (High  $y^+$ -mesh) would be the clear choice between the two. Not only is it the model that showed the smallest average deviation from the experimental results for the total drag, but it also predicted the component-wise trends of the experimental data with the most accuracy. Unfortunately it is computationally expensive, requiring all the components of the specific Reynolds stress tensor to be solved directly. Since the  $k-\omega$  SST model offers reasonable accuracy and requires only two equations to be solved, it is a viable alternative to the RSM (High  $y^+$ -mesh). An additional advantage offered by the  $k-\omega$  SST is the low  $y^+$ -mesh on which it runs. While this does increase the cell count of the mesh, it also addresses the issue of the blended region ( $5 < y^+ < 30$ ). That is, the flow field around the train body is very complex with areas of stagnation, separation and the like. Elements that lie in regions such as these see low to no velocity. If a high  $y^+$ -mesh is made use of, it is therefore impossible to avoid the blended region and in many cases the  $y^+$ -values of the elements will lie in the valid region for a low  $y^+$ -mesh. A low  $y^+$ -mesh does not face the same challenge; its valid region for  $y^+$ -values lies between zero and five (heat transfer is not considered here) and the blended region can be altogether avoided with sufficient refinement of the boundary-layer mesh. It is therefore a much simpler task to build a mesh for which all elements lie in the valid  $y^+$ -region, hereby lessening the degree of numerical uncertainty of a solution obtained from such a mesh.

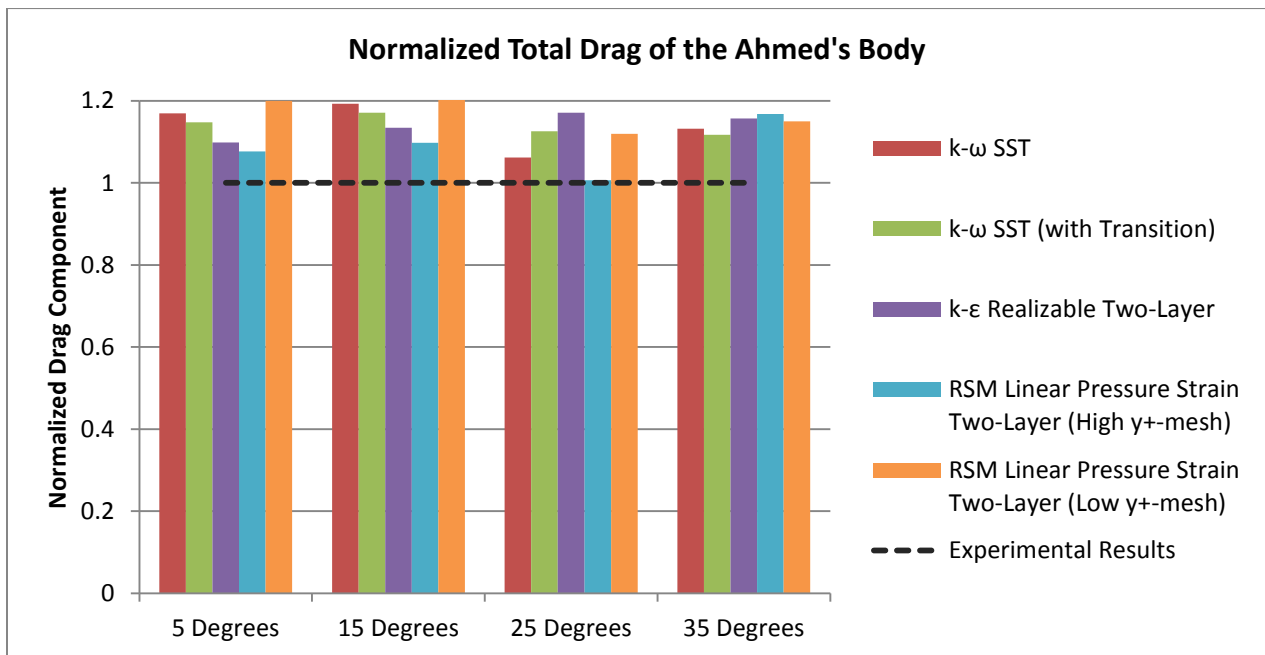


Figure 61: The total drag of the Ahmed's body as obtained from various turbulence models. The total drag results obtained from the various turbulence models were normalized by the experimental value of the total drag as obtained by (Ahmed, et al., 1984). All simulation results were obtained for slope inclination angles of five, fifteen, twenty-five and thirty-five degrees respectively.

Slope Angle [Degrees]	Percentage Deviation from Experimental Values for Total Drag [%]				
	k- $\omega$ SST	k- $\omega$ SST (with Transition)	k- $\epsilon$ Realizable Two - Layer	RSM LPS Two - Layer (High $y^+$ )	RSM LPS Two - Layer (Low $y^+$ )
5	16.93	14.76	9.83	7.66	19.99
15	19.26	17.07	13.41	9.78	23.34
25	6.14	12.58	17.07	0.65	11.90
35	13.17	11.74	15.69	16.75	15.01
<b>Average Deviation [%]</b>	13.87	14.03	14.00	8.71	17.56
<b>Max.Dev - Avg.Dev [%]</b>	5.38	3.03	3.07	8.04	5.78
<b>Min.Dev - Avg.Dev [%]</b>	-7.73	-2.30	-4.17	-8.06	-5.66
<b>Deviation Range [%]</b>	13.11	5.33	7.23	16.10	11.44

Table 7: The deviation percentage from the experimental values for total drag associated with each respective turbulence model. Results are given for slope angles of five, fifteen, twenty-five and thirty-five degrees. The abbreviation “LPS” stands for “Linear Pressure Strain”.

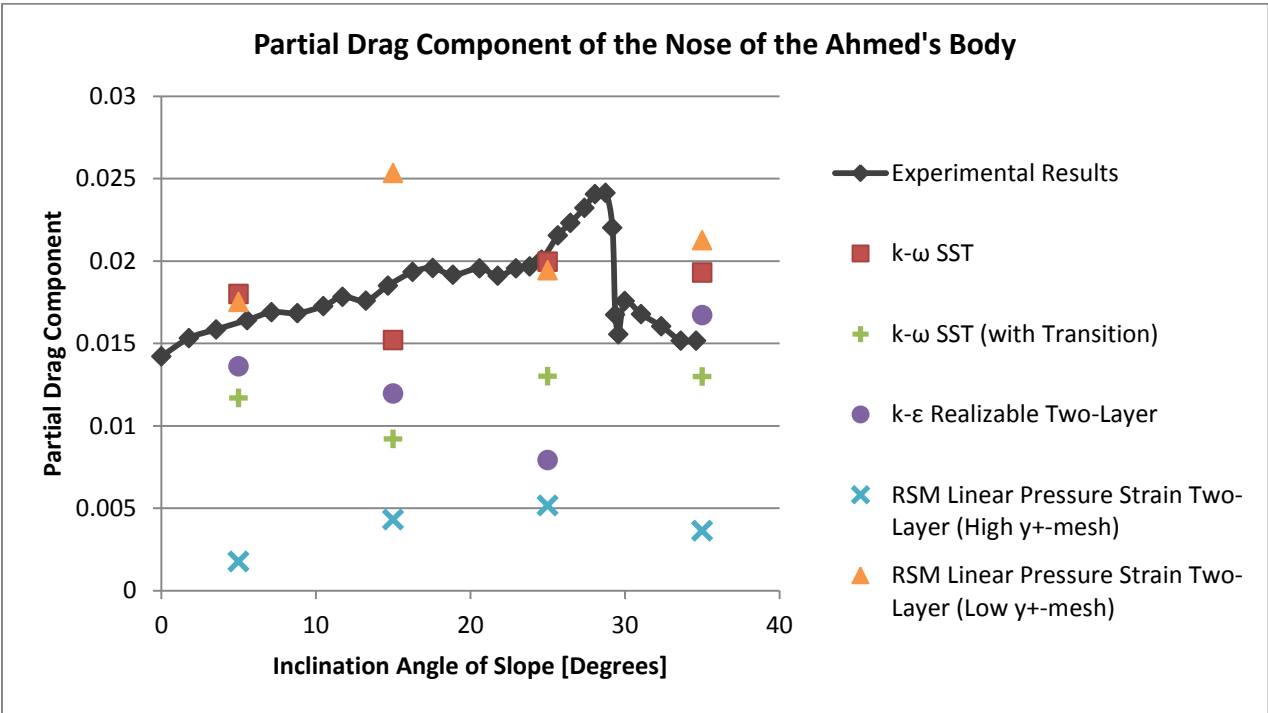


Figure 62: The Partial Drag Component of the Nose of the Ahmed’s body as obtained by various turbulence models plotted together with the experimental values of the same as obtained by (Ahmed, et al., 1984). All simulation results were obtained for slope inclination angles of five, fifteen, twenty-five and thirty-five degrees respectively.

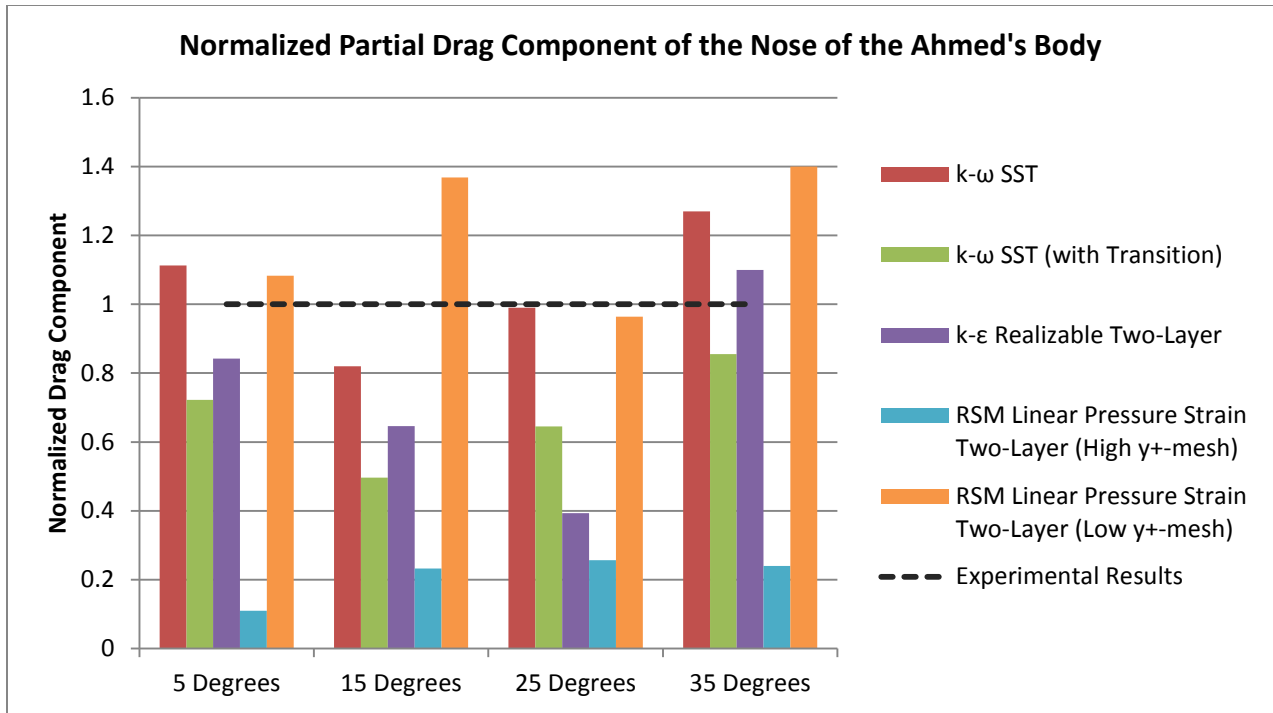


Figure 63: The Nose Partial Drag component of the Ahmed's body as obtained from various turbulence models. The drag results obtained from the various turbulence models were normalized by the experimental value of the nose drag component as obtained by (Ahmed, et al., 1984). All simulation results were obtained for slope inclination angles of five, fifteen, twenty-five and thirty-five degrees respectively.

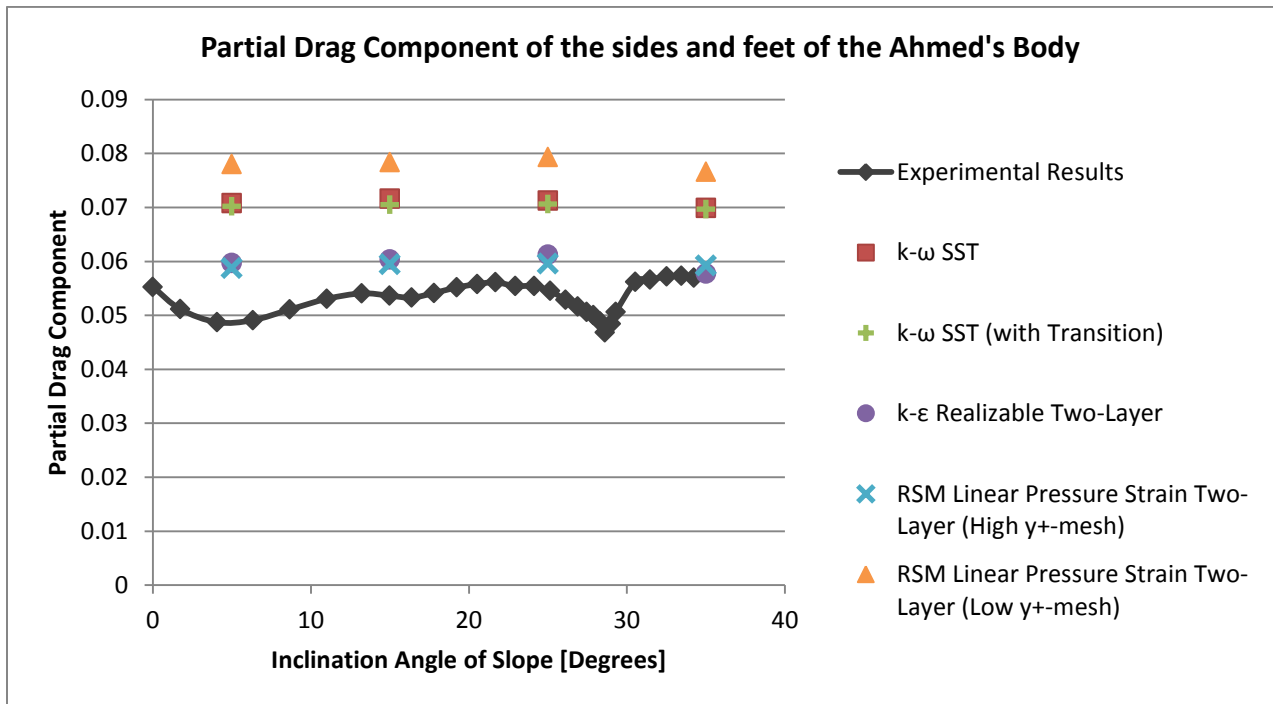


Figure 64: The Partial Drag Component of the sides and feet of the Ahmed's body as obtained by various turbulence models plotted together with the experimental values of the same as obtained by (Ahmed, et al., 1984). All simulation results were obtained for slope inclination angles of five, fifteen, twenty-five and thirty-five degrees respectively.

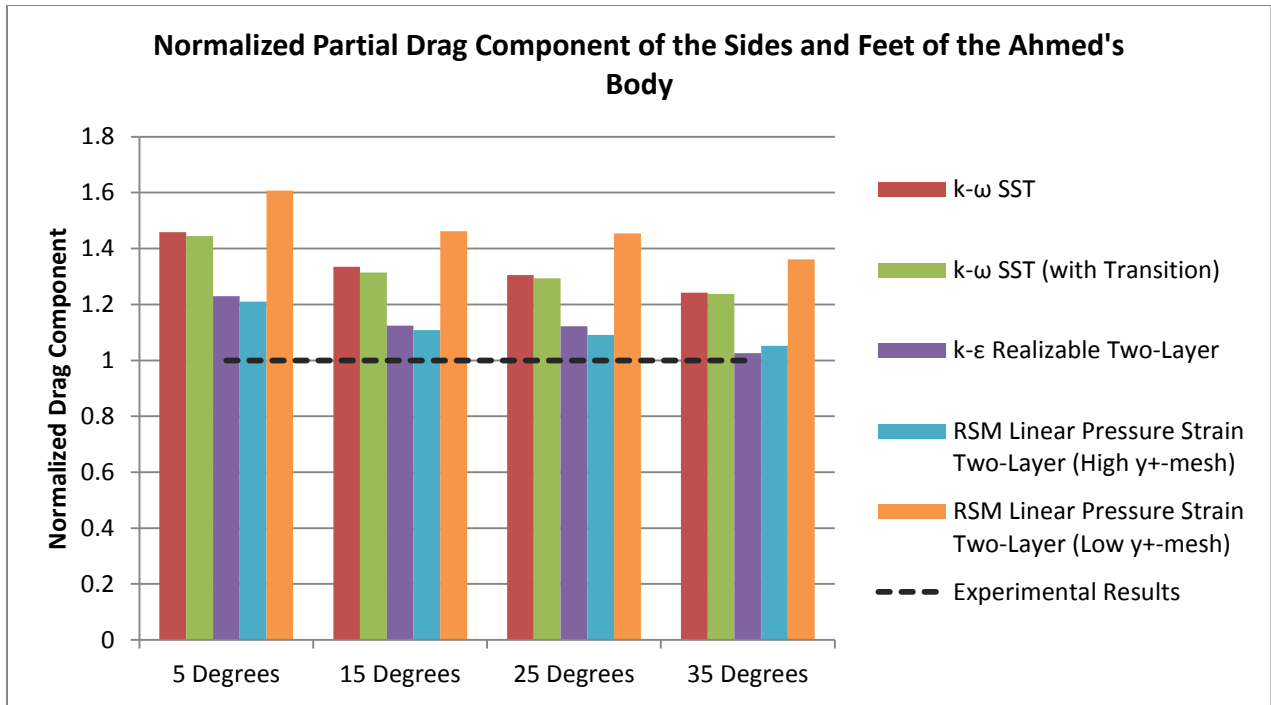


Figure 65: The “Sides and Feet” Partial Drag component of the Ahmed’s body as obtained from various turbulence models. The drag results obtained from the various turbulence models were normalized by the experimental value of the “Sides and Feet” drag component as obtained by (Ahmed, et al., 1984). All simulation results were obtained for slope inclination angles of five, fifteen, twenty-five and thirty-five degrees respectively.

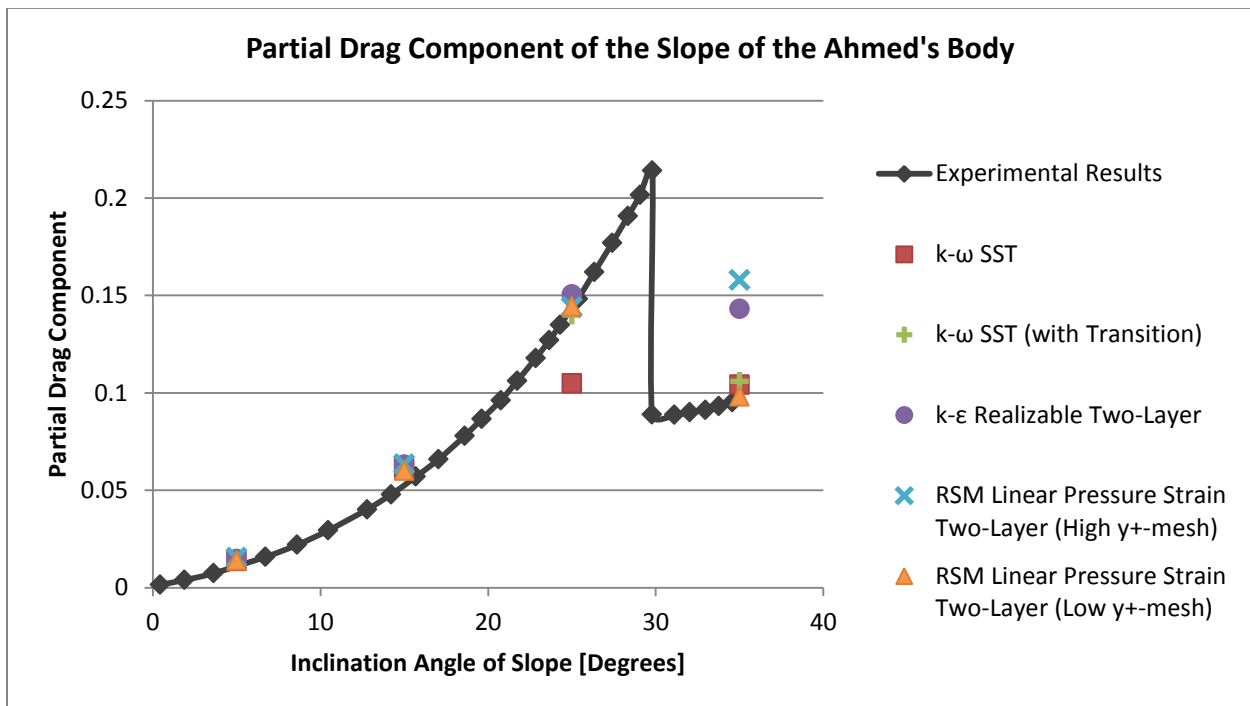


Figure 66: The Partial Drag Component of the Slope of the Ahmed’s body as obtained by various turbulence models plotted together with the experimental values of the same as obtained by (Ahmed, et al., 1984). All simulation results were obtained for slope inclination angles of five, fifteen, twenty-five and thirty-five degrees respectively.

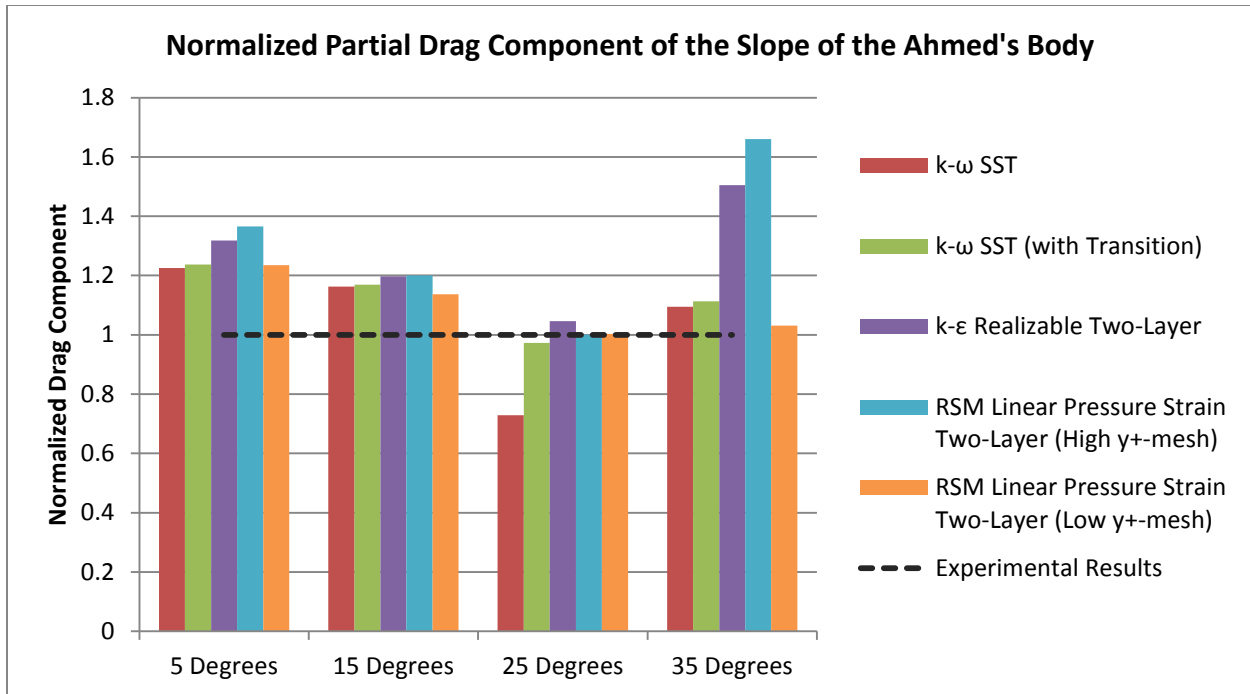


Figure 67: The Slope Partial Drag component of the Ahmed's body as obtained from various turbulence models. The drag results obtained from the various turbulence models were normalized by the experimental value of the slope drag component as obtained by (Ahmed, et al., 1984). All simulation results were obtained for slope inclination angles of five, fifteen, twenty-five and thirty-five degrees respectively.

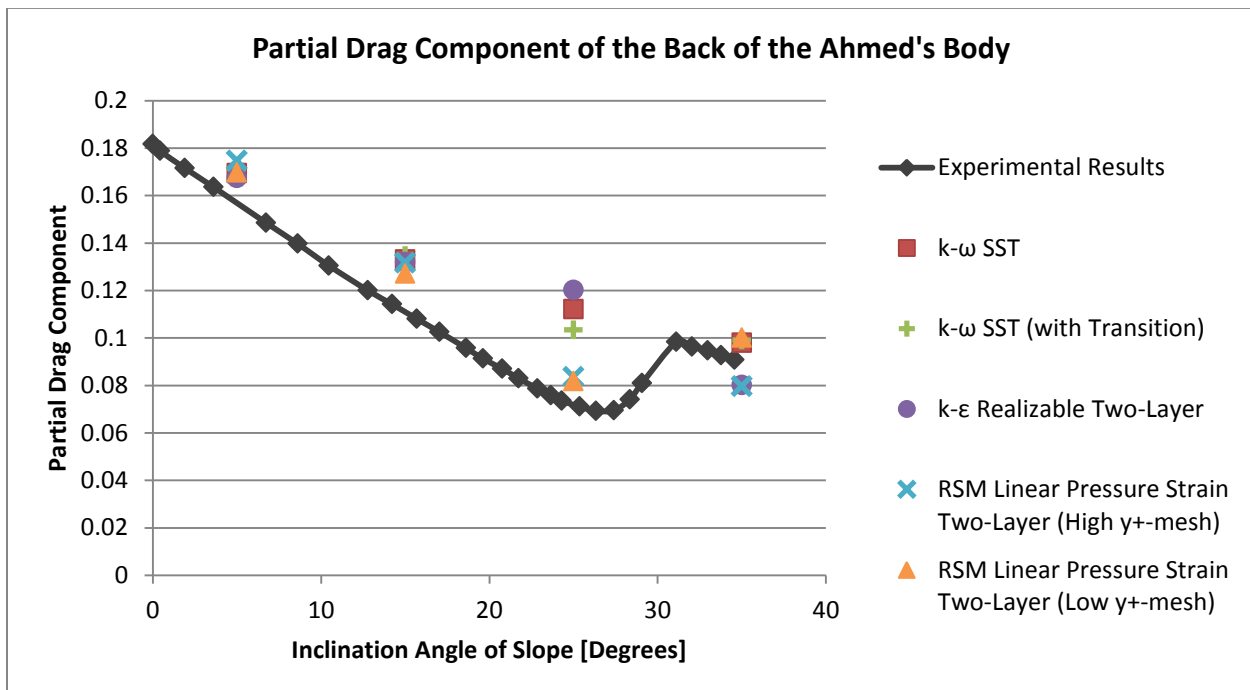


Figure 68: The Partial Drag Component of the Back of the Ahmed's body as obtained by various turbulence models plotted together with the experimental values of the same as obtained by (Ahmed, et al., 1984). All simulation results were obtained for slope inclination angles of five, fifteen, twenty-five and thirty-five degrees respectively.

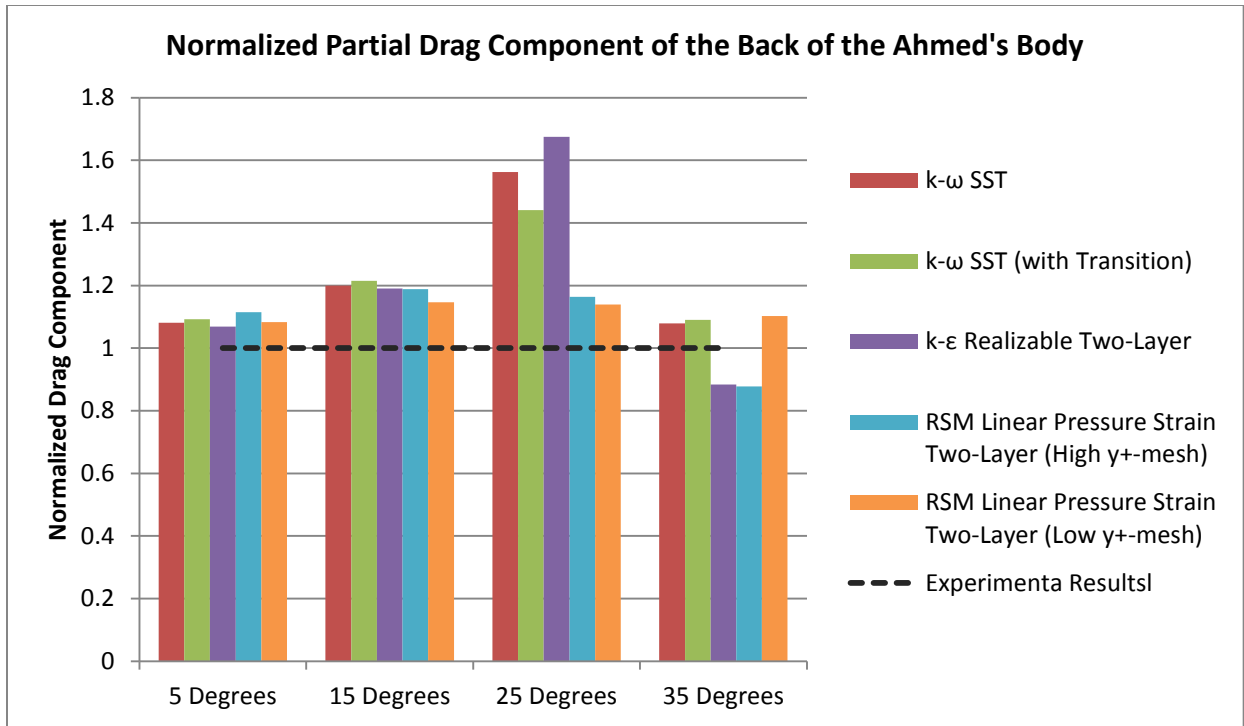


Figure 69: The Back Partial Drag component of the Ahmed's body as obtained from various turbulence models. The drag results obtained from the various turbulence models were normalized by the experimental value of the back drag component as obtained by (Ahmed, et al., 1984). All simulation results were obtained for slope inclination angles of five, fifteen, twenty-five and thirty-five degrees respectively.

### 3.5. Minimization of drag on Ahmed’s body

The algorithm that was discussed above (see section 2.5.2.3) and which is intended to be used for the optimization of the high-speed train is known as the SHERPA algorithm. Since a theoretical discussion pertaining to this algorithm has already been completed, it will not be repeated here. Rather, this section will investigate the ability of the SHERPA algorithm to accurately predict the optimal design of the Ahmed’s body, i.e., the inclination angle of the slope that yields the minimum drag. This is a convenient benchmark case, since the ideal inclination angle is known to be approximately 9.23° from the experimental values published in literature (Ahmed, et al., 1984).

In the previous section (see section 3.4) various turbulence models were considered. Based on the numerical results obtained from these models it was decided that the k- $\omega$  SST as well as the RSM (high y+-mesh) were viable options, with the Reynolds’ stress model displaying the superior performance. Both these turbulence models were thus considered for this validation study of the SHERPA algorithm. The optimization parameters were identical for both cases (Table 8) with the only variable being the turbulence model in question. In so doing the differences in performance of the optimization algorithm in each instance can be attributed to the effect of the turbulence model only.

<b>Optimization Type:</b>	Weighted sum of all objectives
<b>Number of Designs to Run:</b>	40
<b>Input Parameter:</b>	Inclination Angle
<b>Parameter Type:</b>	Continuous
<b>Range:</b>	[1.0, 35.0]
<b>Resolution:</b>	137
<b>Response:</b>	Mean Drag Coefficient
<b>Goal:</b>	Minimize Mean Drag Coefficient

Table 8: The parameters that describe the single-objective optimization of the slope of the Ahmed’s body for the total drag coefficient

From the results of the optimization study (see Table 9) it is clear that while both turbulence models perform reasonably well, the RSM shows the better performance of the two. Not only does it predict the trend of the total drag coefficient as a function of the inclination angle best (see Figure 70), but it also predicts an optimal inclination angle that deviates with only 2.49% from the true optimal angle. Additionally the RSM turbulence model over-predicts the optimal drag coefficient by 13.56% while the k- $\omega$  SST performs less favourably and over-predicts the optimal drag coefficient by 23.19%. Furthermore, the k- $\omega$  SST model has particular trouble capturing the trend of the total drag coefficient for inclination angles ranging from approximately 24.25° to 31°. Since the strength of the longitudinal trailing vortices increase as the inclination angle tends to 30° a plausible hypothesis for this inability to capture the total drag coefficient in this region may be the k- $\omega$  SST model’s difficulty in predicting anisotropic flow behaviour. In light of the fact that the presence of anisotropic flow phenomena in the flow field surrounding the train is likely, the RSM is the most suitable choice of turbulence model to capture the external flow field. It is worth noting however, that the k- $\omega$  SST is less computationally expensive than the RSM and while the RSM performed better, the k- $\omega$  SST was still able to reasonably predict the trend of the total drag coefficient and find an optimal inclination angle with a deviation of

18.74% from the true optimal angle. Both these turbulence models are therefore viable options based on the results of the optimization study.

Finally then, while it is expected that all optimization algorithms should be able to solve this single parameter, uni-modal problem, SHERPA's unique, self-taught nature is revealed by the concentration of data points as seen in Figure 70; the largest concentration of design points lie in the vicinity of the optimal inclination angle, with the other design points sparsely distributed over the remaining angles. It is however, important to notice the dependency of the answer on the selected turbulence model; the general trend of the total drag coefficient was captured in both cases (k- $\omega$  SST as well as RSM) and the numerically determined optimal inclination angle that was identified in each respective case, lay in the vicinity of the true minimum but the RSM model performed considerably better than the k- $\omega$  SST model (see Table 9). Clearly then, it is not simply a matter of choosing an appropriate search algorithm but a turbulence model that is able to supply the search algorithm with reliable data.

	<b>RSM</b>	<b>k-<math>\omega</math> SST</b>	<b>Experimental</b>
<b>Optimal Inclination Angle [Degrees]</b>	9	7.5	9.23
<b>Deviation from Experiment [%]</b>	2.49	18.74	-
<b>Minimized Drag Coefficient</b>	0.2605	0.2826	0.2294
<b>Deviation from Experiment [%]</b>	13.56	23.19	-

Table 9: The results of the optimization studies as obtained by making use of the Linear Pressure-Strain as well as the k- $\omega$  SST turbulence models respectively and the deviation of said results from the experimental values.

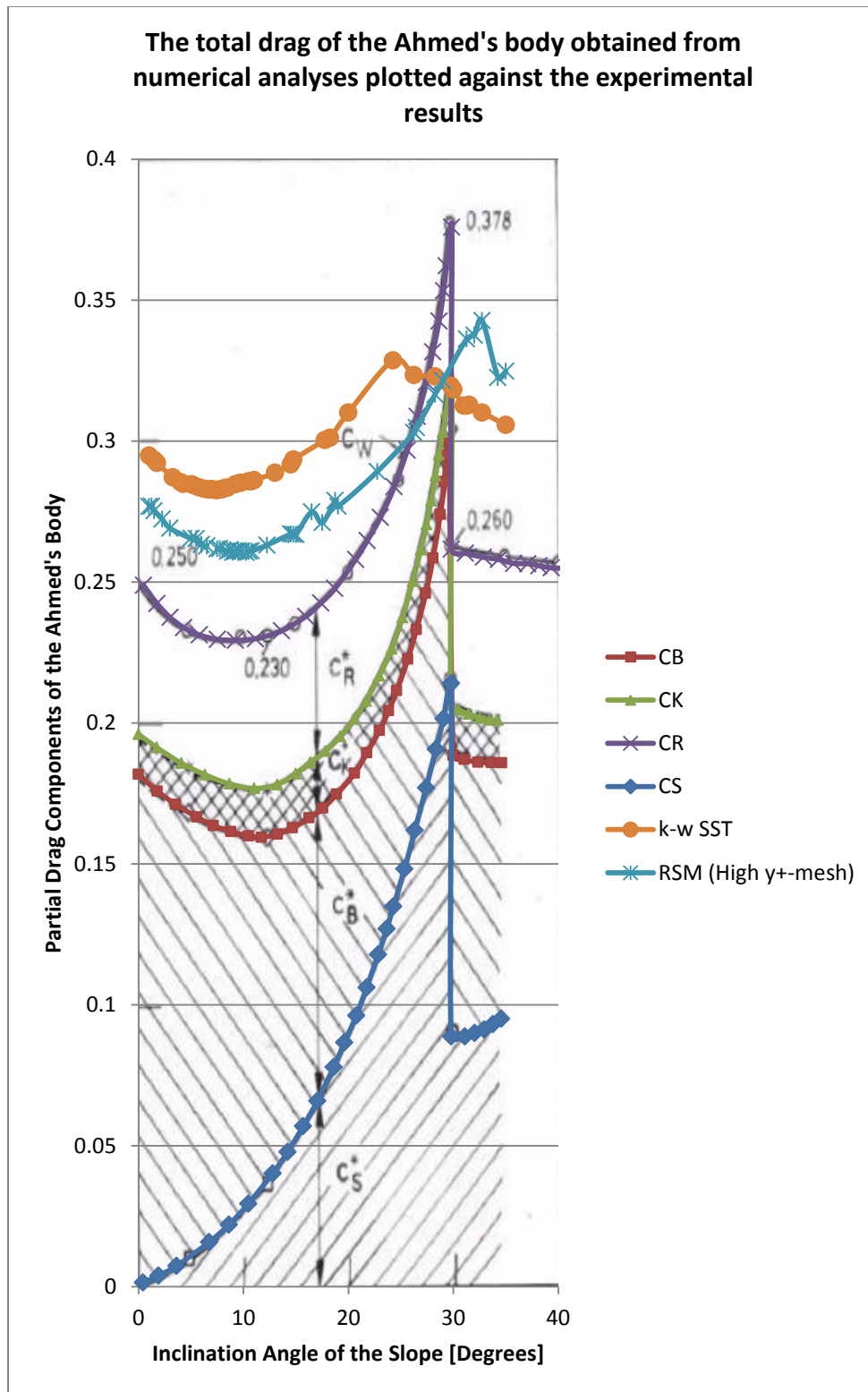


Figure 70: The total drag of the Ahmed's body as obtained from numerical analyses plotted against the experimental results.

## 4. Optimization of the High-Speed Train Nose and Tail for Windless Conditions

The first load case that will be considered for the optimization of the nose and tail geometry, is for the train travelling at high speed in a windless condition. This is considered to be the normal operating condition since there will certainly be days during which the wind loading is negligible if not zero. Of course this is not to say that there will generally speaking be no wind present, but the nature of the wind loading that a train may see can vary significantly. This is not only a function of the wind and its fickle nature (e.g., anything from a gentle breeze to a strong gust is possible) but also as a function of the orientation of the track relative to the wind. There is much uncertainty and many variables once wind is considered and as such it is useful to determine the nose shape for a condition that is devoid of this uncertainty. Furthermore, the train's orientation on any given track may at times be parallel to the direction of the wind and while this loading condition is not identical to windless conditions, they share similarities and as such it is conceivable that a shape that is favourable under windless conditions will also perform well with wind from the front or rear. Finally, the train is approximately four meters high, placing it firmly in the boundary layer of the wind, therefore the velocity of the train in comparison to that of the average wind in this region is such that the effect of the wind on the relative velocity may be negligible in many instances. It is with these general cases that this chapter concerns itself.

### 4.1. Simulated Geometry

The train geometry that the nose optimization will be performed on has been simplified in order to allow for a computationally viable numerical model. Features such as the inter-carriage gaps as well as geometric details such as door handles and windows have been omitted in an attempt to minimize cell count and ease solution convergence. Furthermore, while the cross-section of the train body is identical to that of coaches already being developed by Transnet Engineering in width and height, a further assumption is made that the bogies have been faired. While fairings do not smooth out the bogies entirely, the effect they have in dissipating the energy in the boundary layer is limited in this way. In this model the faired bogies, underbody and train sides have therefore been approximated as smooth surfaces. Clearly then, the number of assumptions and simplifications to the train geometry is considerable. Unfortunately the nature of optimization is such that in and of itself, it is already a computationally expensive process. In addition, the geometry is to be optimized for external flow conditions which imply large computational models as well. It is therefore necessary to simplify the train geometry as far as reasonably possible to ensure that the optimization thereof remains computationally viable. And while the resultant flow field surrounding the train model in question may not be true to reality, the trends that are predicted for the drag, lift and rolling moment as functions of the nose parameters (see Figure 71 and Table 10) may be identified nonetheless. The final simplified train model that was optimized for was 120m long and consisted of six cars of 20m each, two locomotives and four passenger carriages, all of which are located at 75mm above the ground surface in keeping with Transnet standards which requires this minimum clearance between the cowcatcher and the ground.

The geometry of the train nose, and consequently the geometry of the trailing locomotive, that is to be optimized, is illustrated in Figure 71; the profile of the cross-section of the train body (symmetrical about the xz-plane) as well as the side profile of the nose (on the longitudinal symmetry plane) are

shown. The three-dimensional nose shape is obtained by lofting between these profiles while different nose geometries are obtained by varying the values of three control points on the side profile of the nose. These points are the height of the nose tip ( $z_0$ ), the length of the nose ( $L$ ) and the height of the inflection point between the nose tip and the top of the train roof ( $H$ ) (see Figure 71 and Table 10), while the x-coordinate of the control point H ( $x_H$ ), is defined as  $0.5L$ . Since the side profile of the nose was constructed by making use of a spline that is fitted through the control points, constraints were placed at the locations where the nose profile joins the train body in order to avoid impractical nose shapes to be assumed, i.e., the spline must always be tangent to the train body. The range of values over which these control points were allowed to vary can be seen in Table 10. These ranges were chosen in such a way that the nose shapes that are generated by assuming them remain viable, i.e., impractical nose shapes were excluded from the optimization from the onset. The upper bound of the range of nose lengths was not a geometric constraint however, rather from the literature it was found that beyond this point the law of diminishing return applies (see section 2.2.1).

The choice of control points that define the nose shape was informed by work completed in section 2.4. By varying these points the so-called “fastback”, “squareback” or “notchback” configurations could be assumed. This allowed the optimization to be completed over a much larger design space, i.e., a larger range of possible nose shapes could be assumed thereby reducing the number of unexplored designs that necessarily accompany optimization problems. Put differently, the manner in which a given nose shape is parameterized will necessarily constrain the geometries that can be generated. It may very well be that some hypothetical ideal shape lies in this domain of geometries that cannot be assumed and as such that domain cannot be explored. By parameterizing the geometry in such a way that it can assume a large number of shapes, the size of the domain that remains unexplored is reduced. Consequently the probability that the hypothetical ideal can be attained, or at the very least a shape that tends to said “ideal”, is increased.

<b>Variables</b>	L	$Z_0$	H
<b>Description</b>	Varies the length of the nose.	Varies the height of the tip of the nose.	Toggles between “notchback” and “fastback” or “squareback” configurations
<b>Range</b>	$2\text{m} \leq L \leq 7.7\text{m}$	$0.7\text{m} \leq Z_0 \leq 1.5\text{m}$	$2\text{m} \leq H \leq 3\text{m}$

Table 10: Significant geometric parameters that define the shape of the train nose and which could alter the flow that surrounds the train. The permissible ranges for which these parameters will be optimized are also given.

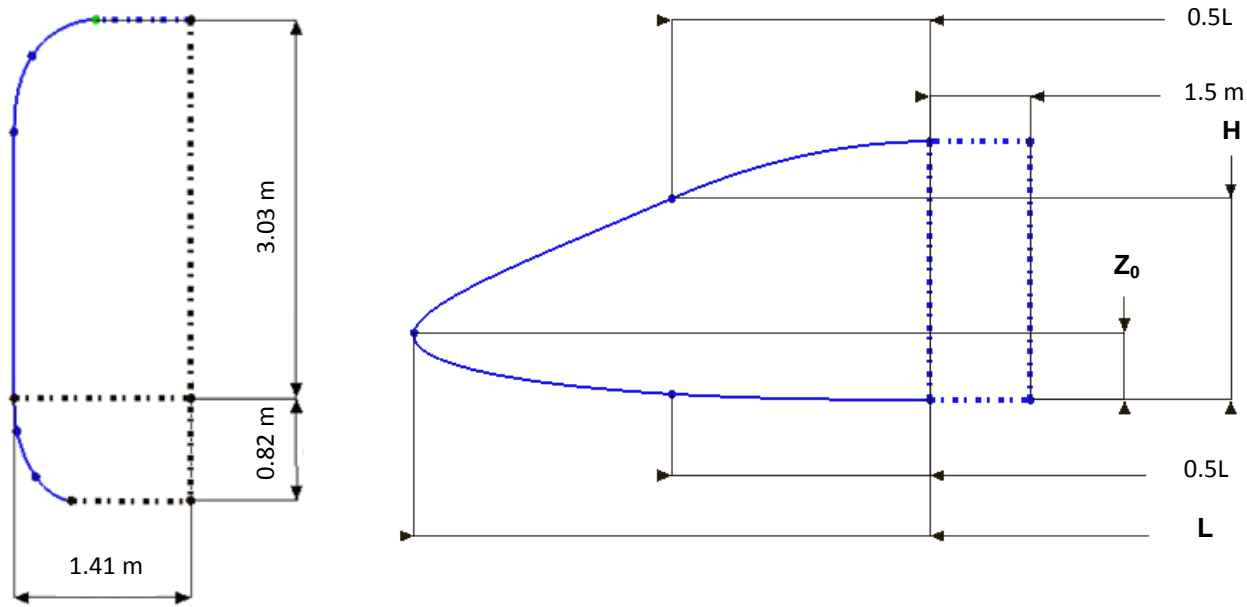


Figure 71: The geometry of the train nose and tail that was to be optimized. Left: The cross-section of the train body, symmetrical about the  $z$ -plane, as seen from the front. Right: The parameterization of the train nose indicated on the side profile thereof.

<p>L=2m  <math>Z_0 = 1.02\text{m}</math>  <math>H = 2.7\text{m}</math></p>	<p>L=4.85m  <math>Z_0 = 1.34\text{m}</math>  <math>H = 2.8\text{m}</math></p>
<p>L=4.85m  <math>Z_0 = 0.7\text{m}</math>  <math>H = 2.4\text{m}</math></p>	<p>L=7.7m  <math>Z_0 = 1.02\text{m}</math>  <math>H = 2.6\text{m}</math></p>

Table 11: Examples of nose geometries that can be generated by varying the parameters as shown in Figure 71.

## 4.2. Configuration of the Computational Model

The boundary conditions, solver-type and flow parameters used for the simulation of the air flow around the train under windless conditions will be discussed here and are used throughout this section unless explicitly stated otherwise. Since the purpose of the simulation is to mimic reality as closely as reasonably possible, the boundary conditions that were used were chosen on this basis and are shown in Table 12 (to be read in conjunction with Figure 72). For this design case the cruising speed of the train is 97.22m/s (350km/h) and the ground and surrounding air are stationary in the physical world. The principles of relative velocity therefore dictate that since the model of the train is stationary in the simulation, the velocity of the inlet air as well as that of the ground must be 97.22m/s. In order to simulate the moving air, velocity inlets were specified at the inlet, side and top faces with a magnitude of 97.22m/s directed along the x-axis (see Figure 72). The motion of the ground was simulated by assigning a moving wall boundary condition to it; once again the velocity was 97.22m/s in the x-direction. A gauge pressure of 0 Pa was specified on the outlet face, hereby implying an averaged atmospheric condition and should the outlet face be adequately located from the train model this holds true to reality. Finally, since the train is symmetrical and the flow surrounding it is expected to be symmetrical on average, a symmetry boundary condition was used (see Figure 72) hereby allowing the cell count of the model to be reduced by half.

As mentioned above, the train is travelling at 350km/h and since a Mach number of above 0.3 is obtained for certain cells in the domain, it is clear that the compressibility of the air ought to be considered. In order to accomplish this, the density of the air must be variable which in combination with the high Mach numbers, necessitates the use of the Coupled solver in STAR-CCM+. An added advantage offered by this solver is the pseudo-time marching approach it makes use of which is able to more accurately capture the time-dependent turbulent eddies surrounding the train body, albeit in a steady state simulation. In order to simulate the behaviour of the air with compressibility effects considered, the ideal gas model was made use of and the air properties are specified as those at standard atmospheric pressure (see Table 13).

Domain Face	Boundary Type	Boundary Value
Ground Face	Moving Wall	[97.22, 0, 0] m/s
Inlet Face	Velocity Inlet	[97.22, 0, 0] m/s
Side Face	Velocity Inlet	[97.22, 0, 0] m/s
Top Face	Velocity Inlet	[97.22, 0, 0] m/s
Symmetry Face	Symmetry	-
Outlet Face	Pressure Outlet	0 Pa Gauge Pressure

Table 12: The boundary conditions used for the simulation of the airflow around the symmetry model of the train under windless conditions.

Property	Magnitude	Unit
Dynamic Viscosity	1.855E-5	Pa-s
Molecular Weight	28.966	kg/kmol
Specific Heat	1003.62	J/kg-K
Thermal Conductivity	0.026	W/m-K
Turbulent Prandtl Number	0.9	-

Table 13: The material properties of air at standard atmospheric pressure.

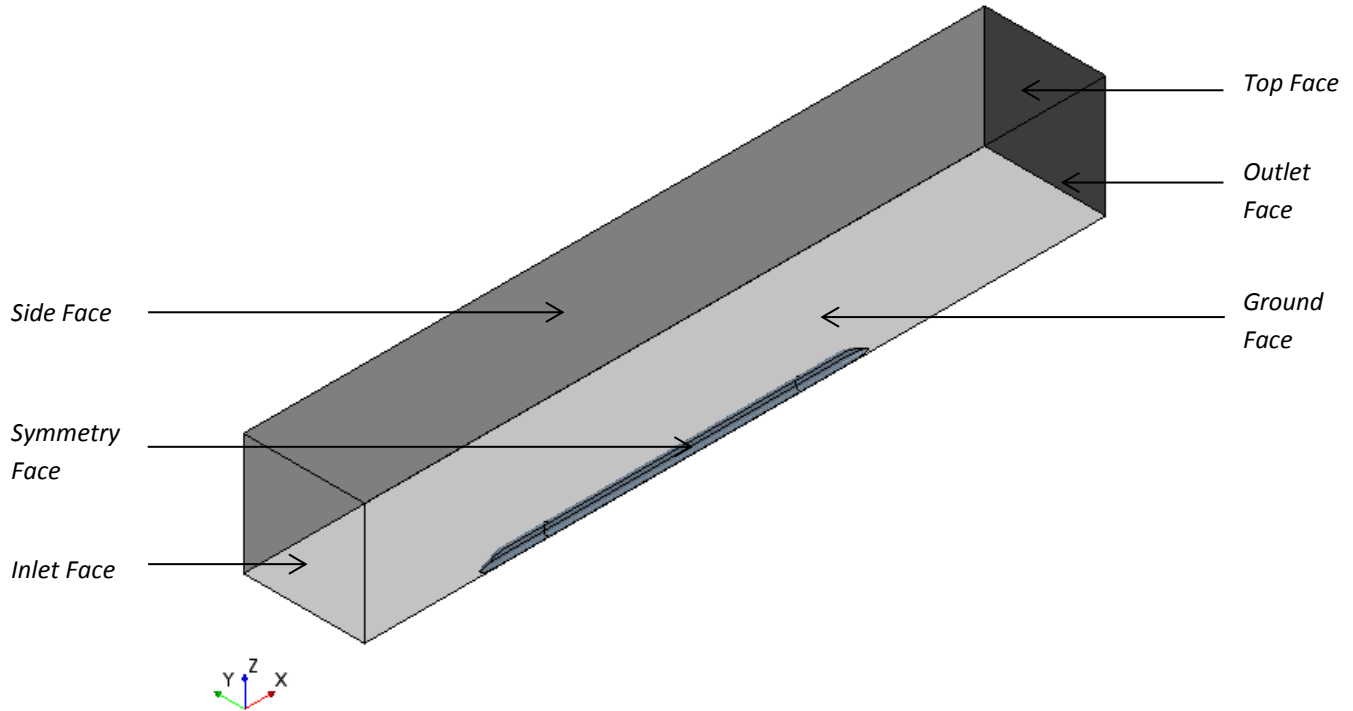


Figure 72: The computational domain, not drawn to scale, of the symmetry model of the train and the chosen nomenclature of the boundary faces.

### 4.3. Grid Convergence Study

The value of ensuring whether the mesh resolution for a given simulation is adequate has already been discussed in section 3.3. In a similar fashion to the aforementioned Ahmed's body validation case (see section 3), the grid convergence index methodology will be used here to determine an adequate grid resolution for the train model as well. Since the meshes, low- and high  $y^+$  respectively, that were constructed for the Ahmed's body in section 3.3.2 have already been validated as converged, they will be transposed onto the train model where after the base size of the train-mesh will be varied to determine convergence. This section will however, not only concern itself with determining an adequate mesh resolution for the train model, but will also consider the performance of the LPS Two-Layer turbulence model in comparison to the SST  $k-\omega$  turbulence model for the various grid refinements, hereby allowing a final decision regarding choice of turbulence model to be made. The nose geometry used throughout this section corresponds to that shown in Figure 71 which is obtained when the nose length ( $L$ ) is 7.7m, the tip height of the nose ( $Z_0$ ) is 1m, and the height of the inflection point ( $H$ ) is 3m.

#### 4.3.1. Transposed Computational Domain

The computational domain that was used for the grid convergence study is the domain that was obtained by transposing the domain of the Ahmed's body onto the train. Similar to the domain used for the simulation of the flow around the Ahmed's body, the domain used for the train is also a symmetrical model (see Table 14 and Figure 73). The characteristic length that was used in the construction of the Ahmed's body domain was the width of the body since it was the larger cross-sectional dimension. In the case of the train however, the larger cross-sectional dimension is its height and it will therefore serve as the characteristic length for the construction of the train domain. As a clarifying example, consider, the width of the Ahmed's body is 0.389m and the distance from the front inlet face to the nose of the body is 3.89m, which implies ten characteristic lengths. Similarly, the height of the train is 3.849m and given an inlet distance of ten characteristic lengths the inlet face of the train domain would be 38.49m from its nose.

It is worth mentioning that while this process was repeated for the outlet length of the train domain, thereby yielding an outlet distance of 76.98m, with the width and height arbitrarily chosen to be ten characteristic lengths each. This is due to the fact that the Ahmed's body was tested in a wind tunnel and the purpose of analyzing it was to mimic the experimental results and consequently choose an appropriate turbulence model. The train will however be travelling in the open and as such it is advantageous to increase the blockage ratio of it relative to the domain, especially considering the velocity at which the train is meant to travel and consequently its resultant flow field.

Domain Dimensions	Symbol of Domain Dimension	Number of Characteristic Lengths	Magnitude [m]
Inlet Distance	$D_i$	10L	38.49
Outlet Distance	$D_o$	20L	76.98
Width	W	10L	38.49
Height	H	10L	38.49

Table 14: Dimensions of the Initial Computational Domain.

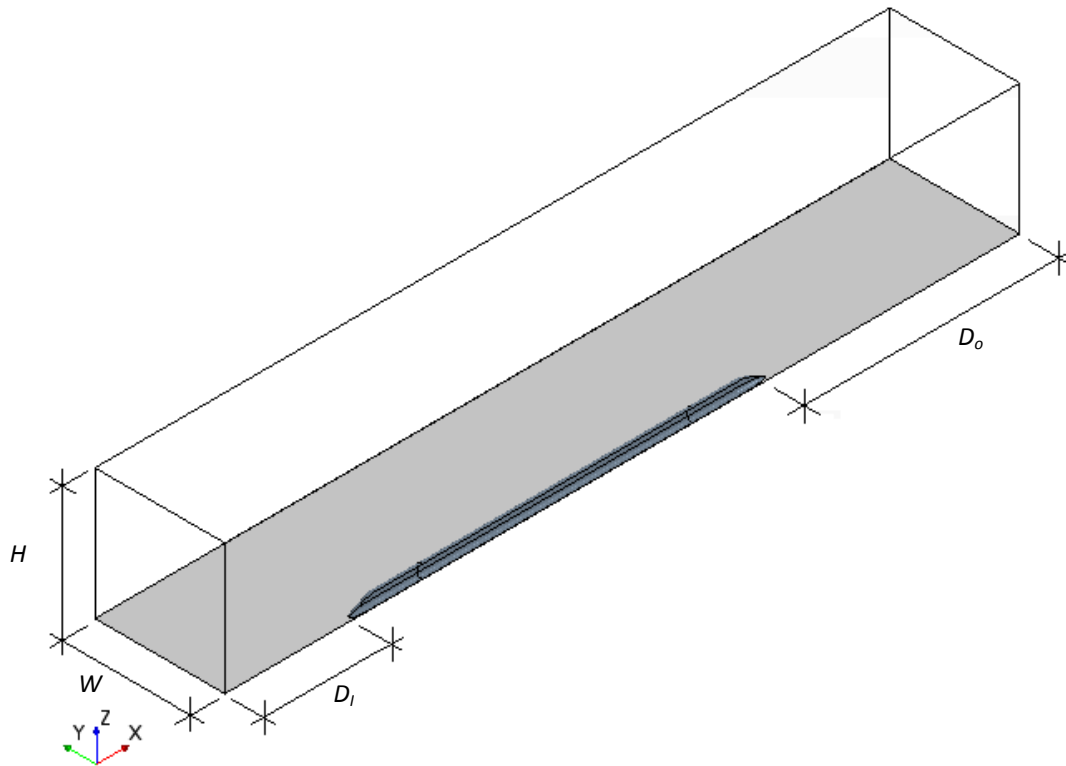


Figure 73: The initial computational domain, not drawn to scale, that was used for the grid convergence study and was obtained by transposing the computational domain of the Ahmed's body.

#### 4.3.2. Mesh Construction

Two mesh types were constructed for the grid convergence study, namely low  $y^+$ - and high  $y^+$ -meshes, which were created by taking the corresponding (low or high  $y^+$ ) mesh that was validated for the Ahmed's body and transposing it onto the train. Both mesh types were considered in order to allow the ability of the LPS two-layer and the SST  $k-\omega$  turbulence models to accurately capture the external flow fields, to be investigated.

There are, however, not only geometric differences between the two bodies, but differences in the flow conditions as well. Thus the mesh for the train had to be altered slightly in order to accommodate for these differences, consider; the velocity of the incoming air in the case of the Ahmed's body was 40m/s, whereas the incoming air in the case of the train travels at 97.22m/s, thus the number of cells through the boundary layer of the train model was increased so as to ensure that the  $y^+$ -values of the respective meshes lie in their permissible regions. Further mesh parameters that were also altered, include the boundary layer stretching factor, the surface element size on the train body, the minimum cell size on the ground and the target size of the surface cells on the ground (see Appendix B for a full discussion, as well as mesh descriptions). In addition to the slightly modified, transposed meshes, coarser meshes were also created for each mesh type, i.e., low- or high  $y^+$ , in an attempt to keep the necessary computational resources manageable (see Appendix B). As an illustrative example, the coarsened, high  $y^+$ -mesh corresponding to refinement level '2' (see Table 15) is shown in Figure 74 and Figure 75.

In accordance with the GCI method, the base cell size of the train model was varied in order to obtain three grid refinement levels for each of the mesh types, i.e., the low  $y^+$ - and high  $y^+$ -meshes. This process was repeated for the transposed mesh as well as the coarsened mesh and the resultant grids with their respective cell counts and corresponding base cell sizes may be seen in Table 15. It is these meshes that will be used in section 4.3.3 to determine grid convergence.

Mesh Refinement Level	Low $y^+$ -Mesh			High $y^+$ -Mesh		
	Base Cell Size [m]	Number of Cells [Millions]		Base Cell Size [m]	Number of Cells [Millions]	
		Transposed Mesh	Coarsened Mesh		Transposed Mesh	Coarsened Mesh
Level 1	2.5	16.57	7.9	2.2	11	8.82
Level 2	3.15	9.61	6.07	2.7	6.46	5.04
Level 3	3.935	5.75	3.37	3.4	3.69	2.87

Table 15: The cell count [millions] and corresponding base cell sizes of the high  $y^+$ - and the low  $y^+$ -meshes, for both the case of the transposed mesh as well as the coarsened mesh respectively. Refinement level one corresponds to the finest mesh and refinement level three to the coarsest.

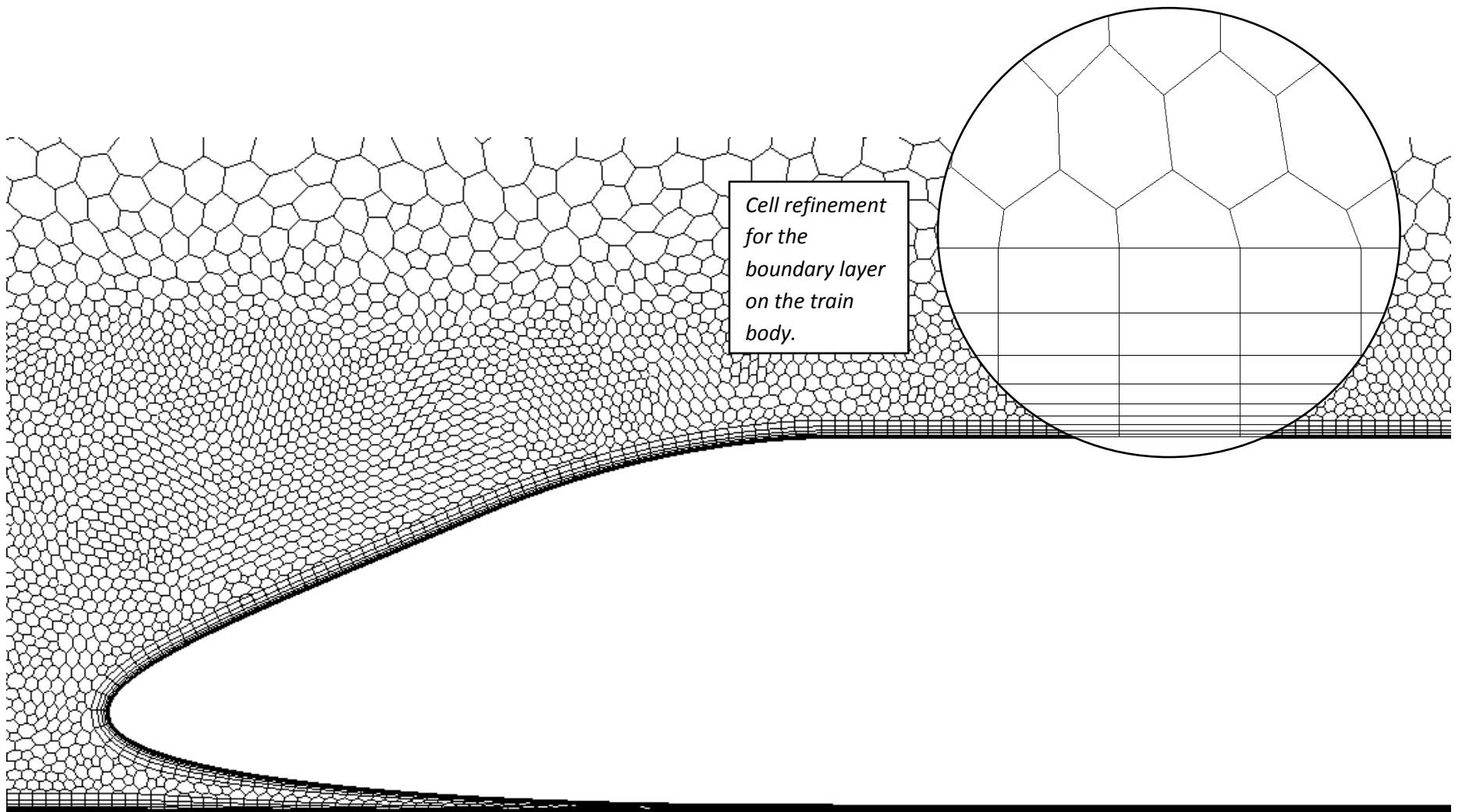


Figure 74: The high  $y^+$ -mesh constructed for the train body shown here at refinement level two on the symmetry plane of the model. The magnified view shows the boundary layer cell refinements for the train body. The nose of the train is shown here at a length ( $L$ ) of 7.7m, inflection point height ( $H$ ) of 3m and nose-tip height ( $Z_0$ ) of 1m.

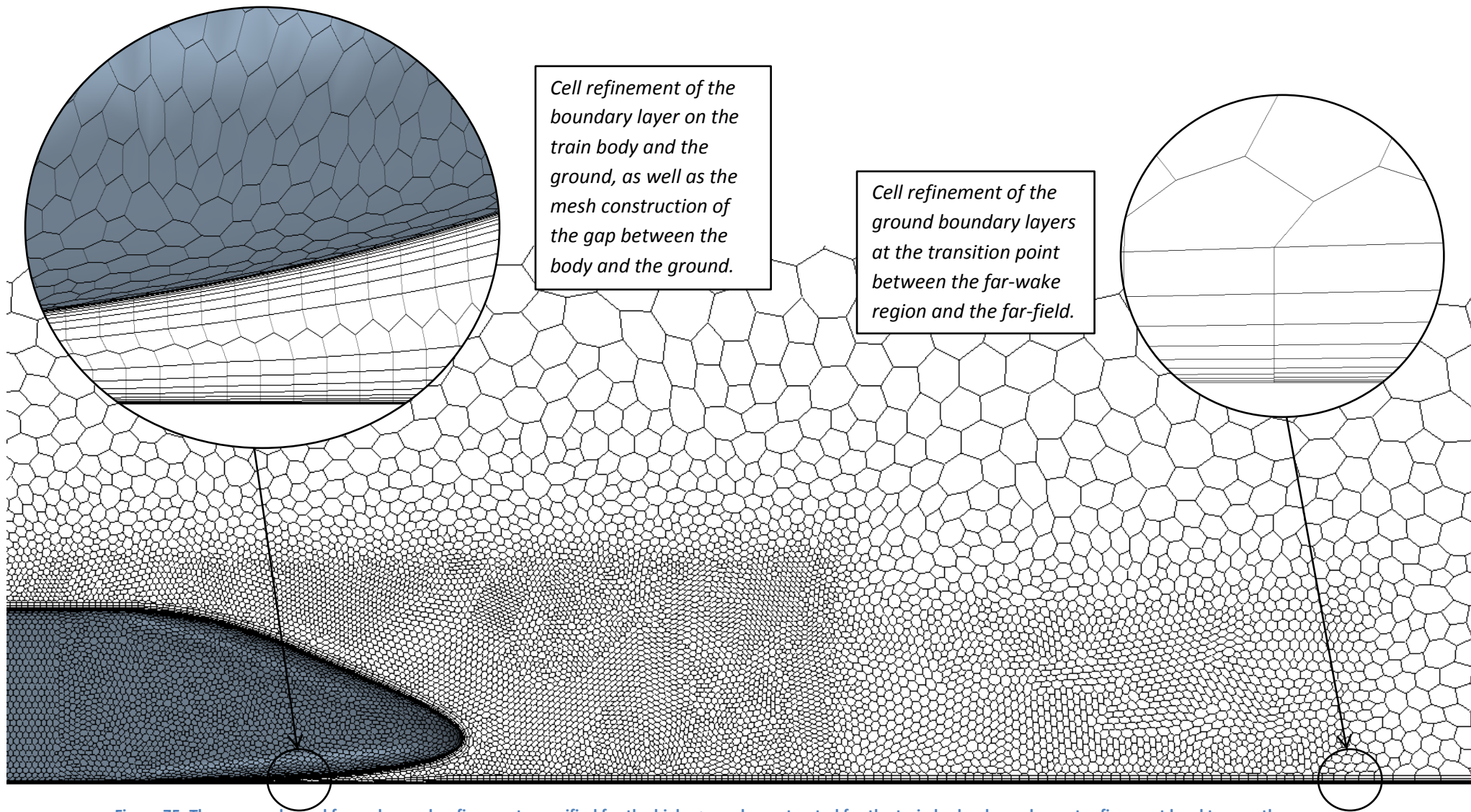


Figure 75: The near-wake and far-wake mesh refinements specified for the high  $y^+$ -mesh constructed for the train body, shown here at refinement level two on the symmetry plane of the model. The magnified views show the boundary layer cell refinements for the high  $y^+$ -mesh on the train body and the ground in the near-wake region (left) as well as on the ground surface at the transition from the far-wake to the far-field region (right). The tail of the train is shown here at a length ( $L$ ) of 7.7m, inflection point height ( $H$ ) of 3m and nose-tip height ( $Z_0$ ) of 1m.

### 4.3.3. Results from the Numerical Analysis

The grid convergence study was conducted for both the low  $y^+$ -mesh, in conjunction with the SST  $k-\omega$  turbulence model, as well as the high  $y^+$ -mesh, in conjunction with the LPS Two-Layer turbulence model. Since the Ahmed's body validation case only considered the drag force seen by the body, with no attention given to the side and lift forces, it is prudent to consider the turbulence models in question's ability to accurately predict these forces as well, especially since the RANS models notoriously have trouble predicting the lift force experienced by bodies in ground proximity (Krajnović, 2008).

Three simulation cases were considered for each mesh type; first, the transposed mesh with a stationary ground boundary condition will be investigated. Since this case mimics the Ahmed's body validation case in terms of mesh construction and boundary conditions, it is expected that the train mesh ought to be converged for this case in accordance with the convergence already proved in section 3.3.3. It is important to note that in addition to the difference in the velocity inlet boundary condition, the side and top boundaries of the train model were assigned symmetry conditions rather than the slip walls that were used in the case of the Ahmed's body. The second case (with boundary conditions as discussed in section 4.2) that was considered was the transposed mesh, this time with moving ground to mimic the train moving through space. This simulation will allow the differences in the performance of the mesh and turbulence models of the moving-ground model, to be compared to that of the stationary ground condition. The third case considered the coarsened mesh which was used together with the moving ground boundary condition. By comparing this case to the second, the validity of coarsening the mesh and its effect on the accuracy of the results can be determined. The results of the GCI approach for the aforementioned scenarios are shown in Appendix C (see Table 44 for the low  $y^+$ -meshes and Table 45 for the high  $y^+$ -meshes respectively). In all cases the geometry of the nose is such as discussed in section 4.3 and shown in Figure 73.

For the first case all the force components acting on the train converged for the high  $y^+$ -mesh. The low  $y^+$ -mesh however only shows convergence for the  $x$ - and  $y$ -forces, while the  $z$ -force remains erratic irrespective of the mesh refinement level. For the second case, the  $x$ - and  $y$ -force components show convergence for both meshes, while the  $z$ -force component now diverges in the case of the high  $y^+$ -mesh as well. Finally, the third case shows that reducing the mesh refinement has no influence on the converged state of the drag and side forces, while the  $z$ -force remains unstable irrespective of mesh-type and turbulence model used (see Appendix C, for all results). Thus the coarser mesh will be used further since it offers similar accuracy to the transposed mesh, yet does not pose the same computational expense.

Moreover, the aforementioned results corroborate the literature, i.e., predicting the lift-force of a body in close ground proximity by making use of RANS-models is notoriously difficult (Krajnović, 2008); the results of the first case show that an RSM model is able to capture the flow beneath the train body when it is still relatively simple, whereas the remainder of the results show that both the RSM model as well as the EDV model fail to achieve this as soon as this flow becomes too complex, i.e., as soon as the ground moves. Thus, the ability of the RSM model to capture complex flow structures ensures its further use, while the results obtained for the lift force necessitates caution for any future work that pertains to it.

## 4.4. Validate Computational Domain

### 4.4.1. Sensitivity Results and Discussion

The computational domain used for the grid convergence study was simply the domain that was transposed from that of the Ahmed's body validation case. As mentioned previously, the flow conditions associated with the validation case and those associated with the train model differ in crucial ways, e.g., the velocity of the incoming air. It is therefore prudent to establish the size of an appropriate computational domain for the train simulation. Such a domain would allow the true external flow field surrounding the train to develop without the boundary conditions applied to the surfaces of this domain interfering with said flow field.

In order to find this adequate domain size, the values of the x-, y- and z-forces acting on the train as a whole, as well as its various sub-components, will be monitored as a function of the boundary locations. Once the forces stabilize, i.e., they no longer vary as a function of the boundary locations, the computational domain has been shown to be large enough. The sub-components of the train that will be monitored are; the nose, coaches and tail of the train as well as the force components acting on the top and bottom of the train (see Figure 76 and Figure 77). The train was divided into a top and bottom portion (see Figure 77) by taking the nose-tip height of the train and using it as the height of a division line, since the nose-tip is typically the stagnation point of the oncoming air after which it will then either flow over or under the body in question.



Figure 76: The subdivision of the train showing the nose (green), coaches (blue) and tail (yellow), with the wind moving in the positive x-direction.



Figure 77: The subdivision of the train showing the top (blue) and bottom (green) halves of it. The train was halved by making use of an xy-plane at the nose-tip height.

While the complete results of this study may be found in Appendix D, in this section attention will only be given to the most important conclusions that could be drawn from it. In order to discuss the aforementioned, Figure 78 and Figure 79 are included here as examples of typical results that were obtained. What is immediately clear is that while some of the x-force components, i.e., total, tail, top and bottom, acting on the train fluctuate with initial adjustments of the boundary location, they do so within a reasonable bound, so that any inlet distance would have been adequate to yield reasonable results. Furthermore, all the x-force components show insensitivity to the inlet boundary location from inlet distance '3' onwards so that it is a conservative location choice. It is thus clear from the results obtained for the x-force component, that not only is it relatively insensitive to the boundary location, but the RS turbulence model is able to capture it also. In contrast, the z-force components, save the lift force acting on the top surface of the train, remain unpredictable irrespective of the boundary location

(see Figure 79). Clearly then, the erratic results for the z-force components cannot be trusted and care should be taken when incorporating them in future work.

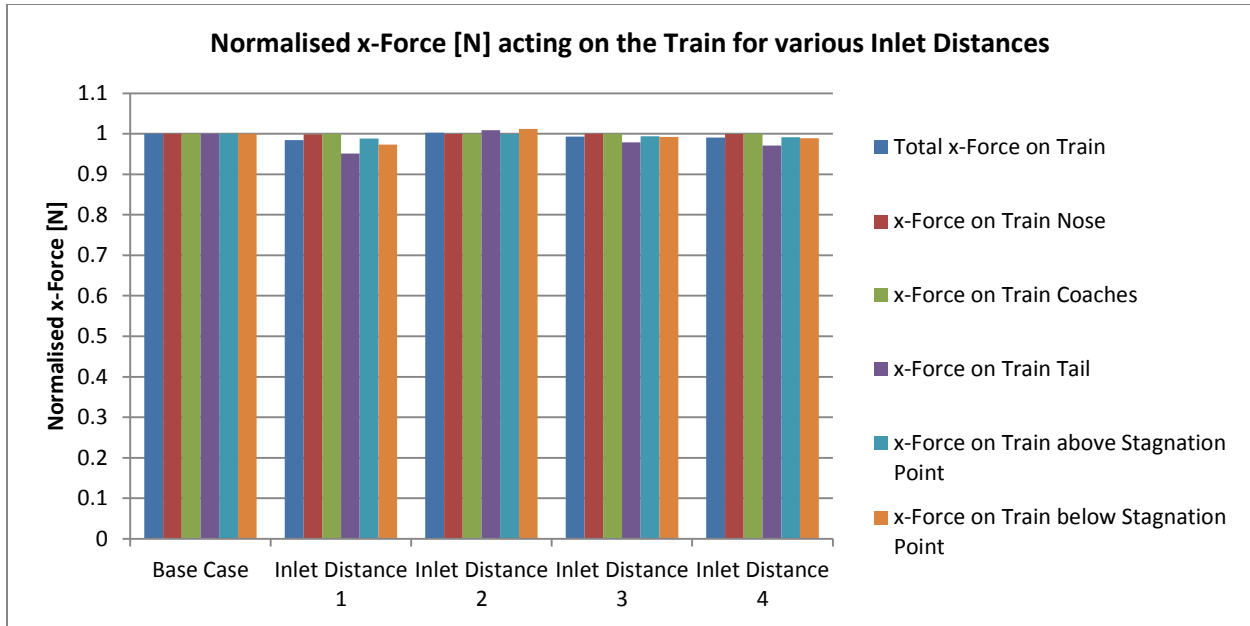


Figure 78: The normalised x-force [N] acting on the train for various domain inlet distances. All forces were normalised by the corresponding value obtained from the base case simulation. The figure shows the forces acting on the train as a whole as well as on the following sub-components; the train nose, coaches and tail as well as the forces acting above and below the stagnation point on the nose.

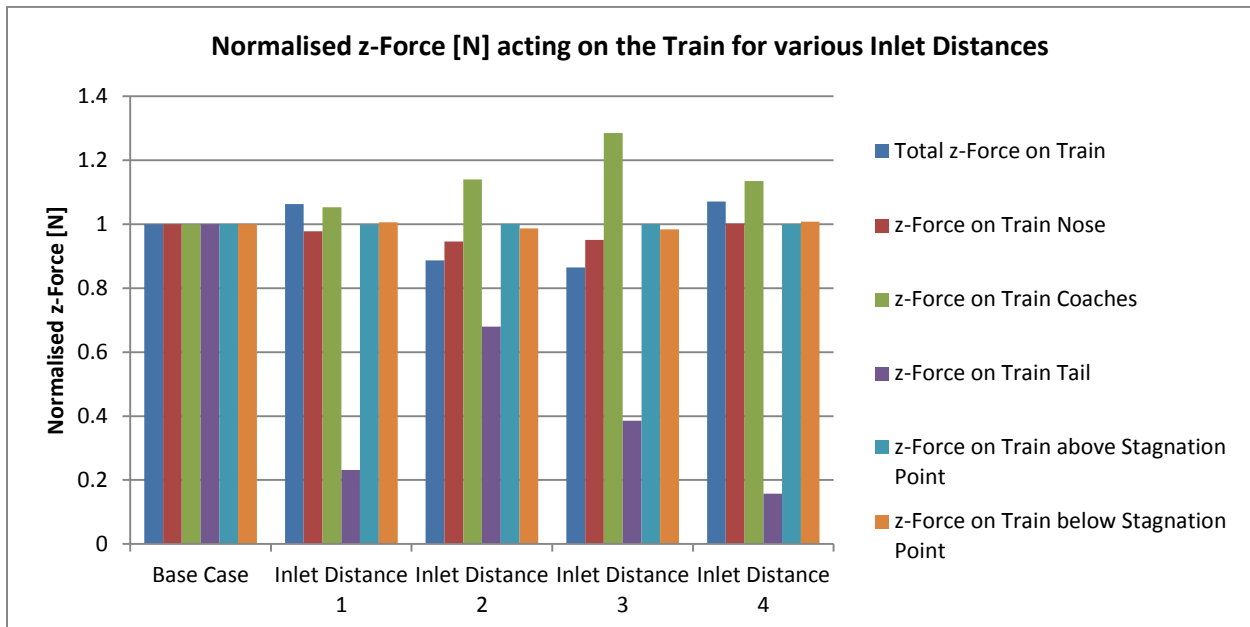


Figure 79: The normalised z-force [N] acting on the train for various domain inlet distances. All forces were normalised by the corresponding value obtained from the base case simulation. The figure shows the forces acting on the train as a whole as well as on the following sub-components; the train nose, coaches and tail as well as the forces acting above and below the stagnation point on the nose.

By following the methodology outlined above, the final domain size that will be used for the optimization was determined to have an inlet length of 446.19m, an outlet length of 1184.68m and a domain height and width of 138.49m as verified by sections ii, iii and iv in Appendix D, respectively (see Table 16). These dimensions were chosen since most of the  $x$ -,  $y$ - and  $z$ -forces with their various sub-components have stabilized as a function of the boundary locations associated with these dimensions. With regard to those  $z$ -force components that have not stabilized as a function of boundary location recall that according to the literature, the RANS models have difficulty predicting the lift force acting on ground vehicles (Krajnović, 2008).

Domain Dimensions	Symbol of Domain Dimension	Number of Characteristic Lengths	Magnitude [m]
Inlet Distance	$D_I$	116L	446.19
Outlet Distance	$D_O$	308L	1184.68
Width	W	36L	138.49
Height	H	36L	138.49

Table 16: The final dimensions that were verified for the computational domain for the symmetry model of the train.

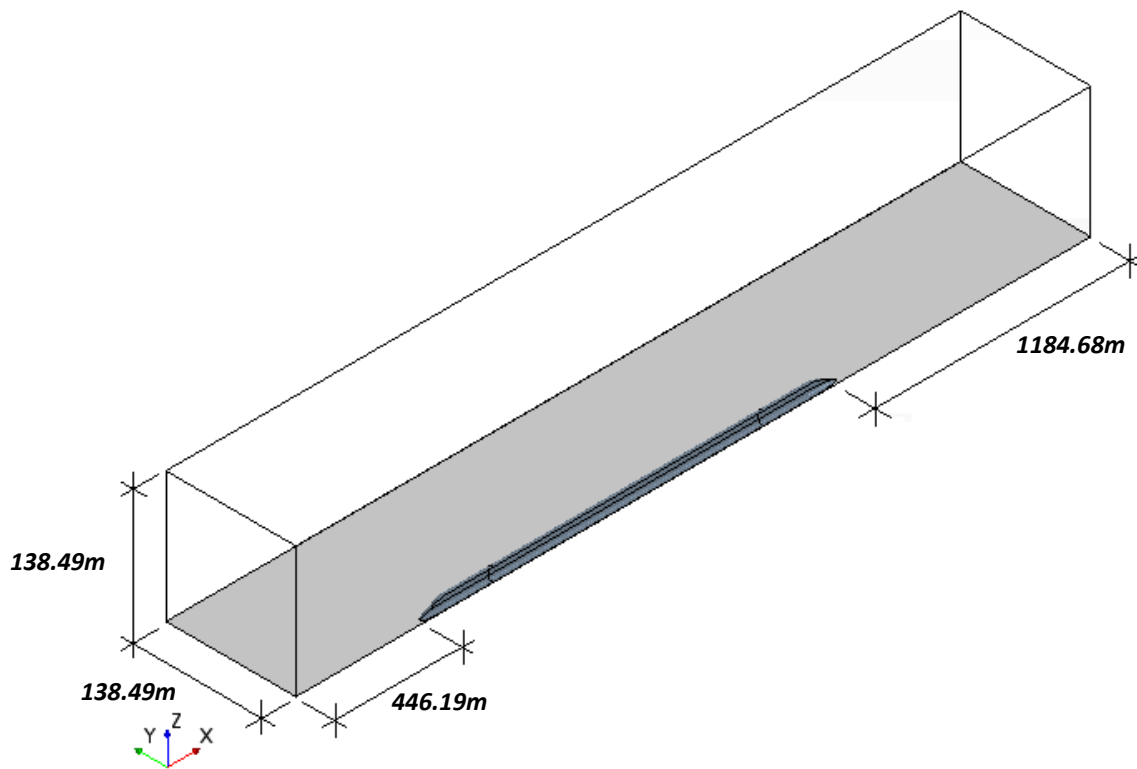


Figure 80: The final computational domain, not drawn to scale, that was used for the grid convergence study and was obtained by transposing the computational domain of the Ahmed's body.

#### 4.4.2. The Unpredictability of the Lift Force and Hypothesis as to the Cause

When considering the results of the boundary location studies, it is clear that the region of instability is the bottom portion of the train (see Figure 141 and Figure 144 in Appendix D), which corroborates (Krajnović, 2008), and that the instability is further located along the coaches and the tail in particular.

The z-force acting on the top region of the train, i.e., the stagnation point on the nose and above, is however stable (see Figure 141 and Figure 144 ) as would be expected from the well-known ability of the RANS models to predict lift on aircraft when bearing in mind that the top portion of the train is not in close ground proximity. Clearly then, the inability of the RANS models to accurately predict lift is a consequence of the force fluctuations beneath, rather than above, the body in question.

Since force is simply a consequence of pressure acting over an area, it is the inaccurate pressure prediction that leads to the inaccurate and fluctuating lift force prediction. It is already known that the Reynolds stress models solve the components of the Reynolds stress tensor directly and as such account for complex turbulent structures, e.g., turbulence anisotropy, secondary flows etc., yet even this model that does not make the Boussinesq assumption fails to accurately capture the flow beneath the train. The underlying issue must thus be more complex than simply modelling or solving for the Reynolds' stress tensor. This study proposes the following hypothesis in an attempt to explain this behaviour;

The transport equations that need to be solved for the six Reynolds stress components contain terms which require modelling themselves, these are the turbulence diffusion term, the dissipation term and the pressure-strain term, the latter of which is considered the most difficult to model. Thus the Reynolds stress model not only averages the flow-field as all RANS models do, hereby introducing inaccuracies, but the idea that the Reynolds' stress models solve for the specific Reynolds' stress tensor directly is also somewhat misleading since modelling is not entirely divorced from this process of "direct solving". In addition, the RSM that was used namely the Linear Pressure-Strain Two-Layer model as formulated by (Gibson & Launder, 1978), assumes a first-order pressure-strain relationship when solving for the pressure-strain term; this applies for the slow and the rapid pressure-strain terms as well as their respective wall-reflection terms.

For flows that exhibit highly non-linear pressure-strain relationships, such as the incredibly turbulent and swirling flows beneath the train body, it is not unexpected that the linear approximation of the pressure-strain term is inaccurate. At this point consider the pressure distributions of the flow in the x-, y- and z-direction; the pressure gradient in the x-direction is not expected to be extreme for the same reason that the velocity variation in the x-direction is not expected to be extreme along the length of the body (see Figure 81,  $x=33.87\text{m}$  through to  $101.6\text{m}$  and Figure 82,  $x=0\text{m}$  through to  $101.6\text{m}$ ) as is known from the theory, with the region of greatest variation on the aforementioned expected to be beneath the train (see Figure 81,  $x=0\text{m}$  in comparison with  $x=33.87\text{m}$  through to  $101.6\text{m}$ ). In the case of the y-direction, the pressure distribution is once again not expected to vary much along the width of the train, in fact, had the nose and tail with their associated three-dimensional flow behaviours not been considered, it would have been reasonable to simulate flow over the train as a two-dimensional model with only a slight error expected in the results. Along these directions then, the linear pressure-strain relation is expected to yield reasonable results. Should the velocity-, and thus implicitly the pressure-, distribution over the train in the z-direction be considered however, the distribution above the train and that below it have very different forms; on the top portion of the train (see Figure 82) there exists a no-slip condition at the train walls and above the train body is free-stream air. Beneath the train (see Figure 81) however, there are no-slip conditions on both the train wall as well as the moving ground so that the pressure distribution assumes a decidedly non-linear form (consider the velocity profiles shown in Figure

81 along the z-direction, at all x-values ). It would seem then that the inability of RANS models to predict lift acting on vehicles in ground proximity lies in the extreme non-linearity of the pressure-strain beneath the train and in the case of the Linear Pressure-Strain Two-Layer model, the first-order pressure-strain assumption that is made. In fact, it is very plausible that even the quadratic pressure-strain model will be unable to capture these non-linearities in the z-direction and when considering that the linear pressure-strain models allow for the two-layer formulation, it seems the initial choice to make use of it has been validated, not to mention the difficulty of convergence when the quadratic model is used.

It is further worth mentioning that all Reynolds stress models offered by STAR-CCM+ employs the Kolmogorov theory of small scale universal equilibrium, i.e., at sufficiently high Reynolds numbers, local isotropy for dissipating scales is postulated, thus the dissipation term is modelled as isotropic. This assumption is clearly not valid in the wall region where length scales are small and anisotropy consequently large, which further adds to the problem of inaccuracy, particularly in the near-wall region. The Linear Pressure-Strain model does however allow for a Two-Layer approach which was used for the simulation of the train. This formulation algebraically describes the turbulent dissipation rate and the turbulent viscosity as functions of wall distance in the viscosity dominated near-wall region, whereas the quadratic pressure-strain model only allows for the use of wall-functions and does not resolve the viscous-affected near-wall region. The choice of the Linear Pressure-Strain Two-Layer model is thus believed to be superior to that of the Quadratic Pressure-Strain model since neither can truly capture the flow beneath the train body, but at the very least the Two-Layer model resolves the viscous sub-layer.

Considering that the Linear Pressure-Strain Two-Layer model, which already solves the Reynolds' stress tensor directly hereby inherently accounting for complex flow effects such as turbulence anisotropy etc., is unable to accurately predict the lift force acting on the train, it is clear that should an accurate prediction of the lift force be required, LES or DNS should be made use of. Since it is not reasonable to combine an already expensive optimization simulation with another computationally expensive simulation such as LES, the lift force will not be optimized for because it remains unstable and unpredictable and as such will only serve to add noise to the optimization simulation.

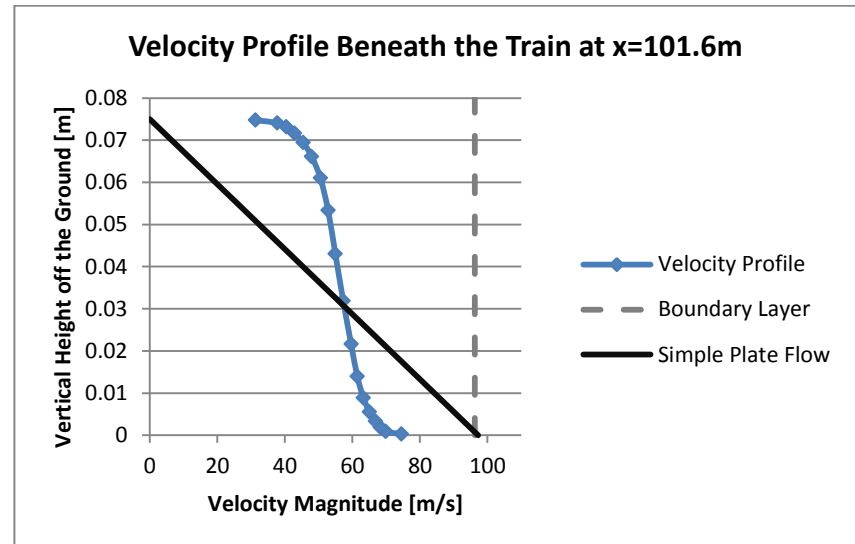
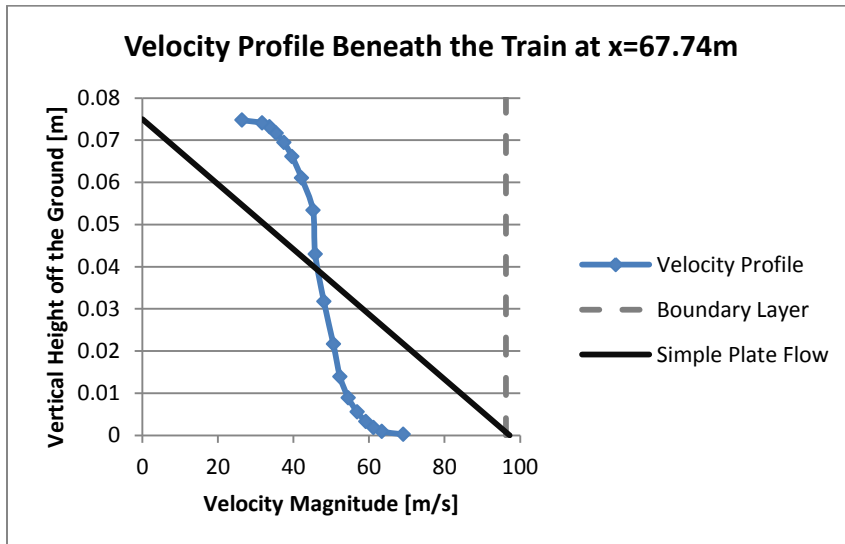
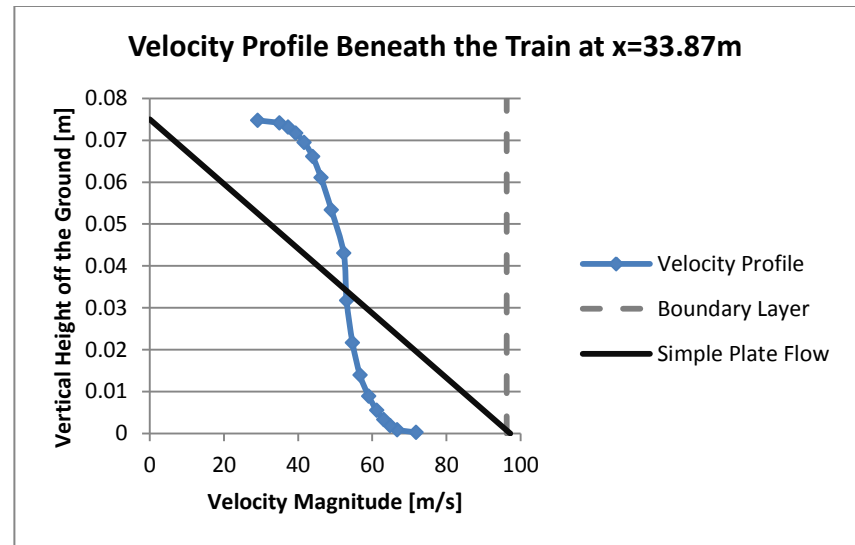
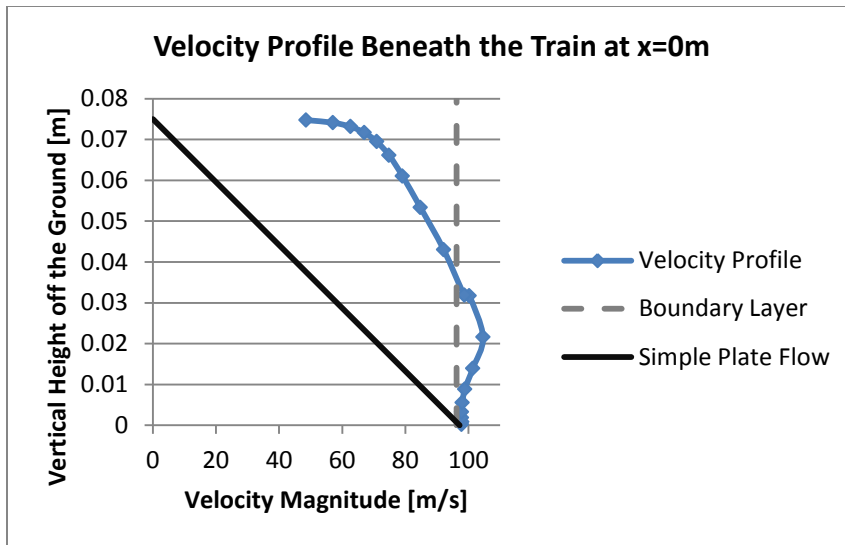


Figure 81: Velocity magnitude profiles as a function of the vertical height off the ground ( $z$ -axis) beneath the train, i.e., below the stagnation point height of the train nose ( $Z_0$ ), taken along the longitudinal symmetry plane of the train ( $y=0$ ) at  $x=0\text{m}$ ,  $33.87\text{m}$ ,  $67.74\text{m}$  and  $101.6\text{m}$ .

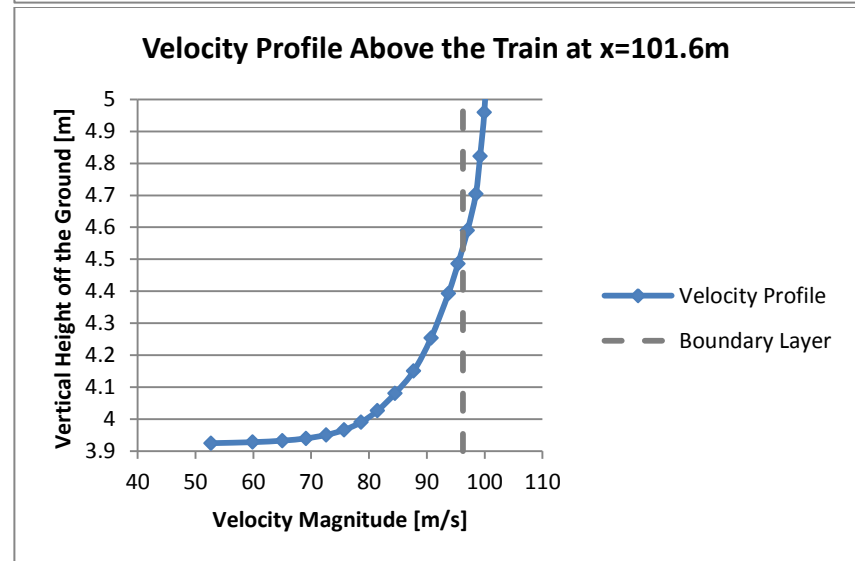
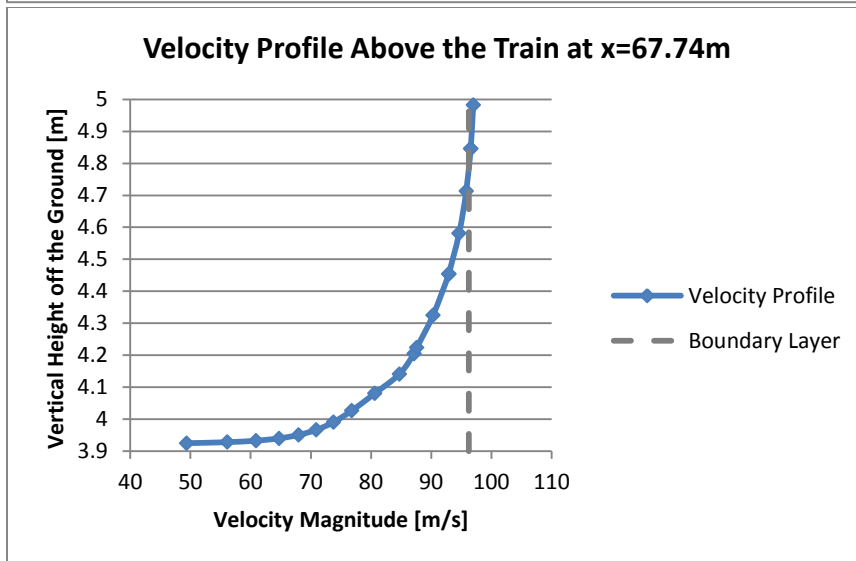
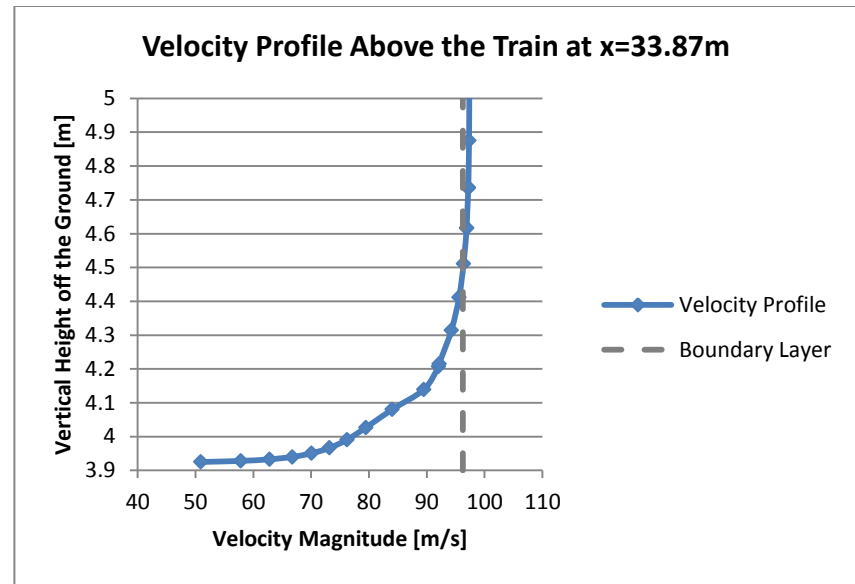
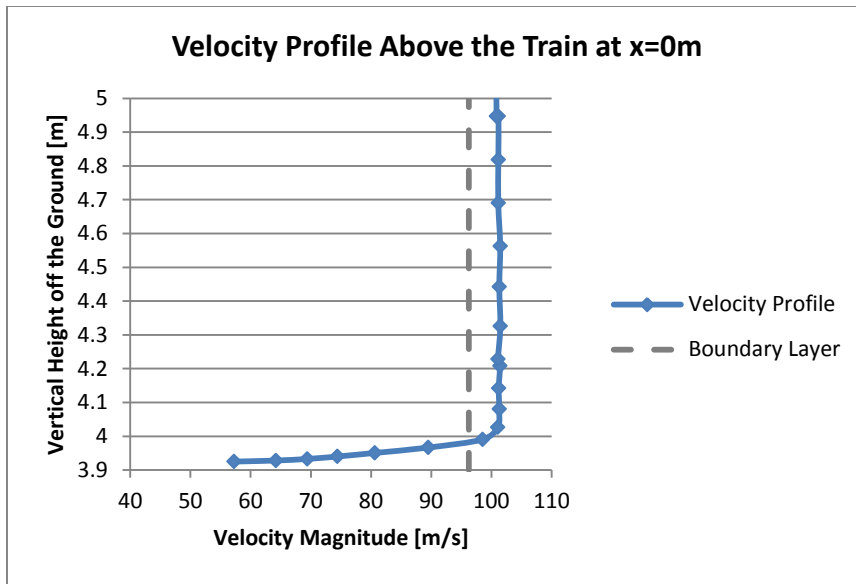


Figure 82: Velocity magnitude profiles as a function of the vertical height off the ground ( $z$ -axis) above the train, i.e., above the stagnation point height of the train nose ( $Z_0$ ), taken along the longitudinal symmetry plane of the train ( $y=0$ ) at  $x=0\text{m}$ ,  $33.87\text{m}$ ,  $67.74\text{m}$  and  $101.6\text{m}$ .

## 4.5. Optimization of the Nose and Tail Geometry

This section of the document concerns itself with the optimization of the train nose geometry (see section 4.1) for windless conditions. The geometry of the computational domain with the various faces' associated boundary condition types were given in section 4.2. The grid that was used here was validated in section 4.3 and finally the domain size and turbulence model used was validated in section 4.4.

The optimization process itself occurred in four steps; the first step was the discretization of the design space by conducting a design sweep of the variables in question. The resultant design points were then simulated in the second step by making use of the validated computer model. The various force responses, i.e., x-, y- and z-force components, were captured for each design point with the particular force component of interest being the total drag acting on the train. The data obtained could then be used for the construction of a surrogate model in the third step. Finally, the nose and tail geometry could be optimized for the total drag acting on the train in the fourth step, by making use of the surrogate model obtained in the third step together with the SHERPA algorithm, where after conclusions regarding the optimized design could be made.

### 4.5.1. Discretization of the Design Space

The three variables that parameterize the nose (see Figure 71 and Table 10) were discretized in such a way as to allow for the design to be considered at five levels (see Table 17), in other words a five-level full factorial design study was performed which effectively implies 125 design points in total. The reason for the study being conducted at five levels was to ensure that possible curvature in the response function was accurately modelled and that the probability of omitting unpredictable localized behaviour was reduced.

Nose Parameter	Design Level 1	Design Level 2	Design Level 3	Design Level 4	Design Level 5
Nose Length [L]	2	3.425	4.85	6.275	7.7
Nose Tip Height [Z <sub>0</sub> ]	0.7	0.9	1.1	1.3	1.5
Inflection Point Height [H]	2	2.25	2.5	2.75	3

Table 17: The three variables that parameterize the nose geometry and their respective values for the five design levels considered for the design sweep.

### 4.5.2. Simulation of the Design Points

The design points as determined in the first step were simulated in STAR-CCM+ by making use of the validated computational model and the resultant, total drag force associated with each design point may be seen in Table 64 in Appendix H. In order to provide clarity on the external flow field surrounding the train, so as to ease understanding during future discussions, an example of said flow field is shown in Figure 83. Broadly speaking, the following flow phenomena can be observed.

As the incoming air collides with the nose-tip it stagnates, giving rise to a high-pressure region (see Figure 83, magnified view, left). Following the air over the top length of the body, it can be seen to accelerate along the length of the nose reaching its maximum velocity where the nose slant transitions

to the train roof, giving rise to a low-pressure region. Thereafter the boundary layer thickness grows visibly as is expected from the literature. It is interesting to note that as the air reaches the rear of the train it once again accelerates, before its velocity rapidly decreases in the near-wake region (see Figure 83, magnified view, right). If the air beneath the train is followed, it can also be seen to accelerate rapidly from the stagnation point on the nose, to the region of uniform cross-section beneath the train body (see Figure 83, magnified view, left). It then gradually decelerates, where after an air velocity below 60m/s is maintained, except for the region where the nose initially starts diverging away from the ground; an area of localized acceleration presents itself here, giving rise to a low-pressure region. Finally, as expected, the separated wake region exhibits low air velocities which trail the tail for quite some distance. The defined, dark blue line present at the rear is reminiscent of a longitudinal vortex, which is expected to be irrotational given the absence of external forces, which are necessary in order to achieve rigid-body motion.

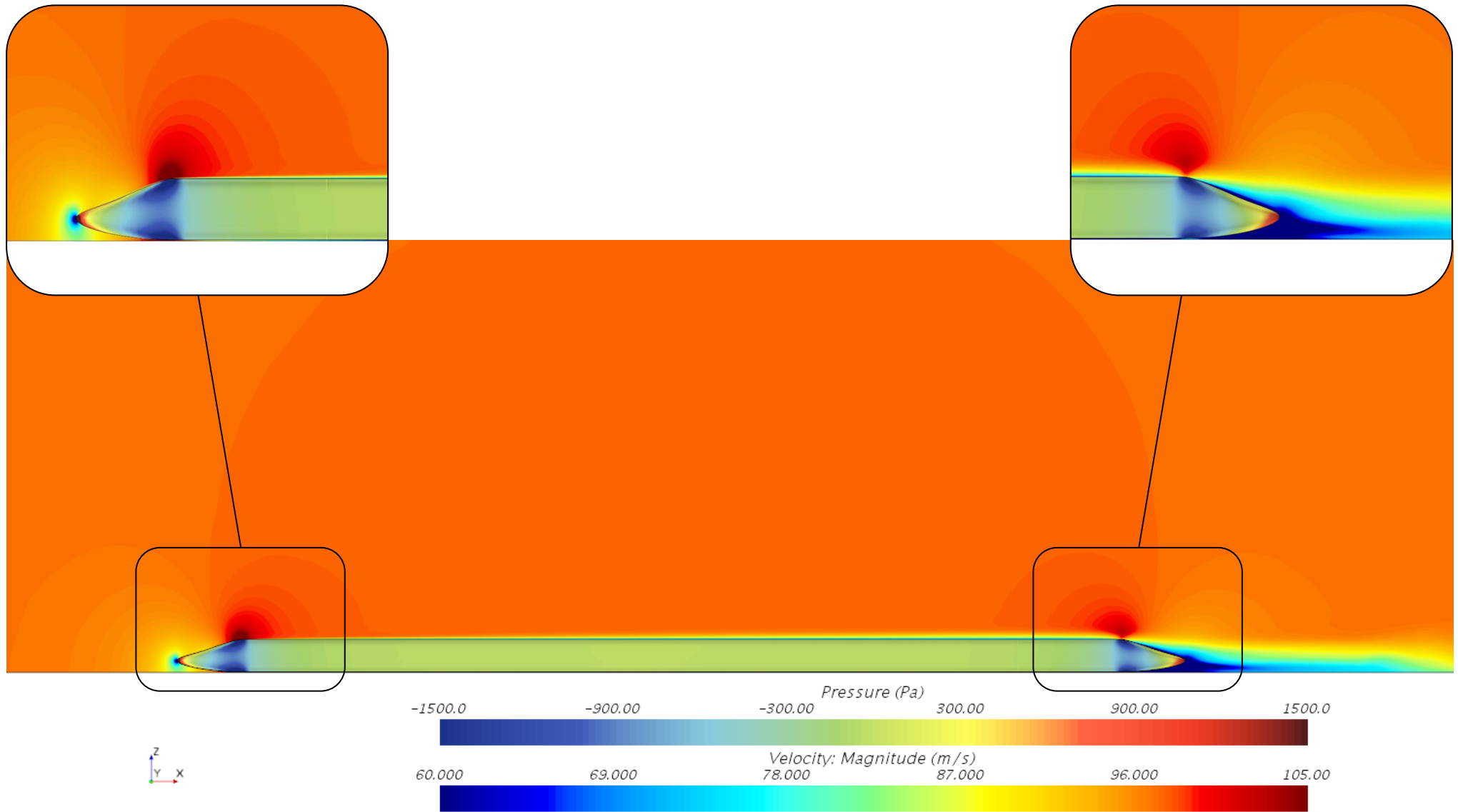


Figure 83: The external velocity field surrounding the train for the optimized nose geometry in windless conditions as seen from the side. The stagnation point on the tip of the nose is shown in the magnified view on the left, while the wake region trailing the tail is shown in the magnified view on the right. The corresponding pressure field acting on the train as a consequence of the velocity field is also shown on the three-dimensional body.

### 4.5.3. Response Surface Model

#### 4.5.3.1. Surrogate Model Construction

The various force responses associated with the design points determined in the first step, were obtained from the simulations performed in STAR-CCM+ in the second step. However, since minimizing the total drag force acting on the train was the goal of the optimization study, these were the only results that were considered as input values for the construction of the surrogate models which were created in HEEDS MDO. For the sake of being thorough, two surrogate models were constructed to allow for the algorithm to optimize the train nose geometry. The resultant, optimized train nose geometry as obtained from each respective surrogate model could then be compared to the literature and the superior surrogate chosen.

The first metamodel that was created, the results of which are discussed here, made use of the radial basis function along with the thin plate spline technique for the interpolation and smoothing of the data. The resultant coefficient of multiple determination ( $R^2$ ) for this model was one, the root mean squared error (RMSE) measured at the fitted data points was zero and the average residual for the cross validation was  $-5.60E-13$ . Thus the RBF surrogate model gave every indication that it would be highly predictive. The second metamodel that was created, made use of the Kriging interpolation method with a Gaussian fitting function with a second-order polynomial used for the polynomial portion of the fit (see Appendix E, section i, ii and iii for complete results). Furthermore, “Fast Kriging” was chosen as a tuning method and the resultant shape factor was 3.01527. This of course expands the influence of a given data-point which allows for a smoother meta-model, but the trade-off is an increase in the average value of the residual for the cross validation ( $-1.20E-28$ ). The  $R^2$ -value for this model was also one and the RMSE value was zero, as can always be expected from using the Kriging method as it interpolates the design points.

In both instances the surrogate models were smoothed due to the presence of numerical noise. This noise could possibly be attributed to the fact that a transient flow field was solved as a steady one. Alternatively the RSM model, which solves the specific Reynolds stress tensor, captured the highly turbulent nature of the flow, which led to the erratic behaviour of the solution. This smoothing of the data is not necessarily an inaccurate course of action. In fact, it could possibly yield superior results to data that haven't been smoothed since it would allow for tendencies to be more clearly identified.

#### 4.5.3.2. Surrogate Model Description

##### 4.5.3.2.1. The Total Drag acting on the Train as a Function of a Variable Nose Length

The results obtained for the total drag force acting on the train as a function of the various geometric parameters, as determined from the RBF surrogate model, will be discussed here (refer to Appendix E, section i for Kriging results). The nose-tip and inflection point heights are indicated on the x- and y-axes, with the drag force response shown on the z-axis. The nose length will act as a “slider” of sorts in order to generate the various surfaces associated with each respective value thereof, i.e., the surrogate model will be expressed as a collection of response surfaces (refer to Appendix E, section ii and iii for the response surfaces generated with the nose-tip and inflection point heights acting as “sliders”).

As the nose length tends to its minimum value, i.e., 2m, the response of the total x-force becomes increasingly noisy (see Figure 84). While it is possible that this behaviour has been predicted accurately, it seems more plausible that the noise in the solution is a consequence of the inability of the turbulence model to accurately capture the flow phenomena that are present in the case of the blunt nose geometry. This hypothesis is strengthened further when the more predictable behaviour of the total x-force as well as the smoother associated response surfaces with an increase in nose length are considered (see Figure 84, bottom through to Figure 86). Be that as it may, the results seem to indicate that for shorter noses, the minimum values for the inflection point height ( $H=2\text{m}$ ) and the nose-tip height ( $Z_0=0.7\text{m}$ ) yield the least aerodynamically efficient shape (see Figure 84, top). With an increase in nose length ( $L \approx 3.425\text{m}$ , see Figure 84, bottom) the location of maximum drag force migrates from the minimum value for the inflection point ( $H$ ) and the minimum value for the nose-tip height ( $Z_0$ ), to the minimum value for  $H$  and the maximum value for  $Z_0$ . This location for the maximum total drag force remains unchanged with a further increase in nose length (see Figure 85 through to Figure 86). The maximum drag force therefore corresponds to the minimum value of the inflection point, irrespective of nose-tip height or nose-length.

Another interesting phenomenon that can be observed here is that the minimum total drag force is located in the vicinity of the maximum nose-tip ( $Z_0$ ) and inflection point ( $H$ ) height, irrespective of nose length. As the nose length increases however, the total drag force decreases (compare Figure 84 and Figure 86) and the region in which the minimum x-force is expected to be found becomes more concentrated (compare Figure 85 to Figure 86). From the results given here, the optimized train nose geometry is thus expected to be long, in fact from the theory it is expected to assume the maximum length of 7.7m. What is further expected is that the value for  $H$  will tend towards its maximum rather than its minimum (see Figure 84 through to Figure 86), with the nose-tip height displaying similar behaviour. Finally, there is a clear relationship for the total x-force as a function of nose length; an increase in nose length leads to a decrease in drag, as expected from the theory. There is, however, a more complex relationship between the nose-tip and the inflection point height and the resultant drag force, so that a general rule cannot simply be stated for the total x-force as a function of nose-tip or inflection point height;

Consider the case where the inflection point assumes its lower bound ( $H=2\text{m}$ ), the drag force increases for a nose length ( $L$ ) of 3.425m, with an increase in the nose-tip height while the drag force decreases with an increase in nose-tip height when the inflection point assumes its maximum bound ( $H=3\text{m}$ ) for the same nose length (see Figure 84, bottom). However, for the maximum nose length ( $L=7.7\text{m}$ ) and the minimum nose-tip height ( $Z_0=0.7\text{m}$ ) the total x-force as a function of the inflection point height is somewhat more complex, i.e., at the maximum and minimum  $H$ -values, the total drag force has maximums, local and global, respectively, while the minimum drag force lies somewhere between these  $H$ -values. There are clearly considerable interdependencies between the inflection point ( $H$ ) and nose-tip ( $Z_0$ ) heights as well as the nose length ( $L$ ) to a certain extent.

Furthermore, it is interesting to note that the Kriging-model attempts to fit the surface through the data points in a tangent fashion, a consequence of the small value for the shape factor, while the radial basis function does not exhibit the same smoothing behaviour, which makes for a less “curved” response

surface. This is not necessarily a disadvantage, rather it would be prudent to evaluate the optimized train nose obtained from each respective metamodel and compare it to known theory and decide upon a suitable surrogate model then, e.g., the optimal nose length for drag reduction is 7.7m.

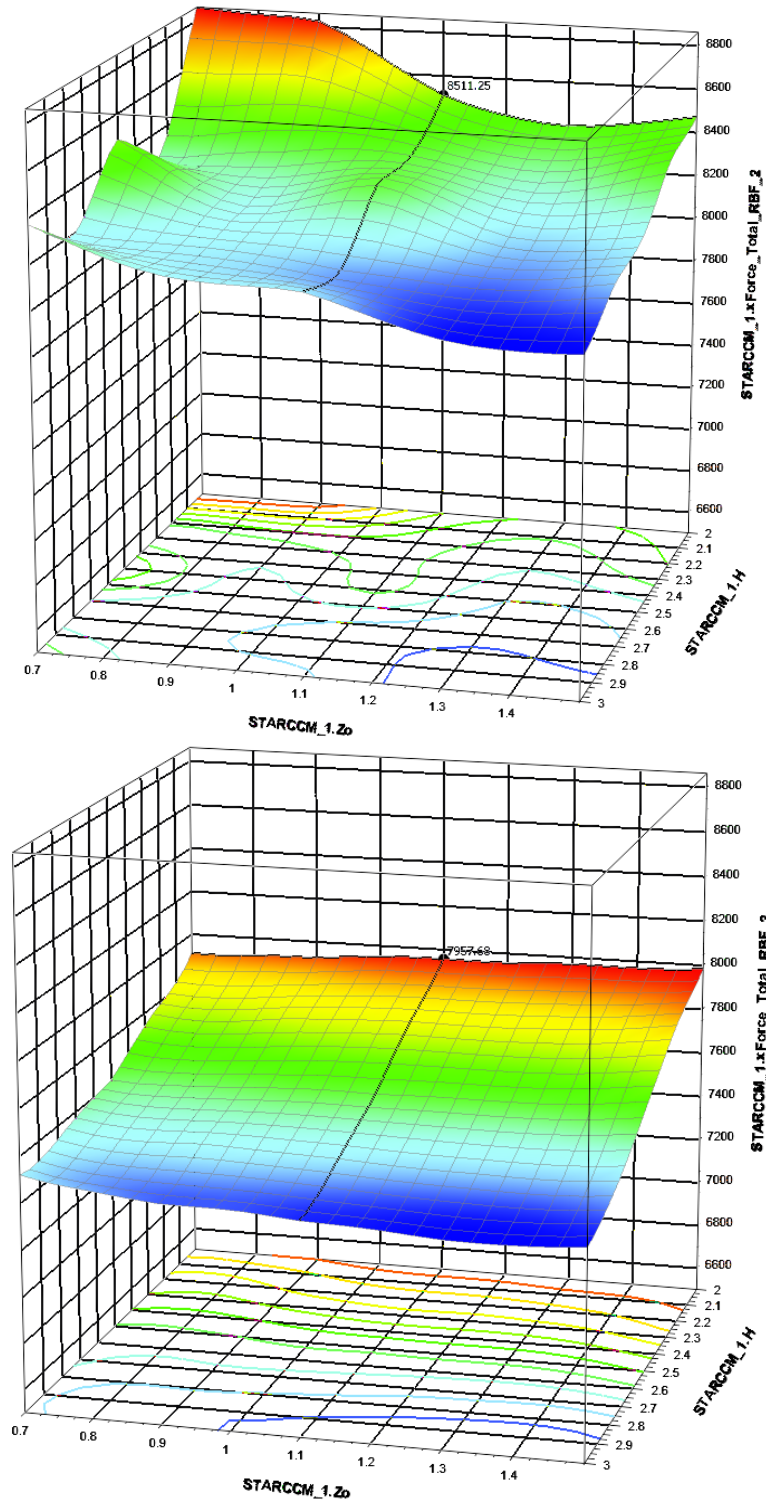


Figure 84: The variation of the total x-force (vertical axis) acting on the train as a function of nose-tip height ( $Z_0$ ) and inflection point height ( $H$ ) for a constant nose length of  $L=2\text{m}$ , top and  $L=3.425\text{m}$ , bottom.

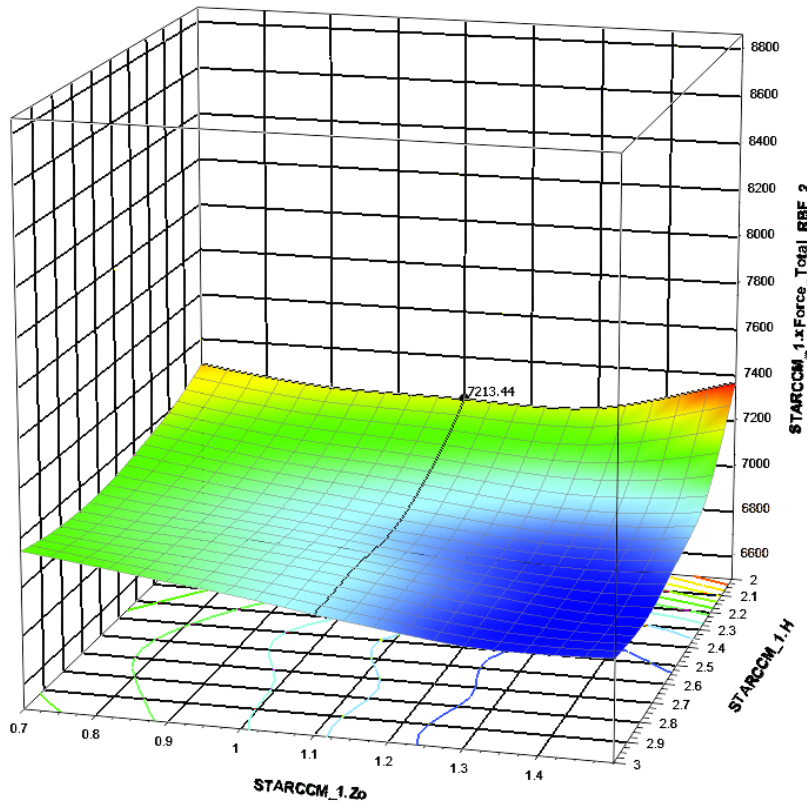
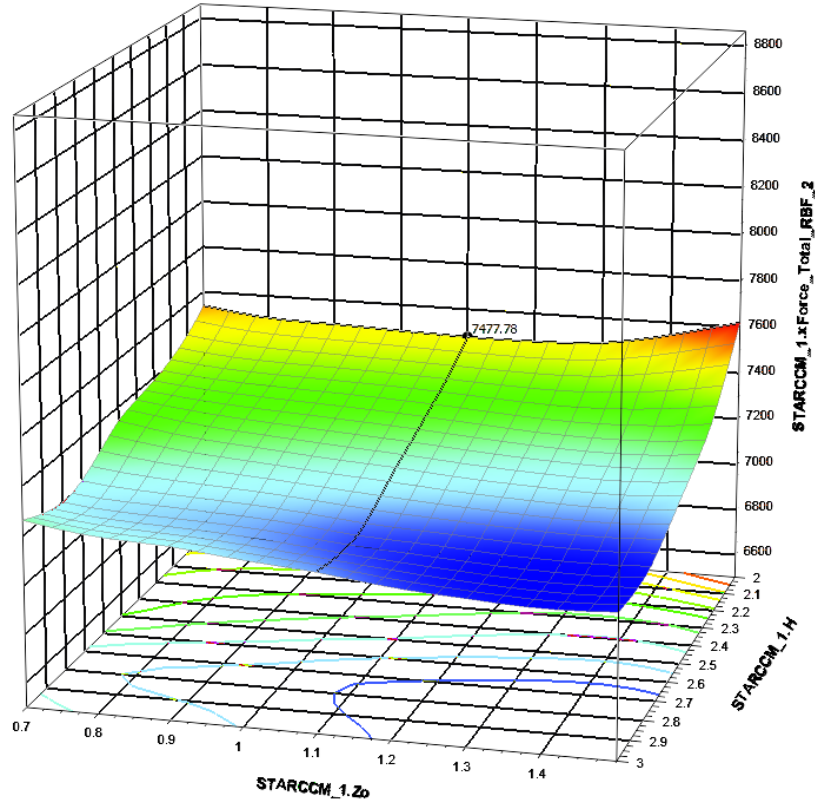


Figure 85: The variation of the total x-force (vertical axis) acting on the train as a function of nose-tip height ( $Z_0$ ) and inflection point height (H) for a constant nose length of  $L=4.85\text{m}$ , top and  $L=6.275\text{m}$ , bottom.

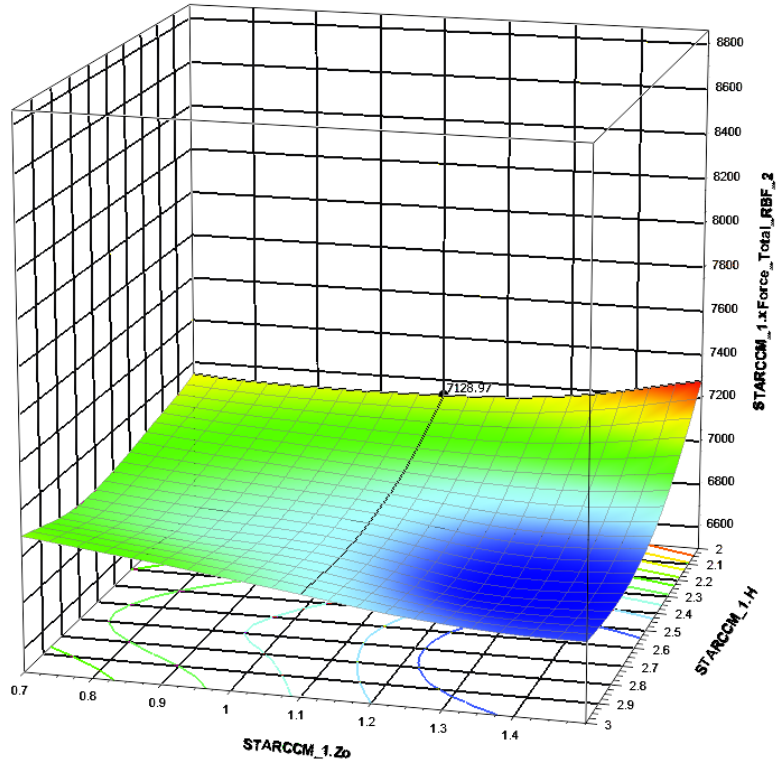


Figure 86: The variation of the total x-force (vertical axis) acting on the train as a function of nose-tip height ( $Z_0$ ) and inflection point height ( $H$ ) for a constant nose length of  $L=7.7\text{m}$

#### 4.5.3.2.2. The Total Drag acting on the Train Sub-Components as a Function of a Variable Nose Length

The response surfaces that describe the behaviour of the various drag components acting on the train as functions of the nose parameters, as obtained from the RBF surrogate model (see Figure 90 through to Figure 95), will be discussed here in order to shed some light as to the nature of the optimal nose geometry.

When the results as shown in Figure 90 through to Figure 92 for the drag force acting on the top and bottom portions of the train are considered, there is a clear correlation between the overall reduction (or approximately vertical translation) of both these forces and an increase in nose length. A longer nose is thus clearly advantageous irrespective of nose-tip or inflection point height. Consider that for a perfectly blunt nose, the pressure drag component that the nose can contribute to the total drag is largest while a lengthening of the nose reduces this pressure drag component and introduces a shear drag component as well. When bearing in mind that it is the pressure drag component that contributes more to the total drag force, it follows that reducing this component reduces the total drag. There are two important flow mechanisms to enforce this; the first is to ensure that the measure of flow separation is limited, so as to ensure a minimal pressure differential across a given body. The second is to avoid flow stagnation as far as is possible, since a stagnant fluid increases the static pressure acting on a body. Lengthening the nose accomplishes both the aforementioned; flow separation at the trailing end of the nose is minimized due to a decrease in the local positive pressure differential while the largest possible mass fraction of air is kept mobile at the largest possible velocity.

With regard to the drag force acting on the top and bottom portions of the train (see Figure 90) there is more instability observable in the results at a nose length of two meters ( $L=2\text{m}$ ) at which point the flow is expected to be more turbulent, hereby making it more difficult for the RANS model to predict the flow, than at the longer nose lengths (see Figure 91 and Figure 92). Yet even so, the over-arching trends of the forces as functions of the nose parameters remain the same irrespective of nose length; the first trend is that as the nose-tip height increases, the force acting on the top portion of the train decreases while that of the bottom portion increases. The nose-tip quite simply seems to act as a divider of the flow as is expected from the literature; the lower the nose tip, the more flow is forced over the top of the train consequently increasing the force it experiences. By raising the nose-tip, the flow stagnates and subsequently divides itself between the bottom and top portions of the train, hereby allowing a larger mass fraction of air to flow beneath the train and consequently increasing the drag force the bottom portion of it experiences.

It is worth noting that the drag force acting on the top and bottom portions of the train is influenced more strongly by the nose-tip height than the inflection point height. Also, the surface that describes the drag force above the train (see Figure 92, left) seems to show a slightly parabolic trend of the force as a function of the inflection point height ( $H$ ) at a fixed nose-tip height ( $Z_0$ ), with the minimum force for a fixed nose-tip height situated closer to the upper bound of the inflection point than the lower bound. When the geometries associated with these inflection point values (see Figure 87) are considered however, the reason for this becomes clear; when the inflection point assumes its lower bound, the nose (and consequently the tail) assumes a “notch-back” configuration. There is thus not only a stagnation point of the air on the nose tip, but also where the hood and the wind-shield meet. Furthermore, this lower location of the inflection point has the added consequence of increasing the inclination of the wind-shield which contributes to the separation of the flow at the trailing-edge of the windshield. When the inflection point assumes its upper-bound however, a “fast-back” configuration is assumed with a stagnation point only present on the nose-tip and separation of the flow at the trailing edge of the windshield. The optimal nose shape (as determined in section 4.5.4.2 ) is in fact very similar to that of the upper-bound shape with the only visible difference being that the nose configuration associated with the upper-bound has a more rounded profile than that of the optimal nose shape. From Figure 92 it is clear that there is very little change in the drag force acting above and beneath the train when the inflection point changes from 2.73m to 3m. One possible reason that the optimal nose shape performs marginally (0.76%) better than the geometry at an inflection point of 3m, could be that for the optimal geometry the flow remains somewhat more attached, since the nose associated with the upper-bound is slightly more rounded. This in turn implies that a larger collection of gradients describes this shape than its optimal counterpart, which affords the flow greater possibility for detachment. A similar parabolic nature is also visible for the drag force acting beneath the train, although not quite as pronounced as that of the drag force acting above the train. This is quite possibly simply a function of the mass fraction of the air that passes over the train rather than beneath it.

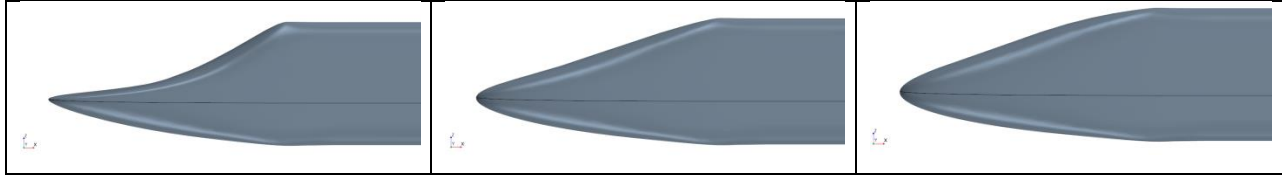


Figure 87: The notch-back (left), optimal (middle) and fast-back (right) configurations for the train nose geometry at a nose length ( $L$ ) of 7.7m, a nose-tip height ( $Z_0$ ) of 1.364m and inflection point heights ( $H$ ) of 2m (lower-bound), 2.73m and 3m (upper-bound) for the left, middle and right noses, respectively.

With respect to the train nose it's clear that an increase in length reduces the drag force experienced by it, irrespective of nose-tip or inflection point height (see Figure 93 through to Figure 95). Furthermore, the range of nose-tip and inflection point heights that are able to yield regions of comparably minimal drag forces acting on the nose expands for an increase in nose length. That is, for the maximum allowable nose length ( $L=7.7\text{m}$ ), there is a reasonably large range of  $Z_0$ - and  $H$ -values that is permissible and would still yield a minimal drag force for the nose. What is clear from Figure 95 (top, left) however, is that the least favourable nose geometries are of the "notch-back" variant. It would thus seem that avoiding the stagnation point where the hood and windshield meet is of great importance to prevent large drag forces acting on the nose. In addition, this appears to ring true for the effect on the total drag force (for longer nose lengths) as well when Figure 85 through to Figure 86 are considered. These figures also indicate a maximum total drag force at an inflection point height of 2m and a nose-tip height of 1.5m for a nose length of 7.7m, a behaviour that is mimicked by the partial drag acting on the train nose. A definite difference in the behaviour of the drag force acting on the train nose in isolation and the drag force acting on the train in total, is the allowable ranges for ' $Z_0$ ' and ' $H$ ' for a given ' $L$ '. As mentioned above, the permissible range for these parameters that still produce a minimal drag force in the case of the train nose, is much larger than for the total drag force acting on the train (see Figure 84 through to Figure 86). Clearly then, there are other factors that come into play when establishing a minimum total drag force than simply ensuring a minimum drag force acting on the train nose.

Another interesting phenomenon to observe is the increase, although modest (1.17% on average from the lower- to the upper-bound of ' $L$ '), of the partial coach-drag force, which seems to be a consequence of the decrease in the nose drag with an increase in nose length. This behaviour appears to indicate that as the nose elongates and tends to a more streamlined configuration, less of the incoming air's energy is dissipated due to stagnation. Consequently, the kinetic pressure available to the air flowing over the coaches is larger, hereby increasing the shear drag experienced by the coaches. Put differently, the larger the mass fraction of air that stagnates on the nose, the larger the pressure recovery required of the air and the smaller the shear drag experienced by the coaches. There is however, a second interesting behaviour exhibited by the partial coach-drag force as a function of ' $Z_0$ ', ' $H$ ' and ' $L$ ' (see Figure 93 through to Figure 95, top, right); the shape of the response surface remains relatively similar with the general vicinity of the maximum and minimum force migrating only slightly. Furthermore, it is important to note that the percentage difference between the minimum and maximum drag forces acting on the coaches as a function of ' $H$ ' and ' $Z_0$ ' for a given nose length is marginal, i.e., 1.21%, 1.13% and 1.31% for nose lengths of 2m, 4.85m and 7.7m, respectively. Moreover, the largest deviation between the minimum and the maximum drag forces across the nose lengths are 1.09% and 1.19% respectively, while the average drag force shows a maximum deviation of 1.17%. Clearly then, while the

drag force acting on the coaches is influenced by the nose shape (and consequently the tail shape as well) the effect is negligible. The aforementioned allows for the assumption to be made that the drag force acting on the coaches is largely insensitive to the nose and/or tail geometry. It is thus a plausible hypothesis that the addition of any number of coaches between the leading and trailing locomotives will not affect the optimal nose, or tail, shape for drag considerations. It is however recommended that the sensitivity of the optimal tail, or nose for that matter, geometry for the boundary layer thickness at the trailing edge of the coaches first be tested before this hypothesis is accepted. Should this hypothesis hold true it is of great industry importance since the train configuration may be adapted as needed without affecting the aerodynamic efficiency, with regard to the drag force, of the locomotives. Answering this question however, lies outside of the scope of this thesis and as such it will not be addressed here. Finally, since the nose geometry has very little influence on the partial coach-drag force, the change in geometry with its resultant flow-field and associated effect on the coaches will only be superficially discussed.

The nose shapes associated with the minimum and maximum drag forces acting on the coaches for nose lengths of 2m, 4.85m and 7.7m, are shown in Figure 89. From the figure it would seem that the strongest determining factor in establishing a minimal drag force on the coaches is the nose-tip height which remains unchanged at 1.34m. In contradiction with what is predicted by the research done on automobiles (see section 2.4.1 and (Buchheim, et al., 1981)), in the case of this specific train, i.e., the MC25, a lower stagnation point (see Figure 89, right) does not decrease the total drag acting on the train. Rather, both the total drag as well as the partial coach-drag is smaller the higher the nose-tip. This may be due to the fact that the nose-tip acts as a flow-divider of sorts, i.e., the higher the stagnation point, the larger the mass fraction of flow that is forced beneath the train which sees slower moving air than the region above it (see Figure 100).

It is known from the simulation results that for the flow beneath the train coaches the compressibility effects are negligible which allows for the assumption that density remains approximately constant to be made, thus the mass flow rate can only be altered by either a change in cross-sectional area or velocity. Considering the control volume beneath the coaches, we can see that the cross-sectional area along the length of the train remains constant. Thus, had the sides of the train been sectioned off in order to form a duct of sorts, the only variable requiring integration remaining is the velocity of the fluid ( $\dot{m} = \rho A \int V$ ). This is however not the case, with air being able to escape from the sides beneath the train along its length. For the sake of simplification and clarification purposes, while acknowledging that this is a simplification, the flow beneath the train along its length on its symmetry plane will be considered (see Figure 81); At  $x=0$  ( see Figure 81, top left), the location just after the nose, there is a velocity profile greater than the linear velocity profile which would be expected of flow beneath a stationary body (the train) and a moving plate (the ground). Clearly then, this is a function of the local acceleration due to the nozzle effect of the train nose geometry. Thus the mass flow rate at  $x=0m$  is also greater than that expected of the simple moving plate scenario.

When the velocity profiles at the remaining x-coordinates are considered it is clear that not only has the velocities associated with said profiles decreased, but that the profiles have also roughly stabilized (see Figure 81,  $x = 33.87m, 67.74m, 101.1m$ ). There is however the matter of the effect that this has on mass

flow to address. Since the summation of the mass flow rate of air that enters and exists the control volume beneath the train must equal zero, a reduction in the velocities associated with the velocity profile implies an increase in area. We however know that geometrically speaking, for any given nose configuration, the train geometry remains unaltered. Thus the only manner in which the cross-sectional area for any given mass-fraction of air could increase, is if it were to alter direction, i.e., exit along the train side. Hence the process of accelerating the air beneath the train nose due to the surface taper, has the effect that rather than choose the path of most resistance along the length of the train with a smaller cross-section (consider Poiseuille's Law), a certain mass fraction of air flows out at the sides of the train since it offers both the shorter flow path as well as the larger cross-sectional area. Thus there is effectively a smaller mass fraction of air that travels along the remainder of the train length, which in turn travels at a lower velocity for the given cross-sectional area. Furthermore, after the initial transient behaviour beneath the train nose, the velocity beneath the train coaches remains approximately constant (see Figure 81,  $x = 33.87\text{m}, 67.74\text{m}, 101.1\text{m}$ ) exhibiting only slight fluctuations in the velocity profile as air flows to and from the flow field surrounding the train and that beneath it. Since the predominant drag contributor for the coaches, i.e., shear drag, is a function of velocity, reducing the velocity of the air limits the partial coach-drag.

In fact, it is only the partial nose-drag component of the train that obeys the behaviour as predicted by (Buchheim, et al., 1981), i.e., the lower the stagnation point on the nose, the lower the drag force acting on the body. However in the case of an automobile for which (Buchheim, et al., 1981) published results, the nose comprises a large portion of the vehicle length, it thus follows that a reduction in the nose drag yields an overall reduction in drag, while this is not the case for a train where it is the coaches which comprises the largest portion of the total length.

Finally, there is the matter of the effect that the variation of the nose parameters have on the partial drag of the tail. At a nose length of 2m the behaviour of the partial drag of the tail is erratic and unpredictable (see Figure 93 bottom, left), so too is the behavior of the partial drag acting on the coaches (see Figure 93 top, right) as well as the total drag (see Figure 84) acting on the train. When considering that the partial drag of the coaches remains erratic irrespective of the nose length but that the partial tail-drag, as well as the total drag acting on the train, stabilizes with an increase in nose length, it seems to indicate that the instability shown in the total drag behaviour at a nose length of 2m (see Figure 84) is a consequence of the unstable partial tail-drag component at the same nose length. This appears to corroborate the prior hypothesis that the surrogate model is untrustworthy at small ' $L'$ '-values.

With an increase in nose length, the behaviour of the partial tail drag becomes more predictable with the locations of the maximum and minimum force remaining roughly similar. This predictability of the minima and maxima indicates a trustworthy solution. Furthermore the approximate locations of the minimum and maximum total drag force of the train are shared by the corresponding minimum and maximum partial tail-drag components for a given nose length, which does seem to indicate the weight that the tail geometry contributes to the optimized solution – neglecting the tail when optimizing for the nose (and tail for that matter) geometry therefore does not seem to be a prudent course of action should it at all be possible to avoid. Bearing the marked influence of the tail geometry on the optimal

solution in mind, it was deemed a reasonable course of action to investigate the geometries (see Figure 88) and associated flow phenomena for both the minimum and maximum partial tail drag locations. Unfortunately the discussion pertaining to the flow phenomena will be speculative since the flow results for the given design configurations aren't readily available.

As is shown clearly by Figure 88, the nose-tip height that leads to both the minimum as well as the maximum partial tail drag is the same at 1.5m ( $Z_0=1.5m$ ). Since the nose length is constant at 7.7m for both cases, the variable that thus leads to either a minimum or maximum partial drag can only be the inflection point height; when the inflection point assumes its lower-bound ( $H=2m$ ), the partial tail drag is a maximum. Conversely, when the inflection point assumes a value just short of its maximum ( $H=2.9m$ ), the partial tail drag is a minimum. A possible clarification for this behaviour is that since the inflection point regulates the nose (or tail, in this case) gradient and a lower inflection point implies a more rapid transition in effective cross-sectional flow area, the pressure differential that is imposed on the flow is greater for a lower inflection point height. This in turn leads to more severe flow separation which is one of the largest contributors of the pressure drag component experienced by a body. When holistically considering the train geometry in the light of the aforementioned and bearing in mind that the pressure differential across the nose and the tail is essentially the drag contributor that is being optimized for, it follows that the marked influence of the tail on the total drag of the train is due to an imbalance of the corresponding pressure acting in the nose. That is, for a given configuration, the partial nose drag is considerably larger than the partial tail drag that can be generated by the same geometry and it is the configuration as shown in Figure 88 on the right, for which this imbalance is greatest.

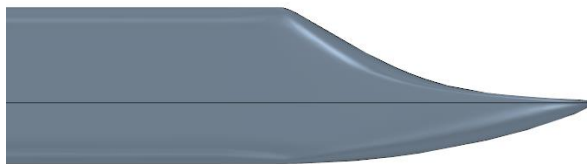
<b>Nose Length of Seven Meters (L=7.7m)</b>	
<i>Minimum Drag Force [N] on Tail</i>	<i>Maximum Drag Force [N] on Tail</i>
	
$Z_0 = 1.5m$ $H = 2.9m$	$Z_0 = 1.5m$ $H = 2m$

Figure 88: The tail (and thus nose) configurations at the maximum length of 7.7m that yield the minimum (left) and maximum (right) drag force on the tail. The nose-tip ( $Z_0$ ) and inflection point ( $H$ ) heights of each respective configuration is also given.

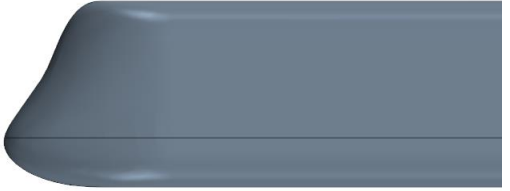
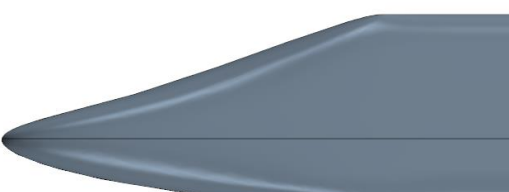
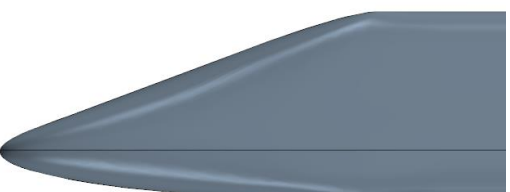
<b>Nose Length of Two Meters (L=2m)</b>	
<i>Minimum Drag Force [N] on Coaches</i>	<i>Maximum Drag Force [N] on Coaches</i>
 <p><math>Z_0 = 1.34\text{m}</math> <math>H = 3\text{m}</math></p>	 <p><math>Z_0 = 1.02\text{m}</math> <math>H = 2.7\text{m}</math></p>
<b>Nose Length of Four Meters (L=4.85m)</b>	
<i>Minimum Drag Force [N] on Coaches</i>	<i>Maximum Drag Force [N] on Coaches</i>
 <p><math>Z_0 = 1.34\text{m}</math> <math>H = 2.8\text{m}</math></p>	 <p><math>Z_0 = 0.7\text{m}</math> <math>H = 2.4\text{m}</math></p>
<b>Nose Length of Seven Meters (L=7.7m)</b>	
<i>Minimum Drag Force [N] on Coaches</i>	<i>Maximum Drag Force [N] on Coaches</i>
 <p><math>Z_0 = 1.34\text{m}</math> <math>H = 2.6\text{m}</math></p>	 <p><math>Z_0 = 1.02\text{m}</math> <math>H = 2.6\text{m}</math></p>

Figure 89: The various nose geometries shown at different nose lengths, i.e., 2m, 4.85m and 7.7m respectively. At each given nose length the values for the nose-tip ( $Z_0$ ) and inflection point (H) height that yields the minimum (left column) and maximum (right column) drag force are given.

**L=2m**

*The portion of the train above the stagnation point*

*The portion of the train below the stagnation point*

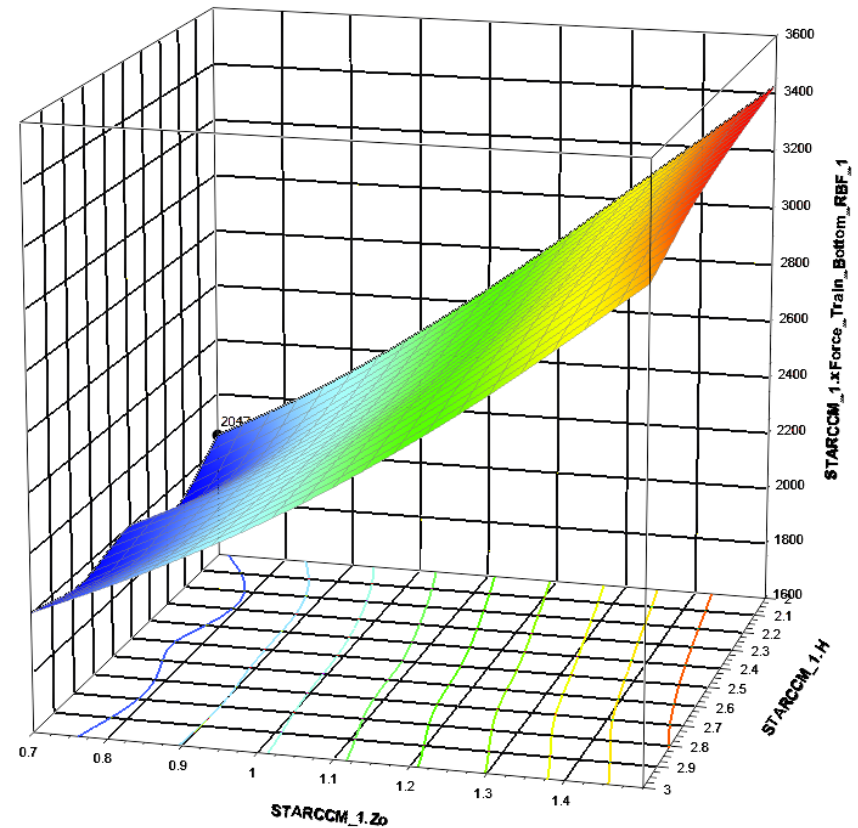
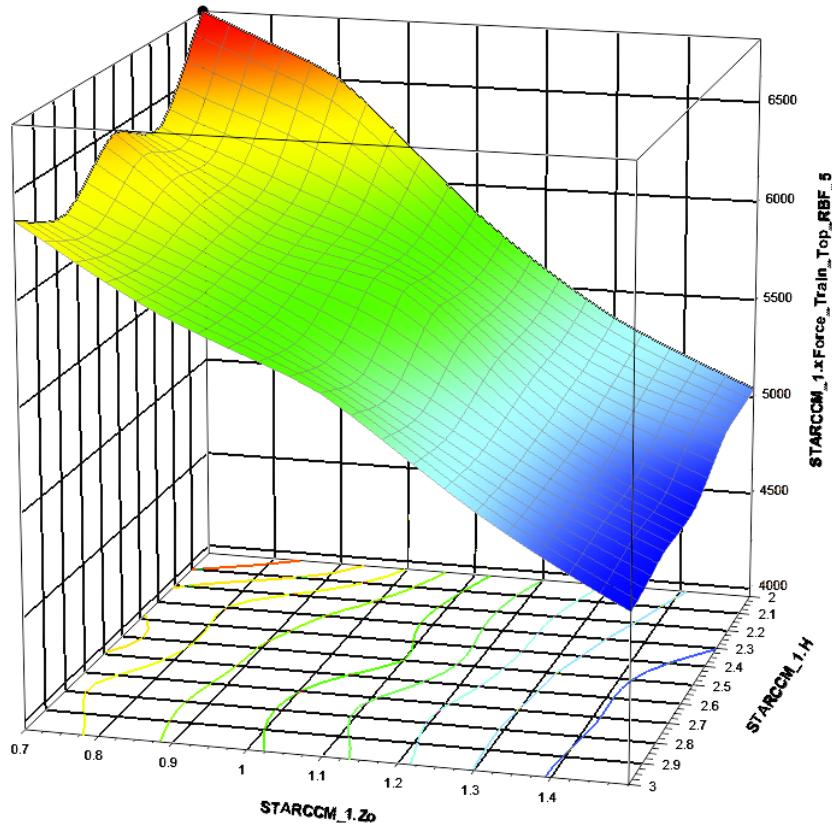
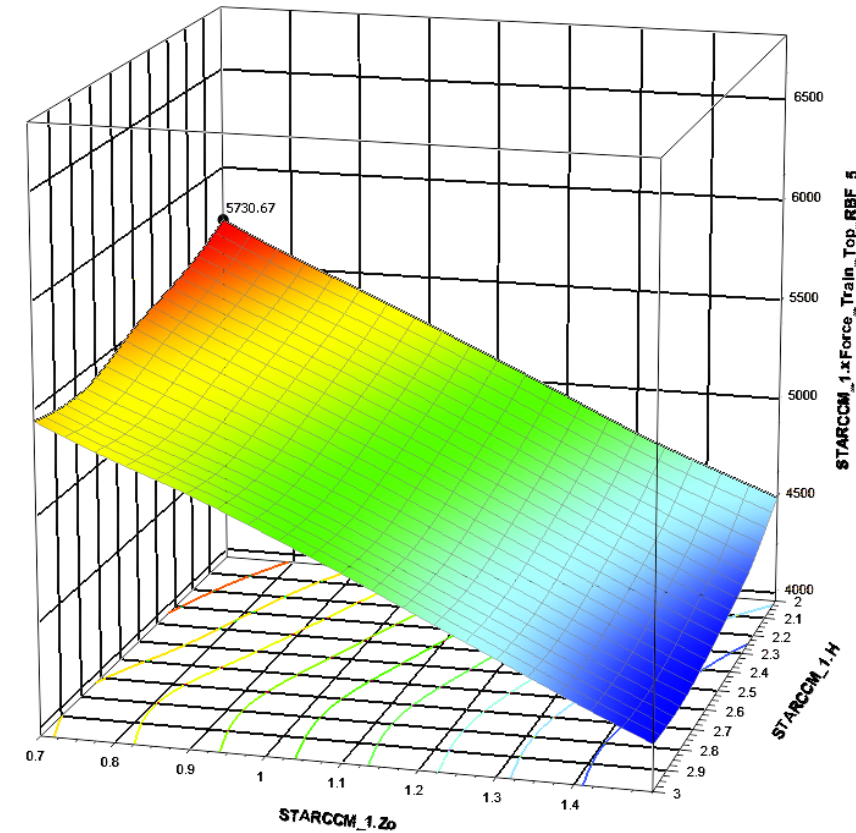


Figure 90: The behaviour of the drag force [N] components for the portion of the train above the stagnation point (left) and below the stagnation point (right) as a function of the nose-tip ( $Z_0$ ) and the inflection point height (H), for a constant nose length of 2m.

**L=4.85m**

*The portion of the train above the stagnation point*



*The portion of the train below the stagnation point*

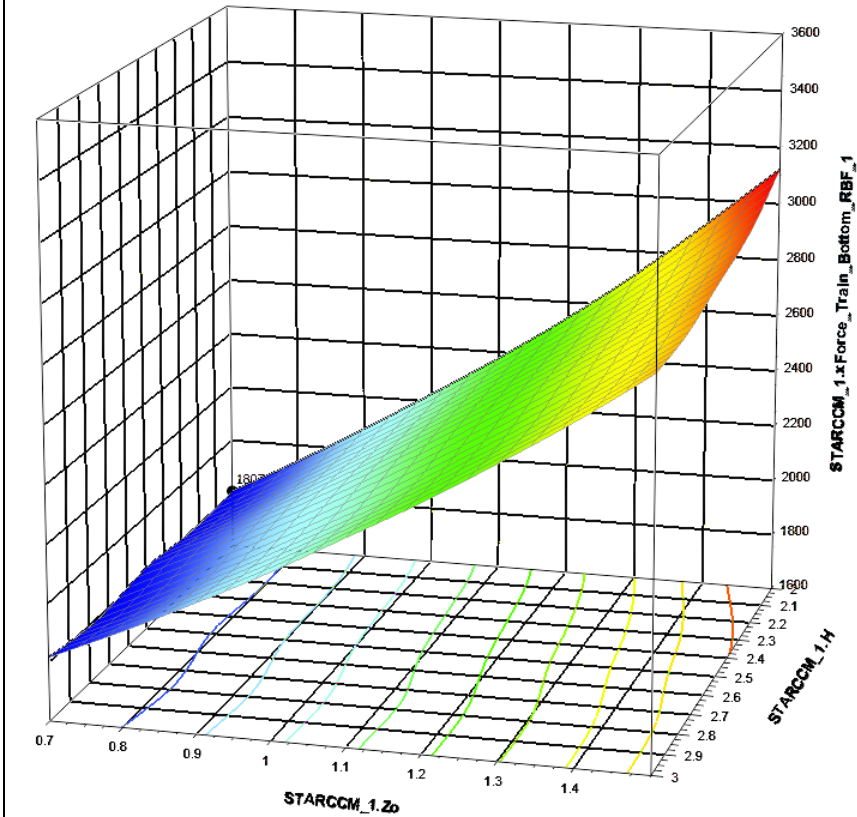


Figure 91: The behaviour of the drag force [N] components for the portion of the train above the stagnation point (left) and below the stagnation point (right) as a function of the nose-tip ( $Z_0$ ) and the inflection point height (H), for a constant nose length of 4.85m.

**L=7.7m**

*The portion of the train above the stagnation point*

*The portion of the train below the stagnation point*

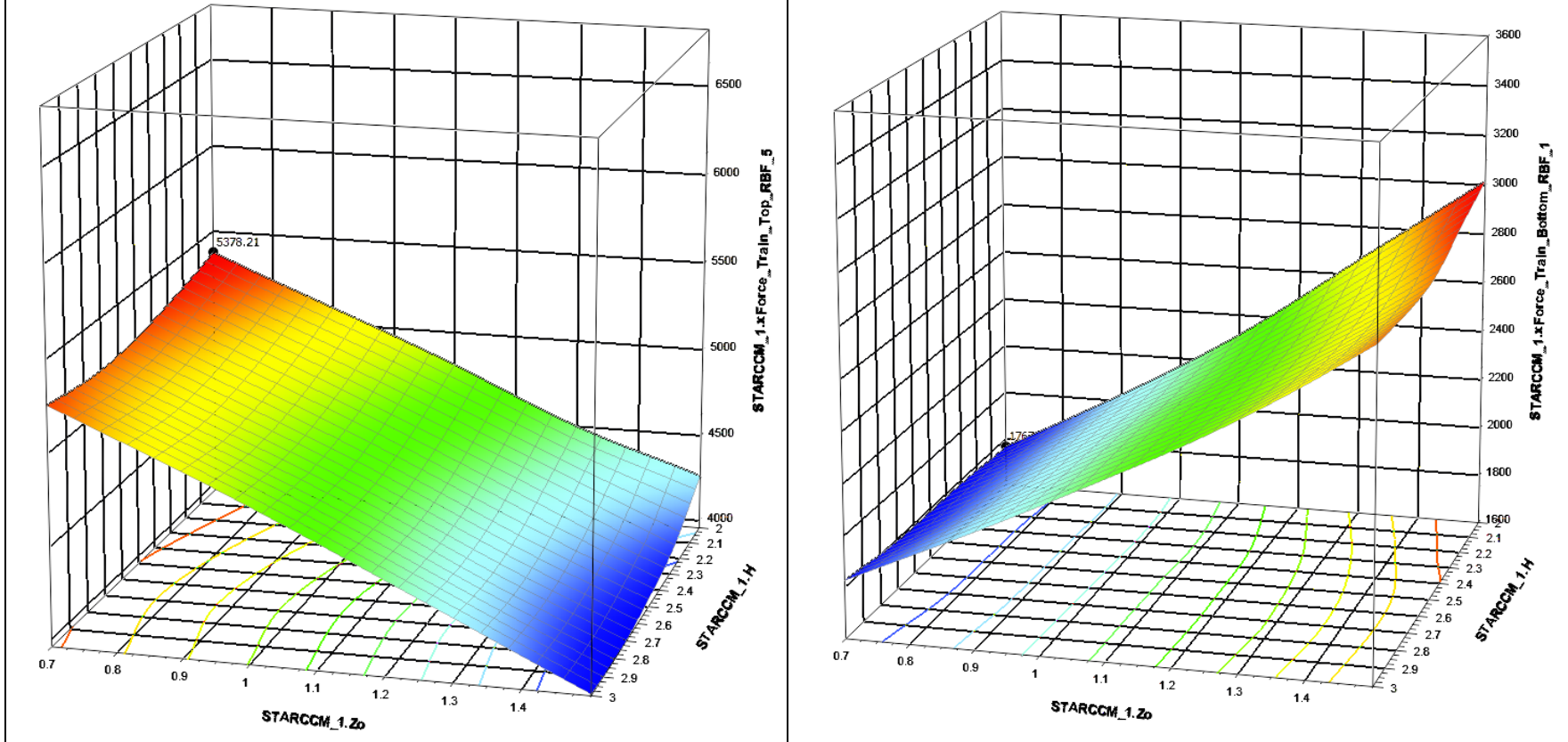
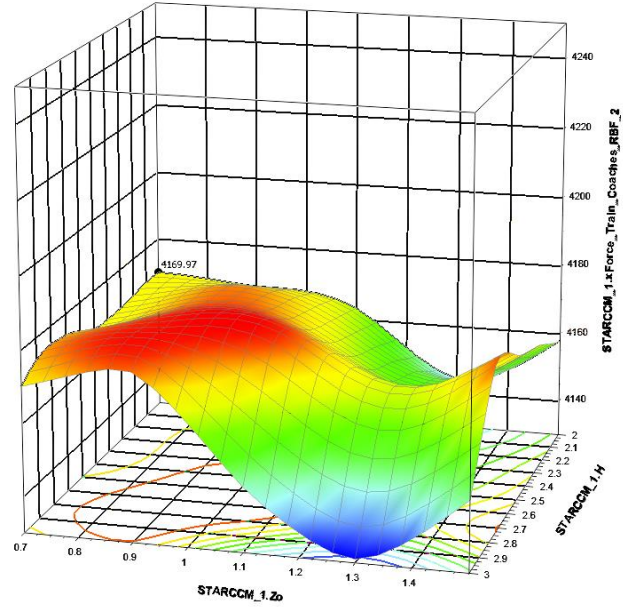
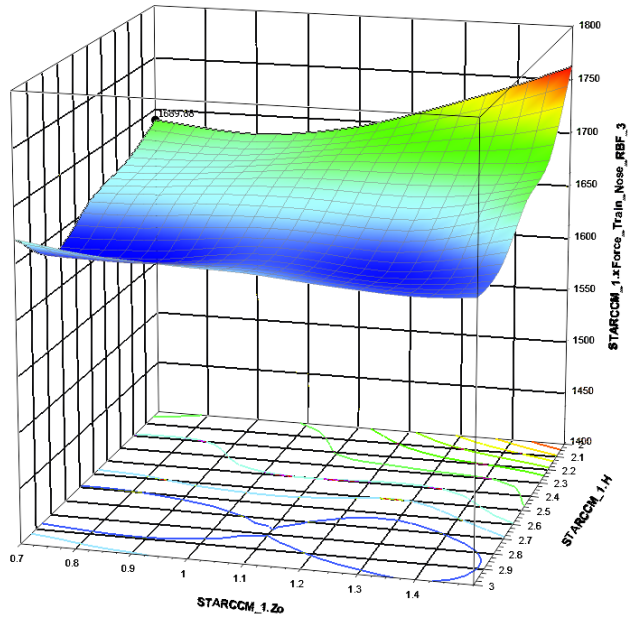


Figure 92: The behaviour of the drag force [N] components for the portion of the train above the stagnation point (left) and below the stagnation point (right) as a function of the nose-tip ( $Z_0$ ) and the inflection point height (H), for a constant nose length of 7.7m.

**L=2m**

*The Nose Portion of the Train*

*The Coaches Portion of the Train*



*The Tail Portion of the Train*

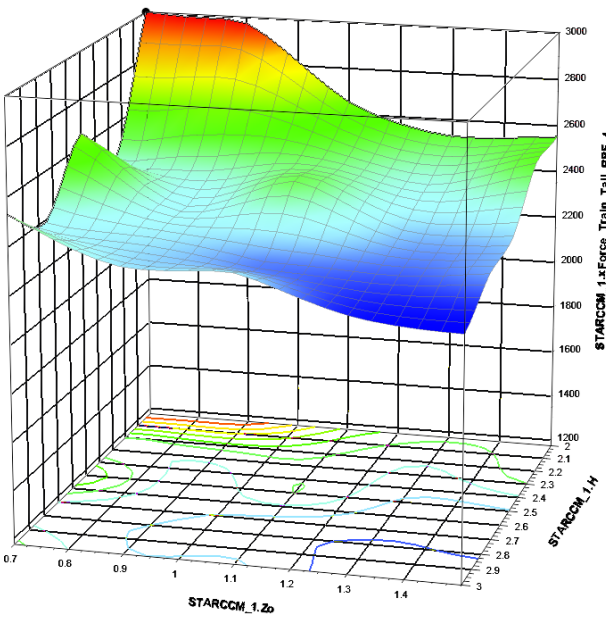
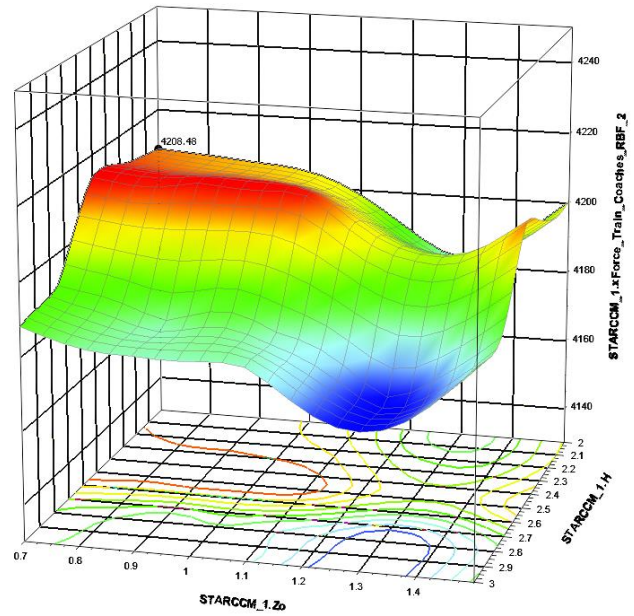
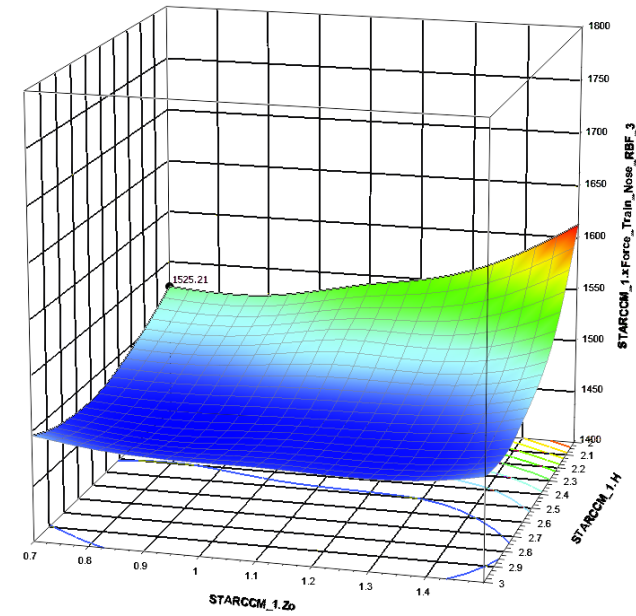


Figure 93: The behaviour of the drag force [N] components for the train nose (top, left), coaches (top, right) and train tail (bottom, left) as a function of the nose-tip ( $Z_0$ ) and the inflection point height ( $H$ ), for a constant nose length of 2m.

**L=4.85m**

*The Nose Portion of the Train*

*The Coaches Portion of the Train*



*The Tail Portion of the Train*

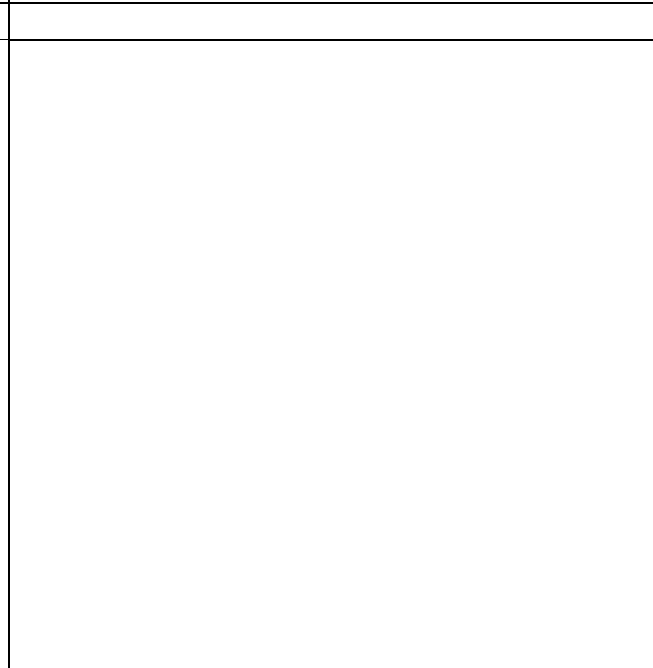
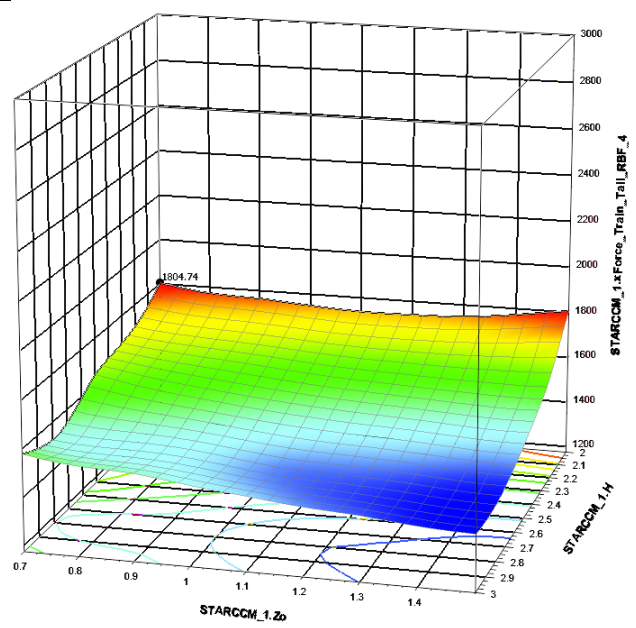
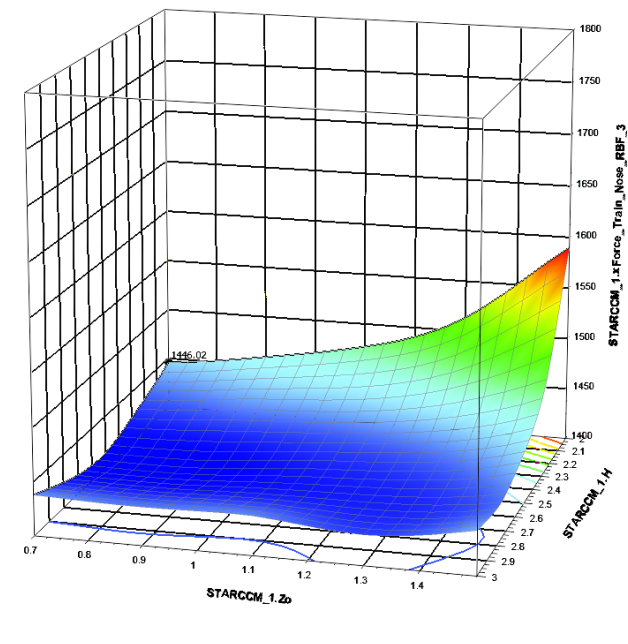


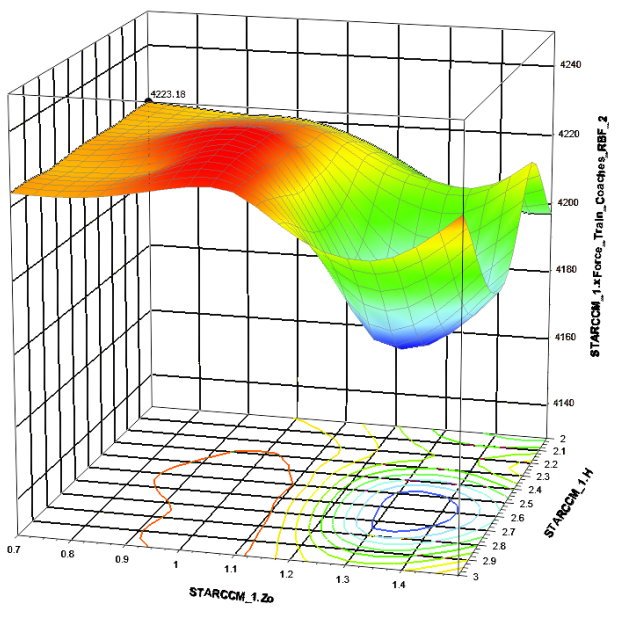
Figure 94: The behaviour of the drag force [N] components for the train nose (top, left), coaches (top, right) and train tail (bottom, left) as a function of the nose-tip ( $Z_0$ ) and the inflection point height ( $H$ ), for a constant nose length of 4.85m.

**L=7.7m**

*The Nose Portion of the Train*



*The Coaches Portion of the Train*



*The Tail Portion of the Train*

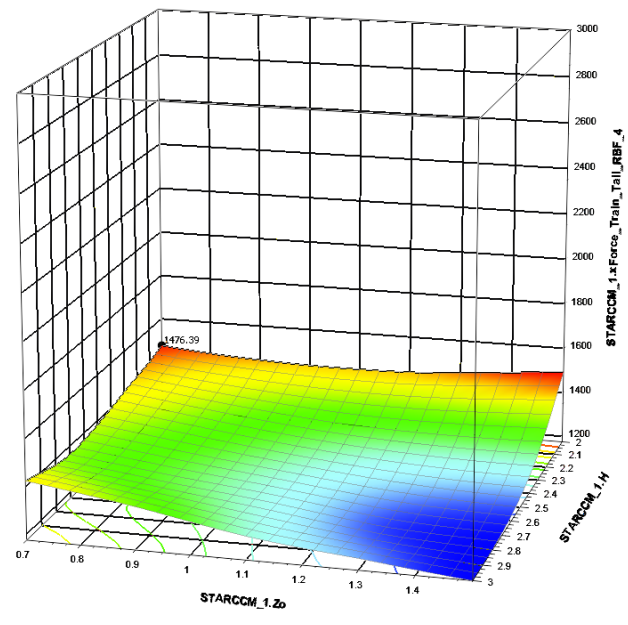


Figure 95: The behaviour of the drag force [N] components for the train nose (top, left), coaches (top, right) and train tail (bottom, left) as a function of the nose-tip ( $Z_0$ ) and the inflection point height (H), for a constant nose length of 7.7m.

#### 4.5.4. Optimization Algorithm Results

##### 4.5.4.1. Surrogate Models Discussion

As mentioned before, two surrogate models were created, one by making use of the radial basis function (RBF) and the other by making use of Kriging interpolation. From the results obtained for each model, one was not clearly superior to the other, with both showing similar behaviour of the total drag force as a function of nose-tip height, inflection point height and nose length (see Figure 84 to Figure 86 as well as Appendix E). The SHERPA algorithm was thus used to explore the design spaces as modelled by both surrogates in order to determine the optimal nose geometry as well as which surrogate is superior.

It is however, important to note that the number of design points made available to a given optimization study changes the way in which the algorithm samples the design space. This is due to the fact that for optimization studies, the design space is sampled as the study proceeds so that changing the number of allowable evaluations, changes the sampling method which leads to different trends and relationships being predicted. Consider as an example that the SHERPA algorithm samples closer to the region where it identifies the optimal point to be located, rather than spacing the design points equally as a design of experiments might do, which can serve to artificially skew data. It was therefore thought to be a prudent course of action to validate that the results obtained from the surrogate are independent from the number of evaluations allowed. The results of this independence study performed on both surrogate models are shown in tables Table 18 and Table 19.

In the case of the RBF surrogate model, fifty evaluations were sufficient to find the values for the parameters (see Table 18) that yielded a geometry that had been optimized for the total drag force (6798.08N acting on the half-model). The solution for the optimized total drag force (6793.09N acting on the half-model) as determined by making use of the Kriging model, was also converged by fifty evaluations, although for slightly different values of the geometric parameters (see Table 19). It is however, interesting to note that the ideal nose length obtained by making use of the Kriging surrogate model is 7.529m, while that predicted by making use of the RBF model is 7.7m. Since an ideal nose length of 7.7m is expected from the theory, the results obtained from the RBF metamodel will be used and considered for discussion, as well as further studies. Yet, when the relatively small discrepancies in the results predicted by the two metamodels are considered, it is likely that the Kriging model would have yielded trustworthy results as well.

Radial Basis Function Surrogate Model							
Number of Evaluations	Correlation Coefficient			Optimized Parameter Value			Total x-Force [N]
	H	L	Z <sub>0</sub>	H	L	Z <sub>0</sub>	
50	-0.41	-0.89	-0.14	2.73	7.7	1.364	6798.08
150	-0.55	-0.91	-0.38	2.73	7.7	1.364	6798.08

Table 18: The Pearson correlation coefficients obtained for the various nose parameters and the total x-force working on the half-model of the train for an increasing number of evaluations. The parameter values determined for the optimized train nose geometry are also listed for the given number of evaluations along with the minimized total drag force. All results shown here were obtained from the surrogate model created by making use of the radial basis function.

Kriging Surrogate Model							
Number of Evaluations	Correlation Coefficient			Optimized Parameter Value			Total x-Force [N]
	H	L	Z <sub>0</sub>	H	L	Z <sub>0</sub>	
50	-0.13	-0.84	-0.49	2.73	7.529	1.38	6793.09
150	-0.36	-0.92	-0.36	2.74	7.529	1.38	6793.07

Table 19: The Pearson correlation coefficients obtained for the various nose parameters and the total x-force working on the half-model of the train for an increasing number of evaluations. The parameter values determined for the optimized train nose geometry are also listed for the given number of evaluations along with the minimized total drag force. All results shown here were obtained from the surrogate model created by making use of the Kriging interpolation function.

#### 4.5.4.2. Optimization Results

The correlation plot obtained for the optimization of the train nose geometry, by making use of the RBF metamodel, is shown in Figure 96. The Pearson correlation coefficient for the nose length indicates a strong negative correlation and given the clear way in which the raw data points follow the same trend as that represented by the red linear regression fit (see Figure 96 and Figure 97, middle graph), the correlation coefficient value may be trusted. Both the inflection point height as well as the nose-tip height show moderately strong negative correlations, i.e., -0.48 and -0.45 respectively. However, when the raw data are considered (see Figure 96 and Figure 97, top and bottom graphs) there is some visible uncertainty and scattering of the data. The overall trend is, nevertheless, captured well which is visible in the concentrated nature of the design evaluations and the fact that the design points aren't arbitrarily scattered across the entire design space. Be that as it may, there are still erratic design points present which artificially skew the data to a certain degree and as such the values of the correlation coefficients for these parameters (H and Z<sub>0</sub>) should be treated with a measure of suspicion.

Furthermore, the complex inter-dependent relationship between the values of the inflection point (H) and the nose-tip height (Z<sub>0</sub>) was not only discussed in section 4.5.3.2.2, but can also be seen from both the histogram as well as the raw data plots (see Figure 96). Consider the very clear sampling bias for the nose length (L); the largest number of evaluations is performed for the longer nose lengths, not so for the inflection point and nose-tip height. In both cases, there are three distinct values which are identified as possible optimal values above the others. In the case of the raw data this is observable as three distinct horizontal lines, while the histogram displays three distinct columns which correspond to the same values of H and Z<sub>0</sub> as the raw data plot lines.

The top and bottom figures shown in Figure 97 illustrate the aforementioned more clearly. This biased clustering of points seen in Figure 97 is a function of the SHERPA algorithm's natural behaviour to find possible optimal points and to explore in those regions specifically, rather than to space points equally as a DOE might do. The graph illustrating the H-value and corresponding drag force for a given design, for example, sees a large concentration of design evaluations around an inflection point height of 2.73m (H = 2.73m). Closer inspection shows that these design points assumed various values for the nose length (L) and nose-tip height (Z<sub>0</sub>), but that those values that appeared most frequently were 7.7m and 1.364m, respectively. Similarly for a nose-tip height of 1.364m (see Figure 97, bottom) the nose-length and inflection point height that present themselves most often are 7.7m and 2.73m, respectively. This serves to prove the effectivity of the SHERPA algorithm; it identifies the optimal value of a given parameter relatively quickly and then varies the other parameters to achieve the desired goal.

It is thus not unexpected that the optimal design as identified by the algorithm has a nose length of 7.7m, an inflection point height of 2.73m and a nose-tip height of 1.364m. Finally, the minimum drag force that is associated with this optimized nose geometry is predicted to be 6798.08N for the half-model. Since this design was not used to construct the surrogate model, it is prudent to simulate this optimal design and compare the results from the CFD to that predicted by the surrogate. This will not only affirm the validity of the optimized geometry but also the quality of the meta-models that were constructed. It is however worth noting that there are multiple designs that perform only fractionally worse than the optimal design. Consider for example the relationship between the total x-force and the inflection point height (see Figure 97, top); there are multiple designs that lie between inflection point height of 2.6m and 2.8m which performs comparatively well with regard to the optimal design. In the case of the nose-tip height ( $Z_0$ ), there is broadly speaking a decrease in the x-force with an increase in  $Z_0$  until a value of 1.3m is reached, where after the total drag force remains approximately constant with a slight increase visible for values approximately above 1.4m (see Figure 97, bottom).

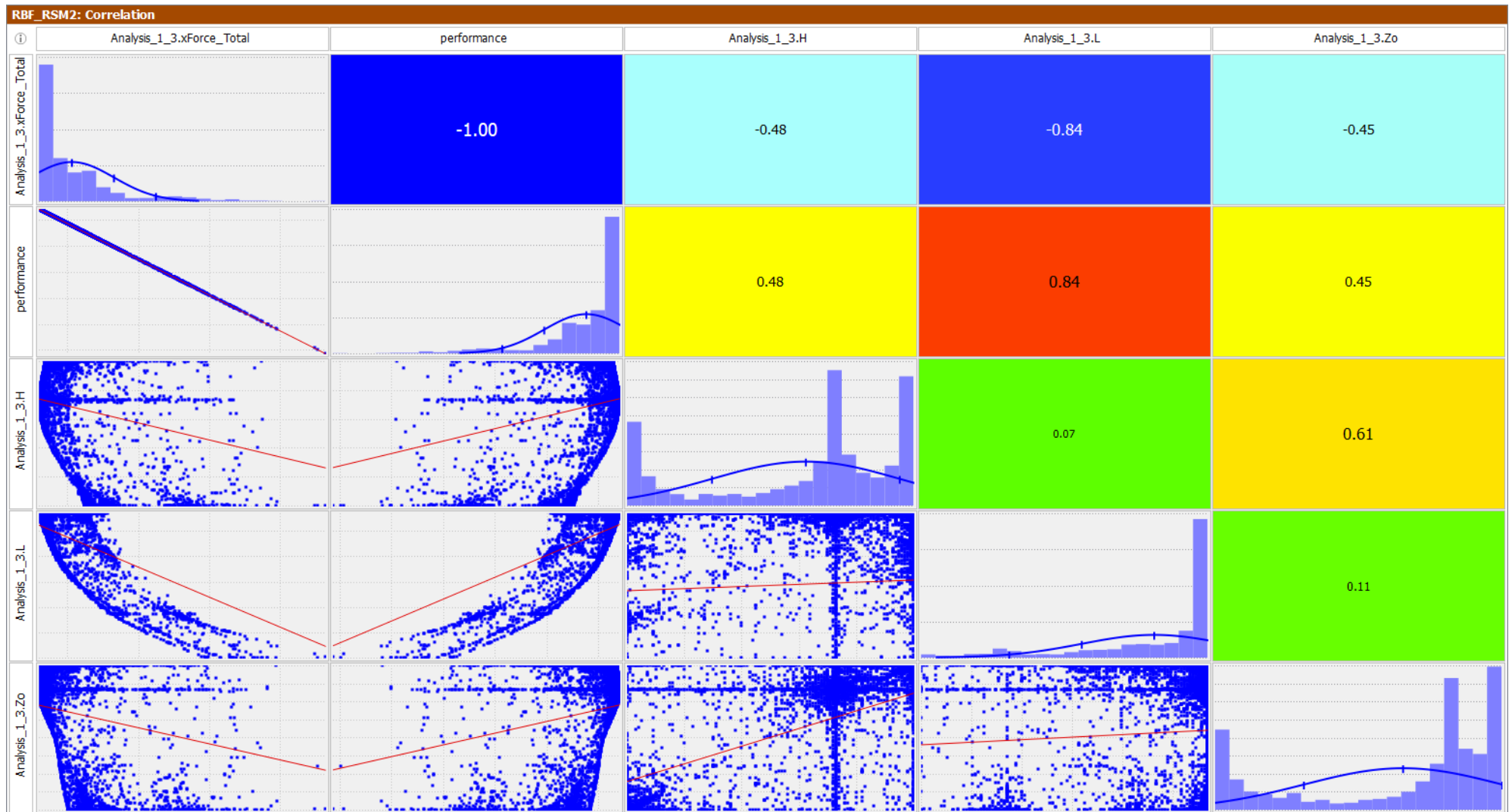


Figure 96: The correlation plot that was obtained by making use of the Radial Basis Function Metamodel which was explored by the SHERPA optimization algorithm. The Pearson correlation coefficients are given along with the raw data for the total drag force as a function of inflection point height, nose length and nose-tip height respectively.

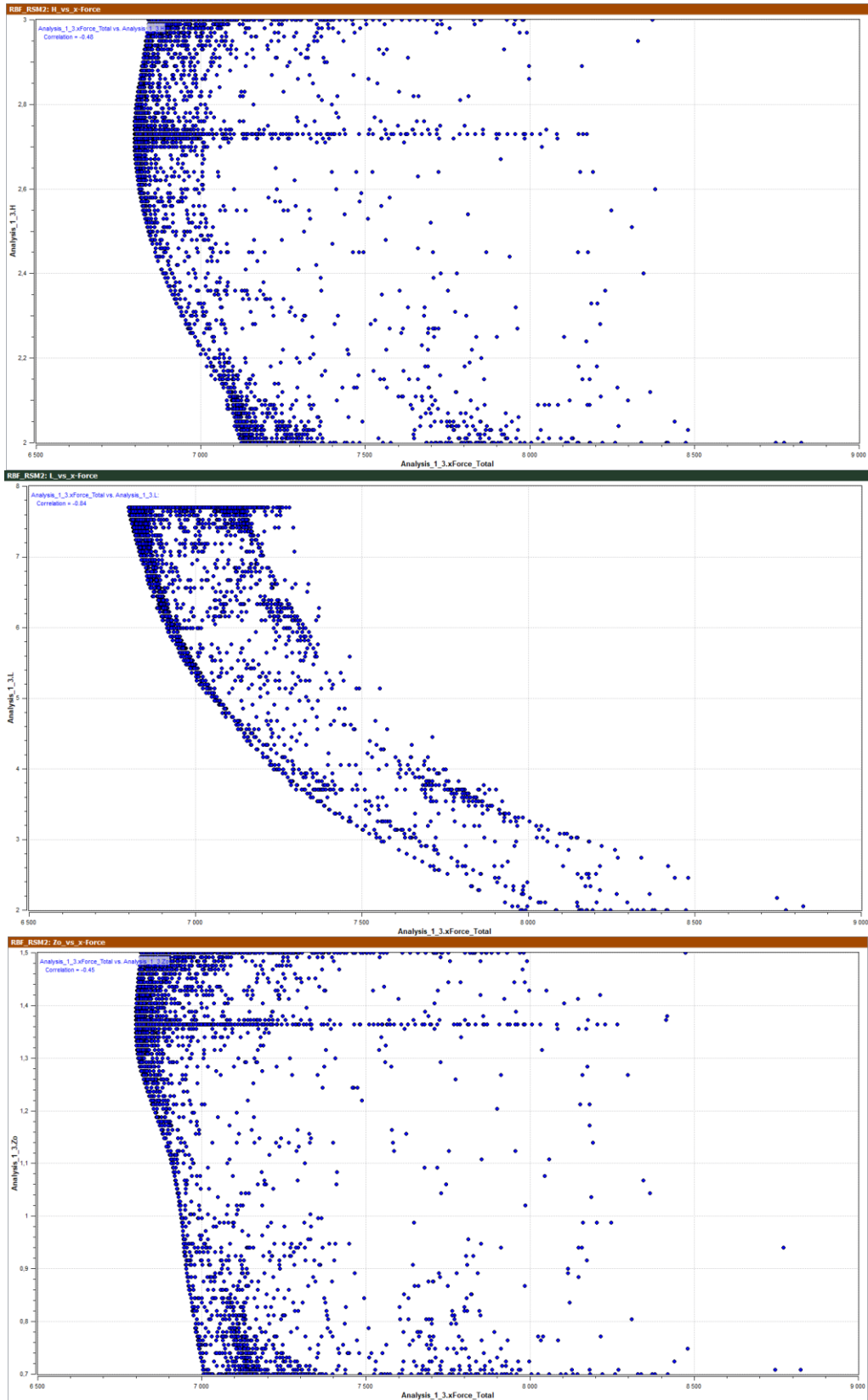


Figure 97: The raw data obtained from the optimization study that shows the relationship between the total x-force acting on the train and the inflection point height (top), nose length (middle) and nose-tip height (bottom).

#### 4.5.4.3. Validation of the Surrogate Model

The optimal design as predicted by the radial basis function metamodel and the SHERPA algorithm has a nose length of 7.7m, an inflection point height of 2.73m and a nose-tip height of 1.364m (see Figure 98) with a predicted total drag force of 6798.08N for the half-model. The external flow field surrounding this geometry was simulated with the assistance of CFD software in order to allow for comparison with the values predicted by the metamodel (see Table 20) and hereby validate said surrogate's accuracy.

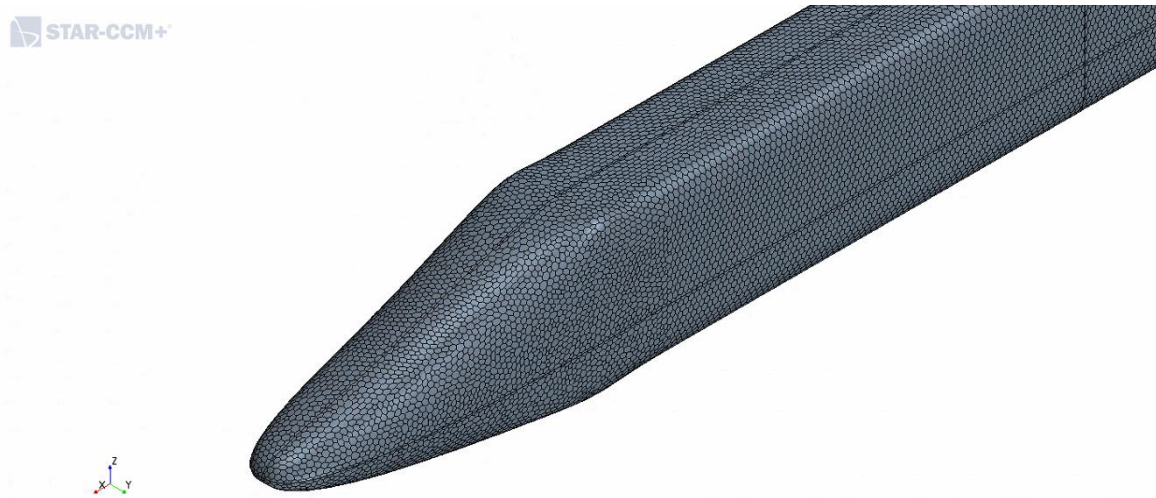


Figure 98: The final geometry of the train nose that was optimized for drag, shown here as a full-model with the body-adjacent polyhedral mesh.

The magnitude of the drag force acting on the various geometric portions of the train, i.e., the nose, coaches, tail, top and bottom thereof, as relayed by the surrogate (see Table 20), were obtained by making use of linear interpolation since the resolution used for the exploration of the meta-model was finer than the resolution used for the construction of said model. In other words, the minimum total drag force acting on the half-model as determined by the SHERPA algorithm (6798.08N) is associated with certain geometric parameters, these are  $L=7.7\text{m}$ ,  $H=2.73\text{m}$  and  $Z_0=1.364\text{m}$ . Save for the nose length however, these values were not used to construct the metamodel and as such the response of any given force component at these geometric parameters is not available. Thus in order to obtain indicative force values at these geometric parameters, linear interpolation was made use of and the resultant force-values can be seen in Table 20. The aforementioned clarifies why it is that there are two values listed for the total x-force; the first value is the summation of the interpolated components (6802.30N) whereas the second is the exact value as predicted by the SHERPA algorithm (6798.08N). It is however worth noting that while there is a discrepancy in the results, the two values only differ by 0.06 per cent from one another. It would thus seem that for a nose length of 7.7m the linear interpolation approximation is reasonable for the discretization size in question. This is further affirmed by the deviation percentages from the simulation results for the various train portions as listed in Table 20. Once again the largest deviations from the simulated results are those values predicted by the meta-models for the bottom portion of the train and specifically for the coaches.

It is thus in these areas that significant changes in the flow behaviour is expected over reasonably small discretized spaces (the deviation percentages associated with the remaining portions of the train affirm this, see Table 20), hereby indicating that the flow in these regions is more non-linear than elsewhere around the train body. The aforementioned therefore serves to affirm the previously hypothesized extreme non-linearities in the flow beneath the train, especially in the vicinity of the coaches. These non-linearities are indicative of a large measure of turbulence in the flow and the eddies which necessarily accompany said flow can make the prediction thereof challenging, especially for anisotropic turbulent flows.

It is thus expected that while the meta-model may perform well for a streamlined nose, its predictive accuracy may deteriorate as the nose, and thus necessarily the tail, tend to blunter configurations. The results as tabulated in Table 20 for the half-model of the train has however, proven the predictive accuracy of the surrogate model for streamlined nose geometries at the very least.

<b>Drag Force [N]</b>			
<b><i>Geometric Portion of Train</i></b>	<b><i>Simulation Results</i></b>	<b><i>Surrogate Results</i></b>	<b><i>Deviation [%]</i></b>
<i>Nose</i>	1431.77	1425.84	-0.41
<i>Coaches</i>	4229.37	4182.92	-1.10
<i>Tail</i>	1201.32	1193.54	-0.65
<i>Top</i>	4187.41	4169.47	-0.43
<i>Bottom</i>	2675.05	2632.83	-1.58
<i>Total</i>	6862.46	a) 6802.30	-0.88
		b) 6798.08	-0.94

**Table 20:** The drag force components that were predicted for the various geometric portions of the half-model of the train, i.e., the nose, coaches and tail as well as the top and bottom portions thereof. The values that are listed as simulation results were obtained from the CFD analysis whereas the surrogate results were obtained from the meta-model which required interpolation to be used to obtain the respective force-component values associated with the optimal nose shape. With regard to the total drag force acting on the train, two values are given for the surrogate results; value (a) 6802.30N is the summation of the various force components obtained from interpolation. Value (b) 6798.08N is the value that was obtained when running the SHERPA algorithm on the response surface that describes the behaviour of the total x-force acting on the half-model of the train.

#### **4.5.4.4. Concluding Remarks on the Optimized Design**

From the results of the optimization study it was found that the nose configuration that yielded the largest drag force had an inflection point ( $H'$ ) of 2m, a nose tip height ( $Z_o'$ ) of 0.7m and a nose length ( $L'$ ) of 2m and an associated total drag of 8862.5N acting on the train body. The nose configuration that yielded a minimum total drag force of 6798.08N has already been discussed at length above. There is thus a 30.36 percent reduction in the drag force from the worst to the best case scenarios. Given this considerable improvement in aerodynamic performance, attention will now be paid to the flow field associated with the optimized nose geometry and the features accompanying it.

The velocity field that surrounds the train (see Figure 100 and Figure 99) exhibits many of the features that have come to be expected from the aerodynamics of an object travelling through a fluid. There is a clear stagnation region present at the tip of the nose (see Figure 99) where a fraction of the air is brought to a complete halt while yet another fraction is impeded at the very least. Following the flow from this stagnation point over the upper portion of the train, a separation region can be observed on

the slant of the nose indicated by a lower velocity and higher pressure region. It may at first seem counter intuitive that an optimal nose design should display a separation region on its slant. However, when the separated wake at the tail and its accompanying high pressure region is considered, it follows that an attempt will be made by the optimization algorithm to increase the pressure acting on the nose and inducing separation is a very effective way to accomplish this.

Furthermore, the slant of the nose roughly acts as a nozzle by decreasing the effective cross-sectional area available to the flow hereby accelerating it from stagnation at the nose tip to a maximum velocity in the region where the trailing end of the slant transitions into the roof (see Figure 99, left). Hereafter the flow is subjected to a moderate pressure gradient, relative to that acting across the nose and tail slants that is, where a steady growth of the boundary layer can be observed along the train roof (see Figure 100). This of course indicates the expected loss in kinetic energy of the flow adjacent to the train body with the boundary layer along the roof reaching its maximum thickness of 0.95m at  $x/L=0.79$  and maintaining it through to  $x/L=0.81$  before thinning out once more. Given that this maximum thickness is 24.68% of the total train height and that it is known from the literature that the boundary layer of the train is expected to be highly three-dimensional and anisotropic (Baker, 2008), the need for the use of the RSM turbulence model becomes clear and the choice of turbulence model validated. The aforementioned is further confirmed when the boundary layer growth along the sides of the train is considered (see Figure 101), with a maximum thickness of 3.46m ( i.e., 89.87% of the total train height) observable from  $x/L=0.82$  through to  $x/L=0.89$ . Clearly then, there is a considerable measure of interaction between the anisotropic boundary layer flow and the train body. It would thus seem that simply using the eddy-viscosity term to describe the flow in question would have been a gross oversimplification whereas the Reynolds stress turbulence models use wall functions to determine the Reynolds stress components in the boundary layer region, hereby yielding a more comprehensive description of the flow field.

As mentioned above, the boundary layer acting along the train roof starts thinning again past the  $x/L=0.81$  point and reaches a local minimum at the point where the roof transitions into the tail-slant. This is of course indicative of faster moving air and the question as to the mechanism that drives this acceleration arises. The first hypothesis that was pursued is that there exist longitudinal vortices along the length of the train which reach their maximum intensity in the region where the boundary layer is thinnest. The Q-Criterion was thus employed in order to identify the regions in the flow field where vorticity rather than strain dominates (see Figure 102). From the results shown in Figure 102, it is clear that there are indeed vortices present along the train length and furthermore the value for the Q-Criterion is considerable in the region just preceding the thinning boundary layer (see Figure 102, magnified view on the top, right). On closer inspection however, a few phenomena can be observed; first, there are positive values for the Q-Criterion observable from immediately after the stagnation region on the nose (see Figure 102, magnified view on the top left) until the region just preceding the wake trailing the tail. However, when the convolution integrals of the velocity on the yz-plane is considered at various x-locations along the train length (where  $x=0m$  is the nose tip), it becomes clear that a positive value for the Q-Criterion doesn't necessarily indicate the presence of a vortex (see Figure 103 and Table 21).

In fact, for the range of x-coordinates from 0m to 10m, there are no coherent vortex structures observable. Yet, the flow in this region shows positive Q-Criterion values. It is thus plausible that this positive value simply indicates the anisotropic, swirling nature of the flow adjacent to the body. The beginnings of a vortex formation can be seen at an x-location of 15m with three vortices ultimately visible at a location of 40m down the length of the train (see Figure 103 and Table 21). Unfortunately in the region where the velocity of the air is largest locally in the region of the tail slant (see Figure 99 (right), Figure 100 and Figure 101), there aren't intense vortex structures observable despite a large value for the Q-Criterion (see Table 21, from  $x=105\text{m}$  to  $110\text{m}$ ), rather a decay in the vortices can be seen. Thus the hypothesis of the longitudinal vortices reaching a maximum intensity in the region of local acceleration of the air, hereby facilitating advanced mixing and consequently introducing large measures of kinetic energy from the free-stream into the boundary layer leading to its thinning, has been proven false.

An alternative hypothesis was thus required to attempt to explain the local acceleration of the air in the region where the train roof transitions into the nose-slant. A plot of the streamlines of the flow on the symmetry plane (see Figure 104) seems to indicate that the flow adjacent to the body remains attached in this region rather than separating. As such, the no-slip condition holds and the flow follows the contour of the train body. The flow in the far-field however, maintains its velocity and while it does deflect somewhat, the deflection isn't nearly as extreme as the flow adjacent to the body (see Figure 100). Finally, a plot of the shear stress acting on the tail (see Figure 105) further indicates that the flow remains attached along its length. A plausible hypothesis could thus be that this local deflection of the streamlines has a localized increase in volume as an effect, hereby influencing the density in the region (see Figure 106). This reduction in air density leads to an associated reduction in pressure which has the effect of accelerating the nearby air. When considering the velocity convolution integrals at  $x=105\text{m}$  to  $x=115\text{m}$  this hypothesis does seem to be corroborated by the increase in velocity of the air in the vicinity where the nose tapers in. The final feature of interest in the external flow field is the longitudinal vortices trailing the train which form at the tip of the tail (see Figure 102). These vortices are expected in the near wake region as is known from the literature (Baker, 2008), until ultimately decaying in the far wake region.

Finally, there is the matter of the pressure field surrounding the train (see Figure 107). A high-pressure region can be observed to the front of as well as around the train nose where the flow stagnates. As the flow accelerates around the trailing end of the train nose due to the decrease in cross-sectional flow area, a notable reduction in the pressure of the air can be observed. Hereafter the pressure increases somewhat as a consequence of the no-slip condition at the train wall and the associated boundary layer growth with its accompanying viscous effects. Along the length of the coaches the cross-sectional area remains constant and as such there are no local pressure differentials to accelerate the flow, leading to the roughly constant pressure distribution seen in Figure 107. This, however, does nothing to affect the overarching pressure differential acting across the train as a whole, which still serves as a driver of the air across the train body.

One of the most striking features of the pressure field is the measure of symmetry that it displays. However, when considering that the total drag of an object is the summation of the shear and pressure

drag it experiences, the pressure field appears coherent. That is, it was the geometry of the nose and tail of the train that was varied so as to ensure a minimum drag force. Now consider that the geometry of the coaches remains constant and as such the associated shear drag will remain roughly constant also, the variation in the nose and tail geometry therefore changes primarily to the pressure drag. Thus, in order to establish a minimum total drag a minimum pressure drag must be ensured. It therefore follows that the smaller the pressure differential across the train, the smaller the total drag force acting on it and it is a pressure field that tends to symmetry that ensures exactly that.

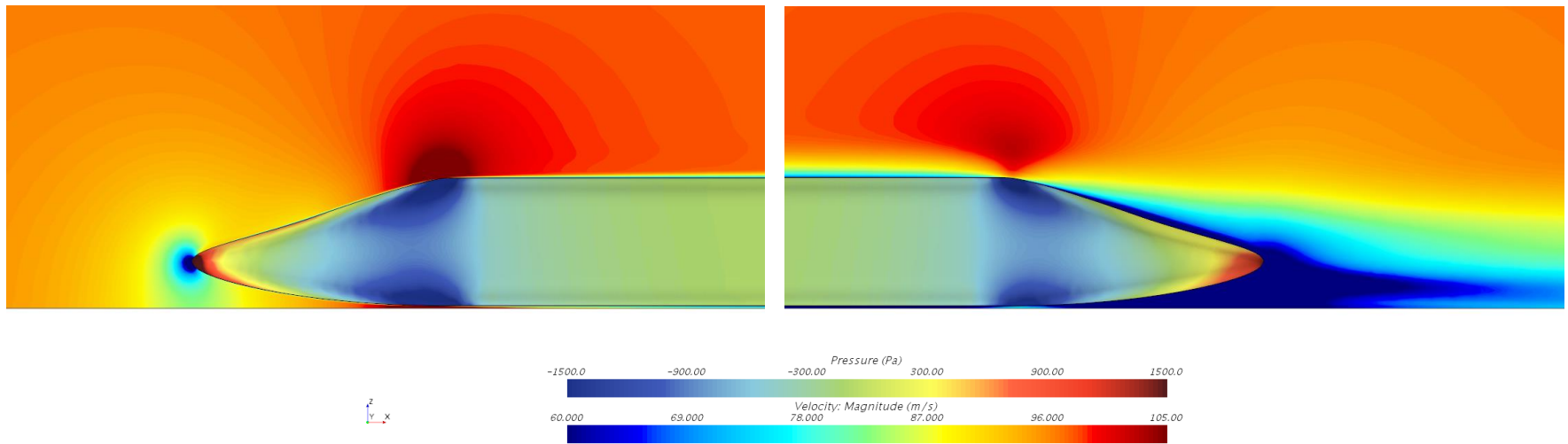


Figure 99: The distribution of the velocity field around the train is shown on the symmetry plane, and the pressure field acting on the train nose (left) and tail (right), is shown on the three dimensional body, for the optimized nose design.

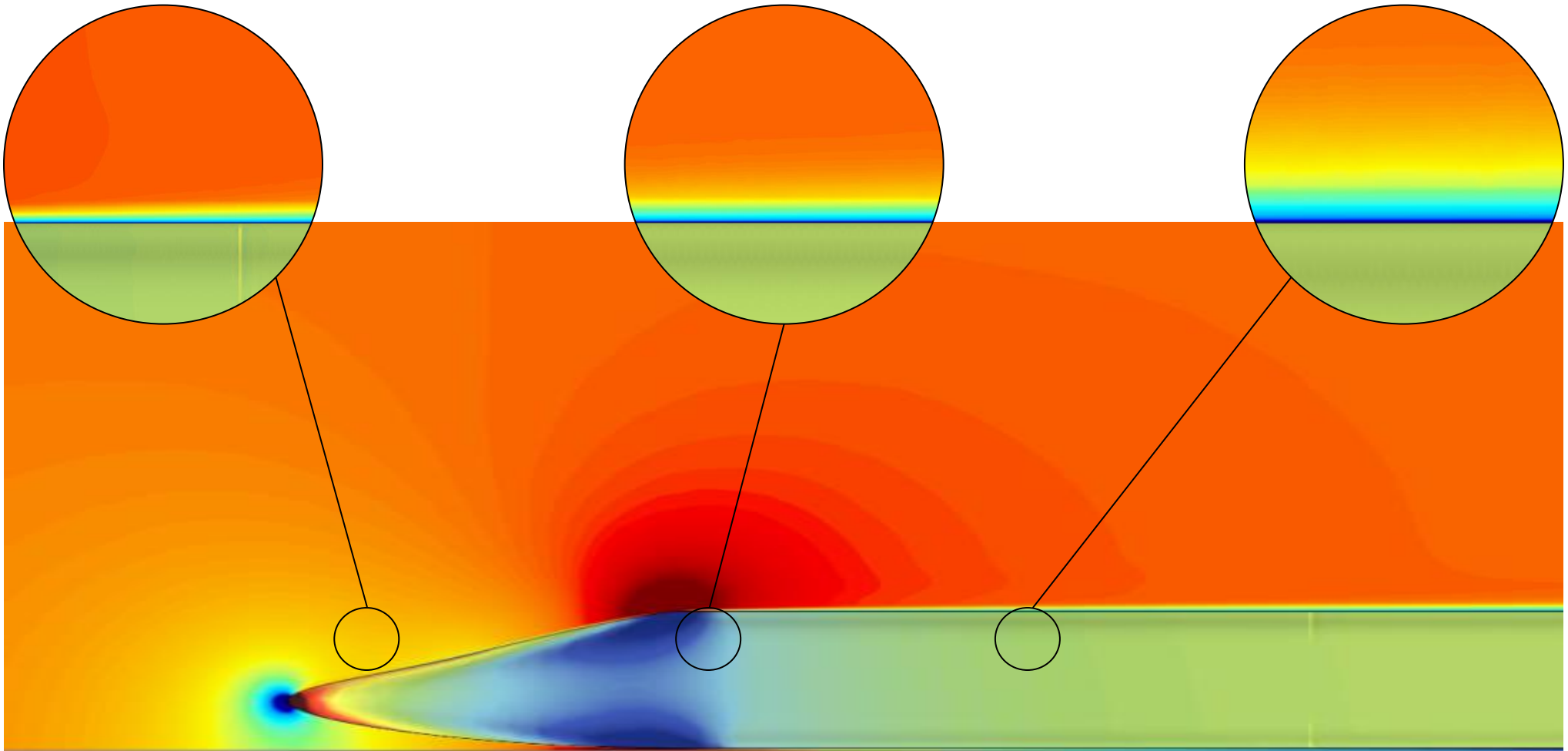


Figure 100: The external velocity field surrounding the train for the optimized nose geometry in windless conditions as seen on the symmetry plane, from the side. The stagnation point on the tip of the nose as well as the wake region trailing the tail are clearly visible, while the considerable growth of the boundary layer along the length of the train body can be seen in the magnified views on the left, middle and right. The corresponding pressure field acting on the train as a consequence of the velocity field is also shown on the three-dimensional train body.

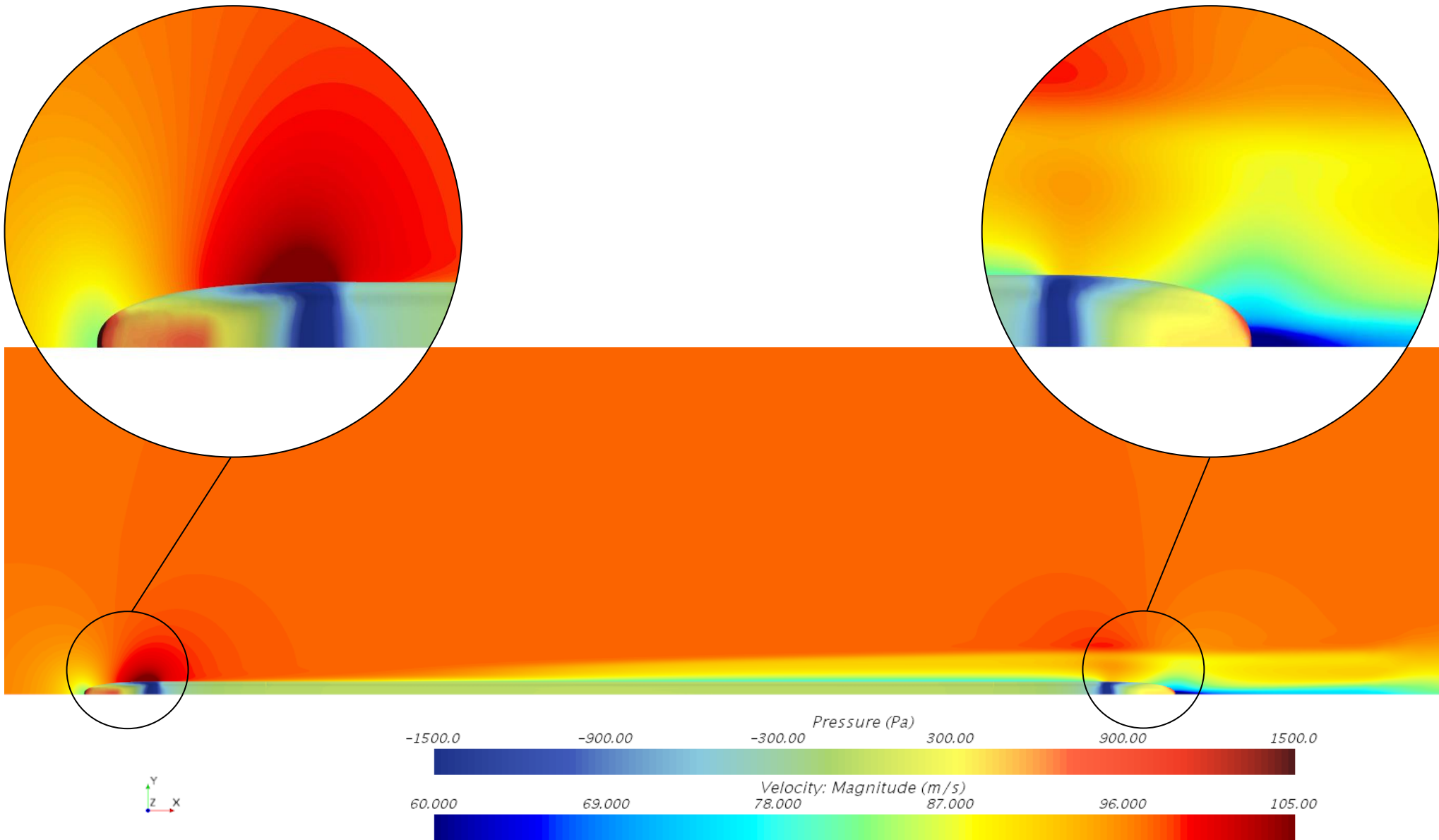


Figure 101: The external velocity field surrounding the train for the optimized nose geometry in windless conditions as seen on the xy-plane, from the top. The stagnation point on the tip of the nose and separated region over it, as well as the wake region trailing the tail are clearly visible. The considerable growth of the boundary layer along the length of the train body can also be clearly seen. The corresponding pressure field acting on the train as a consequence of the velocity field is also shown on the three-dimensional train body.

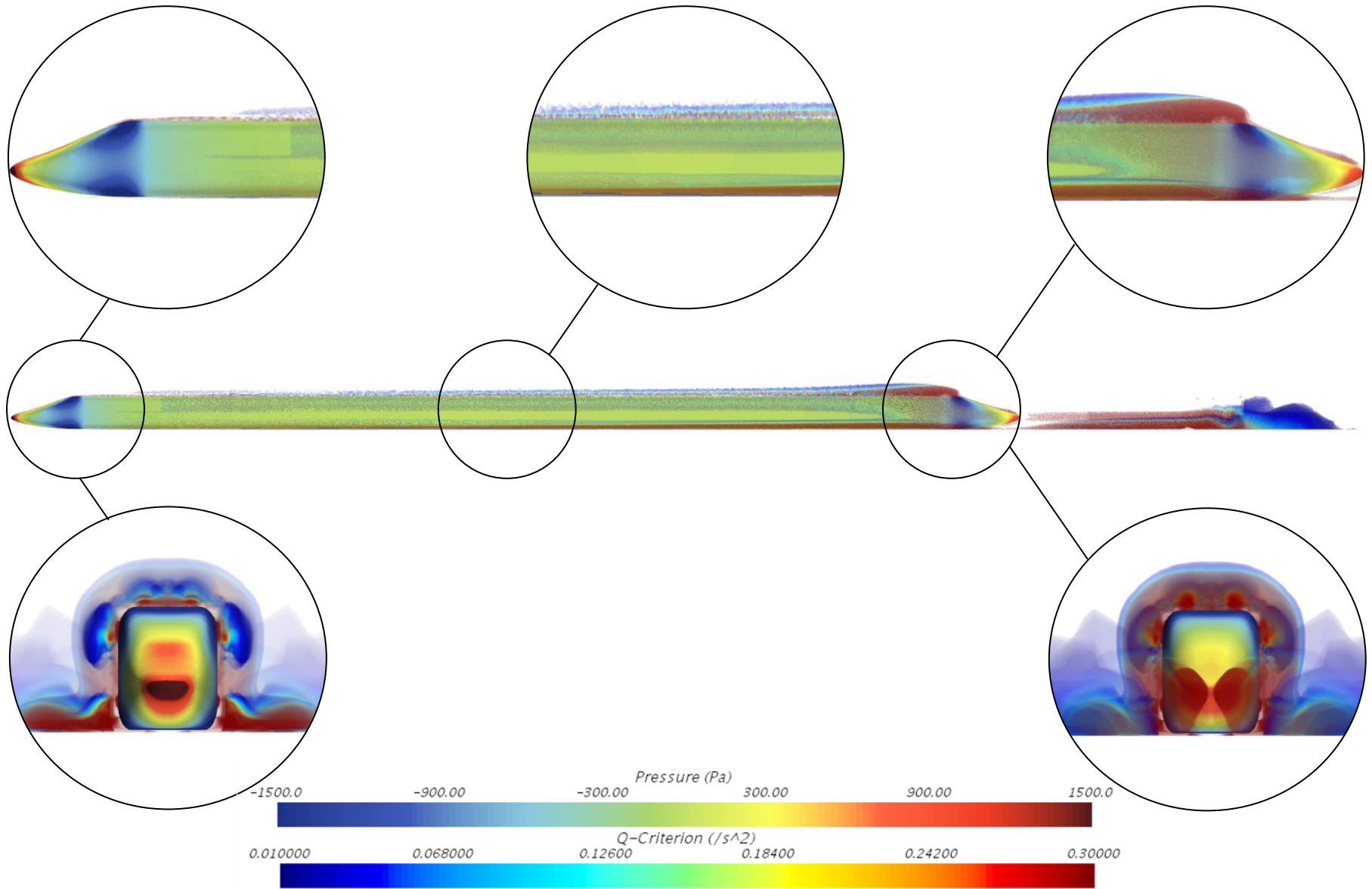


Figure 102: The distribution of the Q-criterion around the train body which was fitted with an optimized nose and tail geometry. The turbulent nature of the boundary layer can be clearly seen in the magnified view on the top left, as well as the magnified view in the top middle which also indicates the measure of boundary layer growth. Finally, longitudinal vortices can be observed in the magnified view on the top, right; these are prevalent along the roof and sides of the train (see magnified views on the bottom left and right) and can further be found trailing the tail (see bottom, right). The static pressure acting on the train is also shown on the three-dimensional body.

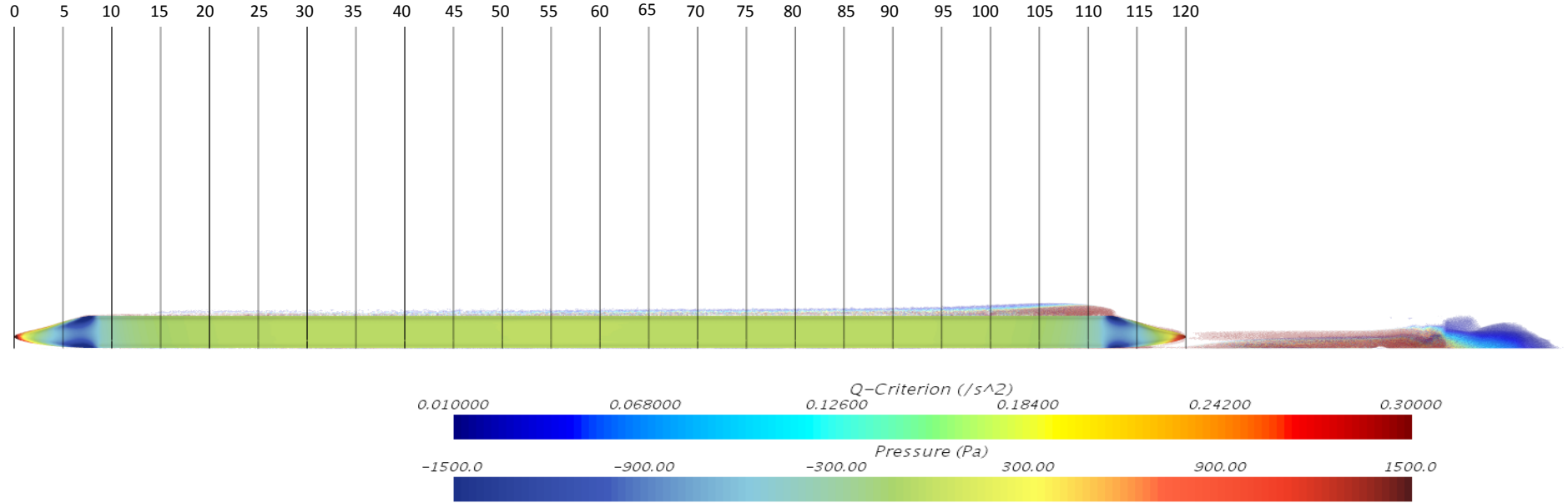
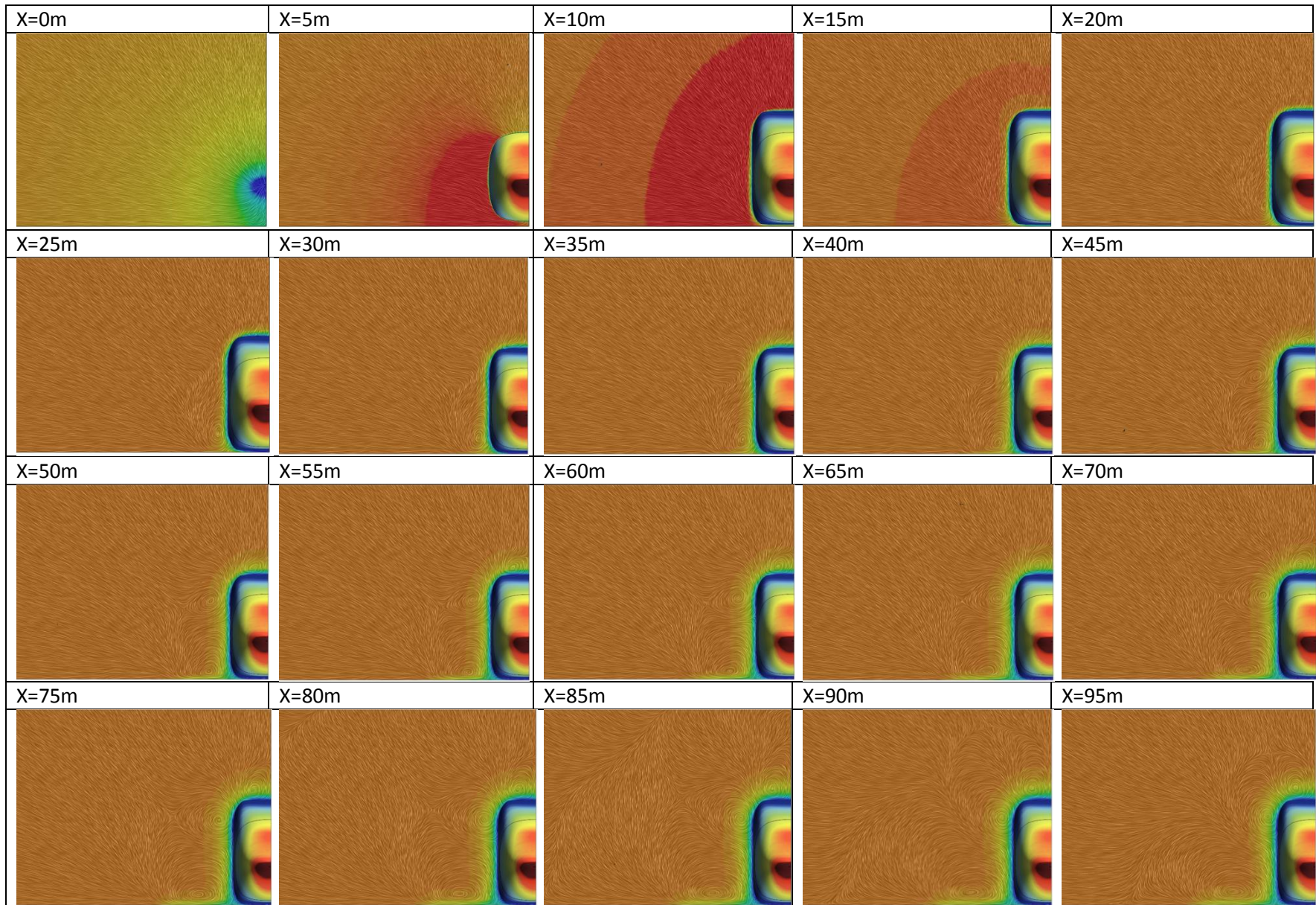


Figure 103: The Q-Criterion of the flow surrounding the train is shown, along with the locations of the various planes on which the convolution integral of the velocity is indicated in Table 21. All locations are indicated in meters, with  $x=0m$  located at the nose tip of the train. The static pressure acting on the train is also shown, plotted on the three-dimensional body.



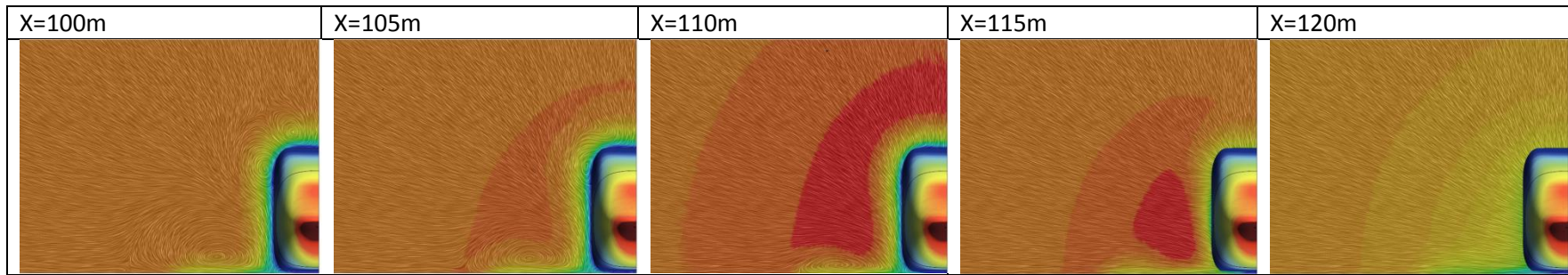


Table 21: The convolution integrals of the velocity of the flow surrounding the train body, is shown at various locations of the yz-Plane. The locations of the planes as indicated above, can be seen in Figure 103, where all locations are indicated in meters with x=0m located at the nose tip of the train. The static pressure distribution acting on the nose is also indicated on the three-dimensional body.

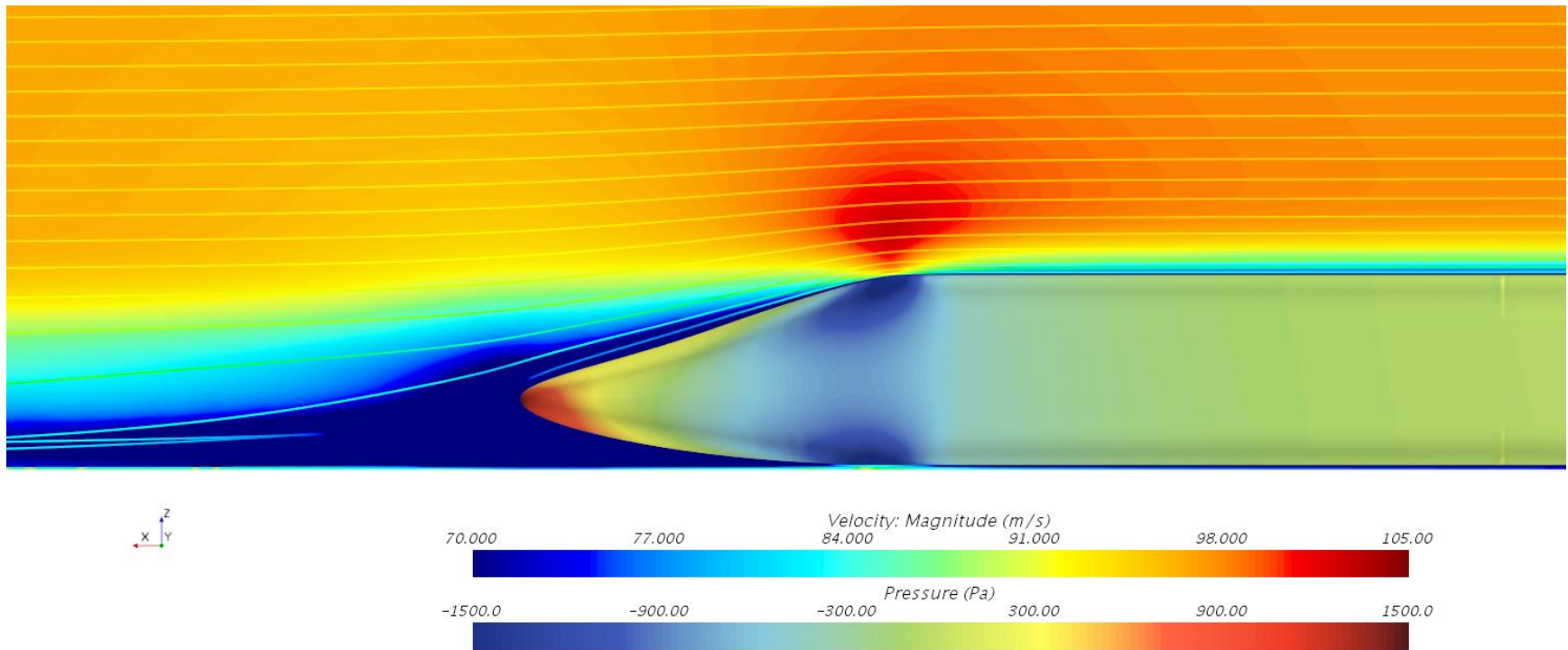


Figure 104: The velocity streamlines of the flow as indicated over the tail of the train on the symmetry plane. Also shown is the velocity distribution on the symmetry plane as well as the static pressure distribution acting on the three-dimensional train body.

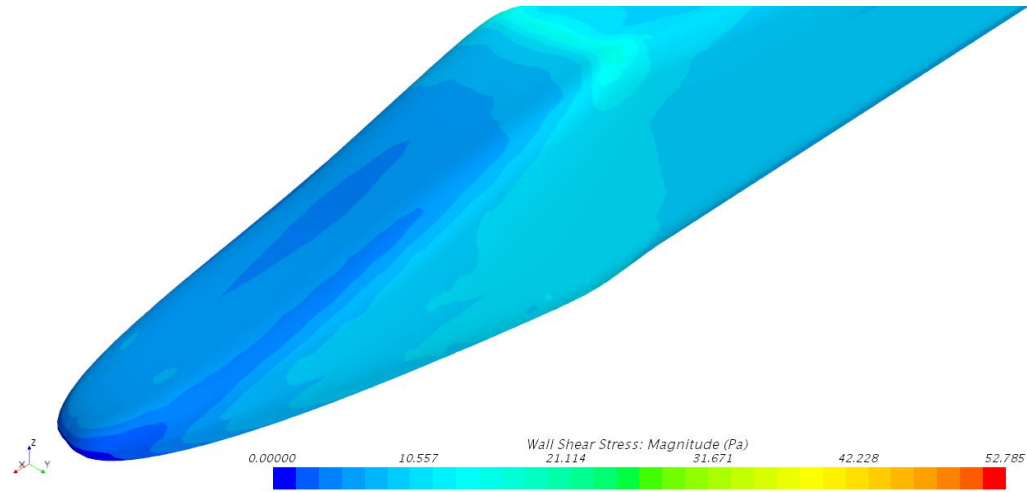


Figure 105: The distribution of the wall shear stress as shown over the tail portion of the train body.

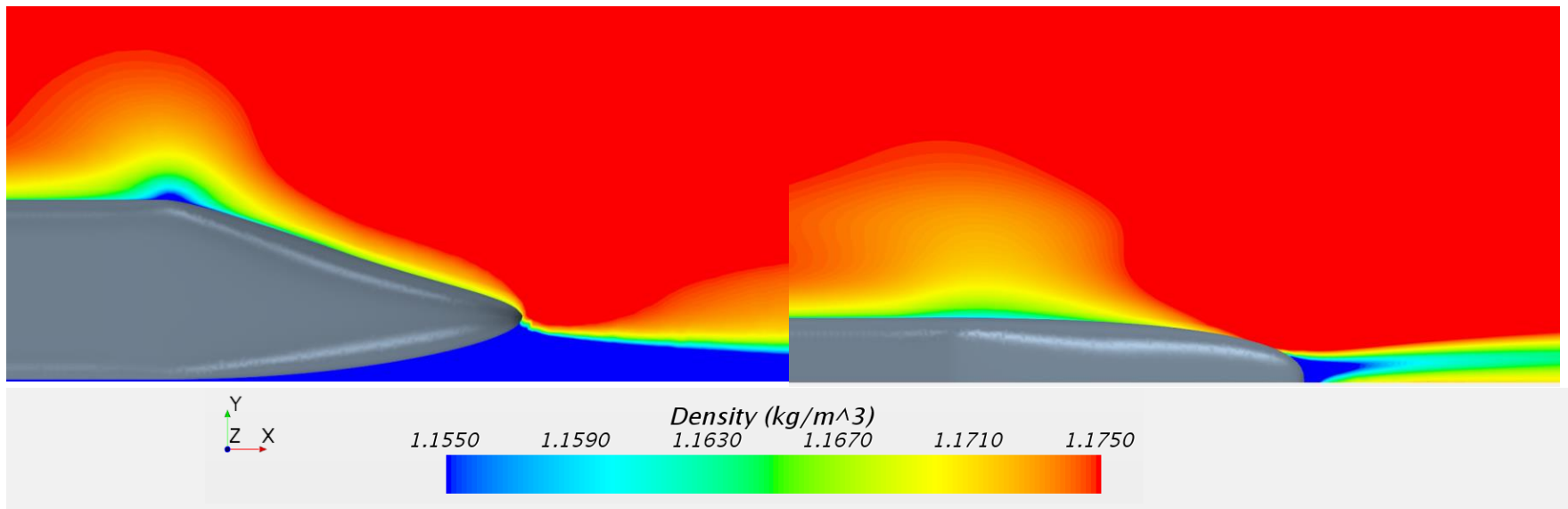


Figure 106: The density distribution surrounding the optimized tail shape. Left: Density shown on the symmetry plane. Right: Density shown on the xy-plane at  $z = 1.364\text{m}$ .

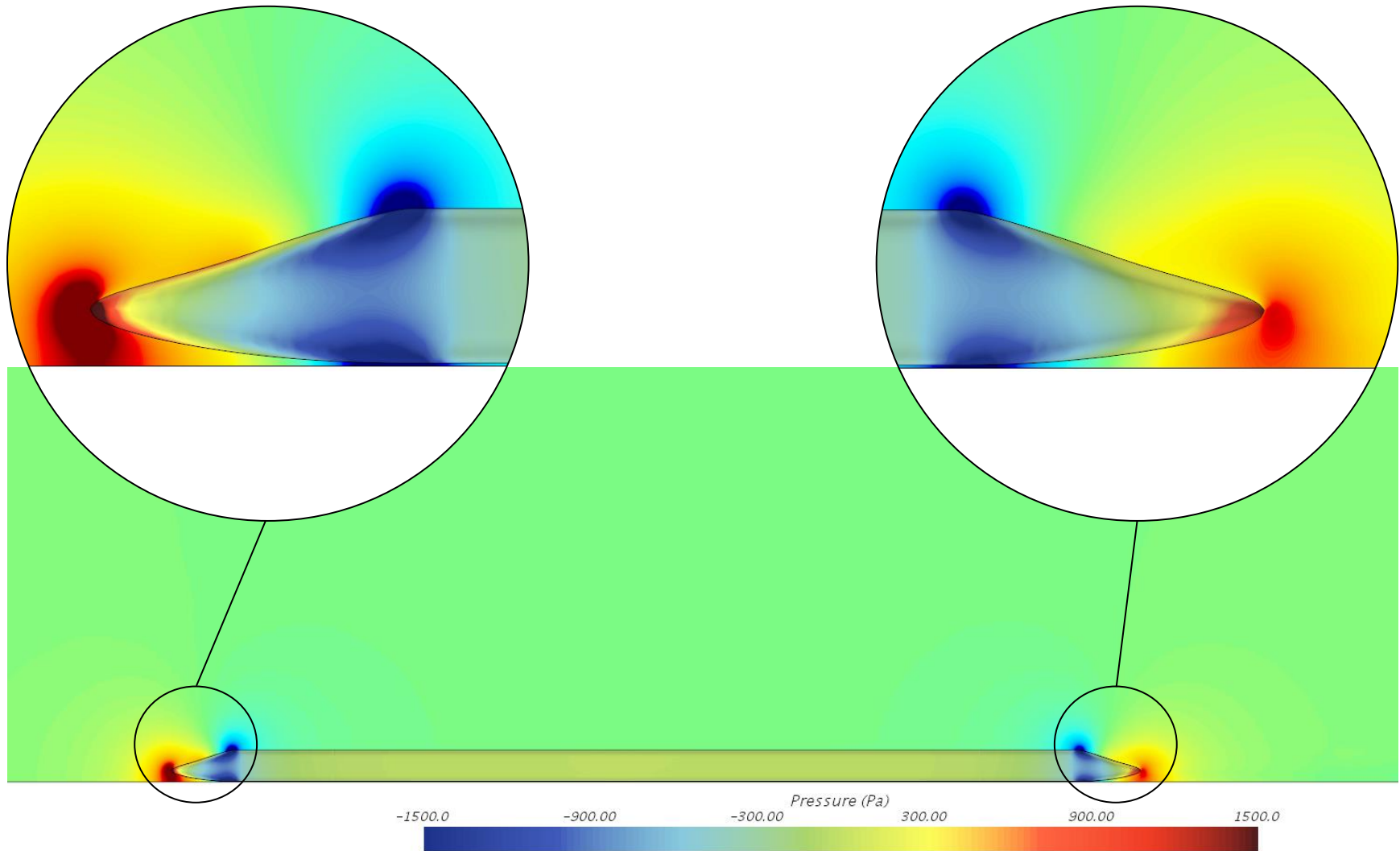


Figure 107: The external pressure field surrounding the train for the optimized nose geometry in windless conditions is shown. The stagnation point on the tip of the nose is clearly visible in the magnified view on the left while the wake region trailing the tail of the train is visible in the magnified view on the right. The static pressure acting on the three-dimensional train body is also shown.

## 5. Optimization of the High-Speed Train Nose and Tail for Crosswind Conditions

The second load case that will be considered for the optimization of the train nose is crosswind conditions, with the reduction of the total drag acting on the train and the leeward rolling moment acting on the leading vehicle being the optimization objectives. As was the case with windless conditions, the top cruising speed of the train of 350km/h will be considered here. However, the wind speed at which the train will be optimized for here is 110km/h at a height of 10m above the ground which is the uppermost boundary of wind speeds that MeteoSwiss considers safe for rail traffic to continue operating unhindered (MeteoSwiss, 2014). As such it was deemed a reasonable condition for optimization since the geometry yielded by optimizing under these circumstances would thus be the most stable that would ever conceivably be put into practical use. The travel condition that the train is subjected to is therefore not the average condition that is expected, rather it is that condition which is anticipated to be worst under which the train is still expected to be resilient.

Since both the track, as well as the angle of the incoming wind relative to the track ' $\beta$ ' (as shown in Figure 110) are variable, the worst-case condition of the wind direction being perpendicular with regard to the track ( $\beta = 90^\circ$ ) was considered. Given the velocity at which the train is travelling, the effective yaw angle ( $\psi$ ) is rather small (see Figure 111 bottom, left) and while it is known from the literature that larger yaw angles, i.e., in the approximate region of 40 degrees (see section 2.2.2, Figure 26 and Figure 27) are a larger threat to train stability, yaw angles of this magnitude can only be obtained by reducing the train speed. Since the objective of this study was however, to produce the most stable train travelling at cruising speed while being exposed to extreme crosswind conditions, these larger yaw angles will not be considered here. Finally, with regard to the wind conditions, it is important to note that the transient case of gust loading will also not be considered.

### 5.1. Configuration of the Computational Model

The geometry of the train nose as well as the parameters that define it, along with their associated ranges are identical to those discussed in section 4.1. The solver type and material properties of the air that were used for crosswind conditions are also identical to those used under windless conditions (see section 4.2). Furthermore, the mesh that was constructed for these conditions is identical to that which was validated and utilized under windless conditions. Section 4.3 may thus be referred to for a full description of the construction and validation of the mesh in question. The boundary conditions used for the simulation of the air flow around the train under crosswind conditions are however, dissimilar to those used for windless conditions and will be discussed below.

As mentioned previously, it is critical to the accuracy and relevance of the results, for the simulation to mimic reality as closely as possible. For the case of a train travelling under crosswind conditions this can prove to be particularly challenging. In reality, the ground remains stationary with the train travelling at 97.22m/s across it while the wind blows over the train in a given direction ( $\beta$ ). Furthermore the wind, like all fluids moving over a surface, exhibits a boundary layer in proximity to the ground. While the wind's profile may be dependent on the local topography and somewhat erratic, i.e., have turbulent

eddies and gusts present, its mathematical approximation may be modelled by making use of the logarithmic wind profile (see equation 17 through to equation 19) or similar. The velocity profile that results as a consequence of this interaction of the wind relative to the moving train can be determined by making use of vector algebra and the resultant expression is given by equation 20 (see also Figure 110 and Figure 111 top, right). Moreover, the yaw angle, that is the angle of the wind relative to the moving train, can be similarly determined from vector algebra and trigonometric functions and its expression is given by equation 21 (see also Figure 110 and Figure 111 bottom, left).

In the simulation environment however, the train body remains stationary and the boundary conditions must be relied upon to imitate the aforementioned behaviour. The velocity profile of the wind relative to the moving train (see equation 20) was therefore specified at the front and side inlets of the domain (see Figure 108) in conjunction with the associated yaw angle (see equation 21). However, the velocity profile specified as per equation 20, already accounts for the motion of the train across the ground. The option of specifying a “moving wall” boundary condition over the entire ground surface to account for this relative velocity is thus eliminated. Furthermore, the mathematical expression as per equation 20 must be preserved until the incoming air reaches the train body and no further boundary layer development may be permitted since it is already accounted for. Thus a few challenges are posed; first the mathematical integrity of the incoming air as per equation 20 and equation 21 must be preserved until the train body is reached. Secondly, the effects of the air flowing between the train body and the ground must be accounted for without doing the same. Finally, once the air has interacted with the train, the flow should be allowed to develop as it would in the presence of the stationary ground at the leeward side of the body.

The ground was thus divided into three distinct regions; the area in front of, beneath and behind the train (see Figure 108 and Figure 109). The region in front of the train was assigned a slip wall condition so as to ensure that the relevant velocity and yaw angle profiles remain unaltered. In order to allow for the development as well as the dissipation of the flow field on the leeward side of the train, the region behind the body was kept stationary and assigned a no-slip wall condition. Finally, the region beneath the train body was assigned a moving wall condition with a velocity component along the positive x-direction (see Figure 108 and Figure 109) of 97.22m/s, hereby imitating the motion of the train across the ground while simultaneously preserving the mathematical accuracy of the velocity and yaw angle profiles of the incoming air. Furthermore the outlet faces of the domain (see Figure 108) were assigned gauge pressures of 0 Pa, hereby implying atmospheric conditions and should they be adequately located from the train model this corresponds to reality. The final boundary to address is the top boundary which was assigned a symmetry condition simply in order to preserve the velocity and yaw angle profiles as stipulated at the given height from the ground.

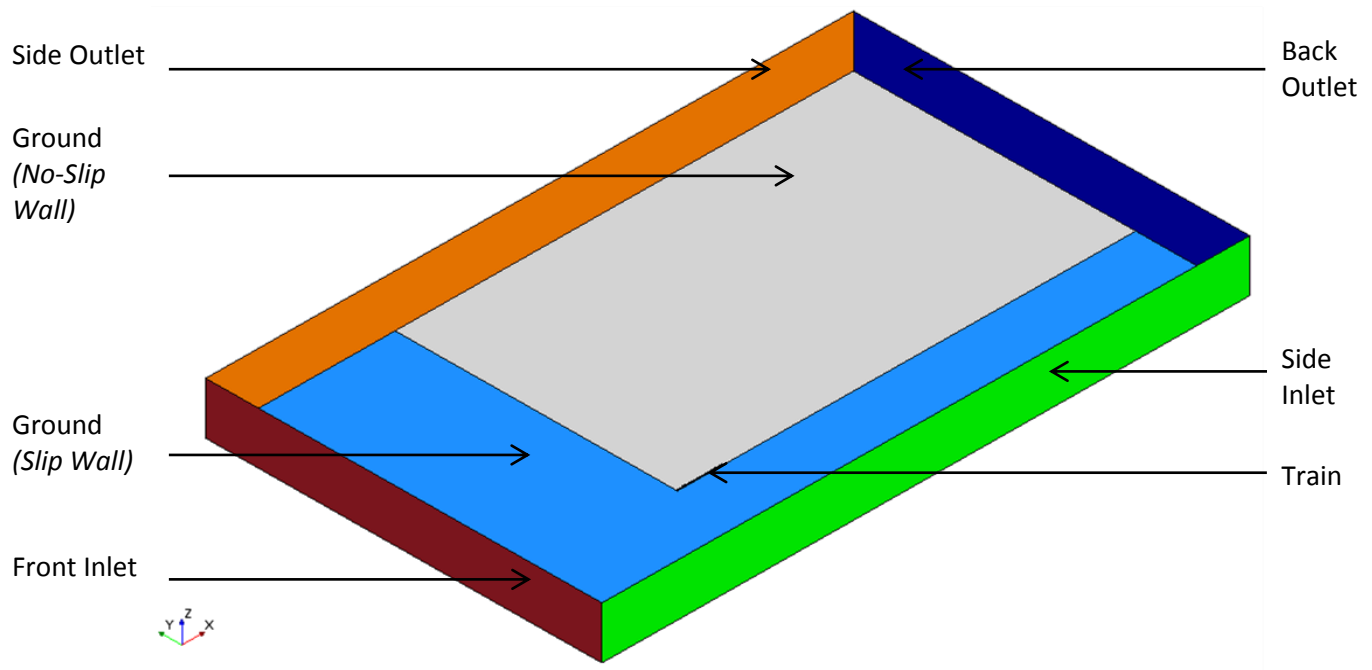


Figure 108: The computational domain of the full model of the train under crosswind conditions showing the chosen nomenclature of the boundary faces.

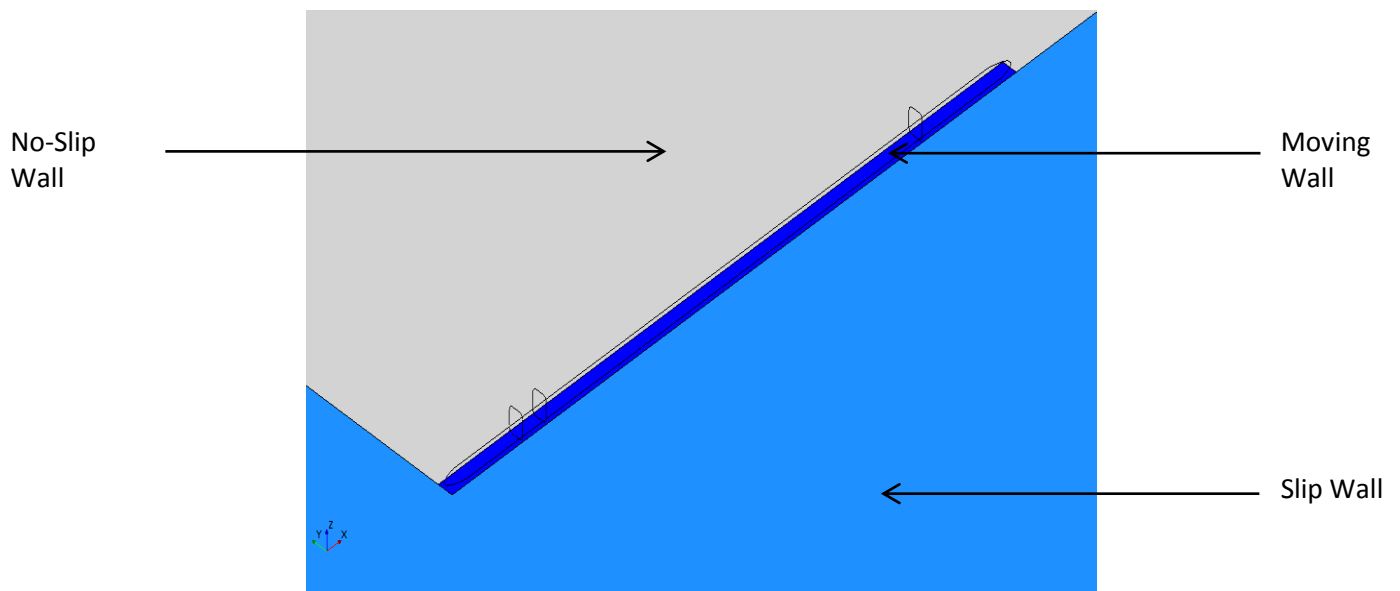


Figure 109: A magnified view of the three distinct ground regions and associated boundary conditions used for the simulation of the train under crosswind conditions, i.e., the slip wall on the windward and front side of the train, the no-slip, stationary wall on the leeward side and finally the no-slip, moving wall beneath the train with a positive velocity component of 97.22m/s along the x-axis.

Description of the logarithmic wind profile:

$$u(z) = \frac{u_\tau}{\kappa} \ln\left(\frac{z+z_0}{z_0}\right) \text{ for } z \leq z_h \quad (17)$$

And;

$$u(z) = \frac{u_\tau}{\kappa} \ln\left(\frac{z_h+z_0}{z_0}\right) \text{ for } z > z_h \quad (18)$$

Given that;

$$u_\tau = \kappa u_{Ref} \left( \ln\left(\frac{z_{Ref}+z_0}{z_0}\right) \right)^{-1} \quad (19)$$

Where;

Symbol	Description	Value	Unit
$u(z)$ :	Wind Velocity as a function of vertical height off the ground (z)	Variable	[m/s]
$z$ :	Height above the ground	Variable	[m]
$\kappa$ :	Von Karman constant	0.4	-
$z_0$ :	Roughness Height	0.5	[m]
$z_h$ :	Height above the ground after which a constant velocity is applied	1000	[m]
$u_{Ref}$ :	Reference Velocity of Wind at the Reference Height (100km/h)	30.56	[m/s]
$z_{Ref}$ :	Reference Height where the Wind assumes its Reference Velocity	10	[m]
$v$ :	Train Velocity (350km/h)	97.22	[m/s]
$\beta$ :	Wind direction relative to the track	90	[Degrees]

Table 22: The various constants and variables used both for the description of the logarithmic wind profile, as well as the wind's behaviour relative to the moving train.

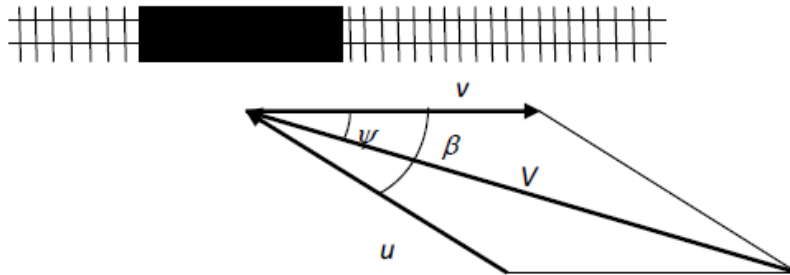


Figure 110: The velocity vector diagram for a train exposed to a crosswind (Baker, 2014).

The velocity profile of the wind relative to the moving train:

$$V^2 = ((u(z) \cos \beta + v)^2 + (u(z) \sin \beta)^2) \quad (20)$$

The angle of the wind relative to the moving train:

$$\tan(\psi) = \frac{u(z) \sin \beta}{u(z) \cos \beta + v} \quad (21)$$

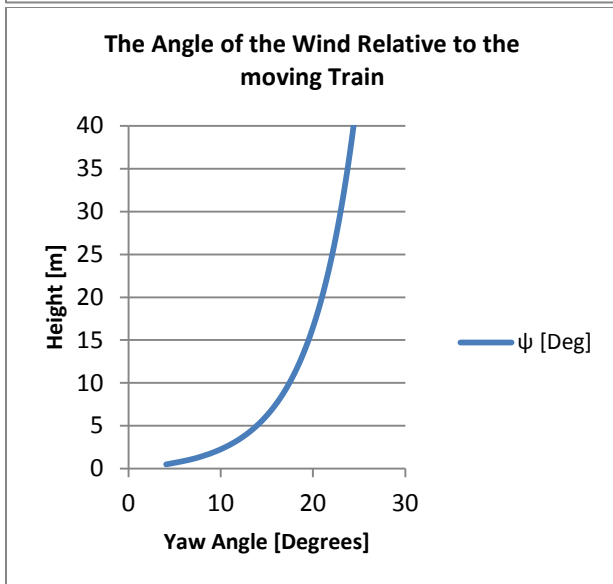
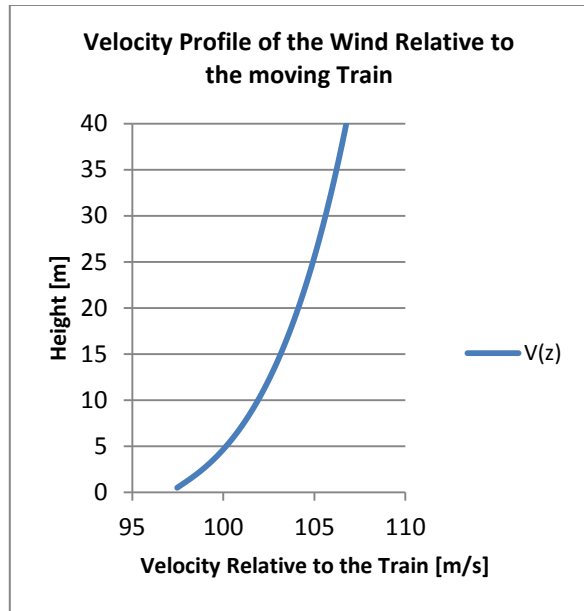
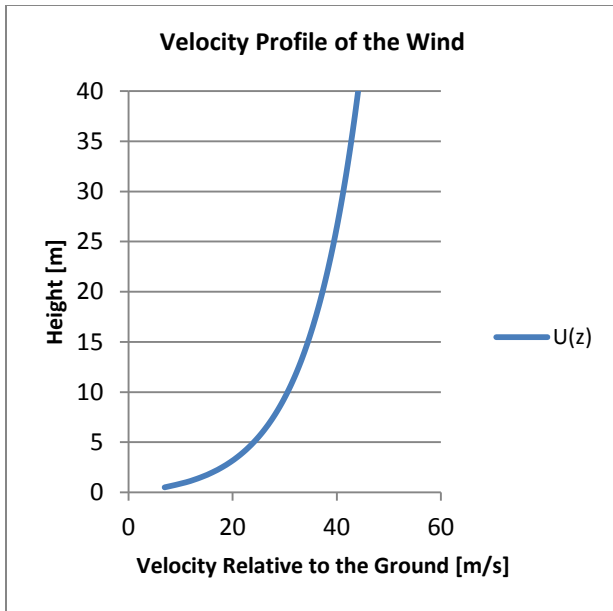


Figure 111: Parameters of the wind relative to the ground (top, left) as well as the moving train (top, right and bottom, left).

## 5.2. Validation of Computational Domain

The computational domain that was used as the base case for the domain validation study under crosswind conditions is simply the full model of the symmetry model that was validated for windless conditions in section 4.4 (see Figure 108 for the relevant nomenclature and read alongside Table 23). However, since not only the boundary conditions but also the associated flow phenomena under crosswinds vary considerably from windless conditions, simply using the aforementioned model of the full domain (as listed in Table 23) would not have been a prudent course of action. Rather, the x-, y- and z-forces acting on the train as a whole as well as its various sub-components, i.e., the nose, coaches, tail, top and bottom portions (see Figure 76 and Figure 77) thereof, will be monitored as a function of the boundary locations. The process to be followed and reasoning behind determining an adequate computational domain was discussed at length in section 4.4 and Appendix D, and may be referred to for a more detailed discussion. The nose geometry that was used for the validation of the computational domain, i.e., throughout section 5.2, is shown in Figure 112 while the values of the parameters associated with this nose shape are given in Table 24.

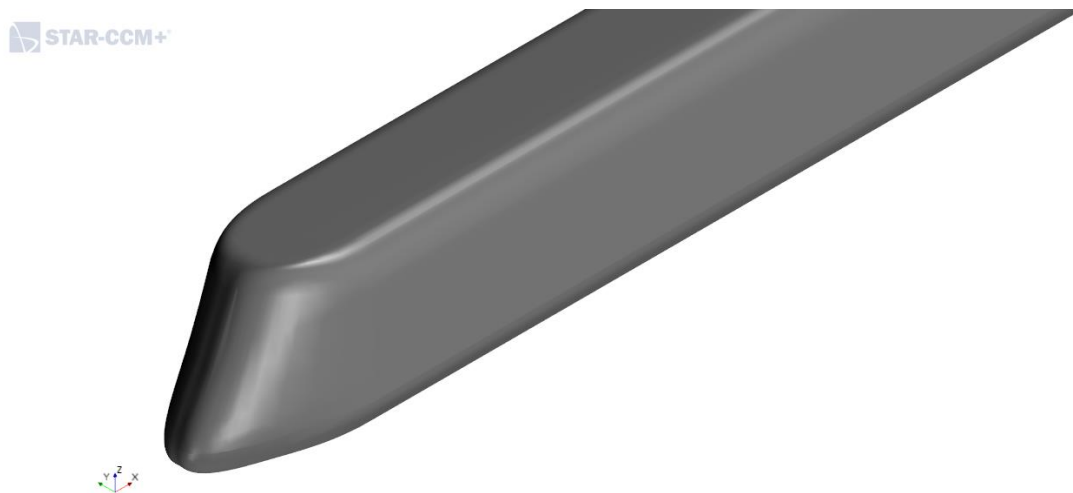


Figure 112: The geometry of the nose that was used throughout the process of validating the computational domain for crosswind conditions.

Domain Dimensions	Magnitude [m]
Front Inlet Distance	446.19
Side Inlet Distance	138.49
Back Outlet Distance	1184.68
Side Outlet Distance	138.49
Height	138.49

Table 23: The dimensions of the “base case” computational domain for a train exposed to crosswind conditions.

Variables	L	Z <sub>0</sub>	H
Value [m]	2	0.7	3

Table 24: The values of the parameters that govern the nose geometry. These values remained constant throughout the process of validating the computational domain.

While the complete results of this domain effect study may be found in Appendix F, in this section attention will only be given to the most important conclusions that could be drawn from it. In order to discuss the aforementioned, Figure 113 and Figure 114 are included here as examples of typical results that were obtained. From Figure 113 it is clear that all the side force components, except the y-force acting on the tail, are roughly insensitive to the location of the front inlet boundary and as such these force components can be trusted. The unpredictable nature of the side force acting on the tail however, not only disqualifies it for further use, but also indicates the possibility of erratic flow conditions which cannot be captured by a steady-state model. When the behaviour of the lift force components as a function of the boundary location is considered (see Figure 114), it is clear that a larger measure of sensitivity reigns. While most of the z-force components do ultimately stabilize with increasing inlet distance, the lift acting on the nose does not. Since this force component contributes to the moment of the leading locomotive about the leaside rail, it is important to use it with caution in future work, since its erratic behaviour could render results that make use of it, untrustworthy.

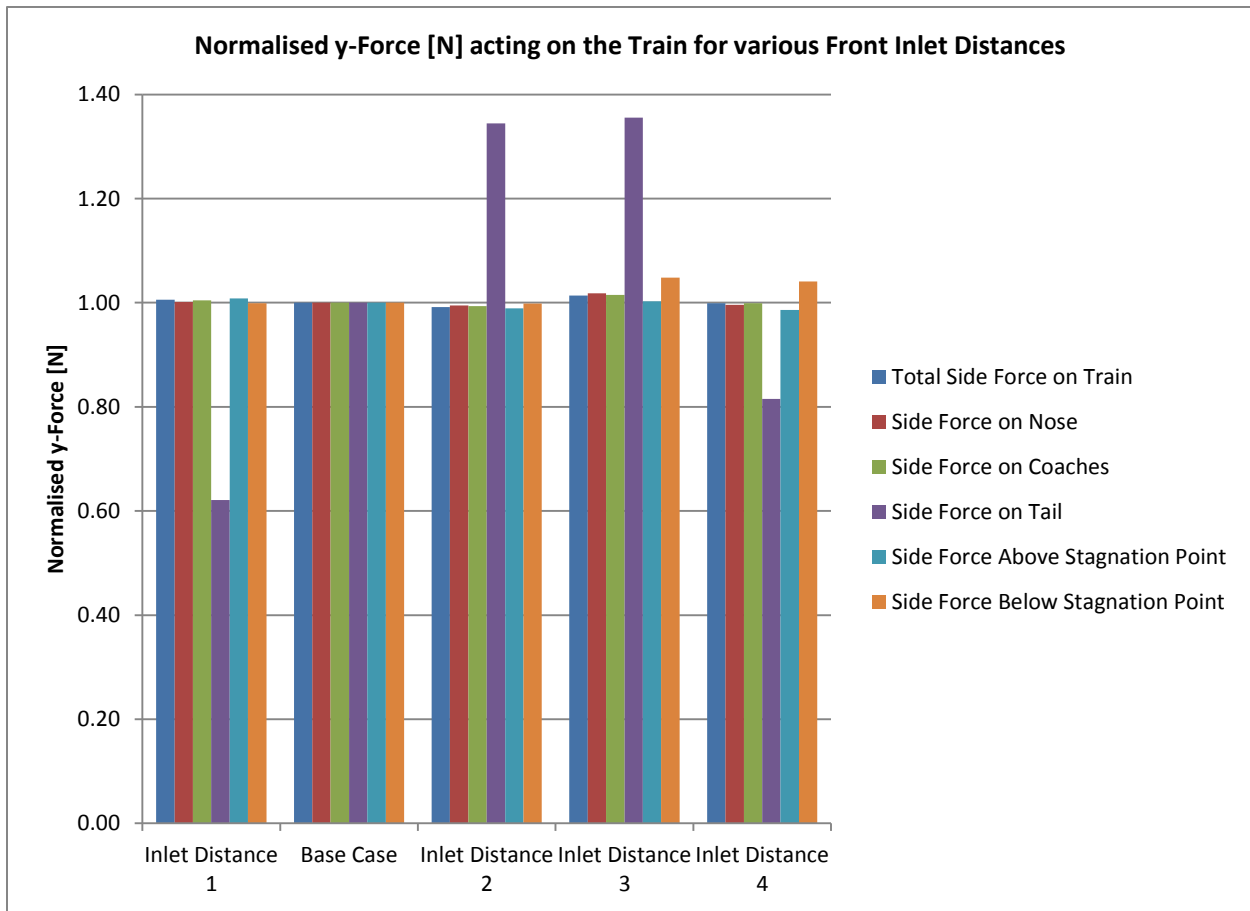


Figure 113: The Normalised y-force [N] acting on the Train as a whole as well as its sub-components given for the various locations of the front inlet face.

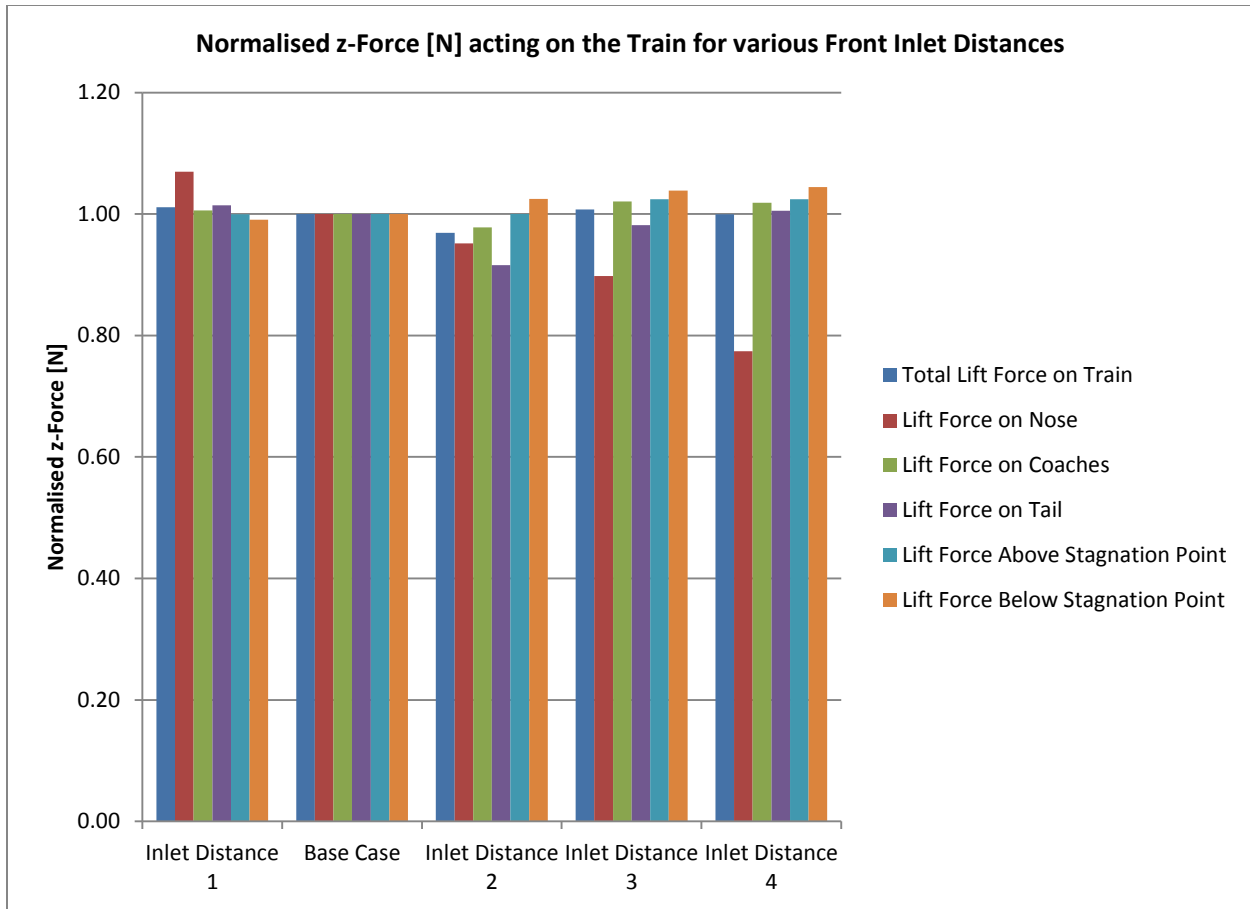


Figure 114: The Normalised z-force [N] acting on the Train as a whole as well as its sub-components given for the various locations of the front inlet face.

Since the force results as a function of boundary location were normalised in order to observe their sensitivity and associated trend with regard to boundary location more clearly, the actual force values as a function of the back outlet boundary are given in Table 25 through to Table 27 as an example of the typical magnitude that can be expected from the various force sub-components. A clear understanding of these values is invaluable in the creation of sensible optimization goals.

Consider for example the partial nose drag acting on the train; while the fluctuations in value is still extreme, the effect of the nose component on the total drag of the train is negligible (see Table 25). Optimising for the partial drag of the train nose could thus prove to be nonsensical as a function of the noise that could be introduced into the solution. However, given what little effect the nose drag has on the total drag of the train body it is not necessary to include it in the optimization objective of reducing the total drag acting on the train body, although it was not excluded in this thesis. The matter of reducing fuel consumption will thus be addressed by utilizing the aforementioned goal function.

The second matter at hand is that of safety and as is known from the literature (Baker, 2014), the largest role player in this regard is the leeside rolling moment. Given the nature of the optimization goal, only the side and lift force components need be considered. It is furthermore important to bear in mind the

nature of the high-speed train in question, i.e., a train with a power car and a non-powered driving trailer. In other words, the non-powered driving trailer is not weighed down with equipment in the same manner as the power car. Thus, when considering the partial side force results as given in Table 26, it is clear that the nose is of greatest concern since the force acting per meter length is greatest for this vehicle in the train body. Also, in the event that this role of leading vehicle, or “nose”, is assumed by the driving trailer, there is the added concern of the comparably small mass of the body in question.

With regard to the lift force acting on the train body, the force experienced by the coaches is greatest, followed by the tail and finally the nose. However, when the average magnitudes of the side and lift forces are considered it is clear that the side, and not the lift force, is the greatest contributor to crosswind instability.

Thus, from the results garnered from the study to determine an adequate computational domain size, an objective function became clear, i.e., minimizing for the leeside rolling moment of the nose in particular. This finding is further corroborated by (CEN, 2010) which states: “The crosswind stability of a train is given by the cross wind stability of the most cross wind sensitive vehicle in the train consist.” Finally, private communications with Prof. Chris Baker of the University of Birmingham revealed that for a train with a power car and a non-powered driving trailer, this will always be the driving trailer when it is at the front of the train due to the low pressures around the nose that result in higher side forces than on the other vehicles.

At this point it is prudent to recall that the lift force acting on the nose of the train remained sensitive to the location of the front inlet boundary (see Figure 114). Unfortunately it is not practical to continue enlarging the computational domain in hopes that this force component will stabilize given the extreme computational expense already posed by the optimization problem. Thus an initial attempt will be made to optimize for the train nose while considering all forces and moments contributing to the rolling moment coefficient. However, in the event that this solution is noisy, the lift force acting on the nose will be omitted and the optimization redone.

Simulation Case	Drag Force [N]					
	Nose	Coaches	Tail	Bottom	Top	Total
<i>Outlet Distance 1</i>	332.64	10183.14	7650.02	4755.47	13410.33	18165.80
<i>Base Case</i>	270.48	10216.62	7726.49	4765.69	13447.90	18213.59
<i>Outlet Distance 2</i>	332.31	10217.45	7666.09	4768.98	13446.87	18215.84

Table 25: The x-force [N] components acting on the Train as a whole as well as its sub-components, given for the various locations of the back outlet face.

Simulation Case	Side Force [N]					
	Nose	Coaches	Tail	Bottom	Top	Total
<i>Outlet Distance 1</i>	54017.29	60025.76	-910.05	27318.49	85814.51	113133.01
<i>Base Case</i>	54469.28	60675.17	-917.31	27725.97	86501.17	114227.15
<i>Outlet Distance 2</i>	53958.28	60057.05	-945.09	27391.26	85678.97	113070.23

Table 26: The y-force [N] components acting on the Train as a whole as well as its sub-components, given for the various locations of the back outlet face.

Simulation Case	Lift Force [N]					
	Nose	Coaches	Tail	Bottom	Top	Total
Outlet Distance 1	6482.31	72534.65	10446.11	-110048.17	199511.23	89463.07
Base Case	6409.95	72800.04	10366.66	-111921.81	201498.46	89576.65
Outlet Distance 2	6342.27	72186.88	10328.25	-110897.64	199755.05	88857.41

Table 27: The z-force [N] components acting on the Train as a whole as well as its sub-components, given for the various locations of the back outlet face.

Finally, given the above discussion (see also Appendix F) regarding the domain for the full model under crosswind conditions and the sensitivity of the results to the location of the boundaries, the final dimensions of the computational domain are indicated in Table 28. These dimensions are also depicted in Figure 115.

Domain Dimensions	Symbol of Domain Dimension	Magnitude [m]
Front Inlet Distance	$D_{FI}$	546.19
Side Inlet Distance	$D_{SI}$	338.49
Back Outlet Distance	$D_{BO}$	1084.68
Side Outlet Distance	$D_{SO}$	738.49
Height	H	138.49

Table 28: The dimensions of the final computational domain for a train exposed to crosswind conditions

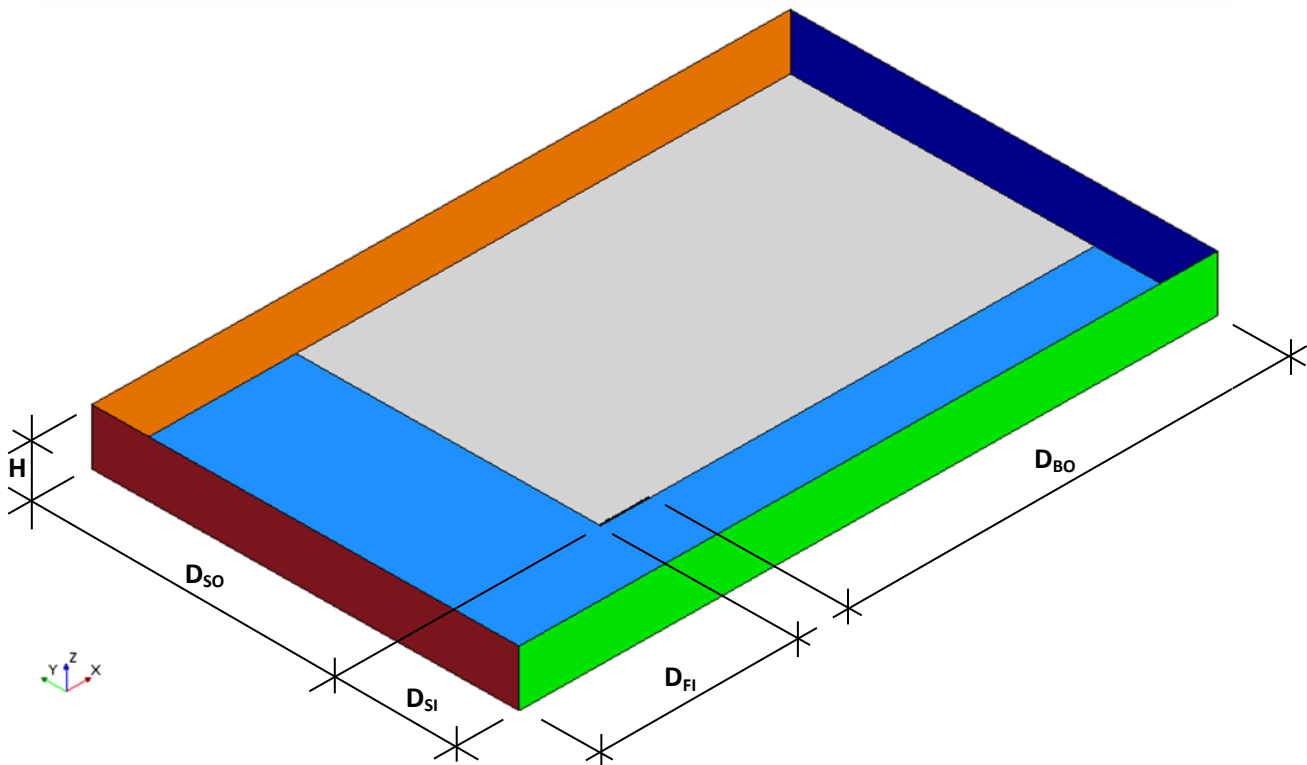


Figure 115: The computational domain of the full model of the train under crosswind conditions showing the chosen nomenclature of the domain dimensions.

### 5.3. Optimization

This section of the document concerns itself with the optimization of the train nose geometry when exposed to crosswind conditions. The optimization goals that were decided upon for these conditions were based on Transnet's specifications of a train that is stable when exposed to crosswinds while being as fuel efficient as possible. The literature review (see section 2.2) revealed that these two considerations do in fact pose challenges in rail applications and are prudent to address. Furthermore, the results for the various force components that were obtained during the process of validating the computational domain revealed that the most crosswind sensitive vehicle in the train is the nose (see section 5.2 for a comprehensive discussion), hereby earmarking it as the vehicle for which the leeside rolling moment ought to be minimized.

Since this objective is not as familiar as the total drag acting on the train body, it will be expressed here so as to provide clarity on the matter. According to Prof. C.J. Baker in private communications, it is irrelevant what point in the train body is used for moment calculations and as such the center of gravity was chosen. The Transnet standard for the maximum center of gravity height is 98 inches or about 2.49m and the HST will run on standard gauge which has a rail width of 1.435m. Taking moments about the leeside rail thus yields the following expression;

$$M_{R,LS} = F_{S,LL} \times COG_{TE} + F_{L,LL} \times \frac{1}{2} \times w_{rail} + M_{x,LL} \quad (22)$$

Where;

- $M_{R,LS}$  : The leeside rolling moment coefficient acting on the leading locomotive
- $F_{S,LL}$  : The side force acting on the leading locomotive
- $COG_{TE}$  : Transnet's height limit on the center of gravity, i.e., 2.49m
- $F_{L,LL}$  : The lift force acting on the leading locomotive
- $w_{rail}$  : The width of the standard gauge rail, i.e., 1.435m
- $M_{x,LL}$  : The moment working about the longitudinal (x-) axis of the leading locomotive

The optimization process itself occurred in two steps; the first was the sampling of the design space by making use of the Latin hypercube statistical method given twenty-seven sample points. For each of the given sample points the various x-, y- and z-force components as well as the leeside rolling moment of the leading locomotive were captured. The data obtained from this step were used for the construction of a surrogate model. The second step optimized the nose geometry of the train for total drag as well as the leeside rolling moment acting on the nose by making use of the surrogate model obtained in the first step and the SHERPA algorithm. Finally conclusions regarding the optimized design as yielded in the second step will be drawn and the resultant flow field discussed.

### 5.3.1. Response Surface Model

The Latin Hypercube statistical method was employed in an attempt to generate as random a sample of design points as possible, given the three variables that parameterize the nose (see Figure 71 and Table 10). In total, there were twenty-seven design points (see Table 29) which is equivalent to a three-level full-factorial design sweep with the same number of parameters, with the added benefit that the designs that were generated by making use of the Latin Hypercube are better distributed and more representative of the design space (see Figure 116 to Figure 118). Given the domain size and turbulent nature of the flow, which has an effect on the number of iterations until convergence, a five-level full-factorial simply wasn't computationally viable. The smaller number of design points do of course have implications on the accuracy of the surrogate model and it is the hope that the more randomized scatter of data will compensate for the lack thereof. Once again the various force responses associated with the design points in question that were used for the construction of the surrogate model were obtained from simulations performed in STAR-CCM+.

<i>Design Point</i>	<i>Nose Length</i>	<i>Stagnation Point Height</i>	<i>Inflection Point Height</i>
1	5.540	1.374	2.613
2	7.688	1.096	2.119
3	7.076	1.446	2.880
4	4.119	1.238	2.205
5	4.472	0.910	2.247
6	2.603	0.802	2.718
7	4.004	1.174	2.334
8	6.054	1.202	2.495
9	7.480	1.116	2.997
10	4.869	1.006	2.652
11	6.446	1.341	2.027
12	4.661	0.767	2.558
13	4.961	1.231	2.535
14	6.831	0.740	2.830
15	7.026	0.829	2.406
16	2.691	0.969	2.701
17	5.173	0.869	2.430
18	3.577	1.421	2.953
19	2.256	1.267	2.905
20	6.304	1.481	2.038
21	3.073	1.295	2.784
22	2.936	0.709	2.453
23	2.171	1.391	2.778
24	3.315	0.898	2.080
25	5.696	1.068	2.324
26	3.895	1.043	2.274
27	5.866	0.954	2.173

Table 29: The twenty-seven design points that were generated by making use of the Latin Hypercube statistical method and their near-random associated parameter values.

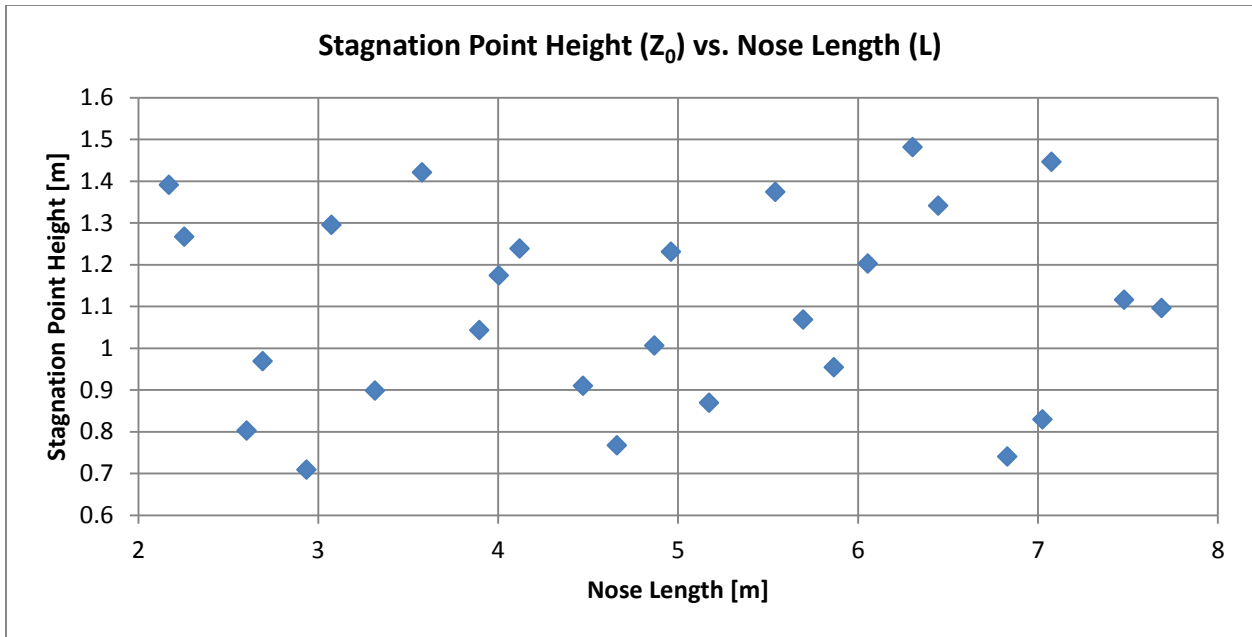


Figure 116: The spread of design points generated by the Latin Hyper-Cube sampling method, shown here for the stagnation point height ( $Z_0$ ) plotted against the nose length ( $L$ ).

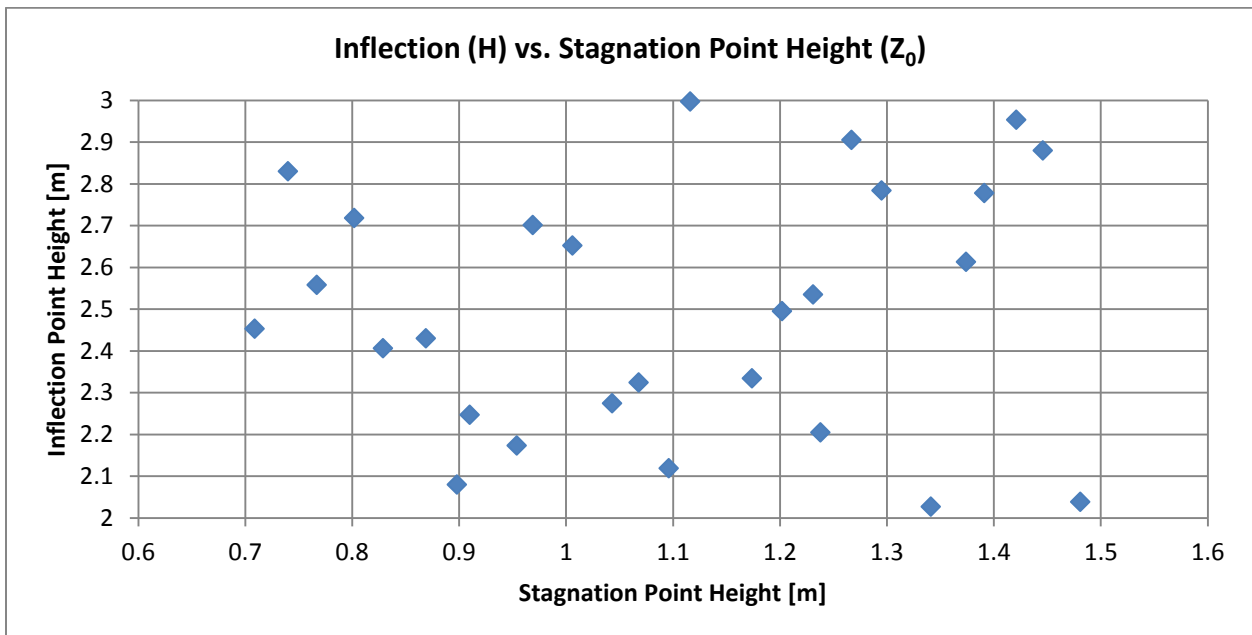


Figure 117: The spread of design points generated by the Latin Hyper-Cube sampling method, shown here for the inflection point height ( $H$ ) plotted against the stagnation point height ( $Z_0$ ).

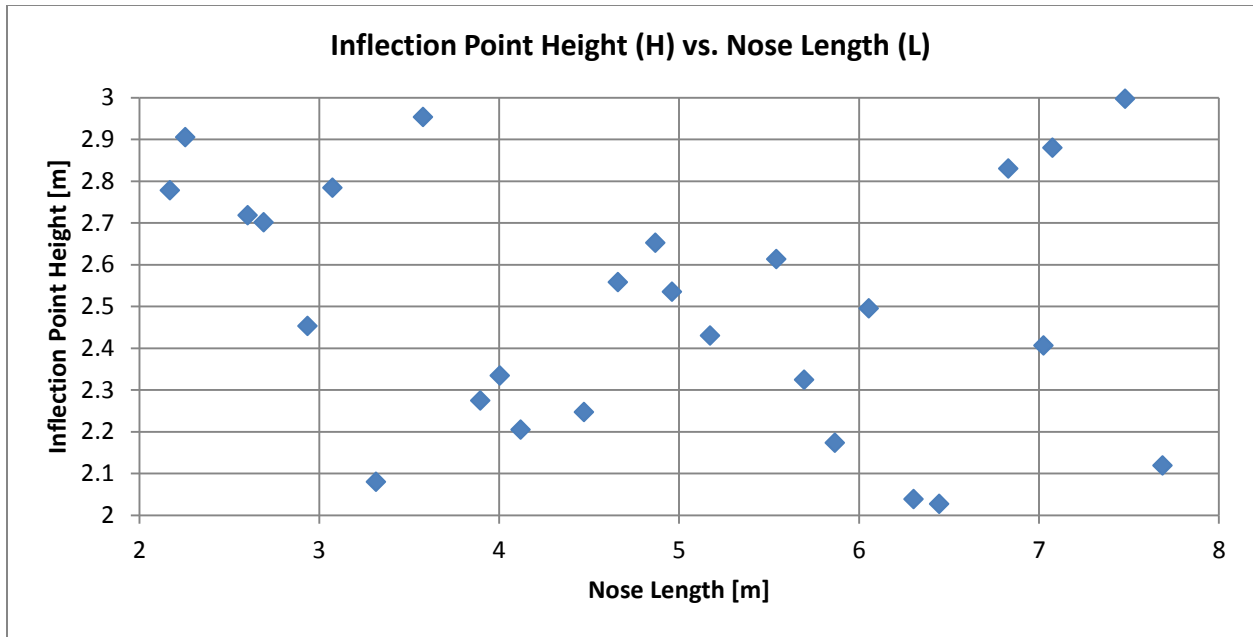


Figure 118: The spread of design points generated by the Latin Hyper-Cube sampling method, shown here for the inflection point height (H) plotted against the nose length (L).

In order to facilitate a discussion regarding the resultant surrogate model, which is represented by a collection of response surfaces and was created by making use of the radial basis function (RBF) together with the thin spline method, the two objective functions, i.e., the total drag force acting on the train as well as the leaside rolling moment acting on the leading locomotive are plotted against the nose-tip and inflection point height while the nose length acts as a “slider” of sorts, that toggles between the collection of response surfaces.

### 5.3.1.1. Total Drag Force

The total drag force acting on the train as a function of nose-tip and inflection point height will be discussed at nose lengths of 2.171m, 4.930m and 7.688m, i.e., the lower bound, midpoint and upper bound of the nose length (L) range as determined by the Latin Hypercube sampling method (see Figure 119). Consideration will further be given to possible trends that exist as a function of the nose length. Finally, since the optimization case for windless conditions considered the flow phenomena that may occur around a train as well as their accompanying implications on the total drag acting on the train, the discussion below will be concise and will rather refer back to applicable sections in the document when necessary.

As is the case under windless loading conditions, an increase in nose length brings about a decrease in the total drag force experienced by the train under crosswind conditions also. Broadly speaking the location of minimum drag for a given nose length remains similar, irrespective of the nose length, i.e., larger values of both the nose-tip height ( $Z_0$ ) as well as the inflection point height (H). It is however, clear from Figure 119 that the general region that allows for a minimum drag to be actualized at a given nose length reduces with an increase in nose length, with the longest nose length (L=7.688m) exhibiting the greatest sensitivity to the values of the nose-tip and inflection point height. The general region of the

maximum drag force shows the opposite behaviour; for short nose lengths the region of maximum drag is approximately confined to low values of nose-tip and inflection point height. As the nose length increases however, the region expands to include all values of the nose tip height for low values of the inflection point height, a behaviour that is cemented the longer the nose length. Clearly then, the critical parameter to be managed at a given nose length is the inflection point (height, ' $H$ '), thus the "fastback" configuration is preferable for the reduction of drag under crosswind conditions.

At any given nose length, ' $L$ ', and for all values of the nose-tip height, ' $Z_0$ ', there is a decrease in the total drag force with an increase in the inflection point height. Furthermore, as is clear from Figure 119, the effect of increasing the inflection point height is more pronounced for shorter nose lengths (see Figure 119,  $L = 2.171\text{m}$  and  $4.930\text{m}$ ) than for a long nose (see Figure 119,  $L = 7.688\text{m}$ ). It would thus seem that the "notch" where the hood and the windshield meet is what ought to be avoided when drag reduction is the objective, possibly due to the additional stagnation region it necessarily implies (see also section 4.5.3.2.2). For shorter nose lengths (see Figure 119,  $L = 2.171\text{m}$  and  $4.930\text{m}$ ) the trend of the total drag force as a function of a variable nose-tip height for a constant inflection point value can be divided into roughly two regions; lower values of the inflection point height (' $H$ ') and larger values of the inflection point height. For lower  $H$ -values (approximately ' $H \leq 2.5\text{m}$ ') there exists a somewhat parabolic relationship for the drag force as a function of a variable nose-tip height (see Appendix E, section iii and 4.5.3.2.2). For larger  $H$ -values however, the total drag force reduces with an increase in the nose-tip height. A possible explanation for this behaviour is that the larger the  $H$ -value, the less influential the  $Z_0$ -value is in determining the geometry of the nose and tail. Said differently, an inflection point that is located fairly high off the ground implies a "fastback" configuration and it is the function of ' $Z_0$ ' in this scenario to simply smooth the geometry, while a lower  $H$ -value allows for the "notchback" configuration to be assumed. Finally for longer nose lengths the total drag force decreases with an increase in ' $Z_0$ ' for all values of the inflection point height, with larger  $H$ -values simply exhibiting a more pronounced reduction. This behaviour is possibly once again a consequence of the nature of the notch that can be realized for a long nose, i.e., the severity of the notch and the associated adverse pressure gradient that are associated with a longer nose is not as extreme as that which can be actualized for shorter nose lengths. The flow over longer noses is thus more inclined to avoid stagnation and remain attached.

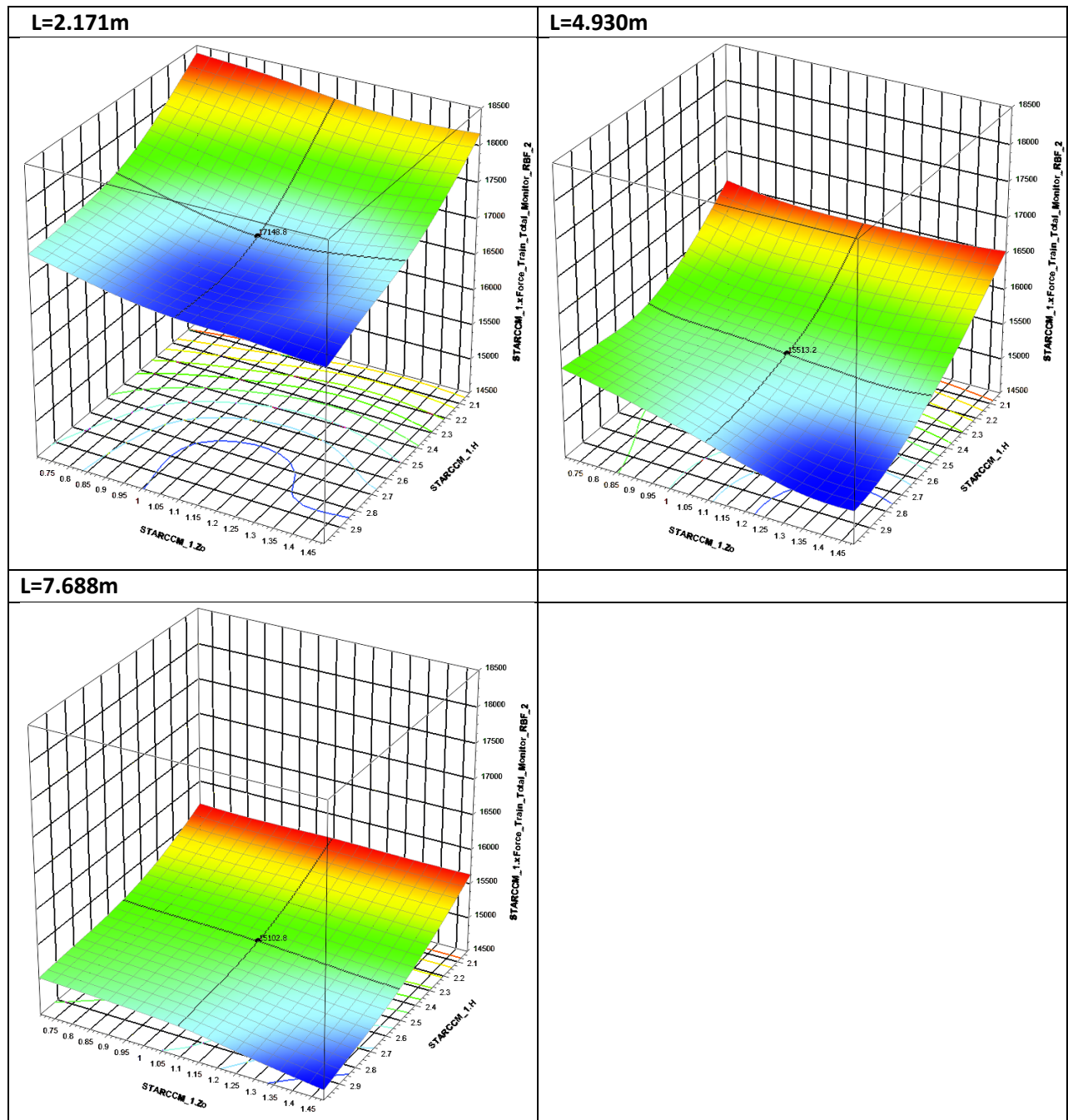


Figure 119: The variation of the total x-force (vertical axis) acting on the train as a function of nose-tip height ( $Z_0$ ) and inflection point height ( $H$ ), shown here for nose lengths of 2.171m, 4.930m and 7.688m.

### 5.3.1.2. *Leeside Rolling Moment*

This section of the document considers the effects of the geometric variables on the leeside rolling moment acting on the leading locomotive. The surrogate model for the rolling moment is shown in Figure 120 for nose lengths of 2.171, 4.930 and 7.688 meters. What is immediately noticeable is the reduction in the leeside rolling moment with an increase in nose length. In order to investigate the phenomena that could bring about this trend, the flow field associated with two of the geometries generated by the Latin Hypercube sampling method that shares similar nose-tip and inflection point heights but have different nose lengths, will be considered. Figure 121 shows plots of the static pressure acting on these two locomotive geometries, i.e., that of design point one and design point twenty-three as per Table 29. The results of the study showed that the lift force acting on the leading locomotive is too erratic to be of any use and as such it will not be discussed here (see Figure 123). Furthermore, since it is known that the largest contributor to the leeside rolling moment is the side force (see Figure 122), the effect of the nose length on it will be studied. In the case of the blunt nose, a larger stagnation region is visible on the windward side than for the longer nose. Additionally, the blunt nose exhibits a more pronounced region of fast moving air on its leeward side. Thus the increase in the side force as a function of the decrease in nose length is driven by at least two mechanisms. Consider first the stagnation region on the windward side; as the nose length decreases, the nose surface tends to a flat plate perpendicular to the oncoming flow and since the wind is coming in at an angle the stagnation region is now offset from the symmetry plane, rather than located on and distributed symmetrically around it as is expected under windless conditions. In addition, the blunt nose serves to accelerate the incoming air faster than the longer nose as a consequence of the more aggressive change in cross-sectional flow area that it poses. Thus the blunt nose not only produces a more extreme suction peak on the leeward side, but the air travelling along this side also reaches its top velocity faster thus ensuring that a larger portion of this side of the leading locomotive sees an overall lower pressure. Consequently the pressure differential acting across the blunt nose is more aggressive than that of the longer nose, hereby increasing the side force and thus the magnitude of the leeside rolling moment acting on the leading locomotive. Finally, contrary to what was expected, the blunt nose associated with design point twenty-three did not show any separation along its length. Had the flow indeed separated on the leeside of the blunt nose, the static pressure in the region would have increased hereby reducing the pressure differential. Thus a blunt nose under crosswind conditions does not necessarily offer the benefit of flow-separation on its leeside.

Furthermore, Figure 120 shows that the maximum rolling moment is located at the upper bound of both the nose-tip as well as the inflection point height. At this maximum nose-tip height ( $Z_0$ ) it can be seen that a decrease in the value of the inflection point ( $H$ ) from its upper to its lower bound, is accompanied by a decrease in the rolling moment acting on the leading locomotive also, with the effect being more pronounced for longer nose lengths (see Figure 120,  $L=4.930\text{m}$  and  $L=7.688\text{m}$ ). A plausible hypothesis is that this behaviour is a consequence of the location of the center of pressure for the given geometric variables. Consider that for any given nose length ( $L$ ) with a nose-tip height that remains constant at its maximum height, increasing the inflection point increases the surface area above the nose-tip (see Table 32). As such, there is not only a larger area over which the flow can exert pressure, but the point through which the force works is also raised. This effect is more pronounced for longer nose lengths

simply because raising the inflection point on a longer nose results in a greater surface area than for a blunt nose. Similarly, raising the nose-tip height also has the effect of increasing the fraction of surface area that is exposed to the incoming crosswind further off the ground, though more pronounced than in the case of the inflection point. In so doing the moment arm acting about the leeside rail is effectively increased, hence the rather pronounced effect of the nose-tip height on the rolling moment for a given inflection point (see Figure 120). In fact, for the maximum nose length (see Figure 120,  $L=7.688\text{m}$ ) an increase in the nose-tip height necessarily leads to an increase in rolling moment, irrespective of inflection point height. For shorter nose lengths however, the aforementioned only holds true for larger values of the inflection point; a phenomenon that will receive more attention later.

With regard to the location of the global minimum rolling moment, it can be seen from Figure 120 that it is located at the lower-bound of the nose-tip height ( $Z_0$ ), irrespective of nose length ( $L$ ). This behaviour of the rolling moment as a function of nose-tip height further serves to affirm the aforementioned hypothesis that a lower nose-tip ensures a lower center of pressure and consequently a smaller moment arm about the leeside rail thus ensuring a minimum. The behaviour of the minimum rolling moment location as a function of the inflection point is, however, not as simple; for a blunt nose shape (see Figure 120,  $L = 2.171\text{m}$ ) a value of  $H = 2.415\text{m}$  yields a minimum, thereafter the inflection height that yields a minimum moment steadily increases with an elongation of the nose until it plateaus at  $H = 2.706\text{m}$  for nose lengths equal to, or greater than  $4.378\text{m}$ . Consider the geometries where the nose-tip height and nose length are a minimum, with the inflection point ( $H$ ) being the only variable. When viewed in conjunction with Figure 120,  $L = 2.171\text{m}$  it can be seen that neither a minimum nor a maximum value of ' $H$ ' is advantageous for the minimization of the rolling moment. The hypothesis as to why that is the case, rests on the very same flow mechanism that was described when the effect of nose length on the flow field and the resultant leeside rolling moment was considered. That is, when the inflection point assumes its minimum bound (Table 30, left) a steep "windshield" region is created which serves to accelerate the leeside air travelling along this curvature more aggressively, thus increasing the effective pressure differential. Similarly, when the inflection point assumes its upper-bound (Table 30, right), the nose slant in its entirety assumes a steep gradient and acts to accelerate the air. The inflection point thus assumes an intermediate value that allows for a more gradual nose slant, so as to ensure a smaller pressure differential and associated minimum leeside moment. Thus it is clear from the results (see Figure 120 and Table 32) that the influence of the inflection point on the rolling moment depends on the nose-tip height of the given train geometry, with its effects being reversed almost entirely for the minimum and maximum nose-tip heights.

Finally there is the matter of the local minimum (see Figure 120,  $L = 4.930\text{m}$ ) that presents itself most notably for nose lengths between, and including,  $L = 3.275\text{m}$  and  $L = 6.033\text{m}$ . When attention is given to the geometries associated with the local (e.g., Table 31, right) and global (e.g., Table 31, left) minima it becomes clear that, as mentioned above, there is a relationship between the nose tip and inflection point height that produces a minimum leeside moment acting on the leading locomotive. To summarize, there are two flow mechanisms at play to ensure a minimum leeside rolling moment for any given nose length which are in tension with one another; on the one hand a lower inflection point height ensures that a smaller area is available to the crosswind to exert pressure on and in so doing the moment is

reduced. On the other hand lowering the inflection point height increases the gradient of the “windshield” hereby accelerating the air more aggressively. Conversely, increasing the inflection point height (within bounds) effectualizes a more modest gradient which allows for a more moderate acceleration of the air on the leeside of the nose, hereby reducing the pressure differential acting across the nose. From the results it would seem that the factor that determines which of the above flow phenomena dominates and to what extent it does so, is the nose-tip height. For lower nose-tips a smoother nose slant gradient is favoured at the expense of an increased surface area, while higher nose-tips favour a smaller surface area at the expense of a steeper “windshield” and the more aggressive acceleration that accompanies it.

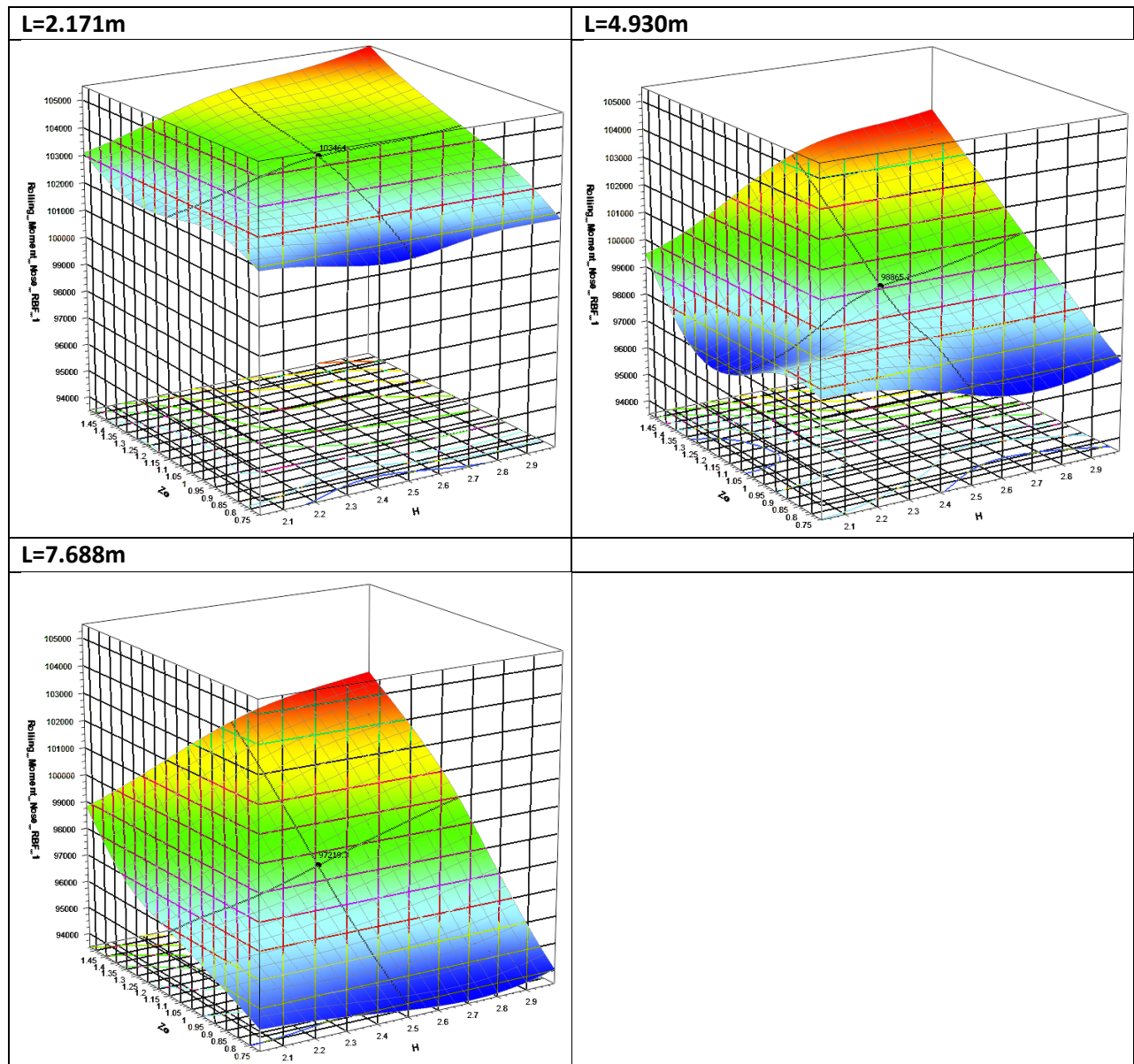


Figure 120: The variation of the leeward rolling moment (vertical axis) acting on the leading locomotive as a function of nose-tip height ( $Z_0$ ) and inflection point height ( $H$ ), shown here for nose lengths of 2.171m, 4.930m and 7.688m.

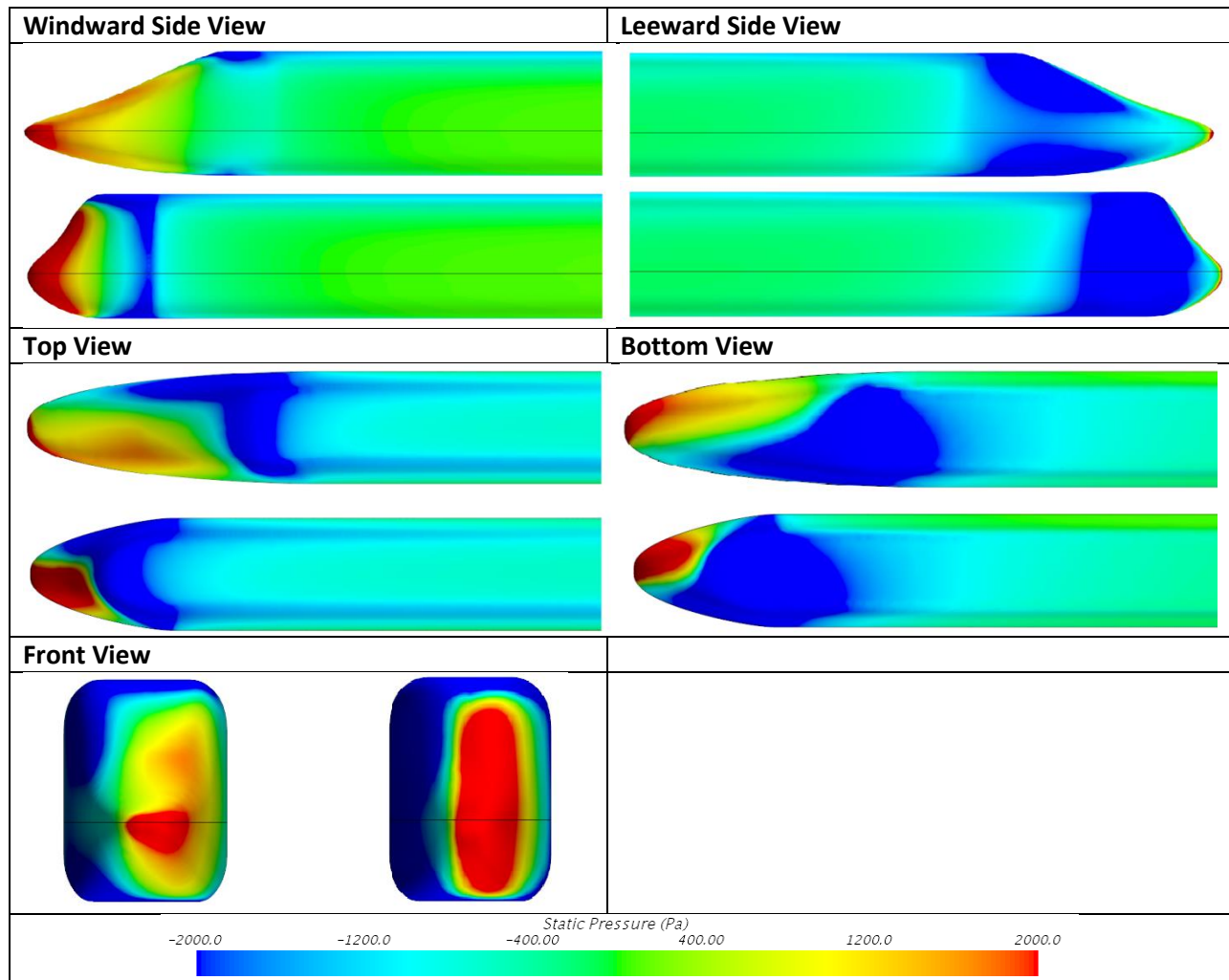


Figure 121: The static pressure (Pa) distribution over the surface area of the leading locomotive under crosswind conditions, shown here for two geometries. At the top, or the left (for the “Front View”); Design Point 1, as per Table 29. At the bottom, or the right (for the “Front View”); Design Point 23, as per Table 29 .



Table 30: The effect of a variable inflection point (H) on the nose geometry of the train for a constant nose length of  $L = 2.171\text{m}$  and nose-tip height of  $Z_0 = 0.709\text{m}$ . The value of the inflection point is 2.027m, 2.512m and 3m from left to right respectively.

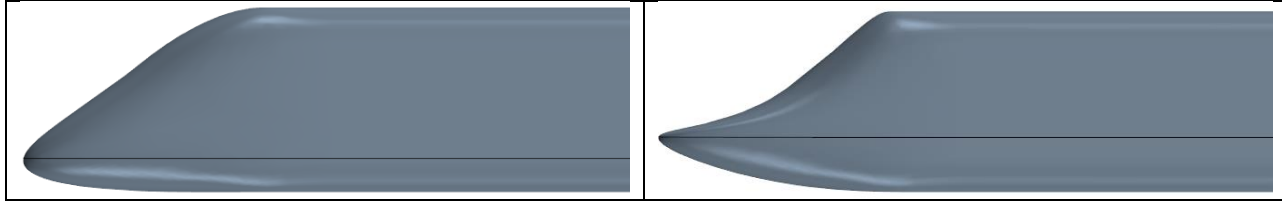
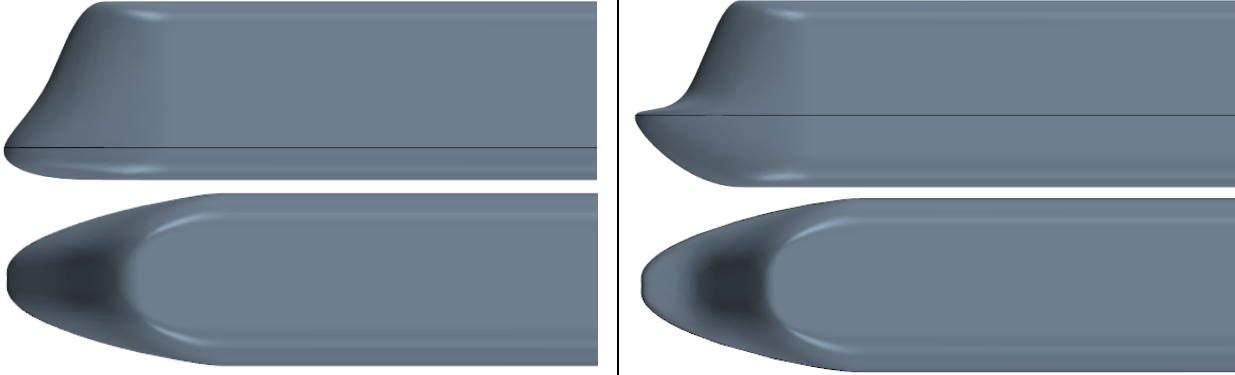
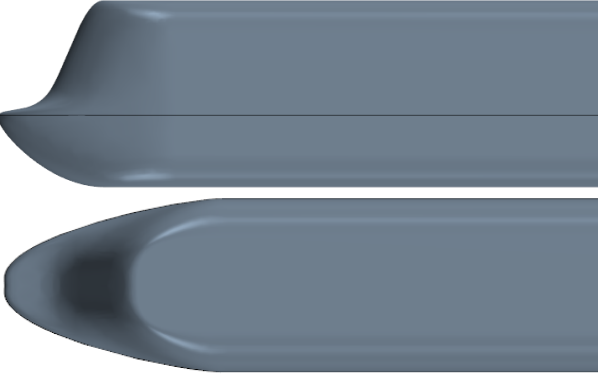
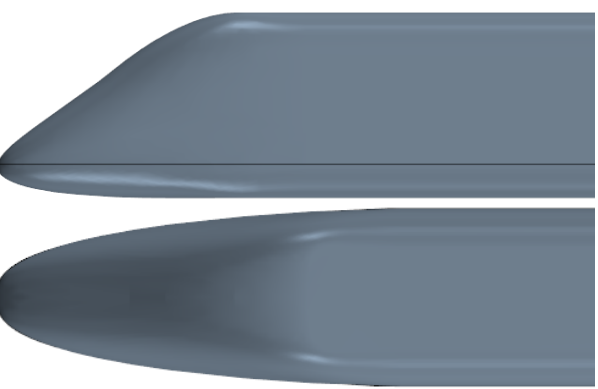
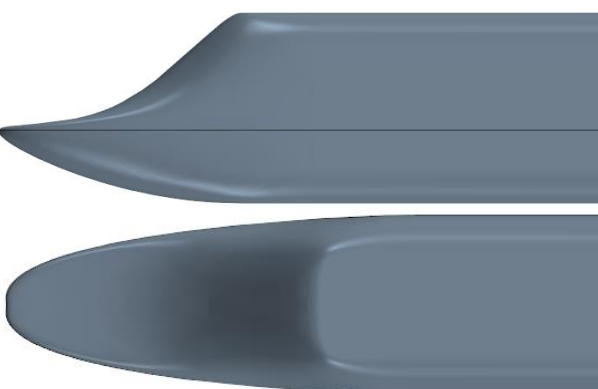
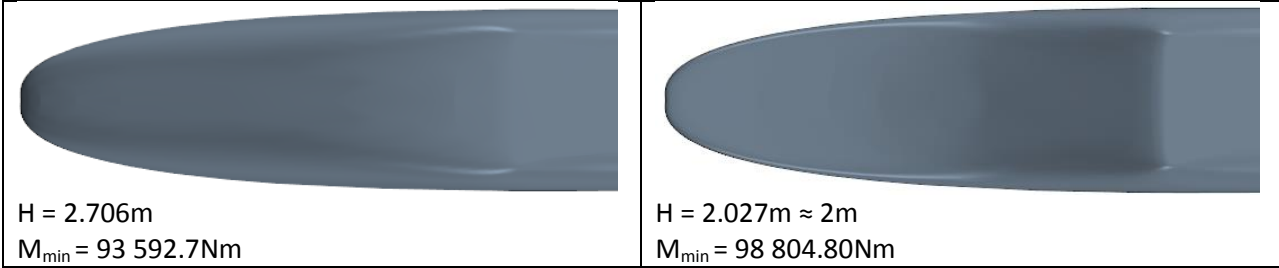


Table 31: The nose geometries associated with the global (left) and local (right) minimum leeside rolling moment acting on the leading locomotive, shown here for a constant nose length (L) of 4.930m. Left:  $Z_0 = 0.709\text{m}$  and  $H = 2.706\text{m}$ . Right:  $Z_0 = 1.172\text{m}$  and  $H = 2.027\text{m}$ .

Nose-tip Height : Lower-bound ( $Z_0=0.709\approx 0.7\text{m}$ )	Nose-tip Height: Upper-bound ( $Z_0=1.481\approx 1.5\text{m}$ )
<b>Minimum Leeside Rolling Moment</b>	
L=2.171m	
 <p data-bbox="190 1045 407 1108">H = 2.415m <math>M_{\min} = 101\ 317\text{Nm}</math></p>	 <p data-bbox="823 1045 1040 1108">H = 2.027m <math>\approx 2\text{m}</math> <math>M_{\min} = 103\ 092\text{Nm}</math></p>
L=4.930m	
 <p data-bbox="190 1556 391 1619">H = 2.706m <math>M_{\min} = 96\ 343\text{Nm}</math></p>	 <p data-bbox="823 1566 1049 1629">H = 2.027m <math>\approx 2\text{m}</math> <math>M_{\min} = 99\ 471.1\text{Nm}</math></p>
L=7.688m	
	

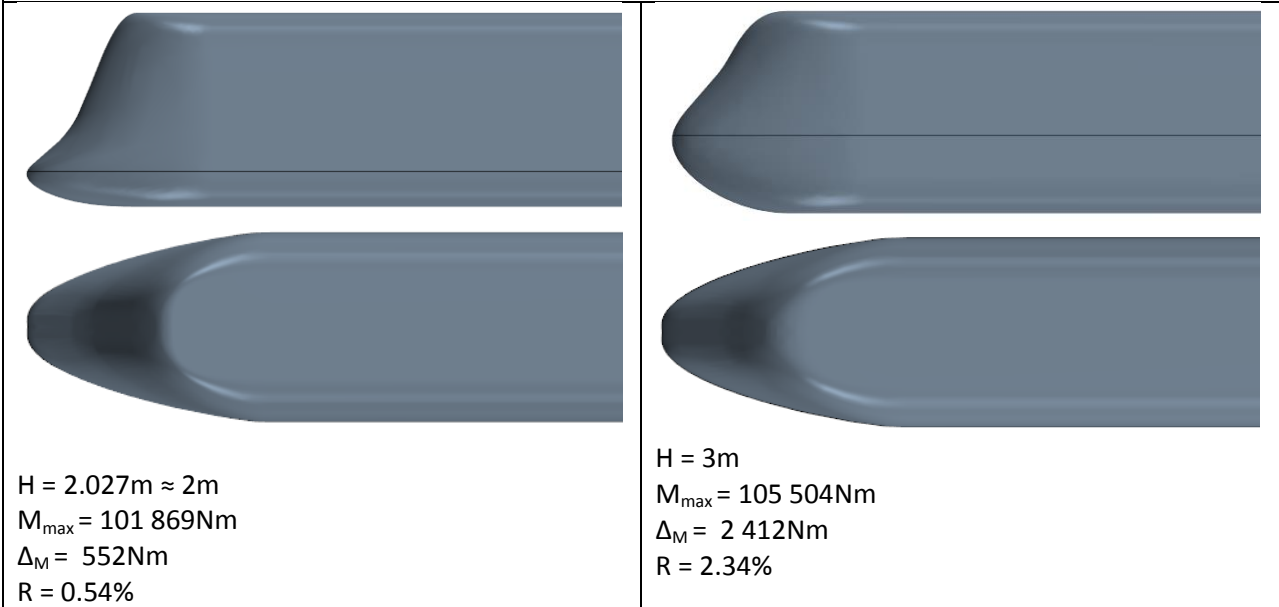


**Maximum Leaside Rolling Moment**

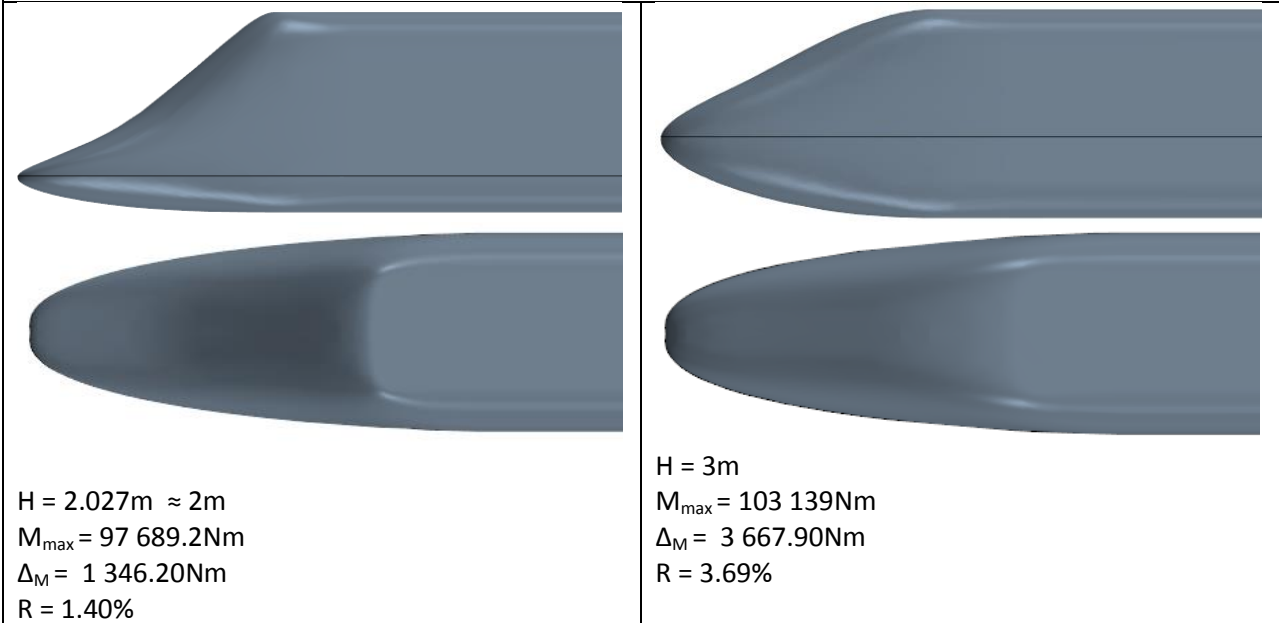
Given;

$$R = \left( \frac{M_{Max} - M_{Min}}{M_{Min}} \right) * 100$$

L=2.171m



L=4.930m



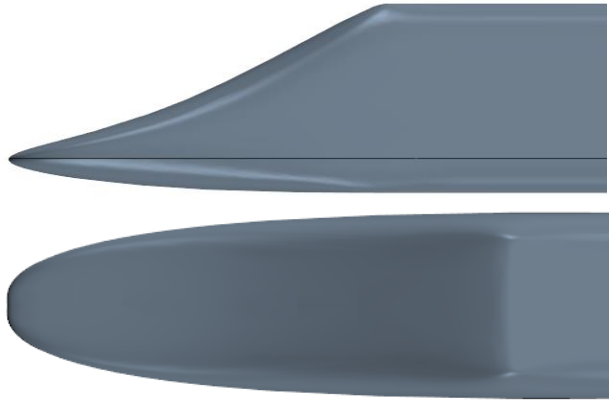
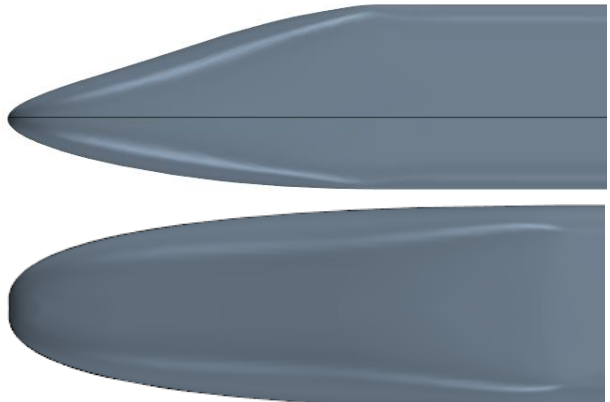
L=7.688m	
	
<p>H = 2.027m <math>\approx</math> 2m  <math>M_{\max} = 94\,268.9\text{Nm}</math>  <math>\Delta_M = 676.2\text{Nm}</math>  R = 0.72%</p>	<p>H = 3m  <math>M_{\max} = 102\,151\text{Nm}</math>  <math>\Delta_M = 3\,346.20\text{Nm}</math>  R = 3.39%</p>

Table 32: A comparative table showing first the nose geometries that ensure a minimum leaside rolling moment for nose lengths of L = 2.171m, 4.930m and 7.688m given at the location of both the minimum (left column) as well as the maximum (right column) nose-tip heights. Thereafter the very same geometric variables and responses are considered such that a maximum leaside moment is obtained. The table further gives the difference ( $\Delta_M$ ) between the maximum and minimum moments obtained at a constant nose-tip height and nose length. The percentage change (R) for the same is also given.

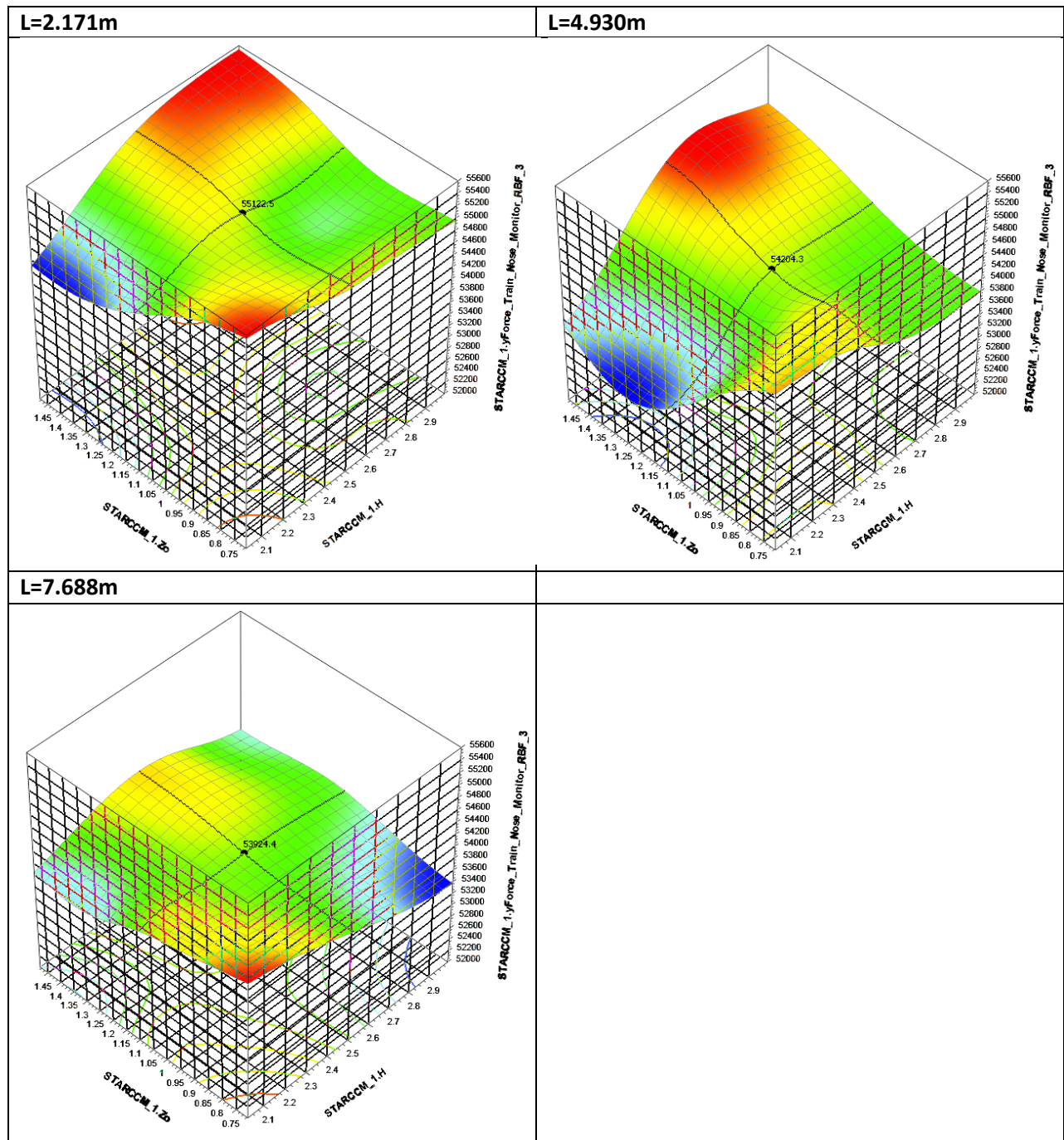


Figure 122: The variation of the side-force (vertical axis) acting on the leading locomotive as a function of nose-tip height ( $Z_0$ ) and inflection point height ( $H$ ), shown here for nose lengths of 2.171m, 4.930m and 7.688m.

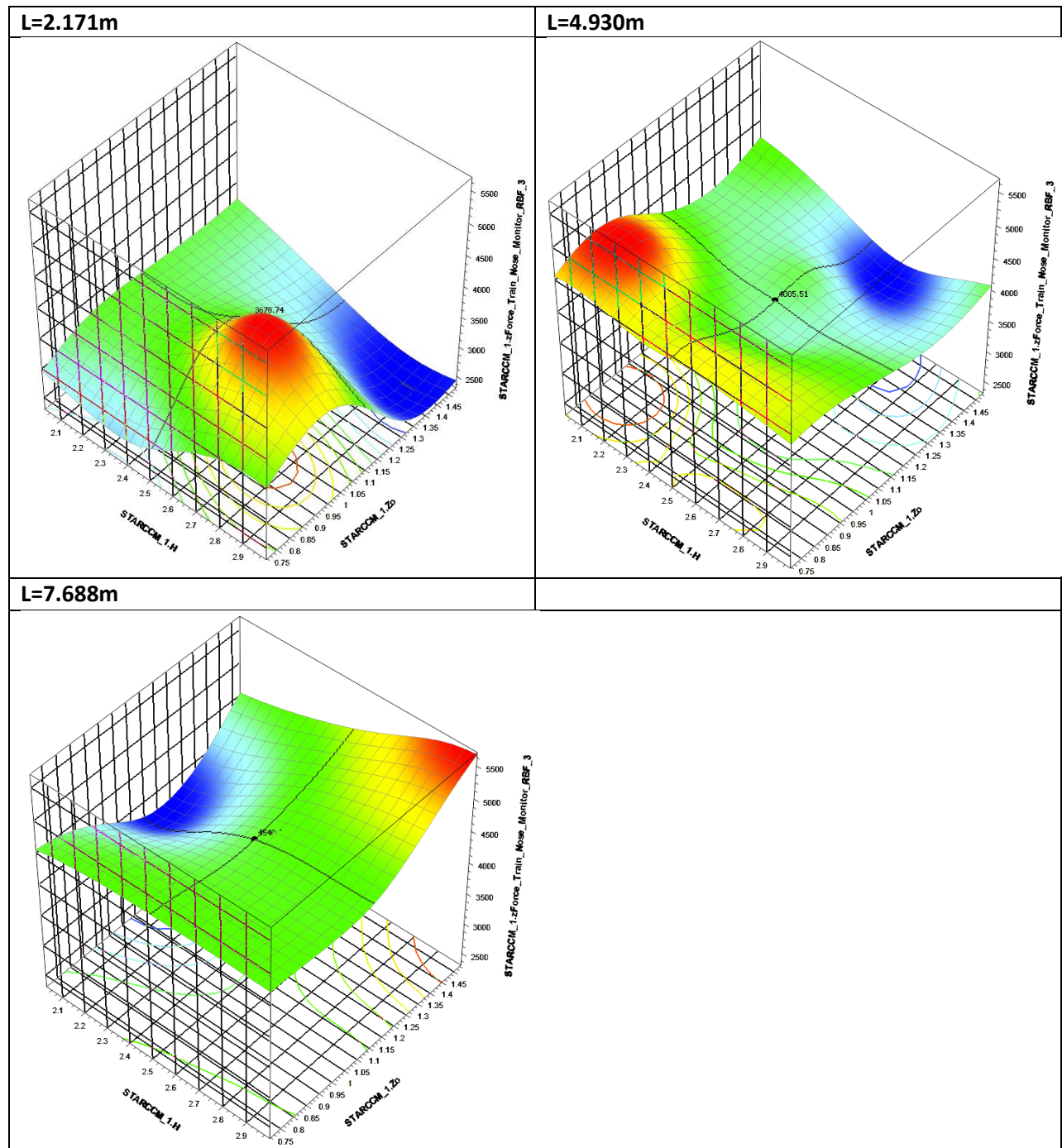


Figure 123: The variation of the lift-force (vertical axis) acting on the leading locomotive as a function of nose-tip height ( $Z_0$ ) and inflection point height (H), shown here for nose lengths of 2.171m, 4.930m and 7.688m.

### 5.3.2. Optimization Results

The surrogate model that was used for this optimization study was created by making use of the radial basis function together with the thin spline method and is discussed in detail in section 5.3.1. As mentioned previously, the reduction of the total drag force acting on the train and the rolling moment about the leaside rail acting on the leading vehicle are the objectives of this study. The multi-objective optimization process itself was conducted by making use of the SHERPA algorithm which was allowed 1000 evaluations and an archive size of 30. Once the design space had been explored, there was found to be two strong correlations, i.e., the well-known relationship between the nose length ('L') of the train and the total drag force acting on it, which yielded a correlation of -0.83 (see Figure 124). The second is the relationship between the nose-tip height ('Z<sub>0</sub>') of the train and the rolling moment acting on its leading vehicle about the leaside rail, which yielded a correlation of 0.87 (see Figure 125). Since the flow mechanisms responsible for the aforementioned behaviours have already been discussed it will not be repeated here, rather section 5.3.1.1 and section 5.3.1.2 may be referred to for a comprehensive discussion on the total drag force and the rolling moment about the leaside rail, respectively.

The results of the optimization process further showed that, within the boundaries placed on the study, a maximum total drag force of 18.06kN could be obtained for a nose geometry where L = 2.342m, H = 2m and Z<sub>0</sub> = 1.324m, while a minimum drag force of 14.63kN is achievable for L = 7.7m, H = 3m and Z<sub>0</sub> = 1.5m. Thus a maximum drag reduction of 23.50% is possible given the geometric parameters and their permissible ranges (see Table 10 and Figure 71). In the case of the leaside rolling moment, a maximum reduction of 12.60% is possible where a nose geometry with L = 2.285m, H = 2.97m and Z<sub>0</sub> = 1.484m yields a maximum rolling moment of 105.30kNm and a nose geometry where L = 7.7m, H = 2.71m and Z<sub>0</sub> = 0.7m yields a minimum rolling moment of 93.51kN-m. While the aforementioned values indicate the maximum achievable percentagewise improvement of the design for a given response, it is worth considering the Pareto front (see Figure 126) that resulted from the optimization study since it relays a collection of optimal designs rather than geometric extremes that would have been disregarded a priori. These results show a 3.18% increase from the minimum (14.63kN) to the maximum drag force (15.09kN) and a 9.40% increase between the minimum (93.51kN-m) and maximum rolling moment (102.30kN-m), (see Figure 126 and Table 33). It is thus clear from the aforementioned that, for the collection of optimal results, it is the rolling moment response that is more sensitive to a change in the geometric parameters, while the performance of the drag force remains approximately unaffected (within 0.46kN) by the same. Bearing this in mind, it is recommended to opt for the nose configuration associated with the minimum rolling moment, i.e., point 'a' (see Table 33 and Figure 126).

Design Point (as per Figure 126)	Geometric Description			Drag Force [kN]	Rolling Moment [kN-m]
	Nose Length [m]	Inflection Point Height [m]	Nose-tip Height [m]		
'a'	7.7	2.71	0.7	15.09	93.51
'b'	7.7	3	1.108	14.92	98.91
'c'	7.7	3	1.5	14.63	102.30

Table 33: The geometric description as well as the force and moment responses, as per surrogate model, of the extreme points of the Pareto front (see Figure 126, point 'a' and 'c') as well as its "trade-off" point (see Figure 126, point 'b').

The question of the predictive accuracy of the surrogate model, and consequently the results obtained by its use, arises however. Thus, in order to validate the model points ‘a’, ‘b’ and ‘c’ as per Table 33 and Figure 126, where point ‘b’ is the trade-off point between the two optimization objectives, were simulated and the results obtained from the computational models were compared to the values predicted by the surrogate model. From the results of this comparative study (see Table 34) it is clear that the surrogate model is highly accurate with the largest discrepancy between predicted and simulated results being 1.59%. It is however worth noting that all three design points that were used for the cross-validation study lies on the Pareto front and consequently all three geometries assumed the maximum possible nose length, since the elongation of the nose favours both the reduction of the total drag force as well as the leaside rolling moment. This is not a problem in itself as the optimal solution is expected to lie within the region of longer nose lengths, but it is worth validating the model for shorter nose lengths if flow phenomena about such nose geometries are to be studied; numerical noise could cause possible discrepancies to arise due to the nature of the flow associated with the aforementioned.

Design Point (see Table 33)	Drag Force [N]			Leaside Rolling Moment [N-m]		
	Surrogate Model	Simulation	Deviation [%]	Surrogate Model	Simulation	Deviation [%]
‘a’	15 091.69	15 207.28	0.77	93 512.77	92 852.50	-0.71
‘b’	14 917.60	14 959.71	0.28	98 912.08	98 816.8	-0.10
‘c’	14 626.04	14 858.64	1.59	102 298.71	102 080.42	-0.21

Table 34: A comparison between the results predicted by the surrogate model and the simulation for the total drag force (N) and the leaside rolling moment (N-m) for various geometries.

Now that it has been proven that the results obtained from the Pareto front may be trusted, it is worth considering the three design points, i.e., points ‘a’, ‘b’ and ‘c’ (see Table 35) and their associated flow features. The pressure coefficient acting around the nose circumference of points ‘a’, ‘b’ and ‘c’ on the Pareto front was captured at various locations along the length of the leading locomotive, i.e., at  $x/L = 0.125, 0.25, 0.375, 0.5, 0.75$  and 1 (see Figure 127 to Figure 132), where ‘x’ is measured from the nose-tip and ‘L’ is the total length of the locomotive. The aforementioned graphs are able to cast some light on a flow field that is decidedly asymmetric since the coefficient of pressure is highly descriptive of the nature of the flow at a given location. While it is true that the pressure coefficient is best used for describing incompressible flow due to the unchanging nature of the density, it is still informative when used in a comparative manner, although now  $C_p$ -values significantly larger than one may be expected.

At the x-locations further down the length of the leading locomotive (see Figure 130, Figure 131 and Figure 132) the pressure coefficient curves of the various nose geometries collapse to virtually the same graph with broadly speaking the following flow behaviour; a suction peak can be observed in the vicinity of  $60^\circ$  as the air is accelerated over the curvature of the train roof. Thereafter the air, while still moving considerably faster than the freestream, somewhat stabilizes before once again accelerating over the roof curvature on the leeward side possibly due to a locally induced low pressure region as a consequence of the no-slip condition on the train wall and the inertia of the flow in the far field. There is a noticeable reduction of the air velocity on the leeward face and since flow separation has already been ruled out, it is possibly a consequence of Bernoulli’s principle. While the flow beneath the train is obviously more erratic, a possible consequence of anisotropic turbulence, its behaviour is as would be

expected; the air accelerates as the cross-sectional area decreases, giving rise to a suction peak as well as the increase in air velocity which remains roughly constant until the cross-sectional area expands. The flow behaviour associated with point 'a' shows a few outliers to the aforementioned at  $x/L=1$  (see Figure 132), but it is hypothesized that this is a consequence of numerical error rather than true behaviour. At  $x/L=0.5$ , the  $C_p$ -value on the windward face is mostly negative (see Figure 130), seeming to indicate that the air remains in motion while definite positive values of the pressure coefficient are observable on the windward face at  $x/L = 0.75$  and 1 hereby indicating stagnation regions.

In the case of the  $x$ -locations to the front of the leading locomotive, i.e., on the nose itself (see Figure 127 and Figure 128), the flow behaviour on the leeward face is similar to the aforementioned, while the remainder of the flow field differs in a few key ways; first there is a clear stagnation region in the vicinity of  $45^\circ$  since the "train roof" is now the upper portion of the nose-slant. Bearing this in mind it becomes immediately clear why there is an increase in the air velocity over the "train roof" as the flow follows the camber of the nose. In a similar vein the "train underbody", that is the underside of the train nose, acts to accelerate the incoming air also. What does however prove to be unexpected from Figure 127 and Figure 128, is that both the maximum  $C_p$ -value on the windward face as well as the minimum  $C_p$ -value on the leeward face is generated by point 'a' on the Pareto front which is associated with the minimum leeward rolling moment. Bearing in mind that the largest contributor to the rolling moment is the side force, the results seem to contradict one another. On the other hand, the simulation results (see Table 35) shows very little difference in the value of the side force obtained for the different geometries, thus while point 'a' may show the greatest peaks, the area beneath the curve for the train geometries must be of a similar magnitude. It is only once the  $x$ -moment about the center-of-gravity is considered, that it becomes clear why three optimized geometries with roughly the same values for the side and lift forces are able to yield a difference of roughly 10% for the rolling moment acting about the leeward rail; a reduction in the nose-tip height lowers the center of pressure and consequently the moment taken about the center of gravity is reduced. This not only confirms the hypothesis formulated in section 5.3.1.2 but further illustrates the immense influence that the nose-tip height has on cross-wind stability.

As mentioned previously, it is recommended to make use of the geometry associated with point 'a' and as such, the velocity field along its symmetry plane is shown in Figure 133 while the same is shown from the top on an  $xy$ -plane at a height of  $z=1\text{m}$  in Figure 134. The flow field along the symmetry plane of the train (see Figure 133) shows the typical flow features that are expected; there is a stagnation region visible at the tip of the nose as the flow comes into contact with the train geometry. The air proceeds to accelerate along the curvature where the "windshield" transitions into the train roof with the beginnings of a boundary layer visible in the magnified view on the left. The same magnified view also shows an increase in the air velocity beneath the train nose, probably as a consequence of Bernoulli's principle. In the vicinity of the tail there is also a region of high velocity visible where the train roof transitions into the tail slant. This area is however, not as pronounced as that for the nose region, perhaps due to the asymmetric nature of the flow. Once again it is postulated that the region of accelerated air on the windward side is a consequence of a locally induced low pressure region. On the tail slant the flow seems able to remain more-or-less attached rather than the geometry giving rise to a large separated wake while the blue "fingers" trailing the tail are reminiscent of longitudinal vortices. Finally, section

4.5.3.2.2 may be referred to for a comprehensive discussion on how the oncoming flow in conjunction with the nose geometry affects the total drag acting on the train.

The velocity field viewed from above (see Figure 134) also shows some expected flow features; a stagnation region on the windward side of the nose along with an area of high velocity on the leeward side, as the nose taper accelerates the oncoming air. This pressure differential is what causes the side force acting on the train nose. Along the tail there is a small region of accelerated air on the windward side (see section 4.5.4.4 for a comprehensive explanation), while the leeward side displays a larger region of slower moving air, thus the tail is expected to experience a negative side force. This is however of little concern; not only does the CEN code not earmark the trailing vehicle as a possible source of derailment but when the magnitude of the force, as obtained by simulation, is considered, it further proves to be insignificant (see Appendix G).

An interesting flow phenomenon to take note of is the behaviour of the near-wall flow on the leeward side of the train; initially, i.e., nearer the train nose, there is a considerable retardation of the near-wall flow, then it suddenly shows a velocity increase in the middle of the train before once again decelerating until it reaches the trailing locomotive. This thinning of the slower-moving, near-wall air (see Figure 134) is a consequence of the longitudinal vortices present on the leeward side of the train (see Figure 135); as the radii of the vortices increase, high energy air comes into contact with the low energy air in the near-wall region and serves to energize it. It is also worth noting that when the vortex structures surrounding the train (see Figure 135) are considered alongside the velocity field (see Figure 134), it becomes clear that the velocity associated with the aforementioned leeward vortex, is considerably larger than that of the vortices trailing the train. The trailing vortices do, however, interact with the train body to a larger extent, which further emphasizes the need to accurately model the irrotational vortices present in the flow field. The aforementioned thus serves to justify the initial choice of making use of a Reynolds' stress turbulence model.

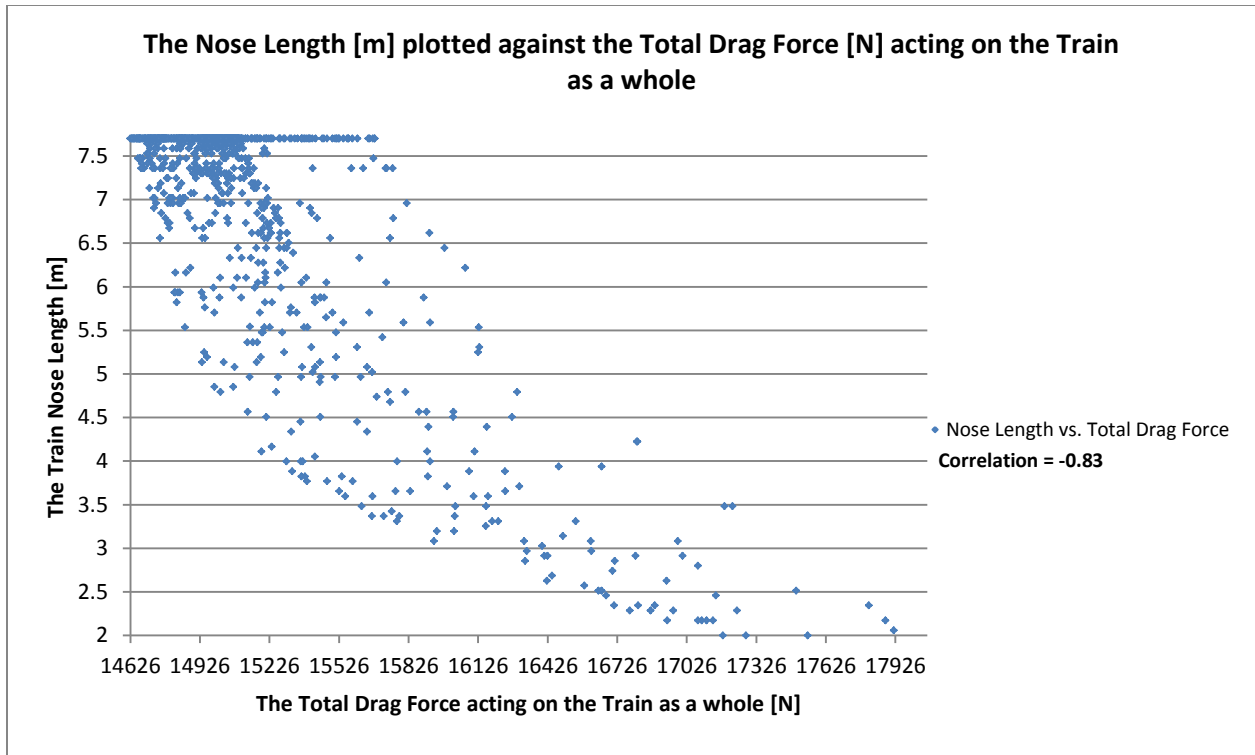


Figure 124: The relationship between the nose length ( $L$ ) and the total drag force acting on the train. The correlation between the two variables is also indicated as -0.83.

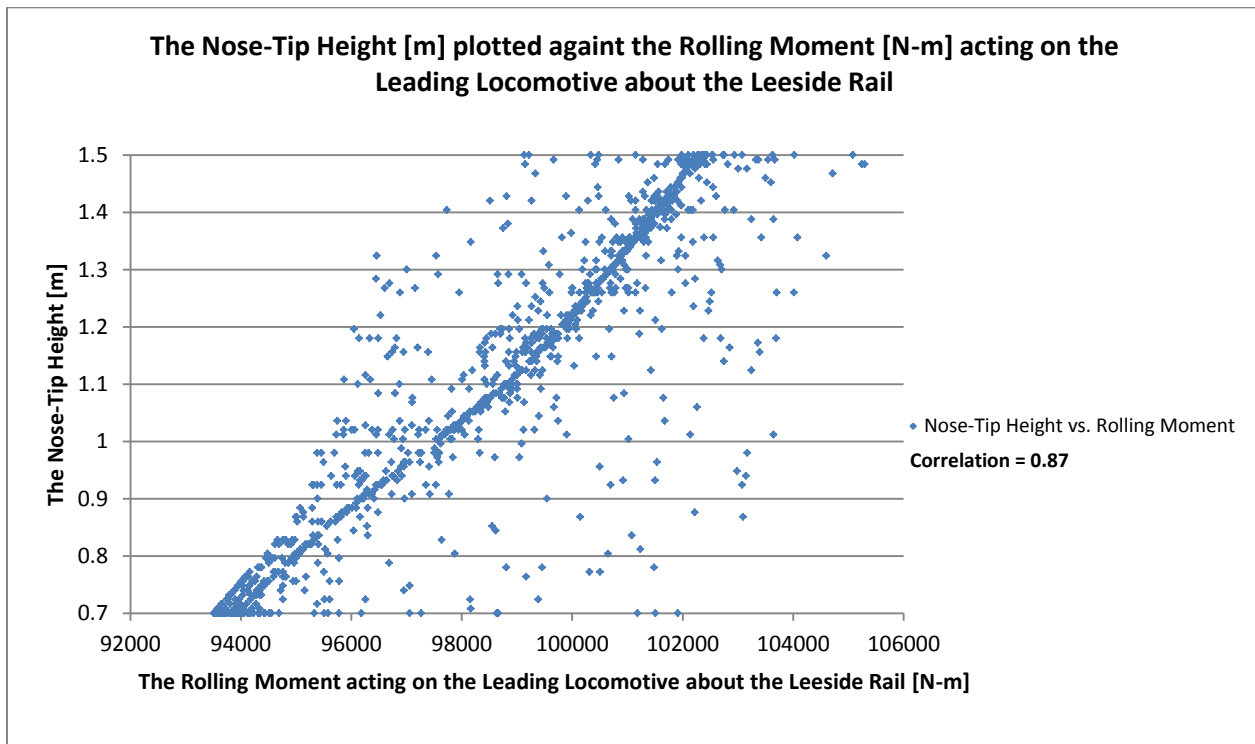


Figure 125: The relationship between the nose-tip height ( $Z_0$ ) and the rolling moment acting on the leading vehicle about the leaside rail. The correlation between the two variables is also indicated as 0.87.

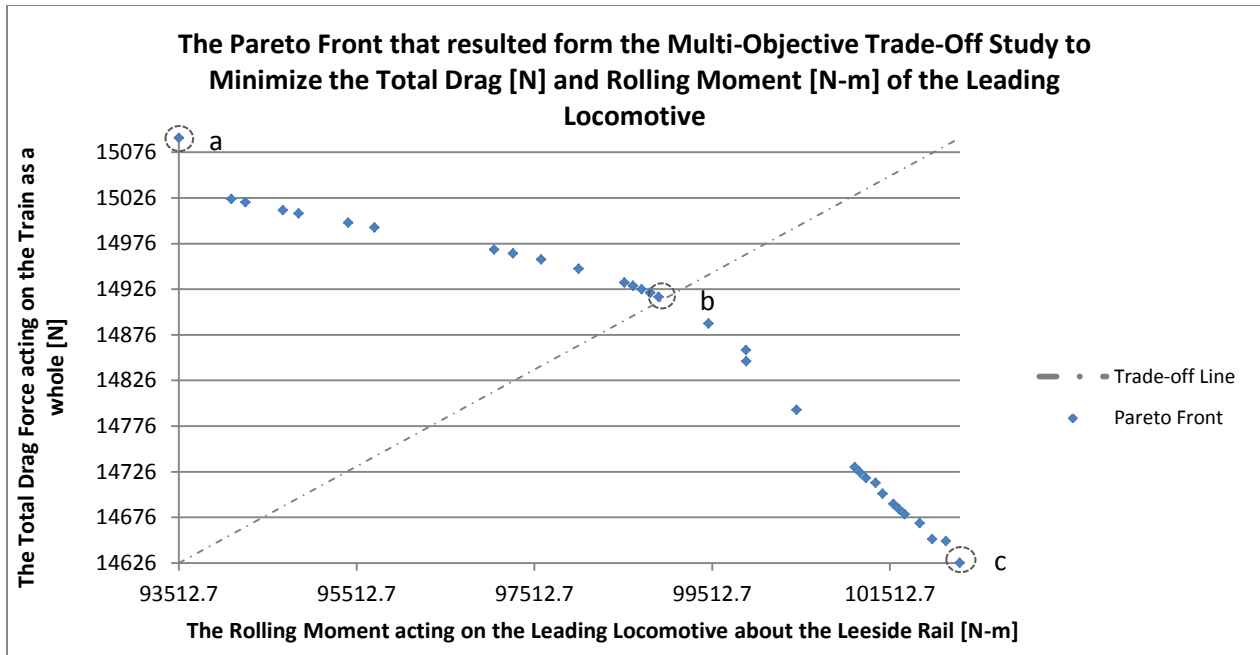


Figure 126: The Pareto front that was obtained from the multi-objective optimization process of minimizing both the total drag as well as the rolling moment acting on the leading vehicle about the leaside rail.

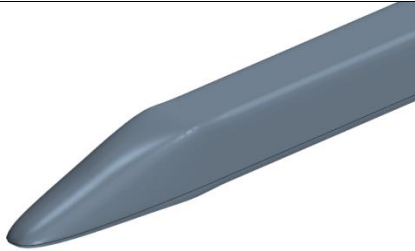
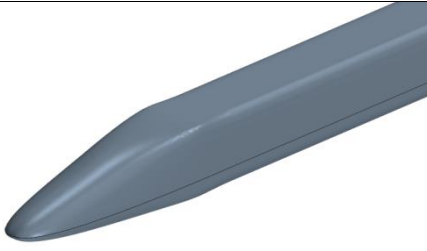
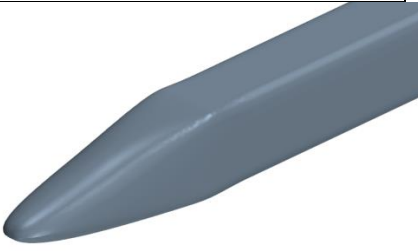
Point 'a'	Point 'b'	Point 'c'
<b>Geometry:</b>		
		
L = 7.7 H = 2.71 Z <sub>0</sub> = 0.7	L = 7.7 H = 3 Z <sub>0</sub> = 1.108	L = 7.7 H = 3 Z <sub>0</sub> = 1.5
<b>Force Responses:</b>		
<b>Nose:</b> F <sub>y,LL</sub> = 53.41kN F <sub>z,LL</sub> = 4.90kN <b>Train:</b> F <sub>x,Train</sub> = 15.21kN	<b>Nose:</b> F <sub>y,LL</sub> = 53.95kN F <sub>z,LL</sub> = 4.40kN <b>Train:</b> F <sub>x,Train</sub> = 14.96kN	<b>Nose:</b> F <sub>y,LL</sub> = 53.53kN F <sub>z,LL</sub> = 4.67kN <b>Train:</b> F <sub>x,Train</sub> = 14.86kN
<b>x-Moment Responses:</b>		
<b>About the Nose COG:</b> M <sub>LL,COG</sub> = -43.60kNm <b>About the Leaside Rail:</b> M <sub>LL,LS</sub> = 92.85kNm	<b>About the Nose COG:</b> M <sub>LL,COG</sub> = -38.61kNm <b>About the Leaside Rail:</b> M <sub>LL,LS</sub> = 98.82kNm	<b>About the Nose COG:</b> M <sub>LL,COG</sub> = -34.51kNm <b>About the Leaside Rail:</b> M <sub>LL,LS</sub> = 102.08kNm

Table 35: The nose geometries corresponding to point a, b and c on the Pareto front is shown here along with their associated force and moment responses (see Figure 126), from left to right respectively. The right-hand-rule is applied with the exception of the moment about the x-axis where the signs are reversed.

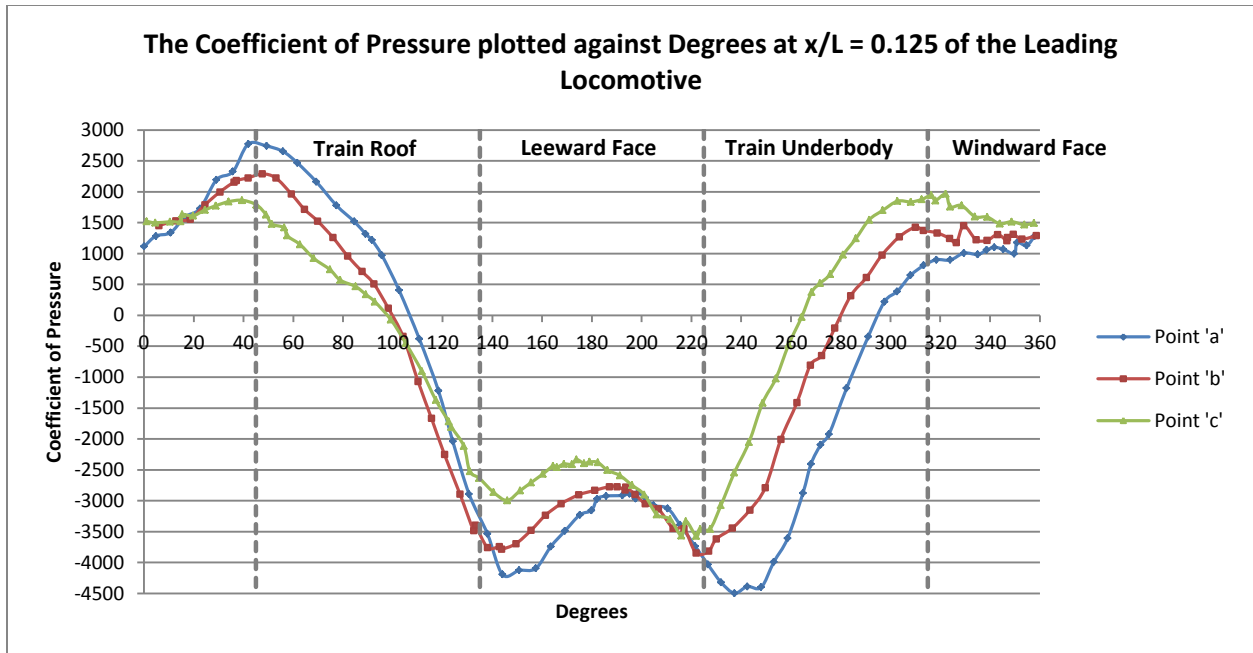


Figure 127: The coefficient of pressure plotted against degrees at  $x/L = 0.125$  of the leading locomotive, where the distance 'x' is measured from the tip of the nose and has been non-dimensionalised by the locomotive length, i.e., 20m. The regions of the train circumference are as follows; Windward Face;  $-45^\circ$  to  $45^\circ$ , Train Roof;  $45^\circ$  to  $135^\circ$ , Leeward Face;  $135^\circ$  to  $225^\circ$ , Train Underbody;  $225^\circ$  to  $315^\circ$ .

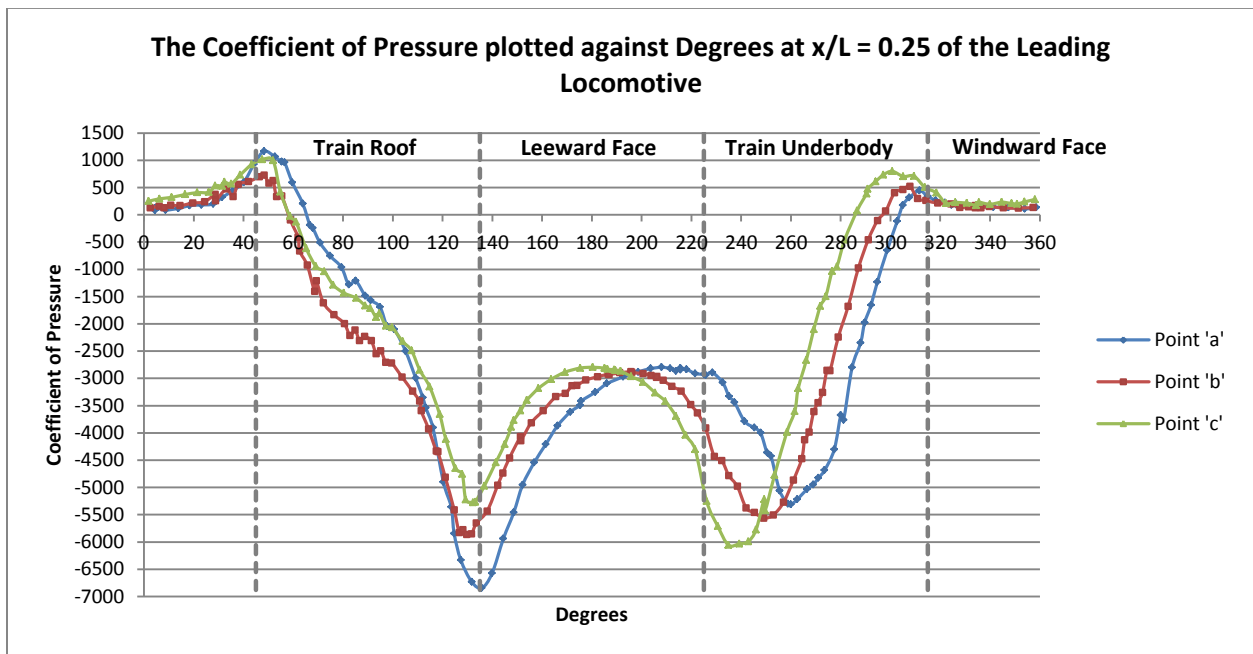


Figure 128: The coefficient of pressure plotted against degrees at  $x/L = 0.25$  of the leading locomotive, where the distance 'x' is measured from the tip of the nose and has been non-dimensionalised by the locomotive length, i.e., 20m. The regions of the train circumference are as follows; Windward Face;  $-45^\circ$  to  $45^\circ$ , Train Roof;  $45^\circ$  to  $135^\circ$ , Leeward Face;  $135^\circ$  to  $225^\circ$ , Train Underbody;  $225^\circ$  to  $315^\circ$ .

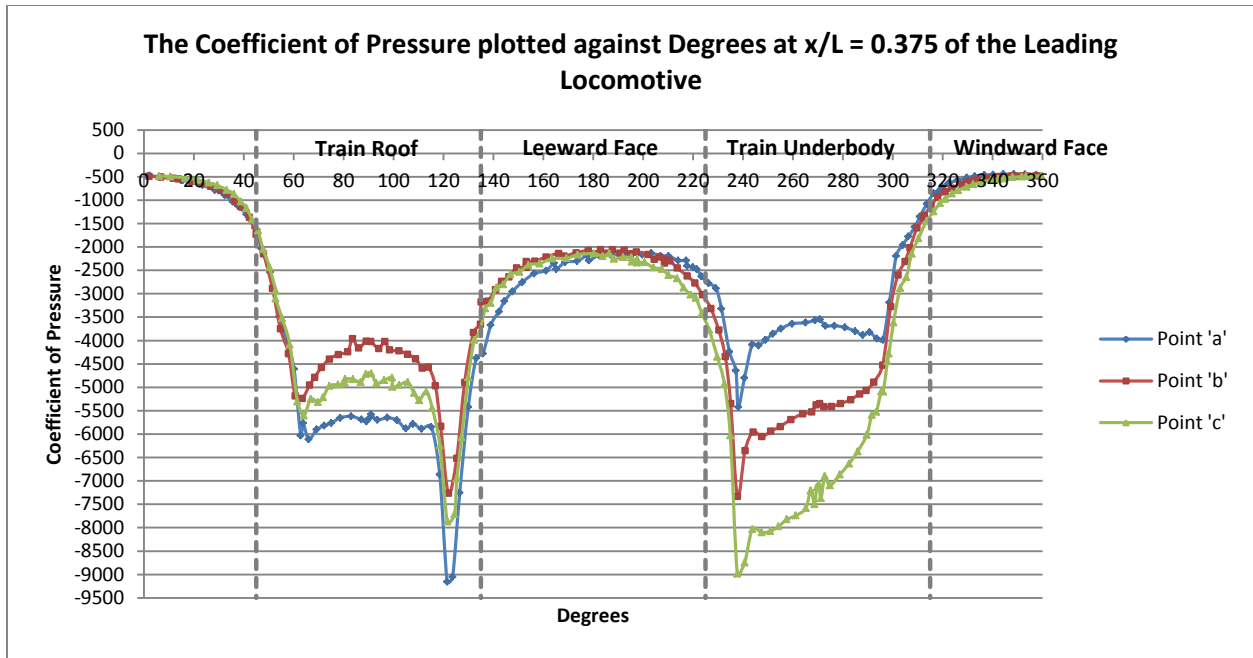


Figure 129: The coefficient of pressure plotted against degrees at  $x/L = 0.375$  of the leading locomotive, where the distance 'x' is measured from the tip of the nose and has been non-dimensionalised by the locomotive length, i.e., 20m. The regions of the train circumference are as follows; Windward Face; -45° to 45°, Train Roof; 45° to 135°, Leeward Face; 135° to 225°, Train Underbody; 225° to 315°.

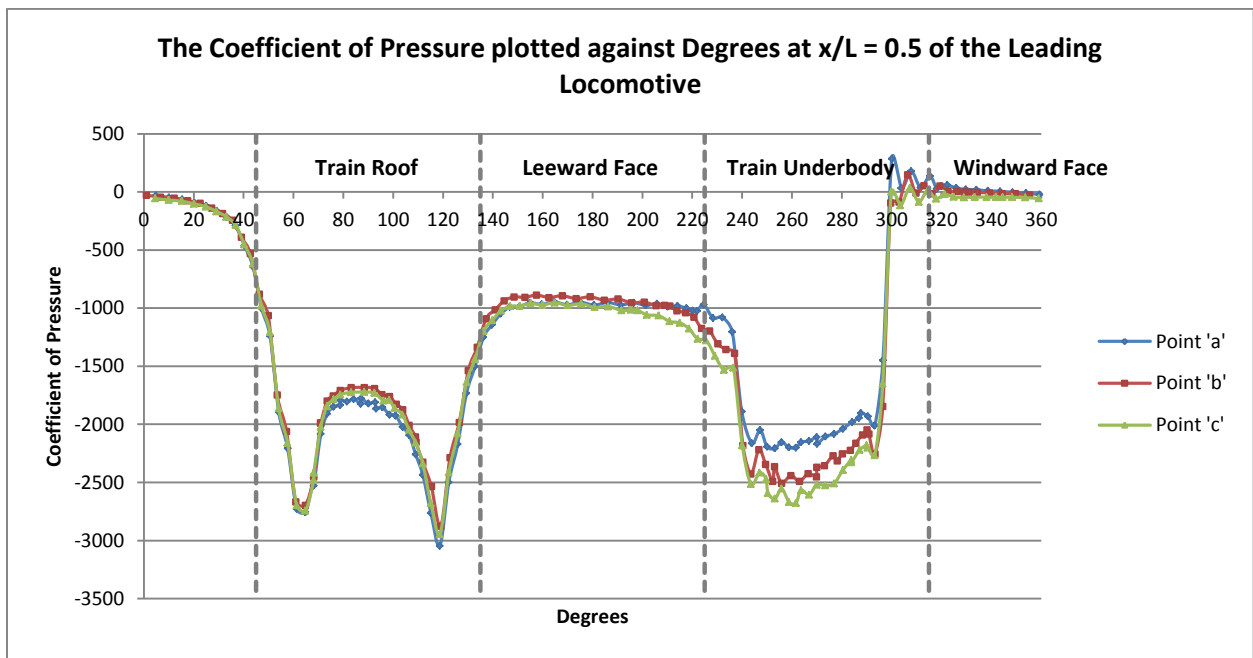


Figure 130: The coefficient of pressure plotted against degrees at  $x/L = 0.5$  of the leading locomotive, where the distance 'x' is measured from the tip of the nose and has been non-dimensionalised by the locomotive length, i.e., 20m. The regions of the train circumference are as follows; Windward Face; -45° to 45°, Train Roof; 45° to 135°, Leeward Face; 135° to 225°, Train Underbody; 225° to 315°.

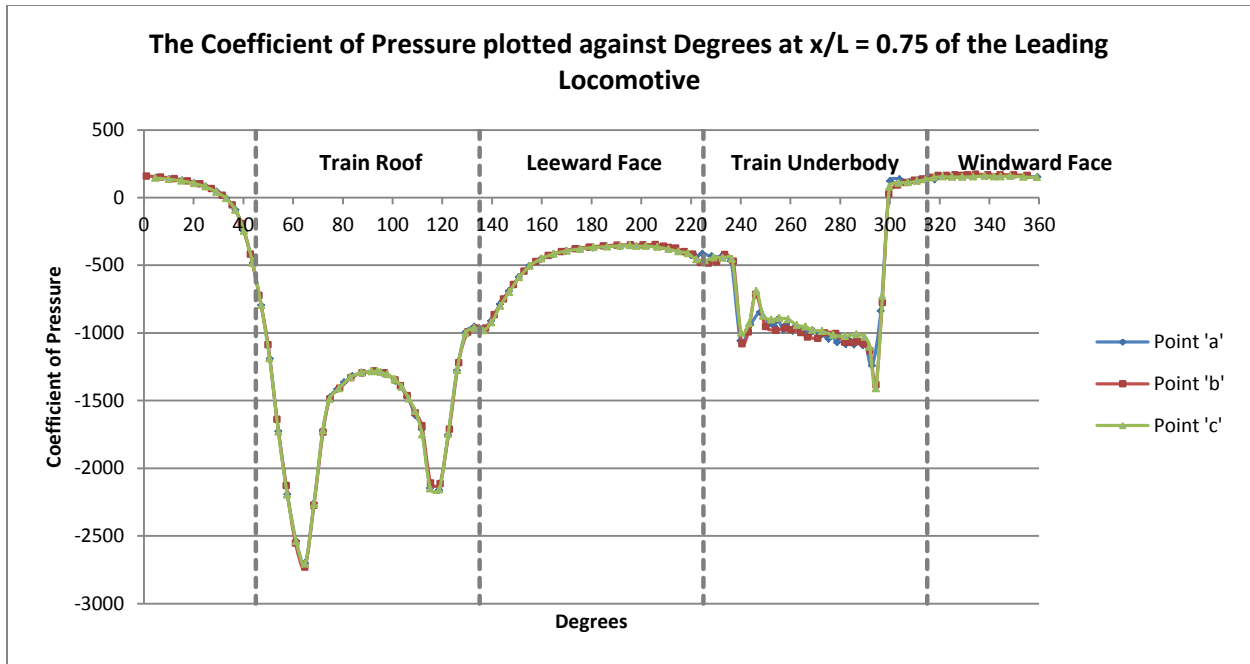


Figure 131: The coefficient of pressure plotted against degrees at  $x/L = 0.75$  of the leading locomotive, where the distance 'x' is measured from the tip of the nose and has been non-dimensionalised by the locomotive length, i.e., 20m. The regions of the train circumference are as follows; Windward Face;  $-45^\circ$  to  $45^\circ$ , Train Roof;  $45^\circ$  to  $135^\circ$ , Leeward Face;  $135^\circ$  to  $225^\circ$ , Train Underbody;  $225^\circ$  to  $315^\circ$ .

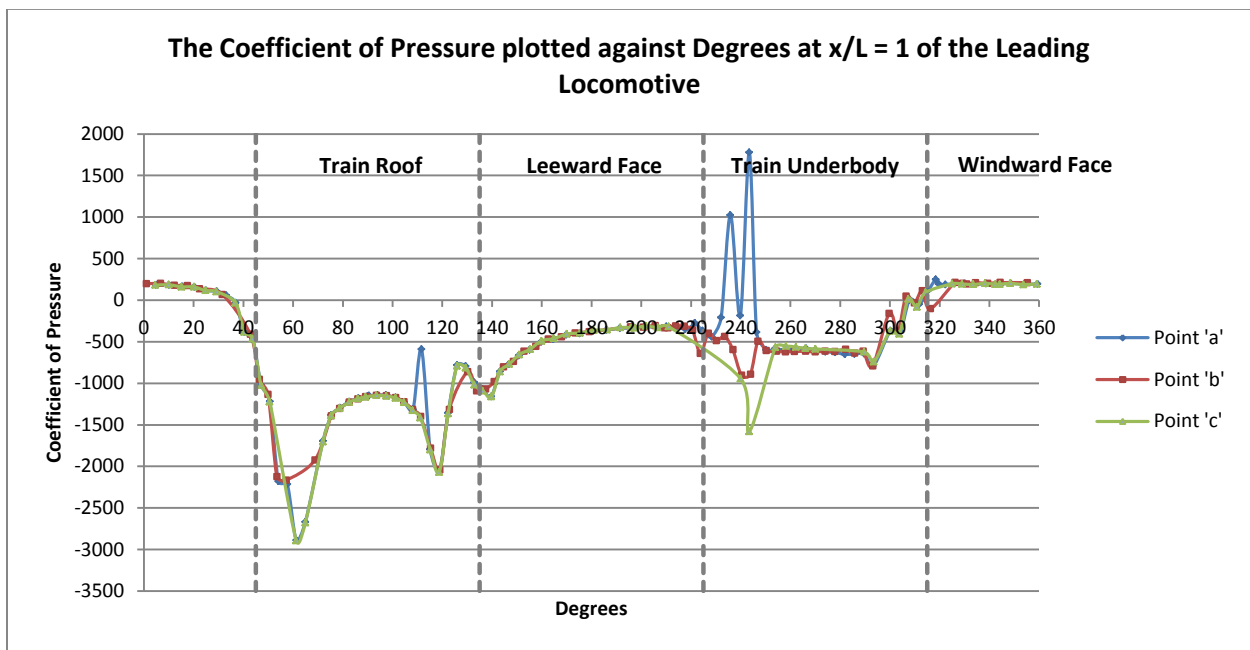


Figure 132: The coefficient of pressure plotted against degrees at  $x/L = 1$  of the leading locomotive, where the distance 'x' is measured from the tip of the nose and has been non-dimensionalised by the locomotive length, i.e., 20m. The regions of the train circumference are as follows; Windward Face;  $-45^\circ$  to  $45^\circ$ , Train Roof;  $45^\circ$  to  $135^\circ$ , Leeward Face;  $135^\circ$  to  $225^\circ$ , Train Underbody;  $225^\circ$  to  $315^\circ$ .

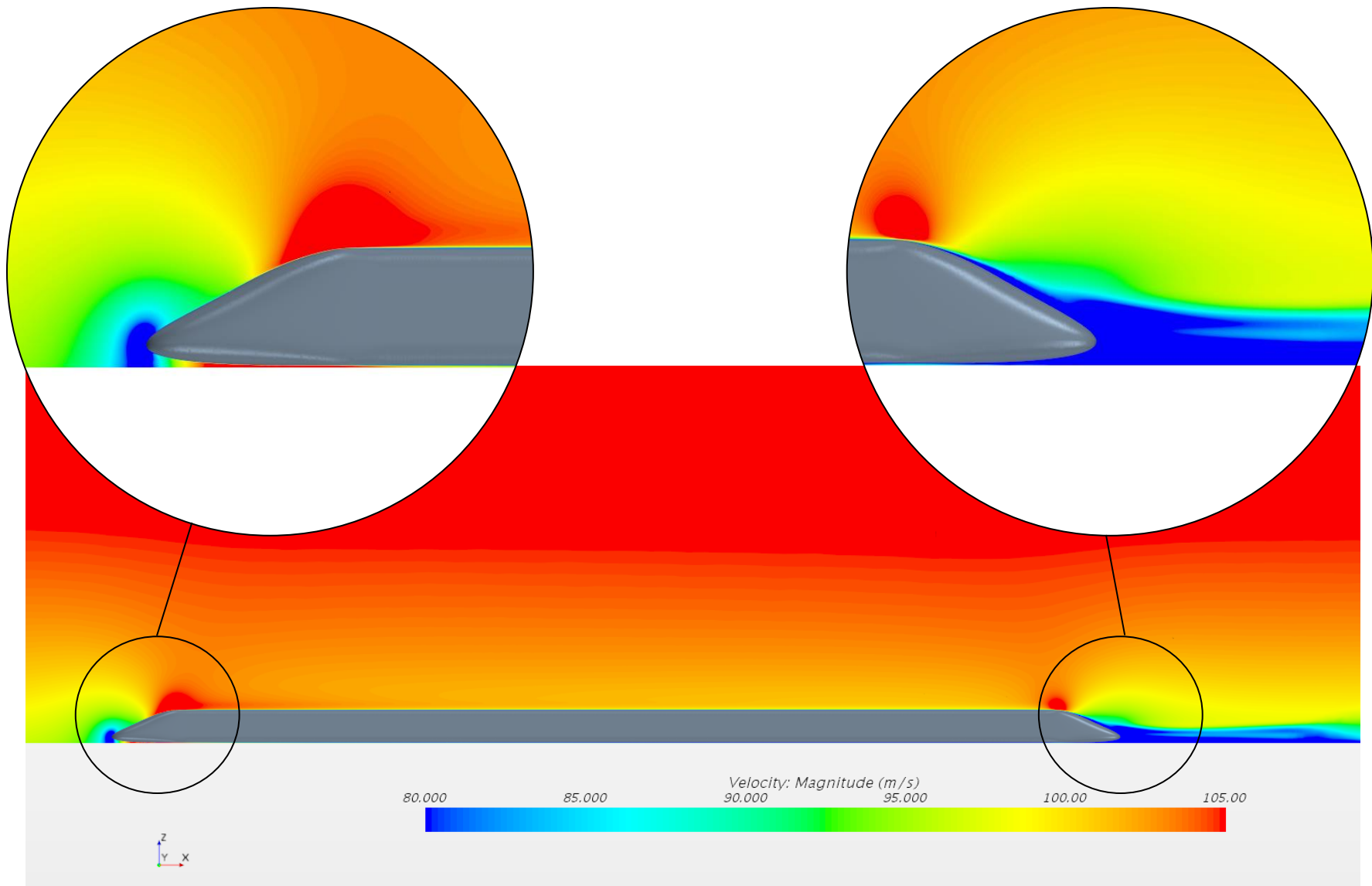


Figure 133: The velocity field surrounding the train geometry associated with point 'a' (see Table 35) on the Pareto front is shown. The velocity field is displayed about the train's symmetry plane, i.e., on the xz-plane. The detail view on the left shows a magnification of the velocity field surrounding the train nose while the detail view on the right shows a magnification of the velocity field surrounding the train tail.

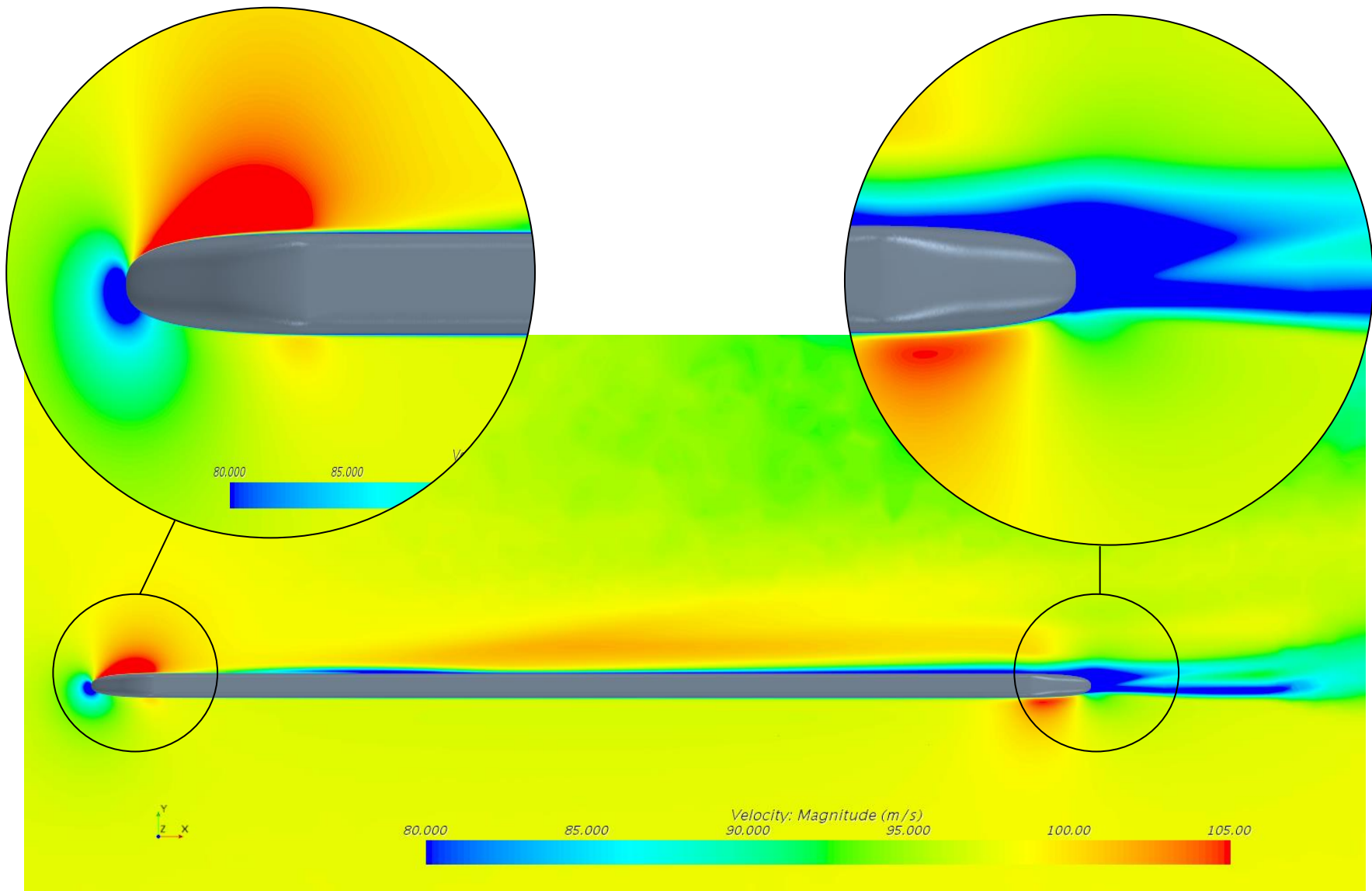


Figure 134: The velocity field surrounding the train geometry associated with point 'a' (see Table 35) on the Pareto front is shown. The velocity field is displayed from the top on a xy-plane located at a vertical height of  $z = 1\text{m}$ . The detail view on the left shows a magnification of the velocity field surrounding the train nose while the detail view on the right shows a magnification of the velocity field surrounding the train tail.

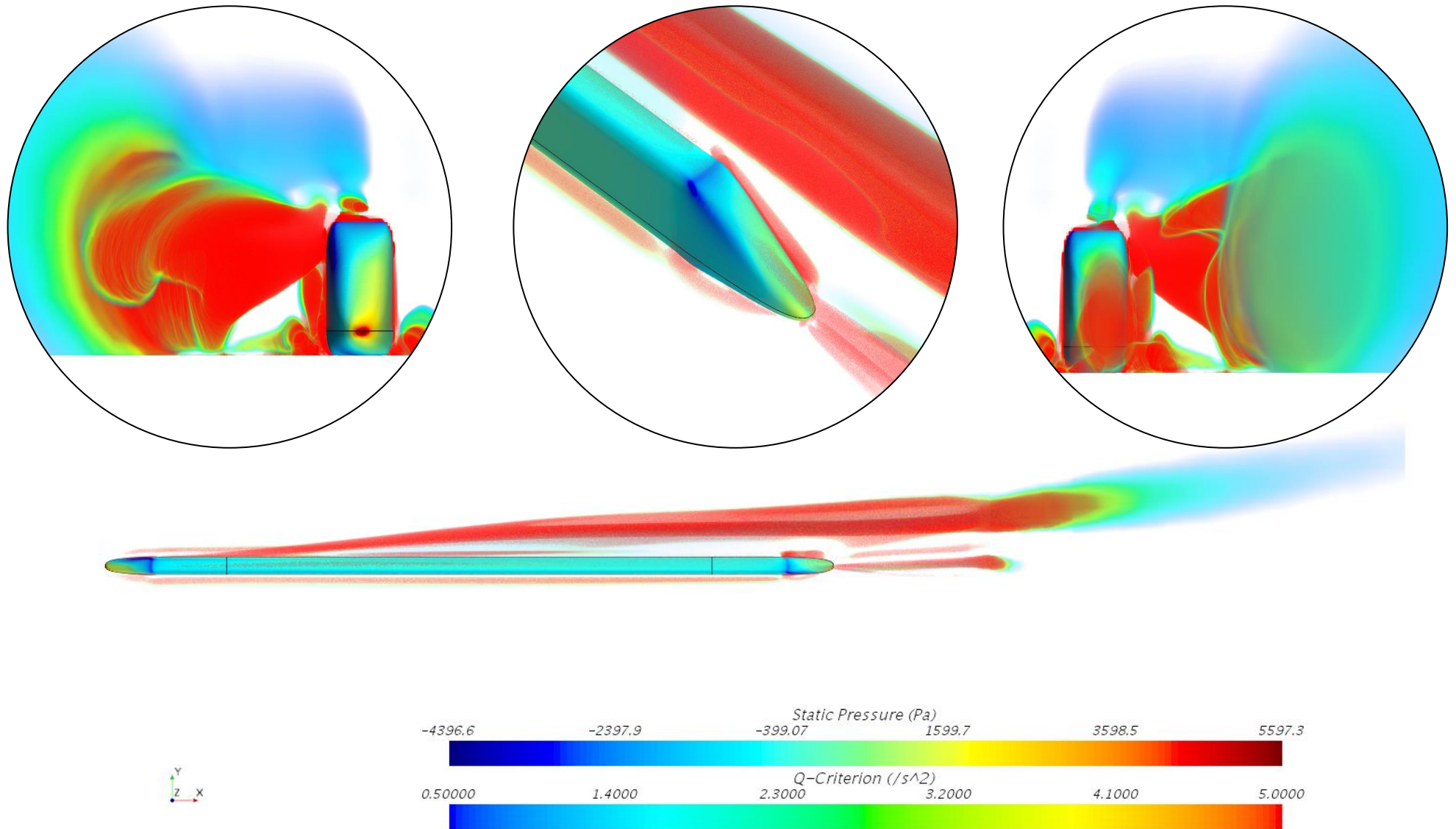


Figure 135: The vortex structures surrounding the train with the nose geometry associated with point 'a' on the Pareto front are shown. The detail view on the left shows a magnified view of the vortices as seen from the front. The detail view in the middle shows the interaction of the irrotational vortices with the tail structure. The detail view on the right shows a magnified view of the vortices as seen from the rear.

## 6. Summary, Conclusions and Recommendations

### 6.1. Summary

The release of the South African government's National Rail Policy has made several targets clear for the future of rail in the country. One of the requirements stipulated is the availability of high speed commuter services to passengers by the year 2050. The primary motivator for the initiative is the reduction of greenhouse gas emissions associated with the transport sector, while a secondary motivator is the economic development of the sector and as such the option of simply importing the necessary vehicles to address the need, was eliminated. Unfortunately, there exists the obstacle of a skills shortage in the rail industry so that achieving the aforementioned poses a challenge.

Transnet Engineering thus decided to start bridging this knowledge gap by implementing several initiatives, one of which is the deliverable obtained from this study, i.e., a nose, or tail for that matter, geometry that has been optimized for windless- as well as cross-wind conditions. As mentioned above, environmental concerns acted as the primary motivator for the implementation of high speed rail and thus the optimization objective of drag reduction is self-explanatory. The second objective in the case of crosswind conditions pertains to the sanctity of human life, i.e., the crosswind stability of the leading vehicle was to be maximized, as per CEN code (CEN, 2010), so as to avoid train derailment as far as possible.

Study revealed that there are a number of challenges faced by high speed rail which include but are not limited to, the aforementioned. The challenges of importance will of course vary from problem to problem, but at the very least the study proved Transnet Engineering's concerns and proposed optimization goals to be valid. While many geometric optimization studies (see section 1.2) have been completed in the past, they have mostly focused on preexisting nose and tail geometries, whereas Transnet Engineering has none. Thus significant parameters to define the geometry had to be determined from previous work which led to the decision of using the nose/tail length, nose- or tail-tip height and finally the inflection point height (see Figure 71) to morph the nose and tail shape.

Due to the magnitude of the problem at hand it was decided to make use of computer simulations, i.e., computational fluid dynamic (CFD) as well as optimization software, to find a solution. Good CFD practice requires the use of a validation case, for which the Ahmed's body (see Figure 57) was chosen. By making use of this model, grid independence could be ensured (see section 3.3), an informed decision with regard to appropriate turbulence models could be made (see section 3.4) and the ability of the chosen optimization algorithm to find an optimal answer, given a converged grid and suitable computational domain size, could be verified (see section 3.5).

In order to address the aim of this study, two computer experiments were conducted; one for windless and the other for crosswind conditions. The mesh that was validated in Chapter 3 was first transposed onto the computational model for windless conditions, where it became evident that some minor changes to the grid were necessary (see Table 36). It was this mesh that was ultimately used for the analysis of crosswind conditions as well. The size of the computational domain was validated for both

cases by extracting the x-, y- and z-force components acting on various sections of the train body and determining the boundary locations at which the components remain insensitive to further changes in the domain. The resultant domains may be seen in Table 16 for windless and Table 28 for crosswind conditions. An exhaustive description of the boundary conditions that were used to mimic the respective flow conditions can be seen in section 4.2 for windless conditions and 5.1 for crosswind conditions. Finally, the total length of the train remained unchanged for both cases at 120m, i.e., two locomotives and four passenger cars. In addition, the profile of the cross-section of the train body remained constant and can be seen in Figure 71.

In order to optimize the nose geometry for a given load case, a response surface was first generated by obtaining data points that describe the design space by making use of simulation. In the case of windless conditions the design space was sampled by making use of a 5-level full factorial experimental design, while in the case of crosswind conditions the Latin Hypercube sampling method with twenty-seven design points was used. The radial basis function with thin spline method was used to connect the data points in order to generate the surrogate models associated with each respective load case. Finally, the SHERPA search algorithm was used to find the optimal solution for windless conditions as well as the Pareto optimal front for crosswind conditions.

## 6.2. Conclusions

The Ahmed's body validation case was completed first. During the study, the back slant angle was systematically varied and the ability of various turbulence models to accurately predict the flow structures associated with a given slant angle as well as the drag coefficient brought about by them, were assessed. It was found that the Linear Pressure-Strain Reynold's stress model (RSM LPS) and the  $k-\omega$  SST model performed best with an average deviation from the experimental results for the total drag of 8.71% and 13.87%, respectively. In addition, the RSM LPS model predicted the component-wise trends of the experimental data with the greatest accuracy and most notably, it was the only model able to capture the behaviour of the partial nose drag component with a variation in the slant angle. This can possibly be attributed to the fact that the RSM LPS model does not make the same isotropic flow distribution assumption after stagnation has occurred, that the eddy viscosity models do. Bearing the importance of the flow structures surrounding the train nose, in particular under crosswind conditions, in mind, the advantageous nature of the RSM LPS turbulence model becomes clear.

The proposed optimization algorithm, i.e., the SHERPA search algorithm, was also evaluated by making use of the Ahmed's body. Both the RSM LPS as well as the  $k-\omega$  SST model were considered with the RSM LPS model able to predict the optimal slant angle within 2.49% of the experimental result and the associated minimum drag coefficient within 13.56%. The  $k-\omega$  SST model did not fare as well and predicted the optimal slant angle and accompanying minimum drag coefficient within 18.74% and 23.19% respectively. The optimization algorithm validation study thus not only revealed that the SHERPA algorithm could be trusted but that the RSM LPS model is an appropriate choice of turbulence model also.

In light of the aforementioned, the optimization study of the train nose and tail under windless conditions was completed with confidence. The optimal geometry was found to have a nose-tip height

of 1.364m, an inflection point height of 2.73m and a nose length of 7.7m. The minimized drag force that resulted is 6.80kN (for the half-model) which is 30.36% less than the maximum drag force that can be actualized by the geometric parameters within their respective ranges. The most prominent correlation coefficient was found to exist between the nose length and the total drag acting on the body with a value of -0.89. In addition, the correlation plot of the aforementioned confirms the relationship found by (Raghunathan, et al., 2002) which states that increasing the length to height ratio of the nose beyond two, has a negligible impact on drag. This in turn served to bolster confidence in the computational model as well as the optimization software. It is further worth mentioning that it was the surrogate model generated by making use of the Radial basis function with the thin spline method, that was able to capture the phenomenon published by (Raghunathan, et al., 2002) and in so doing it cemented its further use for the optimization case of the train travelling under crosswind conditions.

Finally, it was found that the geometry that is most detrimental to the minimization of drag is the “notch back” configuration due to the second stagnation region between the hood and “windshield” that necessarily accompanies it. It is thus not entirely surprising that, although modest, the nose-tip and inflection point heights also influence the total drag force with correlation coefficients of -0.48 and -0.45 respectively.

The matter of the reliability of the aforementioned results has to be addressed however. For this, consider Table 20 which shows the discrepancy between the results predicted by the surrogate model for a given geometry and the simulation values obtained for the identical geometry, which was not used in the construction of the surrogate model; the greatest discrepancy between the results is -1.58% and as such, the surrogate model may be regarded as highly predictive.

Since the crosswind optimization case constitutes a multi-objective optimization namely the reduction of both the total drag acting on the train as well as the moment acting on the leading locomotive about the leese side rail, the deliverable is not a single optimized solution but rather a collection of optimized solutions (see Figure 126). The Pareto front which resulted from this study, indicated that there is only a 3.18% increase in the drag force from point ‘c’ to point ‘a’, while an increase of 9.40% in the rolling moment can be expected from point ‘a’ to point ‘c’. It is thus recommended to favour point ‘a’ since it is able to actualize the greatest reduction in the rolling moment, with little difference in the value of the total drag force. The geometry associated with the aforementioned has an inflection point height of 2.71m, a nose-tip height of 0.7m and a nose length of 7.7m. Furthermore, it is no coincidence that point ‘c’, which yields the maximum rolling moment on the Pareto front, has a nose-tip height of 1.5m. Rather, the correlation plots obtained from the optimization study showed that the most influential parameter in determining the rolling moment of the leading locomotive is the nose-tip height, with a correlation coefficient of 0.87 (see Figure 125). In fact, there is an almost linear relationship between an increase in nose-tip height and the rolling moment.

With regard to the objective of minimizing the total drag acting on the train when subjected to crosswind, the behaviour found by (Raghunathan, et al., 2002) is preserved, i.e., an increase in nose length reduces the total drag acting on the train with a predicted correlation coefficient of -0.83. It is interesting to note that an increase in nose length also has the effect of lowering the rolling moment, so

that it becomes clear that the parameter that causes the conflict between the two objectives is the nose-tip height. Consider that under windless conditions it was determined that an increase in the nose-tip height, has the effect of decreasing the total drag acting on the train. This is a consequence of the air stagnating on the nose-tip and subsequently distributing itself between the upper and lower portions of the train. The air that is now compelled to flow beneath the train quickly short circuits out the sides beneath the train nose, rather than flowing down the length of the train which offers considerably more resistance. For the case of the rolling moment about the leaside rail however, raising the nose-tip, raises the center-of-pressure and thus increases the effective moment arm.

At this point however the question of the reliability of the results and the relationships that were either confirmed or established by the study of the train subjected to windless conditions, arises. Consider then that the greatest deviation between the results predicted by the surrogate model and those predicted by the simulation is 1.59% (see Table 34 for comprehensive results), so that a large measure of confidence in the results presented above is justified.

Finally, there is the question of how a given optimized geometry fares when exposed to the other's load conditions. An interpolation reveals that the nose shape optimized under windless conditions experiences a leaside rolling moment acting on its leading vehicle of 100.73kNm and a drag force of 14.87kN when exposed to the crosswind load case. When comparing these values to those associated with the optimal geometry (point 'a') under crosswind conditions, a reduction of 1.50% in the value of the total drag force from 15.09kN to 14.87kN can be observed, while the rolling moment has increased by 7.72 % from the optimal value of 93.51kNm to 100.73kNm. On the other hand, the nose geometry that was optimized for crosswind conditions now experiences a drag force of 14.01kN when subjected to windless conditions. This constitutes an increase of 3.04% from the minimum achievable drag force of 13.60kN, associated with the nose geometry that was optimized for windless conditions. In conclusion, both nose geometries perform well aerodynamically. The choice of which of these ought to be manufactured and implemented however, lies with the management of Transnet Engineering since the prerogative of which load case, i.e., windless or crosswind, as well as which optimization goal, i.e., drag reduction or crosswind stability is most important, is determined by them.

### 6.3. Recommendations

The following recommendations are made for future work:

- A study into the effect that the thickness of the boundary layer has on the optimal solution could prove useful. Consider; the optimal solutions reported on in this document are for a train with a total length of 120m. Whether these relationships, especially for that of the total drag force acting on the body, remains valid for different train lengths can be of interest.
- In the assumptions discussed in Chapter 1 it was mentioned that geometric irregularities, e.g., inter-carriage gaps were omitted in the train model that was used for the optimization study. There does however, exist the possibility of characterizing a repeat load on the train body to account for these, rather than disregarding them entirely.

- Another characterization possibility for the rail simulation environment is the ballast that lies beneath the train; attention may be given to a representative roughness offered by the ballast or the typical offset that exists between the average height of the exposed ballast surface and the top of the rail.
- As mentioned in section 2.2.3, there exist a number of challenges in rail. It may be that the nose geometry that was optimized for here, while addressing the optimization goals set before it, exacerbates one of these other issues. Attention may thus be given to the effect that the variables reported on here, i.e., nose length, nose-tip height and inflection point height has on one of these challenges.
- The crosswind optimization was completed for a steady incoming wind of 100 km/h at 10m off the ground, without any gust loading being taken into consideration. Attention may thus be given to how the optimized geometry fares when exposed to gust loading.
- This study made use of RANS turbulence models that have an infamous inability to predict the lift force of bodies in close ground proximity. Since the optimization goal used in the crosswind study contains the lift force component, the results obtained from said study may be scrutinized by making use of LES for example.

## Bibliography

- Ahmed, S. R., 1981. Wake structure of typical automobile shapes.. *Transactions of the ASME, Journal of Fluids Engineering.*, Volume 103, pp. 162-169.
- Ahmed, S. R., Ramm, R. & Faltin, G., 1984. *Some Salient Features of the Time-Averaged Ground Vehicle Wake.*, Detroit: SAE Paper 840 300.
- Andersson, E., Haggstrom, J., Sima, M. & Stichel, S., 2004. Assessment of train-overturning risk due to strong cross-winds. *Proceedings of Institution of Mechanical Engineers Part F: Journal of Rail and Rapid Transit*, Volume 218, pp. 213-223.
- Arnold, K. O., 1965. *Untersuchungen über den Einfluss der Absaugung durch einen Einzelschlitz auf die turbulente Grenzschicht in anliegender und abgelöster Strömung.*, TH Braunschweig: Unpublished Report of Institut für Strömungsmechanik..
- Auckland Transport, 2014. *flickr*. [Online]  
Available at: <https://www.flickr.com/photos/aucklandtransport/12940899704/in/photostream/>  
[Accessed 11 December 2018].
- Baker, C. J., 2008. *The Flow Around High Speed Trains*. Milano, Italy, s.n.
- Baker, C. J., 2010. The flow around high speed trains. *Journal of Wind Engineering and Industrial Aerodynamics*, 98(6-7), pp. 277-298.
- Baker, C. J., 2011. *A meta-analysis of train crosswind aerodynamic force coefficient data*. Amsterdam, Holland, s.n.
- Baker, C. J., 2014. A framework for the consideration of the effects of crosswinds on trains.. *Journal of Wind Engineering and Industrial Aerodynamics*, Volume 123, pp. 130-142.
- Baker, C. J., 2014. A review of train aerodynamics Part 1 - Fundamentals. *The Aeronautical Journal*, March, 118(1201), p. 203.
- Baker, C. J., 2014. A review of train aerodynamics Part 2 - Applications. *The Aeronautical Journal*, 118(1202), pp. 345-382.
- Baker, C. J. et al., 2009. Crosswind effects on road and rail vehicles. *Vehicle Systems Dynamics*, 47(8), pp. 983-1022.
- Baker, C. J. et al., 2001. *The slipstream and wake of a high speed train*. s.l., s.n., pp. 83-99.
- Baker, C. J., Gilbert, T. & Jordan, S., 2013. *The validation of the use of moving model experiments for the measurement of train aerodynamic parameteres in the open air*. Sydney, Australia, s.n.

- Baker, C. J. et al., 2012. Transient aerodynamic pressures and forces on trackside and overhead structures due to passing trains. Part 1 Model scale experiments. *Journal of Rail and Rapid Transit*, Volume 228, pp. 36-69.
- Baker, C. J. et al., 2012. Transient aerodynamic pressures and forces on trackside and overhead structures due to passing trains. Part 2 Standards applications. *Journal of Rail and Rapid Transit*, Volume 228, pp. 36-69.
- Baker, C. J. et al., 2013. *Full-scale measurement and analysis of train slipstreams and wakes. Part 2 Gust analysis*. s.l., s.n.
- Baker, C. J. et al., 2013. *Full-scale measurement and analysis of train slipstreams and wakes: Part 1 Ensemble averages*. s.l., s.n.
- Beagles, A. E. & Fletcher, D. I., 2012. *The aerodynamics of freight; approaches to save fuel by optimising the utilisation of container trains*. London, s.n.
- Bearmann, P. W., 1979. *Bluff body flows applicable to vehicle aerodynamics*. Niagra Falls, s.n., pp. 1-11.
- Bouferrouk, A. et al., n.d. *Calculation of the cross wind displacement of pantographs*. Milano, Italy, s.n.
- Brockie, N. J. W. & Baker, C. J., 1990. The aerodynamic drag of high speed trains. *Journal of Wind Engineering and Industrial Aerodynamics*, Volume 34, pp. 273-290.
- Buchheim, R., 1983. *Aerodynamik bei leichten Nutzfahrzeugen - heute und morgen*. s.l., s.n.
- Buchheim, R., Deutenbach, K. R. & Lückoff, H. J., 1981. *Necessity and Premises for Reducing the Aerodynamic Drag of Future Passenger Cars*. Detroit: SAE Paper 810185.
- Buchheim, R. & Leie, B., 1982. *The development of the new Audi 100 - a new approach in aerodynamic passenger car design*. Wolfsburg, s.n.
- Buchheim, R., Leie, B. & Lückoff, H. J., 1983. Der neue Audi 100-Ein Beispiel fuer Konsequente Aerodynamische Personenwagen-Entwicklung. *ATZ*, Volume 85, pp. 419-425.
- Buchheim, R., Piatek, R. & Walzer, P., 1979. *Contribution of aerodynamics to fuel economy improvements for future passenger cars*. Washington , s.n.
- Carr, G. W., 1968/9. *The Aerodynamics of Basic Shapes for Road Vehicles, Part 2, Saloon Car Bodies*, s.l.: MIRA-Rep. No. .
- CEN, 2010. *Railway Applications - Aerodynamics - Part 6: Requirements and test procedures for cross wind assessment*, s.l.: BS EN 14067-6:2010.
- CEN, 2010. *Railway Applications - Aerodynamics requirements and test procedures for aerodynamics in tunnels*, s.l.: BS EN 14067-5:2006+A1:2010.

CEN, n.d. *Railway Applications - Aerodynamics Part 3 Aerodynamics in tunnels*, s.l.: BS EN 14067-3:2003.

Chase, N. et al., 2014. *A Benchmark Study of Multi-Objective Optimization Methods*, East Lansing: Red Cedar Technology.

Chase, N. et al., Retrieved on: 24 November 2016. *A Benchmark Study of Optimization Search Algorithms*, East Lansing: Red Cedar Technology.

China Daily, 2007. *Four die after train derails in China*. [Online]  
Available at: [http://www.chinadaily.com.cn/china/2007-02/28/content\\_816203.htm](http://www.chinadaily.com.cn/china/2007-02/28/content_816203.htm)  
[Accessed 11 05 2017].

Coles, D. & Wadcock, A. J., 1979. A Flying-Hot-Wire Study of Two-Dimensional Mean Flow Past a NACA 4412 Airfoil at Maximum Lift. *AIAA-Journal*, 17(4), pp. 321-328.

Cook, N. J., 1986. *The Designer's Guide to Wind Loading of Building Structures: Static Structures*. s.l.: Butterworths, ISBN-10: 0408008709.

Copley, J., 1987. The three-dimensional flow around railway trains. *Journal of Wind Engineering and Industrial Aerodynamics*, 26(1), pp. 22-52.

Deb, K., 2001. *Multi-Objective Optimization using Evolutionary Algorithms*. Chichester, United Kingdom: Wiley.

Deb, K., Pratap, A., Agarwal, S. & Meyarivan, T., 2002. A fast and elitist multi-objective genetic algorithm: NSGA-II. *IEEE Transactions on Evolutionary Computation*, 6(2), pp. 182-197.

Department: Transport , June 2017. *National Rail Policy. Draft White Paper*, s.l.: Department: Transport Republic of South Africa.

Diedrichs, B., 2003. *On computational fluid dynamics modelling of crosswind effects for high-speed rolling stock*. s.l., s.n.

Diedrichs, B., 2005. *Computational methods for crosswind stability of railway trains*, s.l.: KTH Engineering Sciences report TRITA AVE.

Dorigati, F., 2013. *Rail vehicles in crosswinds; analysis of steady and unsteady aerodynamic effects through static and moving model tests.*, Birmingham, UK: PhD thesis, University of Birmingham.

East Japan Railway Company, 2006. *Current Measures in Response to the Uetsu Line Accident*. [Online]  
Available at: <http://www.jreast.co.jp/E/press/20060101/index.html>  
[Accessed 11 05 2017].

Ferreira, A. D. & Vaz, P. A., 2004. Wind tunnel study of coal dust release from train wagons. *Journal of Wind Engineering and Industrial Aerodynamics*, 92(5), pp. 65-577.

Gawthorpe, R. G., 1978. Aerodynamics of trains in the open air. *Railway Engineer International*, 3(3), pp. 7-12.

George, A. R., 1979. *Aerodynamics of simple bluff bodies including effects of body shape, ground proximity and pitch.* Niagra Falls, s.n., pp. 71-81.

Gibson, M. M. & Launder, B. E., 1978. Ground effects on pressure fluctuations in the atmospheric boundary layer. *Journal of Fluid Mechanics*, 86(3), pp. 491-511.

Gustafsson, M. et al., n.d. *Railway pollution - sources, dispersion and measures. A literature review, Swedish National Road and Transport Research Institute (VTI)*, s.l.: Report 602, ISSN: 0347-6030.

Hemida, H. N., 2006. *Large eddy simulation of the flow around simplified high speed trains under side wind conditions*, Goteborg, Sweden: Licentiate of Engineering thesis, Chalmers University of Technology.

Hinterberger, C., Garcia-Villalba, M. & Rodi, W., n.d.. *Large Eddy Simulation of flow around the Ahmed body*, Karlsruhe: Institute for Hydromechanics, University of Karlsruhe.

Hucho, W. H., 1986. *Aerodynamics of road vehicles*. London: Butterworths.

Hucho, W. H., Janssen, L. J. & Emmelmann, H. J., 1976. *The Optimization of Body Details - A Method for Reducing the Aerodynamic Drag of Road Vehicles.*, Detroit: SAE Paper 760 185.

Hummel, D., 1978. On the vortex formation over a slender wing at large angles of incident.. *AGARD CPP*, Volume 247, pp. 15-1 - 15-17.

Ido, A., Saitou, S., Nakade, K. & Iikura, S., 2008. *Study on under-floor flow to reduce ballast flying phenomena*. Seoul, s.n.

Janssen, L. J. & Hucho, W. H., 1975. Aerodynamische Entwicklung von VW olf und Scirocco.. *ATZ*, Volume 77, pp. 1-5.

Johnson, T., 2013. *Development of a pantograph sway probability model*, Birmingham, UK: International Workshop on Train aerodynamics .

Johnson, T. & Dalley, S., 2002. 1/25 scale moving model tests for the TRANSAERO Project.. *TRANSAERO - A European Initiative on Transient Aerodynamics for Railway System Optimisation.*, Volume 79, pp. 123-135.

Jordan, S. C., Johnson, T., Sterling, M. & Baker, C. J., 2008. Evaluating and modelling the response of an individual to a sudden change in wind speed. *Building and Environment*, Volume 43, pp. 1521-1534.

Kaltenbach, H. J., n.d. *DeuFraKo Project - Aerodynamics in Open Air (AOA) WP 1 Underfloor Aerodynamics* , s.l.: Summary Report.

Krajnović, S., 2008. *Improvement of aerodynamic properties of high-speed trains by shape optimization and flow control*. s.l., 8th World Congress on Railway research (WCRR2008).

- Kwon, H. B. & Park, C. S., 2006. *An experimental study on the relationship between ballast flying phenomenon and strong wind under high speed train*. Montreal, s.n.
- Langtry, R., Kuntz, M. & Menter, F. R., 2004. *Drag Prediction of Engine-Airframe Interference Effects with CFX-5*, Reno: AIAA Paper 2004-0392.
- Langtry, R. & Menter, F. R., 2009. A Correlation-Based Transition Model using Variables for Unstructured Parallelized CFD Codes.. *AIAA Journal*, 47(12).
- Lay, W. E., 1933. Is 50 miles per gallon possible with correct streamlining?. *SAE Journal*, Volume 32, pp. 144-156 and 177-186.
- Lienhart, H., Becker, S. & Stoots, C., n.d. *ERCRAFT Classic Database*. [Online] Available at: [http://cfm.mace.manchester.ac.uk/cgi-bin/cfd/db/prpage.cgi?82&EXP&database/cases/case82/Case\\_data&database/cases/case82&cas82\\_head.html&cas82\\_desc.html&cas82\\_meth.html&cas82\\_data.html&cas82\\_refs.html&cas82\\_resol.html&1&1&1&0&0&unknown](http://cfm.mace.manchester.ac.uk/cgi-bin/cfd/db/prpage.cgi?82&EXP&database/cases/case82/Case_data&database/cases/case82&cas82_head.html&cas82_desc.html&cas82_meth.html&cas82_data.html&cas82_refs.html&cas82_resol.html&1&1&1&0&0&unknown) [Accessed 19 07 2017].
- Lienhart, H., Stoots, C. & Becker, S., 2000. *Flow and turbulence structures in the wake of a simplified car model (Ahmed model)*. Stuttgart, s.n.
- Li, R., Xu, P., Peng, Y. & Ji, P., 2016. Multi-Objective optimization of a high-speed train head based on the FFD method. *Journal of Wind Engineering and Industrial Aerodynamics*, Volume 152, pp. 41-49.
- Liu, Y. & Moser, A., 2003. *Numerical modeling of airflow over the Ahmed body*. s.l., s.n., pp. 507-512.
- Mair, W. A., 1969. Reduction of base drag by boat-tailed afterbodies in low-speed flow.. *Aeronautical Quarterly*, Volume 20, pp. 307-320.
- Mair, W. A. & Stewart, A. J., 1985. The flow past yawed slender bodies, with and without ground effects. *Journal of Wind Engineering and Industrial Aerodynamics*, 18(3), pp. 301-328.
- Menter, F. R., 1992. Influence of freestream values on k-w turbulence model predictions.. *AIAA-Journal*, 30(6), pp. 1657-1659.
- Menter, F. R., 1994. Two-Equation Eddy-Viscosity Turbulence Models for Engineering Applications. *AIAA-Journal*, 32(8), pp. 269-289.
- Menter, F. R., 2009. Review of the shear-stress transport turbulence model experience from an industrial perspective.. *Int. J. of Comp. Fluid Dynamics*, 23(4), pp. 305-316.
- Menter, F. R., 2011. *Turbulence Modelling for Engineering Flows*, s.l.: ANSYS Inc..
- Menter, F. R., Langtry, R. & Völker, S., 2006. Transition Modelling for General Purpose Codes.. *Journal of Flow Turbulence and Combustion*, 77(1-4), pp. 277-303.

- MeteoSwiss, F. O. o. M. a. C., 2014. *The Federal Council. The portal of the Swiss government.* [Online] Available at: <https://www.meteoswiss.admin.ch/home/weather/gefahren/explanation-of-the-danger-levels/wind.html> [Accessed 2017].
- Ming, L., Bin, L., Miao, Y. & Dahai, W., 2016. *Multi-Objective Integrated Optimization of the Aerodynamic Shape Design of the Head-Type for a High Speed Electric Multiple Unit*. Stirlingshire, Proceedings of the Third International Conference on Railway Technology: Research, Development and Maintenance.
- Monnoyer, F., Lorriaux, E. & Bourabaa, N., 2006. *Aerodynamic optimization of railway motor coaches*, s.l.: The World Congress on Railway Research.
- Morel, T., 1978. The effect of base slant on the flow pattern and drag of three-dimensional bodies with blunt ends.. In: *G. Sovran, T. Morel and W.T. Mason, ed. Aerodynamic Drag Mechanisms of Bluff bodies and Road Vehicles.* . New York: Plenum Press, pp. 191-226.
- Nouzawa, T. et al., 1992. *Unsteady wake analysis of the aerodynamic drag of a notchback model with critical afterbody geometry*. Detroit, s.n.
- O'Neil, H., 2008. Gauge modelling of West Coast Main Line tilting trains. *Proceedings of the Institution of Mechanical Engineers Part F: Journal of Rail and Rapid Transit*, Volume 222, pp. 235-253.
- Potthoff, J., 1982. *The aerodynamic layout of UNICAR research vehicle.* Wolfsburg, s.n.
- Pratap, A., Deb, K., Agarwal, S. & Meyarivan, T., 2000. *A fast elitist non-dominated sorting geneticalgorithm for multi-objective optimization: NSGA-II*, Kanpur, India: in KanGAL report 200001, Indian Institute of Technology.
- Quinn , A. D. et al., 2010. A full-scale experimental and modelling study of ballast flight under high-speed trains. *Proceedings of the Institution of Mechanical Engineers, Part F: Journal of Rail and Rapid Transit*, 224(2), pp. 61-74.
- Quinn, A. & Hayward, M., 2008. *Full scale aerodynamic measurements underneath a high speed train*. Milano, Italy, s.n.
- Raghunathan, R. S., Kim, H. D. & Setoguchi, T., 2002. Aerodynamics of high speed railway trains. *Progress in Aerospace sciences*, 38(6-7), pp. 469-514.
- RAPIDE, 2001. *Railway aerodynamics of passing interaction with dynamic effects.* , Cologne, Germany: Synthesis report, Aerodynamics Workshop.
- Roache, P. J., 1998. *Verification and Validation in Computational Science and Engineering*. Albuquerque, New Mexico: Hermosa Publishers.
- Rochard, B. P. & Schmid, F., 2000. *A review of methods to measure and calculate train resistances*. s.l., s.n.

- Sanz-Andres, A., Laveron, Cuerva, A. & Baker, C., 2004. Vehicle-induced loads on pedestrian barriers. *Journal of Wind Engineering and Industrial Aerodynamics*, Volume 92, pp. 403-426.
- Schulte-Werning, B., Heine, C. & Matschke, G., 2003, 2, pp 332 -333. *Unsteady wake characteristics of high speed trains*. s.l., s.n.
- Scibor-Rylski, A. J., 1984. *Road Vehicle Aerodynamics*. 2nd ed. London: Pentech Press.
- Scibor-Rylski, A. J., 1984. *Road Vehicle Aerodynamics*. 2nd ed. London: Pentech Press.
- Shuanbao, Y. et al., 2014. Optimization design for aerodynamic elements of high speed trains. *Computers & Fluids*, Volume 95, pp. 56-73.
- Sims-Williams, D., Dominy, R. & Howell, J., 2001. *An investigation into large scale unsteady structures in the wake of real and idealised hatchback car models*. Detroit, s.n.
- Sterling, M., Baker, C. J., Jordan, S. C. & Johnson, T., 2008. *A study of the slipstreams of high speed passenger trains and freight trains*. s.l., s.n.
- Strelets, M., 2001. Detached Eddy Simulation of Massively Separated Flows. *AIAA Paper 2001-0879*.
- Tain, H. Q., 2007. *Train Aerodynamics*. Beijing: China Railway Publishing House.
- Temple, J. & Johnson, T., 2003. *RSSB Review of slipstream effects on platforms*, s.l.: Rail Safety and Standards Board.
- Terram, n.d. *Terram*. [Online]  
Available at: <http://www.terram.com.au/market-sector/railways/?aaopen=ballast-over-weak-subgrades>  
[Accessed 11 December 2018].
- The Railway Technical Website, 2018. *The Railway Technical Website*. [Online]  
Available at: <http://www.railway-technical.com/trains/rolling-stock-index-1/bogies.html>  
[Accessed 11 December 2018].
- TSI, 2008/232/EC. *EU Technical Specification for Interoperability Relating to the 'Rolling Stock' Sub-System of the Trans-European High-Speed Rail System*, s.l.: HS RST TSI.
- TSI, 2008/232/EC. *EU Technical Specification for Interoperability Relating to the 'Rolling Stock' Sub-System of the Trans-European High-Speed Rail System*, s.l.: HS RST TSI.
- Vardy, A. E., 2008. Generation and alleviation of sonic booms from rail tunnels. *Proceedings of the Institution of Civil Engineers - Engineering and Computational Mechanics*, 161(3), pp. 107-119.
- Vino, G. et al., 2005. Flow structures in the near wake of the Ahmed model. *Journal of Fluids and Structures*, Volume 20, pp. 673-695.

Watanabe, S., Hiroyasu, T. & Miki, M., 2002. *Neighborhood Cultivation Genetic Algorithm for Multi-Objective Optimization Problems*. s.l., s.n., pp. 198-202.

Wilcox, D. C., 2006. *Turbulence modelling for CFD. 3rd ed.* , s.l.: DCW Industries, Inc..

Wu, D., 2004. *Predictive prospects of unsteady detached-eddy simulations in industrial external aerodynamic flow simulations.*, Aachen, Germany: Diploma thesis, Lehrstuhl für Strömungslehre und Aerodynamisches Institut .

Your Dictionary, n.d. *Your Dictionary*. [Online]

Available at: <https://www.yourdictionary.com/cowcatcher>

[Accessed 11 December 2018].

## Appendix

### Appendix A

This appendix is supplementary to section 3.4 in Chapter 3. Described herein, is the construction of the prism layer mesh that was used for the Ahmed's body validation case, in conjunction with turbulence models which make use of a high, or all,  $y^+$  - boundary layer mesh.

#### Prism Layer Mesh Construction

##### *High $y^+$ -mesh:*

The k- $\epsilon$  model as well as the Reynolds stress model makes use of a wall function to model the near-wall flow behaviour and does not solve the vicious sublayer directly. The  $y^+$ -value for this mesh must lie in the following region;  $30 < y^+ < 300$ .

Determine the first cell height:

$$C_f = 0.058Re^{-0.2} \quad (23)$$

$$\therefore C_f = 0.058(768\,000)^{-0.2} = 3.858 \times 10^{-3} \quad (24)$$

$$\tau_w = \frac{1}{2} C_f \rho V_\infty^2 \quad (25)$$

Substitute Eq. 24 into Eq. 25:

$$\tau_w = \frac{1}{2} (3.858 \times 10^{-3})(1.18415)(40^2) = 3.65 \quad (26)$$

$$U_\tau = \sqrt{\frac{\tau_w}{\rho}} \quad (27)$$

Substitute Eq. 26 into Eq. 27:

$$U_\tau = \sqrt{\frac{3.65}{(1.18415)}} = 1.76 \text{ m/s} \quad (28)$$

Select  $y^+ \approx 196.61$ ;

$$y = \frac{y^+ \mu}{U_\tau \rho} \quad (29)$$

Substitute  $y^+$ -value and Eq. 28 into Eq. 29:

$$y = \frac{196.61(1.85508 \times 10^{-5})}{1.76(1.18415)} = 1.75 \times 10^{-3} \text{ m} \quad (30)$$

Furthermore, the high  $y^+$ -prism layer mesh consisted of three elements that were stretched by a factor of 1.3. The total height of the prism layer corresponds to that of the low  $y^+$ -mesh, i.e., seven millimeters.

### *Low $y^+$ - Mesh*

The SST  $k-\omega$  model resolves the viscous sublayer directly and as such  $y^+ \approx 1$ . However, since heat transfer is not considered in the simulation  $y^+$  -values of less than five are also acceptable. It is worth noting at this point that the Reynolds number for this problem is large and as such, a very fine mesh resolution in the near-wall region can be expected;

Determine the first cell height:

Select  $y^+ \approx 1.247^*$ ;

$$y = \frac{y^+ \mu}{U_\tau \rho} \quad (31)$$

Substitute  $y^+$ -value and Eq. 28 into Eq. 31:

$$y = \frac{1.247(1.85508 \times 10^{-5})}{1.76(1.18415)} = 1.11 \times 10^{-5} \text{ m} \quad (32)$$

*\*(This  $y^+$ -value was not chosen arbitrarily; rather multiple simulations were performed for various  $y^+$ -values. The  $y^+$ -value that was ultimately chosen, is that value which yielded acceptable  $y^+$ -values for all the elements in the domain yet also yielded the least number of cells through the prism layer thickness.)*

## Appendix B

This appendix is supplementary to section 4.3.2 in Chapter 4. It describes the modifications made to the transposed Ahmed's body mesh along with the reasoning for said modifications. The procedure followed to coarsen the transposed mesh in order to ensure that it is more computationally manageable, is also discussed.

Since the construction of the Ahmed's body mesh has already been discussed at length in section 3.3.2, only a brief overview of the parameters used to create said mesh are given in Table 36 and Table 37. These tables also relay the parameters used to create the mesh that was transposed onto the train from the Ahmed's body as well as a third, coarser mesh that was created in an attempt to manage the cell count associated with the train simulation. Consider first, the differences between the Ahmed's body mesh and the transposed mesh; what is immediately noticeable from Table 36 and Table 37 is the increased number of cells through the boundary layer of the train model in comparison to that of the Ahmed's body. These cells were added in order to ensure that the  $y^+$ -values of the respective meshes lie in their permissible regions, since the train experiences a marked increase in the velocity of the incoming air. The boundary layer stretching factor of the transposed meshes were also increased to this end, i.e., to ensure valid  $y^+$ -values while simultaneously attempting to keep the cells added per mesh to a minimum. Furthermore, the surface element sizes on the train body of the transposed mesh had to be decreased slightly in order to avoid erratic indentations of the boundary layer mesh. The minimum surface cell size on the ground of the transposed low  $y^+$ -mesh was also reduced to 2.13 percent of the base size, in an attempt to improve the aspect ratios of these cells and while this approach may have been successful, it did lead to a considerable increase in the cell count of the mesh. Another factor which contributed to the considerable cell count associated with the transposed mesh is the target size of the surface cells on the ground. This led to the construction of a third, coarser, more computationally manageable mesh. The coarsened grid assumed a minimum surface cell size on the ground of 10 percent of the base size, while the target size was increased to 100 percent of the base size. The surface cell size specification on the train body was abandoned entirely and since the train falls inside the "near-wake" region, the surface cells will tend to 5.12 percent of the base size.

Low $y^+$ -Mesh Grid Specifications	Ahmed's Body Mesh	Train Body Mesh	
		Transposed Mesh	Coarsened Mesh
<b>Far-field</b>			
Boundary Layer Stretching Factor	1.1	1.5	1.5
Number of cells normal to ground	3	10	10
Surface cell size on ground as percentage of base size;			
<i>Minimum</i>	10	2.13	10
<i>Target</i>	30	30	100
<b>Proximity of the body, the near-wake and far-wake</b>			
Boundary Layer Stretching Factor	1.4	1.5	1.5
Number of cells normal to ground	15	24	24
Surface cell size on ground as percentage of base size;			
<i>Minimum</i>	10	2.13	10
<i>Target</i>	30	30	100
Volume cell size as percentage of base size;			
<i>Near-Wake</i>	5.12	5.12	5.12
<i>Far-Wake</i>	7.68	7.68	7.68
<b>Body Surface</b>			
Boundary Layer Stretching Factor	1.3	1.3	1.5
Number of cells normal to surface	20	24	24
Surface cell size on body as percentage of base size;			
<i>Minimum</i>	2.13	2.1	-
<i>Target</i>	4.27	4.24	-

Table 36: The mesh settings used for the construction of a low  $y^+$ -mesh for the Ahmed's body, the transposed mesh for the train body and the coarsened mesh for the train body.

High $y^+$ -Mesh Grid Specifications	Ahmed's Body Mesh	Train Body Mesh	
		Transposed Mesh	Coarsened Mesh
<b>Far-field</b>			
Boundary Layer Stretching Factor	1.1	1.5	1.5
Number of cells normal to ground	3	10	10
Surface cell size on ground as percentage of base size;			
<i>Minimum</i>	10	10	10
<i>Target</i>	30	30	100
<b>Proximity of the body, the near-wake and far-wake</b>			
Boundary Layer Stretching Factor	1.3	1.5	1.5
Number of cells normal to ground	3	9	9
Surface cell size on ground as percentage of base size;			
<i>Minimum</i>	10	10	10
<i>Target</i>	30	30	100
Volume cell size as percentage of base size;			
<i>Near-Wake</i>	5.12	5.12	5.12
<i>Far-Wake</i>	7.68	7.68	7.68
<b>Body Surface</b>			
Boundary Layer Stretching Factor	1.3	1.5	1.5
Number of cells normal to surface	3	10	10
Surface cell size on body as percentage of base size;			
<i>Minimum</i>	2.13	2.1	-
<i>Target</i>	4.27	4.24	-

Table 37: The mesh settings used for the construction of a high  $y^+$ -mesh for the Ahmed's body, the transposed mesh for the train body and the coarsened mesh for the train body

## Appendix C

This appendix is supplementary to section 4.3.3 in Chapter 4. Described here is the GCI method completed on three cases; first, for the transposed mesh with a stationary ground boundary condition. Second, the transposed mesh with a moving ground boundary condition and third, the coarsened mesh with a moving ground. The purpose of this study was not only to investigate the effect of a moving ground on the various force components, but also to ensure the ability of the coarsened mesh to yield accurate results.

For the first case, i.e., the transposed mesh with a stationary ground boundary condition, the low  $y^+$ -mesh shows convergence for the  $x$ - and  $y$ -forces while the  $z$ -force displays erratic behaviour as a function of mesh refinement level. In contrast, all the force components for the train have converged for the high  $y^+$ -mesh and as such the grid may be considered as converged as well. Since the low and high  $y^+$ -meshes are identical save for the boundary layer construction and bearing in mind that the  $y^+$ -values for the low  $y^+$ -mesh all lie in the permissible range, the divergence of the  $z$ -force for the low  $y^+$ -mesh is probably due to the choice of turbulence model. This may be more clearly seen in Figure 176 (see Appendix I), which shows the  $z$ -force components for the nose, tail, coaches, top and bottom of the train. What is evident from the figure is that it is the  $z$ -force components of the coaches and the tail of the train specifically, which have not converged. In addition, the  $z$ -force on the bottom of the train fluctuates slightly more than that of the top. It is therefore plausible that the turbulence beneath the coaches and tail of the train is anisotropic in nature, which would clarify why it is that the forces predicted by the SST  $k-\omega$  do not reach stability while those predicted by the LPS Two-Layer model, which is better suited to anisotropic turbulence, does.

The second case is that of the train with a transposed mesh but with a moving ground. While the  $x$ - and  $y$ -force components remain converged for both the low  $y^+$ - and the high  $y^+$ -meshes, the  $z$ -force component now diverges in the case of the high  $y^+$ -mesh as well. Since the high  $y^+$ -mesh remains unchanged between the first and second case, the reason for the divergence can only be the turbulence introduced by the movement of the ground. This is further indicated by the fact that both mesh types show an increase in divergence in the lift force from the first to the second case. Furthermore Figure 176 (Appendix I) shows that once again the portions of the train that are responsible for this divergence in the lift force are the coaches and tail. The lift force predicted for the nose region of the train by the LPS Two-Layer turbulence model in conjunction with the high  $y^+$ -mesh has however stabilized and may be trusted.

The final case that was considered for the grid convergence study is that of the coarsened mesh with a moving ground. From Table 44 and Table 45 it is clear that coarsening the mesh has no influence on the converged state of the drag and side forces. The lift force however remains unstable irrespective of mesh-type and turbulence model used. Figure 176 (Appendix I) further shows that the cause of the instability of the lift force for the low  $y^+$ -mesh is the erratic behaviour of the nose, coaches and tail of the train. In contrast the high  $y^+$ -mesh indicates a stabilized lift force on the nose and tail of the train so that the instability is due only to the coaches, specifically at the bottom half of the train. Therefore, even though the total lift force of the train has not converged for the high  $y^+$ -mesh, that of the nose and tail can be informative. The lift values predicted for the tail should however be used cautiously since the  $z$ -

force of the transformed mesh has not stabilized to the same extent as that of the coarsened mesh. This is presumably due to the fact that the coarser elements aren't able to capture the turbulent eddies as accurately. Be that as it may, it is clear that there is not a compromise in accuracy for the x- and y-forces when the coarser mesh rather than the transformed mesh is used (see Table 46 and Table 47), while the z-force component displays erratic behaviour irrespective of mesh or turbulence model used; it would therefore be unwise to use the lift force as an optimization objective since it would only serve to add noise to the solution. In addition the coarser mesh offers a less computationally expensive model hereby making the optimization of the train nose viable. Finally, as indicated by Table 48 and Table 49 the variation in x- and y-forces as a function of mesh refinement level is negligible and based purely on the values relayed in these tables it is immaterial which mesh is chosen. However, when considering Figure 174 (Appendix I) it is clear that the drag force for the nose, tail and bottom of the train in the case of the low  $y^+$ -mesh have only stabilized at mesh refinement level two, i.e., the deviation in the forces fall below five percent from those associated with mesh refinement one. The drag force on the nose of the train in the case of the high  $y^+$ -mesh also only stabilized at mesh refinement level two, while all other forces are stable throughout. For the case of the side force acting on the train (Figure 175, Appendix I) both the low  $y^+$ - as well as the high  $y^+$ -meshes show force components that are stable throughout.

It would thus seem from the aforementioned that the coarsened high  $y^+$ -mesh with grid refinement level two used in conjunction with the LPS Two-Layer turbulence model is better suited to capturing the flow field around the train than the SST  $k-\omega$  model. Not only is the LPS Two-Layer model able to capture the lift force over the nose and tail of the train with reasonable accuracy but it also performs better for the drag force (Figure 174) and comparably well for the side force (Figure 175). As mentioned before, the superior performance of the LPS Two-Layer turbulence model may be attributed to its direct calculation of the components of the specific Reynolds stress tensor, as is the case with all Reynolds stress turbulence models. This allows the model to predict complex flows more accurately since the transport equations for the Reynolds stresses inherently account for complex effects such as turbulence anisotropy and irrotational vortices, both of which can present themselves in the external flow field surrounding the train. Since there may be instances where flow structures like the longitudinal, irrotational vortices interact with the train body to a larger extent, it is advisable to use the LPS Two-Layer model since the accurate prediction of these flows is essential to solving the forces acting on the train, or at the very least capturing their trends as a function of nose shape. The LPS Two-Layer model will therefore be used for the optimization of the train, not only because of the aforementioned but also because of this model's superior predictive abilities which were displayed in the Ahmed's body validation case, especially in the vicinity of the nose, and discussed in section 3.4.1.

Low y+-Mesh									
Mesh Refinement Level	Transposed Mesh [Stationary Ground]			Transposed Mesh [Moving Ground]			Coarsened Mesh [Moving Ground]		
	x-Force [N]	y-Force [N]	z-Force [N]	x-Force [N]	y-Force [N]	z-Force [N]	x-Force [N]	y-Force [N]	z-Force [N]
Refinement 1	7157.01	47527.10	308.90	6514.50	62315.73	-2583.88	6544.26	62353.87	-2654.39
Refinement 2	6923.76	48387.32	-210.52	6530.45	62320.07	-1430.31	6530.58	62408.19	-1684.99
Refinement 3	6880.94	44724.02	630.36	6550.64	62299.44	-958.47	6561.41	62467.74	-983.01
$f_{h=0}$	6871.31	47263.12	1148.16	6454.40	62314.56	-631.89	6555.18	61788.73	859.80
<b>Order of Convergence</b>	-3.20	2.74	0.91	0.44	2.94	-1.69	1.85	0.21	-0.74
<b>Relative Error</b>									
$\epsilon_{12}$	-0.0326	0.0181	-1.6815	0.0024	0.0001	-0.4464	-0.0021	0.0009	-0.3652
$\epsilon_{23}$	-0.0062	-0.0757	-3.9943	0.0031	-0.0003	-0.3299	0.0047	0.0010	-0.4166
<b>Grid Convergence Index</b>									
<b>GCI<sub>12</sub></b>	-0.0499	0.0069	3.3962	0.0115	0.00002	0.9443	0.0021	0.0113	1.6549
<b>GCI<sub>23</sub></b>	-0.0095	0.0290	8.0674	0.0146	0.0001	-0.6978	0.0047	0.0124	-1.8878
$\frac{GCI_{i+1,i+2}}{r^p GCI_{i,i+1}}$	1.03	0.98	1.47	1.00	1.00	-1.81	1.00	1.00	-1.58

Table 38: The results of the Grid Convergence Index study completed for the Low y+-Mesh. The transposed mesh as well as the coarsened mesh, as discussed in section 4.3.2, was considered. In the case of the transposed mesh both a stationary as well as a moving ground boundary condition was considered, while the coarsened mesh only considered a moving ground boundary condition. All results were obtained by making use of the SST k- $\omega$  turbulence model.

High y+-Mesh									
Mesh Refinement Level	Transposed Mesh [Stationary Ground]			Transposed Mesh [Moving Ground]			Coarsened Mesh [Moving Ground]		
	x-Force [N]	y-Force [N]	z-Force [N]	x-Force [N]	y-Force [N]	z-Force [N]	x-Force [N]	y-Force [N]	z-Force [N]
Refinement 1	7758.95	48576.28	2628.71	7074.80	66529.12	-2063.39	7028.79	66665.56	-2480.97
Refinement 2	7828.64	48594.28	2525.76	7129.06	66656.38	-1628.74	7125.61	66801.57	-1944.64
Refinement 3	7860.09	48751.95	2692.33	7121.68	66847.75	-1235.98	7250.28	66910.84	-782.09
$f_{h=0}$	7885.96	48573.96	2795.31	7137.60	66276.44	2446.54	6692.08	67357.27	-2940.34
Order of Convergence	-1.46	3.97	0.88	-3.65	0.75	-0.19	0.45	-0.39	1.38
Relative Error									
$\epsilon_{12}$	0.0090	0.0004	0.0392	0.0077	0.0019	-0.2106	0.0138	0.0020	-0.2162
$\epsilon_{23}$	0.0040	0.0032	0.0659	-0.0010	0.0029	-0.2411	0.0175	0.0016	-0.5978
Grid Convergence Index									
GCI <sub>12</sub>	-0.0205	0.0001	0.0792	-0.0111	0.0047	-2.7321	0.0599	-0.0130	0.2314
GCI <sub>23</sub>	-0.0092	0.0005	0.1334	-0.0015	0.0071	-3.1276	0.0761	-0.0104	0.6400
$\frac{GCI_{i+1,i+2}}{r^p GCI_{i,i+1}}$	0.99	1.00	1.04	0.99	1.00	1.27	0.99	1.00	1.28

Table 39: The results of the Grid Convergence Index study completed for the High y+-Mesh. The transposed mesh as well as the coarsened mesh, as discussed in section 4.3.2, was considered. In the case of the transposed mesh both a stationary as well as a moving ground boundary condition was considered, while the coarsened mesh only considered a moving ground boundary condition. All results were obtained by making use of the LPS Two-Layer turbulence model.

Low y+-Mesh									
Mesh Refinement Level	x-Force [N]			y-Force [N]			z-Force [N]		
	Transposed Mesh	Coarsened Mesh	Deviation [%]	Transposed Mesh	Coarsened Mesh	Deviation [%]	Transposed Mesh	Coarsened Mesh	Deviation [%]
Refinement 1	6514.50	6544.26	0.46	62315.73	62353.87	0.06	-2583.88	-2654.39	2.73
Refinement 2	6530.45	6530.58	0.00	62320.07	62408.19	0.14	-1430.31	-1684.99	17.81
Refinement 3	6550.64	6561.41	0.16	62299.44	62467.74	0.27	-958.47	-983.01	2.56

Table 40: The values obtained for the various force components at grid refinements levels 1,2 and 3, for the transposed and coarsened low y+-meshes (in conjunction with the SST k- $\omega$  model). The deviation percentage between the force values obtained from the various meshes is also listed.

High y+-Mesh									
Mesh Refinement Level	x-Force [N]			y-Force [N]			z-Force [N]		
	Transposed Mesh	Coarsened Mesh	Deviation [%]	Transposed Mesh	Coarsened Mesh	Deviation [%]	Transposed Mesh	Coarsened Mesh	Deviation [%]
Refinement 1	7074.80	7028.79	-0.65	66529.12	66665.56	0.21	-2063.39	-2480.97	20.24
Refinement 2	7129.06	7125.61	-0.05	66656.38	66801.57	0.22	-1628.74	-1944.64	19.39
Refinement 3	7121.68	7250.28	1.81	66847.75	66910.84	0.09	-1235.98	-782.09	-36.72

Table 41: The values obtained for the various force components at grid refinements levels 1,2 and 3, for the transposed and coarsened high y+-meshes (in conjunction with the LPS Two-Layer model). The deviation percentage between the force values obtained from the various meshes is also listed.

Coarsened Low y+-Mesh used in conjunction with the SST k- $\omega$ Turbulence Model						
Mesh Refinement Level	x-Force [N]	Deviation [%]	y-Force [N]	Deviation [%]	z-Force [N]	Deviation [%]
Refinement 1	6544.26	-0.21	62353.87	0.09	-2654.39	-36.52
Refinement 2	6530.58	0.47	62408.19	0.10	-1684.99	-41.66
Refinement 3	6561.41		62467.74		-983.01	

Table 42: The percentage deviation between the subsequent x-, y- and z-force components associated with their respective grid refinement levels for the coarsened Low y+-Mesh.

Coarsened High y+-Mesh used in conjunction with the LPS Two-Layer Turbulence Model						
Mesh Refinement Level	x-Force [N]	Deviation [%]	y-Force [N]	Deviation [%]	z-Force [N]	Deviation [%]
Refinement 1	7028.79	1.38	66665.56	0.20	-2480.97	-21.62
Refinement 2	7125.61	1.75	66801.57	0.16	-1944.64	-59.78
Refinement 3	7250.28		66910.84		-782.09	

Table 43: The percentage deviation between the subsequent x-, y- and z-force components associated with their respective grid refinement levels for the coarsened High y+-Mesh.

Low y+-Mesh									
Mesh Refinement Level	Transposed Mesh [Stationary Ground]			Transposed Mesh [Moving Ground]			Coarsened Mesh [Moving Ground]		
	x-Force [N]	y-Force [N]	z-Force [N]	x-Force [N]	y-Force [N]	z-Force [N]	x-Force [N]	y-Force [N]	z-Force [N]
Refinement 1	7157.01	47527.10	308.90	6514.50	62315.73	-2583.88	6544.26	62353.87	-2654.39
Refinement 2	6923.76	48387.32	-210.52	6530.45	62320.07	-1430.31	6530.58	62408.19	-1684.99
Refinement 3	6880.94	44724.02	630.36	6550.64	62299.44	-958.47	6561.41	62467.74	-983.01
$f_{h=0}$	6871.31	47263.12	1148.16	6454.40	62314.56	-631.89	6555.18	61788.73	859.80
<b>Order of Convergence</b>	-3.20	2.74	0.91	0.44	2.94	-1.69	1.85	0.21	-0.74
<b>Relative Error</b>									
$\epsilon_{12}$	-0.0326	0.0181	-1.6815	0.0024	0.0001	-0.4464	-0.0021	0.0009	-0.3652
$\epsilon_{23}$	-0.0062	-0.0757	-3.9943	0.0031	-0.0003	-0.3299	0.0047	0.0010	-0.4166
<b>Grid Convergence Index</b>									
<b>GCI<sub>12</sub></b>	-0.0499	0.0069	3.3962	0.0115	0.00002	0.9443	0.0021	0.0113	1.6549
<b>GCI<sub>23</sub></b>	-0.0095	0.0290	8.0674	0.0146	0.0001	-0.6978	0.0047	0.0124	-1.8878
$\frac{GCI_{i+1,i+2}}{r^p GCI_{i,i+1}}$	1.03	0.98	1.47	1.00	1.00	-1.81	1.00	1.00	-1.58

Table 44: The results of the Grid Convergence Index study completed for the Low y+-Mesh. The transposed mesh as well as the coarsened mesh, as discussed in section 4.3.2, was considered. In the case of the transposed mesh both a stationary as well as a moving ground boundary condition was considered, while the coarsened mesh only considered a moving ground boundary condition. All results were obtained by making use of the SST k- $\omega$  turbulence model.

High y+-Mesh									
Mesh Refinement Level	Transposed Mesh [Stationary Ground]			Transposed Mesh [Moving Ground]			Coarsened Mesh [Moving Ground]		
	x-Force [N]	y-Force [N]	z-Force [N]	x-Force [N]	y-Force [N]	z-Force [N]	x-Force [N]	y-Force [N]	z-Force [N]
Refinement 1	7758.95	48576.28	2628.71	7074.80	66529.12	-2063.39	7028.79	66665.56	-2480.97
Refinement 2	7828.64	48594.28	2525.76	7129.06	66656.38	-1628.74	7125.61	66801.57	-1944.64
Refinement 3	7860.09	48751.95	2692.33	7121.68	66847.75	-1235.98	7250.28	66910.84	-782.09
$f_{h=0}$	7885.96	48573.96	2795.31	7137.60	66276.44	2446.54	6692.08	67357.27	-2940.34
Order of Convergence	-1.46	3.97	0.88	-3.65	0.75	-0.19	0.45	-0.39	1.38
Relative Error									
$\epsilon_{12}$	0.0090	0.0004	0.0392	0.0077	0.0019	-0.2106	0.0138	0.0020	-0.2162
$\epsilon_{23}$	0.0040	0.0032	0.0659	-0.0010	0.0029	-0.2411	0.0175	0.0016	-0.5978
Grid Convergence Index									
GCI <sub>12</sub>	-0.0205	0.0001	0.0792	-0.0111	0.0047	-2.7321	0.0599	-0.0130	0.2314
GCI <sub>23</sub>	-0.0092	0.0005	0.1334	-0.0015	0.0071	-3.1276	0.0761	-0.0104	0.6400
$\frac{GCI_{i+1,i+2}}{r^p GCI_{i,i+1}}$	0.99	1.00	1.04	0.99	1.00	1.27	0.99	1.00	1.28

Table 45: The results of the Grid Convergence Index study completed for the High y+-Mesh. The transposed mesh as well as the coarsened mesh, as discussed in section 4.3.2, was considered. In the case of the transposed mesh both a stationary as well as a moving ground boundary condition was considered, while the coarsened mesh only considered a moving ground boundary condition. All results were obtained by making use of the LPS Two-Layer turbulence model.

Low y+-Mesh									
Mesh Refinement Level	x-Force [N]			y-Force [N]			z-Force [N]		
	Transposed Mesh	Coarsened Mesh	Deviation [%]	Transposed Mesh	Coarsened Mesh	Deviation [%]	Transposed Mesh	Coarsened Mesh	Deviation [%]
Refinement 1	6514.50	6544.26	0.46	62315.73	62353.87	0.06	-2583.88	-2654.39	2.73
Refinement 2	6530.45	6530.58	0.00	62320.07	62408.19	0.14	-1430.31	-1684.99	17.81
Refinement 3	6550.64	6561.41	0.16	62299.44	62467.74	0.27	-958.47	-983.01	2.56

Table 46: The values obtained for the various force components at grid refinements levels 1,2 and 3, for the transposed and coarsened low y+-meshes (in conjunction with the SST k- $\omega$  model). The deviation percentage between the force values obtained from the various meshes is also listed.

High y+-Mesh									
Mesh Refinement Level	x-Force [N]			y-Force [N]			z-Force [N]		
	Transposed Mesh	Coarsened Mesh	Deviation [%]	Transposed Mesh	Coarsened Mesh	Deviation [%]	Transposed Mesh	Coarsened Mesh	Deviation [%]
Refinement 1	7074.80	7028.79	-0.65	66529.12	66665.56	0.21	-2063.39	-2480.97	20.24
Refinement 2	7129.06	7125.61	-0.05	66656.38	66801.57	0.22	-1628.74	-1944.64	19.39
Refinement 3	7121.68	7250.28	1.81	66847.75	66910.84	0.09	-1235.98	-782.09	-36.72

Table 47: The values obtained for the various force components at grid refinements levels 1,2 and 3, for the transposed and coarsened high y+-meshes (in conjunction with the LPS Two-Layer model). The deviation percentage between the force values obtained from the various meshes is also listed.

Coarsened Low y+-Mesh used in conjunction with the SST k- $\omega$ Turbulence Model						
Mesh Refinement Level	x-Force [N]	Deviation [%]	y-Force [N]	Deviation [%]	z-Force [N]	Deviation [%]
Refinement 1	6544.26	-0.21	62353.87	0.09	-2654.39	-36.52
Refinement 2	6530.58	0.47	62408.19	0.10	-1684.99	-41.66
Refinement 3	6561.41		62467.74		-983.01	

Table 48: The percentage deviation between the subsequent x-, y- and z-force components associated with their respective grid refinement levels for the coarsened Low y+-Mesh.

Coarsened High y+-Mesh used in conjunction with the LPS Two-Layer Turbulence Model						
Mesh Refinement Level	x-Force [N]	Deviation [%]	y-Force [N]	Deviation [%]	z-Force [N]	Deviation [%]
Refinement 1	7028.79	1.38	66665.56	0.20	-2480.97	-21.62
Refinement 2	7125.61	1.75	66801.57	0.16	-1944.64	-59.78
Refinement 3	7250.28		66910.84		-782.09	

Table 49: The percentage deviation between the subsequent x-, y- and z-force components associated with their respective grid refinement levels for the coarsened High y+-Mesh.

## Appendix D

This appendix is supplementary to section 4.4.1 and 4.4.2 in Chapter 4, and describes the sensitivity study that was completed in order to ensure that the size of the computational domain was adequate. That is, to ensure that the study results are independent of the boundary locations of the domain. The study further allowed for erratic force components to be identified.

### i. Determine Adequate Blockage Ratio

The first variable that was addressed was that of the blockage ratio of the computational domain to the train. Since the blockage ratio is a function of the cross-sectional area of the train, which remains constant, and the cross-sectional area of the domain, it is varied by varying the domain cross-section. For this study the domain has a square cross-section so that by varying the height of the domain, the width is varied accordingly. It is important to first determine a reasonable blockage ratio for the simulation since one that is too small will affect the flow field greatly and lead to poor predictions of the inlet and outlet distances of the domain.

The values of the variables that define the nose geometry used for this study are given in Table 50 and are in keeping with those that have been used in the study thus far, i.e., the streamlined nose used in section 4.3. The computational domain used for the initial, base case is that of the transposed Ahmed's Body validation case as given in Table 14. Save for the domain height, and thus per implication the domain width, the computational domain remains unchanged for section i in all other respects. The various domain heights that were considered for this study are given in Table 51 and the effects these changes had on the various x-, y- and z-force components are shown in Figure 136, Figure 137 and Figure 138.

Variables	L	Z <sub>0</sub>	H
Value [m]	7.7	1	3

Table 50: The values of the nose length (L), nose-tip height (Z<sub>0</sub>) and inflection point height (H) of the nose geometry used for the study of an adequate blockage ratio.

Simulation Case	Base Case	Domain Height 1	Domain Height 2	Domain Height 3
Domain Height [m]	38.49	88.49	138.49	188.49

Table 51: The various simulation cases that were considered in order to determine an adequate blockage ratio and their associated domain heights. Since the domain cross-section is square the domain height and width are necessarily equal.

Figure 136 shows the x-forces working on the train. Based on these results domain height two (138.49m) appears to be adequate to ensure the blockage ratio is such that the external flow field surrounding the train is able to develop fully, since all forces seem to have stabilized as a function of boundary location at this height. Furthermore, the percentage difference in the x-force components between domain height two and three are negligible, i.e., 0.22, 0.25, 0.29, 0.02, 0.81, -0.05 for the total, nose, coaches, tail, bottom and top respectively. Using a similar approach the necessary domain height to ensure the y-force components are independent of boundary location was determined to be domain height two (138,49m) as well (see Figure 137). At this height all the y-force components have stabilized and the percentage difference between the corresponding forces at consecutive domain heights, i.e., domain height two and three, are negligible; -0.32, -0.11, -0.92, -0.07, -0.71 and -0.17 for the total, nose, coaches, tail, bottom and top respectively.

Finally, as is illustrated by Figure 138, the z-force components of the train as a whole as well as the nose, coaches and tail remain unstable and erratic throughout with ranges of 29.45%, 6.98%, 24.42% and 17.76% respectively. In contrast it does seem that the z-forces acting on the top and bottom portions of the train, i.e., above and below the stagnation point on the nose, stabilizes, the z-force above the stagnation point in particular. These force components can thus be used for explanatory purposes and be indicative of flow behaviour and trends. However, they should still be treated with a measure of caution since the z-force components over the nose, coaches and tail remain erratic and a change in nose shape may affect the stability of the flow over the top and bottom portion, e.g., a transition from a streamlined to a blunt nose. It is here that the inability of the RANS models to predict lift on vehicles in the vicinity of the ground is made clear as stated by (Krajnović, 2008). A domain height of 138.49m (domain height two) was thus chosen as the base height with which the remainder of the boundary location study was conducted.

A boundary location study to determine adequate inlet and outlet locations of the domain with a height of 138.49m was completed for the nose geometry as described in Table 50. The dimensions of the final domain that resulted from this study are given in Table 52, while the results of the complete study may be found in Appendix J. It was however found that a blunt rather than a streamlined nose, which was used for the study in question, requires the larger computational domain. This is due to the greater measure of disturbance to the surrounding air as the train passes through it. The resultant flow separation and larger wake requires a larger domain to effectively capture the external flow field that surrounds the train without the boundary locations disrupting the natural development of it. Therefore, for sections ii, iii and iv which considers the necessary inlet distance of the domain, the necessary outlet distance thereof and the validation of the blockage ratio determined in this section (i) respectively, a blunt nose will be made use of.

<b>Domain Dimensions</b>	<b>Magnitude [m]</b>
Inlet Distance	146.19
Outlet Distance	584.68
Width	138.49
Height	138.49

**Table 52: The values of the dimensions of the computational domain that was validated for a streamlined train nose.**

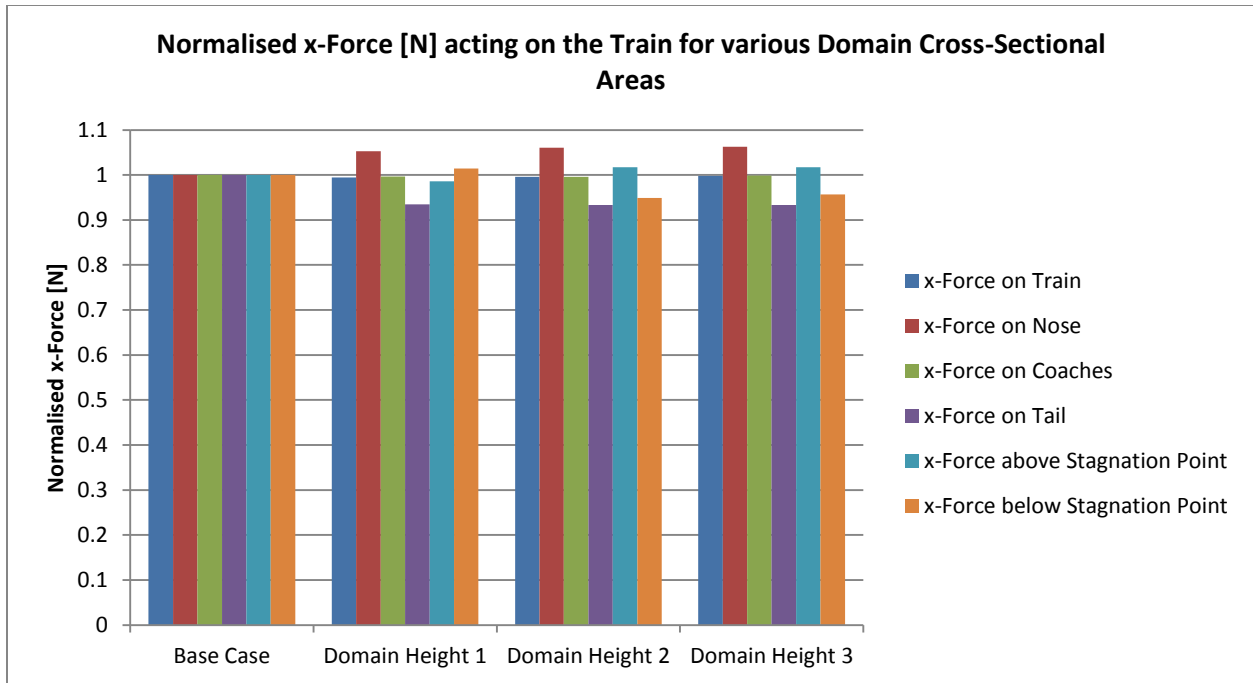


Figure 136: The normalised x-force [N] acting on the train for various domain cross-sectional areas. All forces were normalised by the corresponding value obtained from the base case simulation. The figure shows the forces acting on the train as a whole as well as on the following sub-components; the train nose, coaches and tail as well as the forces acting above and below the stagnation point on the nose.

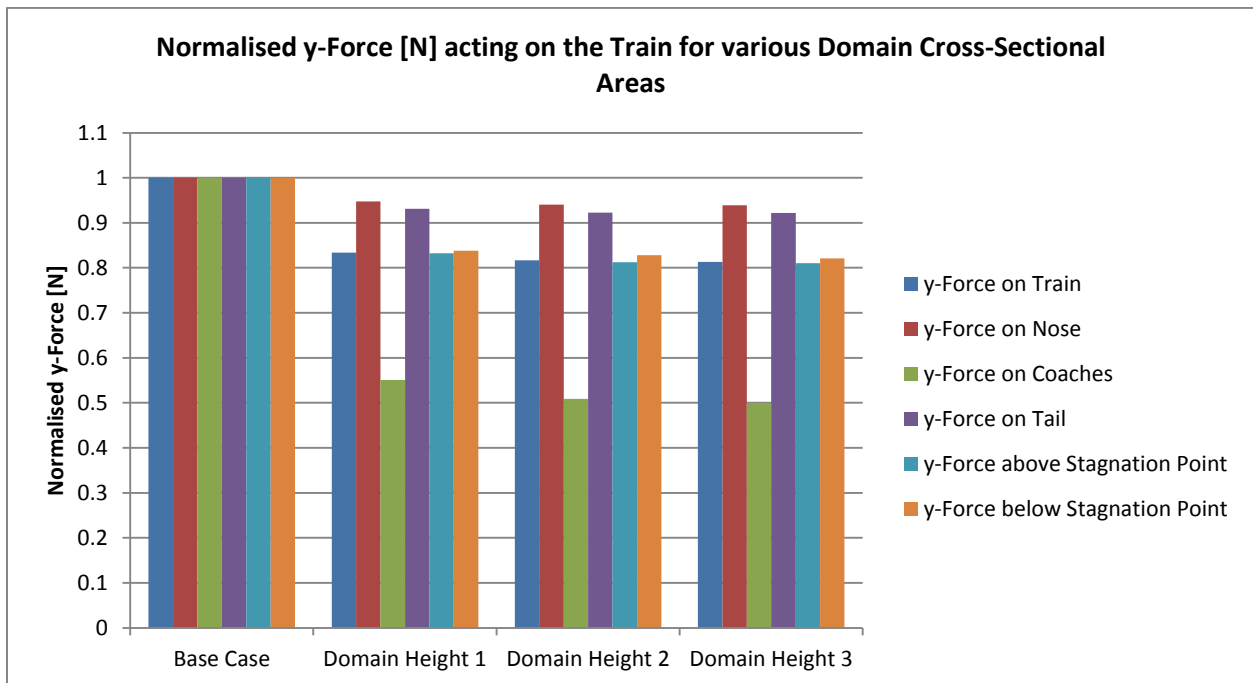


Figure 137: The normalised y-force [N] acting on the train for various domain cross-sectional areas. All forces were normalised by the corresponding value obtained from the base case simulation. The figure shows the forces acting on the train as a whole as well as on the following sub-components; the train nose, coaches and tail as well as the forces acting above and below the stagnation point on the nose.

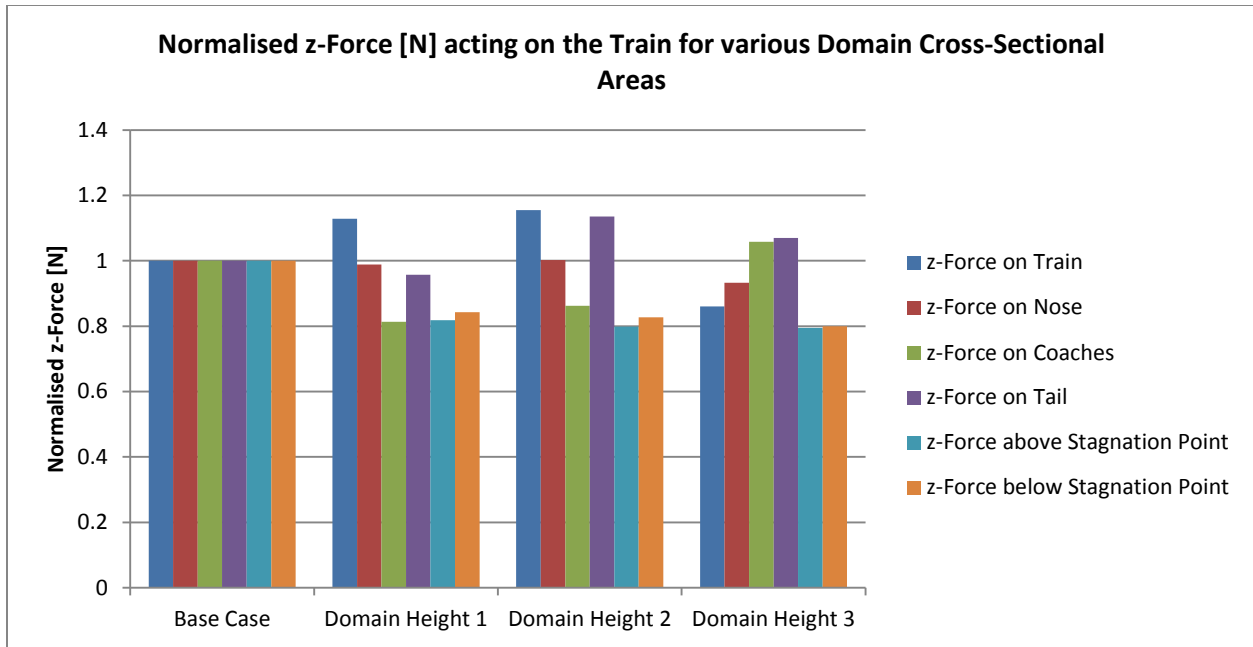


Figure 138: The normalised z-force [N] acting on the train for various domain cross-sectional areas. All forces were normalised by the corresponding value obtained from the base case simulation. The figure shows the forces acting on the train as a whole as well as on the following sub-components; the train nose, coaches and tail as well as the forces acting above and below the stagnation point on the nose.

## ii. Determine Adequate Inlet Distance

This section will concern itself with finding an inlet boundary location that is sufficiently far away from the nose of the train, so as not to interfere with the train’s natural external flow field. The domain that was validated for a streamlined nose will act as a base case for this section (see Table 52) with the various values that the inlet distance will assume given in Table 53 below. All other dimensions given in Table 52 will however remain unchanged for all the cases considered in this section (section ii). Furthermore, as mentioned above, a blunt nose (see Table 54) will henceforth be used for the validation of the computational domain. The effect that moving the inlet boundary has on the x-, y- and z-force components are shown in Figure 139, Figure 140 and Figure 141 .

Simulation Case	Base Case	Inlet Distance 1	Inlet Distance 2	Inlet Distance 3	Inlet Distance 4
Inlet Distance [m]	146.19	246.19	346.19	446.19	546.19

Table 53: The various simulation cases that were considered in order to determine an adequate inlet distance and their associated values.

Variables	L	Z <sub>0</sub>	H
Value [m]	2	0.7	3

Table 54: The values of the nose length (L), nose-tip height (Z<sub>0</sub>) and inflection point height (H) of the nose geometry used for the study of an adequate inlet distance.

The procedure for finding an adequate inlet distance to the domain is similar to that discussed in section i and will therefore be addressed here in a brief manner; there are two primary concerns when choosing an adequate boundary location, the first is whether the force has stabilized as a function of the boundary location, i.e., it doesn’t display erratic behaviour as a function of boundary location. The

second concern is at what point the percentage difference in results for subsequent distances is such that the smaller distance can be used without compromising on accuracy or the measure of stability of the answer. Based on the aforementioned it was found that inlet distance three (446.19m) was the minimum distance which could be used to ensure a stabilized x-force, especially of the x-force components acting on the train tail and the portion above and below the stagnation point (see Figure 139). The total x-force acting on the train also show a measure of instability initially (base case through to inlet distance two) which later subsides (inlet distance two through to inlet distance four). The measure of the total x-force fluctuations are, however, such that any inlet distance could have been used and a reasonably accurate result obtained. In contrast the y-force acting on the train is insensitive to the inlet boundary location and any inlet distance would yield a stabilized y-force result (see Figure 140).

Finally, the z-force remains erratic irrespective of the inlet distance with the only z-force component remaining stable as a function of inlet distance, the force acting above the stagnation point (see Figure 141). The instability of the z-force would therefore more likely seem to be a function of the z-force acting on the lower portion of the train. Furthermore, the coaches and tail show a greater measure of instability than the train nose. This would seem to suggest that the turbulence generated below the train is anisotropic in nature with the measure of anisotropy increasing down the length of the train which corresponds to the developing boundary layer theory. From the aforementioned the necessary inlet distance that ensures that stability of the solution is maintained, save for the z-forces that remain erratic throughout, is inlet distance three (446.19m).

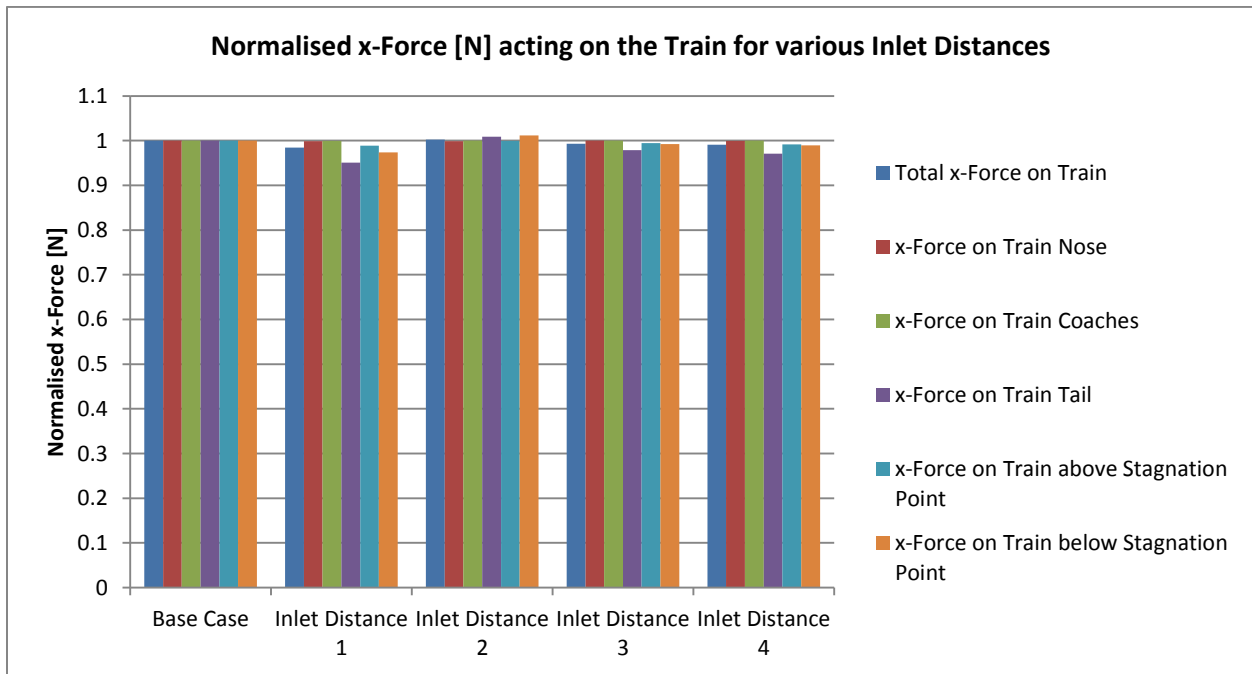


Figure 139: The normalised x-force [N] acting on the train for various domain inlet distances. All forces were normalised by the corresponding value obtained from the base case simulation. The figure shows the forces acting on the train as a whole as well as on the following sub-components; the train nose, coaches and tail as well as the forces acting above and below the stagnation point on the nose.

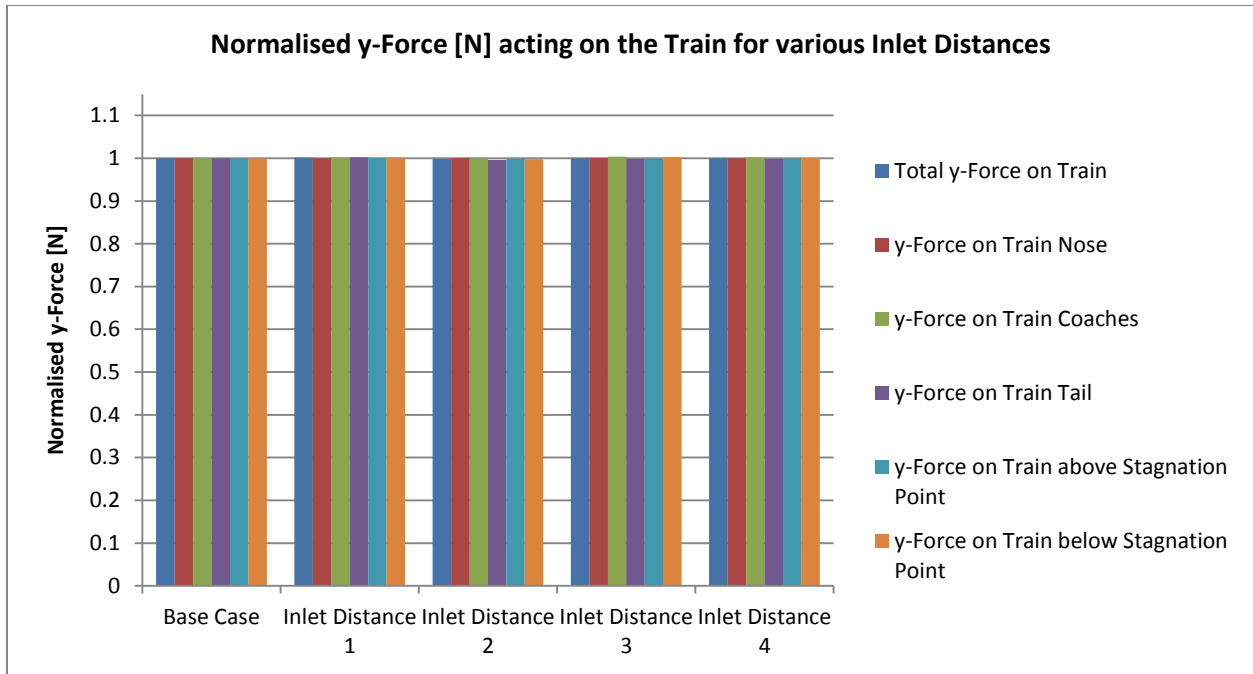


Figure 140: The normalised y-force [N] acting on the train for various domain inlet distances. All forces were normalised by the corresponding value obtained from the base case simulation. The figure shows the forces acting on the train as a whole as well as on the following sub-components; the train nose, coaches and tail as well as the forces acting above and below the stagnation point on the nose.

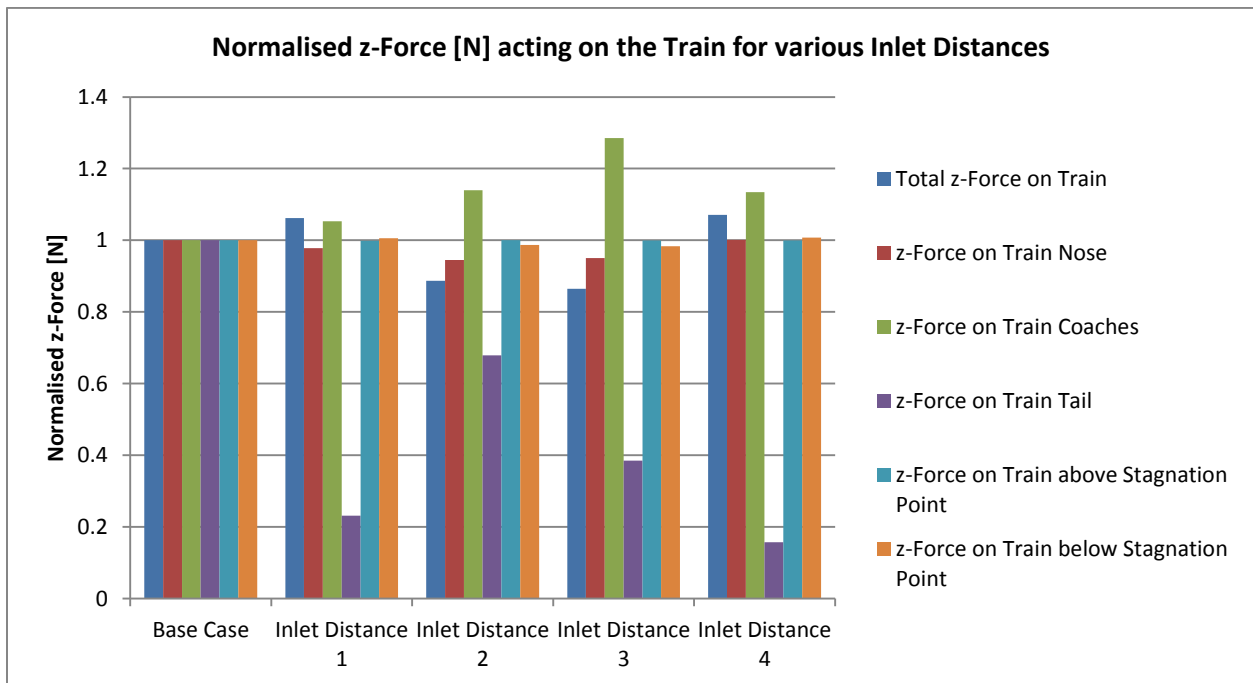


Figure 141: The normalised z-force [N] acting on the train for various domain inlet distances. All forces were normalised by the corresponding value obtained from the base case simulation. The figure shows the forces acting on the train as a whole as well as on the following sub-components; the train nose, coaches and tail as well as the forces acting above and below the stagnation point on the nose.

### iii. Determine Adequate Outlet Distance

The final domain dimension that was investigated was the outlet distance necessary for the various forces and their respective components to stabilize. In a similar fashion to the investigation of the necessary inlet distance (446.19m), the base domain was not that of the transposed Ahmed's body, but rather that of the validated domain for a streamlined nose (see section i and Table 52). Table 55 shows the various outlet distances that were investigated; this was the only domain dimension that was varied, in all other respects the domain remained identical to that relayed in Table 52. Once again a blunt train nose (see Table 56) was used to find an adequate outlet distance, since these nose shapes generate larger trailing wakes. The results of this study, i.e., the behaviour of the various x-, y- and z-force components as a function of outlet distance is shown in Figure 142, Figure 143 and Figure 144.

Simulation Case	Base Case	Outlet Distance 1	Outlet Distance 2	Outlet Distance 3	Outlet Distance 4
Inlet Distance [m]	584.68	784.68	984.68	1184.68	1384.68

Table 55: The various simulation cases that were considered in order to determine an adequate outlet distance and their associated values.

Variables	L	Z <sub>0</sub>	H
Value [m]	2	0.7	3

Table 56: The values of the nose length (L), nose-tip height (Z<sub>0</sub>) and inflection point height (H) of the nose geometry used for the study of an adequate outlet distance.

Consider first the x-force and its various components acting on the train; Figure 142 shows that the total drag force acting on the train is stable throughout and the small fluctuations that it does display is negligible, i.e., a range of 1.01% across all outlet distances. Similarly the x-force acting on the nose and coaches is also stable throughout with a range of 0.12% and 0.13% respectively. In contrast the drag force on the top portion of the train remains unstable, but with a relatively small range of 1.61% across all cases. Thus, while it has not stabilized, its fluctuations are such that the error of a predicted value is negligible. The tail portion displays similar behaviour to the top portion of the train, albeit with a slightly larger range of 3.24%. The x-force acting on the lower portion of the train however, does not only remain unstable as a function of outlet distance but its associated range is also rather large at 8.43%. Clearly then the source of instability for the drag force is located in the bottom region of the train and is driven specifically by the unstable drag force acting on the tail of the train. Based on the results for the x-force outlet distance three (1184.68m) was chosen as the minimum outlet distance necessary, since both the total as well as the tail drag force seem to be more stable from here onwards, i.e., the percentage difference in the values of the forces at successive outlet distances decrease. Based on the results for the side force shown in Figure 143, outlet distance three is also adequate to ensure stability of the y-force components. The only exception to this is the side force acting on the bottom portion of the train. It is also clear from the figure that the side force acting on the tail is once again more unstable than those acting on the nose and coaches. This behaviour therefore corroborates that which was observed for the drag forces as well; the turbulence beneath the train is such that a simple RANS turbulence model is not able to capture it accurately, with the source of this anisotropic turbulence being the tail of the train where irrotational vortices and the like are expected.

Finally, the z-forces remain erratic as a function of the outlet distance, save for the lift force acting on the top portion of the train. Behaviour similar to that of the z-forces as a function of the inlet distance is displayed here and may be referred back to, to avoid repetition.

#### **iv. Blockage Ratio Validation**

This section of the document will serve to validate the domain height, and consequently the blockage ratio, initially validated in section i and Appendix J, and used for sections ii and iii. This is necessary since the train nose geometry used to validate the aforementioned blockage ratio was streamlined, while it was found that a blunt nose geometry requires the larger computational domain. Two simulation cases will thus be run, the first for domain height two (138.49m) and the second for domain height three (188.49m) (see Table 51). For both cases the blunt nose geometry described in Table 54 and Table 56 will be used, while the inlet and outlet distances will be those validated in sections ii and iii, i.e., 446.19m and 1184.68m respectively. The effect of varying the blockage ratio on the x-,y- and z-force components will be considered and a conclusion drawn on the aptness of blockage ratio two, or domain height two for that matter. The results of these analyses are shown in Table 57, Table 58 and Table 59.

The maximum deviation between corresponding x-forces (see Table 57) is 4.09% for the drag force on the lower portion (below the stagnation point) of the train. In the case of the side forces acting on the train, the largest deviation is -2.38% for the y-force component acting on the coaches (see Table 58). Finally the deviation in results of the z-forces (see Table 59) is once again erratic with the smallest being -0.42% on the top portion of the train and the largest being 87.54% and located on the tail of the train. Clearly then neither the accuracy of the x-force and its components, nor that of the y-force and its components are adversely affected by an increase, or decrease, in the domain height (and corresponding increase in domain width). Furthermore, as predicted by the literature, the behaviour of the z-force remains erratic. It is, however, interesting to note that the regions of instability of the z-force are those regions where turbulence is prevalent; the coaches and tail of the train. It is also the tail region, which experiences the greater measure of turbulence, which shows the greatest fluctuation with an increase in domain size. The aforementioned would thus seem to indicate that the forces have stabilized as a function of domain size and that the remaining instability is a function of the large measure of turbulence present in the model and the inability of the RANS turbulence models to predict this complex flow behaviour. It is thus safe to say from the aforementioned that the domain height two (138.49m) has been validated as adequate for the model irrespective of nose type, i.e., streamlined or blunt.

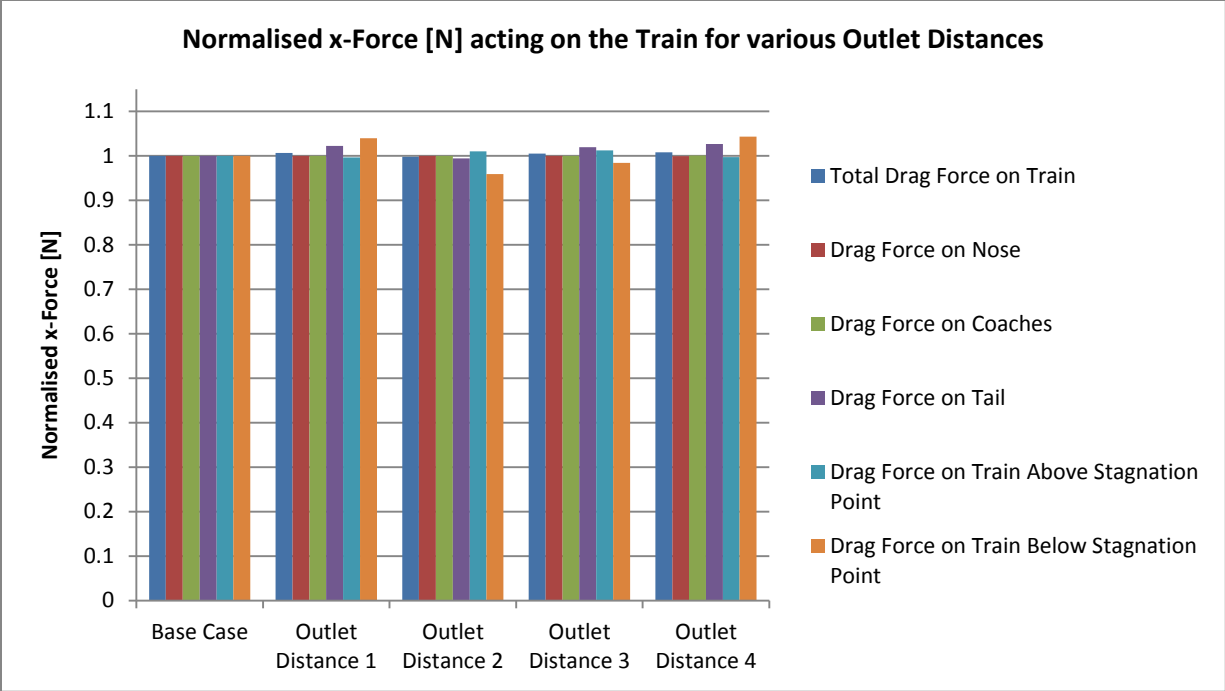


Figure 142: The normalised x-force [N] acting on the train for various domain outlet distances. All forces were normalised by the corresponding value obtained from the base case simulation. The figure shows the forces acting on the train as a whole as well as on the following sub-components; the train nose, coaches and tail as well as the forces acting above and below the stagnation point on the nose.

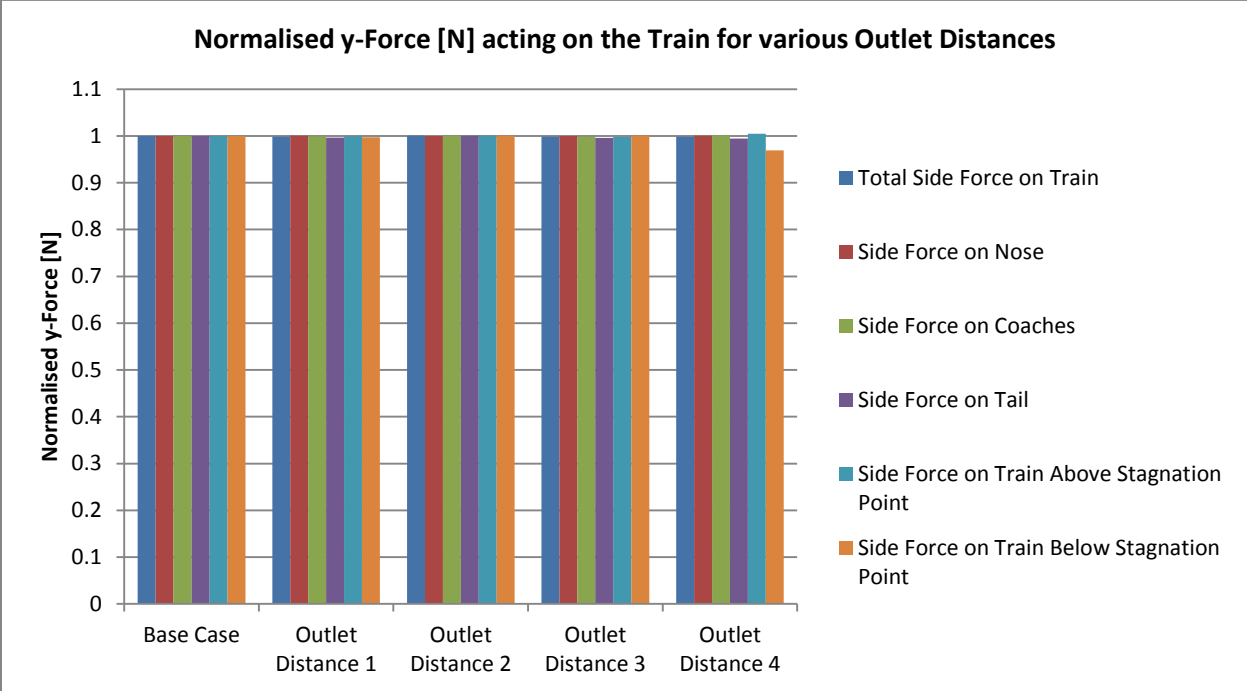


Figure 143: The normalised y-force [N] acting on the train for various domain outlet distances. All forces were normalised by the corresponding value obtained from the base case simulation. The figure shows the forces acting on the train as a whole as well as on the following sub-components; the train nose, coaches and tail as well as the forces acting above and below the stagnation point on the nose.

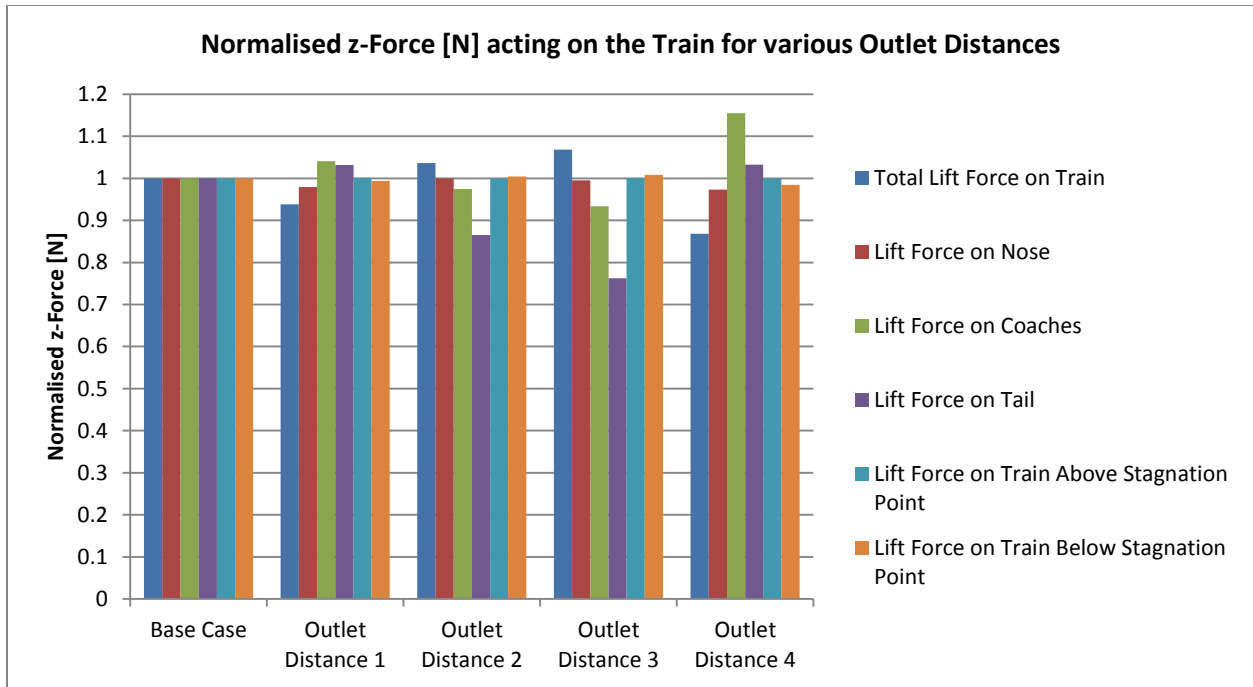


Figure 144: The normalised z-force [N] acting on the train for various domain outlet distances. All forces were normalised by the corresponding value obtained from the base case simulation. The figure shows the forces acting on the train as a whole as well as on the following sub-components; the train nose, coaches and tail as well as the forces acting above and below the stagnation point on the nose.

Simulation Case	Drag Force [N]											
	Nose	Deviation [%]	Coaches	Deviation [%]	Tail	Deviation [%]	Bottom	Deviation [%]	Top	Deviation [%]	Total	Deviation [%]
Domain Height 2	1672.19	0.24	4149.38	-0.13	2471.14	2.97	1934.81	4.09	6357.89	-0.11	8292.71	0.87
Domain Height 3	1676.13		4143.91		2544.45		2013.90		6350.59		8364.48	

Table 57: The drag force and its various components acting on the train as a whole as well as its various sub-divisions, i.e., nose, coaches, tail, top and bottom. The results are given for a train with a blunt nose for domain height two and three as specified in Table 51 and the inlet and outlet distances verified in sections ii and iii, respectively.

Simulation Case	Side Force [N]											
	Nose	Deviation [%]	Coaches	Deviation [%]	Tail	Deviation [%]	Bottom	Deviation [%]	Top	Deviation [%]	Total	Deviation [%]
Domain Height 2	36506.60	-0.08	9095.54	-2.38	26927.12	-0.44	12316.64	-1.47	60212.62	-0.30	72529.26	-0.50
Domain Height 3	36479.07		8878.68		26808.29		12135.87		60030.17		72166.04	

Table 58: The side force and its various components acting on the train as a whole as well as its various sub-divisions, i.e., nose, coaches, tail, top and bottom. The results are given for a train with a blunt nose for domain height two and three as specified in Table 51 and the inlet and outlet distances verified in sections ii and iii, respectively.

Simulation Case	Lift Force [N]											
	Nose	Deviation [%]	Coaches	Deviation [%]	Tail	Deviation [%]	Bottom	Deviation [%]	Top	Deviation [%]	Total	Deviation [%]
Domain Height 2	-4726.30	-0.96	2015.33	-28.71	233.34	87.54	-23542.56	1.02	21064.93	-0.42	-2477.63	13.28
Domain Height 3	-4681.07		1436.69		437.62		-23783.75		20977.00		-2806.75	

Table 59: The lift force and its various components acting on the train as a whole as well as its various sub-divisions, i.e., nose, coaches, tail, top and bottom. The results are given for a train with a blunt nose for domain height two and three as specified in Table 51 and the inlet and outlet distances verified in sections ii and iii, respectively.

## Appendix E

This appendix is supplementary to section 4.5.3.1, 4.5.3.2 and 4.5.4.1, in Chapter 4. Contained herein are the results of a comparative study that was completed on order to evaluate the ability of the RBF and Kriging interpolation methods, to generate a representative response surface model for the problem at hand. Section i shows the results obtained for the total drag force acting on the train, where the nose length (L) acts as a “slider” and Kriging was made use of to create the surrogate model. The results obtained by making use of the RBF method are discussed in 4.5.3.2.1. Section ii and iii, however, show the results obtained for the total drag force acting on the train with the nose-tip ( $Z_0$ ) and inflection point heights (H) acting as the “sliders”, respectively as determined from the two surrogate models, i.e., the Kriging and the RBF surrogate models.

### i. Variable Nose Length: Kriging Surrogate Model

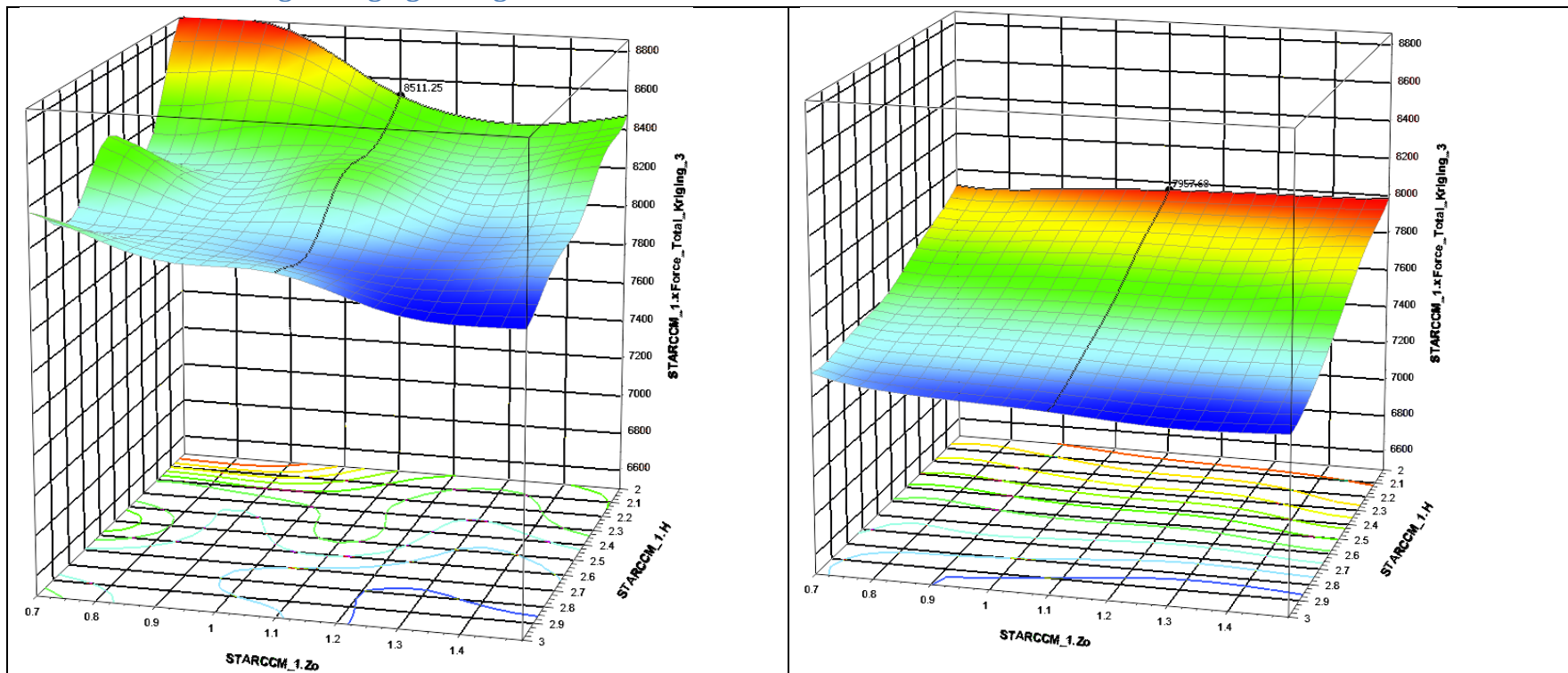


Figure 145: The variation of the total x-force (vertical axis) acting on the train as a function of nose-tip height ( $Z_0$ ) and inflection point height (H) for a constant nose length of  $L=2\text{m}$ , left and  $L=3.425\text{m}$ , right.

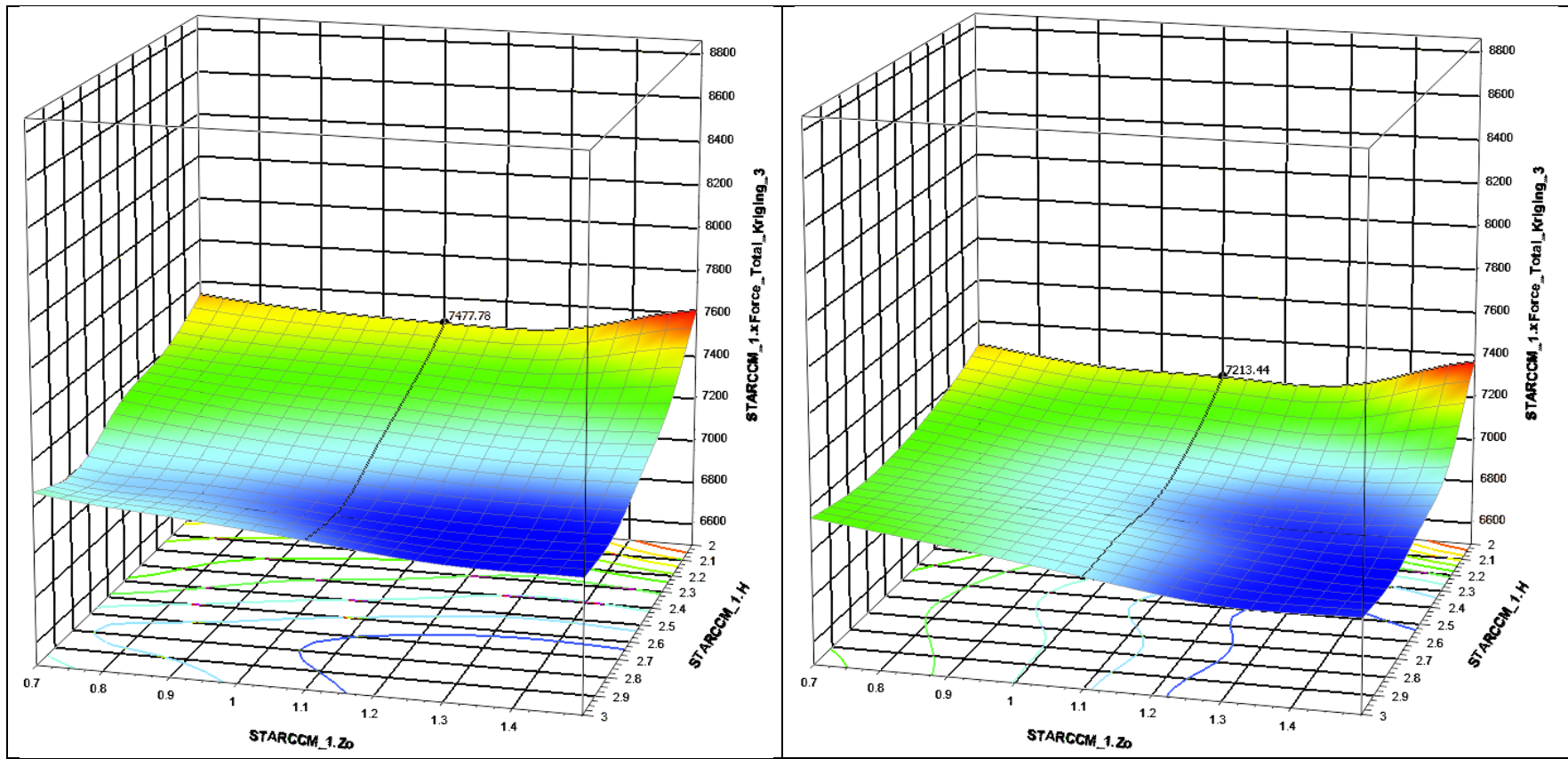


Figure 146: The variation of the total x-force (vertical axis) acting on the train as a function of nose-tip height ( $Z_0$ ) and inflection point height ( $H$ ) for a constant nose length of  $L=4.85\text{m}$ , left and  $L=6.275\text{m}$ , right.

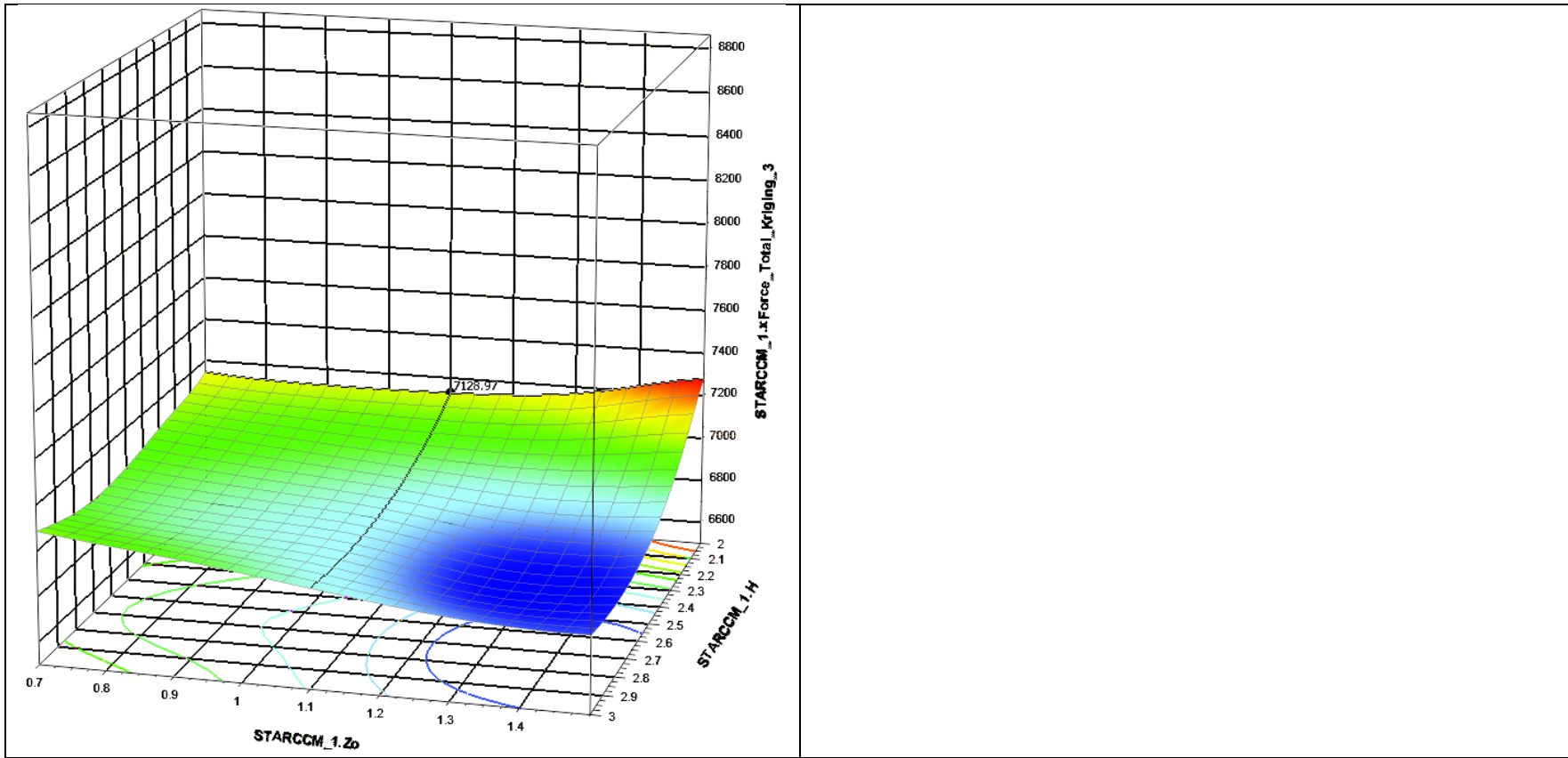


Figure 147: The variation of the total x-force (vertical axis) acting on the train as a function of nose-tip height ( $Z_0$ ) and inflection point height ( $H$ ) for a constant nose length of  $L=7.7\text{m}$

## ii. Variable Nose-Tip Height: RBF vs. Kriging

The results obtained for the response of the total drag force acting on the train as a function of the nose length and inflection point height with variable nose-tip height, corroborates the results obtained for a variable nose length in section 4.5.3.2.1 above; Figure 148 through Figure 152 also show noisy data for blunt noses, i.e., for nose lengths tending toward the minimum boundary ( $L=2m$ ), which corresponds with the data shown in Figure 84, top.

Additionally, an increase in the length of the train nose sees a decrease in the total drag force experienced by the train, irrespective of inflection point or nose-tip height (see Figure 148 through Figure 152). It is however clear from the figures that the effect of elongating the nose is greatest for a larger, although not necessarily maximum, inflection point value ( $H$ ). In fact, for  $L$ -values tending towards the maximum nose length, the  $x$ -force values exhibit an almost parabolic shape, albeit a skewed parabola, with the minimum located between the minimum and maximum bounds and in closer proximity to the maximum inflection point. This behaviour is more pronounced the longer the train nose. Furthermore an increase in the  $Z_0$ -values does seem to lead to a decrease in the total  $x$ -force although the extent to which this is the case is difficult to gauge from these figures.

Suffice it to say however, that the results from the response surfaces shown in Figure 148 through Figure 152 at the very least confirm the theory that the longer the train nose, the less the drag. The figures further illustrate the law of diminishing returns as is expected from the theory (Baker, 2014) and also indicate an optimal inflection point value that is expected in closer proximity to the maximum than the minimum  $H$ -value. The aforementioned confirm the conclusions drawn in the preceding section regarding the expected optimal nose geometry.

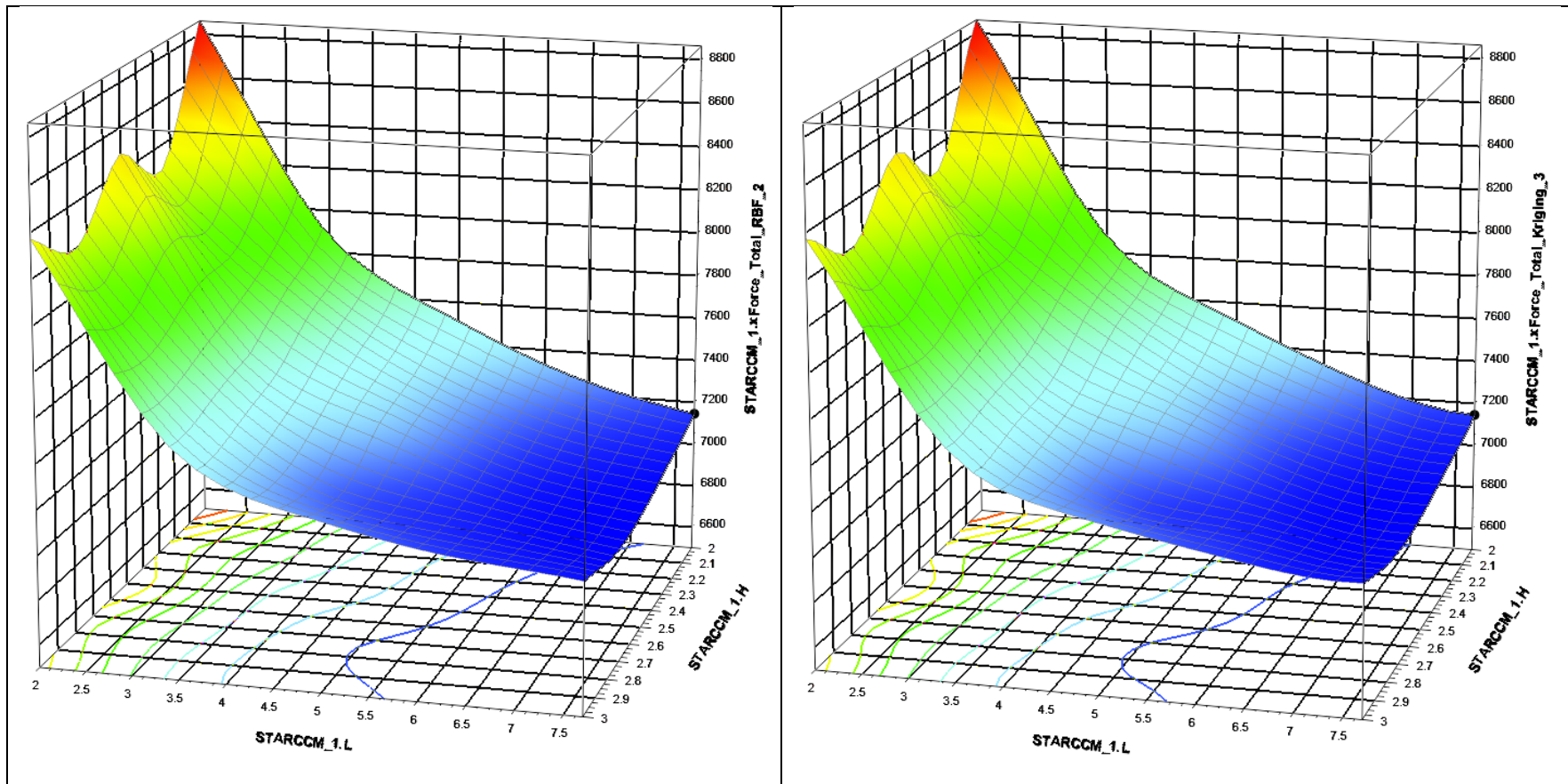


Figure 148: The variation of the total x-force (vertical axis) acting on the train as a function of nose length (L) and inflection point height (H) for a constant nose-tip height ( $Z_0=0.7\text{m}$ ). The response surface on the left was created by making use of the radial basis function (RBF), while that on the right was created by making use of Kriging.

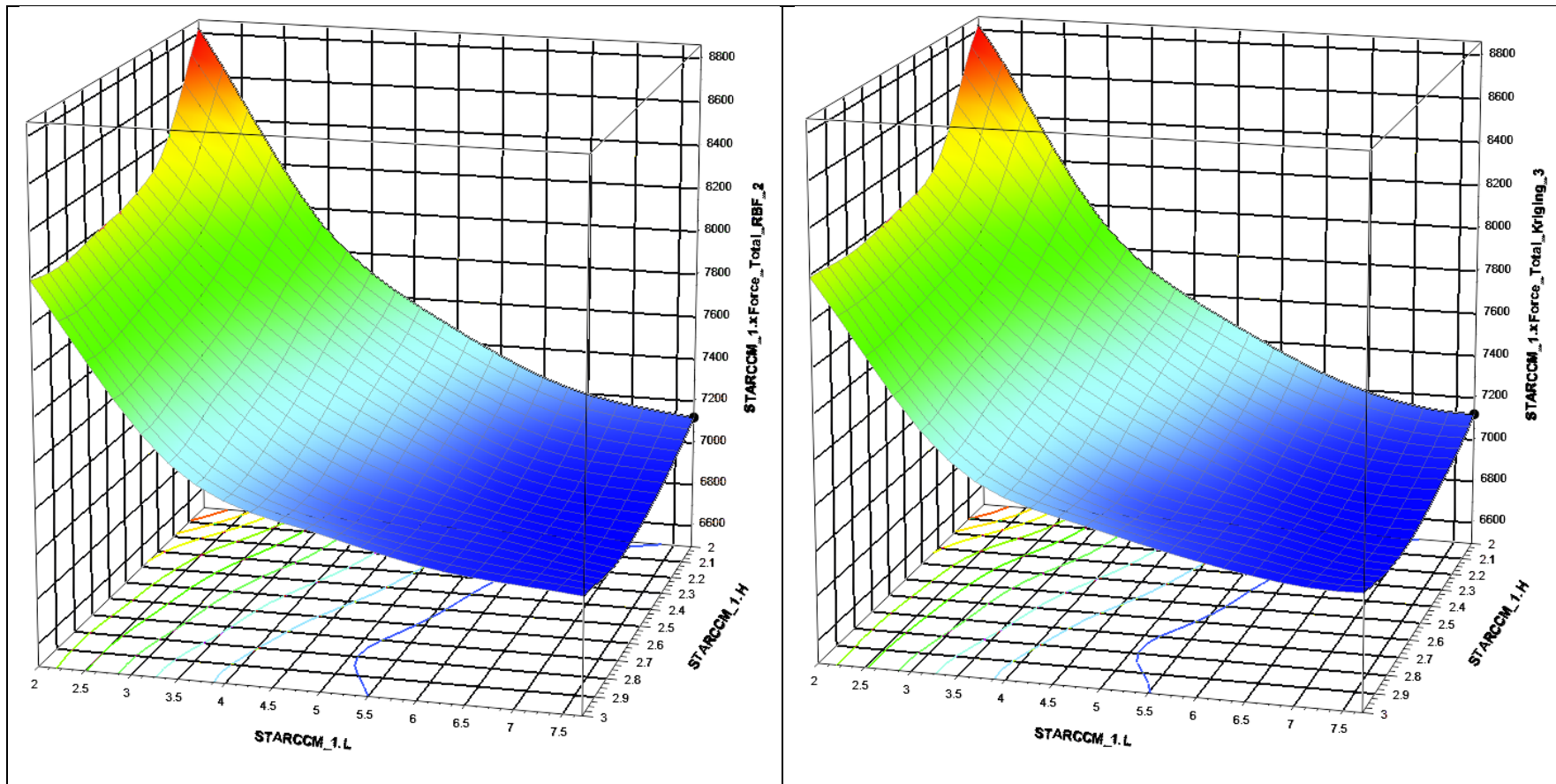


Figure 149: The variation of the total x-force (vertical axis) acting on the train as a function of nose length (L) and inflection point height (H) for a constant nose-tip height ( $Z_0=0.9\text{m}$ ). The response surface on the left was created by making use of the radial basis function (RBF), while that on the right was created by making use of Kriging.

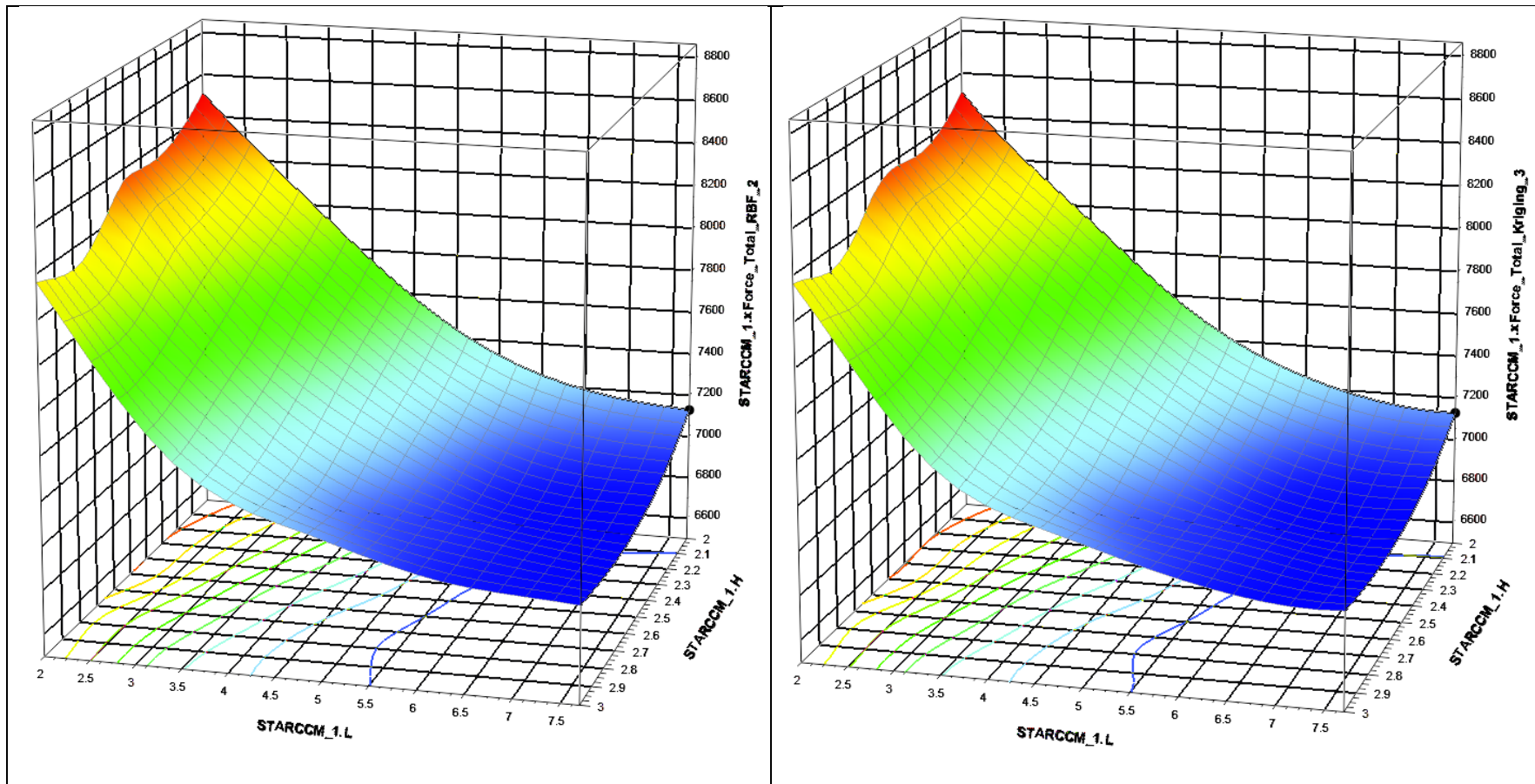


Figure 150: The variation of the total x-force (vertical axis) acting on the train as a function of nose length (L) and inflection point height (H) for a constant nose-tip height ( $Z_0=1.1\text{m}$ ). The response surface on the left was created by making use of the radial basis function (RBF), while that on the right was created by making use of Kriging.

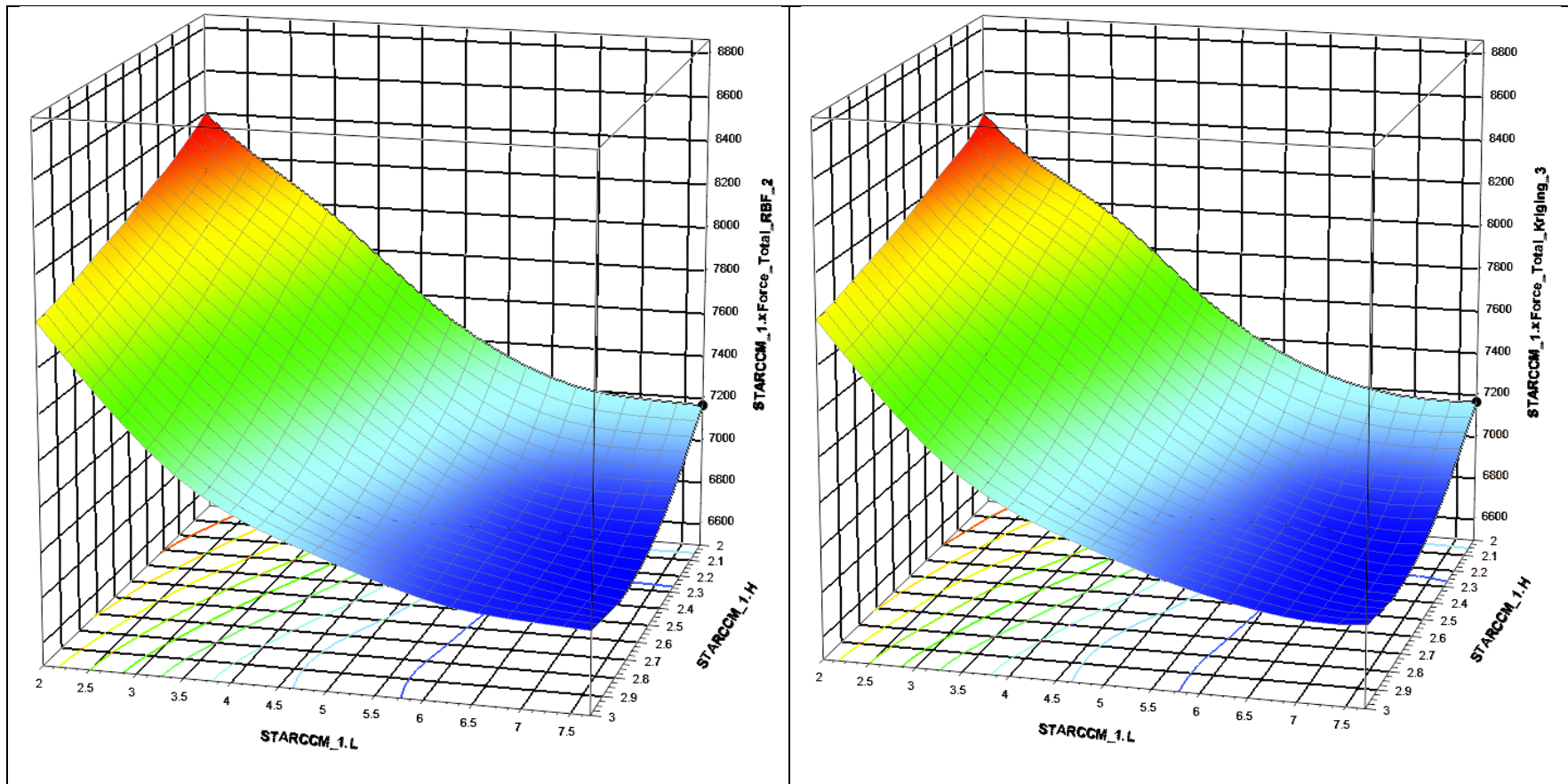


Figure 151: The variation of the total x-force (vertical axis) acting on the train as a function of nose length (L) and inflection point height (H) for a constant nose-tip height ( $Z_0=1.3\text{m}$ ). The response surface on the left was created by making use of the radial basis function (RBF), while that on the right was created by making use of Kriging.

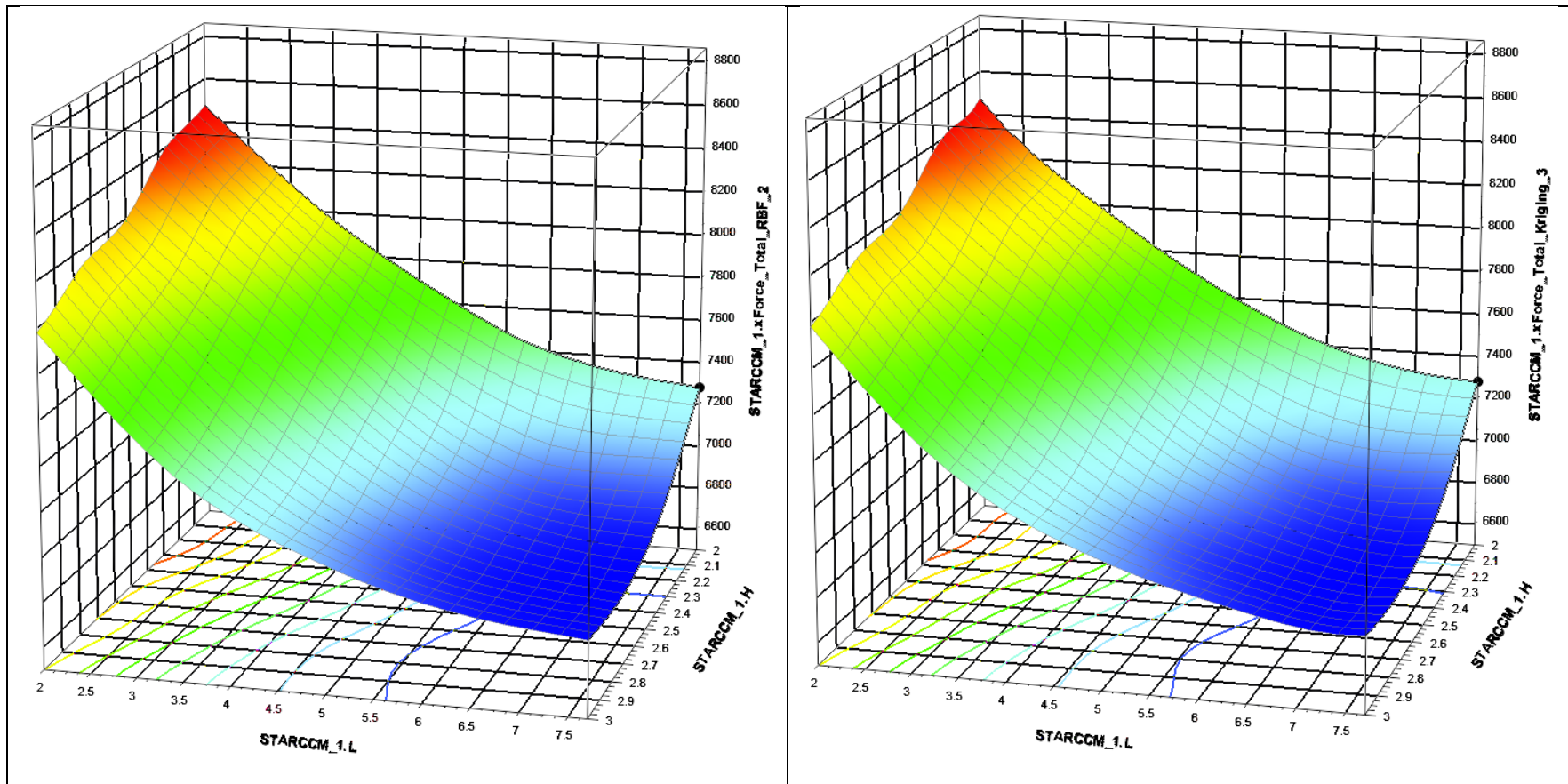


Figure 152: The variation of the total x-force (vertical axis) acting on the train as a function of nose length (L) and inflection point height (H) for a constant nose-tip height ( $Z_0=1.5\text{m}$ ). The response surface on the left was created by making use of the radial basis function (RBF), while that on the right was created by making use of Kriging.

### iii. Variable Inflection Point Height: RBF vs. Kriging

The final train nose parameter that will be discussed is the inflection point height,  $H$ . Once again noisy solution behaviour can be observed for nose lengths ( $L$ ) tending towards the lower bound ( $L=2\text{m}$ ), while the flow behaviour associated with the longer noses, which cause less disturbance to the flow and consequently less turbulence, is more predictable. From Figure 153 through to Figure 155 a decline in the total drag force can be observed with an increase in nose length which corroborates the findings from sections 4.5.3.2.1 and Appendix E, section ii.

For the case where the inflection point assumes its minimum value ( $H=2\text{m}$ ), it can be seen that for nose lengths tending towards the upper-bound, the minimum drag force can be achieved for almost all values of nose-tip height, although a lower nose-tip is more advantageous (see Figure 153). An increase in the inflection point height ( $H=2.5\text{m}$ , see Figure 154), sees a decrease in the total drag force experienced by the train. However, now, as the nose length tends to its maximum a nose-tip height that also tends towards its maximum yields the lowest drag force. This behaviour is exacerbated by a further increase in the inflection point height ( $H$ ), which sees the total drag force decreasing further still.

It is however important to note the smaller region for which these minimal drag forces can be obtained, i.e., the nose length and nose-tip height are required to be closer to their maximum bounds in order to achieve minimal drag (see Figure 155). In contrast, the general region for which minimal drag forces can be obtained when ' $H$ ' assumes its lower bound is much larger, therefore the nose length and nose-tip height exhibit a larger permissible region. Clearly then, the closer the nose tends towards the optimal shape, the more sensitive the total drag force becomes to changes in geometry. This migration of the minimum x-force at the maximum nose length from the lower  $Z_0$ -values, to the higher  $Z_0$ -values with an increase in the inflection point height, confirms the somewhat parabolic nature of the drag force as a function of ' $H$ ' at the maximum nose length.

When all results are considered, both in this section as well as sections 4.5.3.2.1 and Appendix E, section ii, an optimal nose geometry with a relatively high nose-tip and inflection point height is expected, while from the theory it is known that the ideal nose length is 7.7m.

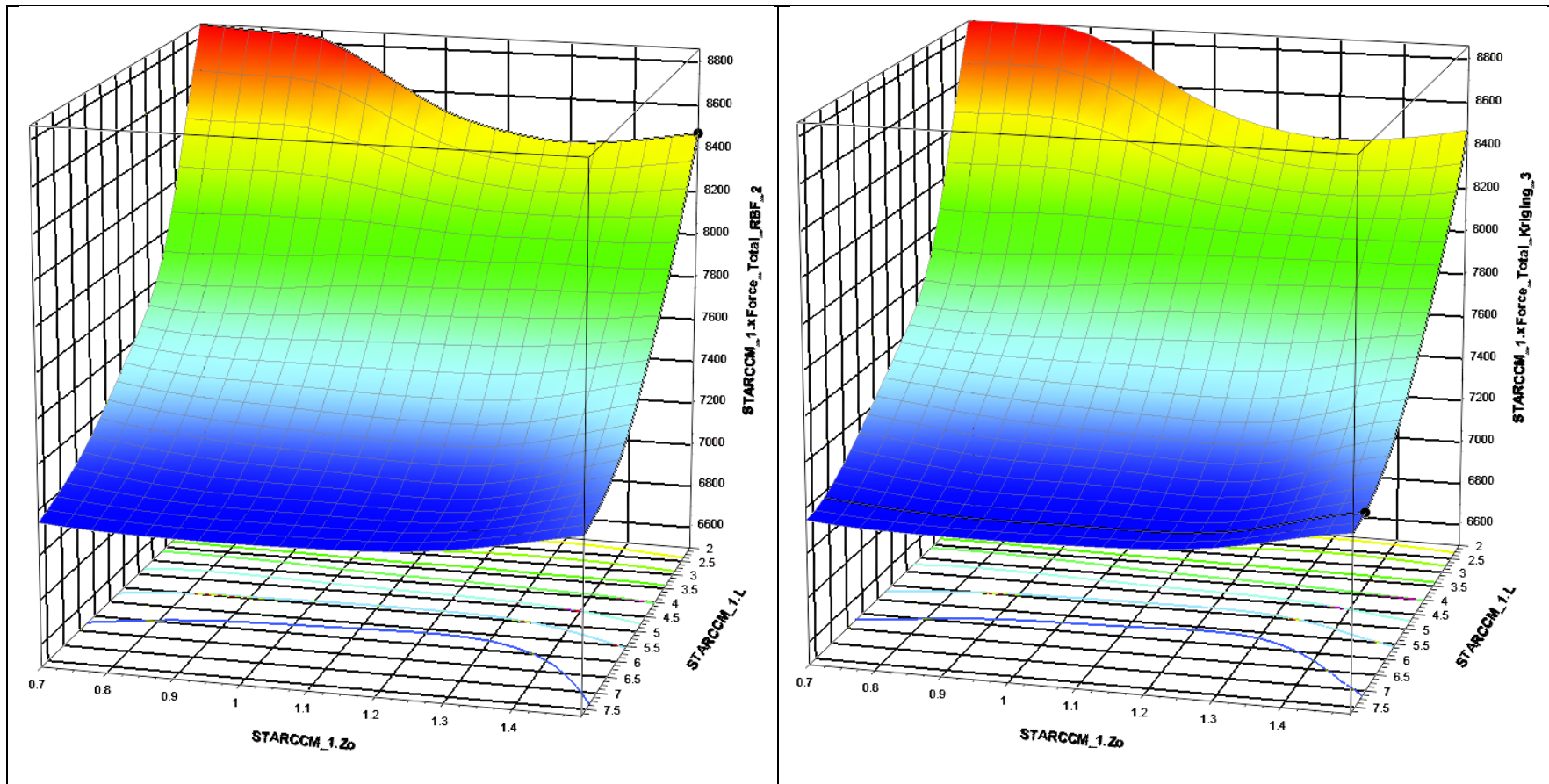


Figure 153: The variation of the total x-force (vertical axis) acting on the train as a function of nose length (L) and nose-tip height ( $Z_0$ ) for a constant inflection point height ( $H=2\text{m}$ ). The response surface on the left was created by making use of the radial basis function (RBF), while that on the right was created by making use of Kriging.

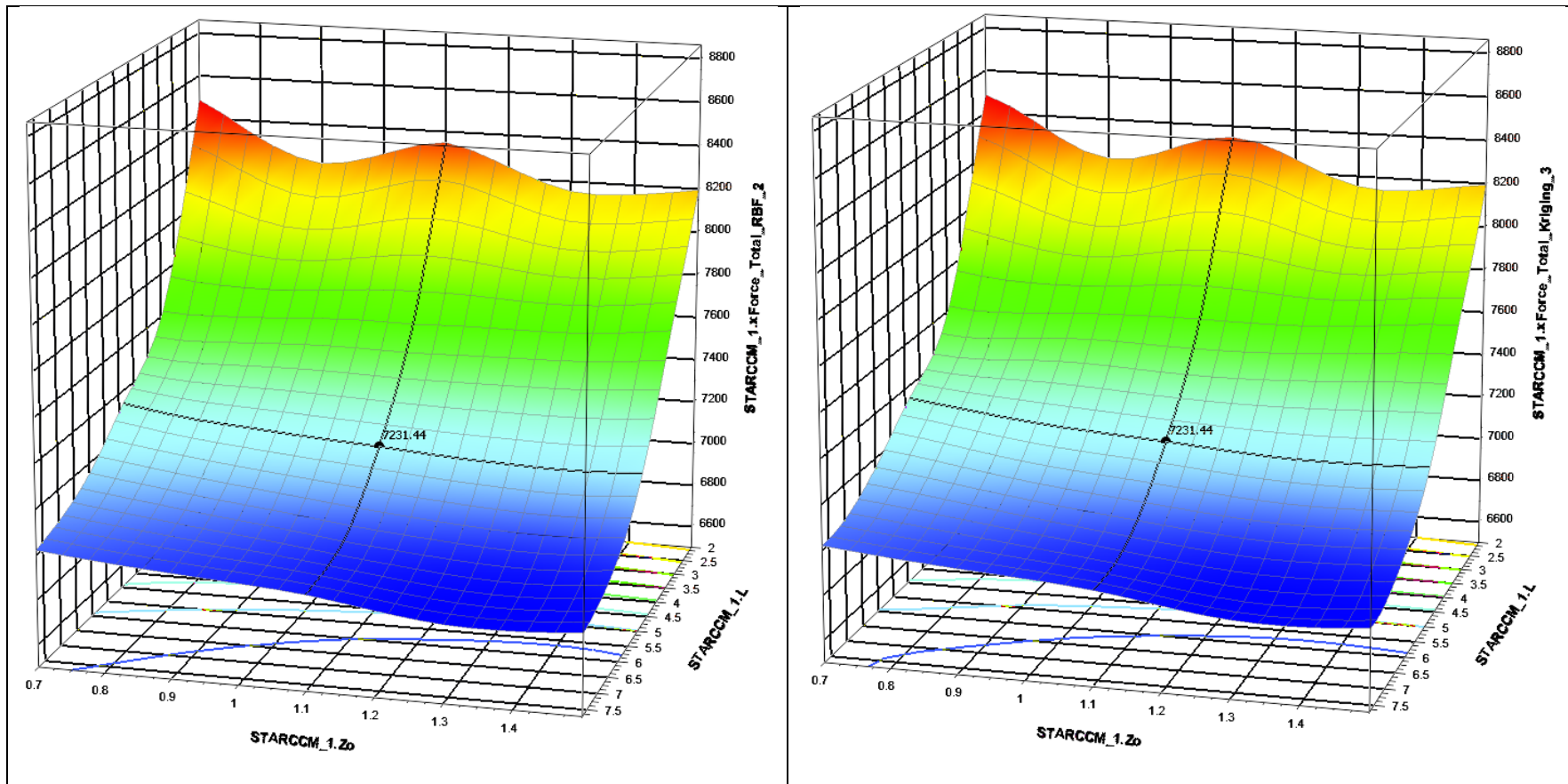


Figure 154: The variation of the total x-force (vertical axis) acting on the train as a function of nose length (L) and nose-tip height ( $Z_0$ ) for a constant inflection point height ( $H=2.5\text{m}$ ). The response surface on the left was created by making use of the radial basis function (RBF), while that on the right was created by making use of Kriging.

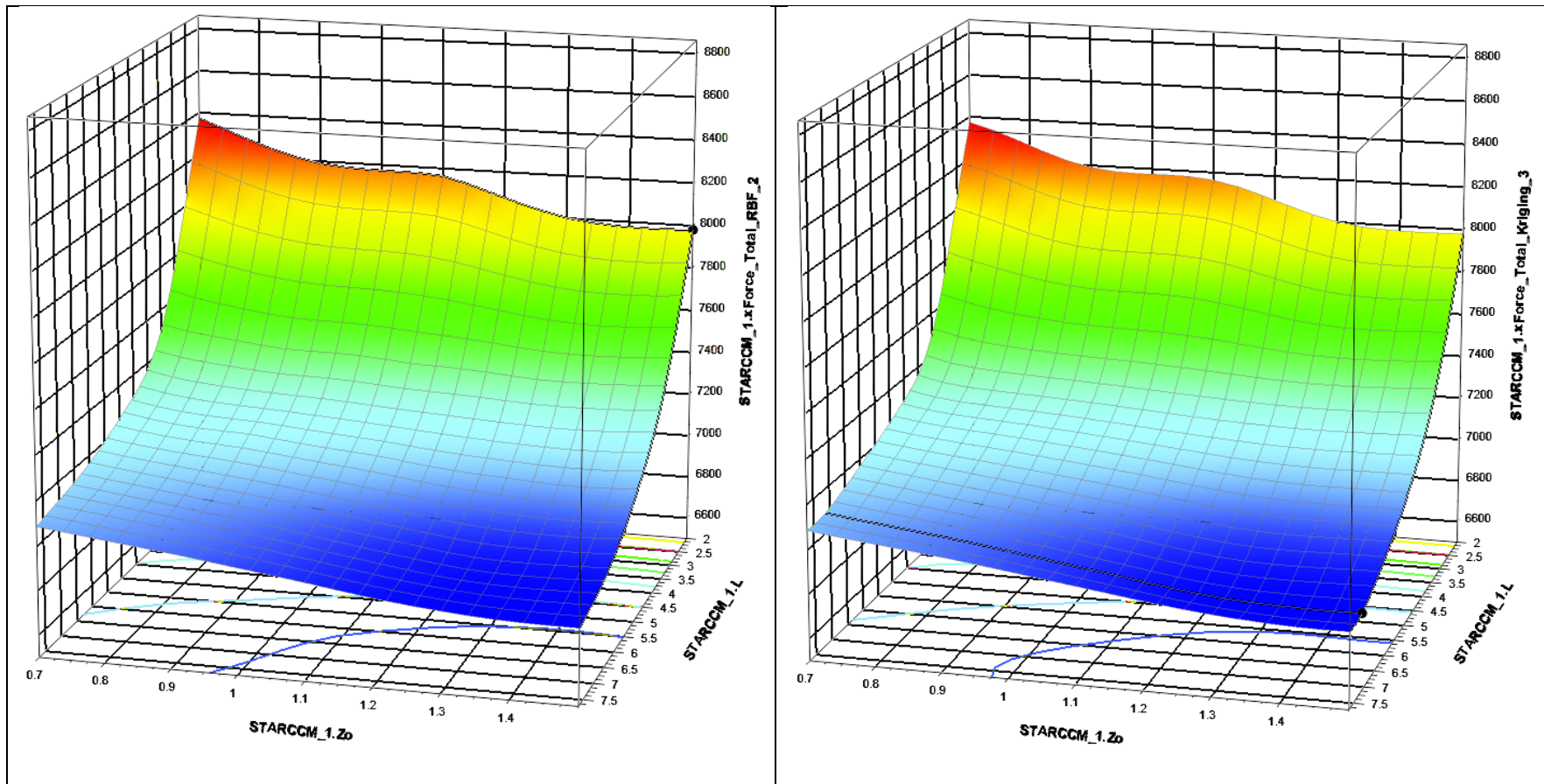


Figure 155: The variation of the total x-force (vertical axis) acting on the train as a function of nose length (L) and nose-tip height ( $Z_0$ ) for a constant inflection point height ( $H=3m$ ). The response surface on the left was created by making use of the radial basis function (RBF), while that on the right was created by making use of Kriging.

## Appendix F

This appendix is supplementary to section 5.2 in Chapter 5. Contained herein are the complete results of the domain effect study that was completed, in order to ensure that the force results obtained from simulation may be trusted. The process that was followed is described and the conclusions that could be drawn from the results are discussed.

### i. Determine Adequate Front Inlet Distance

The process of validating the location of the inlet boundary consisted of systematically translating the front inlet face (see Figure 108) in increments of 50m ( $n=50m$ ). Relative to the location associated with the base case, in total the face was translated 'n'-times in the positive x-direction and '3n'-times in the negative x-direction (as per Figure 108). The various locations of the front inlet face that were considered along with their respective designations are given in Table 60.

The effects that the location of the front inlet face has on the stability of the x-force acting on the train and its various subcomponents are shown in Figure 156 and will be discussed first; the total drag force acting on the train fluctuates marginally (2%) with the location of the front inlet face, as such any of the locations would have been a suitable choice, although there is a definite stabilization observable from inlet 2 and onwards. Similarly the variation in drag force acting on the coaches is negligible, with a maximum deviation of 2%. Despite its behaviour remaining oscillatory, the amplitude of the oscillations is such that any of the front inlet distances would have been a suitable choice. Furthermore, similar observations can be made with regard to the drag force acting on the train tail as well as the force components acting above and below the stagnation point on the nose. It is only the drag force acting on the train nose that displays highly erratic behaviour with a maximum deviation of 43%. This component only stabilizes from front inlet distance 3 onwards. As such, the drag force acting on the train necessitates a minimum front inlet distance of 546.19m.

With regard to the y-force components, the behaviour of the total side force acting on the train as well as the components acting on the nose, coaches and above the stagnation point on the train nose is such that any of the front inlet distances would have been a suitable choice. With regard to the y-force component acting beneath the stagnation point, a maximum deviation of 5% is present with a stable nature observable from inlet 3 onwards. The side force acting on the tail of the train however displays erratic behaviour and remains unstable irrespective of the location of the front inlet face. Bearing in mind that the deviation in the subsequent simulation results between inlet distances 3 and 4 is still considerable at 54% and that there is 596.19m between the tip of the nose and the inlet face at inlet distance 4, it doesn't seem a prudent course of action to increase the front inlet distance further. Not only does the side force acting on the tail show no signs of stabilizing but from a purely computational perspective, increasing the domain further and the number of cells associated with that course of action simply becomes impractical; bear in mind that optimization is already a very computationally expensive endeavor and as such keeping the cell count of a model reasonable is crucial to an acceptable simulation time. Thus with regard to the y-force components a minimum front inlet distance of 546.19m from the nose-tip is required.

Finally there is the matter of the z-force components acting on the train and their behaviour as a function of the location of the front inlet face (see Figure 114). There are a few z-force components that continue fluctuating as a function of the boundary location but their amplitudes are such that the fluctuations are negligible. The maximum deviations of these lift force components as a function of front inlet distance are 4%, 4%, 2% and 5% for the total train body, the coaches, and the portion above the stagnation point and that below it respectively. For these force components any front inlet distance would have been a suitable choice although broadly speaking there is a more stable nature observable from inlet distance three (546.19m) onwards. With regard to the nose and tail of the train, the lift force components acting on them remain unstable irrespective of the inlet boundary location, with the nose showing the larger measure of instability. The maximum deviation the tail component shows as a function of boundary location is 9%, while the instability associated with the nose component is more severe with a maximum deviation of 30%. It is thus prudent to treat results obtained from or by making use of these components with a measure of skepticism.

Simulation Case	Front Inlet Distance 1	Base Case	Front Inlet Distance 2	Front Inlet Distance 3	Front Inlet Distance 4
Front Inlet Distance [m]	396.19	446.19	496.19	546.19	596.19

Table 60: The various simulation cases that were considered in order to determine an adequate front inlet distance and their associated values.

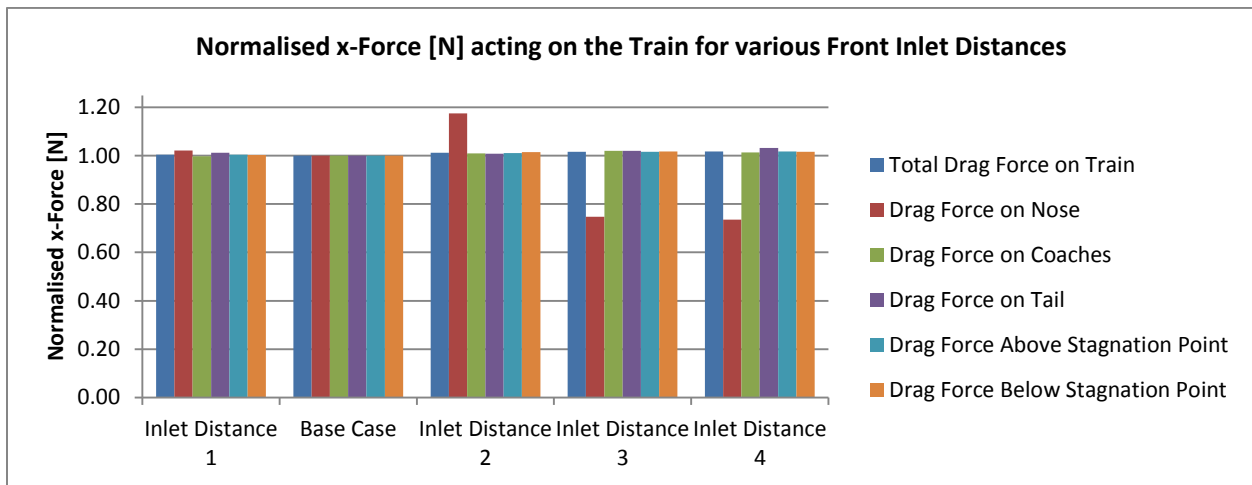


Figure 156: The Normalised x-force [N] acting on the Train as a whole as well as its sub-components given for the various locations of the front inlet face.

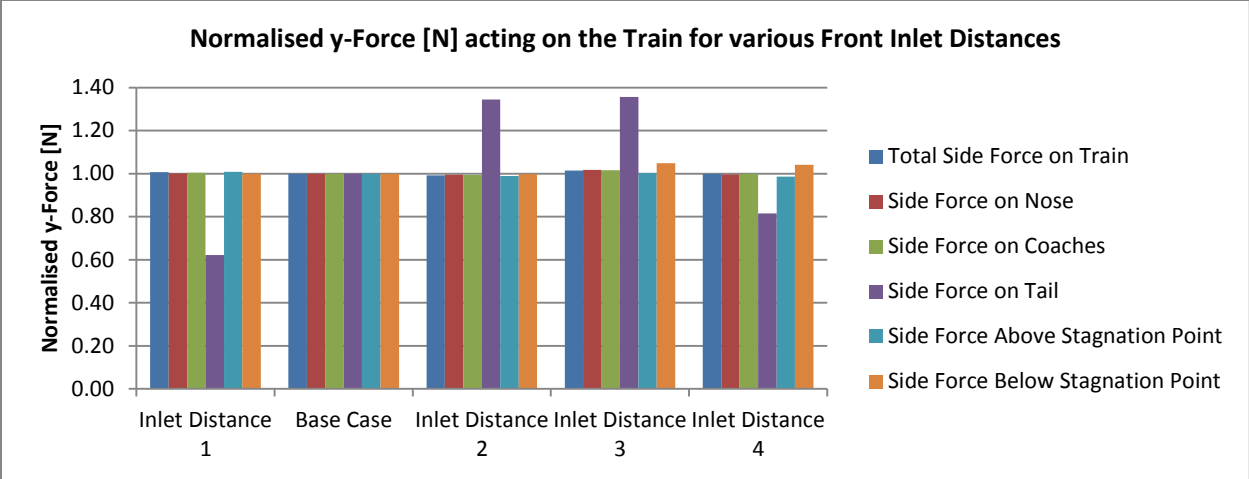


Figure 157: The Normalised y-force [N] acting on the Train as a whole as well as its sub-components given for the various locations of the front inlet face.

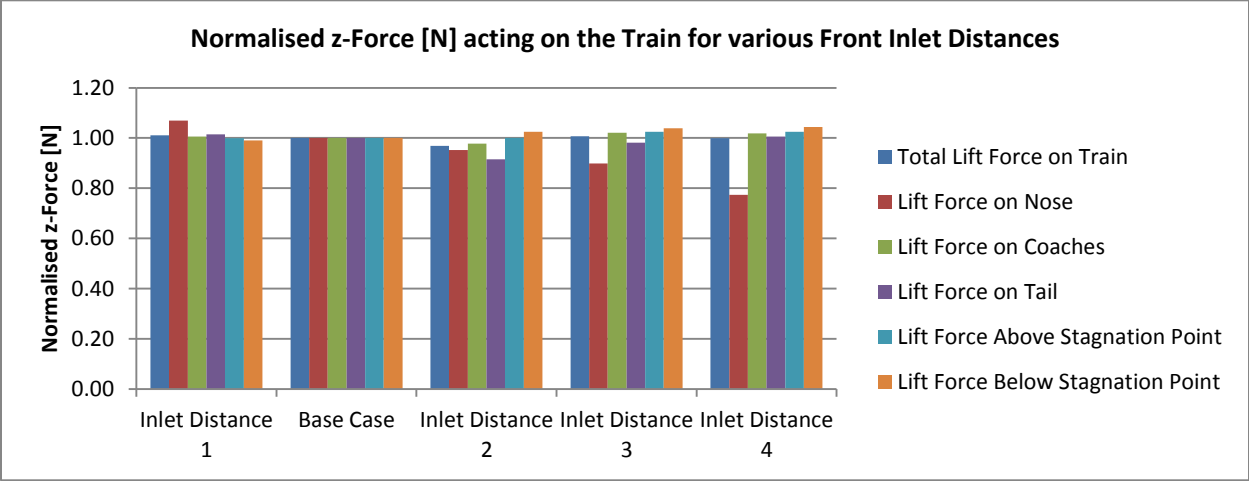


Figure 158: The Normalised z-force [N] acting on the Train as a whole as well as its sub-components given for the various locations of the front inlet face.

**ii. Determine Adequate Side Inlet Distance**

All x-force components, except for the partial nose-drag, acting on the train are stable as a function of the side inlet distance (see Figure 159). Given the measure of instability the nose component exhibits however, it is not practical to further increase the distance between the side inlet face and train, since it could lead to a model that isn't computationally viable. Therefore no further attempt will be made to ensure a partial nose drag component that is insensitive to the side inlet boundary location, rather results that relate to this force component will be treated with caution.

The y-force components acting on the train also show insensitivity to the location of the side inlet boundary (see Figure 160). The only exception to the aforementioned is the side force acting on the tail which remains highly erratic irrespective of boundary location. Thus, as with the x-force components acting on the train, any side inlet distance is acceptable, while bearing in mind that the partial tail side force and those forces associated with it must be treated with the necessary skepticism.

The results of the lift force components as given by Figure 161 are somewhat unexpected since there is an uncannily large measure of insensitivity to the location of the side inlet face visible. The only component that fluctuates somewhat as a function of the boundary location is the lift force acting on the nose; a maximum deviation of 7% is observable. This y-force component does, however, stabilize largely from inlet distance 2 onwards. As such, it is this side inlet distance (338.49m) that was chosen for the final domain configuration.

Simulation Case	Base Case	Side Inlet Distance 1	Side Inlet Distance 2	Side Inlet Distance 3
Side Inlet Distance [m]	138.49	238.49	338.49	438.49

Table 61: The various simulation cases that were considered in order to determine an adequate side inlet distance and their associated values.

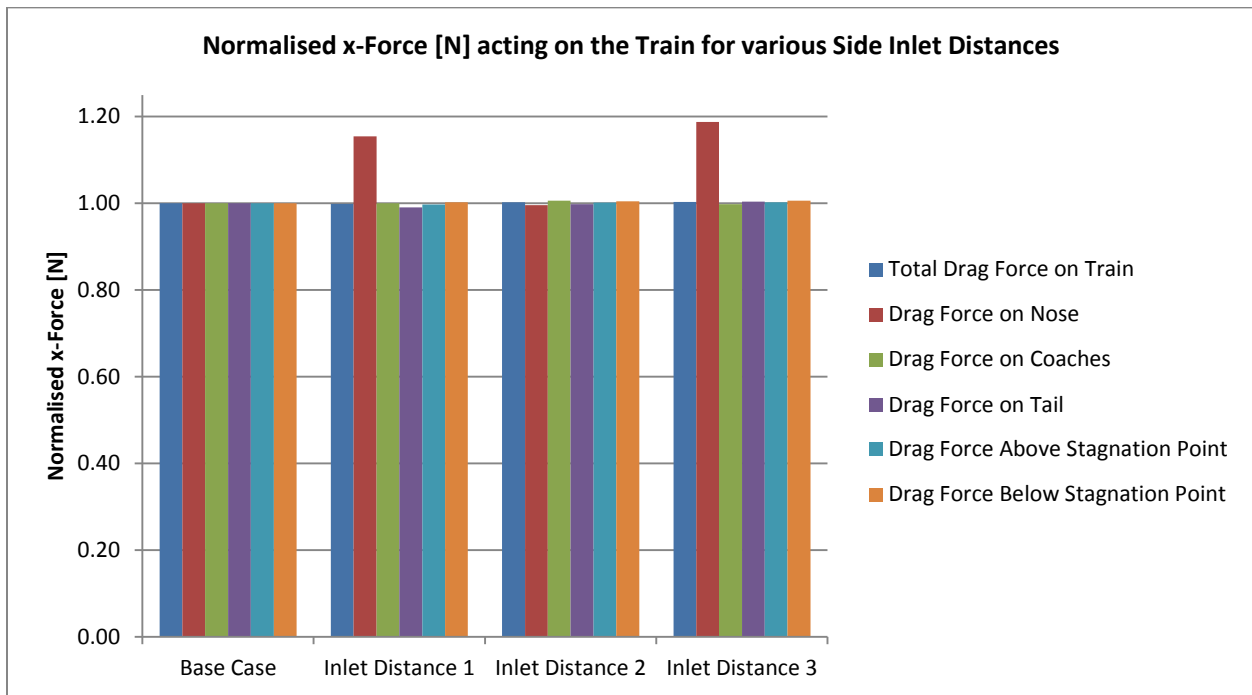


Figure 159: The Normalised x-force [N] acting on the Train as a whole as well as its sub-components given for the various locations of the side inlet face.

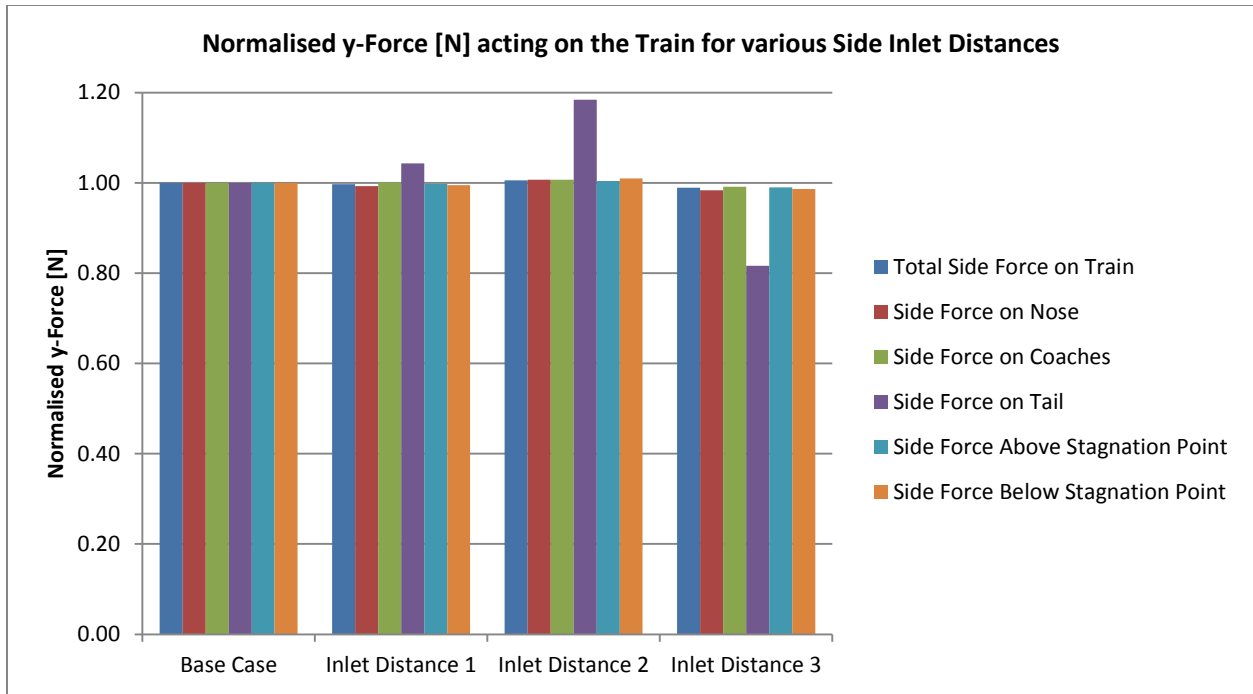


Figure 160: The Normalised y-force [N] acting on the Train as a whole as well as its sub-components given for the various locations of the side inlet face.

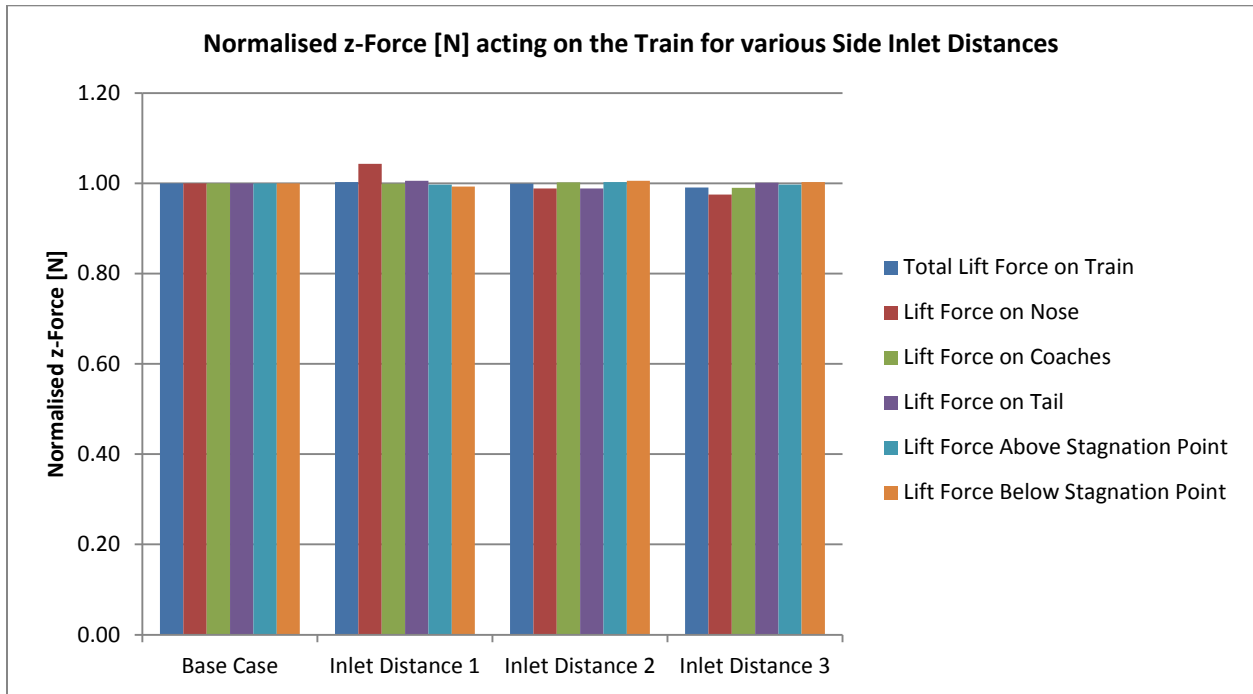


Figure 161: The Normalised z-force [N] acting on the Train as a whole as well as its sub-components given for the various locations of the side inlet face.

### iii. Determine Adequate Back Outlet Distance

With regard to an adequate back outlet distance, the various boundary locations that were assumed are given in Table 62. From the results given in Figure 162 through to Figure 164, it is clear that all the force components are broadly speaking insensitive to the location of the back outlet boundary. There are two exceptions to the aforementioned, i.e., the partial nose drag and the side force acting on the tail. With regard to the y-force acting on the tail, there is some sensitivity visible to the boundary location. However, not only is the maximum deviation percentage small (4%) but the y-force components acting on the tail as a function of the front (see Figure 113) and side inlet distances (see Figure 160) remains unstable also. It is thus redundant to attempt to attain insensitivity for the tail side force as a function of the back outlet boundary, when the force component displays such erratic behaviour as a function of the other boundaries. Finally, the drag force acting on the nose (see Figure 162) displays such unpredictable behaviour that it is unlikely that increasing the distance between the train tail and the back outlet face further, will have a marked impact on the sensitivity of the force component. Thus, rather than attempt to achieve insensitivity for this force component, hereby potentially unreasonably increasing the cell count associated with the model, results that pertain to this force component will simply be treated with caution.

Simulation Case	Back Outlet Distance 1	Base Case	Back Outlet Distance 2
Back Outlet Distance [m]	1084.68	1184.68	1284.68

Table 62: The various simulation cases that were considered in order to determine an adequate back outlet distance along with their associated values.

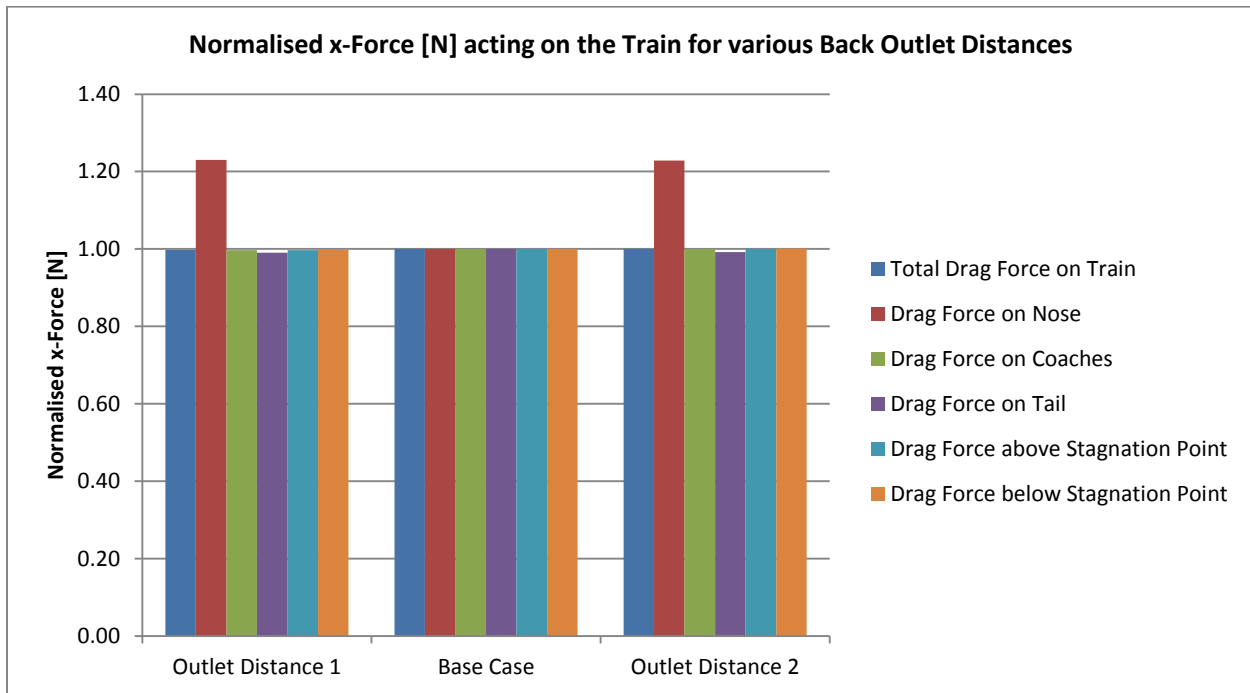


Figure 162: The Normalised x-force [N] acting on the Train as a whole as well as its sub-components given for the various locations of the back outlet face.

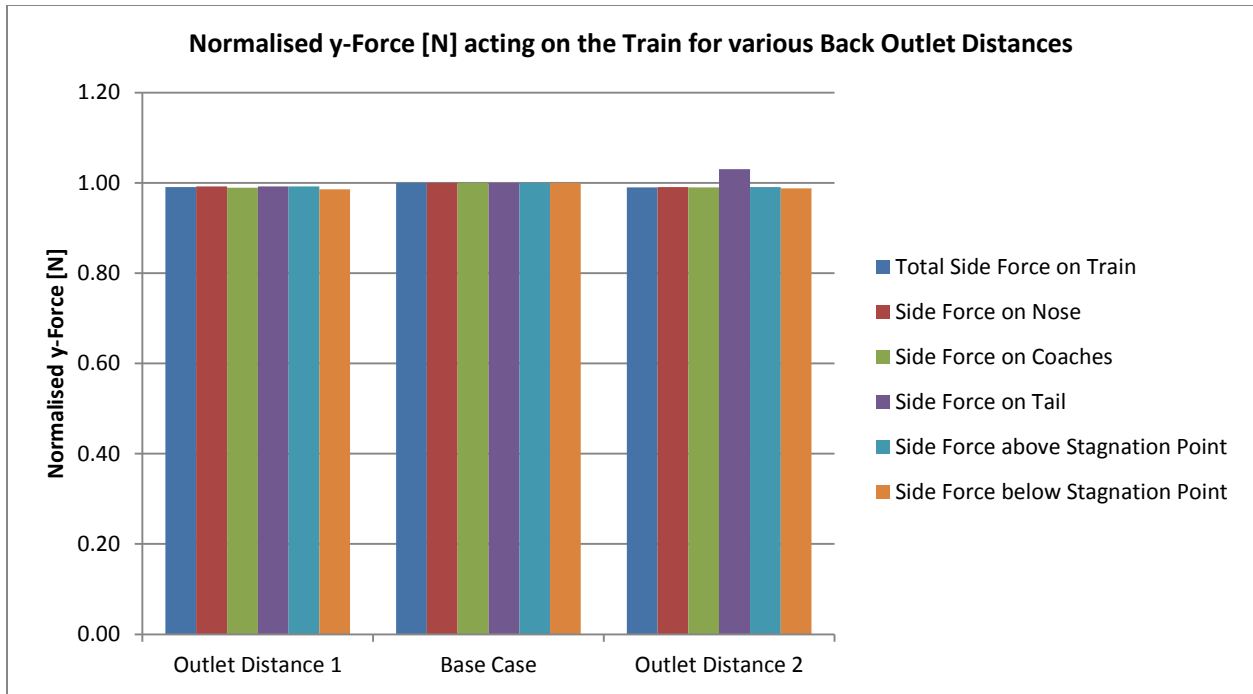


Figure 163: The Normalised y-force [N] acting on the Train as a whole as well as its sub-components given for the various locations of the back outlet face.

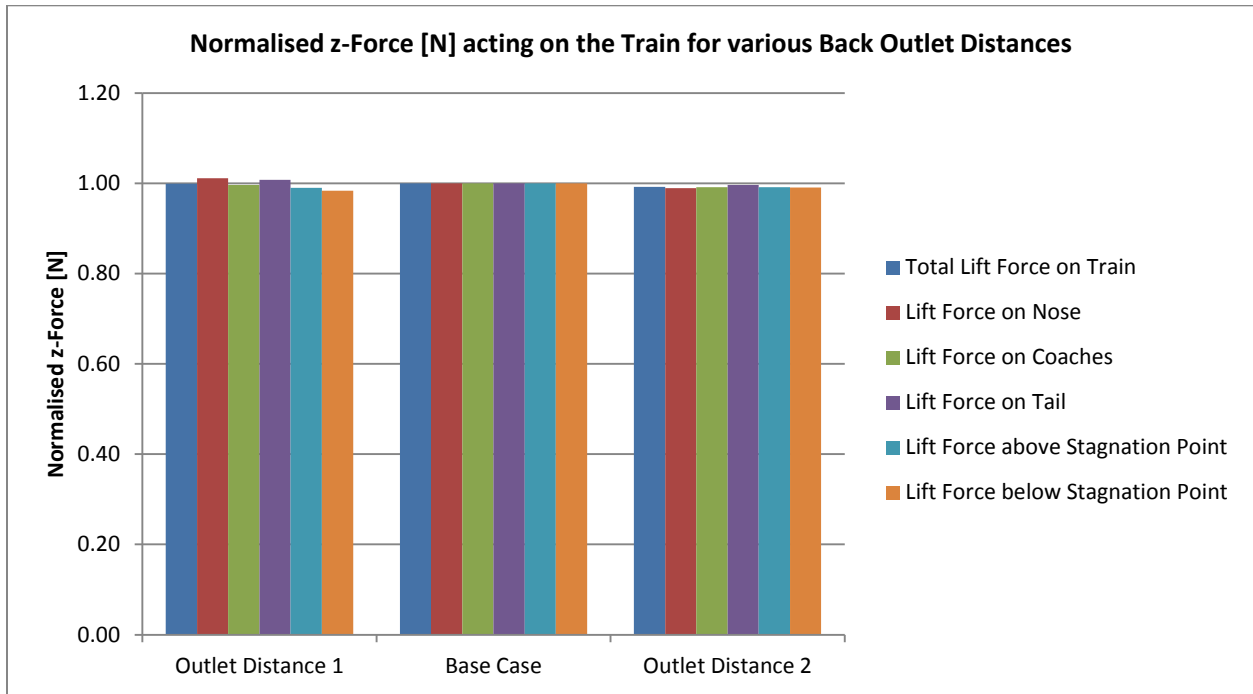


Figure 164: The Normalised z-force [N] acting on the Train as a whole as well as its sub-components given for the various locations of the back outlet face.

#### iv. Determine Adequate Side Outlet Distance

The final boundary location that was investigated was that of the side outlet face (see Table 63). From Figure 165 it's clear that the total drag force, the partial coach-drag as well as the drag acting on the top and the bottom of the train, is insensitive to the boundary location. The drag force acting on the tail however shows some sensitivity as a function of boundary location, before stabilizing from Outlet 3 (738.49m) onwards. The partial drag acting on the nose remains unstable irrespective of boundary location, with a considerable maximum deviation of 246.43%. Thus no further attempt will be made to ensure that this component is insensitive to the location of the boundary.

The effect that the location of the side outlet distance has on the y-force components acting on the train (see Figure 166) is surprisingly uniform save for the partial side force acting on the tail. That is, these components initially show some sensitivity to the boundary location while finally stabilizing at outlet distance 3 onwards. The side force acting on the tail remains erratic irrespective of the boundary location although it does seem to start showing a promising tendency towards stabilization from outlet distance 2 onwards. Once again however, a further increase of the domain size to reach this stable point is not necessarily computationally viable. The final side outlet distance as a function of the side force acting on the train, is thus outlet distance 3 (738.49m).

Finally, there is the matter if the lift force components acting on the train as a function of the side outlet distance to consider; the total lift force, partial nose-lift, partial coach-lift and the lift acting on the portion of the train above the stagnation point are all insensitive to the location of the boundary from side outlet distance 3 (738.49) and onwards. Furthermore, the lift force acting on the tail is insensitive to all locations of the boundary and as such any of the side outlet distances would be a suitable choice. The lift component that seems most sensitive is that of the z-force acting below the stagnation point. This component does however indicate that a reasonable measure of insensitivity has been reached from outlet 3 onwards. Consider that the reduction in the z-force component from outlet 2 to 3 is 6%, while the reduction from outlet 3 to 4 is 4%. Using side outlet distance 3 thus seems to be adequate for predicting the lift force component beneath the train accurately.

Simulation Case	Base Case	Side Outlet Distance 1	Side Outlet Distance 2	Side Outlet Distance 3	Side Outlet Distance 4
Side Outlet Distance [m]	138.49	338.49	538.49	738.49	938.49

Table 63: The various simulation cases that were considered in order to determine an adequate side outlet distance along with their associated values.

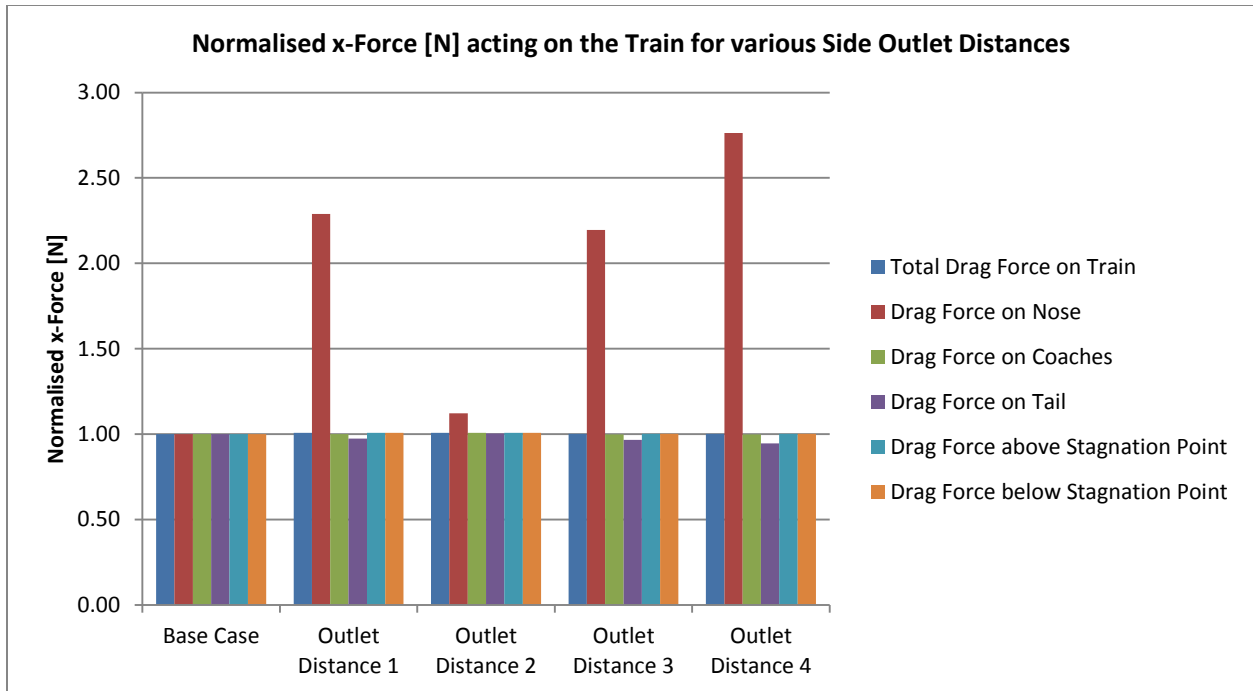


Figure 165: The Normalised x-force [N] acting on the Train as a whole as well as its sub-components given for the various locations of the side outlet face.

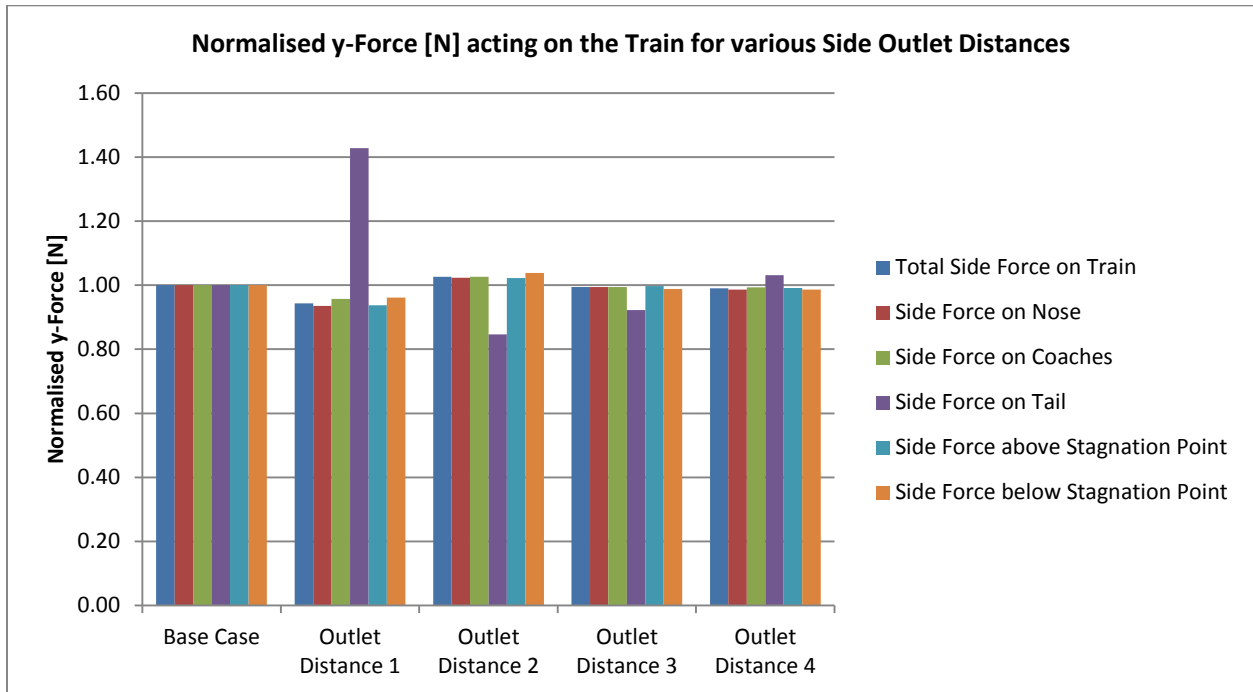


Figure 166: The Normalised y-force [N] acting on the Train as a whole as well as its sub-components given for the various locations of the side outlet face.

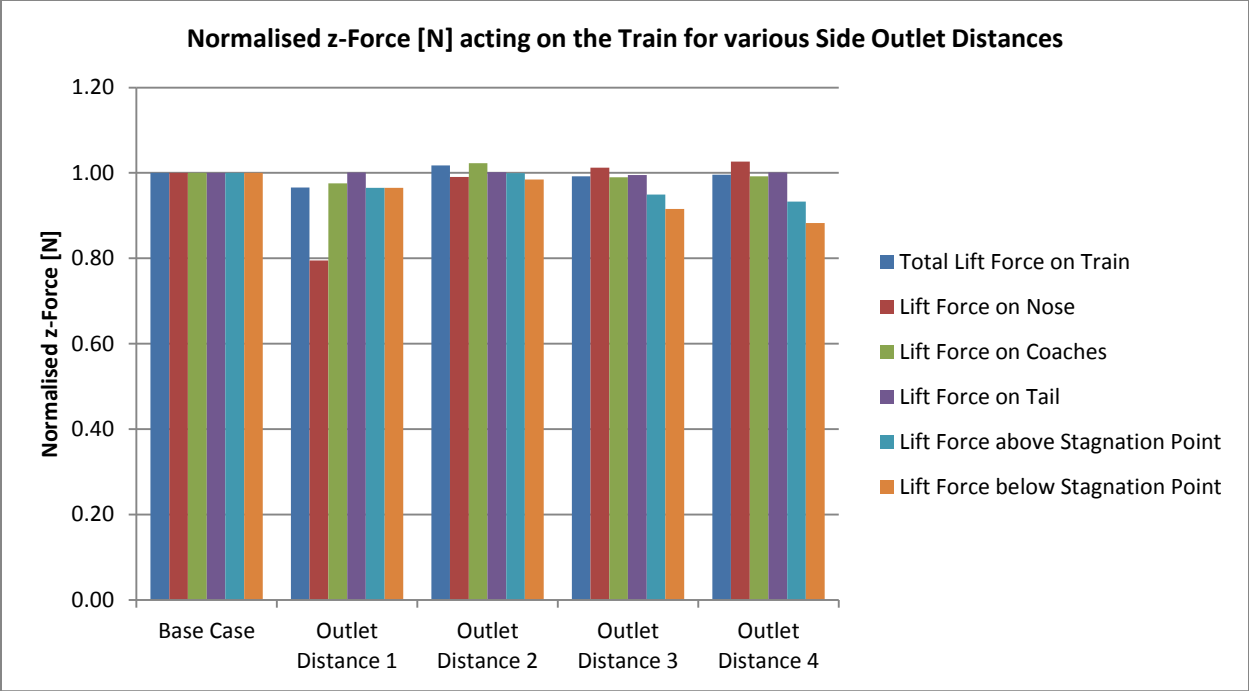


Figure 167: The Normalised z-force [N] acting on the Train as a whole as well as its sub-components given for the various locations of the side outlet face.

## Appendix G

This appendix is supplementary to section 5.3.2 in Chapter 5. Shown here are the force responses acting on the train tail, under crosswind conditions. Section i shows the x-force results while section ii and iii, show the y- and z-force results respectively, and in all instances the nose length (L) acts as the “slider”. From the results it is clear that the magnitudes of the forces acting on the tail are relatively small when compared to those acting on the nose. This appendix thus serves to further prove the importance of ensuring the stability of the train nose, rather than the tail, under crosswind conditions.

### i. x-Force acting on the Tail

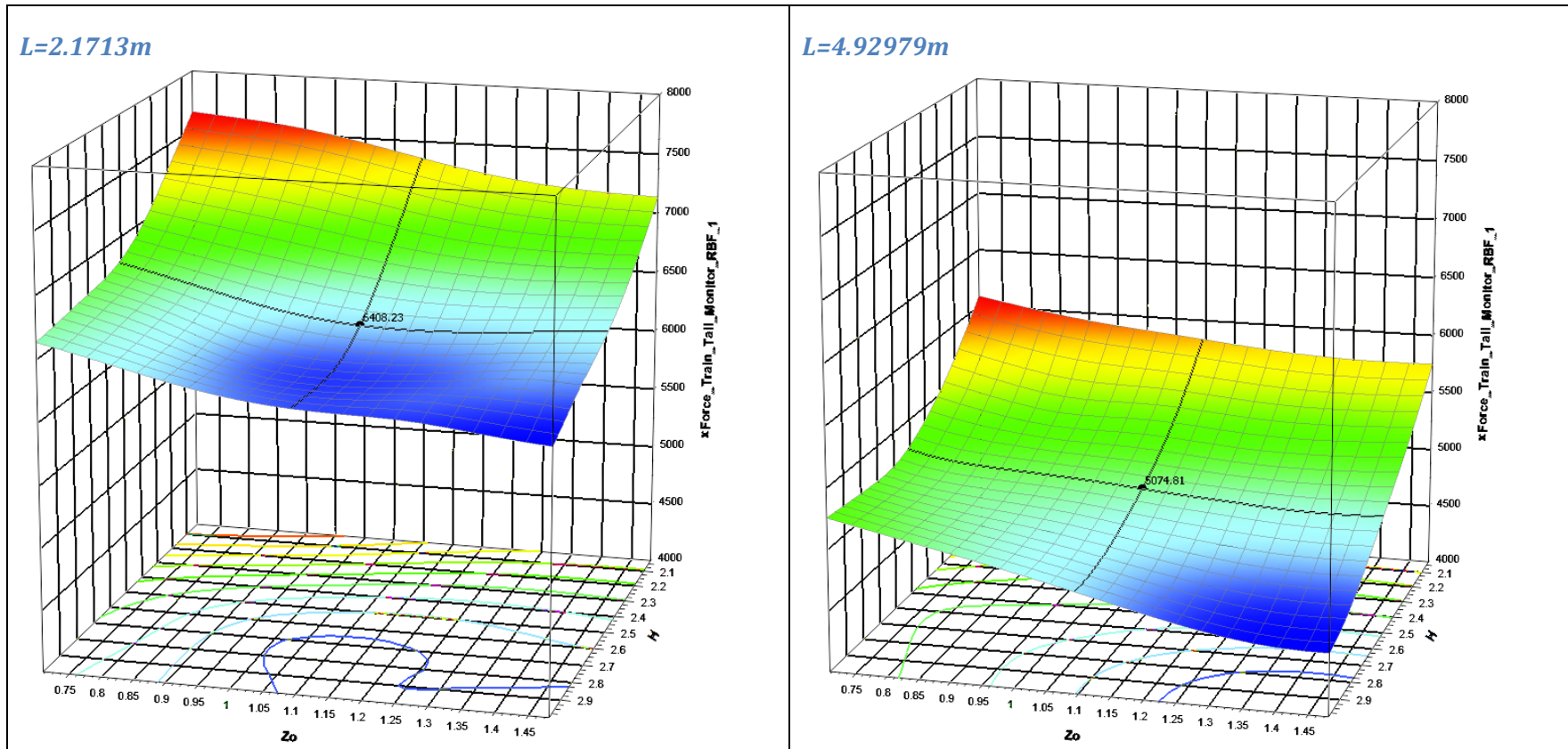


Figure 168: The variation of the x-force (vertical axis) acting on the tail as a function of nose-tip height ( $Z_0$ ) and inflection point height ( $H$ ), shown here for nose lengths of 2.1713m, left and 4.92979m, right.

$L=7.68828m$

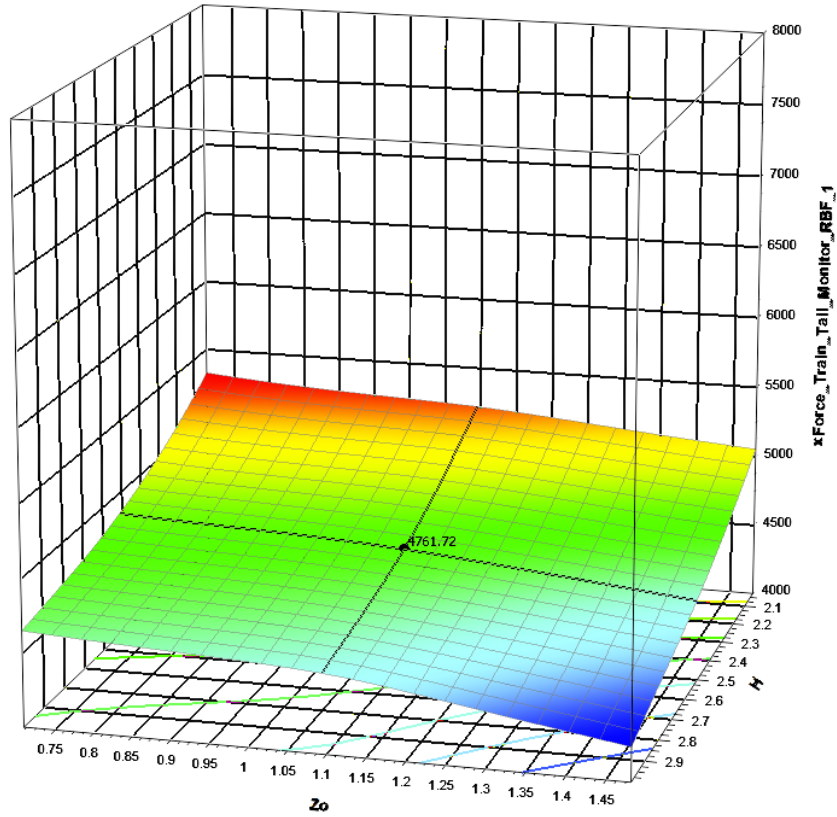


Figure 169: The variation of the x-force (vertical axis) acting on the tail as a function of nose-tip height ( $Z_0$ ) and inflection point height ( $H$ ), shown here for a nose length of 7.68828m.

ii. y-Force acting on the Tail

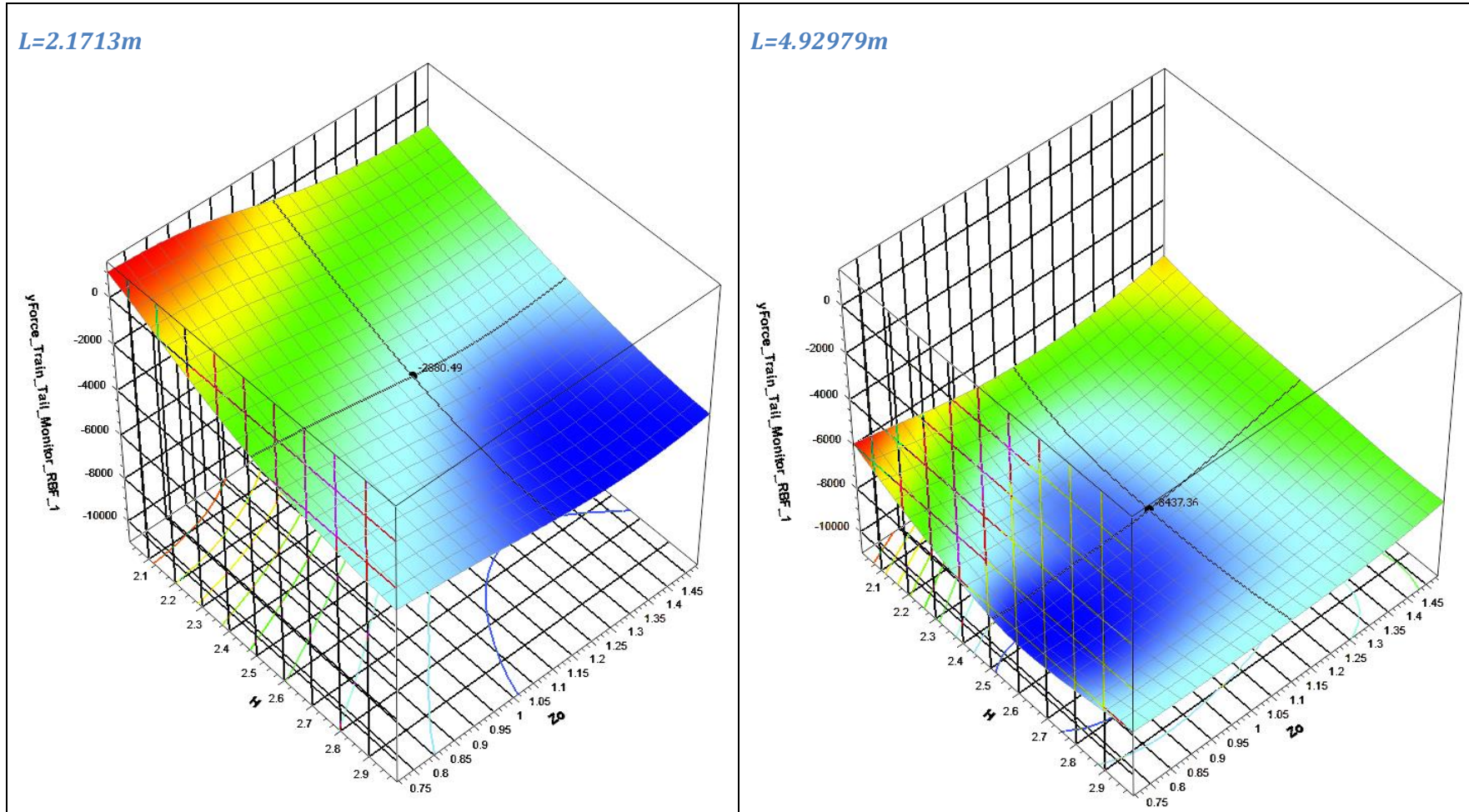


Figure 170: The variation of the y-force (vertical axis) acting on the tail as a function of nose-tip height ( $Z_0$ ) and inflection point height ( $H$ ), shown here for nose lengths of 2.1713m, left and 4.92979m, right.

$L=7.68828m$

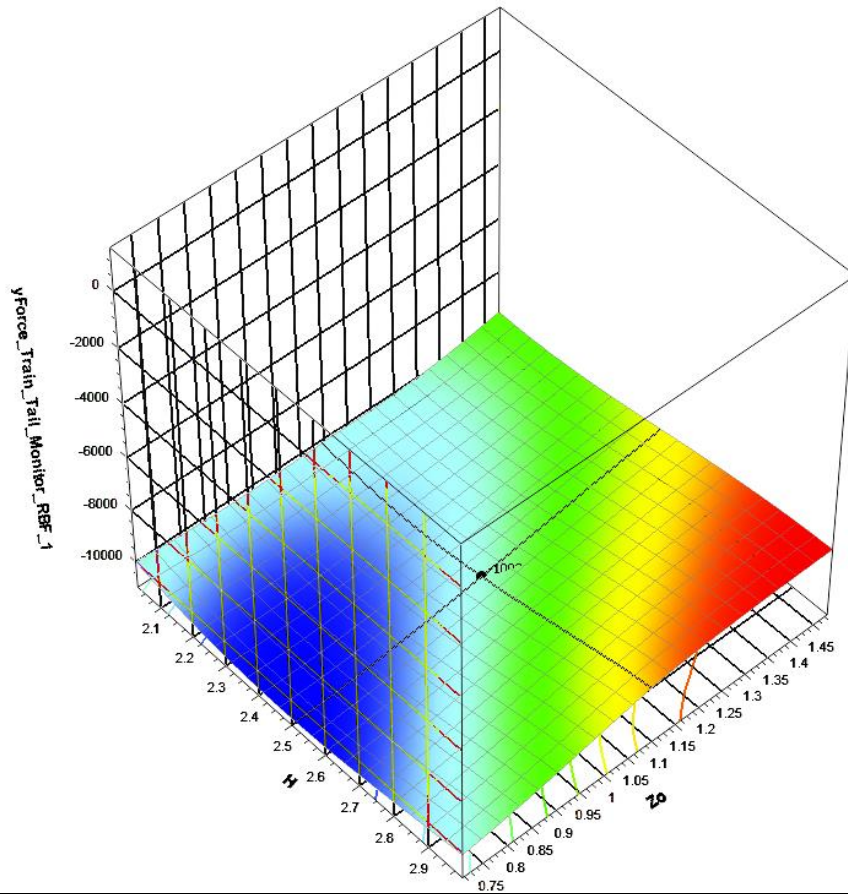
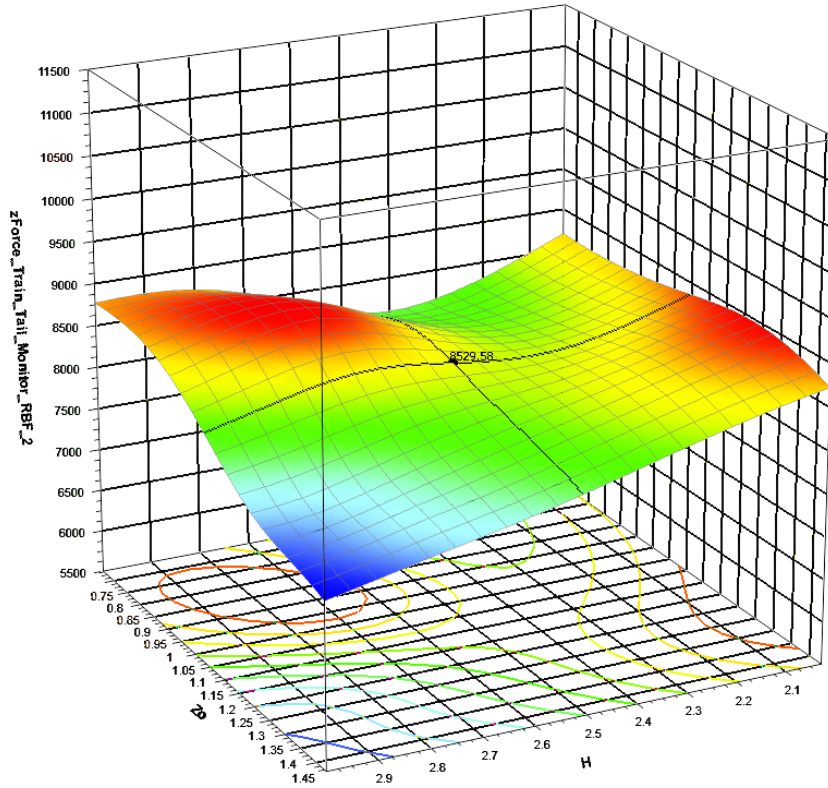


Figure 171: The variation of the y-force (vertical axis) acting on the tail as a function of nose-tip height ( $Z_0$ ) and inflection point height ( $H$ ), shown here for a nose length of 7.68828m.

### iii. z-Force acting on the Tail

$L=2.1713m$



$L=4.92979m$

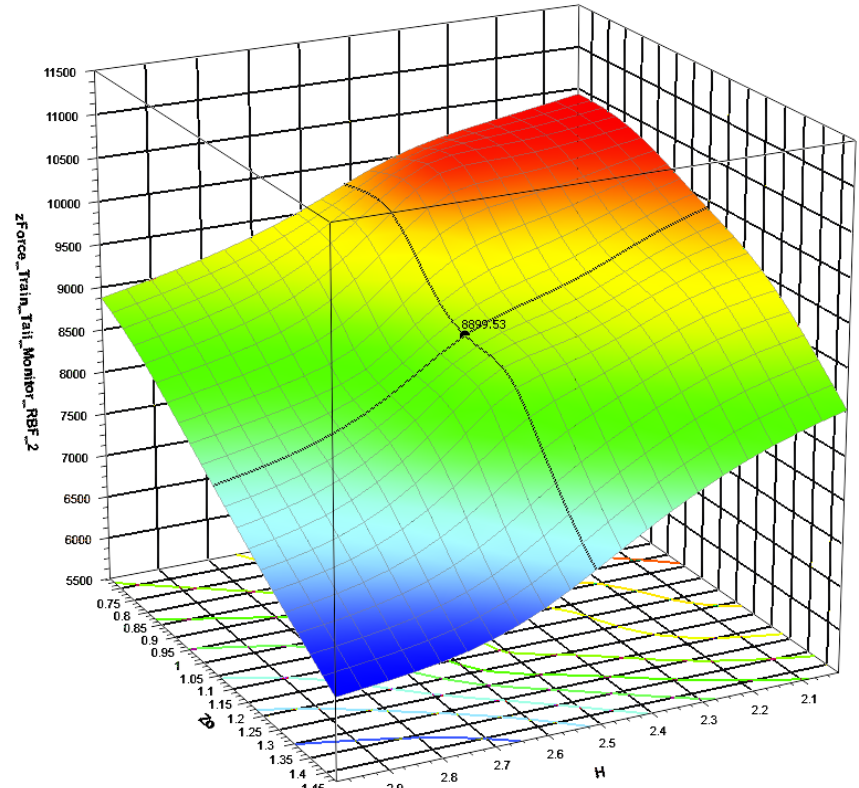


Figure 172: The variation of the z-force (vertical axis) acting on the tail as a function of nose-tip height ( $Z_0$ ) and inflection point height ( $H$ ), shown here for nose lengths of 2.1713m, left and 4.92979m, right.

$L=7.68828m$

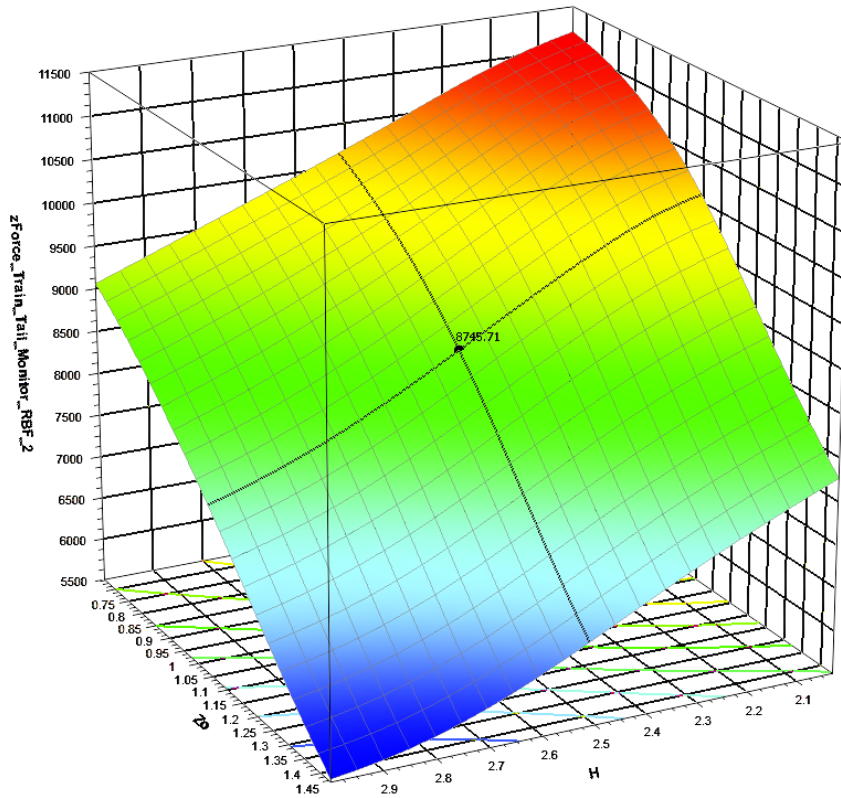


Figure 173: The variation of the z-force (vertical axis) acting on the tail as a function of nose-tip height ( $Z_0$ ) and inflection point height ( $H$ ), shown here for a nose length of 7.68828m.

## Appendix H

This appendix is supplementary to section 4.5.2 in Chapter 4. Shown here is the table containing the 125 design points which were obtained by making use of a 5-level full-factorial design sweep. The points were simulated for a windless condition in STAR-CCM+ in order to allow for the construction of a response surface model.

Design ID	STARCCM_1.xForce_Total	STARCCM_1.H	STARCCM_1.L	STARCCM_1.Zo
1	8862.247316	2	2	0.7
2	8824.256611	2	2	0.9
3	8511.253093	2	2	1.1
4	8398.201742	2	2	1.3
5	8473.161043	2	2	1.5
6	7912.569772	2	3.425	0.7
7	7926.1545	2	3.425	0.9
8	7957.681214	2	3.425	1.1
9	7971.061005	2	3.425	1.3
10	7983.672926	2	3.425	1.5
11	7538.428028	2	4.85	0.7
12	7494.343702	2	4.85	0.9
13	7477.781855	2	4.85	1.1
14	7491.660682	2	4.85	1.3
15	7619.434579	2	4.85	1.5
16	7288.824097	2	6.275	0.7
17	7222.069468	2	6.275	0.9
18	7213.435875	2	6.275	1.1
19	7214.798332	2	6.275	1.3
20	7370.984041	2	6.275	1.5
21	7145.58549	2	7.7	0.7
22	7123.044793	2	7.7	0.9
23	7128.972312	2	7.7	1.1
24	7168.589727	2	7.7	1.3
25	7281.200237	2	7.7	1.5
26	8280.48496	2.25	2	0.7
27	8336.757349	2.25	2	0.9
28	8353.151575	2.25	2	1.1
29	8261.569736	2.25	2	1.3
30	8402.18308	2.25	2	1.5
31	7768.578342	2.25	3.425	0.7
32	7785.09677	2.25	3.425	0.9
33	7811.862756	2.25	3.425	1.1
34	7817.034361	2.25	3.425	1.3
35	7872.032999	2.25	3.425	1.5

36	7400.831879	2.25	4.85	0.7
37	7363.104458	2.25	4.85	0.9
38	7338.540305	2.25	4.85	1.1
39	7305.68654	2.25	4.85	1.3
40	7339.71947	2.25	4.85	1.5
41	7179.558675	2.25	6.275	0.7
42	7097.946824	2.25	6.275	0.9
43	7056.295105	2.25	6.275	1.1
44	7003.714998	2.25	6.275	1.3
45	7041.570341	2.25	6.275	1.5
46	7078.74533	2.25	7.7	0.7
47	7031.652143	2.25	7.7	0.9
48	6991.826864	2.25	7.7	1.1
49	6976.717022	2.25	7.7	1.3
50	7024.53299	2.25	7.7	1.5
51	8483.970005	2.5	2	0.7
52	8216.418774	2.5	2	0.9
53	8348.713451	2.5	2	1.1
54	8153.674511	2.5	2	1.3
55	8194.591372	2.5	2	1.5
56	7617.919414	2.5	3.425	0.7
57	7625.359478	2.5	3.425	0.9
58	7636.94935	2.5	3.425	1.1
59	7643.348385	2.5	3.425	1.3
60	7688.190493	2.5	3.425	1.5
61	7341.719686	2.5	4.85	0.7
62	7271.946544	2.5	4.85	0.9
63	7231.436152	2.5	4.85	1.1
64	7195.199241	2.5	4.85	1.3
65	7203.974686	2.5	4.85	1.5
66	7118.829497	2.5	6.275	0.7
67	7044.792948	2.5	6.275	0.9
68	6975.20502	2.5	6.275	1.1
69	6925.87985	2.5	6.275	1.3
70	6945.081147	2.5	6.275	1.5
71	7020.358851	2.5	7.7	0.7
72	6968.97693	2.5	7.7	0.9
73	6924.218382	2.5	7.7	1.1
74	6845.936459	2.5	7.7	1.3
75	6862.93092	2.5	7.7	1.5
76	8197.026279	2.75	2	0.7

77	8172.077164	2.75	2	0.9
78	8112.296324	2.75	2	1.1
79	8070.027497	2.75	2	1.3
80	8130.398703	2.75	2	1.5
81	7560.125117	2.75	3.425	0.7
82	7535.180231	2.75	3.425	0.9
83	7515.263047	2.75	3.425	1.1
84	7494.573388	2.75	3.425	1.3
85	7506.305918	2.75	3.425	1.5
86	7202.05615	2.75	4.85	0.7
87	7168.150545	2.75	4.85	0.9
88	7120.910413	2.75	4.85	1.1
89	7089.402943	2.75	4.85	1.3
90	7091.240248	2.75	4.85	1.5
91	7105.158293	2.75	6.275	0.7
92	7057.657427	2.75	6.275	0.9
93	6996.630386	2.75	6.275	1.1
94	6922.723301	2.75	6.275	1.3
95	6887.810287	2.75	6.275	1.5
96	7010.250785	2.75	7.7	0.7
97	6954.519884	2.75	7.7	0.9
98	6909.408622	2.75	7.7	1.1
99	6806.053073	2.75	7.7	1.3
100	6814.129151	2.75	7.7	1.5
101	8372.540222	3	2	0.7
102	8190.640897	3	2	0.9
103	8163.915257	3	2	1.1
104	8001.257662	3	2	1.3
105	7980.865643	3	2	1.5
106	7521.737172	3	3.425	0.7
107	7445.603686	3	3.425	0.9
108	7419.69266	3	3.425	1.1
109	7386.309315	3	3.425	1.3
110	7402.850737	3	3.425	1.5
111	7264.38727	3	4.85	0.7
112	7206.727761	3	4.85	0.9
113	7151.316795	3	4.85	1.1
114	7095.084176	3	4.85	1.3
115	7091.547706	3	4.85	1.5
116	7147.503731	3	6.275	0.7
117	7072.140655	3	6.275	0.9

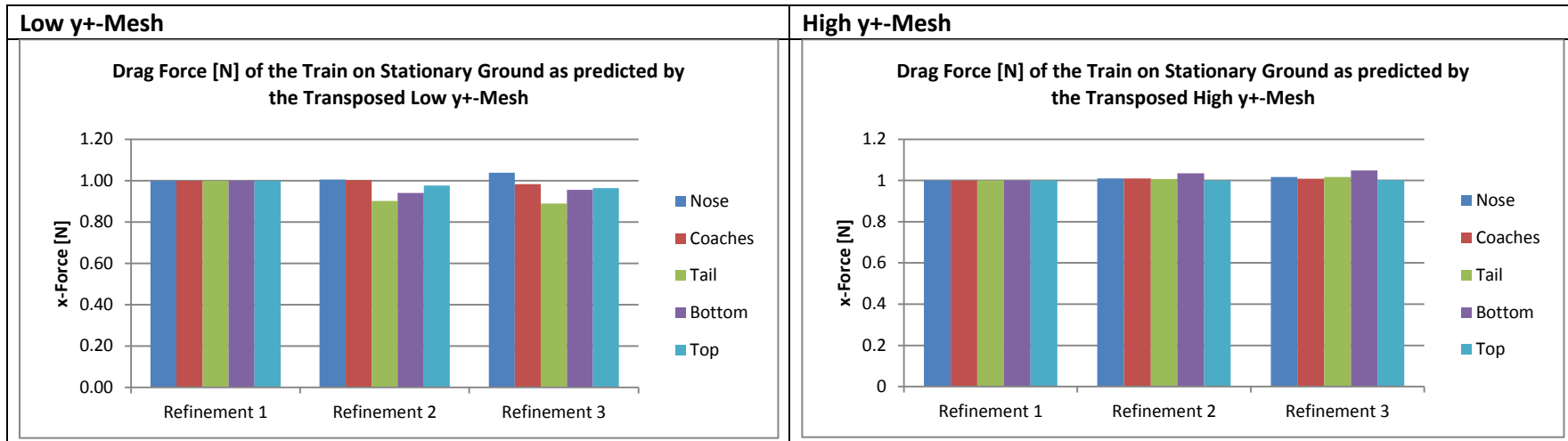
118	6989.696076	3	6.275	1.1
119	6912.661248	3	6.275	1.3
120	6915.774381	3	6.275	1.5
121	7085.775783	3	7.7	0.7
122	7017.477181	3	7.7	0.9
123	6938.422941	3	7.7	1.1
124	6864.200306	3	7.7	1.3
125	6841.458839	3	7.7	1.5

Table 64: The complete table of the 125 design points ran for the various combinations of the parameters that define the train nose geometry and their respective total drag force response.

## Appendix I

This appendix is to be read along with Appendix C, which in turn is supplementary to section 4.3.3. The results of the GCI method for a stationary ground with transposed mesh, moving ground with transposed mesh and moving ground with coarsened mesh, are considered for both the low-, as well as the high  $y^+$ -meshes. The convergence of the x- (see section i), y- (see section ii) and z-force (see section iii) components were monitored so that informed conclusions could be drawn regarding the ability of the computational model to accurately capture the flow features that are associated with the problem at hand.

### i. Drag Forces



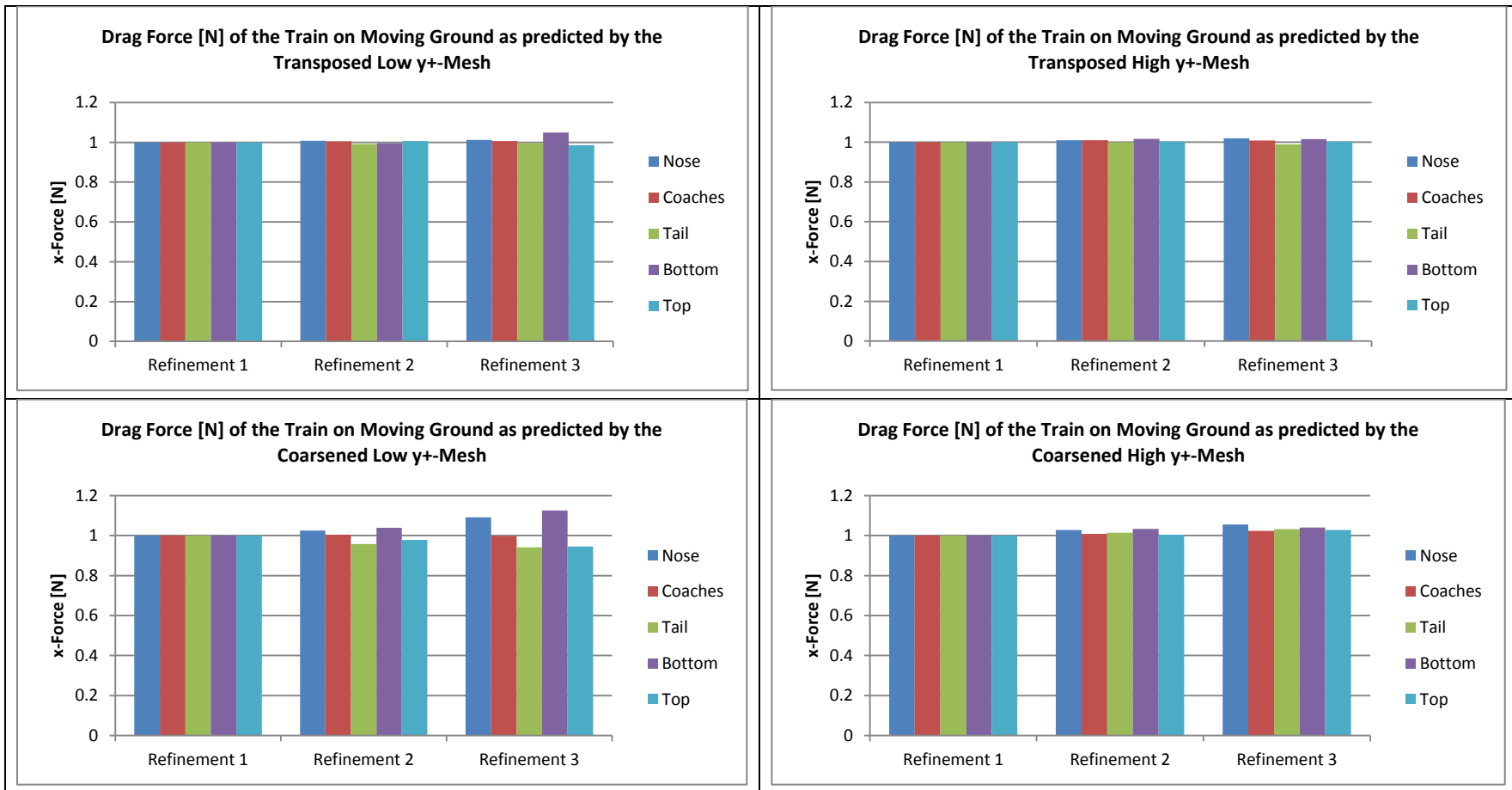
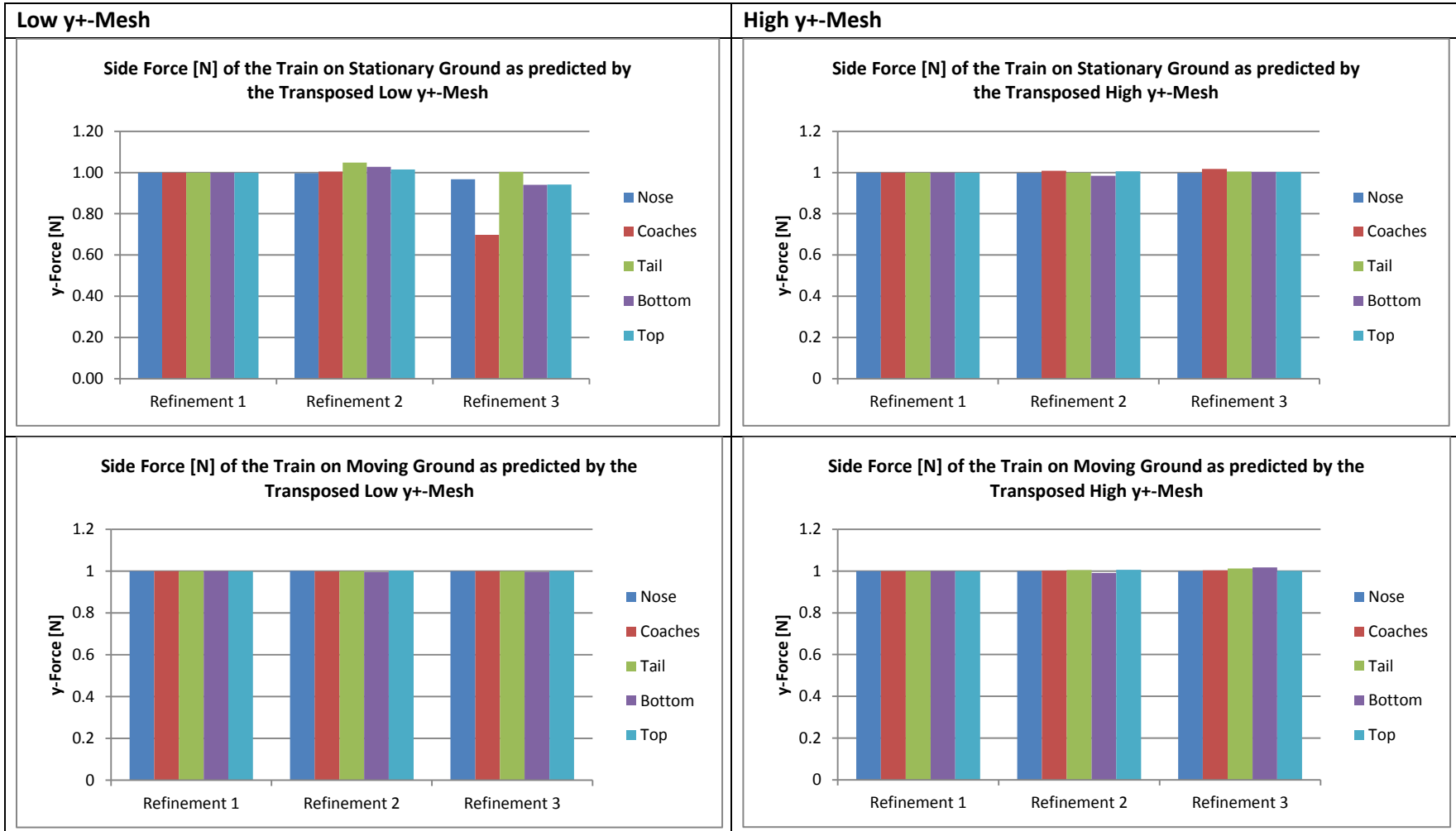


Figure 174: The drag forces [N] acting on the train for the various mesh refinement levels of the Low y+-Mesh (see Table 44) and the High y+-Mesh (see Table 45). The results are given for the leading locomotive (denoted as “nose”), the trailing locomotive (denoted as “tail”) and the coaches between the two. The results are also given for the “bottom” of the train, i.e., the tip of the nose and below it and for the “top” of the train, i.e., that portion of the train body above the nose tip. All forces were normalized by the force-value at mesh refinement level one.

ii. Side Forces



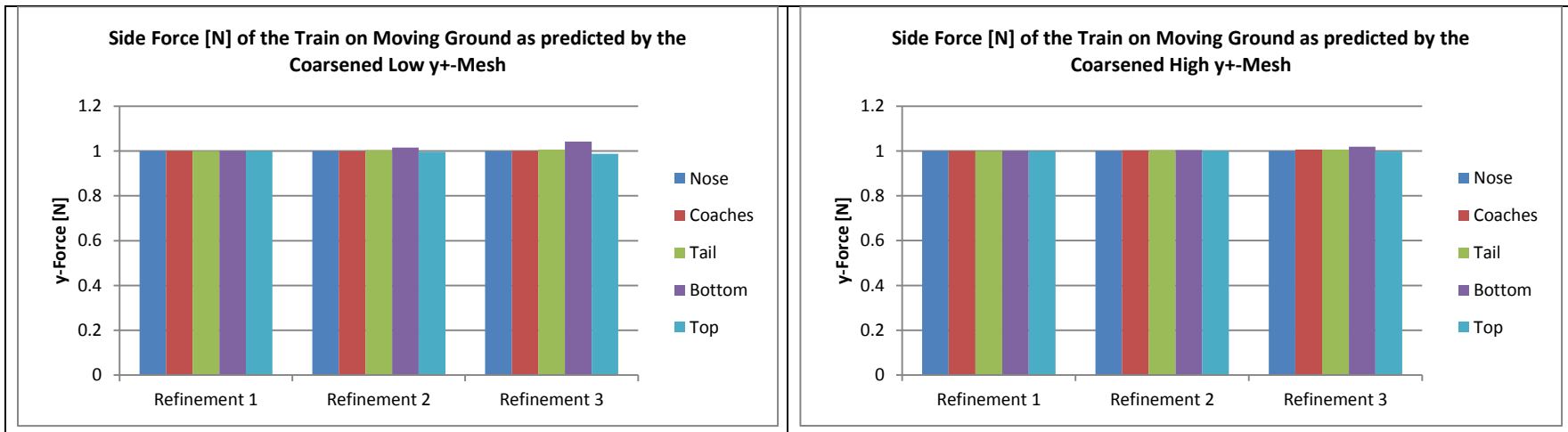
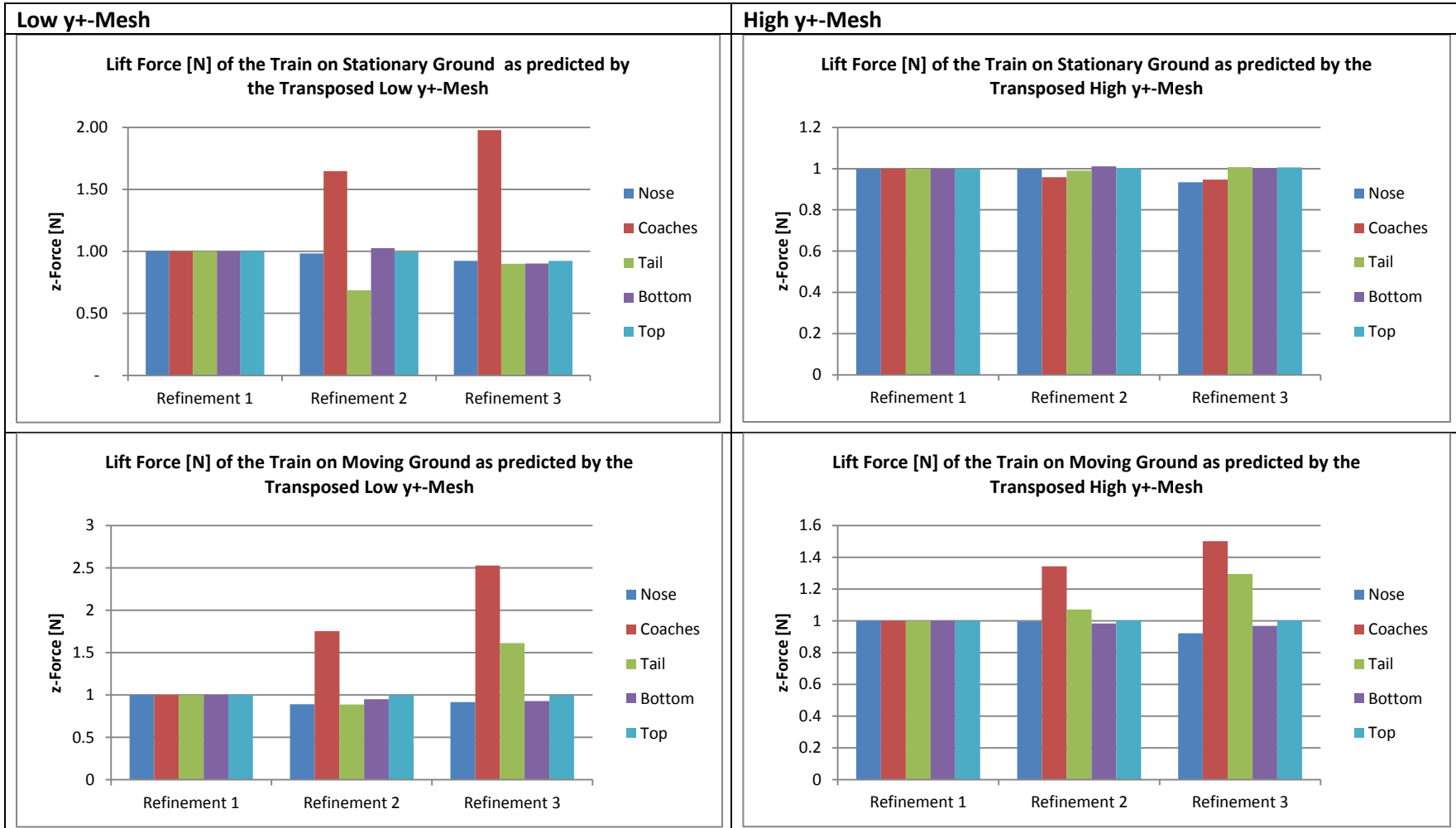


Figure 175: The side forces [N] acting on the train for the various mesh refinement levels of the Low y+-Mesh (see Table 44) and the High y+-Mesh (see Table 45). The results are given for the leading locomotive (denoted as “nose”), the trailing locomotive (denoted as “tail”) and the coaches between the two. The results are also given for the “bottom” of the train, i.e., the tip of the nose and below it and for the “top” of the train, i.e., that portion of the train body above the nose tip. All forces were normalized by the force-value at mesh refinement level one.

### iii. Lift Forces



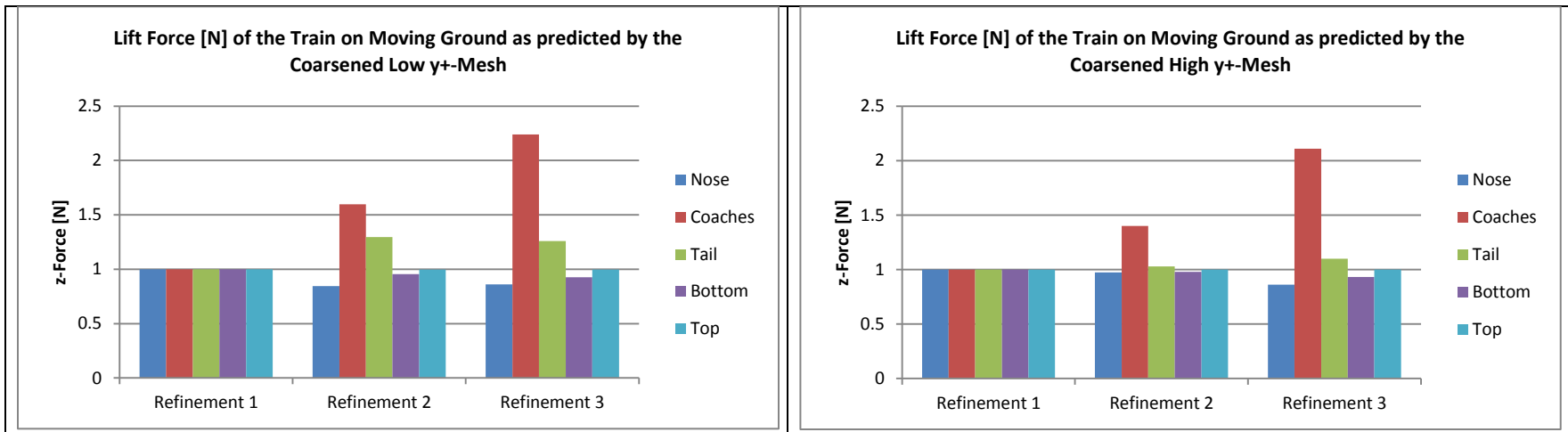


Figure 176: The lift forces [N] acting on the train for the various mesh refinement levels of the Low  $y^+$ -Mesh (see Table 44) and the High  $y^+$ -Mesh (see Table 45). The results are given for the leading locomotive (denoted as “nose”), the trailing locomotive (denoted as “tail”) and the coaches between the two. The results are also given for the “bottom” of the train, i.e., the tip of the nose and below it and for the “top” of the train, i.e., that portion of the train body above the nose tip. All forces were normalized by the force-value at mesh refinement level one.

## Appendix J

This appendix is supplementary to Appendix D. Relayed herein is the process that was followed, in order to validate the size of the computational domain, that was necessary to yield force results that were insensitive to boundary locations, when a streamlined nose geometry was made use of. It was, however, later found that a blunt nose requires a larger domain size. This work is thus included here, to validate the aforementioned.

### i. Inlet Distance

Shown here is the process followed in order to obtain an adequate inlet distance for the computational domain when a streamlined, nose geometry is made use of. As is typical with these studies, the boundary location is deemed appropriate once the force-components acting on the train body remain relatively insensitive when the location is increased further. In all instances a domain height of 138.49m was used, with a description of the nose given in Table 65 and the various locations of the inlet boundary that were considered given in Table 66. From the results “Inlet Distance 2” was deemed appropriate.

Variables	L	Z <sub>0</sub>	H
Value [m]	7.7	1	3

Table 65: The values of the nose length (L), nose-tip height (Z<sub>0</sub>) and inflection point height (H) of the nose geometry used for the study of an adequate inlet distance.

Simulation Case	Base Case	Inlet Distance 1	Inlet Distance 2	Inlet Distance 3
Domain Height [m]	46.19	96.19	146.19	196.19

Table 66: The various simulation cases that were considered in order to determine an adequate inlet distance and their associated values.

Simulation Case	Inlet Distance [m]	Element Count [Million]	Drag Force [N]		Side Force [N]		Lift Force [N]	
			x-Force	Deviation [%]	y-Force	Deviation [%]	z-Force	Deviation [%]
Base Case	46.19	5.28	7096	-0.240	54533	0.224	-2246	-17.542
Inlet Distance 1	96.19	5.36	7079	-0.268	54655	-0.046	-1852	10.475
Inlet Distance 2	146.19	5.42	7060	-0.085	54630	-0.004	-2046	8.602
Inlet Distance 3	196.19	5.47	7054		54628		-2222	

Table 67: The total x-, y- and z-forces obtained from the simulation at various inlet boundary locations. The percentage deviation between subsequent values is also indicated.

Simulation Case	Drag Force [N]					
	Nose	Deviation [%]	Coaches	Deviation [%]	Tail	Deviation [%]
Base Case	1540	-0.844	4149	-0.072	1407	-0.071
Inlet Distance 1	1527	-0.196	4146	-0.169	1406	-0.640
Inlet Distance 2	1524	0.066	4139	-0.072	1397	-0.286
Inlet Distance 3	1525		4136		1393	

Table 68: The drag force acting on the various sub-components of the train, i.e., the nose, coaches and tail, at various inlet boundary locations. The percentage deviation between subsequent values is also indicated.

Simulation Case	Side Force [N]					
	Nose	Deviation [%]	Coaches	Deviation [%]	Tail	Deviation [%]
Base Case	24760	0.158	9280	1.304	20493	-0.185
Inlet Distance 1	24799	0.004	9401	-0.191	20455	-0.039
Inlet Distance 2	24800	-0.040	9383	-0.075	20447	0.073
Inlet Distance 3	24790		9376		20462	

Table 69: The side force acting on the various sub-components of the train, i.e., the nose, coaches and tail, at various inlet boundary locations. The percentage deviation between subsequent values is also indicated.

Simulation Case	Lift Force [N]					
	Nose	Deviation [%]	Coaches	Deviation [%]	Tail	Deviation [%]
Base Case	-3116	-2.953	1424	21.419	-554	0.542
Inlet Distance 1	-3024	-2.447	1729	-17.293	-557	-5.566
Inlet Distance 2	-2950	2.949	1430	-7.552	-526	-3.612
Inlet Distance 3	-3037		1322		-507	

Table 70: The lift force acting on the various sub-components of the train, i.e., the nose, coaches and tail, at various inlet boundary locations. The percentage deviation between subsequent values is also indicated.



Figure 177: The normalised x-force [N] acting on the train for various domain inlet distances. All forces were normalised by the corresponding value obtained from the base case simulation. The figure shows the forces acting on the train as a whole as well as on the following sub-components; the train nose, coaches and tail as well as the forces acting above and below the stagnation point on the nose.

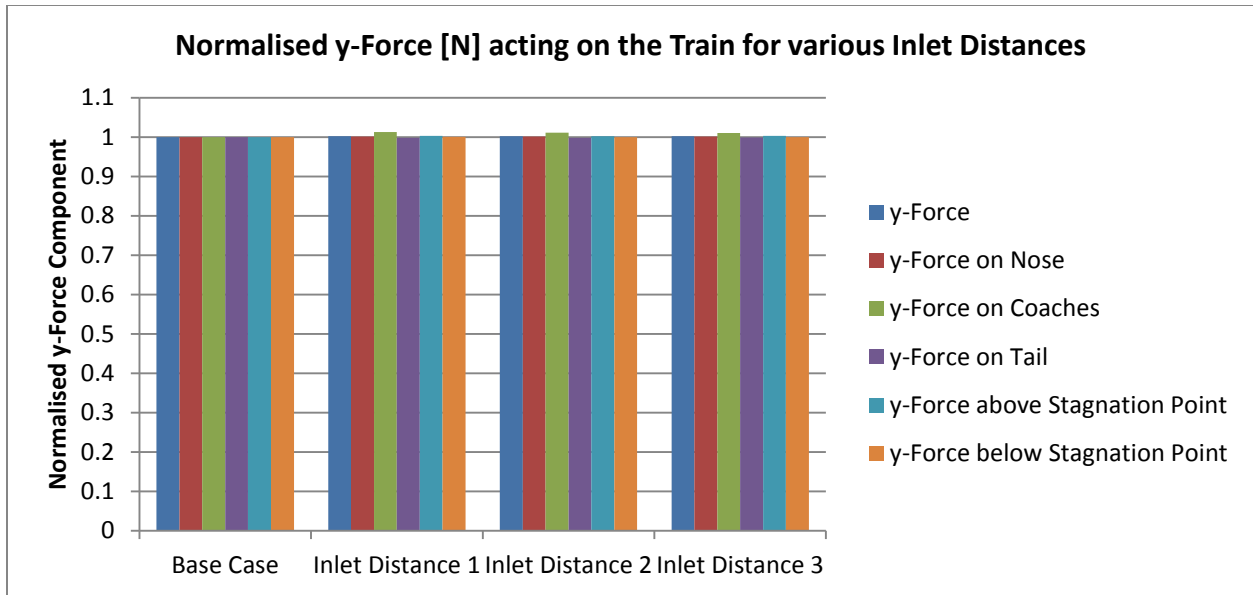


Figure 178: The normalised y-force [N] acting on the train for various domain inlet distances. All forces were normalised by the corresponding value obtained from the base case simulation. The figure shows the forces acting on the train as a whole as well as on the following sub-components; the train nose, coaches and tail as well as the forces acting above and below the stagnation point on the nose.

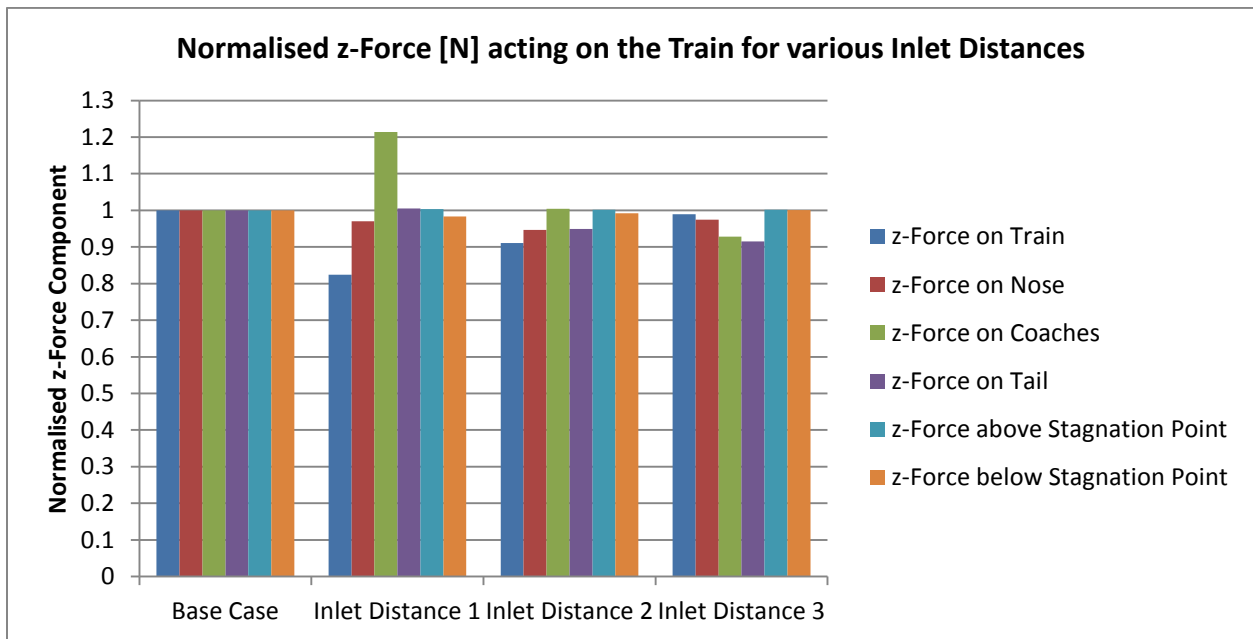


Figure 179: The normalised z-force [N] acting on the train for various domain inlet distances. All forces were normalised by the corresponding value obtained from the base case simulation. The figure shows the forces acting on the train as a whole as well as on the following sub-components; the train nose, coaches and tail as well as the forces acting above and below the stagnation point on the nose.

## ii. Outlet Distance

Shown here is the process followed in order to obtain an adequate outlet distance for the computational domain when a streamlined, nose geometry is made use of. As is typical with these studies, the boundary location is deemed appropriate once the force-components acting on the train body remain relatively insensitive when the location is increased further. In all instances a domain height of 138.49m was used, with a description of the nose given in Table 71 and the various locations of the outlet boundary that were considered given in Table 72. From the results “Outlet Distance 5” was deemed appropriate.

Variables	L	Z <sub>0</sub>	H
Value [m]	7.7	1	3

Table 71: The values of the nose length (L), nose-tip height (Z<sub>0</sub>) and inflection point height (H) of the nose geometry used for the study of an adequate outlet distance.

Simulation Case	Base Case	Outlet Distance 1	Outlet Distance 2	Outlet Distance 3	Outlet Distance 4	Outlet Distance 5	Outlet Distance 6
Domain Height [m]	84.68	184.68	284.68	384.68	484.68	584.68	684.68

Table 72: The various simulation cases that were considered in order to determine an adequate outlet distance and their associated values.

Simulation Case	Outlet Distance [m]	Element Count [Millions]	Drag Force [N]		Side Force [N]		Lift Force [N]	
			x-Force	Deviation [%]	y-Force	Deviation [%]	z-Force	Deviation [%]
Base Case	84.68	5.28	7096	-0.225	54533	0.095	-2246	-14.203
Outlet Distance 1	184.68	5.38	7080	0.254	54585	-0.079	-1927	10.898
Outlet Distance 2	284.68	5.53	7098	-0.056	54542	0.013	-2137	-2.433
Outlet Distance 3	384.68	5.68	7094	0.141	54549	-0.020	-2085	-1.583
Outlet Distance 4	484.68	5.93	7104	0.014	54538	0.040	-2052	-7.943
Outlet Distance 5	584.68	6.1	7105	-0.070	54560	-0.011	-1889	7.041
Outlet Distance 6	684.68	6.2	7100		54554		-2022	

Table 73: The total x-, y- and z-forces obtained from the simulation at various outlet boundary locations. The percentage deviation between subsequent values is also indicated.

Simulation Case	Drag Force [N]					
	Nose	Deviation [%]	Coaches	Deviation [%]	Tail	Deviation [%]
<i>Base Case</i>	1540	0.000	4149	0.048	1407	-1.279
<i>Outlet Distance 1</i>	1540	0.065	4151	-0.024	1389	1.296
<i>Outlet Distance 2</i>	1541	-0.065	4150	0.072	1407	-0.426
<i>Outlet Distance 3</i>	1540	0.000	4153	0.048	1401	0.571
<i>Outlet Distance 4</i>	1540	0.065	4155	-0.024	1409	0.071
<i>Outlet Distance 5</i>	1541	0.000	4154	0.000	1410	-0.355
<i>Outlet Distance 6</i>	1541		4154		1405	

Table 74: The drag force acting on the various sub-components of the train, i.e., the nose, coaches and tail, at various outlet boundary locations. The percentage deviation between subsequent values is also indicated.

Simulation Case	Side Force [N]					
	Nose	Deviation [%]	Coaches	Deviation [%]	Tail	Deviation [%]
<i>Base Case</i>	24760	0.057	9280	-0.129	20493	0.244
<i>Outlet Distance 1</i>	24774	-0.004	9268	-0.076	20543	-0.170
<i>Outlet Distance 2</i>	24773	-0.048	9261	0.076	20508	0.059
<i>Outlet Distance 3</i>	24761	0.004	9268	0.065	20520	-0.088
<i>Outlet Distance 4</i>	24762	0.032	9274	0.086	20502	0.015
<i>Outlet Distance 5</i>	24770	-0.016	9282	-0.032	20505	0.020
<i>Outlet Distance 6</i>	24766		9279		20509	

Table 75: The side force acting on the various sub-components of the train, i.e., the nose, coaches and tail, at various outlet boundary locations. The percentage deviation between subsequent values is also indicated.

Simulation Case	Lift Force [N]					
	Nose	Deviation [%]	Coaches	Deviation [%]	Tail	Deviation [%]
<i>Base Case</i>	-3116	-4.814	1424	2.037	-554	-25.271
<i>Outlet Distance 1</i>	-2966	1.247	1453	-7.020	-414	17.150
<i>Outlet Distance 2</i>	-3003	3.696	1351	5.107	-485	-18.969
<i>Outlet Distance 3</i>	-3114	-0.032	1420	7.535	-393	18.575
<i>Outlet Distance 4</i>	-3113	-3.148	1527	4.912	-466	2.146
<i>Outlet Distance 5</i>	-3015	2.786	1602	-3.246	-476	-0.630
<i>Outlet Distance 6</i>	-3099		1550		-473	

Table 76: The lift force acting on the various sub-components of the train, i.e., the nose, coaches and tail, at various outlet boundary locations. The percentage deviation between subsequent values is also indicated.

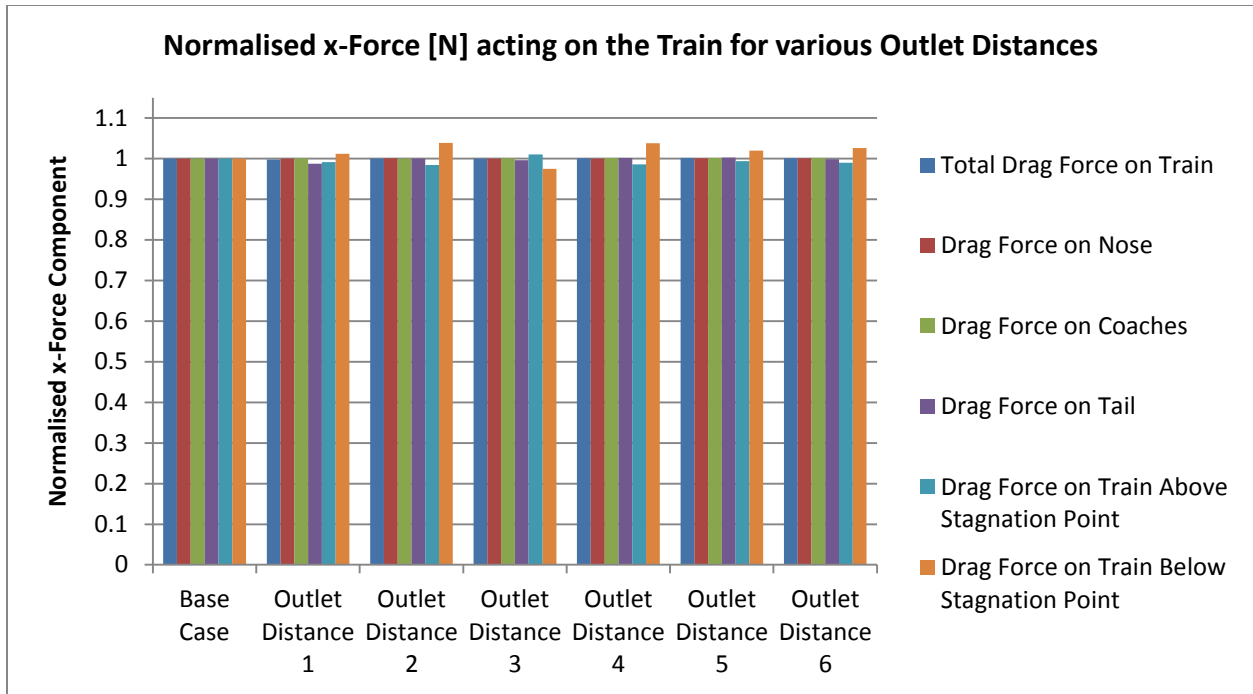


Figure 180: The normalised x-force [N] acting on the train for various domain outlet distances. All forces were normalised by the corresponding value obtained from the base case simulation. The figure shows the forces acting on the train as a whole as well as on the following sub-components; the train nose, coaches and tail as well as the forces acting above and below the stagnation point on the nose.

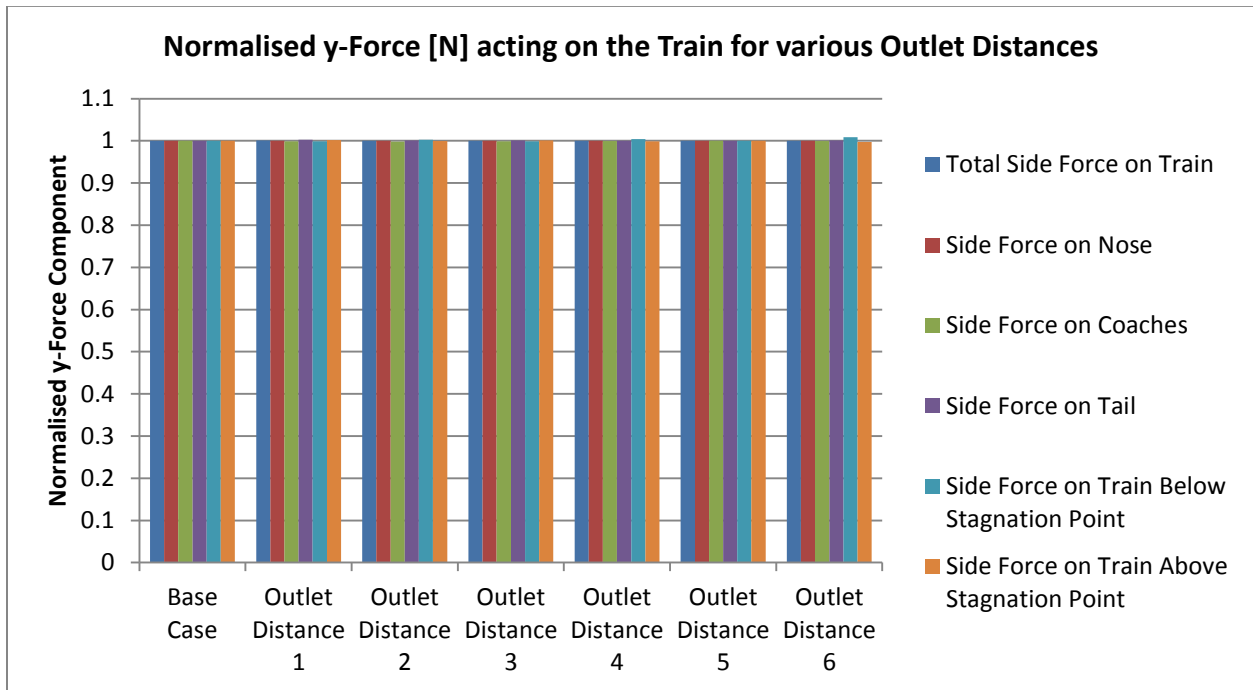


Figure 181: The normalised y-force [N] acting on the train for various domain outlet distances. All forces were normalised by the corresponding value obtained from the base case simulation. The figure shows the forces acting on the train as a whole as well as on the following sub-components; the train nose, coaches and tail as well as the forces acting above and below the stagnation point on the nose.

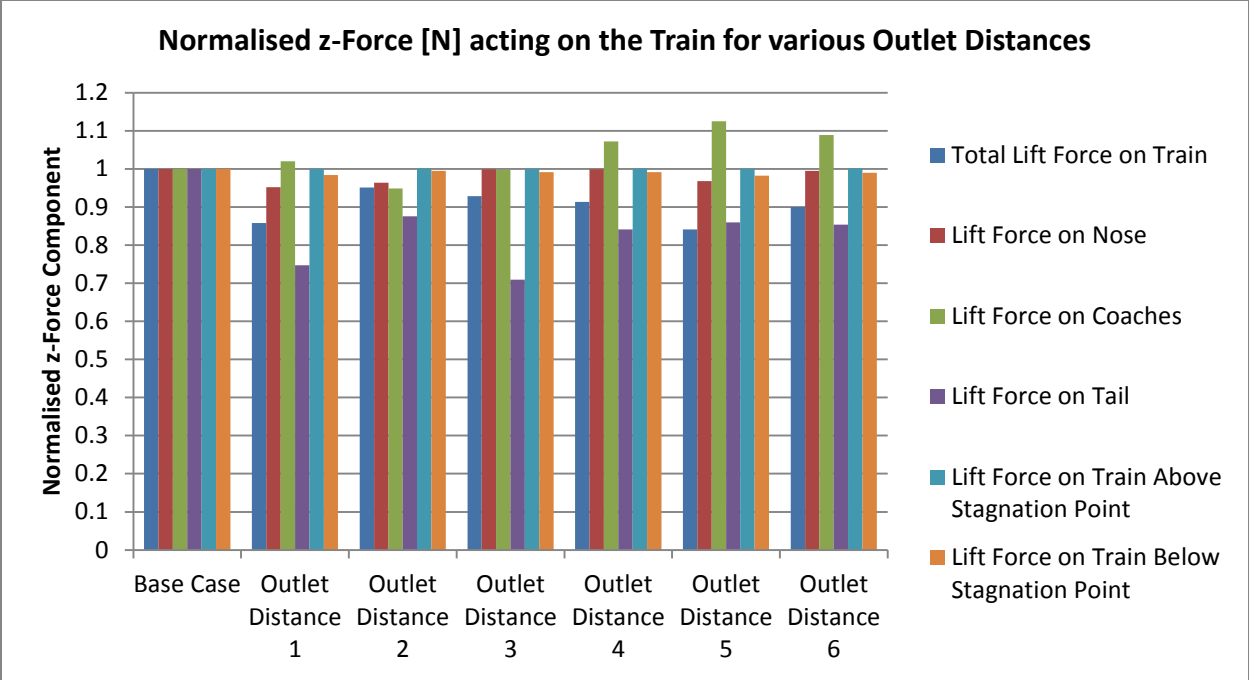


Figure 182: The normalised z-force [N] acting on the train for various domain outlet distances. All forces were normalised by the corresponding value obtained from the base case simulation. The figure shows the forces acting on the train as a whole as well as on the following sub-components; the train nose, coaches and tail as well as the forces acting above and below the stagnation point on the nose.